Transactions of the ASME®



Transactions of the ASME, Journal of Engineering for Gas Turbines and Power (ISSN 0022-0825) is published quarterly (Jan., Apr., July, Oct.) for $125.00 per year by The American Society of Mechanical Engineers, 345 East 47th Street, New York, NY 10017. Second class postage paid at New York, NY and additional mailing offices. POSTMASTER: Send address changes to Transactions of the ASME, Journal of Engineering for Gas Turbines and Power, c/o THE AMERICAN SOCIETY OF MECHANICAL ENGINEERS, 22 Law Drive, Box 2300, Fairfield, NJ 07007-2300.
CHANGES OF ADDRESS must be received at Society headquarters seven weeks before they are to be effective. Please send old label and new address.
PRICES: To members, $36.00, annually; to nonmembers, $125.00.
Add $15.00 for postage to countries outside the United States and Canada.

INDEXED by Applied Mechanics Reviews and Engineering Information, Inc.

# Journal of Engineering for Gas Turbines and Power

Published Quarterly by The American Society of Mechanical Engineers

VOLUME 113 • NUMBER 2 • APRIL 1991

## TECHNICAL PAPERS



(Contents continued on p. 169)

(Contents continued)



ANNOUNCEMENTS

# Integration of a New Process Into an Existing Site: A Case Study in the Application of Pinch Technology[1]

**B. Linnhoff**

**F. J. Alanis**

Department of Chemical Engineering,
Centre for Process Integration,
University of Manchester
Institute of Science and Technology,
Manchester M60 1QD United Kingdom

*New production processes often need to be located in existing sites. Existing sites usually have existing utility systems providing electric power and steam in a limited number of existing mains. A site will have an overall power demand, be nearly balanced, or have a power surplus. Steam consumption, steam generation, power consumption, and power generation of a new process need to be economically assessed against the existing situation on site. Site average and site marginal costs help in this assessment. Changes in overall site production pattern, throughput, energy tariffs, etc., complicate the issue. This paper describes a specific situation. A new Nitric Acid plant is to be located in an existing site. Nitric Acid processes are net energy exporters and contractors tend to offer three basic options: steam export, power export, or a mixed option. The paper discusses how integration of each option affects the balance of the overall site utility system. Boiler feedwater needs to be supplied to the Nitric Acid plant, condensate is returned, the site fuel consumption changes, etc. The true marginal operating cost savings (Nitric Acid processes are energy exporters) are established for each option. The paper then proceeds to consider alternatives. First, it considers whether improvements can be made in the Nitric Acid process and in the existing site utility system separately. Objective targets are set using Pinch Technology and energy cost benefits are improved by 60 percent. Second, the question is posed whether a more fundamental approach would be appropriate. Rather than accepting optimized but separate designs for the Nitric Acid process and the site, could we integrate the Nitric Acid process and the site by allowing individual heat sources and heat sinks in the process to interact with the site utility system individually? This may sound complex and impractical. However, the paper demonstrates how the problem so defined can be tackled using Pinch Technology and how an alternative Nitric Acid process design emerges that is optimized specifically for the site. The design is practical and the energy cost benefits are approximately doubled. The paper is written with two objectives in mind. First, it is hoped to demonstrate the benefits of "site-specific optimization." Second, it is hoped to demonstrate the benefits of Pinch Technology. The problem is totally defined (all data are given) before a solution is attempted. Realistic and clear assumptions are made so that the overall objective is clearly defined in terms of cost. While such black-and-white conditions are not usually given in practice, the benefit is that the reader is free to attempt his or her own solution using either technique or method and compare costs. It is hoped that, in particular, this will stimulate the use of the technique of Exergy Analysis and lead to a constructive dialogue in the literature concerning the relative merits of the techniques of Exergy Analysis and Pinch Technology.*

[1]This paper together with the one directly following (authored by Gaggioli et al.) and the accompanying discussions should be regarded by readers as a whole. The papers explore the relative merits of pinch technology and exergy analysis, and stem from a challenge problem issued by Professor B. Linnhoff at the Advanced Energy Systems Division Symposium of the ASME Winter Annual Meeting, Boston, Massachusetts, December 13–18, 1987. Note contributed by M. J. Moran, Associate Editor.

Contributed by the Advanced Energy Systems Division for publication in the JOURNAL OF ENGINEERING FOR GAS TURBINES AND POWER. Manuscript received by the Advanced Energy Systems Division April 26, 1989; revision received April 6, 1990.

## Background

Figure 1 shows the outline of an existing industrial site. The overall plant energy requirements are supplied by a combined heat and power steam system and external power. Table 1 and Fig. 2 show details of the present use of steam in the existing processes.

A dual pressure Nitric Acid process [1] (Fig. 3 and Tables 2 and 3) is to be built on the site. The contractor offers three basic options:

1 Power import, i.e., maximum steam export (Fig. 4*a*)
2 Power balance, i.e., reduced steam export (Fig. 4*b*)
3 Power export, i.e., no steam export (Fig. 4*c*)

The effect of integrating option (2) into the site is shown in Fig. 5 as an example. The site provides Boiler Feedwater to the Nitric Acid process and accepts back the steam raised and condensate return. Many flows in the existing steam system change as a result. The basis of calculating these changes is given in Appendix I.

A cost summary of the effect of any of the three options, if integrated fully into the existing site, is shown in Fig. 6 for a range of "power-to-fuel" cost ratios. The first feature to be noted is that the power import, power balance, and power export option all intersect at a common point. This should not be a surprise. After all, the power balance option is just a mixture of the other two. At the relevant power/fuel cost ratio there is no economic preference for generating power on site over importing power from the grid. As a corollary, the mixed option is economically comparable. It also follows that the mixed option can never be economically preferable. It may only be preferred for its relative insensitivity to possible fluctuations in energy costs. Without regard to sensitivity, the power import option is best for cheap power and the power export option is best for expensive power.

## Single Process Optimization

The costs in Fig. 6 are based on designs for the Nitric Acid process as per the contractor's base cases. The question is: How much improvement is possible? Usually, we expect some improvements to be possible and the conventional approach would be to perform energy integration studies both for the

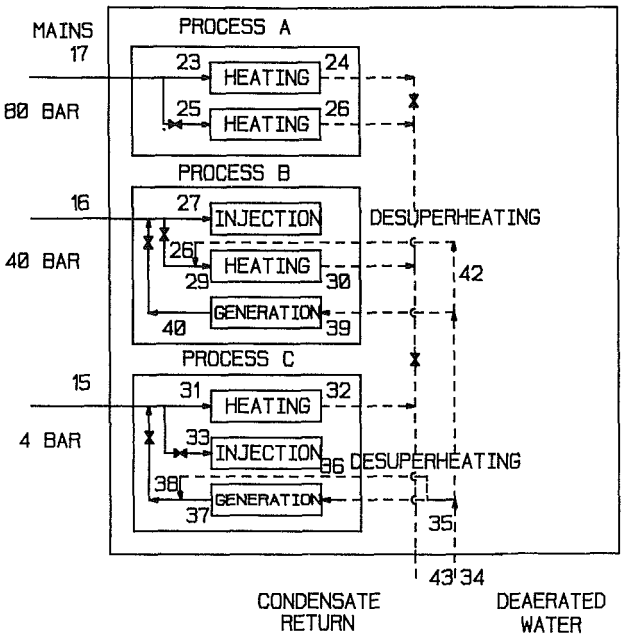


Fig. 2 Site steam distribution

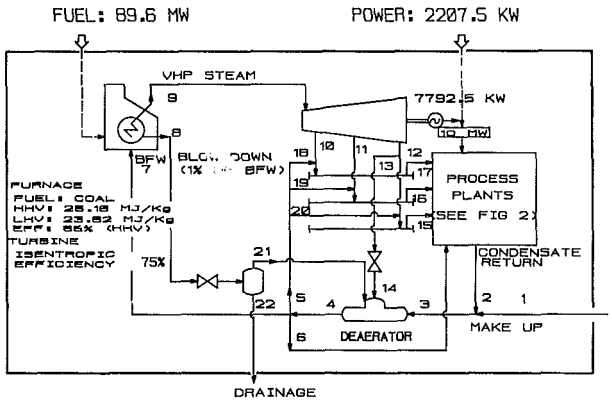


Fig. 1 Existing industrial site

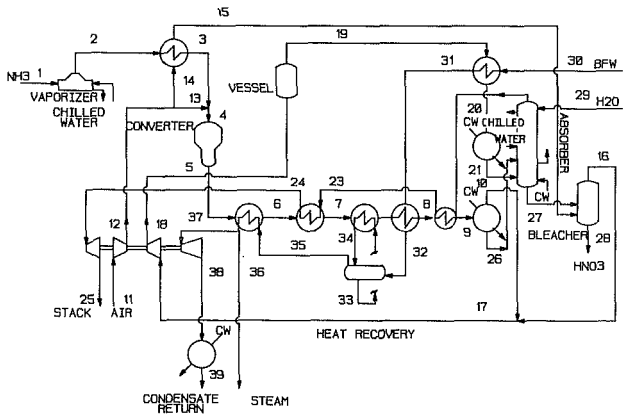


Fig. 3 Dual pressure Nitric Acid process to be built into existing site

Table 1 Heat and mass balance for steam system (Figs. 1 and 2)

| Flow | T, °C | P, bar | H, kJ/kg | m, t/hr | Flow | T, °C | P, bar | H, kJ/kg | m, t/hr |
|---|---|---|---|---|---|---|---|---|---|
| 1 | 20 | ambient | −20.9 | 39.41 | 23 | 295 | 80 | 2653.2 | 14.4 |
| 2 | 80 | 1 | 227.7 | 90.72 | 24 | 80 | 80 | 227.7 | 14.4 |
| 3 | 62 | 1 | 152.4 | 130.13 | 25 | 258.8 | 46 | 2653.2 | 18.0 |
| 4 | 100 | 1 | 312.2 | 138.86 | 26 | 80 | 46 | 227.7 | 18.0 |
| 5 | 100 | 1 | " | 11.99 | 27 | 250.3 | 40 | 2696.2 | 21.6 |
| 6 | 100 | 1 | " | 32.40 | 28 | 250.3 | 8 | " | 25.2 |
| 7 | 100 | 100 | " | 94.476 | 29 | 170.4 | 8 | 2664.2 | 25.543 |
| 8 | 311 | 100 | 1303.2 | 0.94 | 30 | 80 | 8 | 227.7 | 25.543 |
| 9 | 500 | 100 | 3268.2 | 93.53 | 31 | 143.6 | 4 | 2634.2 | 32.777 |
| 10 | 473 | 80 | 3224.2 | 26.05 | 32 | 80 | 4 | 227.7 | 32.777 |
| 11 | 370 | 40 | 3068.9 | 31.14 | 33 | 140 | 3 | 2634.2 | 17.28 |
| 12 | 150 | 4 | 2698.6 | 28.02 | 34 | 100 | 1 | 312.2 | 32.4 |
| 13 | 150 | 4 | " | 8.32 | 35 | 100 | 15 | " | 20.783 |
| 14 | 164 | 1 | " | 8.32 | 36 | 100 | 4 | " | 0.474 |
| 15 | 143.6 | 4 | 2634.2 | 28.8 | 37 | 198.3 | 15 | 2687.2 | 20.783 |
| 16 | 250.3 | 40 | 2696.2 | 36.0 | 38 | 143.6 | 4 | 2634.2 | 21.257 |
| 17 | 295 | 80 | 2653.2 | 32.4 | 39 | 100 | 50 | 312.2 | 10.8 |
| 18 | 100 | 80 | 312.2 | 6.35 | 40 | 266 | 50 | 2692.2 | 10.8 |
| 19 | 100 | 40 | " | 4.86 | 41 | 250.3 | 40 | " | 10.8 |
| 20 | 100 | 4 | " | 0.78 | 42 | 100 | 8 | 312.2 | 0.343 |
| 21 | 100 | 1 | 2570.2 | 0.417 | 43 | 80 | 1 | 227.7 | 90.72 |
| 22 | 100 | 1 | 312.2 | 0.529 | | | | | |

**Table 2 Heat and mass balance for the dual pressure Nitric Acid process**

| Flow | $T$, °C | $P$, bar | $m$ (kg/hr) $N_2$ | $O_2$ | $H_2O$ | $NH_3$ | NO | $NO_2$ | $H(T, P)$, kW |
|---|---|---|---|---|---|---|---|---|---|
| 1 | 7 | 5.5 | - | - | - | 10679.8 | - | - | −3947.7 |
| 2 | 7 | 5.5 | - | - | - | 〃 | - | | −174.0 |
| 3 | 76 | 5.5 | - | - | - | 〃 | - | - | 279.6 |
| 4 | 170 | 3.5 | 126152.7 | 38311.2 | - | 〃 | - | - | 7657.6 |
| 5 | 840 | 3.3 | 126504.0 | 13627.8 | 16946.4 | - | 18064.4 | - | 47259.7 |
| 6 | 753 | 3.3 | 〃 | 〃 | 〃 | - | 〃 | - | 42088.8 |
| 7 | 578 | 3.3 | 〃 | 〃 | 〃 | - | 〃 | - | 31587.8 |
| 8 | 325 | 3.3 | 〃 | 〃 | 〃 | - | 〃 | - | 16466.1 |
| 9 | 135 | 3.16 | 〃 | 11412.3 | 〃 | - | 13909.6 | 6370.4 | 5842.8 |
| 10 | 50 | 3.16 | 〃 | 3995.3 | 931.0 | - | 1538.6 | 20616.1 | 1030.0 |
| 11 | 20 | 1.0 | 141519.0 | 42993.0 | - | - | - | - | −278.0 |
| 12 | 184 | 3.5 | 〃 | 〃 | - | - | - | - | 8272.0 |
| 13 | 184 | 3.5 | 126152.7 | 38311.2 | - | - | - | - | 7378.0 |
| 14 | 184 | 3.5 | 15366.3 | 4681.8 | - | - | - | - | 894.0 |
| 15 | 104 | 3.5 | 〃 | 〃 | - | - | - | - | 440.4 |
| 16 | 67 | 3.0 | 〃 | 〃 | - | - | - | - | 233.6 |
| 17 | 52 | 3.0 | 141870.3 | 8677.1 | 931.0 | - | 1538.6 | 20616.1 | 1267.8 |
| 18 | 225 | 10.2 | 〃 | 8172.8 | 〃 | - | 592.9 | 22066.0 | 9823.0 |
| 19 | 225 | 10.2 | 〃 | 〃 | 〃 | - | 〃 | 〃 | 9823.0 |
| 20 | 159 | 10.2 | 〃 | 〃 | 〃 | - | 〃 | 〃 | 6544.1 |
| 21 | 43 | 10.2 | 〃 | 〃 | 〃 | - | 〃 | 〃 | 713.7 |
| 22 | 18 | 8.9 | 〃 | 3877.0 | 383.0 | - | 15.0 | 23.0 | −491.9 |
| 23 | 297 | 8.9 | 〃 | 〃 | 〃 | - | 〃 | 〃 | 11766.6 |
| 24 | 536 | 8.9 | 〃 | 〃 | 〃 | - | 〃 | 〃 | 22267.7 |
| 25 | 243 | 1.0 | 〃 | 〃 | 〃 | - | 〃 | 〃 | 9232.7 |

| Flow | $T$, °C | $P$, bar | $m$ (kg/hr) $H_2O$ | $HNO_3$ | $H(T, P)$, kW |
|---|---|---|---|---|---|
| 26 | 50 | 3.16 | 15078.0 | 6462.0 | 457.1 |
| 27 | 41 | 3.0 | 36013.4 | 37065.0 | 907.1 |
| 28 | 45 | 3.0 | 〃 | 〃 | 1114.0 |

| | | | $m$ (kg/hr) $H_2O_l$ | $H_2O_q$ | | |
|---|---|---|---|---|---|---|
| 29 | 20 | 10.0 | 24678.4 | - | | −143.3 |
| 30 | 100 | 100.0 | 28727.15 | - | | 2508.0 |
| 31 | 195 | 100.0 | 〃 | - | | 5786.9 |
| 32 | 311 | 100.0 | 〃 | - | | 10399.2 |
| 33 | 311 | 100.0 | 〃 | - | | 10399.2 |
| 34 | 311 | 100.0 | - | 28727.15 | | 20908.6 |
| 35 | 311 | 100.0 | - | 〃 | | 20908.6 |
| 36 | 500 | 100.0 | - | 14186.5 | | 12878.9 |
| 37 | 500 | 100.0 | - | 14540.6 | | 13200.5 |
| 38 | 50 | 0.12 | 1380.0 | 13160.6 | | 9130.5 |
| 39 | 50 | 0.12 | 14540.6 | | | 422.1 |

- Enthalpy figures based on a reference state of 25°C.
- Heats of reaction and/or nonideal mixing are shown by means of boxed figures inside the symbols for the relevant unit operations.

Nitric Acid process design and for the site energy system in order to determine whether there are potential profit improvements. In Pinch Technology terms this is equivalent to reducing the energy consumption of each production system to its "target." The results of such conventional targeting analyses are shown in Figs. 7 and 8 for the Nitric Acid plant and the site system, respectively. The Nitric Acid plant analysis shows that there is a capacity to generate 12 percent more steam at very high pressure (VHP) level and 7.2 ton/hr of steam at low pressure (LP) level. The site system is shown to have opportunity for improvement too. By slightly shifting the pressures of the existing mains at LP and medium pressure (MP) levels, a mismatch between levels and loads can be corrected, allowing more shaft work to be generated from the same total amount of steam.

The net savings with this combination of projects amount to £2.8 million/yr. This represents 60 percent of additional savings over and above the energy cost benefits to be obtained from the Nitric Acid process as per the contractor's base case design.

## Problem

The contention of the present paper is that the optimization carried out so far is by no means all we can do. The plant operating company should evaluate the potential improvements to be obtained by "site-specific optimization." In other words, it should evaluate whether the design of the Nitric Acid process could be changed to take advantage of interaction opportunities between specific heat sources and sinks in the Nitric Acid process and the rest of the site. This idea is expressed pictorially in Fig. 9. In Fig. 9(*a*) the constraints applied in conventional optimization are highlighted. Essentially, we have an optimized, but "separate" process raising a certain amount of steam at high level. In Fig. 9(*b*) we allow for the possibility to undo some of the design inside the Nitric Acid process. Why not allow the process to interact with all three existing site steam mains for both steam generation and consumption? This we call site-specific optimization.

## Site-Specific Optimization by Pinch Technology

It is not the intention of the present paper to provide a Pinch Technology tutorial. Rather the aim is to demonstrate the benefits to be obtained from site-specific optimization and the fact that Pinch Technology is a suitable tool for this task. An outline discussion in terms of Pinch Technology of the solution sequence in Figs. 10–14 is given in Appendix II. A more detailed discussion would be inappropriate as the solution steps in question are well documented elsewhere [2]. Readers with a reasonable knowledge of Pinch Technology will find the Appendix superfluous and will be able to follow Figs. 10–14 from the captions alone. Figure 14 represents the solution obtained at the so-called targeting stage [2]. Figure 15 shows the savings so calculated over the relevant range of power-to-fuel cost ratio. It is apparent that the economics predicted are a sig-

**Table 3 Summary of compression and recovery power in the dual pressure Nitric Acid process**

| | |
|---|---|
| Low-pressure unit | |
| Inlet gas | Air |
| Flow (kg/hr) | 184512.0 |
| Suction temperature (°C) | 20 |
| Suction pressure (bar) | 1.0 |
| Discharge temperature (°C) | 184 |
| Discharge pressure (bar) | 3.5 |
| Shaft power (kW) | 8550 |
| Polytropic efficiency (percent) | 80 |
| High-pressure unit | |
| Inlet gas | Nitrous gas |
| Flow (kg/hr) | 173633.1 |
| Suction temperature (°C) | 52 |
| Suction pressure (bar) | 3.0 |
| Discharge temperature (°C) | 224.5 |
| Discharge pressure (bar) | 10.25 |
| Shaft power (kW) | 8555 |
| Polytropic efficiency (percent) | 79.0 |
| Recovery turbine | |
| Inlet gas | Tail gas |
| Flow (kg/hr) | 173633 |
| Inlet temperature (°C) | 536 |
| Inlet pressure (bar) | 8.9 |
| Discharge temperature (°C) | 243 |
| Discharge pressure (bar) | 1.0 |
| Shaft power (kW) | 13035 |
| Isentropic efficiency (percent) | 81.0 |
| Steam turbine | |
| Flow (kg/hr) | 14540.67 |
| Inlet temperature (°C) | 500 |
| Inlet pressure (bar) | 100 |
| Condenser temperature (°C) | 50 |
| Condenser pressure (bar) | 0.1233 |
| Shaft power (kW) | 4070 |
| Isentropic efficiency (percent) | 80.0 |

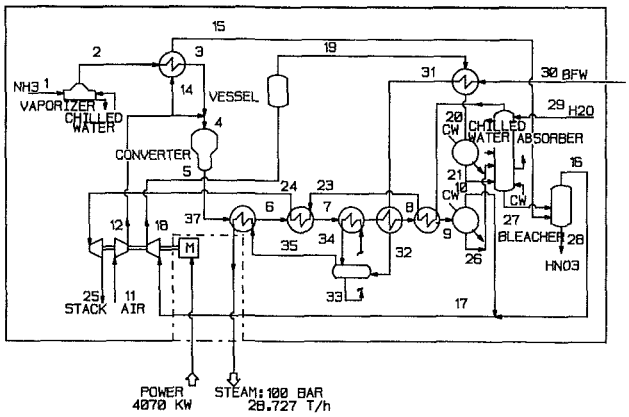


**Fig. 4(*a*) Option 1: power import, total steam export**

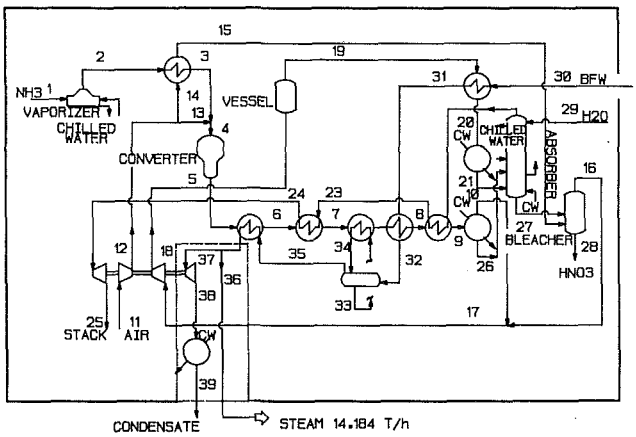


**Fig. 4(*b*) Option 2: power balance, reduced steam export**

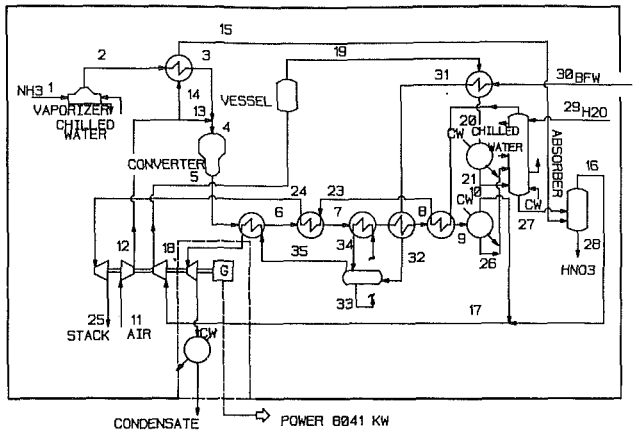


**Fig. 4(*c*) Option 3: power export, no steam export**

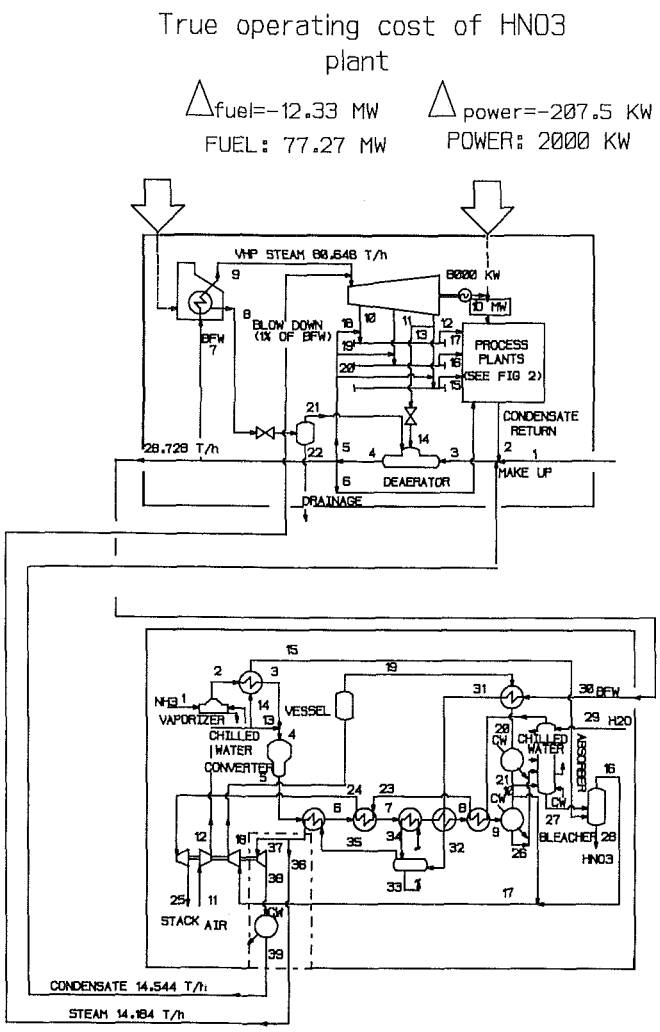


**Fig. 5 Integration of the power balance option (option 2)**

nificant improvement over the conventional optimization approach, with an almost uniform saving of $0.63 million/yr over the entire range of power-to-fuel cost ratios to be considered. This represents approximately 40 percent additional savings over conventional optimization. The "kink" in the profile results from the addition of a condensing steam turbine stage in the central power generating system, which becomes profitable above a certain power-to-fuel cost ratio.

Figure 16 and Tables 4 and 5 show the completed design [6]

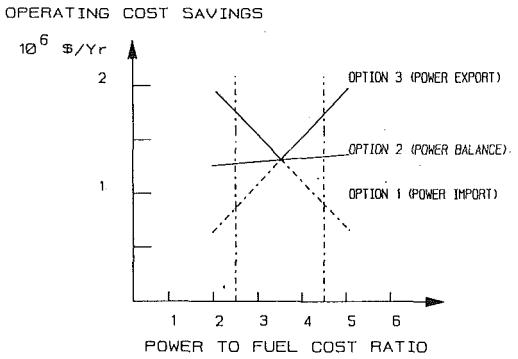


**Fig. 6 Utility cost savings for each of the contractor's options (fuel = $100/kW-yr)**

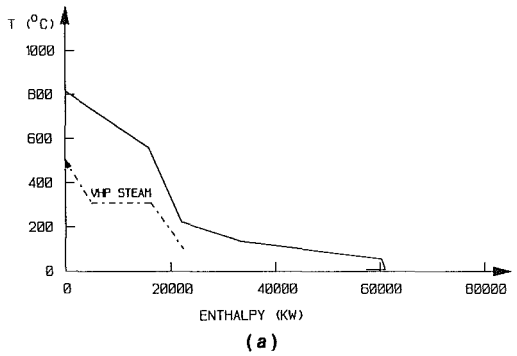


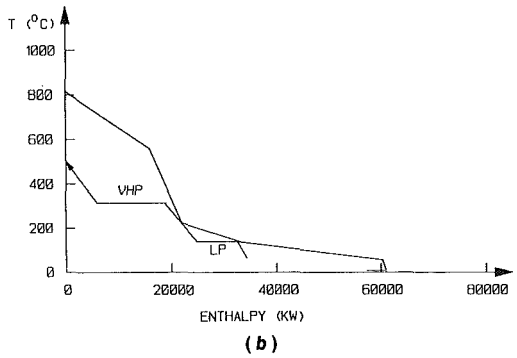


**Fig. 7 Nitric Acid process: (*a*) existing steam generation against the grand composite curve; (*b*) improved steam generation matching to process.**

(for the case without additional condensing stage). It achieves the savings predicted in Fig. 15 and it appears simpler than any of the contractor's options. *The site-specific design is simpler, but not more complicated.* The design takes advantage of site-specific opportunities throughout. The key features are:

1 Small pressure shifts in two of the existing site mains: 40 bar to 46 bar, and 4 bar to 8 bar.

2 Some preheating of central boiler combustion air in the Nitric Acid process.

3 No separate steam based power train in the Nitric Acid process; instead, electricity is imported for the helper motor.

4 Steam generation at VHP level only.

The first feature should be uncontroversial. Overall changes in steam flow rates are such that the mains and the steam turbine stages can be assumed to be able to cope with volumetric steam flows at the new pressures (less than 30 percent). The second feature, i.e., air preheat for the central boiler to be picked up from the Nitric Acid process, may not be acceptable in a given practical situation. Such a constraint is

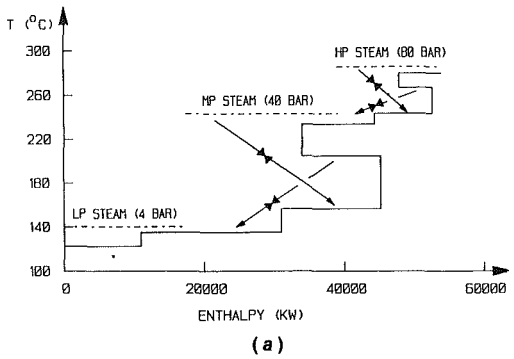


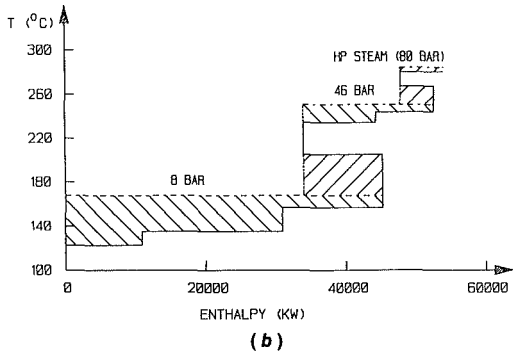


**Fig. 8 Existing site: (*a*) grand composite curve of site as is. Superimposed (broken line) are the actual steam levels and loads as supplied; (*b*) improved utility matching to process on site**

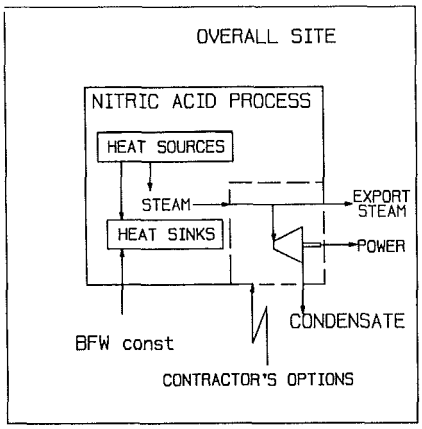


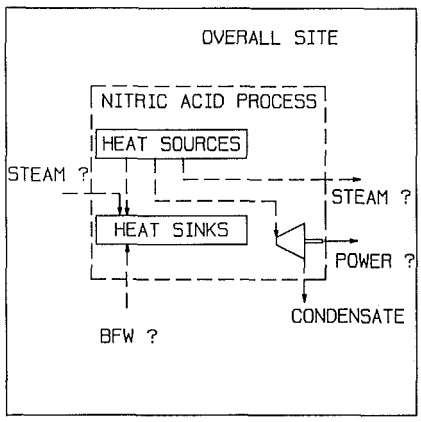


**Fig. 9 Overall site interactions: (*a*) as proposed by the contractor; (*b*) aim: total integration; all utilities options depend upon total site characteristics**

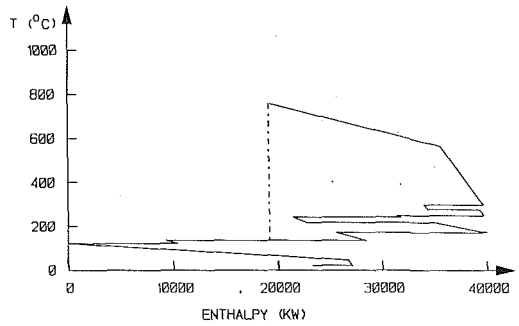


Fig. 10 Overall grand composite curve for site plus Nitric Acid process

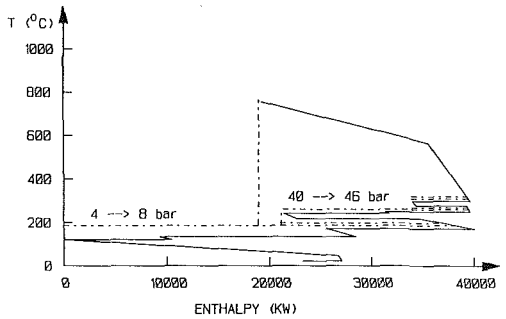


Fig. 11 Introducing steam at the most suitable pressure levels for the overall system

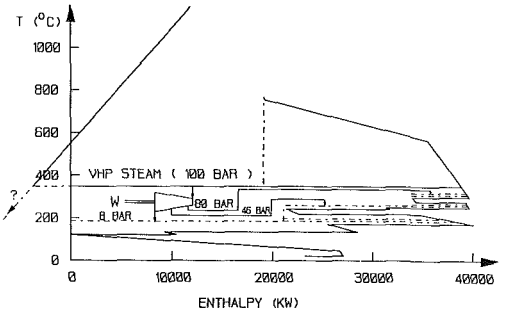


Fig. 12 Introducing a steam turbine cycle to exploit available driving force and to be compatible with existing steam system

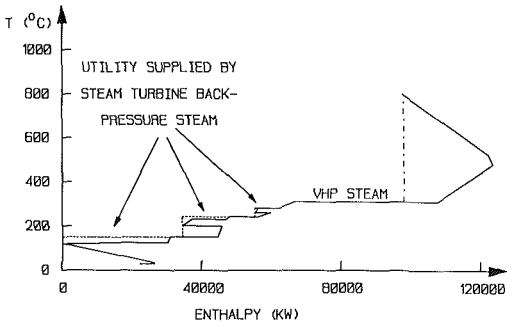


Fig. 13 Steam turbine system/rest of the site interactions (including BFW preheat, 100 bar steam generation, and superheat)

easily allowed for in Pinch Technology [15]: Fig. 17 is the equivalent of Fig. 14 for targeting without process-recovered air preheat [14]. Figure 18 shows the cost disadvantges from the constraint so imposed. The choice is the designer's. The third feature is unquestionably practical and implies significant capital cost savings. The fourth feature highlights the difference between process optimization on a separate basis and site-specific optimization. Whereas the former approach indicates that steam should be generated at LP level as well as VHP level (see Fig. 7*b*), site-specific optimization indicates that it is BFW preheat, and VHP steam generation, that are most profitable.

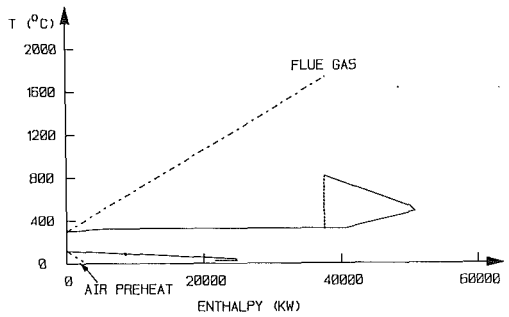


Fig. 14 Energy targets for total integration: overall site, steam cycle, flue gas, and combustion air preheat

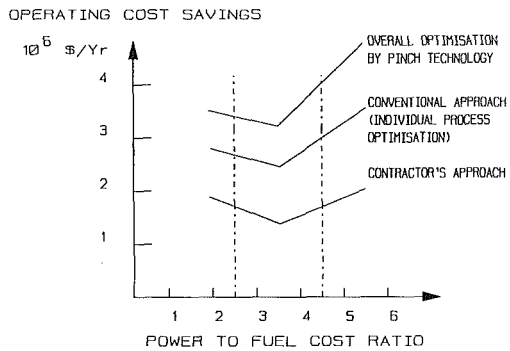


Fig. 15 Economic comparison: overall optimization by Pinch Technology against the conventional approach and the contractor's approach

## Concluding Remarks

The example is fully documented with all data given as necessary to establish energy costs for any solution. Conventional optimization (i.e., process and site system separately) resulted in 60 percent energy cost savings over the base case design. Site-specific optimization resulted in approximately 40 percent additional savings.

It is hoped that the inherent simplicity of the final design will persuade the reader that site-specific optimization does not need to stand for complexity. On the contrary, it may help simplify the interface between process and site by taking advantage of hidden opportunities on both sides of that interface.

The reader may accept this but still be concerned that the designer's job is made more complex. This is not so. The detailed reasoning behind Figs. 10–14 is straightforward once a working expertise in Pinch Technology has been obtained. The approach cuts through an apparently complex problem with ease, so much so that different operating cases, capital costs, plant layout constraints, opportunities in process chemistry and scheduling, data uncertainty, economic uncertainty, etc., are all taken care of adequately in practice.

## Acknowledgments

The authors express their sincere thanks to Mr. B. L. Pretty of Linnhoff March, Inc. for his comments and help in the execution of the project and the preparation of the manuscript.

**Table 4 Heat and mass balance for the Nitric Acid process in Fig. 16**

| Flow | $T$, °C | $P$, bar | $m$ (kg/hr) $N_2$ | $O_2$ | $H_2O$ | $NH_3$ | NO | $NO_2$ | $H$ ($T$, $P$), kW |
|---|---|---|---|---|---|---|---|---|---|
| 1 | 7 | 5.5 | - | - | - | 10679.8 | - | - | −3947.7 |
| 2 | 7 | 5.5 | - | - | - | 〃 | - | - | −174.0 |
| 2.*a* | 49 | 5.5 | - | - | - | 〃 | - | - | 102.0 |
| 3 | 76 | 5.5 | - | - | - | 〃 | - | - | 279.6 |
| 4 | 170 | 3.5 | 125152.7 | 38311.2 | - | 〃 | - | - | 7657.6 |
| 5 | 840 | 3.3 | 126504.0 | 13627.8 | 16946.4 | - | 18064.4 | - | 47259.7 |
| 6 | 604 | 3.3 | 〃 | 〃 | 〃 | - | 〃 | - | 33114.5 |
| 7 | 224.5 | 3.3 | 〃 | 〃 | 〃 | - | 〃 | - | 9982.0 |
| 7.*a* | 224.5 | 3.3 | 40352.5 | 4347.0 | 5405.6 | - | 5762.2 | - | 3184.1 |
| 7.*b* | 224.5 | 3.3 | 86151.5 | 9280.8 | 11540.8 | - | 12302.2 | - | 6797.9 |
| 8 | 135 | 3.16 | 126504.0 | 11412.3 | 16946.4 | - | 13909.6 | 6370.4 | 5842.8 |
| 9 | 132 | 3.16 | 〃 | 〃 | 〃 | - | 〃 | 〃 | 4988.7 |
| 10 | 50 | 3.16 | 〃 | 3995.3 | 931.0 | - | 1538.6 | 20616.1 | 1030.0 |
| 11 | 20 | 1.0 | 141519.0 | 42993.0 | - | - | - | - | −278.0 |
| 12 | 184 | 3.5 | 〃 | 〃 | - | - | - | - | 8272.0 |
| 13 | 184 | 3.5 | 126152.7 | 38311.2 | - | - | - | - | 7378.0 |
| 14 | 184 | 3.5 | 15366.3 | 4681.8 | - | - | - | - | 894.0 |
| 14*a* | 135 | 3.5 | 〃 | 〃 | - | - | - | - | 618.0 |
| 15 | 103.5 | 3.5 | 〃 | 〃 | - | - | - | - | 440.4 |
| 16 | 67 | 3.0 | 〃 | 〃 | - | - | - | - | 233.6 |
| 17 | 52 | 3.0 | 141870.3 | 8677.1 | 931.0 | - | 1538.6 | 20616.1 | 1267.8 |
| 18 | 225 | 10.2 | 〃 | 8172.8 | 〃 | - | 592.9 | 22066.0 | 9823.0 |
| 19 | 225 | 10.2 | 〃 | 〃 | 〃 | - | 〃 | 〃 | 〃 |
| 19*a* | 135 | 10.2 | 〃 | 〃 | 〃 | - | 〃 | 〃 | 5331.1 |
| 19*b* | 57 | 10.2 | 〃 | 〃 | 〃 | - | 〃 | 〃 | 1420.6 |
| 20 | 52 | 10.2 | 〃 | 〃 | 〃 | - | 〃 | 〃 | 1144.6 |
| 21 | 43 | 10.2 | 〃 | 〃 | 〃 | - | 〃 | 〃 | 713.7 |
| 22 | 18 | 8.9 | 〃 | 3877.0 | 383.0 | - | 15.0 | 23.0 | −491.9 |
| 23 | 107 | 8.9 | 〃 | 〃 | 〃 | - | 〃 | 〃 | 3418.5 |
| 23*a* | 196.5 | 8.9 | 〃 | 〃 | 〃 | - | 〃 | 〃 | 7350.9 |
| 23*b* | 214 | 8.9 | 〃 | 〃 | 〃 | - | 〃 | 〃 | 8119.8 |
| 24 | 536 | 8.9 | 〃 | 〃 | 〃 | - | 〃 | 〃 | 22267.7 |
| 25 | 243 | 1.0 | 〃 | 〃 | 〃 | - | 〃 | 〃 | 9232.7 |
| 25*a* | 225 | 1.0 | 〃 | 〃 | 〃 | - | 〃 | 〃 | 8461.0 |
| 25*b* | 184 | 1.0 | 〃 | 〃 | 〃 | - | 〃 | 〃 | 6734.4 |
| 25*c* | 137 | 1.0 | 〃 | 〃 | 〃 | - | 〃 | 〃 | 4730.6 |
| 25*d* | 83 | 1.0 | 〃 | 〃 | 〃 | - | 〃 | 〃 | 2428.4 |

| Flow | $T$, °C | $P$, bar | $m$ (kg/hr) $H_2O$ | $HNO_3$ | $H$ ($T$, $P$), kW |
|---|---|---|---|---|---|
| 26 | 50 | 3.1 | 15078.0 | 6462.0 | 457.1 |
| 27 | 41 | 3.0 | 36013.4 | 37865.0 | 907.1 |
| 28 | 45 | 3.0 | 〃 | 〃 | 1114.0 |
| 29 | 20 | 10.0 | 24678.4 | - | −143.3 |
| | | | $m$ (kg/hr) $H_2O_1$ | $H_2O_q$ | |
| 30 | 100 | 100.0 | 96087.74 | - | 8332.8 |
| 31 | 107 | 100.0 | 〃 | - | 9186.9 |
| 32 | 107 | 100.0 | 62938.81 | - | 6017.6 |
| 33 | 107 | 100.0 | 33147.93 | - | 3169.3 |
| 34 | 156 | 100.0 | 〃 | - | 5148.9 |
| 35 | 156 | 100.0 | 2102.02 | - | 326.5 |
| 36 | 156 | 100.0 | 35668.4 | - | 5540.5 |
| 37 | 196.5 | 100.0 | 〃 | - | 7284.3 |
| 38 | 107 | 100.0 | 58316.31 | - | 5575.7 |
| 39 | 107 | 100.0 | 4622.5 | - | 441.96 |
| 40 | 156 | 100.0 | 〃 | - | 718.03 |
| 41 | 107 | 100.0 | 16958.7 | - | 1621.4 |
| 42 | 107 | 100.0 | 41358.6 | - | 3954.2 |
| 43 | 196.5 | 100.0 | 〃 | - | 8446.1 |
| 44 | 196.5 | 100.0 | 16958.7 | - | 3463.3 |
| 45 | 196.5 | 100.0 | 52627.1 | - | 10747.6 |
| 46 | 196.5 | 100.0 | 32877.8 | | 6714.2 |
| 47 | 500 | 100.0 | - | 32877.8 | 29846.6 |
| 48 | 196.5 | 100.0 | 61107.9 | - | 12479.6 |

| | | | (kg/hr) Combustion air | | |
|---|---|---|---|---|---|
| 49 | 25 | - | 100569 | | 0.0 |
| 50 | 107 | - | 〃 | | 2302.2 |
| 51 | 168 | - | 〃 | | 4043.4 |

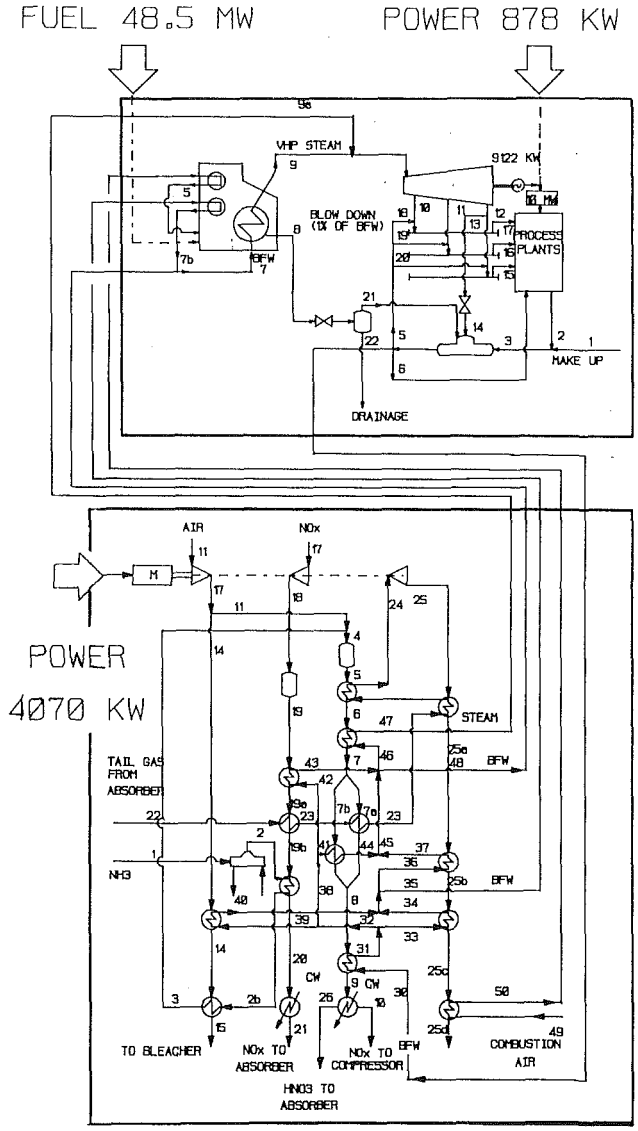


**Fig. 16 Flowsheet for the targeted case in Fig. 14 (see Tables 4 and 5). Stream splits result from applying the Pinch Design Method [6] for maximum energy recovery.**

Also, we are grateful to the member companies of the UMIST Consortium for Process Integration for financial support, case study data, and technical feedback.

## References

1 Hanvin, R. L., Leroy, D. G., and Roudier, L. R., "Single-Pressure or Dual-Pressure Nitric Acid Process," *Proceedings of the British Sulphur Corporations Third International Conference on Fertilizers*, London, Nov. 12–14, 1979.

2 Linnhoff, B., Townsend, D. W., Boland, D., Hewitt, G. F., Thomas, B. E. A., Guy, A. R., and Marsland, R. H., "User Guide on PROCESS INTEGRATION for the Efficient Use of Energy," IChemE, Rugby, United Kingdom, 1982.

3 Linnhoff, B., and Turner, J. A., "Heat-Recovery Networks: New Insights Yield Big Savings," *Chemical Engineering*, Nov. 2, 1981, pp. 56–70.

4 Linnhoff, B., and Vredeveld, D. R., "Pinch Technology Has Come of Age," *Chem. Eng. Prog.*, July 1984, pp. 33–40.

5 Tjoe, T. N., and Linnhoff, B., "Using Pinch Technology for Process Retrofit," *Chemical Engineering*, Apr. 28, 1986, pp. 47–60.

6 Linnhoff, B., and Hindmarsh, E., "The Pinch Design Method for Heat Exchanger Networks," *Chemical Engineering Science*, Vol. 38, No. 5, 1983, pp. 745–763.

7 Linnhoff, B., "Pinch Technology for the Synthesis of Optimal Heat and Power Systems," ASME *Journal of Energy Resources Technology*, Vol. 111, No. 3, 1989, pp. 137–147.

8 Linnhoff, B., and Ahmad, S., "Supertargeting: Optimal Synthesis of Energy Management Systems," ASME *Journal of Energy Resources Technology*, Vol. 111, No. 3, 1989, pp. 121–130.

9 Ahmad, S., and Linnhoff, B., "Supertargeting: Different Process Structures for Different Economics," ASME *Journal of Energy Resources Technology*, Vol. 111, No. 3, 1989, pp. 131–136.

10 Townsend, D. W., and Linnhoff, B., "Heat and Power Networks in Process Design, Part 1: Criteria for Placement of Heat Engines and Heat Pumps in Process Networks," *AIChE Journal*, Vol. 29, 1983, pp. 742–748.

11 Townsend, D. W., and Linnhoff, B., "Heat and Power Networks in Process Design, Part 2: Design Procedure for Equipment Selection and Process Matching," *AIChE Journal*, Vol. 29, No. 5, 1983, pp. 748–771.

12 Linnhoff, B., and Polley, G. T., "Total Process Design Through Pinch

**Table 5 Heat and mass balance for the steam system in Fig. 16**

| Flow | $T$, °C | $P$, bar | $H$, kJ/kg | $m$, kg/h |
|---|---|---|---|---|
| 1 | 20 | Ambient | −20.9 | 39418.1 |
| 2 | 80 | 1 | 227.7 | 90435.14 |
| 3 | 62 | 1 | 152.23 | 129853.24 |
| 4 | 100 | 1 | 312.2 | 138263.64 |
| 5 | 100 | 1 | 312.2 | 9752.41 |
| 6 | 100 | 1 | 312.2 | 32424.49 |
| 7 | 196.5 | 100 | 735.2 | 63209.93 |
| 7*a* | 100 | 100 | 312.2 | 96086.74 |
| 7*b* | 196.5 | 100 | 735.2 | 2102.02 |
| 8 | 311 | 100 | 1303.2 | 960.86 |
| 9 | 500 | 100 | 3268.2 | 62449.07 |
| 9*a* | 500 | 100 | 3268.2 | 32876.8 |
| 10 | 473 | 80 | 3224.2 | 11577.6 |
| 11 | 391 | 46 | 3094.7 | 24391.86 |
| 12 | 227 | 8 | 2793.2 | 51168.78 |
| 13 | 227 | 8 | 2793.2 | 7987.62 |
| 14 | 211 | 1 | 2793.2 | 7987.62 |
| 15 | 170.4 | 8 | 2664.2 | 53975.51 |
| 16 | 258.8 | 46 | 2692.2 | 28515.15 |
| 17 | 295 | 80 | 2653.3 | 14400.00 |
| 18 | 100 | 80 | 312.2 | 2822.4 |
| 19 | 100 | 46 | 312.2 | 4123.3 |
| 20 | 100 | 8 | 312.2 | 2806.72 |
| 21 | 100 | 1 | 2570.2 | 422.78 |
| 22 | 100 | 1 | 312.2 | 538.08 |

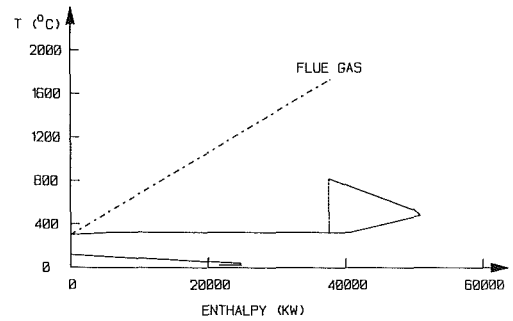


**Fig. 17 Energy targets for partial integration (without air preheat)**

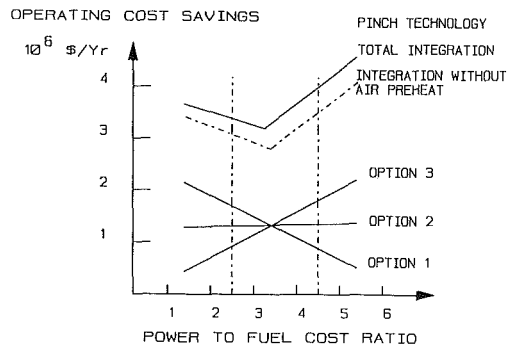


**Fig. 18 Economic comparison: operating cost savings implications for the targeted case without air preheat**

Technology," Paper No. 38c, presented at the AIChE Spring Meeting, New Orleans, LA, Mar. 6-10, 1988.

13 Linnhoff, B., and Eastwood, A. R.,"Overall Site Optimisation by Pinch Technology," *Chem. Eng. Res. Des.*, Vol. 65, 1987, pp. 408-414.

14 Linnhoff, B., "The Process/Utility Interface," presented at the Second International Meeting on National Use of Energy, Liege, Belgium, Mar. 10-12, 1986.

15 Linnhoff, B., and de Leur, J., "Appropriate Placement of Furnaces in the Integrated Process," presented at the IChemE Symposium on Understanding Process Integration II, UMIST, Manchester, United Kingdom, Mar. 22-23, 1988.

# APPENDIX I

## Process Assumptions

A project such as that discussed here with all practical constraints and uncertainties would take several man-months to complete. Many data would remain ill-defined and many decisions would be taken in the absence of full information. The case study in this paper, by contrast, is fully defined based on simplifying assumptions. This may appear naive. Let us bear in mind, however, that without such simplifying assumptions no solution could ever be "checked." Let us also bear in mind that, once in a while, we should try and see just what we can do to find optimal designs. While it is true that the intangibles of real design mean that there is never a strict optimum, would we not feel more comfortable if at least we knew that, were all the information given, we would definitely be able to find the optimum solution? In this spirit, let us accept the following simplifying assumptions:

- **Operating Cases.** All calculations are based on one single operating case.
- **Existing Processes.** Nothing is known about the existing processes on site except their power consumption, their steam consumption, the steam generated from them, and the condensate return condition. In addition, Table 1 shows where steam could be consumed at a lower level and where it could be generated at a higher level. The same information is represented by means of throttle valves in Fig. 2. For example, the throttle valve between stream No. 37 and stream No. 38 indicates that steam generation (stream No. 37) could take place at higher pressure (the saturation pressure at the temperature of stream No. 37) than the mains ($T_{38}$). Likewise, the throttle valve between stream No. 31 and stream No. 33 indicates that the consumption of steam at $T_{33}$ is at lower pressure than the mains. The possible changes in temperature and hence pressure of steam supplied and generated are the only measure of change to be contemplated with regard to the existing process plants. Given that the individual processes are separate and independent no heat recovery from one process to another process is to be considered other than through the existing site steam mains.
- **Steam Mains.** The numbers of steam mains and central turbine stages on site are to remain unchanged. Slight pressure changes (± 20 percent) in the mains are usually practical and therefore permitted.
- **Nitric Acid Process.** Figure 3 and Tables 2 and 3 give a complete heat and material balance. No changes are to be contemplated to any of the flow rates, temperatures, or pressures of any of the streams highlighted in Fig. A1. This includes T24 (set at 536°C), the recovery turbine inlet temperature. Higher turbine inlet temperatures would result in a need for multistage cooling. Also, they would result in significant changes to the design of the reaction vessel (for recovery). No information is given regarding reactor and separator design. The problem as defined in Fig. A1 is purely a heat and power recovery problem. It is not a complete chemical process design problem.

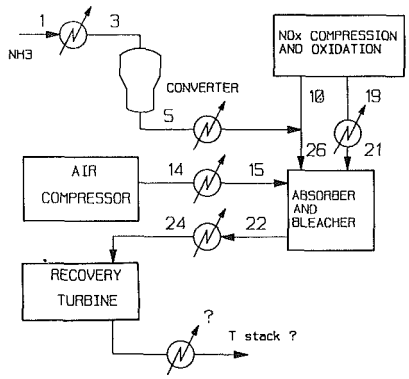


**Fig. A1 Nitric Acid process streams for integration**

## Cost Assumptions

- **Capital Costs.** For simplicity, capital costs are not to be considered other than through the observation of a constraint on minimum temperature difference. The existing Nitric Acid Plant design observes a $\Delta T_{min}$ of 28°C. This is to be adhered to. Changes in steam and water flow rates in the existing site system and/or in the Nitric Acid process are to be considered possible at no capital cost implications.
- **Energy Costs.** Each proposed design must achieve a closed heat and material balance based on site fuel import and electricity import or export across the factory fence. For a constant fuel cost of $100/kWyr two economic scenarios are to be considered: one in which the electricity cost is $250/kWyr, that is, a ratio of electricity cost/fuel cost of 2.5, and another in which the electricity cost is $450/kWyr, that is, a ratio of 4.5.

## Basis of Calculation of Changes in Existing System

The steam flow rate into the central turbine determines the fuel consumption in the boiler and the power output for the turbine. To determine this flow rate it is necessary to calculate the LP steam required for deaeration. The amount necessary depends on the total deaerated feedwater and the condensate fed into the deaerator. Therefore, by writing down a heat and mass balance for the deaerator, the correct flow rates are calculated overall. The following assumptions have been mode: (*a*) Pump work for the Boiler Feedwater pump and condensate pump is negligible. (*b*) The specific enthalpy of water (either feedwater or condensate) at any temperature is taken to be equal to the specific enthalpy of saturated water at that temperature. (*c*) The boiler efficiency remains constant at 86 percent: (*i*) Flue gas dew point is 160°C, and (*ii*) $m_{air}Cp_{air} \equiv m_{flue}Cp_{flue}$ for combustion air preheat calculations.

# APPENDIX II

## Outline Discussion of the Solution

The first step is usually to present heat sources and heat sinks in a grand composite curve [2]. Figure 10 is a grand composite curve merging the composite curves of Figs. 7(*a*) and 8(*a*). In other words it represents the overall grand composite curve of existing processes on site, as given, and of the Nitric Acid process notably not yet committing to any heat recovery features. The profile is best summarized as laying open all thermodynamic opportunities within the Nitric Acid process, between the process and the rest of the site, and within the site.

Figure 11 shows a selection of steam levels drawn against this profile. The levels have been chosen so as to represent a

good thermodynamic match to the profile, and to be practically compatible with the existing steam system (i.e., the three existing mains). In other words Fig. 11 shows how much steam should be used/generated and at what levels once the Nitric Acid process has been designed for proper integration into the site.

Figure 12 extends the targeting stage into the buildup of the total utility system [10, 11]. Once again to stay compatible with the existing site arrangements, steam-back pressure turbines are used and the necessary VHP steam is raised partly from flue gas in a central facility and partly from the nitric acid process. The construction allows us to calculate, quantitatively, all steam flows, the power generated, flue gas temperatures, furnace efficiency, and fuel consumption.

Figure 13 probably represents the most difficult step to understand. The fundamental and rigorous rules of Pinch Technology demand monotonic temperature profiles [2], which are not given in Fig. 12. Figure 13 represents a monotonic construction concentrating on heat interfaces and leaving aside those parts of the heat and power system that are not relevant to the process/utility interface. Sometimes the transition from a construction such as given in Figs. 12 and 13 requires iteration.

Figure 14 shows a further simplification of the overall profile by discarding details that are by now recognized as independent (and can therefore be left separate). The resulting overall profile looks simple even though it describes a complex problem. It is now straightforward to vary flue gas flow rates, temperatures, air preheat assumptions, etc., to arrive at optimized combustion [14, 15]. The final values obtained in Fig. 14 are those of the optimized overall solution.

good thermodynamic match to the profile, and to be practically compatible with the existing steam system (i.e., the three existing mains). In other words Fig. 11 shows how much steam should be used/generated and at what levels once the Nitric Acid process has been designed for proper integration into the site.

Figure 12 extends the targeting stage into the buildup of the total utility system [10, 11]. Once again to stay compatible with the existing site arrangements, steam-back pressure turbines are used and the necessary VHP steam is raised partly from flue gas in a central facility and partly from the nitric acid process. The construction allows us to calculate, quantitatively, all steam flows, the power generated, flue gas temperatures, furnace efficiency, and fuel consumption.

Figure 13 probably represents the most difficult step to understand. The fundamental and rigorous rules of Pinch Technology demand monotonic temperature profiles [2], which are not given in Fig. 12. Figure 13 represents a monotonic construction concentrating on heat interfaces and leaving aside those parts of the heat and power system that are not relevant to the process/utility interface. Sometimes the transition from a construction such as given in Figs. 12 and 13 requires iteration.

Figure 14 shows a further simplification of the overall profile by discarding details that are by now recognized as independent (and can therefore be left separate). The resulting overall profile looks simple even though it describes a complex problem. It is now straightforward to vary flue gas flow rates, temperatures, air preheat assumptions, etc., to arrive at optimized combustion [14, 15]. The final values obtained in Fig. 14 are those of the optimized overall solution.

## DISCUSSION

**D. A. Sama[2] and R. A. Gaggioli[3]**

After concerted but unsuccessful efforts by many investigators, applying the computer with brute force to calculate every combination and permutation of heat exchange between a set of streams that needed to be cooled in order to minimize the amounts of hot and cold utilities, the development of "pinch technology" was a milestone. Pinch methods are based on an elegant and clever use of the second law of thermodynamics. We are indebted to Linnhoff, Hindmarsh, Boland, Flower, Hohmann, Townsend, Alanis, and the others who contributed to the development of pinch technology. It has attracted many followers, and justifiably so, as shown once again by this paper.

Nevertheless, several specific and general comments may help the reader's perspective:

1 The authors repeatedly imply that site-specific optimization and process integration are virtually synonymous with pinch technology. However, process integration and site-specific optimization are by no means dependent upon pinch methodology (for example, see our paper with Qian and El-Sayed in this issue).

2 In spite of having made repeated reference to the benefits of considering the power plant and nitric acid process integrally, the authors have neglected to consider the use/generation of steam by process users and the integration of this user subsystem together with the power plant and the nitric acid subsystems.

The authors did not take advantage of considerable "site-specific optimization" opportunities available with the industrial steam user. For example, the exergy content of the saturated steam condensates leaving the process heaters at 80, 46, 8, and 4 bars have a total exergy content of 4630 kW. They are currently returned as boiler feedwater at 80°C with an exergy content of only 510 kW. The difference, 4120 kW of exergy, is wasted as heat loss in the condensate return piping. This represents 11,536 kW of fuel or $1,153,600 per year, and should not be overlooked. The exergy in the saturated condensates can be recovered inexpensively by throttling down to produce flash steam for use at lower pressures. Throttling is effective when the inlet fluid is liquid.

The existing industrial site has rather obvious, serious mismatches between the pressure levels at which steam is generated or extracted and the pressures at which the steam is used for heating. Steam is supplied to the heaters, via let-down valves, as follows:

| | | | | | |
|---|---|---|---|---|---|
| Flow rate (metric tons/hr) | 18.0 | 10.8 | 14.4 | 20.8 | 17.3 |
| Generation pressure (bars) | 80 | 50 | 40 | 15 | 4 |
| Use pressure (bars) | 46 | 8 | 8 | 4 | 3 |

The application of pinch technology or exergy analysis to this obviously "poor" situation enables us to distinguish, in part, differences between the two approaches.

Using traditional pinch technology Linnhoff and Alanis generate the "grand composite" curve (Fig. 11). This curve shows steam supply and usage at the various pressure levels and enables the prediction of changes in steam usage with changes in the pressure levels of either the steam supply or the steam users. Unfortunately, it is impossible, even after after all this effort using pinch technology, to quantify the fuel losses attributable to the obvious mismatches.

Figure 1 of our article in this issue shows the exergy losses in kW at each of the five let-down valves. They total 2900 kW. Since the existing boiler/turbine system operates at a second law efficiency of 36 percent, each unit of exergy represents 1/(0.36), or 2.8, units of fuel. Thus the fuel wasted by these steam let-downs represents about 8120 kW of fuel, which at $100 per kW year is worth about $800,000. Although the preceding losses cannot be totally eliminated, they can be substantially reduced in numerous ways. (For example, see our paper, and notice that the flashing of condensate helps to reduce much of the mismatch effect referred to here.)

The Linnhoff and Alanis approach is to reduce the steam mismatches by changing the pressures and flows of the extracted steam, presuming that the turbine could still operate under these new conditions. For example, the turbine exhaust pressure was essentially doubled, from 4 to 8 bar, while the flow rate through the last stage was increased markedly from 28 to 51 metric tons per hour, increasing the volumetric flow rate (and hence the velocity) into the last stage by 45 percent. It is doubtful that the turbine could even function with such a change, let alone without affecting its efficiency, which was also assumed constant. The claim that this assumption "should be uncontroversial" notwithstanding, certainly it is wishful thinking to assume that such a change is satisfactory, without checking the particular turbine's performance characteristics.

Many potential improvements for the user subsystem and its integration, which go undiscovered by pinch technology can be brought to light by exergy analysis. Exergy analysis can not only help to achieve a given pinch "target" but unlike the pinch methodology, for which the "target" is fixed, can also lead to improvements in the "target" itself.

3 The authors are more tentative about other assumptions they have made, which in our opinion are serious but not as controversial as those regarding steam turbine operation: The authors make the following assumptions regarding modifications to the existing boiler: (*a*) that the boiler does not already have combustion air preheat (by stack gases), (*b*) that even if it does not have air preheat, the boiler (e.g., tubewall temperatures) could tolerate it, (*c*) that even if the boiler does not have air preheat, it could tolerate it without detracting from

[2]Department of Chemical Engineering, University of Lowell, Lowell, MA 01854.

[3]Department of Mechanical University, Marquette University, Milwaukee, WI 53233.

its efficiency, (*d*) that exhaust tailgas from the nitric acid plant turbine is nearby enough for effective *gas-to-gas* heat exchange with boiler, air, and finally (*e*) that boiler feedwater could be heated with boiler stack gas (which presumes that the stack gas is not being used for air preheat already). However, the authors do present conditional results, in case air preheat already exists or cannot be tolerated; in our opinion it is this conditional result that should be the basis for comparisons with the base case (or with the improvements made with other methodologies, such as exergy analysis).The authors cite many "clear and realistic" constraining assumptions in Appendix I. Yet, in order to implement pinch technology, they have made serious presumptions about the equipment.

4 The authors assume that no changes to flow rates, temperatures, or pressures of any of the nitric acid plant streams are to be allowed (such as the inlet temperature to the tailgas expansion turbine). We agree that the chemical process is not to be changed, but there is no reason to disallow rerouting of flow streams and changing of intermediate temperatures that have no effect upon the process. Invoking such conditions, say, so that Pinch Technology procedures can be applied, imposes unnecessary constraints, which limit the potential for energy conservation. For example, in the assumptions of Appendix I, Linhoff and Alanis state that the tail gas temperature entering the expansion turbine after leaving the first converter gas cooler must be set to 536°C, that used by the contractor. However, the converter gas exits the converter at 840°C; and we maintain that full advantage should be taken of this high temperature, to maximize tailgas turbine output. We do not understand the authors' comments about how this would lead to the need for multistage cooling, cause significant changes in the design of the reaction vessel, or be considered a complete chemical process design problem rather than a heat and power recovery problem. In any case, certainly gas expansion turbines do not need to have their inlet temperatures limited to values such as 536°C for materials reasons; temperatures up to 1000°C can be handled without any need for blade cooling, and values higher than 1300°C with cooling.

5 The authors invoke the constraint that for heat exchangers $\Delta T_{min}$ must be greater than 28°C. In our opinion, the minimum $\Delta T$ allowed should depend upon the heat transfer situation; e.g., for gas-to-gas heat transfer it should be greater than this value, for liquid-to-liquid cases it should be less, and for cases with heat transfer between a liquid and a boiling or condensing stream it should be less yet.

6 Finally, we feel compelled to point out that the large energy savings reported by both Linnhoff and Alanis and ourselves are not solely reflections of the value of pinch technology, or of exergy analysis. They are, to a large extent, the result of starting with an obviously poor (at least from an exergy usage point of view) combination of existing site and contractor's design.

## Authors' Closure

We agree that site-specific optimization is a general objective and that there are various ways of pursuing the objective, including Pinch Technology, Thermoeconomics, Exergy Analysis, and even intuition.

We feel that Exergy Analysis is a thought provoker, supporting the intelligent user in open-ended problem formulations. Pinch Technology sets more meaningful targets and gives more design information for the more closely defined problem. Within the boundaries of its applicability, Pinch Technology makes the use of Exergy Analysis or similar procedures unnecessary. However, a good engineer should always look "beyond" his problem and it is here where Exergy Analysis can score. Our aim in research and development is to extend the scope of problems for which Pinch Technology is applicable (i.e., heat and power, total site integration, chemical process reactors and separators, etc.).

its efficiency, (*d*) that exhaust tailgas from the nitric acid plant turbine is nearby enough for effective *gas-to-gas* heat exchange with boiler, air, and finally (*e*) that boiler feedwater could be heated with boiler stack gas (which presumes that the stack gas is not being used for air preheat already). However, the authors do present conditional results, in case air preheat already exists or cannot be tolerated; in our opinion it is this conditional result that should be the basis for comparisons with the base case (or with the improvements made with other methodologies, such as exergy analysis).The authors cite many "clear and realistic" constraining assumptions in Appendix I. Yet, in order to implement pinch technology, they have made serious presumptions about the equipment.

4 The authors assume that no changes to flow rates, temperatures, or pressures of any of the nitric acid plant streams are to be allowed (such as the inlet temperature to the tailgas expansion turbine). We agree that the chemical process is not to be changed, but there is no reason to disallow rerouting of flow streams and changing of intermediate temperatures that have no effect upon the process. Invoking such conditions, say, so that Pinch Technology procedures can be applied, imposes unnecessary constraints, which limit the potential for energy conservation. For example, in the assumptions of Appendix I, Linhoff and Alanis state that the tail gas temperature entering the expansion turbine after leaving the first converter gas cooler must be set to 536°C, that used by the contractor. However, the converter gas exits the converter at 840°C; and we maintain that full advantage should be taken of this high temperature, to maximize tailgas turbine output. We do not understand the authors' comments about how this would lead to the need for multistage cooling, cause significant changes in the design of the reaction vessel, or be considered a complete chemical process design problem rather than a heat and power recovery problem. In any case, certainly gas expansion turbines do not need to have their inlet temperatures limited to values such as 536°C for materials reasons; temperatures up to 1000°C can be handled without any need for blade cooling, and values higher than 1300°C with cooling.

5 The authors invoke the constraint that for heat exchangers $\Delta T_{min}$ must be greater than 28°C. In our opinion, the minimum $\Delta T$ allowed should depend upon the heat transfer situation; e.g., for gas-to-gas heat transfer it should be greater than this value, for liquid-to-liquid cases it should be less, and for cases with heat transfer between a liquid and a boiling or condensing stream it should be less yet.

6 Finally, we feel compelled to point out that the large energy savings reported by both Linnhoff and Alanis and ourselves are not solely reflections of the value of pinch technology, or of exergy analysis. They are, to a large extent, the result of starting with an obviously poor (at least from an exergy usage point of view) combination of existing site and contractor's design.

## Authors' Closure

We agree that site-specific optimization is a general objective and that there are various ways of pursuing the objective, including Pinch Technology, Thermoeconomics, Exergy Analysis, and even intuition.

We feel that Exergy Analysis is a thought provoker, supporting the intelligent user in open-ended problem formulations. Pinch Technology sets more meaningful targets and gives more design information for the more closely defined problem. Within the boundaries of its applicability, Pinch Technology makes the use of Exergy Analysis or similar procedures unnecessary. However, a good engineer should always look "beyond" his problem and it is here where Exergy Analysis can score. Our aim in research and development is to extend the scope of problems for which Pinch Technology is applicable (i.e., heat and power, total site integration, chemical process reactors and separators, etc.).

# Integration of a New Process Into an Existing Site: A Case Study in the Application of Exergy Analysis[1]

**R. A. Gaggioli**
Marquette University,
Milwaukee, WI 53233

**D. A. Sama**
University of Lowell,
Lowell, MA 01854

**Sanhong Qian**
Jiangsu Institute of Chemical Technology,
People's Republic of China

**Y. M. El-Sayed**
Advanced Energy Systems,
Fremont, CA 94539

*This paper presents a case study that demonstrates how exergy analysis can help make intelligent process design decisions in a logical manner. A proposed, new nitric acid plant is to be intergrated into an existing facility wherein a steam system produces part of the facility's power needs and all of the process steam, at three pressures. The objective is to minimize the expenditure for fuel and power under two scenarios: when the ratio R of power to fuel costs is 2.5, and when the ratio is 4. The procedure used was first to carry out exergy analyses of the three principal subsystems: (1) the process utilization, (2) the existing steam/power generation, and (3) the proposed $HNO_3$ plant. Secondly, improvements of each of these subsystems were developed, independently, by systematically eliminating unnecessary thermodynamic inefficiencies. (For the steam plant and for the nitric acid plant, alone, improved reconfigurations have been presented earlier: Sama et al., 1988, 1989, respectively.) Finally, in this article, further opportunities for reducing inefficiencies, by integration of the three subsystems, were exploited. In the contractor's original conceptual design with integration, the facility needs to purchase 77 MW of fuel and 2.2 MW of power. Improved designs developed here save equivalent fuel of over 45 MW when $R = 2.5$ and over 60 MW when $R = 4$ (i.e., 4.5 and 6.0 million dollars per year at a fuel cost of \$100/kW-yr or \$3.35/$10^6$ Btu).*

## Introduction

This paper deals with a challenge problem presented by Linnhoff (1987). Given a conceptual design offered to a chemical firm by an engineering contractor, Linnhoff proposed that advocates of different approaches for improving energy utilization should apply their procedures to improvement of the design. Then the effectiveness of the different techniques could be measured by comparing the results.

Table 1 shows, in the exact form provided by Linnhoff, the information regarding process use and generation of steam in an existing manufacturing facility. Figure 1 shows that information in schematic form, along with the values of enthalpies (relative to saturated liquid at 0°C) that we checked. Also shown in Fig. 1, for discussion later in this paper, are the exergy flows and consumptions we calculated; the exergy numbers are shown in italics. As presented by Linnhoff, Fig. 2 shows the existing industrial steam plant and its flow rates and thermodynamic properties (as well as our exergy numbers). Figure 3 depicts a nitric acid plant, which is to be newly installed, including one of the contractor's three alternative proposals for use of the heat available from the $HNO_3$ process (and our exergies). Table 2 gives the details as presented by Linnhoff of flows, compositions, and thermodynamic properties associated with each stream of the acid plant. Enthalpy figures for each chemical species are relative to 25°C reference, except for Rows 29–38, which are relative to saturated liquid water at 0°C. Some of the information was corrected; rows with corrected entries are indicated by an asterisk. Rows 19 and 31 were changed in order to satisfy an energy balance on the oxidation vessel, and Row 18 for chemical species and energy balances across Compressor C2. Also, the net power output on Fig. 2 was originally shown as 8032 kW, and it has been corrected to 3965 kW in order to satisfy an energy balance on the array of turbines, compressors, and generator. The original data showed a "heat generation" in Unit E6 of Fig. 3 as 24,489 kW. That is the amount assumed in the preliminary version of this paper (Gaggioli et al., 1988). Linnhoff and Alanis (1988) revised this value to the 20493 kW shown in Fig. 3, which we have now adopted so that our results can be compared more easily with theirs.

The objective is to integrate the $HNO_3$ plant into the existing facility in a technically feasible manner that would minimize the net cost for purchased energy—fuel and electric power.

[1]This paper together with the preceding (authored by Linnhoff and Alanis) and the accompanying discussions should be regarded by readers as a whole. The papers explore the relative merits of pinch technology and exergy analysis, and stem from a challenge problem issued by Professor B. Linnhoff at the Advanced Energy Systems Division Symposium of the ASME Winter Annual Meeting, Boston, Massachusetts, December 13–18, 1987. Note contributed by M. J. Moran, Associate Editor.

Contributed by the Advanced Energy Systems Division for publication in the JOURNAL OF ENGINEERING FOR GAS TURBINES AND POWER. Manuscript received by the Advanced Energy Systems Division March 9, 1989; revision received July 2, 1990.

This is to be done under two alternative conditions: when the ratio of electric to fuel costs is $R = 2.5$ and when $R = 4$. While technical feasibility is of course necessary, capital costs, while relevant, need not be considered explicitly.

In all three of the contractor's alternative proposals, the process heat is used to produce Stream 35 (Fig. 3), which is at 80 bar and 473°C, the same conditions as the 80 bar steam extracted from the power-plant turbine (Fig. 2). In the alternative shown in Fig. 3, Stream 35 is used to produce the maximum amount of power possible, in T2; the power produced, along with that from T1, exceeds that needed to drive compressors C1 and C2, by 3965 kW. That 3965 kW together with the 7792 kW produced by the existing turbine (Fig. 1) exceeds the 10 MW overall plant load (Fig. 2); whatever the value of $R$ might be, the excess power could be sold at the corresponding rate.

In another of the three alternatives, the "maximum steam export option," no power was produced with Stream 35, which was all exported from the acid plant, and purchased electric power was used to drive the compressors. The export steam amounts to 30 metric tons per hour, which exceeds the 26 tons/hr needed for process purposes; again, it is presumed that the excess steam could be sold. In the third alternative, the "compromise option," Stream 35 was split, using just the amount needed by T2 to fulfill the compressor power requirements and exporting the remainder. That export, 14.8 tons/hr, was supplied to process use thereby reducing the amount of 80 bar steam extracted from the power-plant turbine (Fig. 2). It can be said that this "compromise option" does integrate the new and the existing facility; in so doing the net power was increased

**Table 1 Process steam consumption and generation**

| Steam Mains | Consumptions | Generation |
|---|---|---|
| *High-pressure 80 bar, 295°C* | 5764 kW @ Mains<br>8145 kW @ 46 bar, 259°C | |
| *Medium-pressure 40 bar, 250°C* | 21.6 tons/hr @ Mains<br>14531 kW @ 8 bar, 170°C, requiring 0.343 tons/hr of 100°C boiler feedwater for desuperheating | 10.8 tons/hr @ 50 bar & 264°C, requiring 10.8 tons/hr of 100°C boiler feedwater |
| *Low-pressure 4 bar, 144°C* | 19430 kW @ Mains<br>17.28 tons/hr @ 3 bar, 140°C | 20.78 tons/hr @ 15 bar & 198°C requiring 20.78 tons/hr of 100°C boiler feedwater plus 0.47 tons/hr for desuperheating |

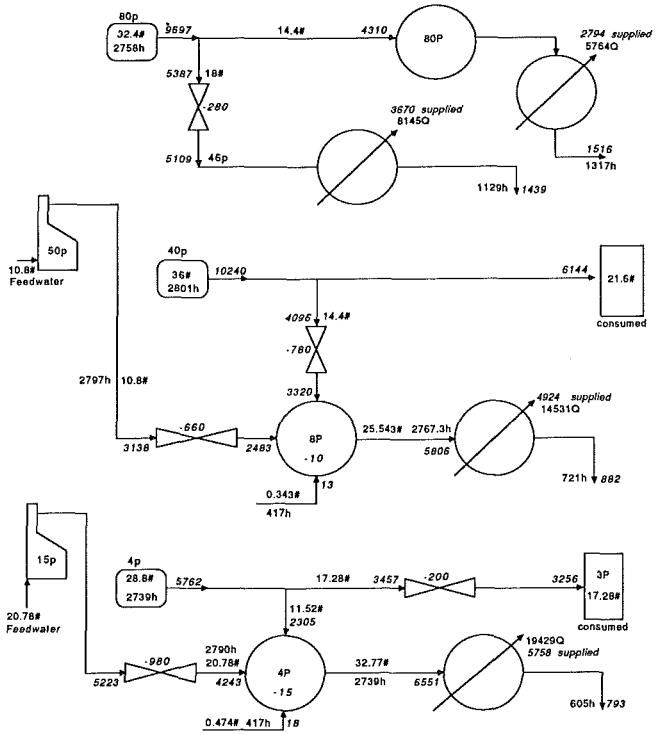


**Fig. 1 Process use and generation of steam (#, tons/hr; *p*, bar; *h*, kJ/kg; *Q*, kW; exergy, kW); N.B.: Exergy numbers are shown in italics**

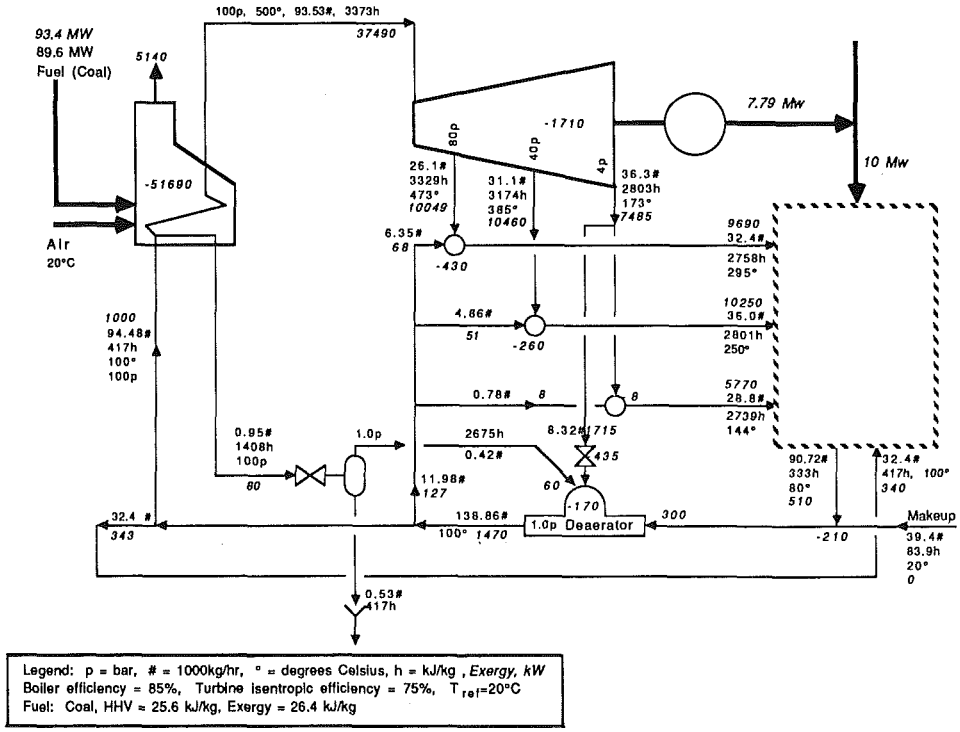


**Fig. 2 Industrial steam plant, base case; N.B.: Exergy numbers are shown in italics**

Table 2 Heat and mass balance of dual pressure Nitric Acid process

| FLOW | T | P | | | m(Kg/hr) | | | | H(T,P) |
|---|---|---|---|---|---|---|---|---|---|
| | (C) | (bar) | N2 | O2 | H2O | NH3 | NO | NO2 | [kW] |
| 1 | 7 | 5.5 | | | | 10679.8 | | | -3947.7 |
| 2 | 7 | 5.5 | | | | 10679.8 | | | -174 |
| 3 | 76 | 5.5 | | | | 10679.8 | | | 279.6 |
| 4 | 170 | 3.5 | 126152.7 | 38311.2 | | 10679.8 | | | 7657.6 |
| 5 | 840 | 3.3 | 126504 | 13627.8 | 16946.3 | | 18064.4 | | 47259.7 |
| 6 | 763 | 3.3 | 126504 | 13627.8 | 16946.3 | | 18064.4 | | 42495.6 |
| 7 | 592 | 3.3 | 126504 | 13627.8 | 16946.3 | | 18064.4 | | 31994.6 |
| 8 | 325 | 3.3 | 126504 | 13627.8 | 16946.3 | | 18064.4 | | 16466.1 |
| 9 | 135 | 3.16 | 126504 | 11412.3 | 16946.3 | | 13909.6 | 6370.4 | 5842.8 |
| 10 | 50 | 3.16 | 126504 | 3995.3 | 931 | | 1538.6 | 20616.1 | 1030 |
| 11 | 20 | 1 | 141519 | 42993 | | | | | -278 |
| 12 | 184 | 3.5 | 141519 | 42993 | | | | | 8272 |
| 13 | 184 | 3.5 | 126152.7 | 38311.2 | | | | | 7378 |
| 14 | 184 | 3.5 | 15366.3 | 4681.8 | | | | | 894 |
| 15 | 103.5 | 3.5 | 15366.3 | 4681.8 | | | | | 440.4 |
| 16 | 67 | 3 | 15366.3 | 4681.8 | | | | | 233.6 |
| 17 | 52 | 3 | 141870.3 | 8677.1 | 931 | | 1538.6 | 20616.1 | 1267.8 |
| 18 | 224.5 | 10.25 | 141870.3 | 8272.8 | 931 | | 592.9 | 22066 | 9823 |
| 18* | 224.5 | 10.25 | 141870.3 | 8677.1 | 931 | | 1538.6 | 20616.1 | 9823 |
| 19 | 224.5 | 10.25 | 141870.3 | 8172.8 | 931 | | 1538.6 | 22066 | 9823 |
| 19* | 236 | 10.25 | 141870.3 | 8172.8 | 931 | | 592.9 | 22066 | 10380.5 |
| 20 | 156 | 10.25 | 141870.3 | 8172.8 | 931 | | 592.9 | 22066 | 6377 |
| 21 | 43 | 10.25 | 141870.3 | 8172.8 | 931 | | 592.9 | 22066 | 713.7 |
| 22 | 18 | 8.9 | 141870.3 | 3877 | 383 | | 15 | 23 | -491.9 |
| 23 | 297 | 8.9 | 141870.3 | 3877 | 383 | | 15 | 23 | 11766.6 |
| 24 | 536 | 8.9 | 141870.3 | 3877 | 383 | | 15 | 23 | 22267.7 |
| 25 | 243 | 1 | 141870.3 | 3877 | 383 | | 15 | 23 | 9237.7 |
| | | | H2O | HNO3 | | | | | |
| 26 | 50 | 3.16 | 15078 | 6462 | | | | | 457.1 |
| 27 | 41 | 3 | 36013.4 | 37865 | | | | | 907.1 |
| 28 | 45 | 3 | 36013.4 | 37865 | | | | | 1114 |
| | | | H2O(L) | H2O(G) | | | | | |
| 29 | 20 | 10 | 24678.4 | | | | | | -143.3 |
| 30 | 100 | 80 | 30036 | | | | | | 2604.8 |
| 31 | 194 | 80 | 30036 | | | | | | 6050.6 |
| 31* | 209.4 | 80 | 30036 | | | | | | 6608.1 |
| 32 | 295 | 80 | 38794.3 | | | | | | 13063 |
| 33 | 295 | 80 | | 38794.3 | | | | | 28591.4 |
| 34 | 295 | 80 | | 30036 | | | | | 22136.6 |
| 35 | 473 | 80 | | 30036 | | | | | 26900.6 |
| 37 | 50 | 0.1233 | 2842.7 | 27193.3 | | | | | 18865.7 |
| 38 | 50 | 0.1233 | 30036 | | | | | | 871.8 |

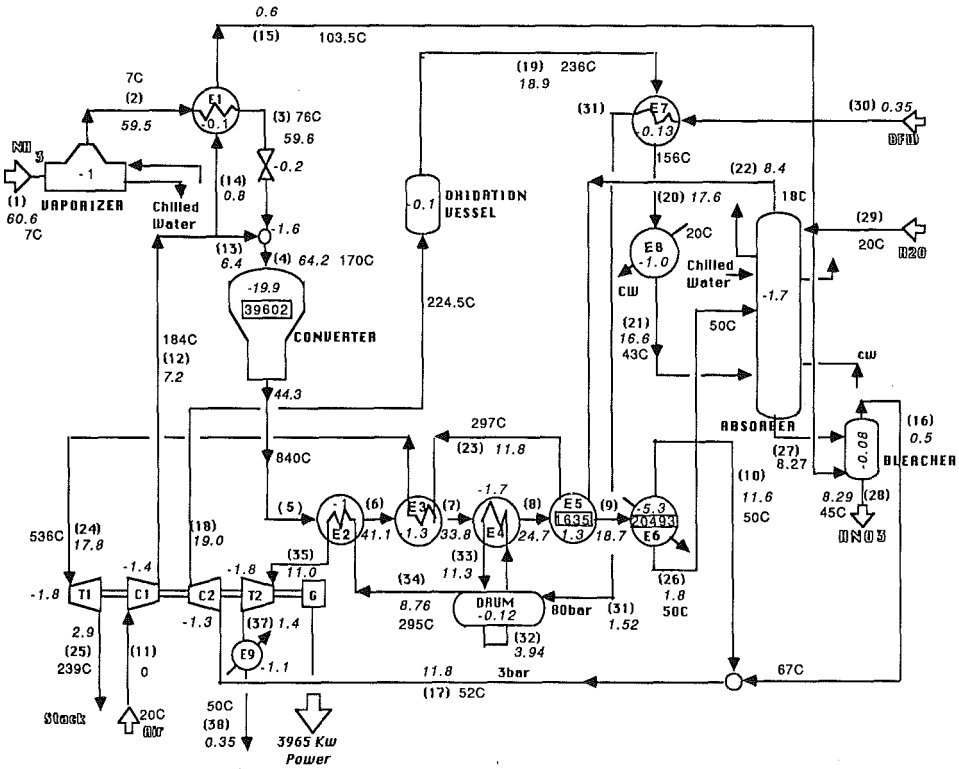


Fig. 3 $HNO_3$ process conceptual design, with exergy (MW); N.B.: Exergy numbers are shown in italics

from 7790 to 7827 kW and the fuel consumption was reduced from 89.6 to 76.7 MW. For the sake of comparison, this option will be taken as the base case, against which results will be measured.

The procedure employed here has three stages: (1) first, to study the exergy utilization of all three subsystems, one at a time, (2) second, led by those analyses, to develop means for improving each subsystem independently, and (3) after that, to explore further opportunities for reducing the exergy inefficiencies by effective integration. This procedure focuses first

on the details and then strives to develop the global ramifications thereof. Admittedly, the success of this process— particularly in stages (2) and (3)— **is proportional to the judgment, intuition and experience of the practitioner.** The lines of reasoning may be tedious. We hope, in the following (*a*) to illustrate the process, (*b*) to pass on some experience, (*c*) to convince the reader that it is worthwhile to pursue the process, to gain first-hand experience, and (*d*) to encourage some readers to develop methodical procedures and tools for facilitating the process.

## Exergy Analyses

As mentioned earlier, Fig. 1-3 show, in italics, the flows and consumptions of exergy in (1) the process use and generation of steam, (2) the steam plant, and (3) the $HNO_3$ plant. The exergies were calculated using the methods from Rodriguez (1980).

**Process Use and Generation of Steam.** The first place to make improvements is in the use/generation of steam at existng processes; that is, to reduce the load on the eventual, integrated steam-power/$HNO_3$ plant. Study of the exergies on Fig. 1 shows many large inefficiencies which appear to be unnecessary, such as: (a) large losses of exergy from the condensate, especially the 1516 kW at 80 bar and the 1439 kW at 46 bar, and (b) significant exergy consumptions at many junctures by throttling of steam—particularly the throttling of 40 and 50 bar steam down to 8 bar and of 15 bar steam to 4 bar, consuming 780, 660, and 980 kW, respectively. It is important to recognize all of the inefficiencies—and they are pinpointed explicitly by exergy analysis whereas other methodologies may allow important inefficiencies to escape notice, for example the large losses of exergy from the condensate. Once the inefficiencies are recognized, various possibilities for reducing them can be developed. Before describing these possibilities, the exergy inefficiencies of the other subsystems will be investigated.

**The Steam Plant.** From the exergy results shown in Fig. 2, it can be concluded that the overall second law efficiency of the plant, the net exergy delivered by the plant divided by the fuel input, is [7790 + 9690 + 10250 + 5770 + 340 − 510]/93430 = 35.7 percent.

The largest inefficiencies are in the boiler, which has a second-law efficiency of 39.1 percent, whereas its first-law efficiency is 86 percent. Of the 93,430 kW of exergy supplied with fuel, 24,500 kW is annihilated by combustion irreversibility and 27,200 kW by heat transfer, while 5140 kW is lost in stack gas effluents. The latter is a little more than 5 percent of the fuel exergy, whereas the stack gas energy is 14 percent of the fuel energy.

The heat transfer consumption, about 30 percent of the fuel exergy, is large compared to the 15 percent for typical electric utility boilers (see Gaggioli et al., 1975, or Petit and Gaggioli, 1980). This is due largely to introducing cold feedwater into the boiler. Therefore, the mean $\Delta T$ between combustion products and $H_2O$ is excessive.

There is little that can be done to reduce the combustion irreversibilities without changing the technology (e.g., using engines or gas turbines in lieu of a boiler). However, preheating of combustion air can provide a modest improvement and, if done in part by stack gases, would also serve to reduce the effluent loss of exergy. However, because the boiler is an existing one, the questions arise, can it be modified structurally to accommodate such changes, and how would its performance change? Since the answers are not available, we precluded the possibilities of air preheating and of heat recovery from stack gases.

There are other inefficiencies shown in Fig. 2 that, although they may appear to be minor, are important, such as the throttling of 4 bar steam to the deaerator, and the desuperheater irreversibility associated with mixing cold water with very hot steam. For example, if the 430 + 260 + 8 ≈ 700 kW of exergy destruction by desuperheating were eliminated, how much fuel would be saved? To answer that question, let us first ask how much "desuperheater fuel" would be saved? That is, how much could the exergy supplied to the desuperheater be reduced and where is that exergy supplied? The desuperheating process consists of the vaporization of liquid, which takes heat from the superheated steam. The exergy which drives this process is given up by the superheated steam, the "fuel" for this process. That steam fuel exergy was acquired from raw fuel exergy in the boiler at an efficiency of 39 percent; therefore if 700 kW of exergy destroyed by desuperheating were saved, input of raw fuel exergy would be reduced by about 700/0.39 = 1795 kW. That would be a significant saving, of 1795/93430 = 1.9 percent. Similar conclusions follow for the exergy destroyed by throttling of 4 bar steam to the dearerator.

**The Nitric Acid Plant.** As shown in Fig. 3, the exergy supplied to the $HNO_3$ plant is 60.6 MW, in the $NH_3$, Stream 1. This represents the theoretical maximum of exergy in products, including the 8.3 MW of desired product $HNO_3$, Stream 28. The exergies of Streams 1 and 28 are almost totally chemical exergy. In the plant at hand, a great amount of that net chemical exergy (60.6 − 8.29 = 52.3 MW) is annihilated by highly irreversible chemical processes, namely the combustion of $NH_3$ in the converter (19.9 MW consumed), the oxidation of NO (0.1 MW), and the absorption of $NO_2$ in the absorber (1.7 MW). To recoup a substantial part of this irreversible consumption would require that the chemical processes be carried out without great irreversibility. Such a study is outside the scope of the present project; improvements are to be sought without any significant changes in the $HNO_3$ production process. Therefore, a practical measure of the upper bound, the maximum recoverable exergy, is 52.3 − 19.9 − 1.7 − 0.1 = 30.6 MW.

The actual net output from the contractor's design shown in Fig. 3 is the 3.965 MW generator output less the 0.35 MW supplied with feedwater (Stream 30); i.e., 3.615 MW net. So the efficiency of utilization of the 30.6 MW is 12 percent. This efficiency is far below the state of the art, about 60 percent, for utilization of combustion-product exergy for power production in power plants (see Gaggioli et al., 1975, or Petit and Gaggioli, 1980).

The most significant inefficiencies shown in Fig. 3 are those associated with:

(*a*) the compressors and turbines, whose function is to transform exergy, as well as the throttling of Stream 3 and its mixing with Stream 13, which annihilate:

| | |
|---|---|
| *C*1 | ≈1.4 MW |
| *C*2 | ≈1.3 MW |
| *T*1 | ≈1.8 MW |
| *T*2 | ≈1.8 MW |
| Throttling, 3-4 | ≈0.2 MW |
| Mixing of 4 & 13 | ≈1.6 MW |
| Transform subtotal | ≈8.1 MW |

(*b*) heat exchangers whose function is to recover exergy, which annihilate:

| | |
|---|---|
| Drum | ≈0.1 MW |
| *E*2 | ≈1.0 MW |
| *E*3 | ≈1.3 MW |
| *E*4 | ≈1.7 MW |
| *E*5 | ≈1.3 MW |
| *E*7 | ≈0.1 MW |
| Recovery subtotal | ≈5.6 MW |

(*c*) exchangers, which, along with *T*1 exhaust (Stream 25), discard energy:

| | |
|---|---|
| *E*6 | ≈5.3 MW |
| *E*8 | ≈1.0 MW |
| *E*9 | ≈1.1 MW |
| *T*1 exhaust | ≈2.9 MW |
| Discard subtotal | ≈10.3 MW |

The total of the foregoing inefficiencies is then 8.1 + 5.6 + 10.3 ≈ 24 kW of exergy either consumed or discarded.

Except for the throttling and mixing, no proposal will be made to reduce the irreversibilities associated with transformations, inasmuch as that would be simply a matter of trading off capital expenditures for better equipment against fuel savings. That tradeoff is outside the scope of the present paper, and to pursue it would becloud the central issue. So we have constrained the values of efficiencies to be equal to those of the turbines and compressors (and boiler) in the original problem.

On the other hand, remedies for the inefficient recovery of exergy by heat transfer and mixing—caused by excessive mean $\Delta T$ between heating and heated streams—will be pursued, and so will the reduction of the large amount of discarded exergy. Particularly notable is the large discard of exergy in *E*6, associated with the rejection of "heat of solution" given up at temperatures from about 135°C down to 50°C.

## Subsystem Improvements

### Process Use and Generation of Steam

*Condensate Losses.* Reduction of the condensate losses is straightforward. These losses are a consequence of the fact that the condensates are at high temperatures and therefore have substantial exergy remaining, as shown by the given information of Fig. 2 since the condensate returns to the steam plant at 80°C, while Fig. 1 shows that it leaves the point of steam use at saturated conditions. Hence that exergy is lost by heat transfer from the condensate return piping. One way that this cause of inefficiency could be reduced might be with thorough insulation of the return piping; such an approach (which would also reduce inefficiencies associated with feedwater heating in the steam plant) would require condensate return at each pressure level.

A more practical way of reducing these inefficiencies is simply to *flash the condensate at each pressure level into flash tanks at the next lower pressure level*, sending the resultant vapor from each flash tank to that next lower pressure main and letting the remaining liquid continue in the cascade downward to lower pressure levels. (It is notable, by the way, that unlike the throttling of vapor, the flashing of liquid destroys relatively little exergy, and yet makes for the practical utilization of the high condensate exergy.) This cascading reduces the amount of steam required from the steam plant at lower pressures, and it also has the "fringe benefit" of reducing the need for throttling of steam (Fig. 1) from the higher to the lower pressures.

*Throttling Inefficiencies.* As is so common, when steam distribution systems are viewed from a first law viewpoint alone, detrimental effects go unrecognized and throttling is used as a matter of course. The exergy consumption from throttling 80 bar steam down to 46 bars can be reduced greatly: *Use the 50 bar process-generated steam at 46 bars instead of throttling it down to 15 bars.* This lowers the amount of 80 bar process steam required from the steam plant. Furthermore, that throttling inefficiency could be eliminated altogether if the pressure of the 40 bar main were raised to 46 bars. The latter modification, however, would require a change in the operating conditions of the extraction turbine. While a change from 40 to 46 bars is probably feasible, this modification was precluded because the permissible changes in the operating conditions of the existing turbine and the effects on performance were unknown. Instead, *a compressor to raise steam from 40 to 46 bars is proposed.* To compress the 5 metric tons per hour (over and above the 10.8 tons available at 50 bars) requires only 60 kW.

The throttling of 50 and 40 bar steam to meet the large 8 bar load can also be readily eliminated: *Use the process-generated steam at 15 bars along with steam obtained by flashing condensate from 46 bars.* Also, because of the large flow rate, it may prove to be worthwhile to *expand the steam from 15 bar to 8 bar through a turbine.* Of course, if the capital expenditure for the turbine cannot be justified, throttling could be used there instead, and the use of the 15 bar steam would still be more efficient than in the original scheme.

Figure 4 shows the results of implementing the proposed changes for process use and generation of steam. The only feature of this revised scheme that is not readily found from analysis of Fig. 1 alone is the proposal to *use a heat pump for supplying 3 bar process steam.* The motivation for the heat pump is the abundance of low-temperature waste heat from the $HNO_3$ process. In return for 720 kW of mechanical exergy, over 3000 kW of thermal exergy can be saved, while both are produced with roughly the same efficiency (≈35 percent).

The net effect of the improvements shown in Fig. 4 is large reductions in the amounts of 80 and 40 bar steam that need to be supplied. While there is an increase in the requirements for 4 bar steam (from 28.8 to 37.3 tons/hr), the exergy content of that steam is much less and hence the amount of fuel necessary to produce it is lower.

*The Steam Plant.* From the analysis by Sama et al. (1988) of the steam plant alone, it is evident that the key to improving performance is in more effective feedwater heating, along with

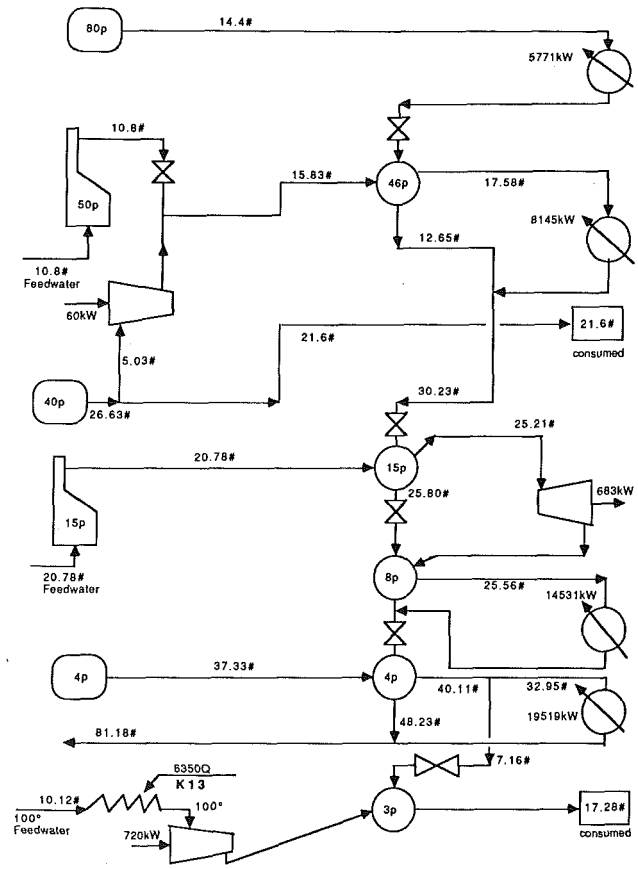


**Fig. 4 Revised use and generation of steam**

the concomitant elimination of irreversible desuperheating. Overall efficiencies of nearly 38 percent can be achieved with various possible reconfigurations for effective feedwater heating. At $R=4$, fuel savings of 10 to 12 percent can be obtained with different reconfigurations. Those improvements can be reached without significant changes in the deaeration subsystem. *More efficient deaeration, along with the elimination of the unnecessary throttling of 4 bar steam, is readily achievable with lower temperature heat* (abundantly available from the acid plant if needed).

It is also clear from the work of Sama et al. (1988) that if the improvement were to be accomplished by making straightforward changes within the steam plant alone, by adding feedwater heaters supplied with bleed steam from the turbine, then the existing turbine might need to be replaced with a larger one, depending upon the amount of 80, 40, and 4 bar steam that, ultimately, needs to be delivered to process use. For the present project, however, it was decided that *replacement of the turbine shall be avoided* because of the expected large capital cost and, as described earlier, the conservative constraint was imposed that *steam flow through each turbine stage should be kept equal to the original* (Fig. 2). Adherence to this constraint dictates some requirements that may be awkward. For example: (*a*) the need to deliver the aforementioned 4 bar steam for process use (37.3 tons/hr), which slightly exceeds the original amount of 4 bar steam exhausted by the turbine (36.3 tons/hr), and (*b*) utilization of the excess of 80 and 40 bar bleed steam over and above that now needed for process use. The constraint limits the possibilities for and/or extent of improvement. Yet, it will be adhered to rigidly inasmuch as we have neither information regarding the extent to which the turbine steam flows can be modified (in amount or pressure) nor of the effects of such modifications.

Nevertheless it was recognized that there is still opportunity for improving the feedwater heating by (*a*) accomplishing some if not all of the feedwater heating with heat integrated from the nitric acid process, and (*b*) using some if not all of the excess turbine-extraction steam, that over and above the requirements for process use.

Furthermore, it could be seen that when $R=4$, as much power should be produced as possible as long as it is produced from raw fuel with a second-law efficiency greater than 25 percent. Therefore, *when $R=4$ excess bleed steam*—produced at 37 percent efficiency even in the original, unimproved steam plant—*should be used to produce power to whatever extent is possible.*

In fact, even when $R=2.5$; needing a fuel-to-power efficiency of 40 percent, the conclusion that maximum power should be produced may be valid, for Sama et al. (1988) report incremental efficiency—additional output divided by additional fuel input—in excess of 40 percent even without integration. (This can be seen, in Sama et al., 1988, by observing in their Table 1 that there is a net "fuel savings" even when $R=2.5$; i.e., savings from decreased purchased power exceeds the cost of additonal fuel.) Sama et al. achieved that incremental efficiency by improving the feedwater heating. So, unless there is more than enough heat available for feedwater heating from the acid plant, it is conceivable that the negative effect of diminished feedwater heating may outweigh the positive effect of using all of the excess bleed steam for power. However, if that were the case, the net effect should not be very large. Hence, at $R=2.5$, *our approach will be to assume that excess bleed steam should be used for power production, and then to check whether diversion of steam to feedwater heating improves overall performance.*

It follows, therefore, that *feedwater heating should be done with heat from the Nitric Acid plant*, to the extent possible without causing an incremental decrease of output from the acid plant exceeding the incremental increase of output from the steam plant. Hence, further details regarding means for improving this subsystem were left for the subsequent integration stage.

Nevertheless, a steam-plant flowsheet was drawn, showing (*a*) the turbine, (*b*) the delivery of steam to the process users in the amounts dictated by Fig. 4, (*c*) the condensate return, and (*d*) the part of the feedwater system, including deaerator, taking the feedwater up to 100°C. From 100° feedwater to the turbine supply, the flowsheet was left blank, to be completed for each integration alternative to be tried. The flowsheet being described here would be identical to that in Fig. 5, except that the dashed box would be empty. (Figure 5 shows the completed flowsheet for one of the reconfigurations to be described later.)

Actually, at first, Item (*d*)—the deaerator subsystem—was not included on the flowsheet; this subsystem was added once it was realized that, since there was such an excessive abundance of heat available below 135°C, this part of the flowsheet could be completed without concern for the details of integration. Note also that this subsystem, adjusted in size, will serve to do the deaeration not only for the steam plant but also for steam to be raised in the acid plant.

*The $HNO_3$ Process.* The focus of this study was on the better utilization of thermomechanical exergy, and prospective changes in the chemical-process flowsheet and operating parameters were not analyzed. That is, the objective was to reduce exergy inefficiencies associated with heat transfer and power production. The key for reducing exergy consumptions associated with heat transfer is, of course, the matching of heating and heated stream temperatures, which depends also upon matching their heat capacities. Therefore, along with the exergies, temperatures have been shown on Fig. 3.

Summarizing Sama et al. (1989), first of all it is readily observed that *the heat to be taken from Stream 19 before introducing it into the absorber could be used much more effectively by heating of tailgas (Stream 22), which could save exergy consumed in E5 and E7 and which could also save much of the discard exergy loss of E8; also, further heating of tailgas with converter gas (such as at E3) might well be eliminated to avoid the discard exergy loss with T1 exhaust.* Implementation of these simple changes alone (utilizing low-temperature converter gas for the feedwater heating formerly done in *E*7) increased the net power output from the Nitric Acid plant from 3.965 to 5.325 MW.

As further means for improving the heat recovery in the $HNO_3$ plant—for reducing the recovery exergy consumptions—Sama et al. proposed (*a*) to raise the steam pressure and (*b*) to employ steam reheat after partial turbine expansion; each of these led to a significant additional power output, up to a maximum of 7.4 MW at 124 bar (1800 psi), an improvement of over 3.4 MW. [Without reheat and a top pressure of 80 bar (1160 psi) the output is 6.4 MW.]

For the heat from the principal source, the converter gas, Fig. 6 compares the matching with the original contractor's heat recovery system and that with a 100 bar top pressure along with reheat. Even though a large improvement is achieved by the reconfiguration, Fig. 6 shows that there is still room for more improvement by reducing the $\Delta T$ at high $T$ and, perhaps, by utilizing the abundance of low-$T$ waste heat. Conceivably these theoretical opportunities can be exploited by making other improvements and by effective integration of the acid and steam plants.

It is apparent from Fig. 6 that the primary cause of remaining temperature differences (recovery exergy consumptions) is the fact that the main heated stream is undergoing phase change. (These exergy consumptions would be shown even more vividly on a diagram with $[1-T_0/T]$ versus $Q$, where the consumption is equal to the area between the cooling and the heating curves; Kalina, 1985.) There are many schemes that might be proposed for reducing those consumptions, such as steam generation at more than one pressure (e.g., see El-Sayed and Gaggioli, 1989),

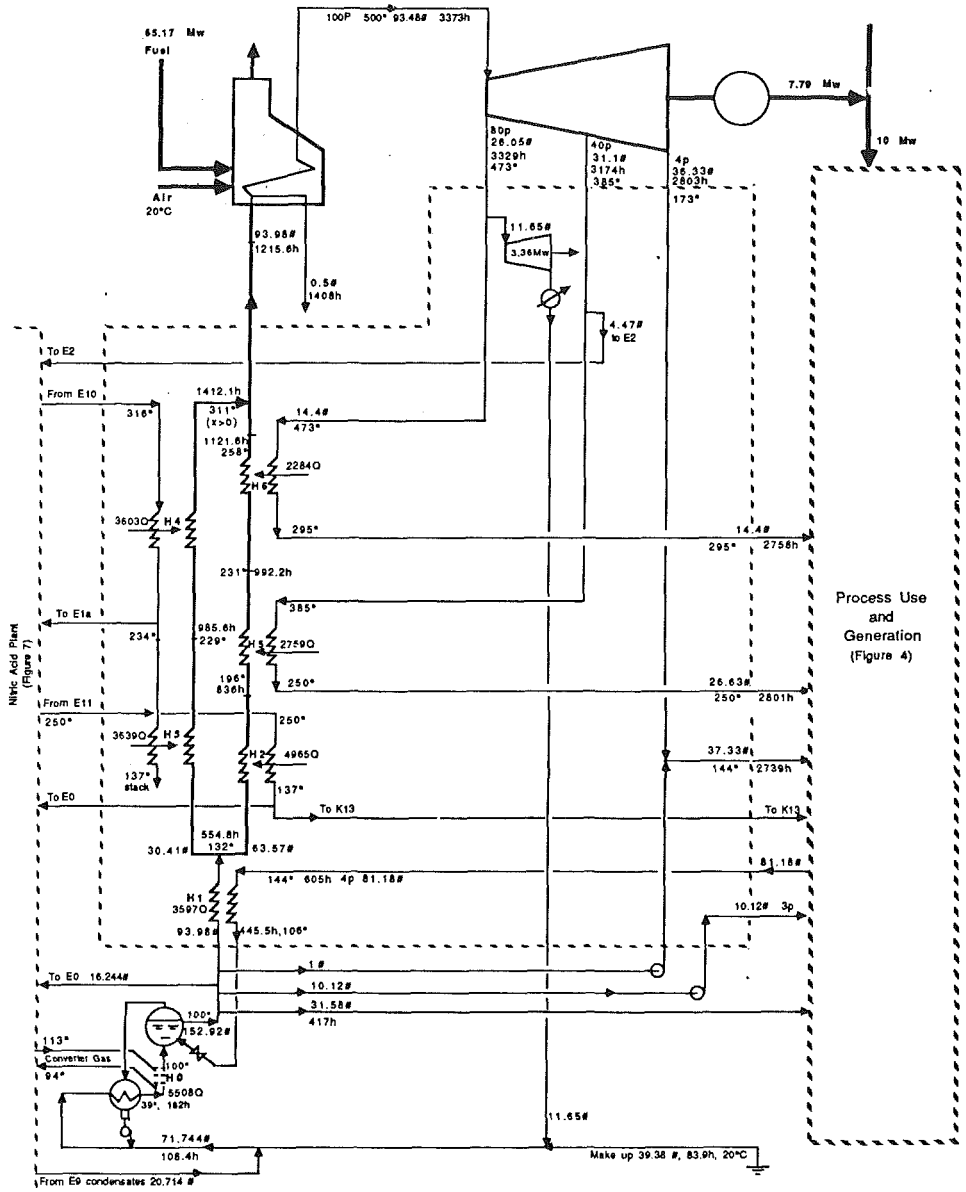


**Fig. 5 Steam plant and feedwater heating for Reconfiguration 1**

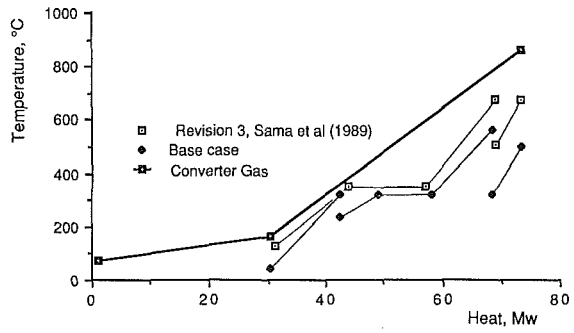


**Fig. 6 Converter gas cooling curve and use of heat in the base case and in Revision 3 of Sama et al. (1989)**

or the use of a binary working fluid (especially since $NH_3$ is at hand; El-Sayed and Tribus, 1985a, 1985b). Above all, though, to help avoid $\Delta T$ associated with phase-change profiles it is clear—especially since the tailgas is a large fraction of the converter gas—that it would pay to *split the converter gas stream and use a large part* (with heat capacity equal to that of the tailgas) *for heating the tailgas* to a much higher temperature before expansion in $T1$. (Then of course, effective use of the gas turbine exhaust heat, for example for feedwater heating, will be important.) Inasmuch as the $T$-$Q$ curves for the split converter gas and the tailgas will then be (essentially) parallel, and hence the heat transfer exergy consumption can be made as small as desired (with added capital cost for heat transfer surface, and for $T1$ as the entrance temperature is raised), *it is clear that tailgas heating for T1 power production is the optimal use of recovered heat, and therefore shall have priority over steam generation or feedwater heating.* A $\Delta T$ of 20°C (38°F) between converter- and tailgas has been adopted, as a reasonable figure for gas-to-gas heat exchangers; with gas leaving the converter at 854°C (14° higher than the original as a result of the heating and turbine-expansion of the $NH_3$, as described below) this leads to an 834°C (1530°F) turbine inlet temperature, quite reasonable with today's gas turbine technology.

It was assumed that the other of the two, split converter gas streams should be utilized, proportionately, in the way illustrated in Fig. 6, subject to some modification upon integration.

Another change, relatively minor (and unecessary), proposed here is the *preheating and turbine expansion of $NH_3$ before the converter*, to reduce large throttling and mixing losses there. (This may be an appropriate place to mention that for a broader, more all-inclusive study it would have been interesting if the given data had included chilled water consumption by the absorber and other users.)

Again, before proceeding to integration, a flowsheet—as complete as possible without integration—was drawn up on the basis of the foregoing decisions. Steam and steam-power generation were absent, as well as the utilization of much of the potentially recoverable heat. Figure 7, but with the dashed box empty, is representative of this incomplete acid plant flowsheet. (Figure 7 shows the complete flowsheet for one of the eventual reconfigurations.)

## Integration

The italicized phrases in the preceding section describe the decisions that were made regarding each of the three principal subsystems independently, and some conclusions that are relevant to the integration of the three. The details of implementation, short of integration, would be shown—if the dashed boxes were empty—by Figs. 5 and 7, as well as by Fig. 4.

What remains to be done? Besides the integration already included (supplying heat to the heat pump) in Fig. 4, the only recognizable opportunity without excessive complications for further integration of the "Process Use and Generation" subsystem with the other two is the use of the 4 bar condensate. It is clear that because of its relatively low temperature ($T = 144°C$) it is suited only for low-$T$ feedwater heating. As shown in Fig. 5 it was simply used directly for heating the deaerated feedwater going to the steam plant (inasmuch as its heat capacity rate is about the same) to 132°C.

Once the deaerating subsystem and heating to 132°C has been completed, for every reconfiguration to be considered all that remains to be done in order to accomplish the integration is: (1) The steam-plant feedwater heating system (for $T >$ 132°C) needs to be designed, including the possibility of power generation from excess bleed steam, in conjunction with (2) the steam and steam-power generation subsystem of acid plant.

The exergy sources ("fuels") available for these heating and power production purposes are:

From the acid plant, (Fig. 7),

(*a*) the thermal exergy of the split converter gas stream that is not employed for heating tailgas, from 854°C down to 137°C, with $mc_p$ = 16.17 kW/°C and $Q$ = 11,600 kW available;

(*b*) the thermal exergy of the hot tailgas exhaust from $T1$, from 422.5°C down to 234°C with $mc_p$ = 43.94 kW/°C and $Q$ = 8170 kW and, after diverting a part of the stream for heating the ammonia, from 234°C down to 137°C with $mc_p$ = 37.5 kW/°C and $Q$ = 3639 kW;

(*c*) the thermal exergy of the converter gas stream leaving the tailgas heater, with $mc_p$ = 43.94 kW/°C and $Q$ = 4965 kW, from 250°C down to 137°C;

(*d*) at 137°C, the combined converter gas streams, with $mc_p$ = 292 kW/°C, which is larger than the combined $mc_p$ in (*a*) and (*c*) because of the exothermic separation.

It was because of the large heat capacity of the converter gas stream below 137°C that the $Q$ of the other sources—like (*a*), (*b*), and (*c*)—were evaluated only down to 137°C; it was apparent that they would not be needed below this temperature.

From the steam plant (Fig. 5), the sources are:

(*e*) the thermomechanical exergy (4500 kW) of the 11.65 tons/hr of 80 bar steam at 473°C bled (along with the 14.4 tons/hr to be delivered to process use) from the turbine;

(*f*) the thermal exergy of the 14.4 tons/hr of 80 bar steam less that at the 80 bar saturated conditions delivered to process use, with $mc_p$ = 12.8 kW/°C and $Q$ = 2284 kW available, from 473°C down to 295°C;

(*g*) the thermomechanical exergy (1500 kW) of the 4.47 tons/hr of 40 bar steam at 385°C bled (along with the 26.6 tons/hr to be delivered to process use) from the turbine;

(*h*) the thermal exergy of the 26.63 tons/hr of 40 bar steam less that at the 40 bar saturated conditions delivered to process use, with $mc_p$ = 20.4 kW/°C and $Q$ = 2759 kW available, from 385°C down to 250°C;

(*i*) the 36.33 tons/hr from the turbine at 4 bar, 173°C (and exergy 7497 kW) less the 37.33 tons/hr of saturated steam (with exergy 7478 kW) to process.

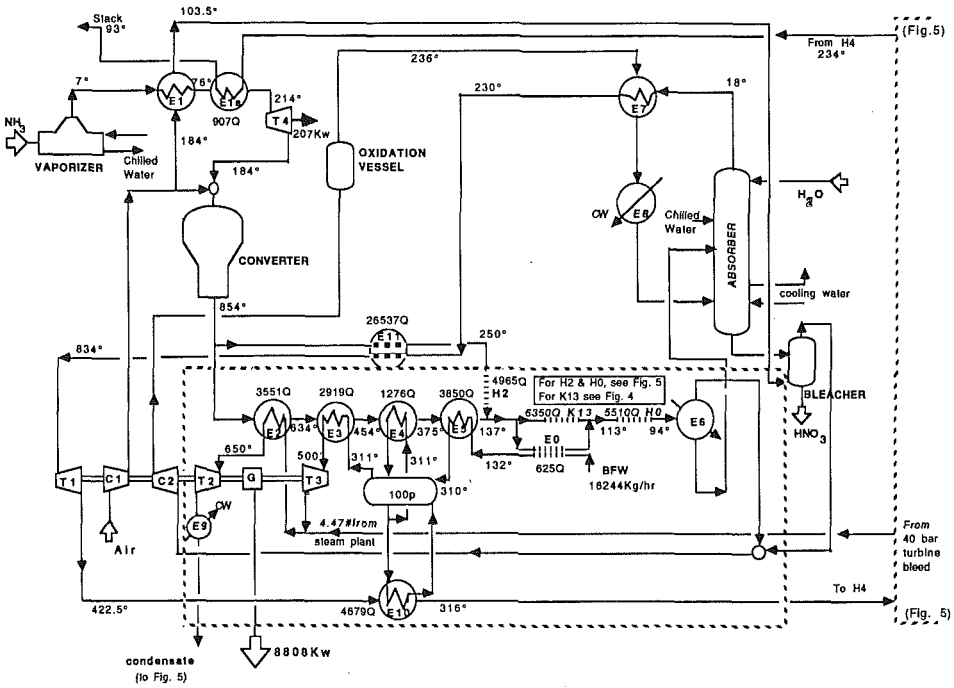


**Fig. 7 Nitric acid plant for Reconfiguration 1**

As mentioned above, to accomplish the integration: (1) The steam-plant feedwater heating system (for $T > 132°$) needs to be designed, in conjunction with (2) the steam and steam-power generation subsystem of the acid plant. Clearly, then, since the steam-plant feedwater must be heated, the order of priorities for efficient utilization of the available heat sources is first to use them *as efficiently as possible* (using reasonable minimum $\Delta T$ in the heat exchangers) for feedwater heating, and *then* to use the remaining heat for power generation in a manner like that discussed by Sama et al. (1989). That is, if the steam-plant feedwater is heated in an optimal manner, no practical opportunity for efficient resource utilization could be lost. The ultimate limits upon overall resource utilization, then, would depend upon the design of the subsystem for utilizing the remaining heat.

**(1) The Steam-Plant Feedwater Heating Subsystem (Reconfiguration 1, Fig. 5).** Before the steam-plant feedwater heating system was designed it was noticed that, while heat from the acid plant would be imported for feedwater heating, there would be no need to transfer heat from the steam plant, namely Sources (*f*) and (*h*) above, to the acid plant. That is, since the specific heat of vapor is less than that of liquid and since the flow rates are less, Sources (*f*) and (*h*) could be used up for feedwater heating.

It was, then, very straightforward to design an "optimal" feedwater subsystem. There would be two heat exchangers for desuperheating the turbine bleed steam, which would then go to process [i.e., for utilizing Sources (*f*) and (*h*)] and the amount of energy to be taken therefrom was known. The remaining amount of energy needed for feedwater heating, which would come from the acid plant, could immediately be evaluated. All that remained, then, was to construct a heat exchanger network for transferring bleed steam and acid plant energy to the feedwater with a minimum of exergy consumption. It is assured that this consumption would be a minimum (and in turn that the amount of acid-plant exergy source left over for producing power would be a maximum) if the network were constructed in a manner that, for every heat exchanger taking heat from the acid plant, had matching heat capacities for the heating and the heated streams (with the $\Delta T$ between streams chosen arbitrarily). It would be straightforward to construct such a network.

The network shown in Fig. 5 does not quite accomplish this objective but it is nevertheless recommended because of its simplicity. The branch stream of feedwater, heated in H4 by tailgas, is almost perfectly matched. Heat exchanger H2 that utilizes Source (*c*), converter gas leaving the tailgas heater at 250°C; could have been matched better; for example, additional converter gas at 250°C might have been extracted from Source (*a*). This would have improved the second-law efficiency of feedwater heating but was judged to be unduly complicated. In the same vein, assumed not worth the complication, the use of the bleed steam en route to process could have been complemented by heat available from Source (*a*).

Once the heat exchanger network was completed, the boiler fuel consumption was calculated. (Even though the average $\Delta T$ between products of combustion and $H_2O$ is lower, the boiler efficiency was assumed to equal the original value (Fig. 2), because the amount of heat to be transferred is lower. If this assumption were not valid, it would be necessary to put a recuperator on the boiler stack to achieve our final results. It should be noted, though, that our results could be improved even more by reducing combustion irreversibility by using air preheat with stack gases or heat from Sources (*a*) through (*h*).)

Another detail needs to be mentioned regarding Fig. 5. Recall, it was assumed that excess bleed steam would be expanded in condensing turbines. Notice that the turbine for expanding the excess 4.47 tons/hr of 40 bar bleed steam is not shown in the figure; the reason is explained forthwith. Finally, we should mention that although Exchangers $H_2$, $H_3$, and $H_4$ (and the deaerator subsystem) are shown schematically on Fig. 5, their actual location might be at the acid plant.

**(2) Acid Plant Steam-Power Subsystem (Reconfiguration 1, Fig. 7).** Reconfiguration 1 seeks to accomplish the steam plant feedwater heating with nitric acid process heat at appropriate temperatures, while producing "maximum" steam power with the remaining process heat, subject to the self-imposed constraint that the steam production would be at 100 bar and to a superheat temperature of 500°C, the same conditions as in the steam plant. As mentioned earlier, the scheme for steam power production at the nitric acid plant was taken to be essentially the same as that developed by Sama et al. (1989), scaled down because of the lesser amount of converter gas available, and modified to account for the availability of hot exhaust from the tailgas turbine. Furthermore, in Sama et al. (1989) steam reheat is incorporated at 40 bar (and up to 650°C). Rather than use a separate condensing turbine for the excess 40 bar steam from the steam-plant turbine, that steam could be joined with that of the nitric acid plant before reheating and expansion. (It had been found by Sama et al. that 40 bar was essentially the optimal pressure for reheating.)

The exergy available for production of steam power is all of that from Source (*a*), the converter gas not used for tailgas heating, plus that portion of Source (*b*), tailgas turbine exhaust, that was not used for feedwater heating, that is, the portion from 422.5°C down to 316°C. For the modified system of Sama et al., it is assured that (subject to the 100 bar, 500°C constraint) no undue exergy consumptions will occur provided the tailgas heat, between these two temperatures, is used in parallel with the converter gas heat. That determines the physical configuration of the system, shown in Fig. 7. Only a single independent decision variable, the design parameter, remains. For example, one can choose the flow rate of feedwater (at 100°C) to the heat exchanger train as the parameter, and then find the minimum value that does not violate the $\Delta T_{min}$ criterion that has been established. In actuality, we did not have to determine the final flow rate parametrically. We assumed that, as in the earlier work of Sama et al. and shown in Fig. 6, the minimum $\Delta T$ would occur at the place where the converter gas reaches 137°C, the place where its heat capacity changes. Then, the energy balances through the heat exchangers and steam turbines determine the flow rate, along with the turbine output power. The results are shown by Fig. 7, and it can be seen that the pinch point is indeed at the assumed location, E5.

Figures 5 and 7, then, show the final results of integration, for Reconfiguration 1. The implications of Reconfiguration 1 on fuel consumption and net power production are shown by the first two rows of Table 3, along with the effective fuel savings (in MW) when $R = 2.5$ and $R = 4$ (and when $R = 4.5$); i.e., "Fuel Savings" = [Base Fuel − Reconfiguration Fuel] + $R^*$ [Reconfiguration Net Power − Base Net Power], at any $R$. (At a fuel cost of say \$100/kW-yr (\$3.35/$10^6$ Btu), the annual monetary savings could be determined by multiplying the "fuel savings" by 100,000.)

While the results are commendable, a few other reconfigurations were investigated in order to test the sensitivity of the results to various assumptions, judgments, and decisions made in the course of developing Reconfiguration 1.

**Reconfigurations 2 and 3.** Reconfigurations 2 and 3 differed from Number 1 only in the change of the constraints on the pressure and/or superheat temperature of steam generation in the acid plant. In Reconfiguration 2, the superheat temperature at the nitric acid plant was raised to 650°C. In Reconfiguration 3, the steam pressure there was also raised, to 124 bars. From the results shown in Table 3, all three reconfigurations lead to substantial reduction of fuel usage. Reconfigurations 2 and 3 make incremental improvements over No. 1, but these savings

Table 3 Comparison of reconfigurations to base case

| | Fuel,F (MW) | Net Power, P | Fuel Savings R = 2.5 | Fuel Savings R = 4 | Fuel Savings R = 4.5 |
|---|---|---|---|---|---|
| Original, Base Case (Contractor's integrated option) | 76.70 | 7.83 | | | |
| Rec'n 1, 100 bar gen'n & power at HNO3 plant 500°C to T3; turbine exp'n of excess 80 bar bleed | 65.17 | 20.22 | 42.51 | 61.09 | 67.29 |
| Rec'n 2, 100 bar gen'n & power at HNO3 plant 650°C to T3; turbine exp'n of excess 80 bar bleed | 65.17 | 20.39 | 42.93 | 61.77 | 68.05 |
| Rec'n 3, 124 bar gen'n & power at HNO3 plant 650°C to T3; turbine exp'n of excess 80 bar bleed | 64.36 | 20.23 | 43.34 | 61.94 | 68.14 |
| Rec'n 4, 100 bar gen'n & power at HNO3 plant 500°C steam to Turbine 3 | 54.64 | 16.88 | 45.10 | 58.26 | 62.79 |
| Rec'n 5, 100 bar gen'n & power at HNO3 plant 650°C steam to Turbine 3 | 54.64 | 17.06 | 45.14 | 58.98 | 63.60 |
| Rec'n 6, 124 bar gen'n & power at HNO3 plant 650°C steam to Turbine 3 | 53.82 | 16.89 | 45.53 | 59.12 | 63.65 |
| Rec'n 7, 100 bar generation at HNO3 plant | 42.60 | 12.29 | 45.25 | 51.94 | 54.17 |

*For a fuel cost of $100/kW-yr ($3.35/million Btu), the annual monetary savings equals 100,000 times the "Fuel Savings."*

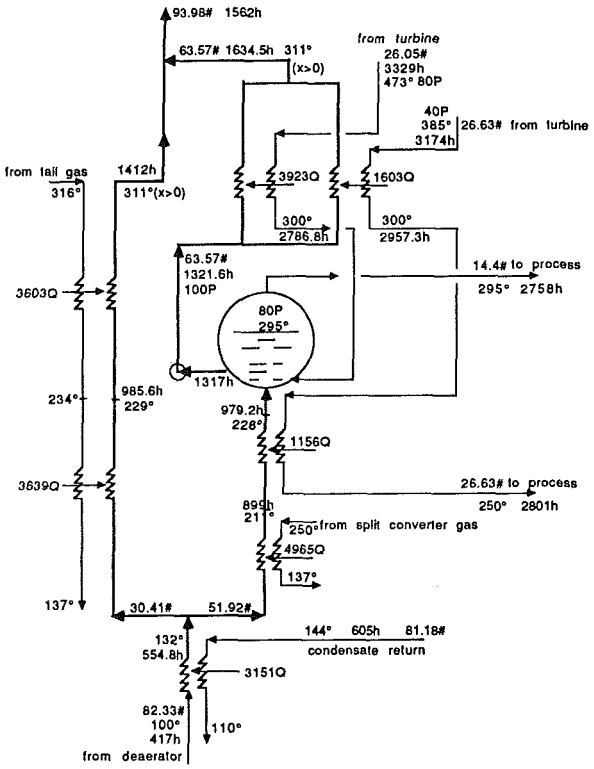


Fig. 8 Steam plant and feedwater heating for Reconfiguration 4

might not justify the added cost of operating at higher top temperature and pressure.

**Reconfigurations 4, 5, and 6.** One of the judgments made during the course of developing the foregoing reconfigurations was that when $R = 4$ maximum power output should be sought and, probably, when $R = 2.5$. Reconfigurations 4, 5, and 6 are like Nos. 1, 2, and 3, respectively, except that the excess steam bled from the power-plant turbine, sources (*e*) and (*g*), is used for feedwater heating rather than for power. The feedwater heating schematic for Reconfiguration 4 is shown in Fig. 8, and the effect is shown in Table 3 by comparing Reconfigurations 1 and 4. Likewise, compare Nos. 2 and 5, and 3 and 6. As expected, when $R = 4$ Nos. 1, 2, and 3 are better. However, it happens that when $R = 2.5$ Reconfigurations 4, 5, and 6 are preferable. Consequently, recognizing that when $R = 2.5$ it might be preferable to strive primarily for even

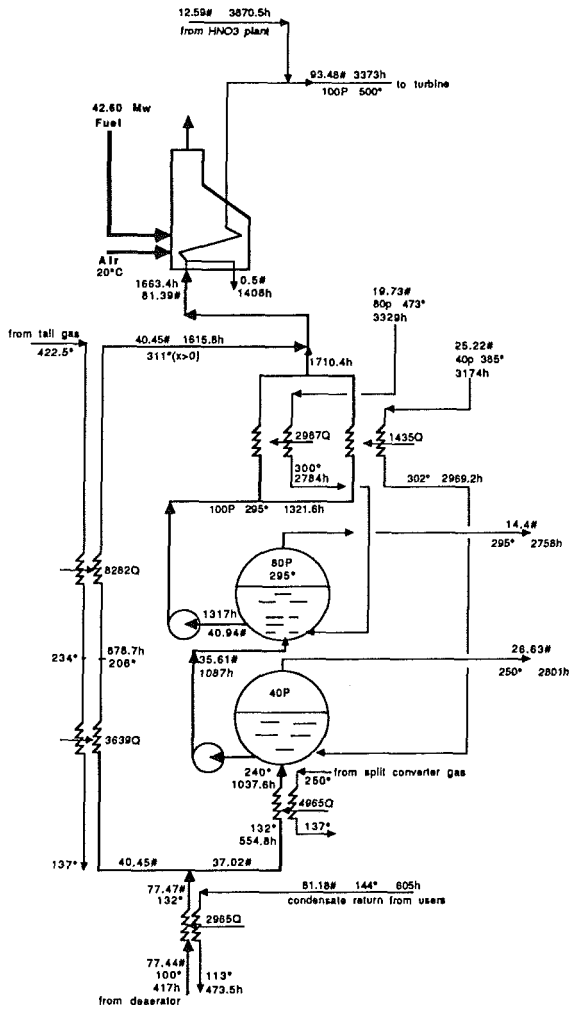


Fig. 9 Steam plant and feedwater heating for Reconfiguration 7

more fuel savings at the expense of power production, another reconfiguration was tried, called No. 7 here.

**Reconfiguration 7.** In this reconfiguration there is no steam power production at the nitric acid plant; all of the recoverable heat is used to produce steam for the original steam plant; see Fig. 9. Interestingly, in this case to satisfy property relation and energy balance constraints, not all of the excess bleed steam

from the original turbine could be used for feedwater heating (at least not without major revision of the networking), so some is used for powering generation. Table 3 shows that, indeed, when $R = 2.5$, this is slightly better than Reconfigurations 4 and 5, but not quite as good as No. 6.

## Closure

We have presented several reconfigurations that improve the performance of the overall plant significantly over the original conceptual design. In fact, we do not recommend any one of the reconfigurations over the others. They differ from one another not only in fuel savings but also in complexity and in capital costs. While Reconfiguration 2 may appear to be the best compromise when $R = 4$, and No. 7 when $R = 2.5$, the trade-off between these factors might well be weighed more carefully before a final recommendation would be made.

Our intention has been, simply, to show that exergy analysis is a valuable tool for achieving substantial improvements in process plant energy utilization, using conventional hardware. They are by no means presented as "the ultimate" results. Yet, to achieve them required diligent and methodical analysis of the exergy numbers along with a basis against which to compare the numbers, together with experience. Indeed, with additional and/or more systematic pursuit, further improvements might be achieved (especially if additional flowsheet complications, or more advanced technologies, or revisions of the nitric acid process were entertained). For examples, the explicit use of second-law efficiencies and costing in ways like those illustrated by El-Sayed and Gaggioli (1987, 1988, 1989) might be employed to help find further improvements. In any case, though, it is granted that in the current state of the art of exergy analysis there is "a very heavy dependence on judgment and past experience," in the words of one reviewer. How can the art be improved, to help overcome this shortcoming? One way, mentioned by another reviewer, is to meld exergy analysis with systematic procedures like pinch technology. Another approach is the development of interactive computer programs (e.g., El-Sayed and Gaggioli, 1987, 1988, 1989). All of these might well be incorporated into expert systems, which incorporate the tools, experience, and judgment of second-law practitioners (e.g., Kowalski, 1987; Melli et al., 1990).

## Acknowledgments

Daniel Finkenthal and William Cooley did the initial work and many of the calculations on this project, as seniors in the ULowell course ME 423, Design of Thermal Systems, Spring 1988. Their work, supported by the Center for Productivity Enhancement at ULowell, was very important, especially for the revisions of the process steam use and generation subsystem. Also, we want to thank all of the reviewers for their patience, diligence, and many helpful comments.

## References

El-Sayed, Y. A., and Gaggioli, R., 1987, 1988, "The Integration of Synthesis and Optimization for Conceptual Designs of Energy Systems," *Second Law Analysis of Thermal Systems*, ASME Vol. I00236 (1987); also, ASME *Journal of Energy Resources Technology*, Vol. 110, pp. 109–113 (1988).

El-Sayed, Y. A., and Gaggioli, R., 1989, "A Guide to the Structural Improvement of Energy Systems," *Thermodynamic Analysis and Improvement of Energy Systems*, International Academic Publishers, Beijing, pp. 175–183 (Pergamon Press, Oxford–New York).

El-Sayed, Y. A., and Tribus, M., 1985a, "Thermodynamic Properties of Water–Ammonia Mixtures—Theoretical Implementation for Use in Power Cycles Analysis," *Analysis of Energy Systems—Design and Operation*, ASME Vol. AES-1, pp. 89–96.

El-Sayed, Y. A., and Tribus, M., 1985b, "A Theoretical Comparison of the Rankine and Kalina Cycles," *Analysis of Energy Systems—Design and Operation*, ASME Vol. AES-1, pp. 97–102.

Gaggioli, R., Patulski, S., Yoon, J., Latus, A., and Obert, E., 1975, "Pinpointing the Inefficiencies in Energy Conversion Systems," *Proc. American Power Conference*, Vol. 37, pp. 656–670.

Gaggioli, R., Qian, S., Sama, D., and El-Sayed, Y., 1988, "Second Law Analysis for Efficient Process Design: Integrating a New $HNO_3$ Plant Into an Industrial Utility System," presented at the Symposium on Energy Systems Analysis, ASME Winter Annual Meeting, Chicago, IL.

Kalina, A., 1985, "A Method of Analysis of Energy-Covnersion Systems," *Analysis of Energy Systems*, ASME Vol. AES-1, pp. 103–108.

Kowalski, A. D., 1987, "Expert System Possibilities for Process Optimization Using Second Law Analysis," *Second Law Analysis of Thermal Systems*, ASME Vol. I00236, pp. 177–182.

Linnhoff, B., 1987, Private communication to attendees at the sessions of the Advanced Energy Systems Division, ASME Winter Annual Meeting, Boston, MA.

Linnhoff, B., and Alanis, F., 1988, "Integration of a New Process Into an Existing Site—A Case Study," *Approaches to the Design and Optimization of Thermal Systems*, ASME Vol. AES-7, pp. 25–40.

Melli, R., Paoletti, B., Razze, M., and Sciubba, E., 1990, "SYSLAM: An Interactive Expert System Approach to Powerplant Design and Optimization," *A Future for Energy*, Proc. of the Florence World Energy Symposium, Florence, Italy, May 31–June 5, Pergamon Press.

Petit, P., and Gaggioli, R., 1980, "Second Law Procedures for Evaluating Processes," *Thermodynamics: Second Law Analysis*, Am. Chem. Soc. Symposium Series, Vol. 122, pp. 15–38.

Rodriguez, L., 1980, "Calculation of Available Energy Quantities," *Thermodynamics: Second Law Analysis*, Am. Chem. Soc. Symposium Series, Vol. 122, pp. 39–60.

Sama, D. A., Qian, S., Finkenthal, D., Cooley, W., and Gaggioli, R., 1988, "Second Law Analysis for Process and Energy Engineering: Use in a Steam/Power Cycle," *Proc. 10th Industrial Energy Technology Conference*, The Energy Laboratory, Texas A&M U., pp. 406–415.

Sama, D. A., Qian, S., and Gaggioli, R., 1989, "A Common-Sense Second Law Approach for Improving Process Efficiencies," *Thermodynamic Analysis and Improvement of Energy Systems*, International Academic Publishers, Beijing, pp. 520–531 (Pergamon Press, Oxford–New York).

from the original turbine could be used for feedwater heating (at least not without major revision of the networking), so some is used for powering generation. Table 3 shows that, indeed, when $R = 2.5$, this is slightly better than Reconfigurations 4 and 5, but not quite as good as No. 6.

## Closure

We have presented several reconfigurations that improve the performance of the overall plant significantly over the original conceptual design. In fact, we do not recommend any one of the reconfigurations over the others. They differ from one another not only in fuel savings but also in complexity and in capital costs. While Reconfiguration 2 may appear to be the best compromise when $R = 4$, and No. 7 when $R = 2.5$, the trade-off between these factors might well be weighed more carefully before a final recommendation would be made.

Our intention has been, simply, to show that exergy analysis is a valuable tool for achieving substantial improvements in process plant energy utilization, using conventional hardware. They are by no means presented as "the ultimate" results. Yet, to achieve them required diligent and methodical analysis of the exergy numbers along with a basis against which to compare the numbers, together with experience. Indeed, with additional and/or more systematic pursuit, further improvements might be achieved (especially if additional flowsheet complications, or more advanced technologies, or revisions of the nitric acid process were entertained). For examples, the explicit use of second-law efficiencies and costing in ways like those illustrated by El-Sayed and Gaggioli (1987, 1988, 1989) might be employed to help find further improvements. In any case, though, it is granted that in the current state of the art of exergy analysis there is "a very heavy dependence on judgment and past experience," in the words of one reviewer. How can the art be improved, to help overcome this shortcoming? One way, mentioned by another reviewer, is to meld exergy analysis with systematic procedures like pinch technology. Another approach is the development of interactive computer programs (e.g., El-Sayed and Gaggioli, 1987, 1988, 1989). All of these might well be incorporated into expert systems, which incorporate the tools, experience, and judgment of second-law practitioners (e.g., Kowalski, 1987; Melli et al., 1990).

## Acknowledgments

Daniel Finkenthal and William Cooley did the initial work and many of the calculations on this project, as seniors in the ULowell course ME 423, Design of Thermal Systems, Spring 1988. Their work, supported by the Center for Productivity Enhancement at ULowell, was very important, especially for the revisions of the process steam use and generation subsystem. Also, we want to thank all of the reviewers for their patience, diligence, and many helpful comments.

## References

El-Sayed, Y. A., and Gaggioli, R., 1987, 1988, "The Integration of Synthesis and Optimization for Conceptual Designs of Energy Systems," *Second Law Analysis of Thermal Systems*, ASME Vol. I00236 (1987); also, ASME *Journal of Energy Resources Technology*, Vol. 110, pp. 109–113 (1988).

El-Sayed, Y. A., and Gaggioli, R., 1989, "A Guide to the Structural Improvement of Energy Systems," *Thermodynamic Analysis and Improvement of Energy Systems*, International Academic Publishers, Beijing, pp. 175–183 (Pergamon Press, Oxford-New York).

El-Sayed, Y. A., and Tribus, M., 1985a, "Thermodynamic Properties of Water-Ammonia Mixtures—Theoretical Implementation for Use in Power Cycles Analysis," *Analysis of Energy Systems—Design and Operation*, ASME Vol. AES-1, pp. 89–96.

El-Sayed, Y. A., and Tribus, M., 1985b, "A Theoretical Comparison of the Rankine and Kalina Cycles," *Analysis of Energy Systems—Design and Operation*, ASME Vol. AES-1, pp. 97–102.

Gaggioli, R., Patulski, S., Yoon, J., Latus, A., and Obert, E., 1975, "Pinpointing the Inefficiencies in Energy Conversion Systems," *Proc. American Power Conference*, Vol. 37, pp. 656–670.

Gaggioli, R., Qian, S., Sama, D., and El-Sayed, Y., 1988, "Second Law Analysis for Efficient Process Design: Integrating a New $HNO_3$ Plant Into an Industrial Utility System," presented at the Symposium on Energy Systems Analysis, ASME Winter Annual Meeting, Chicago, IL.

Kalina, A., 1985, "A Method of Analysis of Energy-Covnersion Systems," *Analysis of Energy Systems*, ASME Vol. AES-1, pp. 103–108.

Kowalski, A. D., 1987, "Expert System Possibilities for Process Optimization Using Second Law Analysis," *Second Law Analysis of Thermal Systems*, ASME Vol. I00236, pp. 177–182.

Linnhoff, B., 1987, Private communication to attendees at the sessions of the Advanced Energy Systems Division, ASME Winter Annual Meeting, Boston, MA.

Linnhoff, B., and Alanis, F., 1988, "Integration of a New Process Into an Existing Site—A Case Study," *Approaches to the Design and Optimization of Thermal Systems*, ASME Vol. AES-7, pp. 25–40.

Melli, R., Paoletti, B., Razze, M., and Sciubba, E., 1990, "SYSLAM: An Interactive Expert System Approach to Powerplant Design and Optimization," *A Future for Energy*, Proc. of the Florence World Energy Symposium, Florence, Italy, May 31–June 5, Pergamon Press.

Petit, P., and Gaggioli, R., 1980, "Second Law Procedures for Evaluating Processes," *Thermodynamics: Second Law Analysis*, Am. Chem. Soc. Symposium Series, Vol. 122, pp. 15–38.

Rodriguez, L., 1980, "Calculation of Available Energy Quantities," *Thermodynamics: Second Law Analysis*, Am. Chem. Soc. Symposium Series, Vol. 122, pp. 39–60.

Sama, D. A., Qian, S., Finkenthal, D., Cooley, W., and Gaggioli, R., 1988, "Second Law Analysis for Process and Energy Engineering: Use in a Steam/Power Cycle," *Proc. 10th Industrial Energy Technology Conference*, The Energy Laboratory, Texas A&M U., pp. 406–415.

Sama, D. A., Qian, S., and Gaggioli, R., 1989, "A Common-Sense Second Law Approach for Improving Process Efficiencies," *Thermodynamic Analysis and Improvement of Energy Systems*, International Academic Publishers, Beijing, pp. 520–531 (Pergamon Press, Oxford-New York).

# DISCUSSION

### B. Linnhoff [2]

The paper "Integration of a New Process Into an Existing Site—A Case Study in the Application of Pinch Technology" by B. Linnhoff and F. J. Alanis which appears in this issue of the *Journal of Engineering for Gas Turbines and Power* is based on a previous paper presented at the 1987 ASME Winter Annual Meeting in Boston. In both papers, we describe an improved site energy system and process design based on simplifying assumptions using Pinch Technology. The simplifying assumptions are necessary to define clearly an overall cost objective.

Gaggioli et al. took up the problem in their paper "Integration of a New Process Into an Existing Site—A Case Study in the Application of Exergy Analysis" and undertook to solve it using exergy analysis. In so doing they altered some of the assumptions set down in our original paper, which, it appears, were not sufficiently highlighted to avoid confusion. The end result is that each party has presented solutions to differing problems.

We are setting out below those assumptions made in the original paper that are key to keeping alternative solutions on a comparable basis but were not observed by Gaggioli et al. :

**1 Gas Turbine Inlet Temperature.** Our paper stipulates that parameters for streams should not be changed. This includes the recovery turbine feed stream. The turbine inlet temperature was thus set at 536°C. Gaggioli et al. increased this temperature to 834°C. It is clear that higher turbine inlet temperatures will improve shaftwork recovery. However, the chosen temperature of 536°C represents a widely accepted practical maximum. For higher temperatures, converter development would be required as well as an expensive (though feasible) air-cooled expander. For temperatures higher than 710°C, we know of no available technology. It appears that Gaggioli et al.'s choice (834°C)

[2]Centre for Process Integration, Department of Chemical Engineering, The University of Manchester Institute of Science and Technology, Manchester M60 1QD, United Kingdom.

simply stems from the process source temperature (854°C) minus a $\Delta T_{min}$ (20°C), without consideration of equipment issues.

For the purpose of comparison, it would not have mattered whether the turbine inlet temperature was constrained to 536°C, or 710°C, or any other temperature. To keep the comparison valid, however, we feel that future studies should adhere to the value we set.

**2 Minimum Approach Temperature.** From experience with industrial applications, we set $\Delta T_{min}$ = 28°C throughout to reflect a likely optimum capital-energy trade-off. Violation of this value is obviously possible and may be of overall financial benefit. However, without capital cost data there is simply no basis for a decision. Once again, the chosen value ought to be adhered to if valid comparisons are to be made. Gaggioli et al. used values for $\Delta T_{min}$ as low as 5°C.

**3 Additonal Site Steam Mains.** In the problem as formulated by ourselves, the separate processes on site use and generate steam interacting with three distinct site steam mains (at 80 bar, 40 bar, and 4 bar). Heat transfer between processes can only be achieved via these existing mains. Other levels of steam are a consequence of steam throttling within processes and do not represent site mains. Additional site mains were to be disallowed; not only would new site mains be uneconomic almost without a doubt but the admission of new mains would also render the problem meaningless. An infinite number of thermodynamic solutions would become possible. Any problem, however complex initially, could be set up cascade fashion and be solved thermodynamically with little regard to capital cost and little or no "method" if there are no restrictions on mains. This would represent an entirely impractical and artificial situation. Gaggioli et al.'s solution sets up such a "thermodynamic cascade" and requires three additonal site steam mains.

The solution offered in our paper requires changes in the existing mains' pressures and flow rates. The ability of turbine generator stages and of steam distribution systems to handle such changes could be a matter of debate. Our changes imply variations in volumetric flow rates in any turbine stage of less than 30 percent.

**4 Condensate Handling System.** In our paper, condensate is shown to return to the deaerator at 80°C (streams No. 24, 26, 30, 32, and 43). That is, the process steam demands shown are net after generation of flash steam. Table 1 confirms this assumption. Nevertheless, Gaggioli et al. assumed that condensate exits each plant at saturated conditions and that additional heat is available between exit conditions and the 80°C we cited. Thus, they violated the heat balance as given per our data and effectively used the heat available from condensate twice.

"Backing out" these four differences from Gaggioli et al.'s solution we account for more than the differences in savings between the two solutions. Note that the effect of a removal of restrictions is open to interpretation in the context of specific solutions; the benefits obtained must depend on the use made of such removal by the solution in question. Our statement, by contrast, is unambiguous as it relates to objective "targeting."

Addressing practical judgment, our solution introduces alternative heat exchangers in the Nitric Acid plant and central boiler, which are in line with the assumptions and constraints set down at the outset and appear feasible in economic and practical terms. Gaggioli et al.'s solution introduces three new stream mains and it requires new expander and converter designs for hitherto unobtainable operating conditions. We emphasize that the assumptions chosen, while intended to enable valid comparisons to be made, also have a sensible and practical engineering basis.

In summary, we feel that a comparison of the two solutions is difficult. There are plain differences in assumptions probably caused by a difference in philosophy. Our solution aims at the best achievable thermodynamic performance subject to clear constraints. Gaggioli et al.'s solution aims at thermodynamic efficiency setting aside many of these constraints. Still, we feel that a comparison of Pinch Technology and Exergy Analysis has been made possible by these two papers. We suggest it has become clear that Pinch Technology views an overall problem globally and that it is less dependent on the structure and equipment selection of any particular solution. The other main difference between the techniques has been highlighted inadvertently by the differences in assumptions made. In an "ideal" design environment (any number of steam levels, etc.) there would be few pinches and Pinch Technology would be of limited use. Exergy Analysis, by contrast, would be an adequate tool to support the knowledgeable designer.

In a more practical environment with given constraints (limits to the number of levels and stages, etc.) there are pinches. Now, Exergy Analysis does not offer the designer formalized help in "translating" equipment considerations into overall system effects. Pinch Technology, by contrast, in its almost abstract targeting rigor, establishes how specific equipment parameters influence an overall solution within given constraints. Pinch Technology allows the designer to formulate consistently the most efficient thermodynamic solutions for complex situations that are practically constrained.

## Authors' Closure

The economic difference between the solutions presented in our paper and in the paper by Linnhoff and Alanis in this issue is clearly shown by Fig. 10 below, which is an adaptation of Fig. 18 of Linnhoff and Alanis.

In view of the uncertainty with regard to whether air preheat is allowable, which even Professor Linnhoff admits, and on which we commented in our Discussion of their paper, we maintain that the comparison between the solutions should be made on a non-air-preheat basis. When one compares the increase in savings above the contractor's design, which is, after all, all that we or Linnhoff and Alanis can take credit for, the results are, in millions of dollars per year:

| | $R$ = 2.5 | $R$ = 4.5 |
|---|---|---|
| Exergy analysis | 4.1 | 6.3 |
| Pinch technology without preheat | 1.4 | 1.7 |
| Pinch technology with air preheat | 1.7 | 2.2 |

In any case, our savings are several times better than the savings from pinch technology.

Professor Linnhoff, however, challenges our results. With all due respect to Professor Linnhoff, we believe that he is trying to impose new constraints which were not set forth when he first posed the challenge problem. There is a virtual one-to-one correspondence between the new constraints that he would like to impose, and those features of our design that

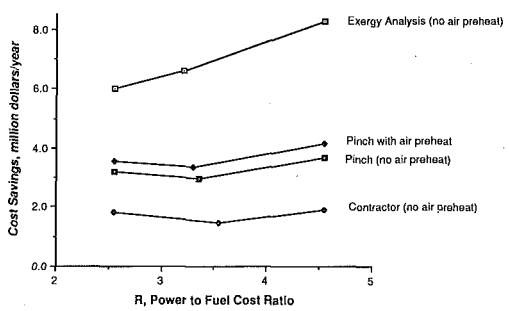


Fig. 10

simply stems from the process source temperature (854°C) minus a $\Delta T_{min}$ (20°C), without consideration of equipment issues.

For the purpose of comparison, it would not have mattered whether the turbine inlet temperature was constrained to 536°C, or 710°C, or any other temperature. To keep the comparison valid, however, we feel that future studies should adhere to the value we set.

**2 Minimum Approach Temperature.** From experience with industrial applications, we set $\Delta T_{min}$ = 28°C throughout to reflect a likely optimum capital-energy trade-off. Violation of this value is obviously possible and may be of overall financial benefit. However, without capital cost data there is simply no basis for a decision. Once again, the chosen value ought to be adhered to if valid comparisons are to be made. Gaggioli et al. used values for $\Delta T_{min}$ as low as 5°C.

**3 Additonal Site Steam Mains.** In the problem as formulated by ourselves, the separate processes on site use and generate steam interacting with three distinct site steam mains (at 80 bar, 40 bar, and 4 bar). Heat transfer between processes can only be achieved via these existing mains. Other levels of steam are a consequence of steam throttling within processes and do not represent site mains. Additional site mains were to be disallowed; not only would new site mains be uneconomic almost without a doubt but the admission of new mains would also render the problem meaningless. An infinite number of thermodynamic solutions would become possible. Any problem, however complex initially, could be set up cascade fashion and be solved thermodynamically with little regard to capital cost and little or no "method" if there are no restrictions on mains. This would represent an entirely impractical and artificial situation. Gaggioli et al.'s solution sets up such a "thermodynamic cascade" and requires three additonal site steam mains.

The solution offered in our paper requires changes in the existing mains' pressures and flow rates. The ability of turbine generator stages and of steam distribution systems to handle such changes could be a matter of debate. Our changes imply variations in volumetric flow rates in any turbine stage of less than 30 percent.

**4 Condensate Handling System.** In our paper, condensate is shown to return to the deaerator at 80°C (streams No. 24, 26, 30, 32, and 43). That is, the process steam demands shown are net after generation of flash steam. Table 1 confirms this assumption. Nevertheless, Gaggioli et al. assumed that condensate exits each plant at saturated conditions and that additional heat is available between exit conditions and the 80°C we cited. Thus, they violated the heat balance as given per our data and effectively used the heat available from condensate twice.

"Backing out" these four differences from Gaggioli et al.'s solution we account for more than the differences in savings between the two solutions. Note that the effect of a removal of restrictions is open to interpretation in the context of specific solutions; the benefits obtained must depend on the use made of such removal by the solution in question. Our statement, by contrast, is unambiguous as it relates to objective "targeting."

Addressing practical judgment, our solution introduces alternative heat exchangers in the Nitric Acid plant and central boiler, which are in line with the assumptions and constraints set down at the outset and appear feasible in economic and practical terms. Gaggioli et al.'s solution introduces three new stream mains and it requires new expander and converter designs for hitherto unobtainable operating conditions. We emphasize that the assumptions chosen, while intended to enable valid comparisons to be made, also have a sensible and practical engineering basis.

In summary, we feel that a comparison of the two solutions is difficult. There are plain differences in assumptions probably caused by a difference in philosophy. Our solution aims at the best achievable thermodynamic performance subject to clear constraints. Gaggioli et al.'s solution aims at thermodynamic efficiency setting aside many of these constraints. Still, we feel that a comparison of Pinch Technology and Exergy Analysis has been made possible by these two papers. We suggest it has become clear that Pinch Technology views an overall problem globally and that it is less dependent on the structure and equipment selection of any particular solution. The other main difference between the techniques has been highlighted inadvertently by the differences in assumptions made. In an "ideal" design environment (any number of steam levels, etc.) there would be few pinches and Pinch Technology would be of limited use. Exergy Analysis, by contrast, would be an adequate tool to support the knowledgeable designer.

In a more practical environment with given constraints (limits to the number of levels and stages, etc.) there are pinches. Now, Exergy Analysis does not offer the designer formalized help in "translating" equipment considerations into overall system effects. Pinch Technology, by contrast, in its almost abstract targeting rigor, establishes how specific equipment parameters influence an overall solution within given constraints. Pinch Technology allows the designer to formulate consistently the most efficient thermodynamic solutions for complex situations that are practically constrained.

## Authors' Closure

The economic difference between the solutions presented in our paper and in the paper by Linnhoff and Alanis in this issue is clearly shown by Fig. 10 below, which is an adaptation of Fig. 18 of Linnhoff and Alanis.

In view of the uncertainty with regard to whether air preheat is allowable, which even Professor Linnhoff admits, and on which we commented in our Discussion of their paper, we maintain that the comparison between the solutions should be made on a non-air-preheat basis. When one compares the increase in savings above the contractor's design, which is, after all, all that we or Linnhoff and Alanis can take credit for, the results are, in millions of dollars per year:

| | $R$ = 2.5 | $R$ = 4.5 |
|---|---|---|
| Exergy analysis | 4.1 | 6.3 |
| Pinch technology without preheat | 1.4 | 1.7 |
| Pinch technology with air preheat | 1.7 | 2.2 |

In any case, our savings are several times better than the savings from pinch technology.

Professor Linnhoff, however, challenges our results. With all due respect to Professor Linnhoff, we believe that he is trying to impose new constraints which were not set forth when he first posed the challenge problem. There is a virtual one-to-one correspondence between the new constraints that he would like to impose, and those features of our design that

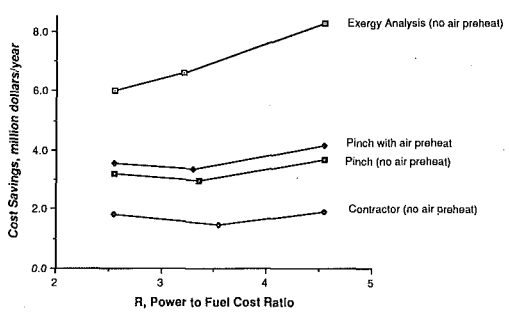


Fig. 10

led to significantly greater economic advantage over his. He claims that we have obtained better results, in part, because we have not observed constraints placed on the solution of the problem for:

1 Gas turbine inlet temperature
2 Minimum approach temperatures
3 Additional site steam mains

He also claims that we did not deal with the condensate handling system properly, and that we ". . . effectively used the heat available from the condensate twice." We disagree on all counts.

To put the issue of unobserved constraints to rest, for the record we present the statement of the original challenge problem.

B. Linhoff and F. J. Alanis
Centre for Process Integration
Department of Chemical Engineering
University of Manchester Institute of Science and Technology
P. O. Box 88, Manchester M60 1QD

Figure 1 shows an existing industrial site. The process plant energy requirements are supplied by a combined heat and power steam system and external power. A dual pressure Nitric Acid process (Fig. 2 and Tables 1 and 2) is to be built on site. The contractor [has offered] three basic options:

1 Maximum steam export (Fig. 3*a*)
2 Maximum power export (Fig. 3*b*)
3 Compromise (Fig. 3c)

The effect of integration option 3(*c*) into the site is shown in Fig. 4.

**Problem:** The client should evaluate other options. Naturally this includes options 3(*a*) and 3(*b*).

More importantly, the client should evaluate nonobvious options where the design of the Nitric Acid process is changed to take advantage of site opportunities, etc.

For this job to be done, Table 3 lists the possible generation and consumption pressures of the existing processes. Some are identical to existing mains pressures, some are not.
Possible:

1 Redesign $HNO_3$ process?
2 Exploit discrepancies between mains pressures and possible consumption/generating pressures in existing consumers?
3 Shift mains pressures?

Also consider: Best options are wanted for $R = 2.5$ and $R = 4.0$ where $R$ = Cost of power/cost of fuel.

10 December 1987

There were no further written or oral instructions, or constraints imposed, although there was the tacit agreement that any solution to the problem should be "practical." The tables and figures referred to in this problem statement are identified in the footnote below.[3] It seems clear to us that the original problem statement does not pose any constraints on gas turbine inlet temperature, approach temperatures, or additional site steam mains. For the interested reader, further comments on this set of issues are found in our Discussion of the Linnhoff and Alanis paper, and in the accompanying footnote.[4]

The remaining issue, brought forth by Professor Linnhoff, is that of the condensate handling system. In full agreement with the original problem statement, the temperature of the condensate returning from the Process Plant to the deaerator was set at 80°C. This is clearly shown in our paper in Fig. 2, Industrial steam plant, base case; the condensate stream leaving the Process Plant (dashed rectangle) is indeed at 80°C. The disagreement is, simply, whether the returning condensate is at 80°C., because process heat was removed down to this level, or because there were heat losses in the condensate return lines from the Process Plant. A crucial test, which can resolve this disagreement, is the application of material and energy balances to the Process Plant, in conjunction with the data presented in the original problem statement. Indeed, upon first addressing this challenge problem, we did that in order to check whether the condensate leaving the loads conformed to the saturated conditions (as a practitioner would expect). That analysis proves that we are correct as we shall elaborate on:

The Process Plant not only uses steam from the power plant, but also generates steam at 50 bar and 15 bar. The use and generation are shown in Table 1 of our paper, exactly as they were given in the original challenge problem. A clear representation of the information from that table is shown in Fig. 1 of our paper. It includes the flows from the steam plant; the steam internally generated; the steam used for heat exchange; and the steam consumed in processes. All these flows and duties are in accordance with the original problem statement. Our Fig. 1 also represents a material and energy balance for the Process Plant; the only information on the figure that was not provided with the original problem statement are the enthalpies of the condensates leaving the heat exchangers (and the exergies, which are not relevant to the issue at hand).

Our Fig. 1 clearly shows that the enthalpies of the condensates leaving the heat exchangers (1317, 1129, 721, and 605 kJ/kg) are those of the saturated condensates at 80, 46, 8, and 4 bar and not that of 80°C water. An energy balance cannot be satisfied if those enthalpies are set to the value of liquid water at 80°C. Further evidence may be seen in the differences between the heat exchanger duties at the four pressure levels as calculated from their Fig. 2 and Table 1, and those specified in the original challenge problem.

| | 80 bars | 46 bars | 8 bars | 4 bars |
|---|---|---|---|---|
| Linnhoff duties, kW | 9,702 | 12,128 | 17,288 | 21,911 |
| Specified duties, kW | 5,764 | 8,145 | 14,531 | 19,430 |

Thus it is not we who are in error when Professor Linnhoff contends, in his Discussion, ". . . the process steam demands shown [by Fig. 2 of his paper] are net after generation of flash steam. Table 1 confirms this assumption." N.B. : Table 1 and Fig. 2 of his paper were not part of the original problem statement; they do not confirm his assumption that the enthapy in the condensates above 80°C was used in the Process Plant; they merely reflect his incorrect assumption. Figure 2 and Table 1 of Linnhoff and Alanis' paper are consistent with their orig-

[3]For the information of those who might be interested, the problem statement was accompanied by:

1 Six figures: "Fig. 1 " is the same as Fig. 2 of our paper (but without our exergy numbers). "Figures 2, 3(*a*), 3(*b*), and 3(*c*)" were variations of the $HNO_3$ plant; "3(*a*) was like our Fig. 3 without a steam turbine but with a motor in its place and export of the steam; "3(*b*)" was equivalent to our Fig. 3 (without exergies); and "Figs. 2 and 3(*c*)" (which were identical) have a steam turbine but without production of excess power and with export of 14,832 kg/h of excess steam instead (at 80 bar and 473°C). "Figure 4" showed the integration of "Fig. 3(*c*)" into "Fig. 1" [into our Fig. 2].

2 Three tables: "Table 1" is presented as Table 2 in our paper; "Table 2" is absent from our paper but is presented as Table 3 of Linnhoff and Alanis' paper in this volume (although for some unknown reason the inlet $T$ and $p$ to the steam turbine have been raised from the original 473°C and 80 bar and the flow rate decreased from 15,215 kg/h); "Table 3" is our Table 1.

[4]In his discussion of our paper Professor Linnhoff raises the issue of the number of site mains. In the first place there was no restriction to the number of site mains in the original problem statement. Furthermore, we would argue that, from the information provided with the original problem statement, there is no reason to believe that additional mains would be needed to serve the (presumably special) users at 46, 8, and 3 bars. (Even if "mains " were needed, our results show that significant fuel savings would result, and therefore the economics of installing them should be investigated. It would be imprudent to jump to the conclusion that "new site mains would be uneconomic without a doubt," let alone to disqualify the idea outright.)

inal problem statement only if the condensate is reduced from the saturation temperature of the mains to the 80°C of Stream 43 by heat losses from the condensate return piping.

In our opinion, Linnhoff and Alanis did not draw the boundary conditions of the problem properly, stopping at the border of the Process Plant, rather than at the boundaries of the heat exchangers within. Thus, they did not take advantage of the "site-specific" opportunities within the Process Plant to save additional fuel.

In conclusion, pinch technology is a systematic procedure that has application in the design of heat exchanger network systems in which the streams to be heated and cooled are known, and whose supply and target temperatures are known, explicitly. But its strength, that it is a systematic procedure, is also one of its weaknesses: It is easy to be lulled into complacency, and miss "implicit" opportunities. We grant that pinch technology has been an important advance. However, we maintain that exergy analysis is a more powerful tool, which brings to light opportunities that go undetected by pinch technology.

# A Computer Method for Thermal Power Cycle Calculation

**E. Perz**
Graz University of Technology,
Graz, Austria

*This paper describes a highly flexible computer method for thermodynamic power cycle calculations (PCC). With this method the user can model any cycle scheme by selecting components from a library and connecting them in an appropriate way. The flexibility is not restricted by any predefined cycle schemes. A power cycle is mathematically represented by a system of algebraic equations. The structure of mathematical cycle models as well as different approaches to set up and solve the resulting equations with computer programs are discussed in the first section. The second section describes the developed method. The mass and energy balance equations are set up and solved with a semiparallel algorithm. As input only the cycle's topology and component parameters must be entered. Information about the calculation sequence and the convergence method can be omitted completely. The example of two simple steam cycles demonstrates the applied technique. The method requires only a few, if any, iterations. Calculation time and storage requirements can be kept low enough to calculate even very complex cycles on personal computers. At the end of the paper input data and results for a complex cycle scheme as it may occur in reality are given to demonstrate the performance finally.*

## Introduction

The general energy-supply and environmental situation requires an improved utilization of energy sources. Therefore the complexity of power generating units has increased considerably. Plant owners are increasingly demanding strictly guaranteed performance. This requires thermodynamic calculations of high accuracy. As a result the expenditure for thermodynamic calculation during design and optimization has grown tremendously. To be competitive constructors are forced to reduce planning and designing time as well as the number of errors by applying computer-aided methods. Moreover the application of computer aided methods allows optimization and case studies, which otherwise would be too time consuming.

At the Institute for Thermal Turbomachinery of Graz University of Technology, several projects concerned with advanced power cycle development have been carried out during the last few years (Jericha, 1983, 1985; Wilplinger, 1986; Jericha et al., 1987; Jericha and Ratzesberger, 1989). At the beginning, programs for each cycle were written to carry out parameter studies. With growing projects a demand for more powerful software tools emerged.

## Existing Packages for Power Cycle Calculation

With computer-aided power cycle calculation (PCC) two requirements must be observed: flexibility and ease of use. Numerous program packages have been developed for PCC. The complexity of these programs covers a wide range. It reaches from programs that can be used for a few fixed cycle schemes, up to packages that allow the modeling of any cycle configuration.

Packages that are restricted to a few cycle schemes are usually easy to handle: Prior to the calculation the user selects a cycle scheme and enters the required parameters, such as temperature at turbine inlet or efficiency of the turbomachine. These packages, however, lack the flexibility that is required for many advanced investigations.

At the other end of the scale, there are highly flexible all-purpose packages. These packages require not only information about the cycle's topology and parameters but also about calculation sequence and convergence method. This makes all-purpose packages very difficult to handle for nonspecialist users.

Somerton et al. (1987) describe a program that can be used for calculation of cycles based upon the Rankine cycle. This package allows the calculation of 28 different cycle schemes.

More flexible programs are necessary for cycle development. Dittmar (1973) used for the first time a flexible program for power cycle development. Other packages for calculation of power cycles have been published by Miedema (1981), Sonnenschein (1982), Sandner (1983), Eisermann et al. (1984), and Ohadi et al. (1985). More theoretical contributions were made by Martensen (1984).

Extremely powerful packages originally developed for chemical engineering problems have also been used for power cycle calculation. Well-known simulators are ASCEND-II (Locke and Westerberg, 1983), ASPEN (Rosen and Scott, 1985), PROCESS, and SPEEDUP (Pantelides, 1988).

For the developments carried out at the Institute for Thermal

Contributed by the International Gas Turbine Institute and presented at the 35th International Gas Turbine and Aeroengine Congress and Exposition, Brussels, Belgium, June 11–14, 1990. Manuscript received by the International Gas Turbine Institute January 23, 1990. Paper No. 90-GT-351.

Turbomachinery of Graz University of Technology those packages were not suitable. While special PCC packages were too restrictive, other packages like PROCESS turned out to be too complex and too large to be run on personal computers. Therefore a new package for power cycle calculation was developed.

## Development Goals

The development goal was a computer program for studying conventional and advanced power cycles. In particular it had to meet the following requirements:

- Flexibility: The user must be able to calculate arbitrary cycle schemes without changing the program.
- Ease of use: The user must only need to provide information about the cycle scheme, but no information about how to carry out the calculation.
- PC-based system: The program's memory requirements must not exceed the 640K limits of DOS personal computers.
- Speed: To carry out case studies easily, calculation time must not exceed a few minutes.
- Expandability: To allow handling of cycles with novel components or unconventional working fluids, the program must be able to add the required capabilities easily.

It was not intended to use the program for the analysis of part-load behavior. The omission of this feature allows use of very simple mathematical models for the components (e.g., the performance of a turbine is determined by constant efficiency).

## System Modeling

Thermodynamic processes are composed as a connection of many standard components, such as turbines, pumps, heat exchangers, etc. It is efficient to use this structure of a system containing standardized components also for mathematical cycle modeling. Therefore the following model structure has been introduced:

The components of a mathematical model are called "units." Units can be connected by:

- Streams, which are connections allowing transport of mass and energy. Streams define the state between two units. The state is characterized by a mass flow and thermodynamic properties such as pressure, enthalpy, or composition.
- Energetic links that allow energy transport only. An example of an energetic link is a shaft.

Mathematically a unit is a collection of all equations that are necessary to describe a single component of a cycle, i.e.:

- Mass balances of a single component.
- Energy balances of a single component.
- Functions that describe the behavior of a particular component (e.g., the calculation of the expansion for a turbine or the pressure drop and the heat loss for a pipe).

A stream is mathematically represented by the equations necessary for the calculation of the thermodynamic properties. To connect two units by a stream means to set equal their thermodynamic and mass flow properties.

To set up a mathematical model of a cycle using this model structure, the units are selected and connected in the desired way by streams and energetic links. Mathematically this means to put all equations together into a system of nonlinear equations. This system must be solved to obtain all states including the efficiency of the cycle. The system can have 1000 unknowns or even more. It is the task of a computer-aided PCC package to set up and solve this system.

## Customary Solution Methods

There are two basically different approaches to solve these equations. First, it is possible to follow perception and to carry out the calculation sequentially, unit after unit. This approach is called the "sequential method." Second, one can take the more abstract way of setting up the entire system of equations and solving it with an appropriate algorithm. The latter approach is called the "equation-oriented method."

**The Sequential Method.** The sequential method does not use the system of equations explicitly. Instead each unit is represented by a transfer function that calculates all output streams from the input streams.

With this method calculation starts at an appropriate point of the cycle with estimated values. The cycle is then calculated unit after unit following the direction of mass flow. Loops are represented by recycle streams and solved iteratively: For recycle streams properties and mass flow are estimated at the beginning of the calculations. Each loop is iterated until all data in the loop are consistent. At the end of a calculation step the result is compared with the estimated starting values. The starting value is modified and the procedure repeated until the result does not change any more.

The advantages of this method are:

- It is easy to implement; new unit models can be added easily.
- Limited memory is required because the system of equations is never used explicitly.

Its disadvantages are:

- It is necessary to identify recycle streams. This means it is necessary to provide information on how to carry out the calculation.
- Flexibility is restricted because flow of information must always be in the direction of mass flow.

**Equation-Oriented Method.** The development of the equation-oriented method has started later, but it has gained importance during the last few years, particularly in academic research. The advantages of this method are:

- It offers more flexibility because there are no restrictions imposed by the flow of information.
- No information on calculation sequence must be provided by the user because all equations are solved simultaneously.

The disadvantages of this method are:

- A large amount of memory is needed to store the system of equations. For a system with $N$ unknowns at least a system matrix of size $N*N$ must be stored. On DOS personal computers with 640K memory available $N$ is limited to about 250 double precision or 370 single precision unknowns.
- It requires a robust algorithm for solving the system of nonlinear equations.
- The user is forced to estimate initial values of sufficient accuracy because all solution methods start from an initial guess for each unknown. These values are iterated until solution is reached.

The two main disadvantages have, however, been overcome during the last few years with the development of hardware making sufficient memory available and of robust algorithms for solving nonlinear equation systems. Nevertheless the user must still provide starting values for iteration.

## The Semiparallel Method

The method presented here combines sequential and equa-

## Nomenclature

$h$ = specific enthalpy, kJ/kg
$m$ = mass flow, kg/s
$p$ = pressure, bar
$P$ = power output, kW
$t$ = temperature, °C
$x$ = relative humidity

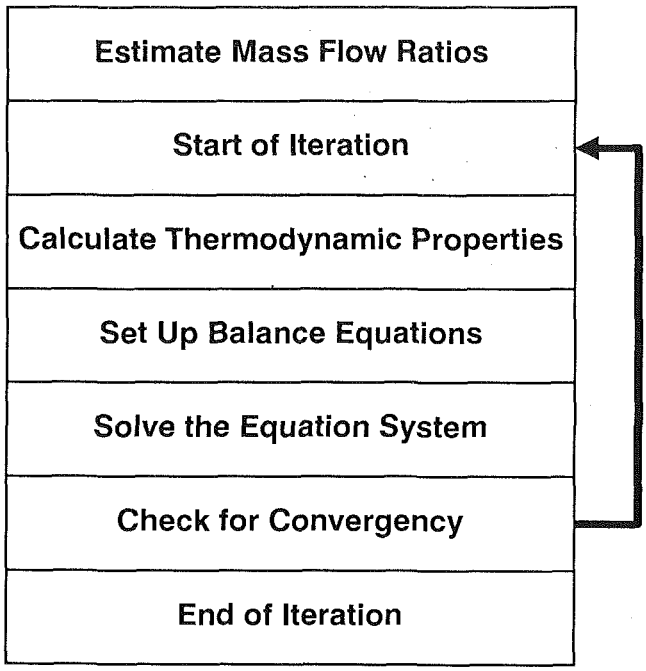


Fig. 1 Calculation scheme

tion-oriented features. While the thermodynamic data are calculated in a way similar to the sequential method, mass and energy balance equations are set up explicitly and solved in parallel. Therefore this new method is called the "semiparallel approach." Similar approaches were used by Miedema (1981) and Sandner (1983).

It takes advantage of the fact that many of the system's equations are linear equations. If all thermodynamic data of a cycle are known, mass and energy balances form a system of linear equations. This can easily be solved with standard algorithms for linear equation system solution like Gauss-Jordon Elimination or Lower-Upper Decomposition. Because only the mass flow rates are unknowns of the linear equation system its size is only a small fraction of that required for the equation-oriented method.

Usually it is not possible, however, to calculate thermodynamic data independently from mass flow rates. Mixing points and under certain circumstances also heat exchangers need mass flow data to calculate thermodynamic properties. The enthalpy behind a mixing point is calculated from the feed streams as follows:

$$h_3 = \frac{m_1}{m_3} h_1 + \frac{m_2}{m_3} h_2 \tag{1}$$

This means that mass flow rates for mixing points must be estimated before the calculation of thermodynamic data, and leads to an iterative process as shown schematically in Fig. 1.

At the beginning mass flow rates are estimated. With this estimate all thermodynamic properties are calculated. By setting up and solving the mass and energy balance equations improved values for the mass flow rates are obtained. These steps are repeated until the solution reaches the required accuracy.

## Examples

To give more insight into this method, the solution processes for two simple Rankine cycles are discussed here. The steps described are exactly the same as the computer program takes.

The cycle scheme as shown in Fig. 2 does not require the iteration process. All thermodynamic properties can be calculated before solving mass and energy balance equations.

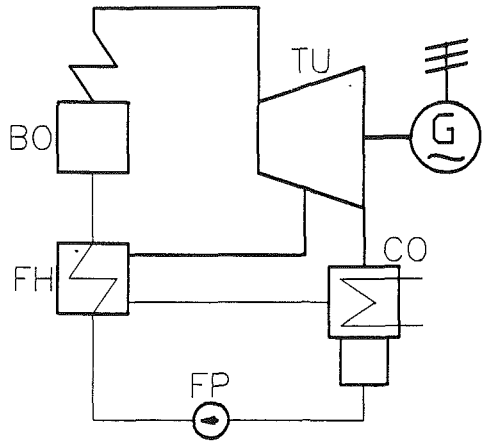


Fig. 2 Sample cycle not requiring iteration: TU = turbine; CO = condenser; FP = feedwater pump; FH = feed heater; BO = boiler

The different preheater scheme of the cycle shown in Fig. 4 leads to a system that must be solved by iteration.

**Cycle Not Requiring an Iterative Solution.** Figure 2 shows a simple Rankine cycle with a single feed heater. The mathematical modeling needs a modified structure as shown in Fig. 3. The turbine model does not allow any diverted streams. Therefore it is represented by two turbines and a splitter. A shaft connects both the turbines and the generator. The numbers 1-9 indicate the streams that are to be calculated.

Live steam conditions, bleeding pressures, condenser pressure, and required temperature differences at the in- and outlet of the preheater are given as well as all pressure drops and efficiencies of the cycle's components.

In advance of the thermodynamic calculation a topological analysis of the system shows the identity of the following mass flows:

$$m_1 = m_2 = m_6 = m_7 = m_8 \tag{2a}$$

$$m_3 = m_5 \tag{2b}$$

$$m_4 = m_9 \tag{2c}$$

Although this topological analysis is not obligatory, it can reduce the required memory considerably. For this example the number of unknowns can be reduced to 1/3, resulting in a reduction of the system matrix size to 1/9. The additional effort in calculation time is negligible and can usually be compensated for by the time saved in the solution of the reduced system.

The next step is to complete the still unknown thermodynamic properties. With given live steam conditions (1) and bleed stream pressure the entire properties of (2) are determined. The properties at (3) and (4) are also fixed, because there is no alteration of properties at a splitter. The expansion in the second turbine gives the properties at the inlet of the condenser (5). The properties at (6), the condenser outlet, are determined by the demand for complete condensation ($x = 0.0$). The outlet pressure of the feed water pump is not yet known, but with the given pressure drop in the boiler, the pressure $p_8$ can be calculated. With the given pump efficiency this allows calculation of the entire properties at (7). The properties at (8) result from the required temperature differences of the preheater. Finally the properties at (9) can be calculated from pressure drop and the required temperature difference of the preheater. The following balance equations can be written:

*Turbines:*

$$m_1 - m_2 = 0 \tag{3a}$$

$$m_3 - m_5 = 0 \tag{3b}$$

$$(h_1 - h_2)m_1 + (h_3 - h_5)m_3 = P \tag{3c}$$

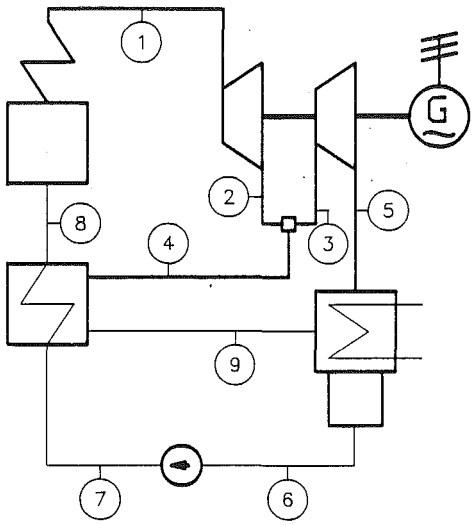


Fig. 3 Model structure for the cycle of Fig. 2

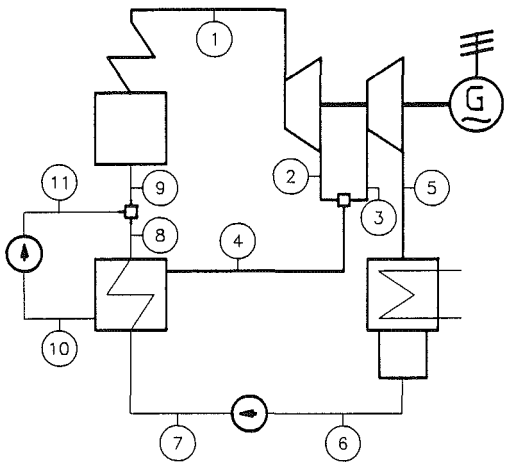


Fig. 4 Model structure for the example cycle requiring an iterative solution

*Splitter:*

$$m_2 - m_3 - m_4 = 0 \tag{3d}$$

*Condenser:*

$$m_5 + m_9 - m_6 = 0 \tag{3e}$$

*Pump:*

$$m_6 - m_7 = 0 \tag{3f}$$

*Preheater:*

$$m_7 - m_8 = 0 \tag{3g}$$
$$m_4 - m_9 = 0 \tag{3h}$$
$$(h_4 - h_9)m_4 - (h_8 - h_7)m_7 = 0 \tag{3i}$$

*Boiler:*

$$m_8 - m_1 = 0 \tag{3j}$$

With regard to the mass flow identities, the system can be transformed to:

$$\begin{aligned}(h_1-h_2)m_1 &+ (h_3-h_5)m_3 &&= P &(4c)\\ m_1 &- m_3 - m_4 &&= 0 &(4d)\\ -m_1 &+ m_3 + m_4 &&= 0 &(4e)\\ -(h_8-h_7)m_1 &+ (h_4-h_9)m_4 &&= 0 &(4i)\end{aligned}$$

The letters following the equation numbers correspond to those of equations (3).

In this system of equations one equation is superfluous. It is difficult to identify this equation, particularly for complex cycle schemes. It is not necessary however to eliminate a certain equation if a mathematical trick is used: An additional unknown is introduced in the system, with coefficient 1.0 in each equation. This unknown must resolve to zero.

**Cycle Requiring an Iterative Solution.** The model of the cycle shown in Fig. 4 has a different preheating scheme: The condensate from the preheater is fed to the main stream and not to the condenser as in the cycle shown in Fig. 3. The resulting energy balance for the mixer is

$$h_9 m_9 = h_8 m_8 + h_{11} m_{11} \tag{5}$$

In this case $h_9$ depends not only on the enthalpies $h_8$ and $h_{11}$ but also on the mass flows. Since the resulting equation system is not linear an iterative solution is necessary. The following mass flow identities can be found by a topological analysis:

$$m_1 = m_2 = m_9 \tag{6a}$$
$$m_3 = m_5 = m_6 = m_7 = m_8 \tag{6b}$$
$$m_4 = m_{10} = m_{11} \tag{6c}$$

The completion of properties is done analogously to the scheme without iteration. Equation (5) can be easily transformed to

$$h_9 = \frac{m_8}{m_9} h_8 + \left(1 - \frac{m_8}{m_9}\right) h_{11} \tag{7}$$

This equation contains only the mass flow ratio $m_8/m_9$ for which an initial value can be estimated. The resulting equations are:

*Turbines:*

$$m_1 - m_2 = 0 \tag{8a}$$
$$m_3 - m_5 = 0 \tag{8b}$$
$$(h_1 - h_2)m_1 + (h_3 - h_5)m_3 = P \tag{8c}$$

*Splitter:*

$$m_2 - m_3 - m_4 = 0 \tag{8d}$$

*Condenser:*

$$m_5 - m_6 = 0 \tag{8e}$$

*Pump:*

$$m_6 - m_7 = 0 \tag{8f}$$

*Preheater:*

$$m_7 - m_8 = 0 \tag{8g}$$
$$m_4 - m_{10} = 0 \tag{8h}$$
$$(h_4 - h_{10})m_4 - (h_8 - h_7)m_7 = 0 \tag{8i}$$

*Mixer:*

$$m_8 + m_{11} - m_9 = 0 \tag{8k}$$

*Boiler:*

$$m_9 - m_1 = 0 \tag{8l}$$

Regarding the mass flow identities, the system can be reduced to

$$\begin{aligned}(h_1-h_2)m_1 &+ (h_3-h_5)m_3 &&= P &(9c)\\ m_1 &- m_3 - m_4 &&= 0 &(9d)\\ &+ (h_8-h_7)m_3 &+ (h_4-h_{10})m_4 &= 0 &(9i)\\ -m_1 &+ m_3 + m_4 &&= 0 &(9k)\end{aligned}$$

After solving this system an improved ratio $m_8/m_9$ can be calculated. With this value the calculation must be repeated until old and new ratio $m_8/m_9$ correspond with required accuracy.

## Implementation

This method has been implemented with the intention to

offer a user-friendly tool for PCC. While the amount of data required as input can be minimized by applying this method, it is necessary to provide additionally a facility to enter input data in a comfortable way.

A special input language was developed to facilitate the description of cycle schemes. Currently it is necessary to write an input file using the system's text editor. As further user support it is planned to use a graphic preprocessor for generation of input files. However, this preprocessor is not yet available.

The carefully designed program does not restrict further developments. Figure 5 shows all units that are currently available. New units can be added if required, although familiarity with the solution method is necessary for their development.

The thermodynamic properties calculation has been completely separated from the other parts of the package by a standardized interface. This increases the flexibility of the package, since new working fluids can be added by simply extending the properties data base. It is also possible to interface the package with other properties data bases. For the calculation of steam properties either the 1967 IFC formulations (Schmidt, 1969) or the NBS/NRC steam tables (Haar et al., 1984) can be chosen.

Implementations of this method are currently running on VAX hardware and DOS personal computers. For implementation the ANSI standard of the C programming language was used.

"C" supports the definition of data structures and user-defined data types, a feature that was used extensively. It is possible for example to create a data type "property-type" that has several components to store pressure, temperature, and all other thermodynamic properties. If a variable "props" of type "property-type" is defined, it can be handled similarly to an array. To reference one of the components of "props" only the component name must be appended to the variable name, e.g., "props.pressure." Due to the ability to define composed data types, data flow within the program can be organized clearly.

Another useful feature of "C" is the capability to allocate memory dynamically. Therefore it is not necessary to reserve memory for the maximum possible unit number of each type at compilation time. Instead the program allocates memory according to input data. The memory for the equation system is also allocated dynamically. Dynamic memory allocation allows reduction of the required storage area, because there are no unused portions as with statically allocated memory.

Figure 6 shows a cycle scheme for a 150 MW steam plant of real scale complexity that has been investigated with this PCC program on a 12 MHz AT personal computer with mathematical coprocessor.

In Table 1 a part of the input file is given as an example for the description language. Table 2 shows the standard output listing. It contains data for all streams and efficiency data.

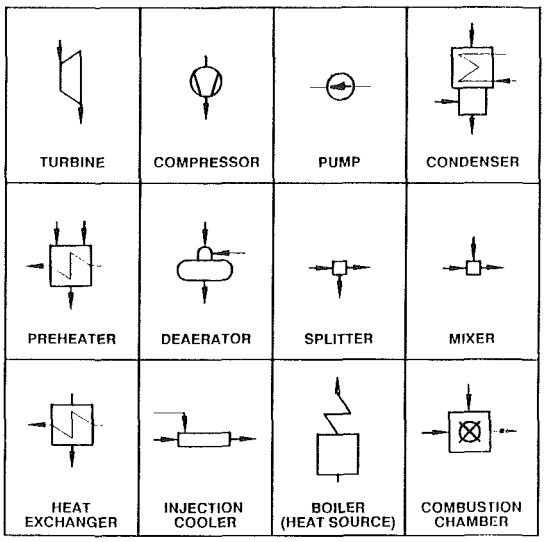


Fig. 5 Currently available units

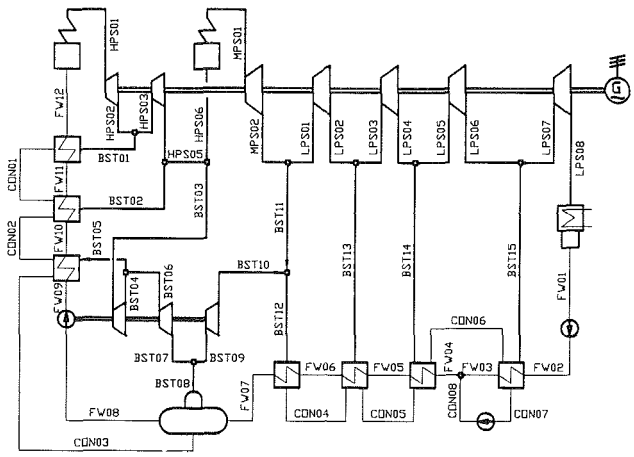


Fig. 6 Sample cycle: 150 MW steam cycle

Table 1 Part of the input file for the cycle of Fig. 6

```
header:   EXAMPLE 150 MW Plant

unit:     turbine
  name:   HP_TURBINE_1
  feed:   HPS01 ( p = 196.12, h = 3374.72 )
  drain:  HPS02 ( p = 52.27 )
          etas = 0.818
          etam = 0.955

unit:     splitter
  name:   HP_BLEEDER_1
  feed:   HPS02
  drain1: HPS03
  drain2: BST01

unit:     turbine
  name:   HP_TURBINE_2
  feed:   HPS03
  drain:  HPS04 ( p = 34.321 )
          etas = 0.913
          etam = 0.955

unit:     splitter
  name:   HP_BLEEDER_2
  feed:   HPS04
  drain1: HPS05
  drain2: BST02

unit:     splitter
  name:   PU_BLEEDER
  feed:   HPS05
  drain1: HPS06
  drain2: BST03

unit:     boiler
  name:   REHEATER
  feed:   HPS06
  drain:  MPS01 ( h = 3543.88 )
          dp = 0.0857
          etak = 0.92

  ....

unit:     mixer
  name:   MIX_POINT_2
  feed1:  BST10
  feed2:  BST11
  drain:  BST12
  quot = 0.05

unit:     pump
  name:   CONDENSATE_PUMP
  feed:   CON07
  drain:  CON08
          eta = 0.80

unit:     shaft
  name:   GENERATOR_SHAFT
  connect:HP_TURBINE_1, HP_TURBINE_2,
          MP_TURBINE, LP_TURBINE_1,
          LP_TURBINE_2, LP_TURBINE_3,
          LP_TURBINE_4
          pw = 150000.0

unit:     shaft
  name:   PUMP_SHAFT
  connect:PUMP_TU_1, PUMP_TU_2,
          PUMP_TU_3, FEEDW_PUMP

composition:
  define: HPS01 (water:1.0)
  ident:  HPS01,ALL
```

**Table 2 Output listing for cycle scheme of Fig. 6**

EXAMPLE 150 MW Plant

STREAMS:

| Name | Comp. | p [bar] | t [Grad] | h [kJ/kg] | s [kJ/kgK] | v [m3/kg] | x [-] | m [kg/s] |
|---|---|---|---|---|---|---|---|---|
| BST01 | 1 | 52.27 | 351.3 | 3069.1 | 6.4327 | 0.0496 | 1.00 | 7.590 |
| BST02 | 1 | 34.32 | 297.4 | 2974.0 | 6.4487 | 0.0695 | 1.00 | 11.007 |
| BST03 | 1 | 34.32 | 297.4 | 2974.0 | 6.4487 | 0.0695 | 1.00 | 17.724 |
| BST04 | 1 | 15.00 | 216.3 | 2838.8 | 6.5424 | 0.1390 | 1.00 | 17.724 |
| BST05 | 1 | 15.00 | 216.3 | 2838.8 | 6.5424 | 0.1390 | 1.00 | 7.697 |
| BST06 | 1 | 15.00 | 216.3 | 2838.8 | 6.5424 | 0.1390 | 1.00 | 10.027 |
| BST07 | 1 | 6.06 | 159.2 | 2698.9 | 6.6228 | 0.3042 | 0.97 | 10.027 |
| BST08 | 1 | 6.06 | 159.2 | 2698.9 | 6.6228 | 0.3042 | 0.97 | 6.642 |
| BST09 | 1 | 6.06 | 159.2 | 2698.9 | 6.6228 | 0.3042 | 0.97 | 3.385 |
| BST10 | 1 | 2.30 | 124.8 | 2558.2 | 6.6911 | 0.7208 | 0.93 | 3.385 |
| BST11 | 1 | 2.30 | 222.1 | 2913.8 | 7.5319 | 0.9820 | 1.00 | 0.753 |
| BST12 | 1 | 2.30 | 124.8 | 2622.1 | 6.8517 | 0.7434 | 0.96 | 4.137 |
| BST13 | 1 | 1.10 | 154.9 | 2785.4 | 7.5921 | 1.7828 | 1.00 | 3.656 |
| BST14 | 1 | 0.451 | 84.8 | 2653.6 | 7.6631 | 3.6319 | 1.00 | 3.346 |
| BST15 | 1 | 0.215 | 61.6 | 2553.9 | 7.7096 | 6.9758 | 0.98 | 4.579 |
| CON01 | 1 | 50.18 | 251.4 | 1092.7 | 2.8041 | 0.0013 | 0.00 | 7.590 |
| CON02 | 1 | 32.95 | 208.3 | 890.5 | 2.4063 | 0.0012 | 0.00 | 18.597 |
| CON03 | 1 | 14.40 | 173.5 | 734.7 | 2.0751 | 0.0011 | 0.00 | 26.294 |
| CON04 | 1 | 2.21 | 109.3 | 458.3 | 1.4104 | 0.0011 | 0.00 | 4.137 |
| FW01 | 1 | 0.023 | 19.5 | 81.6 | 0.2886 | 0.0010 | 0.00 | 78.456 |
| FW02 | 1 | 9.81 | 19.5 | 82.8 | 0.2892 | 0.0010 | 0.00 | 78.456 |
| FW03 | 1 | 8.83 | 58.6 | 246.1 | 0.8134 | 0.0010 | 0.00 | 78.456 |
| FW04 | 1 | 8.83 | 53.9 | 226.4 | 0.7536 | 0.0010 | 0.00 | 94.175 |
| FW05 | 1 | 7.85 | 75.8 | 317.9 | 1.0246 | 0.0010 | 0.00 | 94.175 |
| FW06 | 1 | 6.87 | 99.3 | 416.4 | 1.2982 | 0.0010 | 0.00 | 94.175 |
| FW07 | 1 | 6.06 | 121.8 | 511.5 | 1.5462 | 0.0011 | 0.00 | 94.175 |
| FW08 | 1 | 6.06 | 159.2 | 672.0 | 1.9344 | 0.0011 | 0.00 | 127.111 |
| FW09 | 1 | 254.0 | 163.5 | 705.3 | 1.9486 | 0.0011 | - | 127.111 |
| FW10 | 1 | 253.0 | 198.3 | 855.5 | 2.2798 | 0.0011 | - | 127.111 |
| FW11 | 1 | 252.0 | 241.4 | 1048.0 | 2.6706 | 0.0012 | - | 127.111 |
| FW12 | 1 | 251.1 | 266.7 | 1166.0 | 2.8946 | 0.0013 | - | 127.111 |
| HPS01 | 1 | 196.1 | 541.9 | 3374.7 | 6.3217 | 0.0166 | 1.00 | 127.111 |
| HPS02 | 1 | 52.27 | 351.3 | 3069.1 | 6.4327 | 0.0496 | 1.00 | 127.111 |
| HPS03 | 1 | 52.27 | 351.3 | 3069.1 | 6.4327 | 0.0496 | 1.00 | 119.522 |
| HPS04 | 1 | 34.32 | 297.4 | 2974.0 | 6.4487 | 0.0695 | 1.00 | 119.522 |
| HPS05 | 1 | 34.32 | 297.4 | 2974.0 | 6.4487 | 0.0695 | 1.00 | 108.514 |
| HPS06 | 1 | 34.32 | 297.4 | 2974.0 | 6.4487 | 0.0695 | 1.00 | 90.790 |
| LPS01 | 1 | 2.30 | 222.1 | 2913.8 | 7.5319 | 0.9820 | 1.00 | 90.037 |
| LPS02 | 1 | 1.10 | 154.9 | 2785.4 | 7.5921 | 1.7828 | 1.00 | 90.037 |
| LPS03 | 1 | 1.10 | 154.9 | 2785.4 | 7.5921 | 1.7828 | 1.00 | 86.381 |
| LPS04 | 1 | 0.451 | 84.8 | 2653.6 | 7.6631 | 3.6319 | 1.00 | 86.381 |
| LPS05 | 1 | 0.451 | 84.8 | 2653.6 | 7.6631 | 3.6319 | 1.00 | 83.035 |
| LPS06 | 1 | 0.215 | 61.6 | 2553.9 | 7.7096 | 6.9758 | 0.98 | 83.035 |
| LPS07 | 1 | 0.215 | 61.6 | 2553.9 | 7.7096 | 6.9758 | 0.98 | 78.456 |
| LPS08 | 1 | 0.023 | 19.5 | 2319.0 | 7.9347 | 54.3857 | 0.98 | 78.456 |
| MPS01 | 1 | 31.38 | 539.8 | 3543.9 | 7.3248 | 0.1171 | 1.00 | 90.790 |
| MPS02 | 1 | 2.30 | 222.1 | 2913.8 | 7.5319 | 0.9820 | 1.00 | 90.790 |

COMPOSITIONS:
Composition #1:
Water 1.00

HEAT BALANCE:
Fuel Heat Input[kW]: 368182.0
Turbine Power[kW]: 154232.9
Pump Power[kW]: 4340.4
Thermal Efficiency: 0.40711

STATISTICS:
Calculation started: Thu Jan 04 09:36:27 1990
Calculation finished: Thu Jan 04 09:37:29 1990

More detailed, unit-oriented output can be produced optionally. Computation time for this problem was 62 seconds. The memory requirements were about 320 K.

## Conclusion

A computer method for power cycle calculation has been demonstrated. It allows calculation of arbitrary cycle schemes. The memory requirements of about 320K and the short calculation time of about one minute for cycles of real world complexity enable the calculations to be carried out on personal computers. A user-friendly input language makes the program easy to handle even for inexperienced users.

## Acknowledgments

The author wishes to express his gratitude to Prof. H. Jericha for the opportunity to carry out this work. He also thanks R. Rieger for his support in implementing this method.

## References

Dittmar, H., 1973, "Einsatz eines Programmsystems zur Berechnung von thermodynamischen Kreisprozessen bei den VEW," *VGB Kraftwerkstechnik 53*, No. 2, Feb., pp. 72–77.

Eisermann, W., Hasberg, W., and Tsatsaronis, G., 1984, "Thesis—Ein Rechenprogramm zur Simulation und Entwicklung von Energieumwandlungsanlagen," *Brennstoff-Wärme-Kraft*, Vol. 36, No. 1–2, Jan./Feb., pp. 45–51.

Haar, L., Gallagher, J., and Kell, G., 1984, *NBS/NRC Steam Tables*, Hemisphere Publishing Corporation, Washington–New York–London.

Hausmann, G., and Schmitz, H., 1983, "Ein neues Berechnungsverfahren für Wärmekraftwerks—Kreisläufe," *Brennstoff-Wärme-Kraft*, Vol. 35, No. 12, Dec. pp. 509–520.

Jericha, H., 1983, "A New Combined Gas-Steam Cycle Promising up to 60% Thermal Efficiency," CIMAC, Conference Paper No. T10.1.

Jericha, H., 1985, "Efficient Steam Cycle With Internal Combustion of Hydrogen and Stoichiometric Oxygen for Turbines and Piston Engines," CIMAC, Oslo.

Jericha, H., Wilplinger, H., and Perz, E., 1987, "A Novel High Efficiency Steam Cycle," presented at the ASME Cogen-Turbo Conference, Montreux.

Jericha, H., and Ratzesberger, R., 1989, "A Novel Thermal Peak Power Plant," presented at the ASME Cogen-Turbo III, Nice, France.

Locke, M. H., and Westerberg, A. W., 1983, "The ASCEND-II System—A Flowsheeting Application of a Successive Quadratic Programming Methodology," *Computers and Chemical Engineering*, Vol. 7, No. 5, pp. 615–630.

Martensen, J., 1984, "Kreislaufberechnung und die Graphentheorie," *VGB Kraftwerkstechnik 64*, Vol. 10, Oct., pp. 878–884.

Miedema, J. A., 1981, "CYCLE: A General Computer Code for Thermodynamic Cycle Computations," Ph.D. Thesis, Technische Hogeschool Delft, Netherlands.

Ohadi, M. R., Anderson, M. R., and Foster, A. R., 1985, "TPCSIM—Thermal Power Cycle Simulator," presented at the ASME/IEEE Joint Power Generation Conference, Milwaukee, Paper No. 85-JPGC-Pwr-49.

Pantelides, C. C., 1988, "Speedup—Recent Advances in Process Simulation," *Computers and Chemical Engineering*, Vol. 12, No. 7, pp. 745–755.

Rosen, M. A., and Scott, D. S., 1985, "The Enhancement of a Process Simulator for Complete Energy-Exergy-Analysis," AES-Vol. 1, ASME Winter Annual Meeting, Miami Beach, FL.

Sandner, T., 1983, "Verfahren zur Berechnung von thermodynamischen Kreisprozessen in Dampfkraftanlagen," *VGB Kraftwerkstechnik 63*, Vol. 1, Jan., pp. 1–7.

Schmidt, E., 1969, *Properties of Water and Steam in SI Units*, Springer-Verlag, Berlin–Heidelberg–New York.

Shewchuk, C. F., 1986, "MASSBALL MKII-New Process Simulation System," *Comp.-Aided Eng. of Energy Systems*, Vol. 2, ASME AES-Vol. 2-2, pp. 1–7.

Somerton, C. W., Brouillette, T., Pourciau, C., Strawn, D., and Whitehouse, L., 1987, "RANKINE: A Computer Software Package for the Analysis and Design of Steam Power Generating Units," ASME JOURNAL OF ENGINEERING FOR GAS TURBINES AND POWER, Vol. 109, pp. 222–227.

Sonnenschein, H., 1982, "A Modular Optimizing Calculation Method of Power Station Energy Balance and Plant Efficiency," ASME JOURNAL OF ENGINEERING FOR POWER, Vol. 104, pp. 255–259.

Wilplinger, H., 1986, "Neuer Dampfkreislauf, Thermodynamische Optimierung," Doctoral Thesis, Graz University of Technology, Austria.

# A Comparative Evaluation of Advanced Combined Cycle Alternatives

**O. Bolland**
Thermal Energy Division,
Department of Mechanical Engineering,
The Norwegian Institute of Technology,
7034 Trondheim, Norway

*This paper presents a comparison of measures to improve the efficiency of combined gas and steam turbine cycles. A typical modern dual pressure combined cycle has been chosen as a reference. Several alternative arrangements to improve the efficiency are considered. These comprise the dual pressure reheat cycle, the triple pressure cycle, the triple pressure reheat cycle, the dual pressure supercritical reheat cycle, and the triple pressure supercritical reheat cycle. The effect of supplementary firing is also considered for some cases. The different alternatives are compared with respect to efficiency, required heat transfer area, and stack temperature. A full exergy analysis is given to explain the performance differences for the cycle alternatives. The exergy balance shows a detailed breakdown of all system losses for the HRSG, steam turbine, condenser, and piping.*

## Introduction

In the past two decades, combined gas and steam turbine cycle (CC[1]) plants have successfully been put into operation with very good fuel utilization compared to other types of thermal power plants. CC plants can either be used for the generation of electricity only, or for the generation of electricity and heat. Among thermal power plants that are commercially available, the CC is the type that generates electricity with the highest efficiency. The future outlook for CC plants in Europe is very good. A number of such plants are expected to be built during the 1990s. In Great Britian and the Netherlands, CC plants are becoming very popular.

In the early seventies, CCs were built with typical electrical efficiencies of about 40 percent. Recently, CCs have been built with electrical efficiencies above 50 percent. Two plants are worth mentioning in this respect: Pegus 12 (220 MW) in Utrecht, the Netherlands, which was being put into operation in Feb. 1989 (Frutschi and Plancherel, 1989), and a 1350 MW plant, which is being built in Ambarli, Turkey (Hamann and Joyce, 1989). For both plants the guaranteed net efficiency based on the lower heating value is above 51 percent, which can be regarded as 1989 "state of the art" for CCs.

The increase in the electrical efficiency of CCs in the last few years has mainly been caused by gas turbine improvements. Increased firing temperatures have been introduced for gas turbines with relatively moderate pressure ratios, which has resulted in exhaust gas temperatures above 500°C. This type of gas turbine improvement has a positive influence on the electrical efficiency of the steam cycle.

This paper deals with the potential for improving the steam cycle efficiency in a large CCs (> 400 MW), and thereby increasing the CC electrical efficiency. The steam cycle can be improved by, among other things, decreasing the temperature differences in the heat recovery steam generator (HRSG) and by lowering the condenser pressure. This paper concentrates on another alternative: increasing the CC electrical efficiency for a given gas turbine, by improvements in the *steam cycle configuration*.

*Why* is it necessary to improve the efficiency of the CC? Modern CCs already have a very high efficiency and most improvements in efficiency have disadvantages with respect to investment costs, complexity, and reliability. The economics of a power plant govern how the plant should be built. In this respect there are four main factors to be considered: fuel costs, capital costs, time of construction, and environmental issues. The motivation for further improvements in CC efficiencies is an expected growth in energy prices and environmental aspects. The latter are becoming more and more important, and improved fuel utilization is one measure to reduce emissions from thermal power plants.

**Table 1 Performance data for the selected gas turbines**

| | V94.2 | V94.3[2] | |
|---|---|---|---|
| Net power output | 144.3 | 189.5 | MW |
| Net efficiency | 32.5 | > 35 | % |
| Exhaust gas mass flow | 504.0 | 565.2 | kg/s |
| Exhaust gas temperature | 553.1 | 563.4 | °C |
| Pressure ratio | 10.7 | 16.0 | - |

[1]The terms GuD (Gas und Dampf) and STAG (STeam And Gas) are also commonly used.

Contributed by the International Gas Turbine Institute and presented at the 35th International Gas Turbine and Aeroengine Congress and Exposition, Brussels, Belgium, June 11–14, 1990. Manuscript received by the International Gas Turbine Institute January 17, 1990. Paper No. 90-GT-335.

[2]According to Siemens, performance data for the V94.3 are preliminary.

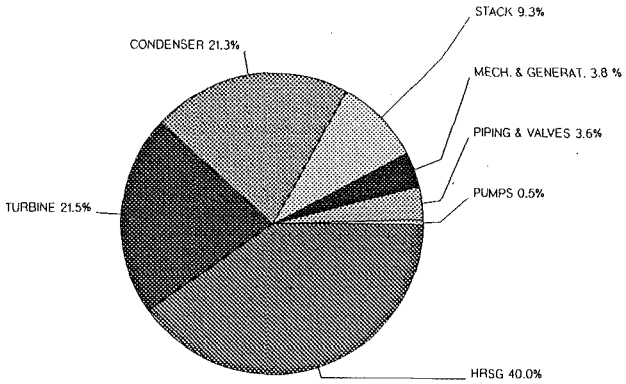


**Fig. 1 Breakdown of exergy losses in a dual pressure steam cycle**

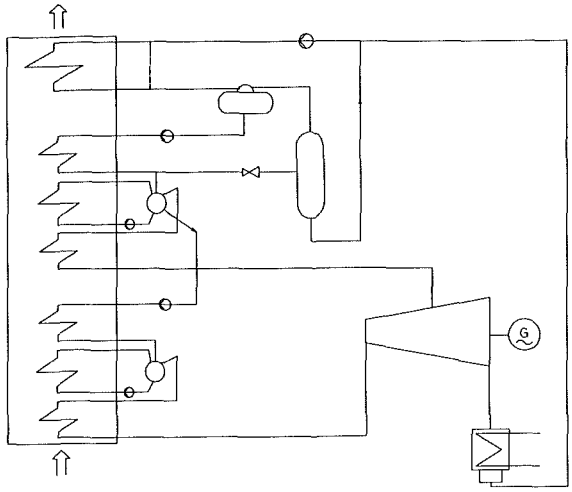

***Fig. 2(a) Flowsheet diagram for the dual pressure cycle***

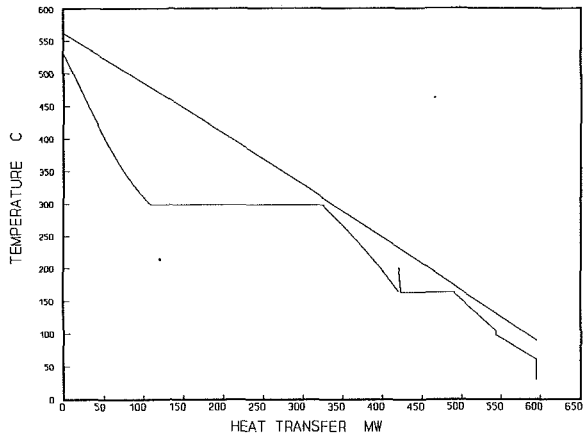


***Fig. 2(b) TQ diagram for the dual pressure cycle***

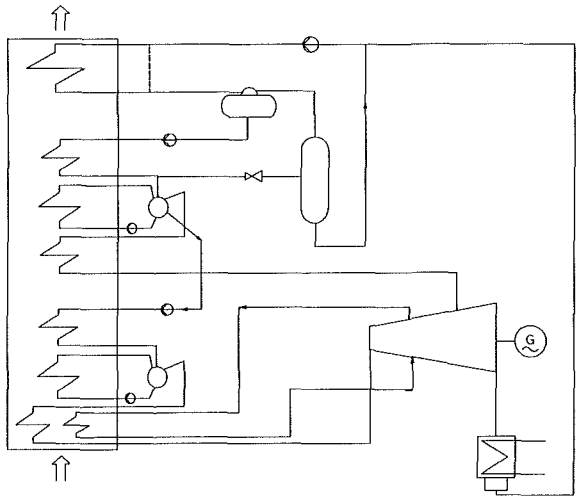

***Fig. 2(c) Flowsheet diagram for the dual pressure reheat cycle***

## Gas Turbines Used in the Study

Two gas turbines were used for the study: Siemens V94.2 and Siemens V94.3. The former of these is at present one of the largest gas turbines in operation anywhere in the world, and is a representative choice for a modern CC gas turbine. The latter is an improved model from Siemens, with a high firing temperature. This machine represents a new generation of gas turbines now being introduced to the market. This new generation consists of machines like the 150 MW class Fr 7F and the 210 MW Fr 9F from General Electric and Alsthom; Westinghouse and Mitsubishi with the 15 MW MF-111 and 150 WM W501F; Siemens with the 60 MW V64.3, 155 MW V84.3, and the 190 MW V94.3. ABB is probably going to make the 200 MW Type 15.

The two gas turbines selected for this study are calculated at ISO conditions with inlet/outlet pressure drops of 10/40 mbar. The thermodynamic cycle data are given in Table 1 (Rukes, 1990).

## Steam Cycle Configurations

Large modern CCs are normally built with a dual-pressure steam bottoming cycle. Figure 1 shows a typical distribution of losses of available work[3] for such a steam cycle. Obviously,

[3]The terms "availabe work," "availability," and "exergy" are synonymous and are going to be used interchangeably.

## Nomenclature

$A$ = heat transfer area, $m^2$
$\tilde{A}$ = nondimensional heat transfer area, see equation (16)
$c$ = efficiency moisture correction factor
CC = Combined Cycle
$C_P$ = specific heat, kJ/kg/K
$e$ = specific exergy, kJ/kg/s
$E$ = exergy, kJ/s, kW
$H$ = specific enthalpy of exhaust, kJ/kg
$h$ = specific enthalpy of $H_2O$, kJ/kg
$HP$ = high pressure
$IP$ = intermediate pressure
LHV = lower heating value, kJ/kg
$LP$ = low pressure
$m$ = mass flow, kg/s
$p$ = pressure, bar
$Q$ = heat flow, kJ/s, kW
$R$ = gas constant, kJ/kg/K
$RH$ = reheat pressure
$s$ = specific entropy, kJ/kg/s
$t$ = temperature, °C
$T$ = temperature, K
$U$ = total heat transfer coefficient, $kW/m^2/K$
$W$ = work, kW
$x$ = steam quality, kg/kg
$\eta$ = efficiency

**Subscripts**

$a$ = ambient
aux = auxiliary
$C$ = cold
$CC$ = combined cycle
$ex$ = exhaust gas
$f$ = fuel
$GT$ = gas turbine
$H$ = hot
HRSG = heat recovery steam generator
$pp$ = pinch-point temperature difference
reh = reheat
$SC$ = steam cycle
$st$ = steam
1, 2, 3 = cycle state points in Fig. 3

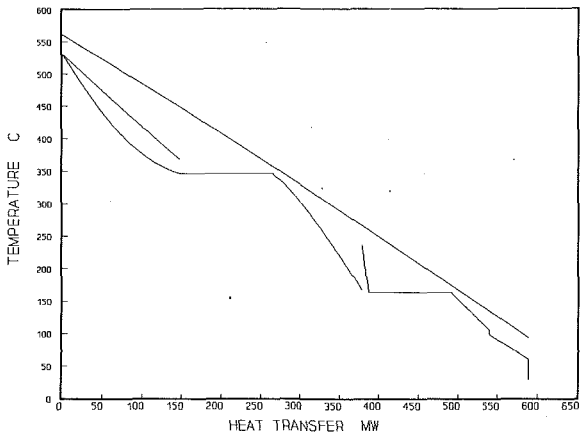


Fig. 2(*d*) TQ diagram for the dual pressure reheat cycle

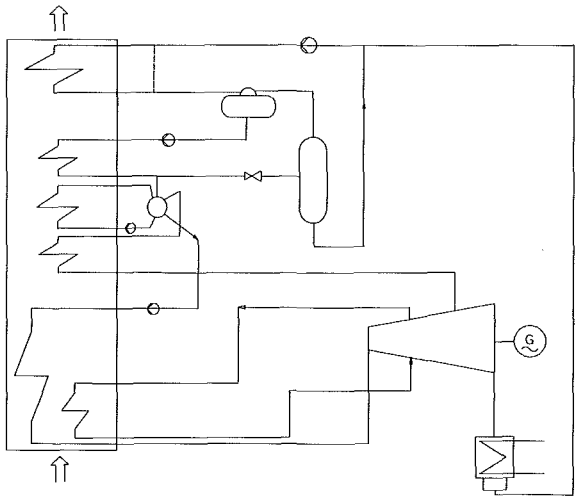


Fig. 2(*e*) Flowsheet diagram for the dual pressure supercritical reheat cycle

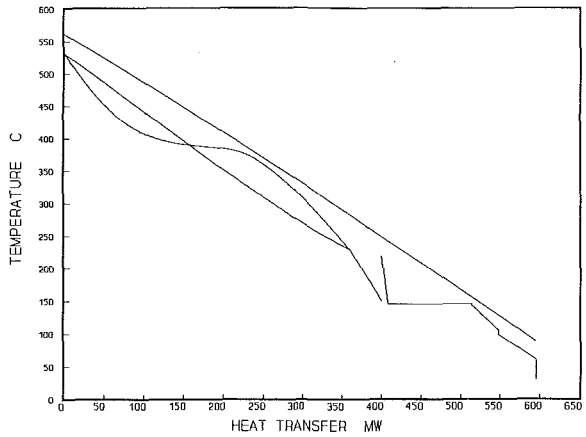


Fig. 2(*f*) TQ diagram for the dual pressure supercritical reheat cycle

the HRSG losses constitute a main share (≈40 percent) of the steam cycle loss of available work. Figures 2(*a–l*) show TQ diagrams and the cycle flowsheet for proposed changes in configuration to decrease loss of available work and thereby improve the steam cycle efficiency. The following cycle configurations are shown in Figs. 2(*a–l*):

2(*a*, *b*) Dual pressure cycle
2(*c*, *d*) Dual pressure reheat cycle
2(*e*, *f*) Dual pressure supercritical reheat cycle
2(*g*, *h*) Triple pressure cycle
2(*i*, *j*) Triple pressure reheat cycle
2(*k*, *l*) Triple pressure supercritical reheat cycle

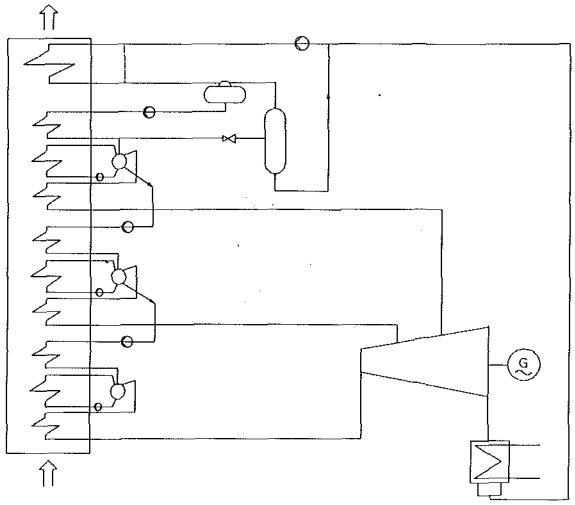


Fig. 2(*g*) Flowsheet diagram for the triple pressure cycle

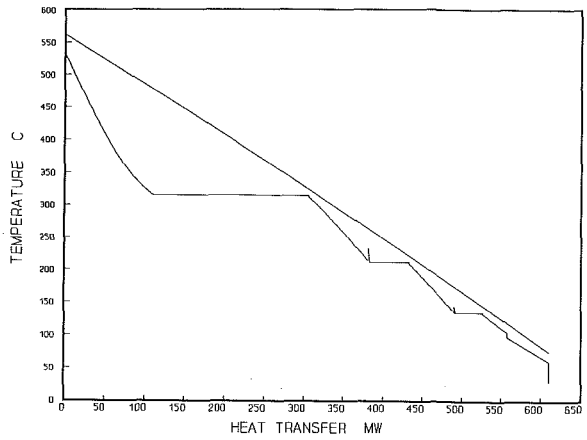


Fig. 2(*h*) TQ diagram for the triple pressure cycle

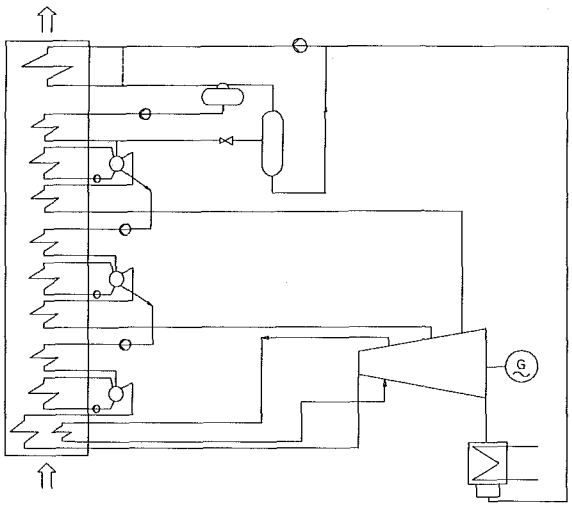


Fig. 2(*i*) Flowsheet diagram for the triple pressure reheat cycle

The choice of preheating and deaeration system needs to be explained. The steam for deaeration is generated in a flashtank outside the HRSG. Hot pressurized water from the LP economizer is throttled before entering the flashtank. The steam that is flashed off goes to the deaerator, and the water leaving the flashtank is used to preheat the feedwater coming from the condenser. To prevent the exhaust gas moisture from condensing, the feedwater should be heated up to a temperature above the dewpoint of the exhaust gas. This is done in the

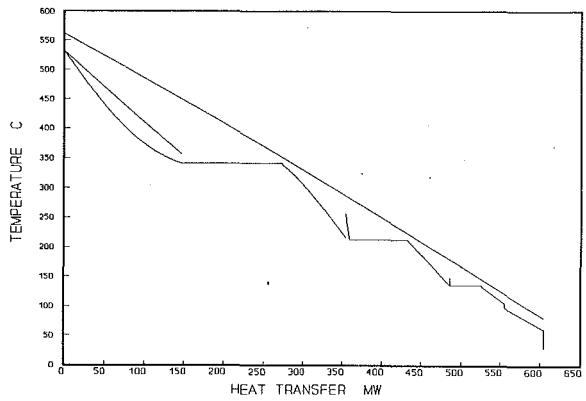


**Fig. 2(*j*) TQ diagram for the triple pressure reheat cycle**

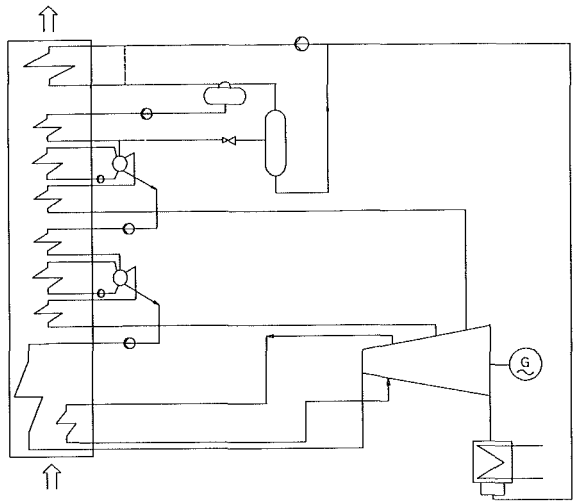


**Fig. 2(*k*) Flowsheet diagram for the triple pressure supercritical reheat cycle**

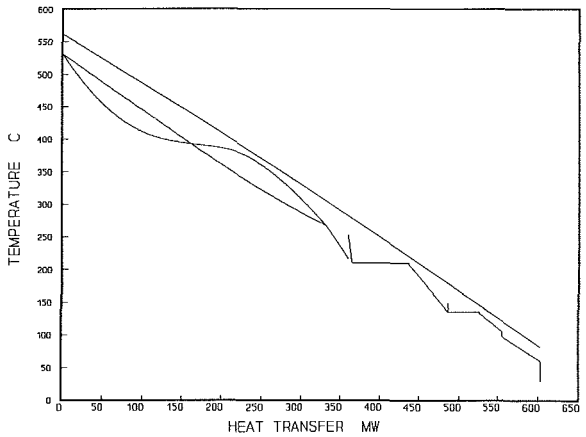


**Fig. 2(*l*) TQ diagram for the triple pressure supercritical reheat cycle**

feedwater preheater with a circulation loop (dashed line in flowsheet figures). The circulation ratio is such that the feedwater temperature entering the HRSG is above the dewpoint of the exhaust gas. In this study the feedwater temperature entering the HRSG is set to 60°C, which is well above the dewpoint of the exhaust gas, normally about 40°C.

## Computational Model

The HRSG model is separated into two basic types of computational model: the subcritical pressure stage and the supercritical pressure stage. The former consists of an economizer, an evaporator with forced circulation, and a superheater. The

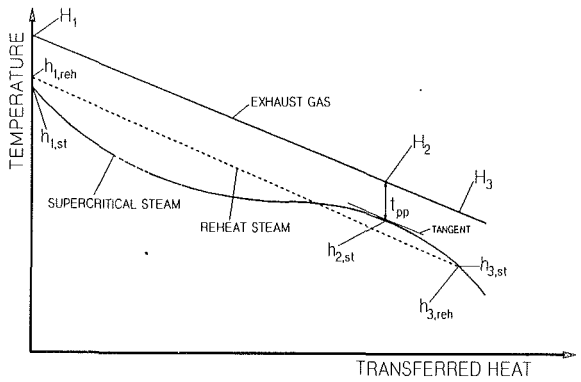


**Fig. 3 TQ diagram for supercritical pressure stage**

latter consists of a once-through heat exchanger. For the HRSG calculations, the exhaust-gas/live-steam approach temperature difference, pinch-point temperature difference, economizer approach temperature difference, live-steam pressure, and pressure drops are given as input. For the subcritical pressure stage the computational procedure is quite straightforward. The procedure applied in this study is similar to the method presented by Chin and Elmasri (1987). The computational procedure for the supercritical pressure stage is more complex since the steam[4] is not undergoing any sudden change of phase and there is no distinct "pinch point." The steam temperature at the pinch point is therefore not as easily found as for the subcritical case. Figure 3 shows a TQ diagram for a supercritical pressure stage. Obviously, the slopes of the two curves have to be equal at the pinch point. Further, the distance between the two curves has to be the specified pinch-point temperature difference, and there must be a heat transfer balance between exhaust gas and steam. With these three requirements formulated in equations (1)–(3), the steam temperature ($t_{2,st}$) at the pinch point can be found

$$m_{st} \cdot C_{P\,2,st} = m_{ex} \cdot C_{P\,2,ex} \tag{1}$$

$$m_{st} \cdot (h_{1,st} - h_{2,st}) = m_{ex} \cdot (H_1 - H_2) \tag{2}$$

$$t_{2,st} = t_{2,ex} - t_{pp} \tag{3}$$

If constant specific heat is assumed for the exhaust gas, the steam temperature at the pinch point can be found more easily

$$t_{2,st} = t_{1,ex} - t_{pp} - \frac{h_{1,st} - h_{2,st}}{C_{P\,2,st}} \tag{4}$$

However, for this study the formulation for variable specific heat is applied. It should be noted that when applying equation (1) caution must be made when evaluating the specific heat ($C_{P\,2,st}$) for steam near the critical temperature. The specific heat changes very rapidly as function of temperature above and near the critical point. For a supercritical stage with reheating, the same procedure can be applied except for equation (2), which has to be rewritten, and an extra heat balance equation needs to be added (equation (6))

$$(h_{1,st} - h_{2,st}) \cdot (H_1 - H_3) = (H_1 - H_2) \cdot (h_{1,st} - h_{3,st}) \tag{5}$$

$$m_{ex} \cdot (H_1 - H_3) = m_{st} \cdot (h_{1,st} - h_{3,st}) + m_{\text{reh}} \cdot (h_{1,\text{reh}} - h_{3,\text{reh}}) \tag{6}$$

The HRSG heat transfer area calculation is carried out by an integration method for each type of heat exchanger (superheater, evaporator, economizer, and preheater). A counterflow heat exchanger model is applied. The integration model ensures that the effect of variable specific heat capacities is taken into account. This is important for high-pressure superheated steam and water near saturation. A counterflow heat exchanger model may not be accurate in all cases, but when comparing heat transfer areas as in this study, such a model should be sufficient.

[4]Water at supercritical pressure can hardly be defined as either water or steam, but it is here referred to as steam.

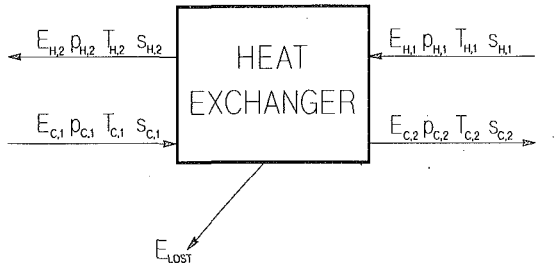


**Fig. 4 Exergy balance of a counterflow heat exchanger**

The steam turbine expansion is broken into a number of sections, which correspond to the number of HRSG pressure stages. Each section is computed by an individual dry isentropic step efficiency. The efficiency for the LP section is corrected for moisture if the expansion crosses into the wet region. The LP expansion is broken into steps, and the efficiency for each step is corrected for moisture when the exit quality is below that for the onset of condensation. This "Wilson line" quality is normally between 0.95 and 0.98. The efficiency degradation is assumed to be an exponential function (7) of mean step steam quality

$$\eta_{\text{step}} = \eta_{\text{dry}} \cdot (1 - (1 - x_{\text{step,mean}})^c) \tag{7}$$

The exponent $c$ is typically in the range 1.0–1.3, and is chosen to be 1.15 for this study. That means the penalty for moisture is a decrease in isentropic efficiency with a factor typically in the range 0.63–0.75 for every extra percent of moisture. The steam turbine model also takes into account a throttle valve loss, steam leakages through the steam turbine seals, LP section leaving loss, and steam turbine and generator auxiliary power requirements.

The condenser model is a water-cooled counterflow heat exchanger. The cooling water pressure drop and the required pump work are calculated.

Heat and exergy balances are carried out for *all components* in the model. To ensure that there are no errors in the model, an overall system heat balance is carried out, as well as an overall exergy balance.

The net efficiency of the CC is here defined as

$$\eta_{CC} = \frac{W_{GT} + W_{SC} - W_{\text{AUX}}}{m_f \cdot \text{LHV}} \tag{8}$$

$W_{GT}$, $W_{SC}$ = power output at the generator terminals
$W_{\text{AUX}}$ = auxiliary power demand and pump work

## Exergy Analysis

Traditional first-law cycle analysis based upon component performance characteristics coupled with energy balances invariably lead to a correct final answer. However, such analysis cannot locate and quantify the sources of loss that lead to that result. This is because the first law embodies no distinction between work and heat, no provision for quantifying the *quality of energy*. These limitations are not a serious drawback when dealing with familiar systems, since an intuitive understanding of the different parametric influences on system performance and a second-law qualitative appreciation of "grade-of-heat" and effect of pressure loss can be developed. When analyzing novel and complex thermal systems, however, such an understanding must be supplemented by more rigorous quantitative methods. Second-law analysis, or exergy analysis, provides these tools. Second-law analysis is no substitute for first-law analysis; it is, rather, a supplement.

The quantity energy can be split into exergy and anergy:

$$\text{Energy} = \text{Exergy} + \text{Anergy}$$

Anergy is energy in equilibrium with the ambient conditions and cannot be converted to work, while exergy is the proportion

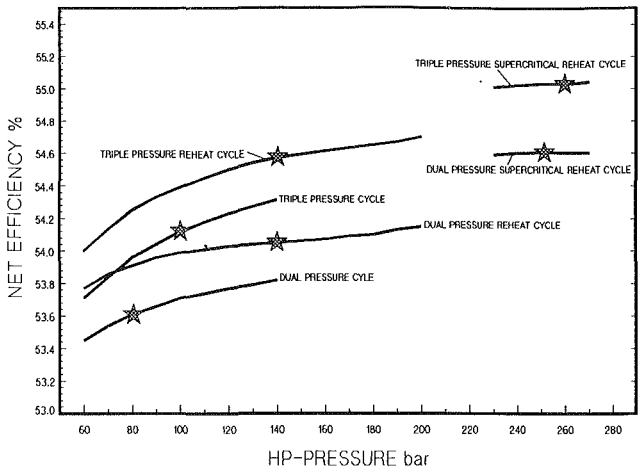


**Fig. 5 Combined Cycle net efficiency as function of HP pressure for the V94.3 gas turbine**

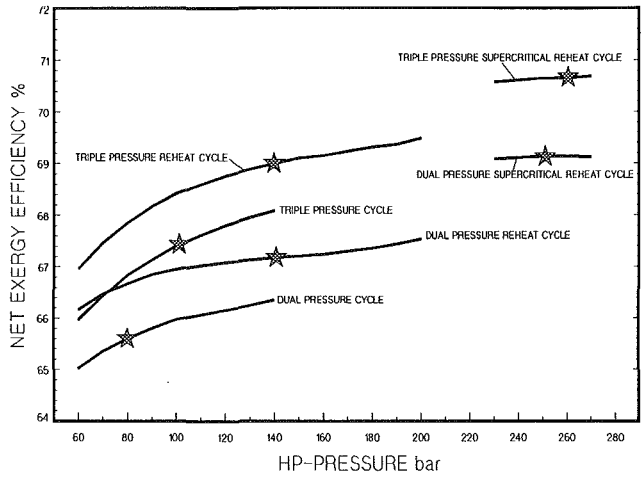


**Fig. 6 Steam cycle net exergy efficiency as function of HP pressure for the V94.3 gas turbine**

of energy that theoretically can be converted to work. The exergy of a flow stream for a given pressure $p_1$ and temperature $t_1$ can be computed by the following expression:

$$e(p_1, t_1) = (h_1 - h_a) - T_a \cdot (S_1 - S_a) \tag{9}$$

where

$$h_a = h(p_a, t_a) \qquad h_1 = h(p_1, t_1)$$
$$s_a = s(p_a, t_a) \qquad s_1 = s(p_1, t_1)$$

For an ideal gas, the term $s_1 - s_a$ can be written

$$s_1 - s_a = \int_a^1 C_P(T)/T \cdot dT - R \cdot \int_a^1 dp/p \tag{10}$$

To quantify the loss of exergy for a component, an exergy balance is applied. Figure 4 shows a counterflow heat exchanger and the quantities related to an exergy balance. The loss of exergy for the heat exchanger is

$$E_{\text{lost}} = E_{\text{in}} - E_{\text{out}} = E_{H,1} + E_{c,1} - E_{H,2} - E_{c,2} \tag{11}$$

The steam cycle is a closed loop. Exergy in a steam leaving a component is transferred to the next component, and is therefore not lost from the system. The exception is at points where exergy is deliberately rejected from the system, such as the HRSG stack and the condenser cooling water. The loss of exergy for all other components in the steam cycle can be calculated in a similar way as shown in the above example. When adding up all losses of exergy plus the generated work, this should equal the exergy of the gas turbine exhaust gas entering the HRSG. At this point the *exergy efficiency* can be defined

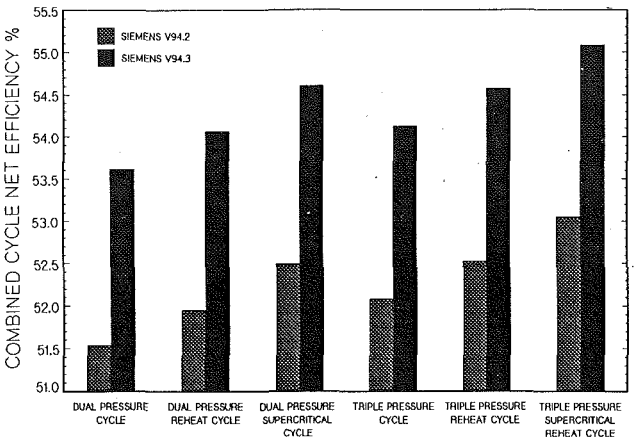


**Fig. 7 Combined Cycle net efficiency for specially chosen HP pressure for the V94.2 and V94.3 gas turbines**

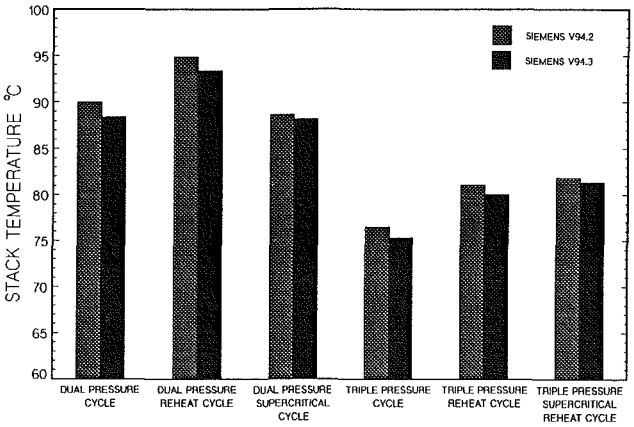


***Fig. 8 Stack temperature for specially chosen HP pressures for the V94.2 and V94.3 gas turbines***

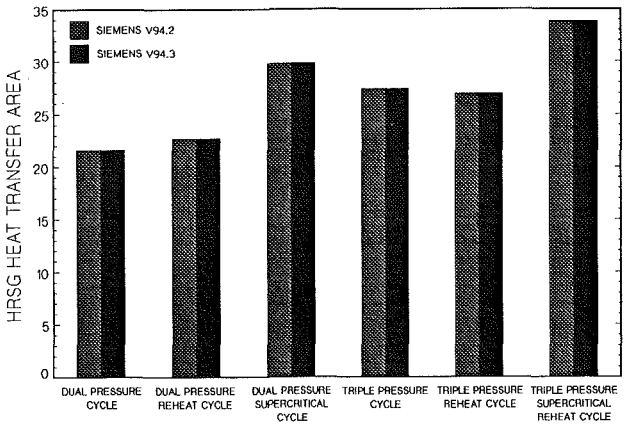


**Fig. 9 HRSG relative heat transfer areas for the V94.2 and V94.3 gas turbines**

$$\eta_{\text{exergy}} = \frac{W_{\text{net,out}}}{E_{\text{HRSG,in}}} = \frac{E_{\text{HRSG,in}} - \Sigma E_{\text{loss}}}{E_{\text{HRSG,in}}} \tag{12}$$

and further, the *maximum thermal efficiency* referred to the exhaust gas is given by

$$\eta_{\text{thermal,max}} = \frac{E_{\text{HRSG,in}}}{Q_{\text{HRSG,in}}} \tag{13}$$

where

$$Q_{\text{HRSG,in}} = m_{ex} \cdot (H_{\text{HRSG,in}} - H_a) \tag{14}$$

and $H_{\text{HRSG,in}}$ is referred to ambient conditions, which means

$$H_a = 0$$

The maximum thermal efficiency describes the thermodynamic limitation for the conversion of heat to work. The exergy efficiency accounts for internal steam cycle "imperfections," such as heat exchanger temperature differences, "mismatched" heat exchanger temperature profiles, heat losses, pressure losses, mixing losses, mechanical losses, generation of entropy in compression and expansion processes and rejection of exergy to the surroundings. By combining equations (12) and (13) a relation between work and heat is obtained

$$W_{\text{net,out}} = Q_{\text{HRSG,in}} \cdot \eta_{\text{thermal,max}} \cdot \eta_{\text{exergy}} \tag{15}$$

## Results and Discussion

Parametric studies were carried out for combined cycles using the Siemens V94.2 and V94.3 gas turbines (representing current "state of the art" and advanced technology, respectively). Thermodynamic cycle data for the gas turbines were presented earlier, and the Appendix contains additional particulars for the various cycle components.

Net exergy efficiencies (equation (12)) and net combined cycle efficiencies (equation (8)) were calculated for the various combined cycles. These efficiencies are presented in Figs. 5 and 6 as functions of the design HP pressure for the HRSG, using the V94.3. At each HP pressure the other live-steam pressures (RH, IP, LP) are optimized with respect to cycle efficiency. Figures 7–9 compare the effects of the two gas turbines on net cycle efficiency, stack temperature, and the required HRSG heat transfer area in each of the cycles.

Introducing reheat improves the efficiency by 0.2–0.4 percentage points compared to the nonreheat cycles, for both the dual and triple pressure cycles. The difference in efficiency between dual and triple pressure cycles is about 0.5–0.6 percentage points, except for smaller HP pressures, where this difference tends to decrease. Supercritical reheat cycles give a higher efficiency than the subcritical cycles. There is also a significant difference in efficiency between the dual and triple pressure supercritical reheat cycles, about 0.5 percentage point.

The variation in exergy efficiency is from 65 percent for the dual pressure cycle at 60 bar HP pressure and up to nearly 71 percent for the triple pressure supercritical reheat cycle. The differences in exergy efficiency correspond, of course, to what has been explained for Fig. 5. It is interesting here to make a comparison between the steam cycle and the Kalina cycle, where in the latter cycle a mixture of ammonia and water is used as working fluid. For the Kalina cycle, Stecco and Desideri (1989) have calculated the exergy efficiency to be 63.2 percent when utilizing exhaust gas heat at 577°C. It should be emphasized, however, that the assumptions used in the present work differ from those of Stecco and Desideri.

In Figs. 5 and 6 the graphs are marked in order to represent a "reasonable" choice of HP pressure for each type of cycle. These choices are mainly based on the steam turbine exit quality for the nonreheat cycles. For the subcritical reheat cycles the HP pressures are chosen to be 140 bar. Increased live-steam pressure normally implies higher HRSG cost, but for the subcritical reheat cycles the HRSG HP stage has a smaller mass flow and also a smaller volumetric flow compared to the nonreheat cycles. The increased tube thickness (and weight) due to higher pressure will be opposed by smaller tube diameters. Table 2 summarizes the results from the calculations with the chosen HP pressures, which are marked in Figs. 5 and 6.

Figures 7–9 are graphic presentations of the data in Table 2. When comparing the CC performance with respect to gas turbine technology (V94.2 versus V94.3), the differences in efficiency (Fig. 7) are about 2.0–2.1 percentage points. These differences are larger than any of the differences between the cycles with a given gas turbine. The potential for CC efficiency improvement therefore mainly relies on gas turbine developments. With the new generation of gas turbines, in this study represented by the Siemens V94.3, it is likely to have CC net efficiencies reaching 54–55 percent.

Figure 8 shows the stack temperature for the different cycles. As can be seen there are only minor differences in stack temperatures when comparing the two types of gas turbine. There is no obvious connection between the stack temperature and efficiency. This means that the CC efficiency is not solely dependent on *how much* of the exhaust gas energy, is utilized, but it is also a question of *how* the exhaust gas energy is utilized.

In Fig. 9 and Table 2 the HRSG heat transfer areas are given in a nondimensional form, which is

$$\tilde{A}_{\mathrm{HRSG}} = U \cdot A \cdot T_a / W_{SC} \qquad (16)$$

where $W_{SC}$ [$W$] is the steam cycle net power output. $T_a$ is a constant for all cases. Equation (16) defines a parameter relating the required $UA$ to the net power output of the steam cycle. Figure 9 shows that there is very little difference in the HRSG heat transfer area between the two gas turbines. As can be seen when comparing Figs. 7 and 9, increased efficiency comes at the expense of a larger heat transfer area. The supercritical cycles, especially, require a large heat transfer area for a given gain in efficiency. It is interesting to note that the triple pressure subcritical reheat cycle requires less heat transfer area than the triple pressure nonreheat cycle. The reason for this is that the reheat results in less mass flow going through the HP economizer and HP evaporator, which constitute most of the heat transfer area for a nonreheat cycle. Besides, the condensate flow rate is less for a reheat cycle compared to a nonreheat cycle, which means less heat transfer and heat transfer area at the cold end of the HRSG.

The effect of supplementary firing in front of the HRSG for three different types of cycles is shown in Fig. 10. The selected cycles are the dual pressure cycle, the triple pressure reheat cycle, and the dual pressure supercritical reheat cycle. All three cycles are calculated with the V94.3 gas turbine. The two subcritical cycles are calculated with different HP pressures along with an optimization of the other live-steam pressures. As can be seen from Fig. 10 supplementary firing does not improve the efficiency of the subcritical cycles irrespective of the HP pressure within the range stated in Fig. 10. On the other hand, the efficiency is slightly improved by the supplementary firing of the dual pressure supercritical cycle.

The difference among the cycles with respect to efficiency is described by means of a first-law method of analysis. A

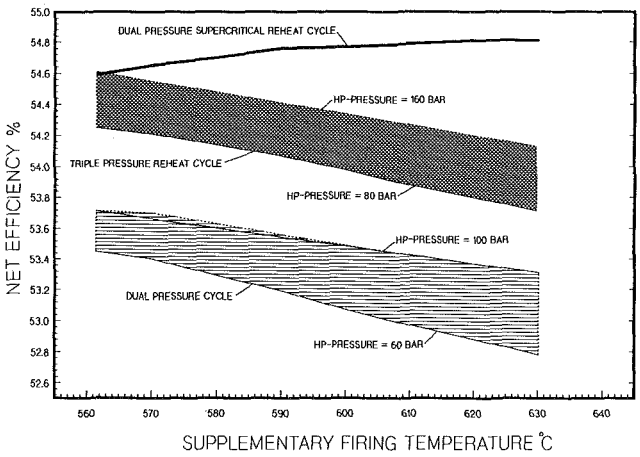


**Fig. 10 Combined Cycle net efficiency as a function of supplementary firing temperature**

**Table 2 Cycle performance**

| Type of cycle | V94.2 $\eta_{CC}$ | V94.3 $\eta_{CC}$ | V94.2 $W_{cc}$ | V94.3 $W_{cc}$ | V94.2 $\tilde{A}_{HRSG}$ | V94.3 $\tilde{A}_{HRSG}$ | V94.2 $t_{STACK}$ | V94.3 $t_{STACK}$ |
|---|---|---|---|---|---|---|---|---|
| Dual pressure | 51.53 | 53.61 | 687.7 | 577.3 | 21.76 | 21.59 | 90.0 | 88.4 |
| Dual pressure reheat | 51.95 | 54.06 | 693.3 | 582.2 | 22.81 | 22.70 | 94.9 | 93.4 |
| Dual pressure supercritical reheat | 52.49 | 54.60 | 700.5 | 588.0 | 29.90 | 29.79 | 88.6 | 88.1 |
| Triple pressure | 52.08 | 54.12 | 695.2 | 582.8 | 27.55 | 27.36 | 76.5 | 75.3 |
| Triple pressure reheat | 52.52 | 54.57 | 701.0 | 587.6 | 27.14 | 26.88 | 81.0 | 80.0 |
| Triple pressure supercritical reheat | 53.05 | 55.03 | 708.0 | 592.7 | 34.09 | 33.90 | 81.8 | 81.3 |

$W_{cc}$ [MW], $\tilde{A}$ [-], t [°C]

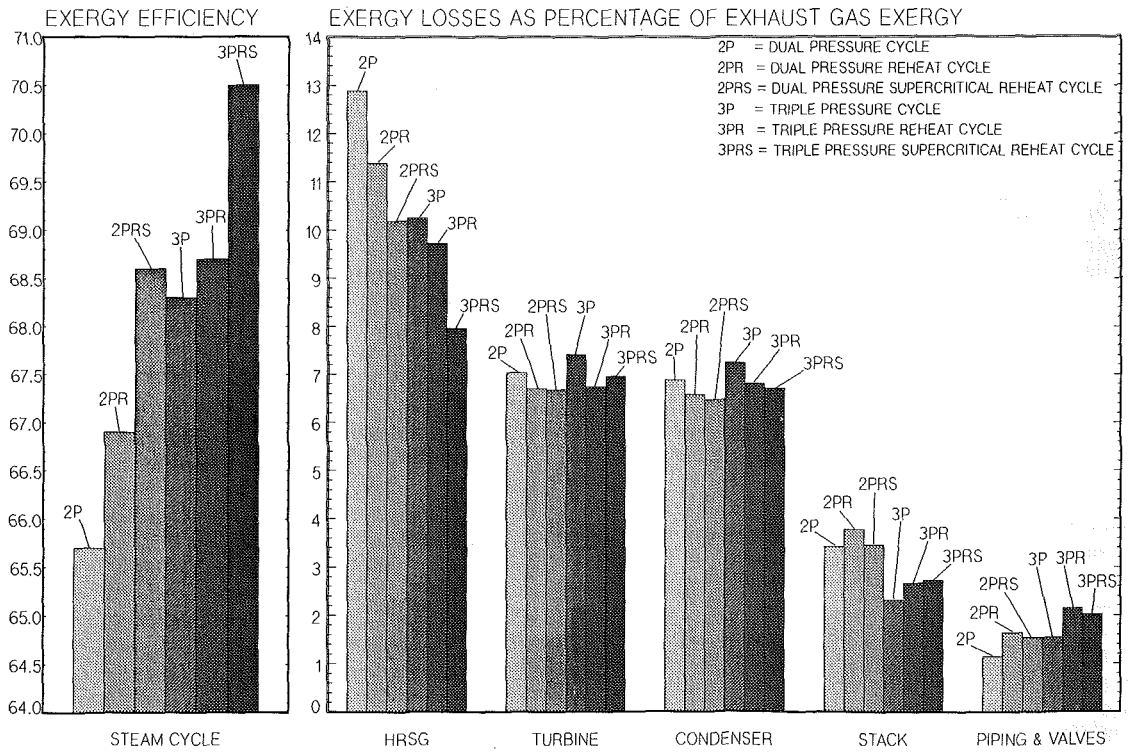


**Fig. 11 Exergy efficiency and exergy loss breakdown for the considered cycles**

second-law or exergy analysis provides information about *why* there are differences in cycle performance. Figure 11 shows a breakdown of exergy losses for different components in the steam cycle with the V94.2 gas turbine, as well as the steam cycle net exergy efficiencies. The main reason for differences in efficiency between the cycles is the decrease in HRSG exergy losses. The steam turbine exergy losses do not differ significantly between the cycles. The variations can be explained by the fact that different mass flows are expanded in the turbines and the efficiencies vary because of differences in exit quality, especially between reheat and nonreheat cycles. The condenser has also rather small variations in exergy losses, but the reheat cycles have slightly lower condenser losses. Even if reheat cycles have a higher steam turbine exit quality, the reduction in condenser steam mass flow implies a smaller loss of exergy. The stack exergy loss is a function of stack temperature, and as can be seen the triple pressure cycles have much smaller losses than the dual pressure cycles. The exergy losses from pipes and valves shown in Fig. 11 are obviously a function of cycle complexity and steam mass flow.

## Conclusions

The combination of the first-law and second-law approaches provides a good tool for the analysis of power cycles. The exergy balance method of analysis enables all loss sources to be *located* and *quantified*. When different steam cycle configurations are compared, the exergy analysis gives a very useful understanding of *why* thermodynamic performance differs from one type of cycle to another.

The triple pressure supercritical reheat steam cycle gives the largest increase in efficiency compared to a "state-of-the-art" dual pressure subcritical steam cycles. On the other hand, the increase in required heat transfer area is large compared to the gain in efficiency. The triple pressure subcritical reheat steam cycle seems to be very interesting. Compared to the dual pressure nonreheat cycle, the increase in efficiency is approximately on percentage point. Supplementary firing is not very interesting as a measure to increase CC efficiency with the types of gas turbine used in this study, except for the supercritical cycles. However, supplementary firing provides flexibility with respect to load control, and from a design point of view, flexibility is added to power output without having to make significantly less efficient cycles.

When comparing the CC efficiency of the two gas turbines used in this study, it is obvious that the new generation of gas turbines now being introduced to the market will increase the CC efficiency by about 2 percentage points. This new generation of gas turbines together with some of the proposed steam cycle configurations will make it possible to reach net efficiencies in the range of 54–55 percent for large combined cycles.

## Acknowledgments

The discussions held with Dr. Maher Elmasri were invaluable during the course of this work.

## References

Bolland, O., 1987, *GuD Power Plant Alternatives for Norwegian Boundary Conditions*, Siemens (KWU) report, Erlangen, Federal Republic of Germany.

Bolland, O., and Loken, P. A., 1987, *Potentials to Improve the Steam Cycle Efficiency in an Unfired Combined Cycle*, SINTEF report STF15 A87053, Trondheim, Norway.

Chin, W. W., and Elmasri, M. A., 1987, "Exergy Analysis of Combined Cycles: Part 2—Analysis of Two-Pressure Steam Bottoming Cycle," ASME JOURNAL OF ENGINEERING FOR GAS TURBINES AND POWER, Vol. 109, pp. 237–243.

Engelke, W., 1989, *Dampfturbinen für GuD-Kraftwerke*, BWK, Vol. 41, No. 7/8, July/Aug., pp. 335–342.

Frutschi, H. U., and Plancherel, A., 1988, "Comparison of Combined Cycles With Steam Injection and Evaporisation Cycles," IGTI-Vol. 3, ASME Cogen-Turbo, pp. 137–145.

Hamann, B., and Joyce, J. S., 1989, "World's Largest Gas Turbines for Ambarli Combined Cycle," *Modern Power Systems*, pp. 61–74, May.

Horlock, J. H., 1987, *Cogeneration—Combined Heat and Power (CHP), Thermodynamics and Economics*, Pergamon Press, New York.

Johnson, D. G., 1982, "Möglichkeiten der Kombi-Kraftwerke mit Hochtemperatur-Gasturbinen," *VGB Kraftwerkstechnik 62*, pp. 167–173, Mar.

Kehlhofer, R., et al., 1984, "Gasturbinenkraftwerke, Kombikraftwerke, Heizkraftwerke und Industriekraftwerke," *Handbuchreihe Energie Technischer Verlag Resch*, Verlag TUV Rheinland, Band 7, Chap. 2.

Kotas, T. J., 1985, *The Exergy Method of Thermal Plant Analysis*, Butterworths, London.

Rukes, B., 1990, Head of Department for Calculating of Heat Cycles and Heat Removal Systems, Siemens AG-KWU Group, The Federal Republic of Germany, Private Communication.

Stecco, S. S., and Desideri, U., 1989, "A Thermodynamic Analysis of the Kalina Cycles: Comparisons, Problems and Perspectives," ASME Paper No. 89-GT-XX.

## APPENDIX

Inputs not mentioned in the body of the paper but used in the calculations cited are:

### Gas Turbines

- Ambient temperature = 15 [°C]
- Ambient pressure = 1.013 [bar]
- Relative humidity = 60 [percent]
- Inlet pressure drop = 10 [mbar]
- Outlet (HRSG) pressure drop = 40 [mbar]
- Auxiliary power for each gas turbine = 400 [kW]

### HRSG

- Pinch point = 10 [K]
- Minimum steam/exhaust approach temperature = 30 [K]
- Economizer approach temperature = 2 [K]
- Pressure drop live-steam pipes:
  Subcritical cycles HP = 5, RH = 7, IP = 7, LP = 10 [percent]
  Supercritical cycles HP = 4, RH = 7, IP = 7, LP = 10 [percent]
- Heat loss live-steam pipes = 1 [K]
- Pressure drop superheaters = 5 [percent]
- Pressure drop evaporators = 5 [percent]
- Pressure drop economizers = 5 [percent]
- Pressure drop feedwater preheater = 4 [bar]
- Deaerator pressure = 1.2 [bar]
- Exhaust gas duct heat loss = 2 [K]
- Maximum steam temperature: HP = 540, RH = 560 [°C]

### Steam Turbine

- Pressure drop throttle valves = 2 [percent]
- Pressure drop reheat return pipe = 3 [percent]
- Isentropic efficiencies: HP = 92, RH = 92, IP = 92, LP = 89 [percent] (subcritical)
- Isentropic efficiencies: HP = 91, RH = 92, IP = 92, LP = 89 [percent] (supercritical)
- Steam leakages through seals: HP = 0.2, RH = 0.2, IP = 0.2, LP = 0.2 [percent]
- LP section leaving loss = 30 [kJ/kg]
- "Wilson line" quality = 0.975
- Auxiliary power fraction = 0.25 [percent] (pump work not included)
- Mechanical/generator efficiency = 98.2 [percent]

### Condenser

- Condenser pressure = 0.04 [bar]
- Cooling water temperature = 15 [°C]
- Allowed cooling water temperature increase = 9 [K]
- Cooling water pressure drop = 1 [bar]

### Pumps

- Mechanical efficiency = 92 [percent]
- Isentropic efficiency = 80 [percent]

# Combined Cycle Enhancement

**H. Jericha**
Graz University of Technology,
Graz, Austria

**F. Hoeller**
Elin-Union,
Vienna, Austria

*The Combined Cycle Plant (CCP) offers the best solutions to curb air pollution and the greenhouse effect, and it represents today the most effective heat engine ever created. At Graz University of Technology work is being conducted in close cooperation with industry to further enhancement of CC systems with regard to raising output and efficiency. Feasibility studies for intake air climatization, overload and part-load control, introduction of aeroderivate gas turbines in conjunction with high-temperature steam cycles, proposals for cooling, and the use of hydrogen as fuel are presented.*

## Introduction

Due to the limitations of a small home market, the actual manufacture of gas turbines in Austria has been restricted to a few technology plants. Even so, Austrian engineers have contributed to the development of the CC throughout its history: F. Pauker [1] obtained the first patents. H. Melan [2] planned the first large CCP with unfired boiler Korneuburg A on the order of the utility NEWAG. It was built by Brown Bovery and Waagner Biro and went into operation in 1960, delivering 75 MW. The same utility a few years later ordered one of the first CCPs with fired high-pressure boiler built by Siemens, and achieved with the Korneuburg B plant, again built by BBC and WB in 1980, a world efficiency record of 47 percent in the acceptance tests [3].

Last year the coauthor's company planned and supervised the erection of the largest yet industrial CCP. It is a retrofit of a GE frame6 of a 40 MW gas turbine built by AEG-Kanis with fired boiler by SGP at an existing high-pressure steam plant. Thus Steyrermuehl Company, one of the largest paper mills in the country, is supplied with power and technological heat in cogeneration.

At the moment work proceeds concerning the following topics:

## Topic 1: Intake Air Climatization

At 40°C ambient air temperature a typical heavy-duty gas turbine develops only about 85 percent of its rated power. In summer in southern European regions and in the tropics long or continuous periods of operation under such conditions are expected. Evaporative cooling with chilled water and even operation of refrigeration plants has been investigated and applied.

The authors propose a scheme using turbomachinery and a cooler to obtain the desired cooling effect for a CCP operating under tropical conditions. Figure 1.1 (scheme A) shows an Air Conditioning Set (ACS) for supercharging the gas turbine of CCP within limits of safe operation as specified by the gas turbine manufacturer. It consists of an air compressor, air cooler, and air expansion turbine; the cooling medium is feed-

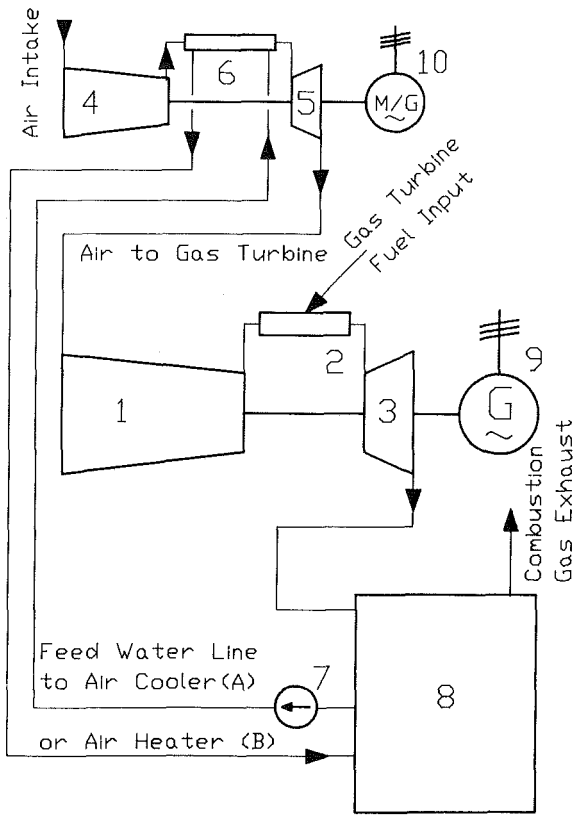


1 Gas Turbine Compressor
2 Combustion Chamber
3 Gas Turbine
4 ACS Compressor
5 ACS Expander
6 Compressed Air Cooler / Air Heater
7 Feed Pump
8 Exhaust Heat Boiler Steam Plant
9 Generator
10 Motor/Generator

**Fig. 1.1 Scheme of air conditioning turboset increasing output of gas turbine and CCP**

Contributed by the International Gas Turbine Institute and presented at the 35th International Gas Turbine and Aeroengine Congress and Exposition, Brussels, Belgium, June 11-14, 1990. Manuscript received by the International Gas Turbine Institute January 18, 1990. Paper No. 90-GT-112.

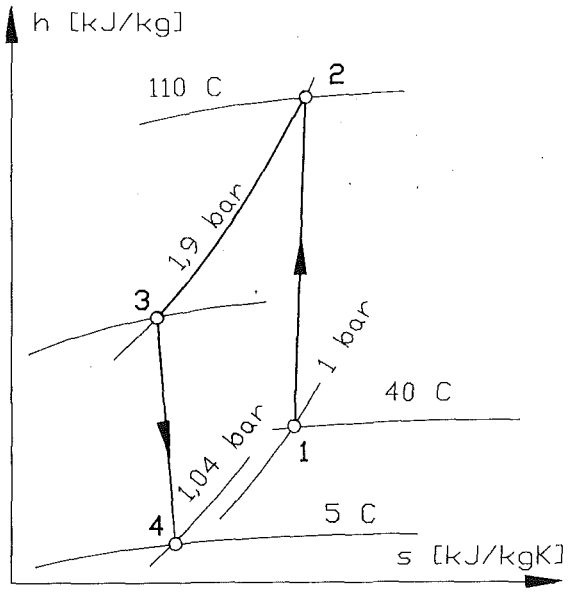


1 Air Intake
2 After Compression in ACS Compressor
3 After Cooler
4 Air at Inlet to Gas Turbine

**Fig. 1.2 ACS operation shown in an enthalpy-entropy diagram for air (mode of operation for increased output)**

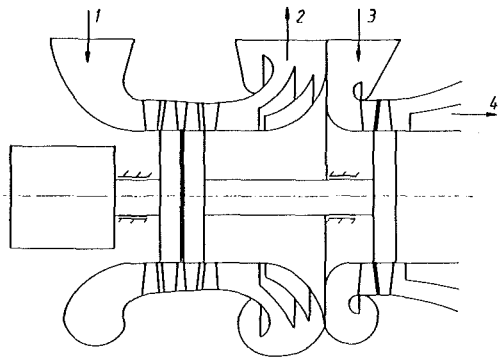


1, 2, 3, 4 *see Fig. 1.2*

**Fig. 1.3 ACS with a counterrotating compressor**

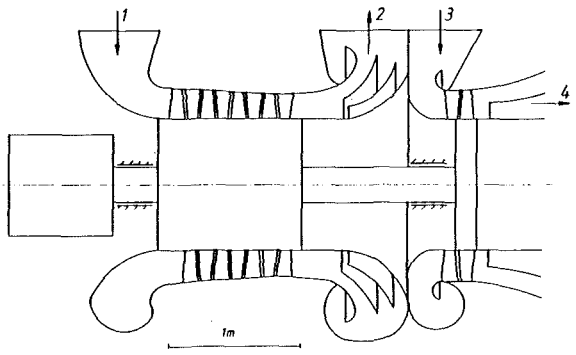


1, 2, 3, 4 see Fig. 1.2

**Fig. 1.4 ACS with a single-shaft four-stage compressor**

water prior to feed heating at ambient temperature. Figure 1.2 denotes the thermodynamic conditions of the ACS in an enthalpy–entropy diagram for air, with changes of state corresponding to compression, cooling, and expansion of the air flow [4].

For a typical heavy-duty industrial gas turbine, for example a GE frame6 40 MW gas turbine, the power balance is as

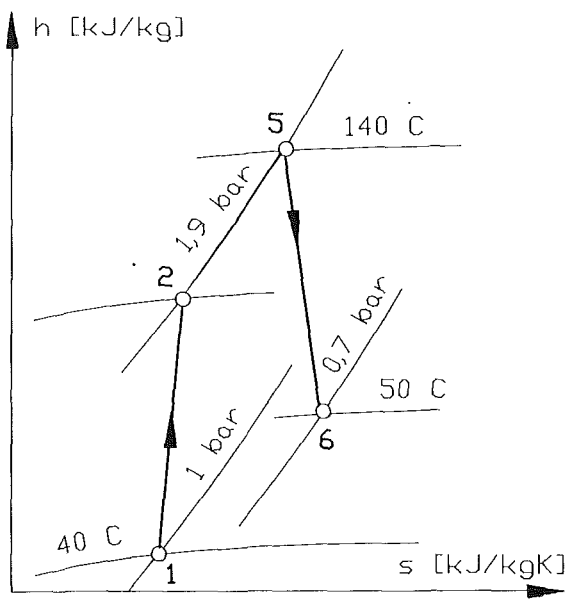


1 Air Intake
2 After Compression in ACS Compressor
5 After Air Heater
6 Air at Inlet to Gas Turbine

**Fig. 1.5 ACS operation shown in an enthalpy-entropy diagram for air (mode of operation for efficient part load)**

follows: To condition the air intake flow from ambient 1 bar/40°C to gas turbine compressor inlet condition 1.04 bar/5°C, about 3.7 MW driving power for the ACS, defined as the difference between ACS compressor and ACS expansion turbine power, is required. Gas turbine power is raised by over 30 percent, so that after deduction of the ACS electrically transmitted driving power, a gain in gas turbine total output of 20 percent results. A further improvement is possible by saving feed heating steam in the steam plant, which can be expanded in the steam turbine with a gain of approximately a further 5 percent of gas turbine power.

The gas turbine thermal efficiency improves by the cooler air intake about as much as the ACS driving work amounts to, even including the electric transmission losses. A possible use of the cooling heat for feedwater heating saves steam extraction from the steam turbine in a CCP and results in an improvement, a small one, in thermal overall plant efficiency.

In a CCP the product of gas turbine exhaust temperature and exhaust mass flow in the operation of an ACS stays constant or is slightly increased. The same is valid for boiler steam production and steam turbine power.

For the same example of a 40 MW gas turbine we studied two different kinds of compressor design: a counterrotating compressor (Fig. 1.3) and a single-shaft four-stage compressor (Fig. 1.4). The dimensions of such an ACS are 1 m rotor drum diameter with 0.2 m blade length and three to four stages for the compressor and 1 m disk diameter and similar blade length for the single-stage expansion turbine. A total bearing span of about 2 m provides ample space for inlet housings and diffusors and outlet casing. The 4 MW motor is driven at 50 Hz.

In operation of a turbomachinery ACS a further operational advantage may be expected. Compressor fouling in gas turbines is caused by air pollution, because particles having passed the filters are centrifuged in the blading, clog blade surfaces, and thus deteriorate compressor performance. Therefore complicated washing procedures or engine shutdown is required. If particles passed an ACS prior to the gas turbine this effect would occur mainly in the ACS compressor and turbine. They are easy to clean and to shut down, while the gas turbine is staying in operation with an air supply via a suitable bypass.

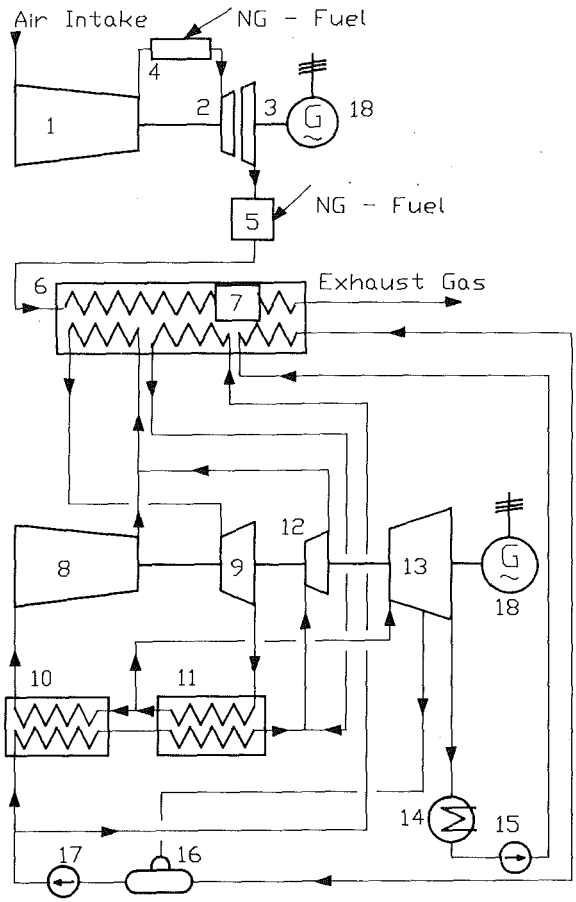


1 Air Compressor
2 Compressor Turbine
3 Power Turbine
4 Combustion Chamber
5 Reheat Combustion Chamber
6 Reheated Combustion Gas
7 Selected Catalytic NOX Reduction
8 Steam Compressor
9 High Temperature Steam Turbine
10 Steam Cooler / Feed Heater
11 Steam Cooler / Boiler Superheater
12 High Pressure Steam Turbine
13 Condensing Turbine
14 Condensor
15 Condensate Pump
16 Deaerator
17 Feed Pump
18 Generator

**Fig. 2.1 Scheme of aeroderivative gas turbine-high-temperature steam combined cycle plant**

So prolonged periods of gas turbine operation with much less need for compressor washing are to be expected. These advantages will have to be balanced against the additional investment costs for the installation of an ACS.

## Efficient Part-Load Operation With ACS

A scheme for efficient part-load operation by heating the gas turbine inlet air was proposed by Frutschi [5] and a thorough investigation of part-load measures regarding their merits in maintaining high part-load efficiency has recently been published by Gyarmathy [6]. Thus variable guide vane compressors with additional throttling at intake serve best together with keeping gas turbine inlet and outlet temperatures at the limits of safe blading operation.

The scheme proposed here can be adapted to efficient part-load operation in a similar way. Supplying feed-heated feedwater from the steam plant to the ACS cooler and transforming it into an air heater, the ACS now supplies heated air at lower pressure to the gas turbine. Thus the mass flow is reduced, but efficient flow conditions remain in the gas turbine compressor (see Fig. 1.1: scheme B). Figure 1.5 shows the thermodynamic conditions of air in ACS. The motor works as a generator and in the same example as cited above it produces about 2.9 MW electric power, improving the part-load efficiency of the plant [7]. Again gas turbine operating conditions provided by the ACS stay within the limits prescribed by the manufacturer. Combined ACS and variable guide vane control in the gas turbine compressor would further allow one to maintain high gas inlet temperature and would thus enhance part-load efficiency.

**Table 2.1 Thermodynamic data of flow scheme of Fig. 2.2**

| Flow | p [bar] | t [Grad] | h [kJ/kg] | s [kJ/kgK] | v [$m^3$/kg] | x [-] | m [kg/s] |
|---|---|---|---|---|---|---|---|
| BST01 | 1.600 | 194.0 | 2860.4 | 7.5876 | 1.3355 | 1.000 | 1.228 |
| BST02 | 0.538 | 96.1 | 2674.4 | 7.6397 | 3.1400 | 1.000 | 1.048 |
| BST03 | 0.160 | 55.3 | 2509.2 | 7.7056 | 9.0654 | 0.961 | 0.980 |
| CON01 | 0.152 | 34.5 | 144.7 | 0.4986 | 0.0010 | 0.000 | 2.028 |
| CON02 | 0.511 | 61.3 | 256.7 | 0.8478 | 0.0010 | 0.000 | 1.048 |
| CST01 | 4.859 | 316.2 | 3098.6 | 7.5327 | 0.5539 | 1.000 | 22.967 |
| CST02 | 0.035 | 26.7 | 2330.9 | 7.7913 | 35.9257 | 0.910 | 19.711 |
| FW01 | 0.035 | 26.5 | 111.1 | 0.3883 | 0.0010 | 0.000 | 21.740 |
| FW02 | 2.423 | 26.5 | 111.4 | 0.3885 | 0.0010 | 0.000 | 21.740 |
| FW03 | 2.326 | 53.3 | 223.4 | 0.7464 | 0.0010 | 0.000 | 21.740 |
| FW04 | 2.233 | 81.2 | 340.0 | 1.0891 | 0.0010 | 0.000 | 21.740 |
| FW05 | 1.592 | 113.2 | 474.7 | 1.4533 | 0.0011 | 0.000 | 22.967 |
| FW06 | 81.380 | 114.3 | 485.2 | 1.4588 | 0.0011 | 0.000 | 22.967 |
| HTS01 | 25.000 | 850.0 | 4265.9 | 8.1798 | 0.2065 | 1.000 | 86.893 |
| HTS02 | 5.061 | 564.0 | 3622.2 | 8.2543 | 0.7611 | 1.000 | 86.893 |
| HTS03 | 4.859 | 316.2 | 3098.6 | 7.5327 | 0.5539 | 1.000 | 86.893 |
| HTS04 | 4.859 | 316.2 | 3098.6 | 7.5327 | 0.5539 | 1.000 | 63.926 |
| HTS05 | 4.664 | 149.2 | 2744.5 | 6.8426 | 0.4000 | 1.000 | 63.926 |
| HTS06 | 25.773 | 375.0 | 3183.4 | 6.9175 | 0.1113 | 1.000 | 63.926 |
| HTS07 | 78.125 | 293.3 | 1471.8 | 3.4812 | 0.0039 | 0.113 | 22.967 |
| HTS08 | 75.000 | 520.0 | 3452.9 | 6.8233 | 0.0461 | 1.000 | 22.967 |
| HTS09 | 25.773 | 370.4 | 3173.0 | 6.9014 | 0.1104 | 1.000 | 22.967 |
| HTS10 | 25.773 | 373.7 | 3180.5 | 6.9131 | 0.1111 | 1.000 | 86.893 |

**Table 2.2 Heat and power balance for steam cycle according to Figs. 2.2 and 2.3**

| | |
|---|---|
| Fuel Heat Input | 94 319 kW |
| Turbine Power | 78 827 kW |
| Pump Power | -248 kW |
| Compressor Power | -28 028 kW |
| Thermal Efficiency | 0.536 |

Table 2.3 Comparison of the available bottoming cycles making use of an aeroderivative gas turbine

| Scheme | Gas Turbine | | | Steam Cycle | | | | Plant |
|---|---|---|---|---|---|---|---|---|
| | Heat Input [MW] | Output [MW] | Efficiency | Output by Exhaust Heat Boiler [MW] | Reheat Input [MW] | Add. Output [MW] | Efficiency | Efficiency |
| CCP | 94.87 | 33.1 | 0.3489 | 11.9 | - | - | - | 0.4743 |
| STIG | 121.98 | 51.4 | 0.4220 | - | - | - | - | 0.4220 |
| CCP with add. firing to 1200°C, with convential high pressure reheat steam cycle | 94.87 | 33.1 | 0.3489 | 11.9 | 138.9 | 60 | 0.430 | 0.4480 |
| CCP with add. firing to 1200°C, with novel steam cycle 25 bar/800°C | 94.87 | 33.1 | 0.3489 | 11.9 | 138.9 | 72 | 0.520 | 0.5015 |
| CCP with add. firing to 1200°C, with novel steam cycle 25 bar/850°C | 94.87 | 33.1 | 0.3489 | 11.9 | 138.9 | 75 | 0.540 | 0.5133 |

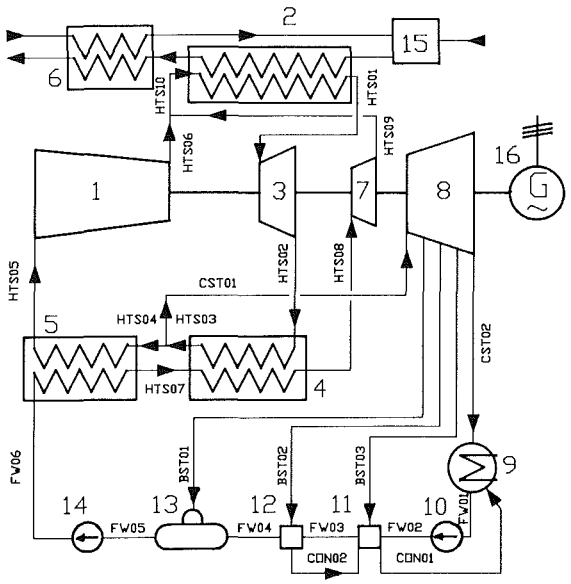


1 Steam Compressor
2 Steam Heater
3 High Temperature Steam Turbine
4 Steam Cooler / Boiler Superheater
5 Steam Cooler / Feed Heater
6 Air Heater
7 High Pressure Steam Turbine
8 Condensing Turbine
9 Condensor
10 Condensate Pump
11,12 Feed Heater
13 Deaerator
14 Feed Pump
15 Combustion Chamber
16 Generator

Fig. 2.2 High-temperature steam cycle: flow scheme with heat input to high temperature steam heater only

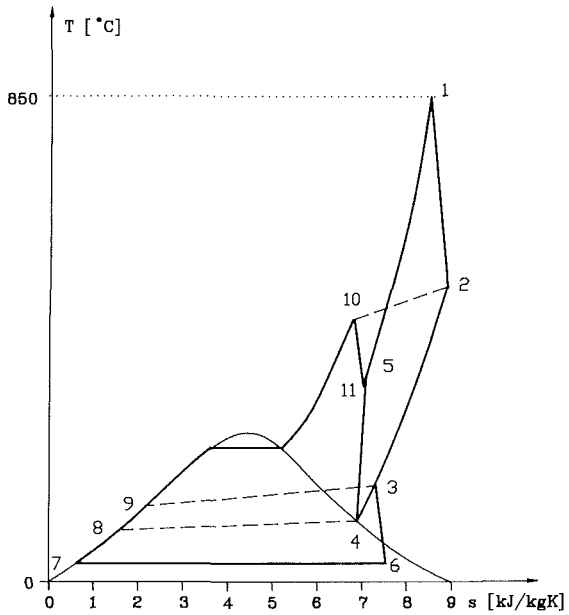


1-2 High Temperature Steam Turbine
2-3, 3-4 Steam Cooler
4-5 Steam Compressor
5-1 Steam Heater
3-6 Condensing Turbine
6-7 Condenser
7-10 Feed Water Heating, Evaporation and Superheating
10-11 High Pressure Turbine
11-5 Merging Point

Full Lines: Changes of State
Dashed Lines: Mass Flow Connections

Fig. 2.3 High-temperature steam cycle: temperature-entropy diagram

## Topic 2: Use of Aeroderivative Gas Turbines in CCP

The use of aeroderivative gas turbines in industrial CCPs has brought about the latest developments in flow calculation, blade cooling, manufacture of high-temperature alloys in single crystal blading and thus very high combustion temperatures, ensuring that high thermal efficiency will be available for power production and cogeneration.

In the US, CCPs with STIG have been successful [8], but in Europe there exists the problem of sufficient makeup water supply. Insufficient well capacity, legal restrictions, and the necessity to install and to operate a large water purification plant have induced most European plant builders to stick to the conventional condensing or cogeneration plant. Besides, emission legislation is to become even more stringent in the future, so that catalytic $NO_X$ reduction plants will have to be installed anyway.

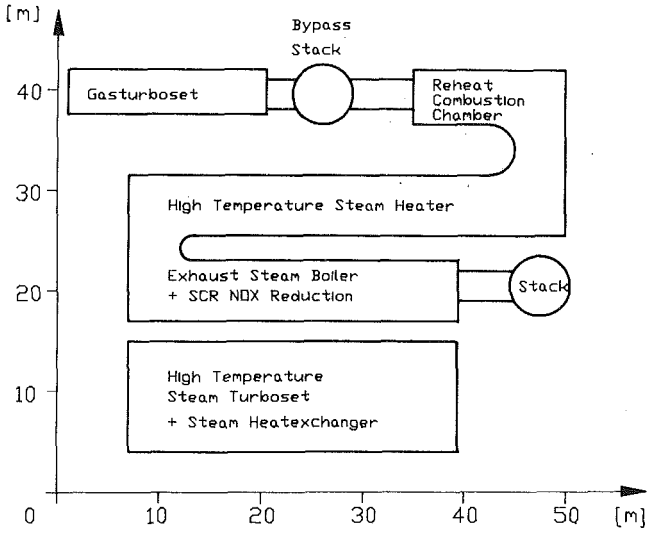


**Fig. 2.4 Site requirements (ground floor arrangement) for 120 MW aeroderivative gas turbine-high-temperature steam combined cycle plant**

Under these boundary conditions all parts of a CCP have to be optimized even for a medium size industrial plant. The use of aeroderivative gas turbines appears to be most reasonable since they fit in output, can be bought from a large production line, and have the highest efficiencies available on the market [9]. Their disadvantages are the requirement of a spare gas generator for replacement during overhaul, the relatively low exhaust temperature of around 400°C, and in comparison to large output gas turbines the impossibility of a reheat scheme from the aerodesign palette. Since a reheat low-pressure gas turbine part would have to be designed specifically for a given plant, a solution could emerge from the inclusion of the reheat in a high-temperature steam plant similar to the one proposed by the author earlier [10]. Combining the aeroderivative gas turbine primary heat input at high temperature with the reheat effect of the novel steam cycle would result in very high CCP efficiency at medium output industrial plants. A similar effect to the Japanese "Moonlight" project with its reheat gas turbine CCP could be achieved, but for machines of far smaller output.

The scheme of such a plant is presented in Fig. 2.1 showing heat input to the GTCC and in reheat to the RCC by natural gas fuel. This heat is transferred to the steam cycle via a metallic high-temperature steam heater and ensuing exhaust heat boiler and feed heater. At the suitable temperature of 250° to 400°C a selective catalytic $NO_X$ reduction plant is incorporated in the boiler.

The novel steam cycle itself has been adapted from nuclear application [10] to atmospheric fossil firing for maximum steam conditions of 25 bar/850°C and 25 bar/800°C, respectively. Figure 2.2 describes the scheme of the novel steam cycle for 50 MW output. Table 2.1 gives the corresponding cycle data. Figure 2.3 is a typical temperature-entropy diagram of the steam cycle; the heat balance and resulting thermal efficiency of heat input only in the high-temperature region are shown in Table 2.2. Figure 2.1 includes the heat input not only from the RCC in the high-temperature region but also the cooling of the exhaust gases to stack temperature.

A comparison of the available bottoming cycles making use of an aeroderivative gas turbine exhaust gases without and with additional firing is made in Table 2.3.

So with the performance data of a GE LM5000 and a high-temperature steam plant as described in the feasibility study published in [10, 11], a CC plant could be developed with a thermal efficiency comparable to plants almost ten times larger with excellent emission properties. The size requirements of such a CCP with 120 MW output are indicated in Fig. 2.4. A comprehensive study of investment costs is presently being conducted; the results will be presented in due course.

## Topic 3: Steam Blade Cooling

Steam blade cooling has been suggested recently [12]. It offers in a CCP the advantage of effective use of heat extracted from the gas turbine blades and nozzles. Expansion in the gas turbine blade path improves due to the elimination of mixing losses of hot gas and ejected cooling air, provided the cooling steam is taken from and is returned to the steam plant. Such a scheme prevents transpiration cooling and requires additional heat shields on the blade surface especially near the leading and trailing edges. Thermal barrier coatings are insufficient in thickness to achieve the required insulation since steam cooling channels cannot be brought near enough to these critical areas. Some kind of ceramic tiling similar to the space shuttle solution could perhaps cope with this task. We are performing heat conduction and strain calculations in the investigation of this problem. Certainly a solution is not in sight nor is one being tested.

## Topic 4: Use of Hydrogen Fuel

The author has reported to ASME Cogen Turbo III [13] on the use of hydrogen fuel for gas turbines and CCPs. A novel peak power plant is presented with internal combustion of hydrogen and oxygen in a steam atmosphere. Thus a very high efficiency of reuse of a most valuable fuel generated by electrolysis from surplus hydraulic sources during periods of low power demand or transported from solar sites is achieved. Work continues with partners in the actual development of an internal steam-cooled $H_2/O_2$ combustion chamber as a first step to the realization of a prototype plant [14].

## References

1 Pauker, F., "Neuere Vorschläge zum Gas-Dampf-Verfahren," Austrian Patent No. 172202, 1947; presented at the 5th World Power Conference, Vienna, 1956.

2 Melan, H., General Report, presented at the 5th World Power Conference, Vienna, 1956.

3 Czermak, H., "Operating Experience Combined Cycles," Panel Discussion, CIMAC Conference, Helsinki, 1981.

4 Elin-Union Patent Applications, Austrian Patent Office, Vienna 1010, Kohlmarkt 8, 1990.

5 Frutschi, H. U., "Control Methods for Cogeneration With Gas Turbines and Combined Cycles," presented at ASME Cogen Turbo, Montreux, 1987.

6 Gyarmathy, G., "On Load Control Methods for Combined Cycle Plants," presented at ASME Cogen Turbo III, Nice, 1989.

7 Elin-Union Feasibility Study, Report on improved thermal energy production to FFF Austrian Research Fonds, in preparation.

8 Kolp, D. A., and Moeller, D. J., "World's First Full STIG LM5000 Installed at Simpson Paper Company," ASME JOURNAL OF ENGINEERING FOR GAS TURBINES AND POWER, Vol. 111, Apr. 1989, pp. 200-210.

9 Pace, R. A., "The Industrial Aeroderivative Gas Turbine," presented at ASME Cogen Turbo II, Montreux, 1988.

10 Jericha, H., "High Temperature Reactor Heat Conversion by Novel High Efficiency Steam Cycle," presented at ASME Cogen Turbo II, Montreux, 1988.

11 Perz, E., et al., "Design of a 50 MW Pilot Plant for a High Efficiency Steam Cycle," ASME Paper No. 88-GT-154.

12 Stambler, I., "EPRI Sees Near Term Potential for Closed Circuit Steam Cooling," *Gas Turbine World*, Feb. 1988.

13 Jericha, H., et al., "A Novel Thermal Peak Power Plant," presented at ASME Cogen Turbo III, Nice, 1989.

14 Sternfeld, H., et al., "Spinning Reserve for Power Plants From Stored Hydrogen," presented at the 6th World Hydrogen Energy Conference, Vienna, 1986.

**I. S. Ondryas**
Project Manager.

**D. A. Wilson**
Project Engineer.

**M. Kawamoto**
Engineer.

Fluor Daniel Power,
Irvine, CA 92730

**G. L. Haub**
Project Engineer,
Kern River Cogeneration Company,
Bakersfield, CA 93380

# Options in Gas Turbine Power Augmentation Using Inlet Air Chilling

*Gas turbine power augmentation in a cogeneration plant using inlet air chilling is investigated. Options include absorption chillers, mechanical (electric driven) chillers, thermal energy storage. Motive energy for the chillers is steam from the gas turbine exhaust or electrical energy for mechanical chillers. Chilled water distribution in the inlet air system is described. The overall economics of the power augmentation benefits is investigated.*

## Introduction

Recent rapid growth in summer electricity demand experienced by most of the U.S. utilities results in the need to build power plants that generate maximum output at summer ambient temperature ratings. Due to their short installation time and low installation cost, gas turbines are often used to meet this peak demand. One disadvantage, however, penalizes the gas turbine peaking plant rating, namely the inversely proportional effect of the ambient temperature on the gas turbine output, which is depicted in Fig. 1. The gas turbines typically produce 30 percent higher output at 20°F than at 95°F. Thus the cost of installing a gas turbine or combined cycle plant rated at 95°F is 20–30 percent higher than that rated at 20°F. This inherent disadvantage of reduced gas turbine output at high ambient temperatures can be mitigated by the reduction of the GT compressor inlet air temperature, which would result in increase of GT output at a given ambient temperature.

The traditional way to decrease the compressor inlet air temperature is the incorporation of an inlet air evaporative cooler, which can reduce the inlet air dry bulb ambient temperature by up to 90 percent of the dry bulb–wet bulb temperature difference. To achieve additional inlet air temperature reduction, alternative methods of inlet air cooling must be used, referred here as inlet air chilling.

## Objectives

- Develop a GT power augmentation concept based on reducing the GT inlet air temperature below the ambient air dew point.
- The power augmentation may be available anytime when the chilled air temperature is below the ambient temperature, but especially during summer on-peak hours.
- GT exhaust heat should be used to generate cooling of the cooling media (chilled water), via absorption chilling; however, other means (electrically driven chillers) may be used for peaking.

## Application of Inlet Air Chilling

The GT inlet air chilling, i.e., air cooling below the ambient wet bulb temperature, can increase the GT capacity needed during peak hours and improve the GT heat rate. Selection of the temperature of the chilled air is important. The temperature at the compressor inlet must be above 32°F to prevent ice buildup on the compressor blades, since the chilled inlet air shall be at 100 percent relative humidity due to moisture condensation during the air chilling process. Due to a major increase in air velocity in the compressor inlet the static

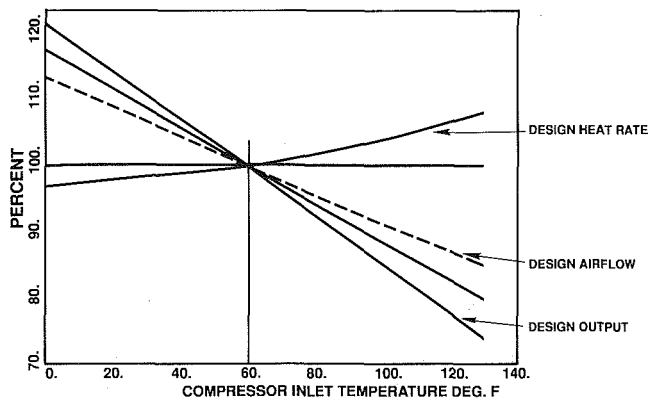


FRAME 7E GT OUTPUT VERSUS COMPRESSOR INLET TEMPERATURE

Fig. 1

Contributed by the International Gas Turbine Institute and presented at the 35th International Gas Turbine and Aeroengine Congress and Exposition, Brussels, Belgium, June 11–14, 1990. Manuscript received by the International Gas Turbine Institute January 16, 1990. Paper No. 90-GT-250.

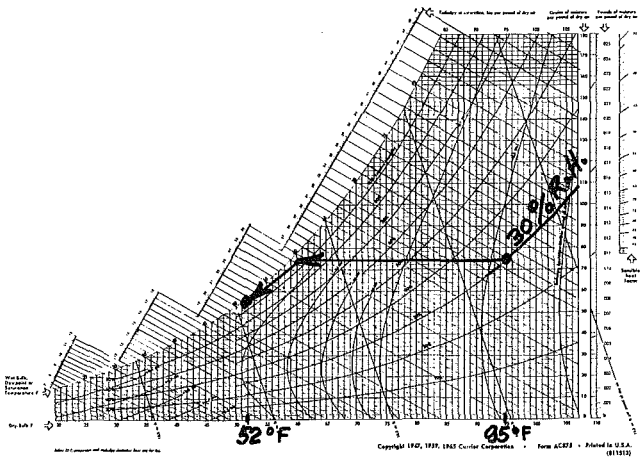


Fig. 2 GT inlet air cooling process

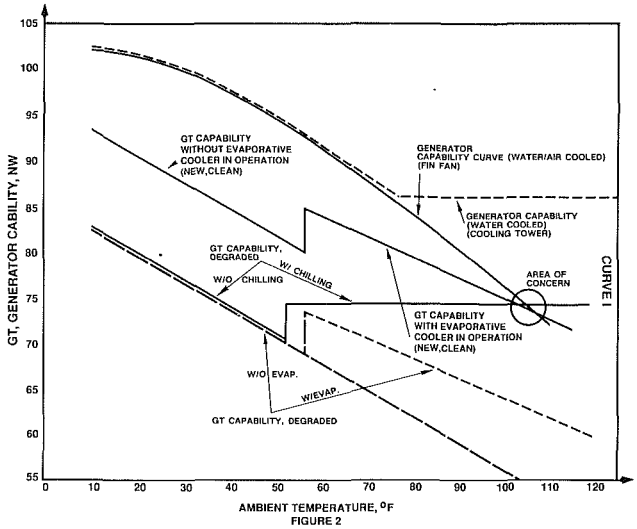


Fig. 3 Generator capability

temperature of air may drop as much as 10°F. To safeguard against this drop the chilled air temperature should be a minimum of 45°F, which includes a 3°F margin.

Figure 1 shows that the output can be increased by 0.36 percent with each 1°F inlet air temperature reduction. If the chilled air temperature is selected at 52°F, then the temperature drop from 95°F is 43°F or 15.5 percent power boost. If the GT unit is or could be equipped with an evaporative cooler, which could reduce the ambient (95°F, 20 percent R.H.) to 72°F (85 percent R.H.) the benefit of air chilling is only (72 − 52) or 20°F or 7.2 percent power boost. The cost of the inlet air chilling equipment must be amortized by the economic benefits from additional power sales during peak or during operation when ambient temperature is above the chilled air temperature.

## Inlet Air Heat Exchange

The ambient conditions (temperature and relative humidity) are important factors. The typical summer average on-peak ambient temperature in the U.S. is 95°F dry bulb. In eastern and midwest locations the relative humidity (R.H.) may be at 90 percent level (wet bulb temperature is ~90°F) and the air enthalpy is ~59 Btu/lb dry air. In the western United States (dry climate), the same 95°F dry bulb temperature shall be associated with 20 percent R.H. (66°F wet bulb) and enthalpy of 34.7 Btu/lb dry air. If the compressor inlet temperature is to be lowered to 52°F dry bulb, 95 percent R.H., the enthalpy is 20.9 Btu/lb dry air. The required heat removal at high humidity location shall be (59 − 20.9) = 38.1 Btu/lb and in the dry climate it will be (34.7 − 20.9) = 13.8 Btu/lb. Thus, the duty of the inlet cooling system in humid climates is much higher than in the dry climates. In either case, moisture separation apparatus should prevent carryover. The cooling process is shown in Fig. 2.

The temperature at the compressor inlet must be above 32°F to prevent ice buildup on the compressor blades, since the chilled inlet air shall be at 100 percent relative humidity due to moisture condensation during the air chilling process. Due to a major increase in air velocity in the compressor inlet, the static temperature of air may drop as much as 10°F, which includes temperature drop in the compressor bellmouth ($\Delta t$ = 4°F) and in the (open) inlet guide vanes (variable or stationary) ($\Delta T$ = ~4°F). Closed variable inlet guide vanes would result in additional pressure drop (~5°F) but this would not apply while inlet air chilling is used. To safeguard against this drop the chilled air temperature should be a minimum of 45°F. Increased wetness in the compressor inlet may induce corrosion, which may require more frequent inspections of compressor inlet.

## GT Inlet Air Cooling Concepts

Several concepts may be offered. The GT operates either in the simple cycle or in the cogeneration or combined cycle. Simple cycle GT shall be able to use all exhaust heat for chilled water generation. For a GT in cogeneration or in combined cycle service, we may need to evaluate the tradeoff of using the exhaust heat for power augmentation in the GT inlet versus the economic benefits of exhaust heat sales.

## Generator Capability

The generator rating has to be verified. If the generator is cooled by cooling water it can be provided from two sources: cooling tower/river, and dry coolers (fin fan type).

Since the generator capability is indirectly proportional to the cooling water temperature, it is possible in the case of dry cooling that the GT output may be increased via inlet air chilling while the generator capability would not increase. This could result in GT exceeding the generator capability with potential overtemperature on the generator winding. The generator rating must be carefully checked. The same applies for air-cooled generators. Examples of the GT and generator capability are shown in Fig. 3.

## Systems Options

The complete inlet air cooling system consists of several systems, such as:

- Water chilling system
- Absorption chiller thermal source
- Chilled water system
- Cooling system

The following options exist for each system;

### Chilling System

- Absorption chiller utilizing:
  - (*a*) Lithium bromide absorbent.
  - (*b*) Ammonia absorbent.
- Mechanical chilling utilizing compression with freon refrigerant.
- Steam jet refrigeration.
- Hybrid chilling system utilizing both absorption and mechanical chilling systems.
- TES (Thermal Energy Storage)

**Absorption Chiller Thermal Source.** A thermal source to provide operating force to absorption chillers was studied based on using:

- Low-pressure steam generated in a new HRSG installed in a simple cycle GT exhaust.
- Tie-in to existing steam export line in cogeneration applications to generate steam through a low-pressure heat exchanger (i.e., reboiler).
- Generation of hot water from the above methods for the ammonia absorption chiller.
- Direct integration of HRSG preheat coil with ammonia absorption chiller to provide desorption heat in simple cycle GTs.

**Chilled Water Distribution System.** Review of the following schemes to provide chilled water to/from the chilled gas turbine inlet air:

- Installation of PVC media similar to the evaporative cooler media downstream of the inlet air filter, using both the evaporative and direct contact principle.
- Installation of chilled water coils using the convection principle (indirect cooling).
- Installation of freon-cooled coils using the convection principle.

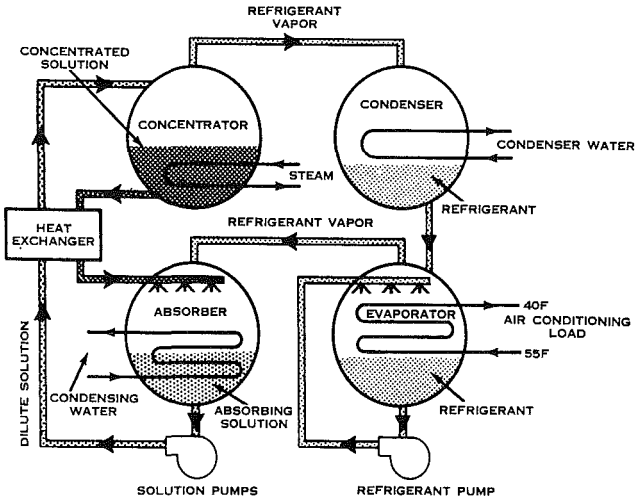


**Fig. 4 Absorption chiller schematics (courtesy of Trane Corp.)**

- Indirect evaporative cooling for distribution of chilled water within the inlet air filter.

**Cooling System.** Study of the following cooling water systems:

- Mechanical draft cooling tower.
- Closed-loop water to air cooled system (fin fan).

## Description of Considered System

The system evaluation is based on retrofitting four General Electric Frame 7E GTGs with inlet air chilling system.

**Existing System: 4 × Frame 7E GTGs**

| | |
|---|---|
| • Power output | 65,000 kW |
| • Heat rate | 12,200 Btu/kWh-LHV |
| • $NO_x$ control—water injection | 70 GPM |
| • Fuel | Natural gas |
| • Barometric air pressure | 14.31 psia |
| • Ambient dry bulb temperature | 95°F |
| • Ambient wet bulb temperature | 70.8°F |
| • Relative humidity | 30 percent |
| • Inlet air enthalpy | 34.7 Btu/lb d.a. |
| • Site elevation (ASL) | 700 ft. |
| • Inlet air flow rate | 2,074,982 lb/h each |
| • Inlet system pressure drop (filter, evaporative cooler, silencer) | 5 in. WC |
| • Openings available: | |
| Inlet duct, 1 opening (W × H) 25′ × 25′ | |
| Filter house, 6 openings 25′ × 5′ | |
| • Evaporative cooler efficiency | 80 percent |
| Temperature after evaporative cooler | 72°F |
| Humidity | 80 percent |
| • Heat Recovery: 80 percent steam quality HRSG for EOR | |
| Inlet temperature | 970°F |
| Stack temperature | 260°F |
| Feedwater temperature | 150°F |
| Steam output @ 800 psig, 80 percent quality | 418,000 lb/h each |
| Gas side pressure drop | 10 in. WC |

**Retrofit With Inlet Air Chilling:**

| | |
|---|---|
| • Retrofitted inlet air temperature (dry bulb) | 52°F |
| • Retrofitted inlet air humidity | 95 percent |
| • Inlet air enthalpy | 21 Btu/lb d.a. |
| • Air chilling duty | 28 mm Btu/H each |
| or | 2333 tons each |

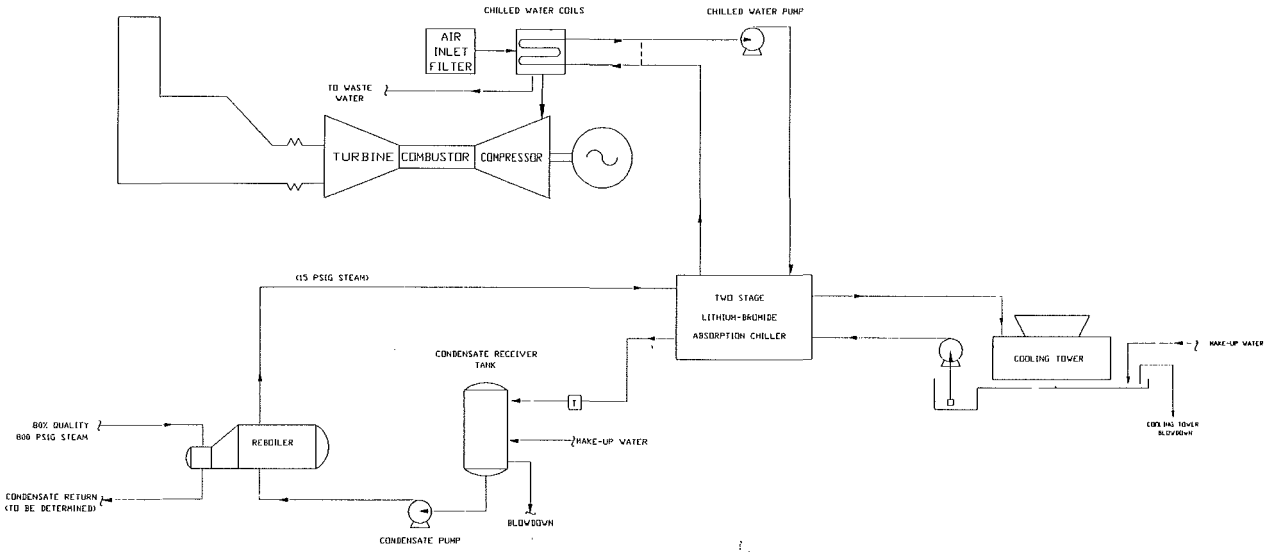


**Fig. 5 Absorption chilling diagram**

## Water Chilling via Absorption Chillers (Fig. 5)

**Absorption Chilling System.** Absorption chilling systems operate with a low-grade thermal source to provide chilled water at 44°F. The system contains refrigerant and absorbent that cycles at low internal pressures. This pressure in the evaporator section will allow evaporation of the refrigerant liquid at a low temperature providing the chilling effect for the incoming chilled water. At slightly higher pressures, the refrigerant vapor and absorbent liquid are combined in the absorber section by their strong affinity for combining. As the vapor is condensed, heat is released into the condenser water coils (cooling water). The resulting solution will be a "strong" absorbing solution of refrigerant and absorbent. This solution is pumped into the absorbing section where the refrigerant is evaporated from the absorbent by a thermal source, either low-pressure steam or hot exhaust gases. In the condenser, the refrigerant vapor is condensed to liquid by cooling water, and the refrigerant liquid is pumped back into the evaporator. The "weak" absorbing solution is recirculated into the absorbing section. An example is shown in Fig. 4.

Ammonia and lithium bromide (LiBr) are two types of absorption chiller that are available for this chilling service.

***Lithium Bromide Absorption Chilling Systems.*** The lithium bromide absorption chilling system can be designed as a single or two-stage chiller. These chillers utilize a design with a lithium bromide water absorption refrigeration cycle. The chilling systems typically provide chilled water at 44°F with return water at 54°F. Consideration was made to lower the chilled water temperature to 42°F; however, this would have reduced the chiller's cooling capacity and efficiency. Chilled water temperatures less than 42°F are not considered practical for absorption units. This is due to the water-based refrigerant used in the chiller, which, when operating between 34°F and 36°F, provides 42°F chilled water and may potentially freeze the chilling unit.

Typical flow calculations for each of the absorption chiller units are based on the following:

- Leaving chilled water temperature = entering temperature − temperature drop
- Leaving condenser water temperature = entering temperature + temperature rise
- Chilled water flow (gpm) $= \dfrac{\text{Cooling load (tons)} \times 24}{\text{temperature drop}}$
- Steam Flow (lb/hr) = Cooling load (tons) × 9.9 (two stage)
  = Cooling load (tons) × 19 (single stage)
- Condenser water flow (gpm) $= \dfrac{\text{Cooling load (tons)} \times 44}{\text{temperature drop}}$

**Single Stage (LiBr).** The chiller design utilizes a single shell hermetic construction that will enhance the integrity of the unit. These chillers operate on low-pressure saturated steam at 15 psig, consuming approximately 19 lb/hr per ton of chilling. Hot water at 270°F can also be used as the thermal energy source. The single-shell design helps prevent air leakage, which can cut the capacity and promote corrosion. A pre-packaged system can be delivered completely assembled with available size range from 101 to 1,660 tons. The single-stage system will operate at a vacuum and may be susceptible to air leakage, which could cause some damage. However, if the proper operating and maintenance procedures are followed, i.e., periodic purging of the system and operation above 42°F, there should be no problems during normal operation. A total loss of power would cause the solution of the absorption chiller to solidify into a solid mass within one hour. Manufacturers that currently produce the single-stage absorption chillers are Trane, Carrier, and York. Cost may be estimated at $250 per ton of refrigeration.

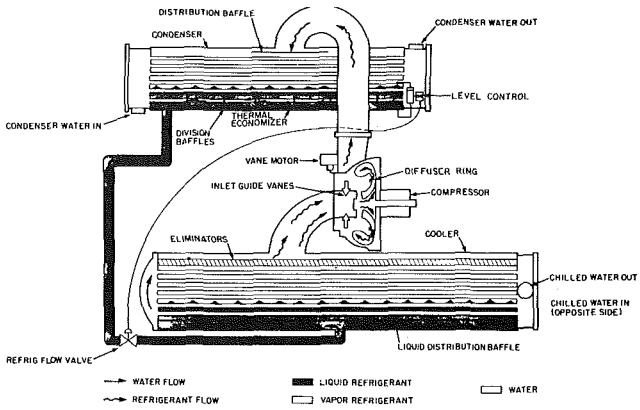


**Fig. 6 Mechanical chiller schematics (courtesy Carrier Air Conditioning Co.)**

**Two Stage (LiBr).** The two-stage lithium bromide absorption chiller system will operate with saturated steam pressures of approximately 114 to 128 psig allowing the unit to consume less steam than a single-stage chiller at 15 psig. The two-stage steam consumption is estimated at 9.9 lb per ton versus 19 lb per ton for the single stage; thus, less steam will be consumed during chiller operation, resulting in a net savings of thermal energy over the single-stage chillers.

The cost estimate for the two-stage chillers is $330 per ton, which is approximately 30 percent more than the single stage and twice the cost of a centrifugal chiller. The chiller size is limited to 1500 tons for the larger chillers. Manufacturers of the two-stage absorption chillers are Hitachi Paraflow, Sanyo-Bohn, and The Trane Company.

**Ammonia Absorption Chilling System.** The ammonia absorption system is an engineered refrigeration system specifically designed for the tons of cooling required. The ammonia system can produce lower chilled water temperature than lithium bromide systems, from +50°F through −50°F chilled medium temperatures. Low-pressure steam (175 to 265 psig) or turbine exhaust gases can be used as the thermal source for the ammonia absorption cycle. However, the ammonia system requires higher capital costs, approximately $650/ton of cooling. Also, larger plot space is required, approximately 30′ × 30′ for a 1,000 ton chiller installation. The ammonia system field installation requires significant structural steel to support the various ammonia storage tanks, heat exchangers, and other vessels. Manufacturers of the Ammonia Absorption Chillers are: Lewis Refrigeration Co., Houston, Texas, and Borsig GmbH.

## Water Chilling Via Mechanical Chillers (Fig. 7)

The Mechanical Chiller is a vapor compression cycle with a compressor, liquid cooler (evaporator), condenser, and compressor drive. Water at 54°F returning from the inlet cooling coils enters the chiller (evaporator) where it is cooled to 44°F by the refrigerant liquid evaporating at a lower temperature. The refrigerant gas produced is compressed to a higher pressure and temperature so that it may be condensed by the cooling water in the condenser. The condensed refrigerant is returned to the evaporator through an expansion/metering valve.

Mechanical chillers may be provided with different types of compressors: reciprocating, screw, or centrifugal. Reciprocating and screw type compressors are generally used for sizes less than 1000 tons. Centrifugal liquid chillers are used for sizes greater than 1000 tons, with factory-assembled units up

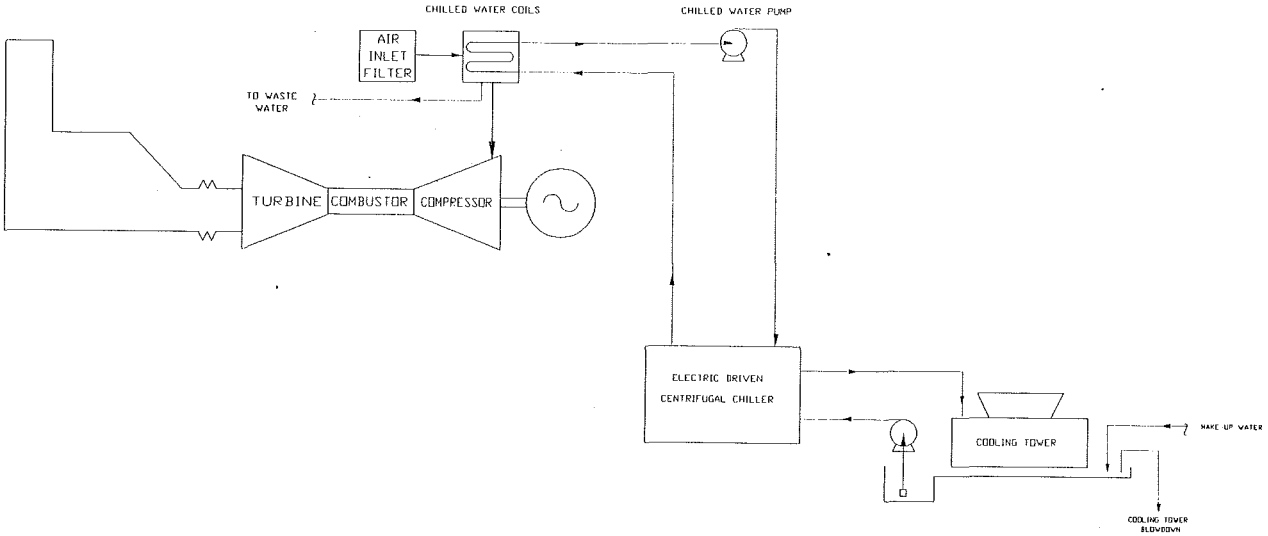


**Fig. 7 Mechanical chilling diagram**

to 1600 tons, and field-assembled machines to about 10,000 tons.

Chillers from 100 tons to 1500 tons are packaged off-the-shelf units that are hermetically sealed. Chillers from 1500 tons to 3000 tons are generally the open-drive centrifugal water chillers. These units are not hermetically sealed because the compressor and motor drive are mounted outside the chiller unit. Three thousand tons and larger are customized units. Manufacturers such as Carrier, Trane, and York are capable of providing chillers in the 1000 ton to 3000 ton size. Each chiller will operate in parallel, to increase availability of the system.

Typical flow calculations for each centrifugal chiller unit are based on the following:

- Leaving chilled water temperature = entering temperature − temperature drop
- Leaving condenser water temperature = entering temperature + temperature rise
- Chilled water flow (gpm) $= \dfrac{\text{Cooling load (tons)} \times 24}{\text{temperature drop}}$
- Condenser water flow (gpm) $= \dfrac{\text{Cooling load (tons)} \times 29}{\text{temperature drop}}$

The temperature rise and drop is generally limited to 10°F. This value can be increased at the expense of derating of the chiller unit. For example, the increase temperature of the cooling water from 10°F to 15°F will derate the chilling capacity of the chiller by approximately 5 percent.

The selection of the 1500 ton centrifugal chiller was based on the cost per ton, delivery, and electrical load requirements. Based on manufacturer's information, the costs per ton for chillers were:

| | |
|---|---|
| 1000–1500 ton chillers | $133/ton |
| 1500–5000 ton chillers | $320/ton |
| Over 5000 ton chillers | $145/ton |

The smaller centrifugals would be the most economical purchase based on capital cost; however, the cost of the installation and required area would be much greater than for the large chillers. The larger tonnage chillers were either too costly or required a large motor driver for their operation. A 5000 ton chiller would require a motor size of approximately 4300 hp. This type of motor would be custom built and associated with long delivery. In addition, these units would require high-voltage electrical devices.

The mechanical chillers need only electricity and condenser water to provide all chilled water requirements; there is no need to provide steam or another thermal energy source. Also, the mechanical chillers provide more tons of cooling in one machine than in other types of chillers. This will result in lower installation costs and less plot space required.

However, the consumption of electricity will reduce the potential output of the plant, reducing the electrical energy generated. Although chlorinated fluorocarbons (CFC) have been in use for years as part of refrigerants used in direct expansion refrigeration such as centrifugal chillers, these CFCs may potentially be banned from use because of their damaging effect on the ozone layer in the atmosphere. The mechanical chillers will require high-voltage electrical devices to support the chiller motors, MCCs, relays, motor starters, etc. This additional cost will increase the overall price of the chillers. Manufacturers of the Mechanical Chillers are: Carrier Corp., The Trane Company, and York, Division of Borg-Warner.

## Thermal Energy Storage Systems

The GT can take advantage of on-peak and midpeak energy costs by using mechanical chillers and the Thermal Energy Storage Systems or TES. The TES system is based on a storage medium with high specific or latent heat, ice, water, or eutectic salts. This storage will contain the cooling produced during the low-cost off-peak hours for utilization during the high-cost on-peak hours.

**Chilled Water Storage.** The design basis requires chilled water to be provided during the peak months of the year, from March to November, during the peak hours, averaging 10 hours per day. During the off-hours, the operator can take advantage of the lower electrical rates by operating the mechanical chillers, producing 44°F chilled water for the TES system. The size of the storage capacity will depend on an economic evaluation of the chilling profile. A full-size TES tank would provide all of the cooling load during the midpeak and peak hours. A partial, load-leveling TES tank will reduce the overall size of the peak cooling load profile and levelize the production of chilled water over the 10 hour period. Estimated size of the TES tank will be:

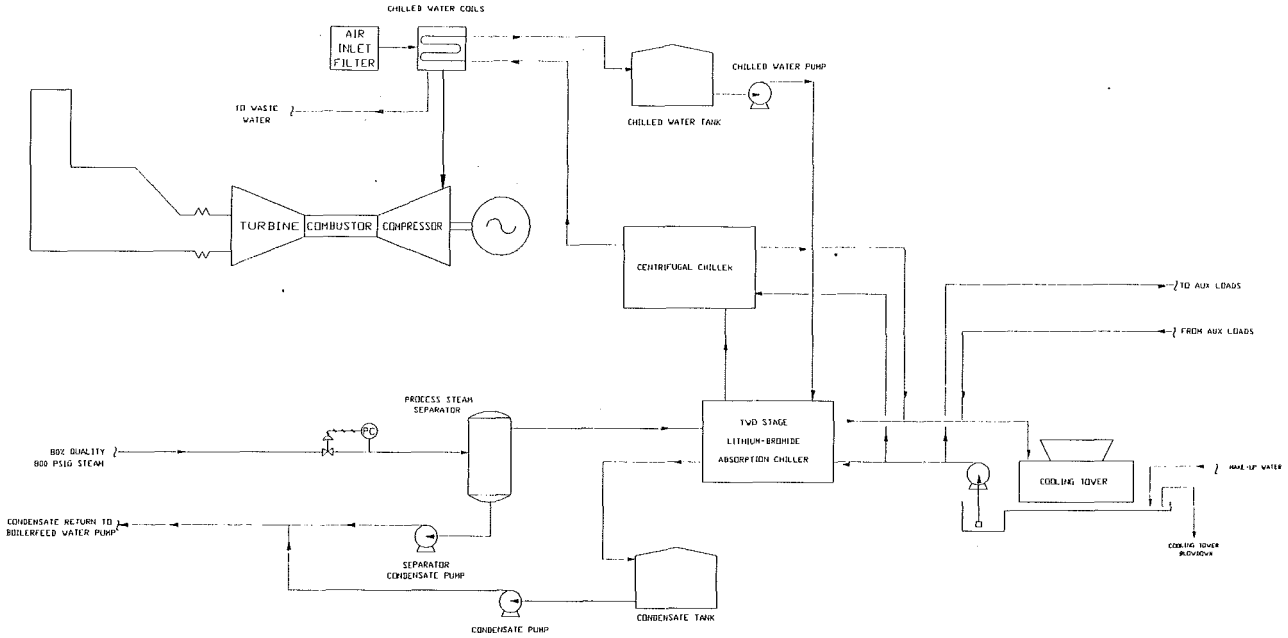


**Fig. 8 Hybrid chilling diagram**

| | Full size (1) | Partial size (2) |
|---|---|---|
| Tank Capacity (gal.) | 15,120,000 | 8,820,000 |
| (bbl) | 360,000 | 210,000 |
| Chiller size (tons) | 7,500 | 4,375 |
| Stored cooling (ton/hr) | 105,000 | 61,250 |

Notes:

1 These values assume that the mechanical chillers will not operate during midpeak and on-peak.
2 These values assume mechanical chiller operation 24 hr/day at an average load.

The size of the tank that will be required for the TES system may result in space constraints and large costs.

**Ice Storage.** The ice storage system can also be used in a scenario similar to the chilled water storage system. The volume of ice required will be from 7 to 14 times less than the water system (based on 144 Btu/lb ice latent heat of fusion versus 10 to 20 Btu/lb water heat capacity). However, the equipment to provide the 85,000 $ft^3$ to 168,000 $ft^3$ of ice will require large real estate.

## Hybrid System (Mechanical/Absorption) (Fig. 8)

The hybrid system is a combination of the lithium-bromide (LiBr) and the mechanical centrifugal chiller systems. The LiBr system will chill the return water from 54°F to 44°F and the mechanical chiller will further reduce the temperature to 38°F. This will be a series type system: two 50 percent capacity trains of absorption and mechanical chillers (reference drawing Fig. 8).

This system will initially take advantage of the steam available at the facility and will enable the mechanical chillers to consume less power during the production of colder chilled water. The system is sized for one-half of the cooling by absorption and the other by centrifugal chilling, which will consume approximately one-half of the total required power than the mechanical chiller system. The 38°F chilled water supply will increase the temperature differential of the cooling coil inlet and outlet (38°F to 54°F). The larger differential temperature will reduce the overall chilled water flow rate, reducing pumping costs as well as piping requirements.

The lower chilled water temperature can be used in the GTG inlet air coils to cool the air from 95°F to 52°F or to 46°F. Application of the hybrid system results in lower chilled water temperatures in the chilled water system associated with less piping and pumping costs. Also, the cooling coils will be more effective, decreasing the overall size requirements.

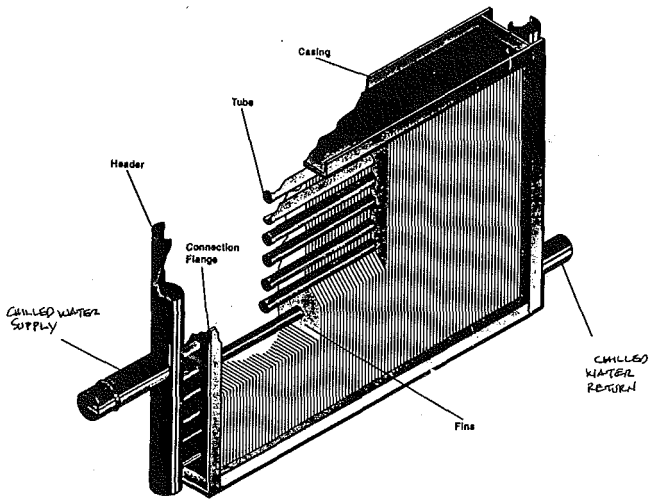


**Fig. 9 Chilled water coils (courtesy of Coil Co. Inc.)**

## Chilled Water Distribution System

The chilled water distribution system will circulate 44°F chilled water from the chilled water plant and into each GTG inlet filter house and return with 54°F water. The inlet cooling system will distribute the chilled water through an indirect or a direct contact heat exchanger that should be installed across the inlet air flow cross section.

The installation of the inlet cooling system will result in permanent increased pressure loss to the inlet of the GTG. General Electric's performance curves have indicated that a 4″ water column pressure drop will result in a 1.45 percent decrease in power output, 0.45 percent increase in heat rate, and an increase in exhaust gas temperature of 2°F. We anticipate that the inlet pressure loss should not exceed 2″ water column.

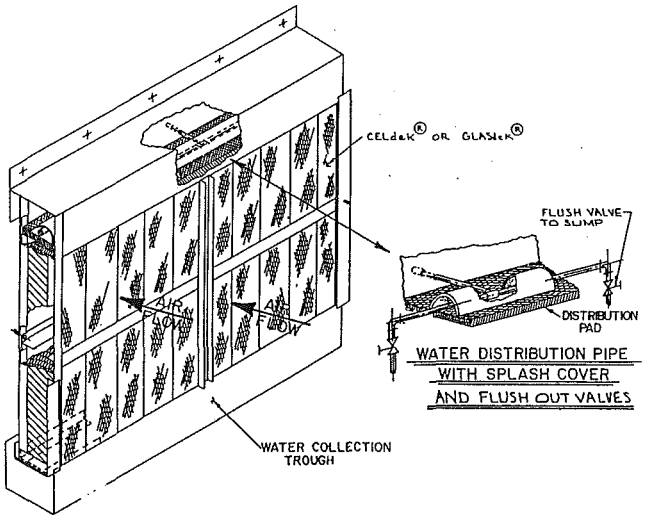


**Fig. 10 Evaporative cooler PVC medium (courtesy of the Munters Co.)**

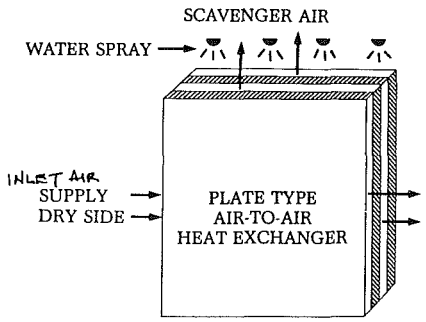


**Fig. 11 Indirect evaporative cooling (courtesy of Des Champs Laboratories Inc.)**

The inlet cooling system should chill the inlet ambient air temperature from 95°F and 30 percent relative humidity (R.H.) to 52°F and 95 percent R.H. This chilling effect will remove both sensible and latent heat, the latter producing condensed water at an approximate rate of 11.5 gpm. The increased humidity in this system will increase the corrosion rate of both existing and new carbon steel components of the GTG inlet air system. It is recommended that either stainless steel or corrosion-resistant material or coatings be used in the construction of new components installed as part of the inlet cooling system.

Please note that the existing direct evaporative cooling is accomplished by passing the GTG inlet supply air through a wetted medium where water is evaporated, absorbing sensible energy and cooling the incoming air to near wet bulb temperatures. This type of cooling changes the Btu content of the air from sensible to latent heat. The water flowing through the medium is not recirculated.

The wetted medium is designed with chevrons where the air must pass through a path, which changes direction to allow full contact with the air and water. This medium can also be utilized as the mist eliminator when not in operation.

**Chilled Water Coils (Indirect Contact Cooling).** A conceptual analysis utilizing copper tube and fin cooling coils with 44°F chilled water for gas turbine inlet cooling confirmed that the industrial type of cooling coil was available for gas turbine inlet cooling applications. Such a coil is shown in Fig. 9.

Each coil system is capable of taking ambient outdoor air at design state point and dehumidifying it to 51°F at 95 percent saturation.

**PVC Media (Direct Contact Cooling).** A conceptual analysis utilizing PVC cooling tower media in direct contact with 44°F chilled water for gas turbine inlet cooling was performed.

The medium is cooling tower packing placed in the straight crossflow position and sprayed with chilled water to create a direct contact chilled water evaporative cooler with an approximately 90 percent relative humidity saturation capacity, shown in Fig. 10.

A computer multiple alternative analysis examined three flow rate conditions consisting of 8, 12, and 16 gallons per square foot of face area and comparing two face velocities of 500 and 750 feet per minute, respectively.

To obtain the 52°F inlet temperature requirement necessitates a face velocity of 500 feet per minute and 12 gallons per square foot, i.e., 12,000 gallons per minute and 1000 square feet of surface area or 750 feet per minute and 16 gallons per square foot, i.e., 650 square feet of surface area and 10,000 gallons per minute, respectively.

The advantage of direct contact cooling is lower first cost and relatively low pressure drop. The disadvantage is the need for extensive water treatment associated with continuous blowdown. Potential for biological buildup exists, resulting in higher maintenance than a closed system. Also, large circulation water quantities are required, depending on performance, from 8 to 16 gallons per square foot.

**Indirect Evaporative Cooling.** The indirect evaporative cooling method lowers the dry bulb temperature without the increased moisture content of the GTG inlet supply air, effectively reducing the wet bulb temperature of the air and the overall energy content.

The indirect method is accomplished by using a plate-type air-to-air heat exchanger, shown schematically in Fig. 11:

- On one side, outside air is directed to one end of the exchanger as scavenger air. Water is sprayed onto the plate surface in contact with this air stream where evaporation takes place, cooling the plate approaching the wet bulb temperature. The water is collected in a sump and is recirculated back into the exchanger. The air is then exhausted above the unit into the atmosphere by an axial fan unit.
- On the other side, the GTG inlet air supply passed across the plate and is cooled by convection to near the wet bulb temperature and passes into the gas turbine.

This type of cooling is effective when there is adequate water available. The dry bulb air temperature can be reduced without increasing the latent heat at minimal cost of water and electricity.

For example, if the outside ambient air temperature is 95°F dry bulb and 71°F wet bulb, the indirect evaporative method of cooling will reduce the GTG inlet dry bulb air temperature to approximately 74°F, effectively reducing the total cooling load by 40 percent. This would translate into approximately 4000 tons of cooling.

Although the indirect cooling system will reduce the inlet air temperature to 75°F, cooling coils will be required to reduce the air temperature further to 52°F. The pressure drop through the indirect cooler is estimated to be from 3″ to 4″ of water, which would reduce the gas turbine power output by approximately 1.45 percent. In addition, the cooling coils will add another 1″ to 1.5″ of water pressure drop.

Due to the overall size of the cooling unit, there may be some problems of system installation. There is limited space available within the filter house for an installation of this type and significant GTG downtime.

The saturated air exhaust from the indirect cooler is located at the filter house, which would defeat the purpose of this system; the air will potentially recirculate back into the inlet, adding the latent heat that was absorbed. Ducting of the air to a different location may not be possible; estimated air flow is 400,000 cfm.

Table 1

| | | CENTRIFUGAL | ABSORPTION | HYBRID |
|---|---|---|---|---|
| 1 | Ambient air temperature (deg. F): | 95 | 95 | 95 |
| 2 | GT compressor inlet air temp.(deg F): | 52 | 52 | 52 |
| 3 | Chilled water temperature (@ coils): | | | |
| 4 | Input (deg F) | 44 | 44 | 44 |
| 5 | Output (deg F) | 54 | 54 | 54 |
| 6 | CHILLING TONS | 10,500 | 10,500 | 10,500 |
| 7 | Chilled water GPM: | 25,200 | 25,200 | 25,200 |
| 8 | Chilled water delta P (psi): | 60 | 60 | 60 |
| 9 | Cooling tower heat rejection (MMbtu/hr): | 192 | 273 | 233 |
| 10 | Generator cooling (MMbtu/hr) | 40 | 40 | 40 |
| 11 | Cooling tower circulating water GPM: | 25,633 | 36,453 | 31,050 |
| 12 | Cooling water delta P/T (psi/°F) | 63/15 | 63/15 | 63/15 |
| 13 | ELECTRICAL POWER | | | |
| 14 | Exist. GTG power (95°F amb.,78°F compr. inlet) | 268,400 | 268,400 | 268,400 |
| 15 | Incr. power with reduced inlet temperatures | 27,500 | 27,500 | 27,500 |
| 16 | Incr. GTG power with reduced inlet temp. | 295,900 | 295,900 | 295,900 |
| 17 | AUXILIARY POWER CONSUMPTION | | | |
| 18 | Chilled water pump (kW): | 786 | 786 | 786 |
| 19 | Cooling tower pump (kW): | 973 | 1,323 | 1,167 |
| 20 | Cooling tower fan (kW): | 280 | 477 | 373 |
| 21 | Makeup water pump (kW): | 7 | 7 | 7 |
| 22 | Conden. water pump (kW): | 0 | 40 | 0 |
| 23 | Chillers Compressor (kW): | 8,400 | 160 | 4,200 |
| 24 | Fin fan cooler (kW): | (764) | (764) | (764) |
| 25 | Total chiller plant auxilary (KW): | 9,682 | 2,029 | 5,769 |
| 26 | Add. power output from chiller project(L15-L25) | 17,818 | 25,471 | 21,731 |
| 27 | STEAM | | | |
| 28 | Steam production (LBS/HR @800 psig): | 1,670,976 | 1,670,976 | 1,670,976 |
| 29 | Steam consumption (LBS/HR @800 psig): | 0 | (200,000) | (100,000) |
| 30 | Net plant steam production (LBS/HR @800 psig) | 1,670,976 | 1,470,976 | 1,570,976 |
| 31 | Chiller Supply Steam (LBS/HR @150 psig): | 0 | 104,000 | 52,000 |
| 32 | WATER CONSUMPTION (Well water) | | | |
| 33 | Cooling tower makeup (GPM): | 605 | 826 | 717 |
| 34 | Demin. water system (GPM): | 0 | 4 | 2 |
| 35 | Net plant water consumption (GPM) | 605 | 830 | 719 |
| 36 | INCOME (ORDER OF MAGNITUDE ESTIMATE) | | | |
| 37 | REVENUES | | | |
| 38 | Net plant electrical power production (KW): | 17,818 | 25,471 | 21,731 |
| 39 | Operating hours/year | 1,500 | 1,500 | 1,500 |
| 40 | Energy payment ( $0.05/KWh) | $1,336,343 | $1,910,318 | $1,629,818 |
| 41 | Capacity payment ( $150/KWy) | $2,672,686 | $3,820,636 | $3,259,636 |
| 42 | Total incremental revenue | $4,009,028 | $5,730,953 | $4,889,453 |
| 43 | INCREMENTAL COSTS | | | |
| 44 | Gas consumption | $1,485,000 | $1,485,000 | $1,485,000 |
| 45 | Heat rate improvement (@-2%) | ($13,680) | ($13,680) | ($13,680) |
| 46 | Annual thermal energy cost (@ $3.0/MMbtu/hr) | $0 | $444,600 | $222,300 |
| 47 | Total thermal costs | $1,471,000 | $1,916,000 | $1,694,000 |
| 48 | | | | |
| 49 | TOTAL INCOME | $2,538,028 | $3,814,953 | $3,195,453 |
| 50 | PROJECT COST (ORDER OF MAGNITUDE ESTIMATE) | | | |
| 51 | MECHANICAL EQUIPMENT | | | |
| 52 | Chillers | $1,600,000 | $3,573,000 | $2,587,000 |
| 53 | Cooling tower | $360,000 | $490,000 | $435,000 |
| 54 | Pumps | $408,000 | $490,000 | $445,000 |
| 55 | Reboiler | $0 | $415,000 | $246,000 |
| 56 | Tanks | $0 | $10,000 | $10,000 |
| 57 | Coils | $1,074,000 | $1,074,000 | $1,074,000 |
| 58 | Total mechanical equipment | $3,442,000 | $6,052,000 | $4,797,000 |
| 59 | ELECTRICAL EQUIPMENT | | | |
| 60 | Transformer | $223,000 | $240,000 | $376,000 |
| 61 | Switchgear | $338,000 | $420,000 | $518,000 |
| 62 | Motor control center | $9,400 | $20,000 | $16,000 |
| 63 | Total electrical equipment | $570,000 | $680,000 | $910,000 |
| 64 | Bulk mat'l/engineering/construction | $6,788,000 | $6,668,000 | $7,093,000 |
| 65 | | | | |
| 66 | Total project cost | $10,800,000 | $13,400,000 | $12,800,000 |
| 67 | PAYBACK PERIOD | | | |
| 68 | Payback period-years (based on 1500 hr/yr) | 4.26 | 3.51 | 4.01 |
| 69 | Cost/kW (L66/L26) | 606 | 526 | 589 |

The circulating water system is an evaporative cooling system similar to the cooling tower, requiring blowdown and a chemical treatment system for biocide and pH control. The rate of blowdown will be determined by the initial condition of the water, evaporation rate, and the level of concentration allowed.

## Absorption Chiller Thermal Source

Absorption chillers require a low-grade thermal source to drive off the lithium bromide from the refrigerant within the concentrator section. This heat source can be a new HRSG in the simple-cycle GT service or a low-grade steam from existing HRSGs in cogeneration or combined cycle service.

Several options exist in facilities with existing HRSGs. Additional coils can be added to recover low-grade heat at levels of 220–300°F in steam or pressurized water form. If the heat recovery exist already at these temperature levels, the steam may be extracted from the process to supply heat to absorption chillers. The value of the extracted steam must be compared to the value of power augmentation during peak hours.

## Cooling System

Cooling water will be required regardless of the type of chiller installation. The water provides a heat sink for the heat that is absorbed by the chilled water. Cooling water flow rates will vary, depending on the type of chiller selected. Normally, mechanical chillers require 2.5 gpm per ton of cooling and

absorption chillers require 3.4 gpm per ton, for cooling water at 85°F inlet and 95°F outlet. However, this design will be an 85°F inlet and 100°F outlet water system to help reduce the required flow rate to 1.7 gpm/ton and 2.3 gpm/ton, respectively.

The chilled water supply should be sized to provide cooling water to the GTG generator, if required.

Three types of cooling towers are available for this service: the wet cooling tower, dry cooling towers, and wet–dry cooling towers.

## Proposed System

Please refer to Figs. 5, 7, and 8, which describe centrifugal, absorption, and hybrid systems.

## Evaluation of Alternatives

While each application of the chilled water concept is unique (i.e., absorption, mechanical, hybrid, etc.) and the associated support equipment availability varies, such as the use of an existing cooling water system, the essential parameters of evaluating the feasibility of the system are essentially common to all installations. The level of detail and complexity of the evaluation should correspond with the available material under consideration.

Table 1, System Evaluation, represents an example of the key parameters to be considered when considering the feasibility of the chilled water concept to combustion turbine projects. This table is designed to evaluate the competing technologies of the centrifugal, two-stage absorption, and hybrid chilling systems. The parameters include electrical power production and consumption, steam consumption, water consumption, anticipated revenues and operating costs, total project cost, and payback period.

As with any economic evaluation, the system studied must first be accurately defined in terms of overall production and consumption requirements. Lines 1 through 36 represent the definition for the sample system.

The operating ambient temperature of the system should be stated as the average temperature at which the chilling system will be in operation. With this temperature as the design point, the effectiveness of the system operation at temperatures other than this can be estimated given the anticipated hours per year at off design conditions. This information will provide the estimated MW hours of operation required to determine the annual electrical energy revenue. Consideration must be given to effects existing evaporative cooling systems may contribute if the installation is to be a retrofit and also the relative humidity at the corresponding temperatures.

Lines 14–30 define the net power production of facility due to installation of the chilling system. In this example, it is assumed that the facility utilizes a direct contact evaporative cooling system to achieve 78°F compressor inlet air temperatures on a 95°F ambient day. In each of the three cases, the auxiliary power consumption varies due the motive force of the chiller (steam or electricity) and cooling system requirements.

If the chilling system is based on steam as the motive force, the total lb/hr consumed should be included in the evaluation.

Water consumption quantities for cooling tower makeup and demineralizer system should be considered even if the source is provided by existing facilities.

After the system production and consumption requirements are defined, the total income can be determined based on financial characteristics of the facility. In this example, the electrical energy and annual capacity revenues are assumed to be \$0.05/kWh and \$150/kW-yr, respectively. These values included cost associated with operation, maintenance, and makeup water cost for both the combustion turbine and chiller facilities. Where applicable, thermal energy costs are assumed to be \$3.00/MM Btu/hr.

Total project engineering, procurement, and installation cost estimates should be developed for each case with the level of detail to assure that unique requirements inherent to the specific case and site conditions are not casually overlooked. Although up to 50 percent of the project cost can be associated with the mechanical and electrical equipment, special circumstances such as the method of providing steam or electricity can alter the outcome of the evaluation.

The final analysis, and obviously the most important, is the expected return on the investment. This evaluation can be a simple payback analysis as presented in Table 1, or as complex as a detailed life-cycle economics analysis. Based on the systems considered in this evaluation, the two-stage ammonia absorption case was determined to be the most attractive option for the facility.

## Conclusions

The gas turbine power augmentation via inlet air chilling can be effectively used to boost power during high ambient temperature usually synchronous with the on-peak power generation, allowing leveling of GT power output. Although the chillers may be expensive equipment, the benefits from on-peak power production can outweigh the cost provided detailed analysis is performed. Caution may have to be paid to the inlet system materials, which may have to be upgraded to stainless steel between the chilled water coils and compressor plenum. The cost of electricity varies in different areas of the country and the energy and capacity rates may be different and evaluated on an individual basis.

## Bibliography


1 *ASHRAE Handbook—1988 Equipment*, American Society of Heating, Refrigeration and Air-Conditioning Engineers Inc. (ASHRAE), 1988.

2 *Trane Air Conditioning Manual*, The Trane Co., 1965.

3 *Open Drive Centrifugal Liquid Chiller*, Carrier Air Conditioning Co. Product Catalog, 1960.

4 "Hitachi Paraflow Two-Stage Steam Absorption Chiller," Gas Energy Inc., 1986.

5 *Commercial Cool Storage Design Guide*, Electric Power Research Institute, May 1985.


# APPENDIX

## Conversion to SI Units

1 ft = 0.3048 m
1 gal = 3.785 liter
1 bbl = 0.1589 $m^3$
1 psi = 6895 Pa
1 btu = 1055 J
1 lbm = 0.4536 kg
1 lbf = 4.448 N
$t$ (°C) = [$t$ (°F) − 32] × 5/9

# Cogenerative, Direct Exhaust Integration of Gas Turbines in Ethylene Production

**D. H. Cooke**

**W. D. Parizot**
Stone & Webster Engineering Corporation,
Houston, TX 77253

*Within the past few years, gas turbines have been integrated into several new world-class ethylene production plants, for the first time using the exhaust as a source of preheated combustible oxygen for the cracking furnaces. The economic inducements and technical impact of such integration on the process are discussed. The general ethylene cracking and recovery process is described, and the various ways of integrating gas turbines are compared, culminating in the current leading designs. Means of providing ambient air backup to protect furnace operation from gas turbine trips are discussed. Furnace group sizing and oxygen demand for the major feedstocks, including naphtha and ethane/propane, are compared with the current range of oxygen and power available from single and dual gas turbines on the world market. Methods of partial integration, where gas turbine integration of the entire ethylene plant would produce more power than can be economically utilized or consume more premium fuel than available, are discussed. Fuel savings relative to ambient air operation are parametrized with percent exhaust oxygen and exhaust temperature. Aeroderivative and industrial gas turbine types are compared. Comparative economics with another means of gas turbine cogeneration, that of auxiliary boiler replacement with a combined cycle in a central utility, are presented.*

## Introduction

Ethylene ($C_2H_4$), an important raw material for the plastics industry, is produced as a gas by "cracking" heavier molecules, such as ethane, propane, and constituents of naphtha or even heavier hydrocarbon mixtures. This is done by heating these feedstocks to temperatures approaching 1600°F (871°C) in tubes passing through radiant cracking furnaces. The heat necessary to produce these high temperatures and to provide the energy consumed by the endothermic cracking reaction requires relatively large amounts of fuel, usually natural gas or methane-rich residue gas derived from the ethylene-producing unit.

Since the early 1980s, many ethylene plant operators worldwide have given serious consideration to integrating gas turbines with the cracking furnaces in order to utilize the exhaust heat cogeneratively to reduce furnace fuel consumption. The most successful manner of doing this has been to utilize the "preheated" residual oxygen entrained in the turbine exhaust products for combustion in the furnace burners.

In order for plant economics to favor gas turbine integration (GTI), there must either be a need for additional power, and an incentive for producing as opposed to purchasing it, or an export market for the power produced. Further, the accumulated savings realized through production of the power and the reduced furnace fuel costs must be sufficient to offset the added capital investment of the gas turbine, and associated ducting and controls for integration, within a relatively short payout period.

The first design featuring direct integration of gas turbine exhaust into cracking furnaces was placed in service in the mid-80s at an Essochem ethylene plant in Mossmorran, Scotland (Foerster, 1984). This design utilized the exhaust of a two-shaft industrial gas turbine driving the charge-gas compressor train. Most GTI applications subsequent to Mossmorran have been done with power-generating gas turbines rather than compressor drive units for simplicity of controls and other reasons discussed in a later paragraph.

The trend toward direct GTI has continued primarily in the Far East, in Taiwan, Korea, and Japan. This in part may be due to favorable legislative and utility-economic situations, as well as the relatively high cost of fuel in that part of the world. From the growing number of Far-Eastern plant users now known to be operating or installing some form of GTI, it appears that this option may be assisting the users in their efforts to produce ethylene at competitive prices.

In typical applications involving GTI, the reliable supply of sufficient oxygen to support the ethylene production process on a 24-hour continuous basis is considered paramount to power generation. Ambient air backup must be provided, so that in the event of a gas turbine trip, furnace burners will automatically shift to ambient air and continue operating without interruption or hazardous conditions.

In most of the plants now under construction or being planned, significant export of power to external utility grid

Contributed by the International Gas Turbine Institute and presented at the 35th International Gas Turbine and Aeroengine Congress and Exposition, Brussels, Belgium, June 11–14, 1990. Manuscript received by the International Gas Turbine Institute January 26, 1990. Paper No. 90-GT-139.

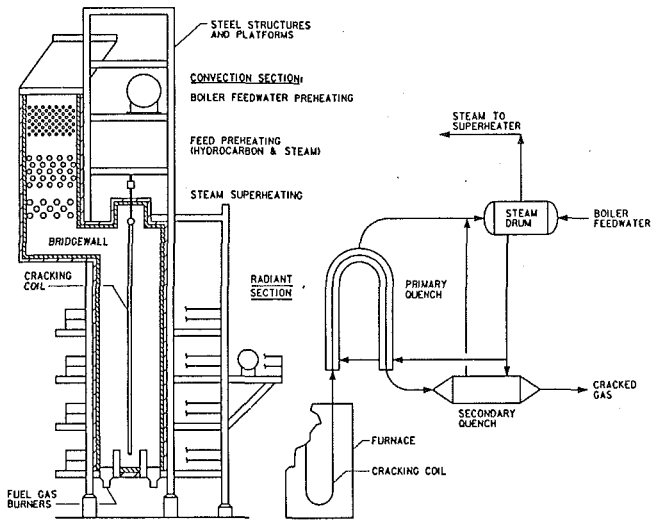


Fig. 1 Cracking furnace and quenching system

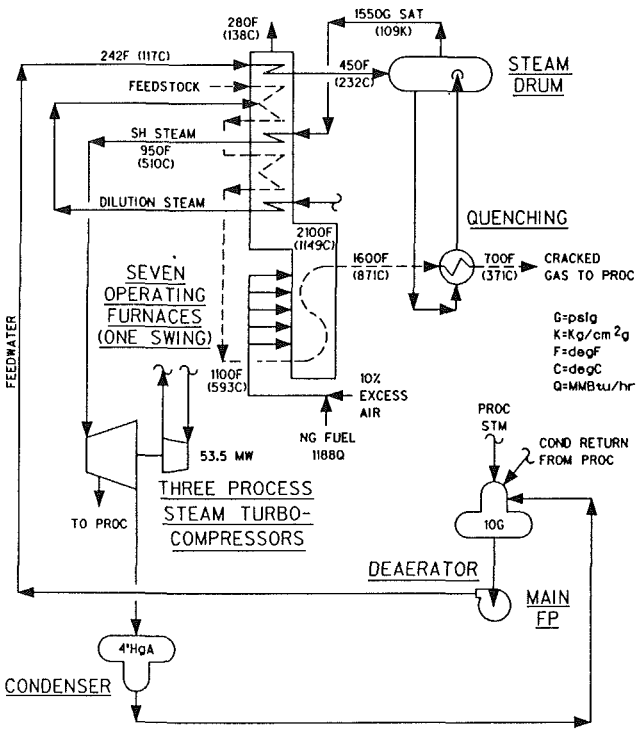


Fig. 2 Typical ethylene plant flow schematic

systems has not been involved. Consequently, production of power has been limited to internal plant needs. In some cases, the amount of power needed, or the amount of premium fuel available for gas turbine consumption, has limited the size of the gas turbine so that insufficient oxygen is available for combustion in all of the ethylene furnaces. In these cases partial integration, involving supply of only part of the furnaces by the gas turbine, or mixing of ambient air into the gas turbine exhaust by forced draft fans, has been found to be economical.

## Ethylene Process Description

Figure 1 (Cooke, 1987) shows a typical ethylene cracking furnace and related heat recovery systems. The cracking reaction occurs at carefully controlled high temperatures, usually between 1250 and 1600°F (677–871°C), in feedstock tubes passing through the radiant firebox of the furnace. The flue gas temperature in the firebox is usually above 2000°F (1093°C). Heat recovery takes place both in the convection section of the furnace and in an external process quenching system. The rapid quenching of the process stream by boiling of feedwater in specially designed external heat exchangers, as shown in Fig. 1, is critical to stop the cracking reaction at precisely the residence time for optimum product yield.

The cracked gas quenching system shown in Fig. 1 is a highly efficient and operationally trouble-free system (Chambers and Potter, 1974). It is applicable for rapid, efficient process stream quenching in many cracking processes. Heat recovery in the convection pass of the furnace is usually accomplished by feedstock preheating, boiler feedwater preheating, and steam superheating.

The cracked gas effluent from the quenching system, although rich in ethylene, is a mixture of many gaseous chemical compounds formed during cracking. Separation, recovery, and purification of the ethylene and other valuable compounds involve many complex downstream processes, which consume large amounts of shaft power and heat.

The quenching process is the source of much of the heat and power required in the downstream processes. Quenching produces high-pressure steam, typically at 1550 psig (109 kg/cm$^2$g), which is subsequently superheated to about 950°F (510°C), in the convection section of the furnace. Figure 2 shows typical conditions in a seven furnace, one billion lb/year (453,000 MTA, Metric Tons per Annum) ethylene plant, where steam from the quenching process is sufficient to drive the three major downstream process turbocompressors. The compressors are usually steam turbine driven, primarily because of the abundance of high-pressure steam, and also because they must operate at variable speeds. Steam turbines are more flexible and efficient for variable speed operation than simple types of gas turbines.

Figure 3 shows schematically a very simplified "*T*-*Q*" plot, which allows visualization of temperature and heat recovery interrelations that take place in the furnaces. The furnace flue gas is heated to near the Adiabatic Flame Temperature (AFT) only locally at the burners. However, the heat transferred from the flue gas to the process fluid at nearly constant firebox temperature (indicated as "saw-toothed") is the same as if the flue gas were cooled along the upper curve starting at the AFT, passing through the "bridgewall" temperature at the transition from the radiant to convection sections, culminating at the stack after most heat available is transferred to the feedwater, steam and feedstock. The visualization of the gas heat transfer as a single curve, pivoting about the "bridgewall point," will be useful in describing GTI effects in the next section.

## Matched Oxygen Gas Turbine Integration

The term "matched oxygen" refers to the situation where the gas turbine exhaust is the sole source of oxygen to the furnace burners, as opposed to supplementary injection of ambient air into the exhaust stream from a gas turbine that is undersized for the number of furnaces being supported. Typically, ethylene plants range in number of operating furnaces from three for small plants to nine for the largest world class facilities. Matched oxygen GTI could refer to a situation where some of the furnaces are integrated, with the remainder exclusively on ambient air, or total integration of the entire furnace facility.

**Compressor Drive Versus Power Generation.** For many years gas turbines have been utilized to drive compressors in some ethylene plants. As an extension of this tradition, the first direct exhaust GTI plant at Mossmorran, Scotland (Foerster, 1984) utilized the exhaust of a two-shaft, compressor drive gas turbine. Since Mossmorran, however, most, if not all, GTI applications have been done with electric power generating gas turbines rather than compressor drive units.

The primary reason for preference of turbine-generator units

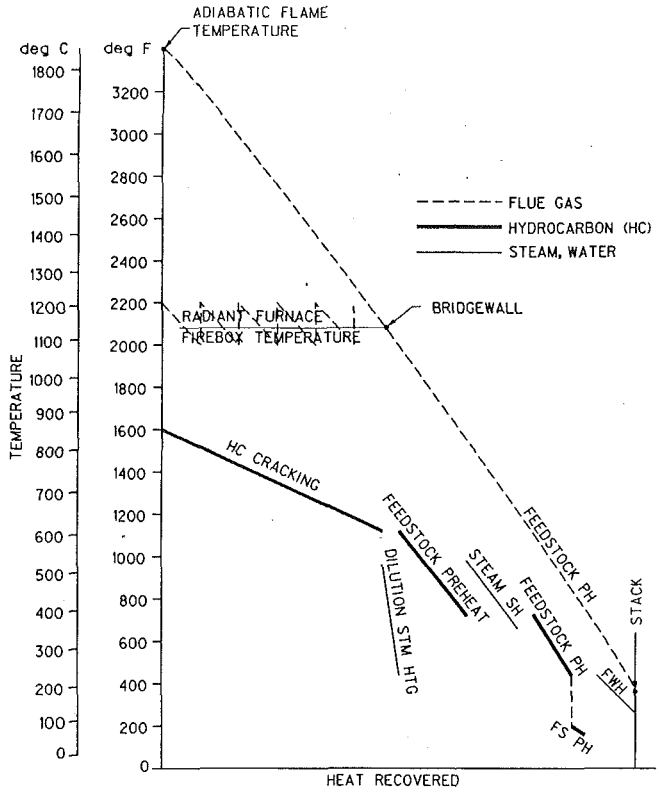


**Fig. 3 Ethylene furnace *T–Q* plot**

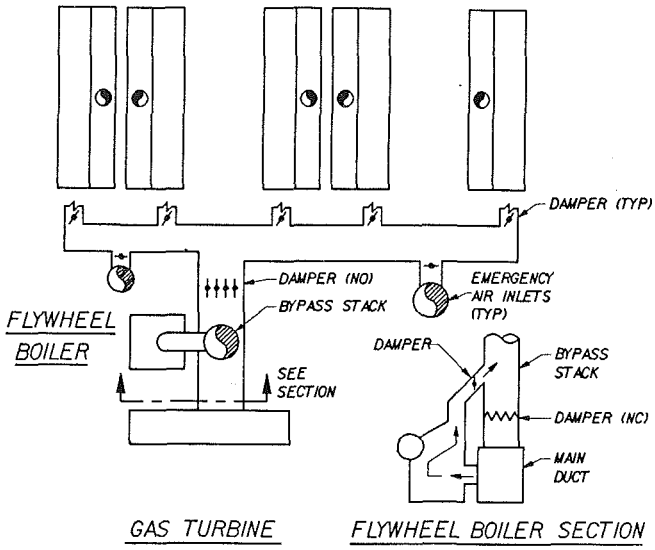


**Fig. 4 Control arrangement**

for GTI is simplicity of controls and plant startup operation. When a gas turbine is used for compressor drive, the operating mode is inherently variable speed with variable exhaust mass flow, in order to respond to process pressure/flow demand. If the exhaust is utilized in the furnaces this superimposes compressor control variations and interferes with stable furnace combustion control. The gas turbine generator, on the other hand, is inherently constant speed (power frequency) with nearly constant exhaust mass flow, which allows stable combustion control.

In a conventional cracking plant, the energy from cracked gas quenching and furnace heat recovery is sufficient to provide major shaft power for process gas compression utilizing steam turbine drives. Steam turbines are more flexible and efficient for variable speed operation than simple types of gas turbines. Design of a gas turbine for variable speed mechanical drive is best accomplished with multiple shafts, while a single-shaft gas turbine is entirely adequate for power generation due to the constant speed of operation regardless of load. Use of gas turbines to drive major compressors therefore tends to increase the cost of the compressor drive package unnecessarily, while steam turbines can accommodate variable speed effectively without increased cost. Furthermore, the use of furnace heat recovery steam for compressor drives is a more logical arrangement under varying furnace/process loads, since furnace heat is closely coupled with compressor drive power demand.

The conclusion of the foregoing considerations is that gas turbine power should not be integrated mechanically, but electrically. For best economy, power from one or more single-shaft gas turbines should be converted into kilowatts in direct connected or geared generators for electrical use inside and outside the ethylene unit. This is also a more favorable arrangement with regard to qualification as a cogenerator under the U.S. Public Utility Regulatory Practices Act (PURPA), which may not fully recognize mechanical shaft power in qualification formulae.

**Gas Turbine Oxygen Sizing and Control Schemes.** The oxygen mass flow of any gas turbine exhaust varies seasonally. The lowest flow occurs during summer peak ambient temperatures when the volumetrically constant compressor intake air flow has the lowest density. The variation between winter and summer may typically be as much as 15 percent. Oxygen demand of the furnaces is also subject to variation, not so much seasonally, but due to normal combustion control fluctuations, variations in feedstock and periodic fluctuations when furnaces must be taken off line for decoking, etc. Simplistically, therefore, a matched oxygen gas turbine should be sized slightly larger in exhaust capacity than the highest oxygen demand expected under peak summer operating conditions.

If there were no means to divert exhaust gas, the gas turbine would have to be operated at continuously varying loads, significantly less than full load, during cooler seasons and periods of lower furnace oxygen demand. This would mean a varying electrical output, which might be acceptable in some circumstances. The more conventional approach, however, is to provide an arrangement similar to that in Fig. 4, where a small economizer section or heat recovery boiler, sometimes called a "Flywheel" boiler, capable of producing medium to low-pressure steam is used to recover heat efficiently from the excess exhaust flow that is not demanded by the furnaces. In this way, the gas turbine can always be operated at maximum electrical load, thus taking full advantage of the capital investment therein. This decoupling of electrical load and frequency control from furnace and process control simplifies overall control design and provides a steady source of power.

Figure 5 is an isometric view of the above arrangement, showing the furnace-induced draft fans that interact with the ambient air inlets to provide backup in the event of a gas turbine trip.

It should be mentioned that sometimes economics or market availability may dictate selecting a gas turbine that is only slightly undersized with regard to oxygen, perhaps just during the summer months. Under these circumstances, a system of relatively small forced draft fans can be used to augment the exhaust by injection of ambient air during oxygen-deficient periods. The use of forced draft fan injection is discussed further under Partial Integration, below.

**Ambient Air Switchover and Transient Operating Provisions.** Figures 4 and 5 illustrate the primary control components for gas turbine exhaust integration with five furnaces, which for the illustration might have four furnaces in process operation with one furnace inactive as a "spare." During normal furnace process operation, dampers in the emergency air inlets

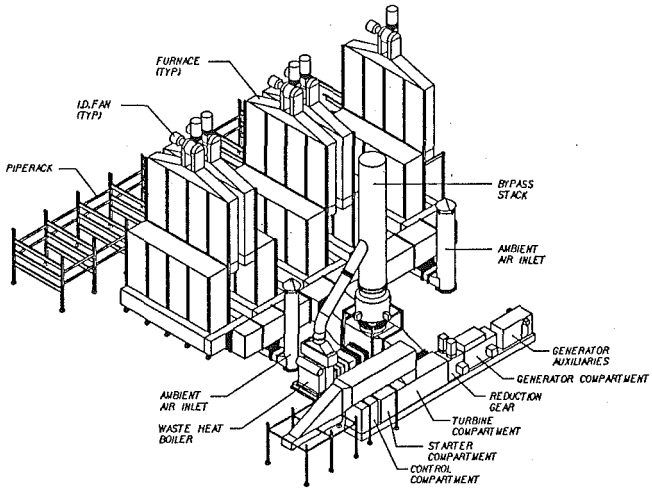


Fig. 5 Gas turbine integrated plant isometric view

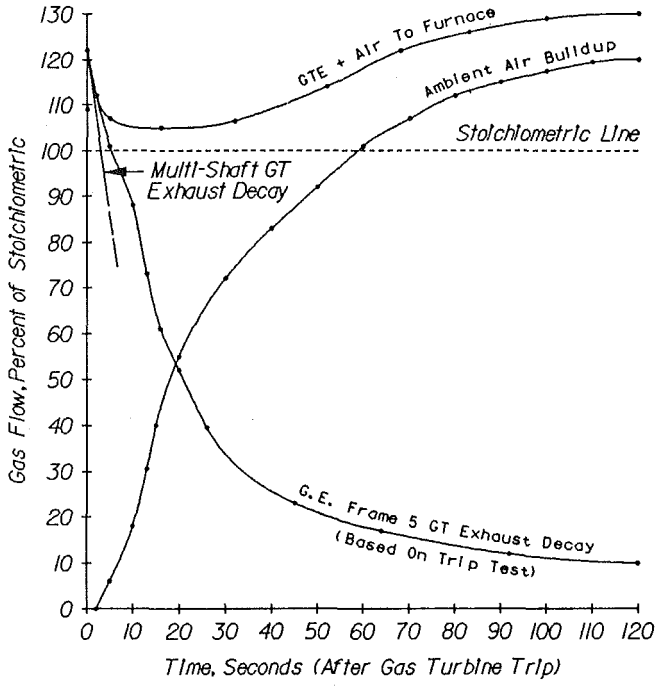


Fig. 6 GTE/air flow versus time following gas turbine trip

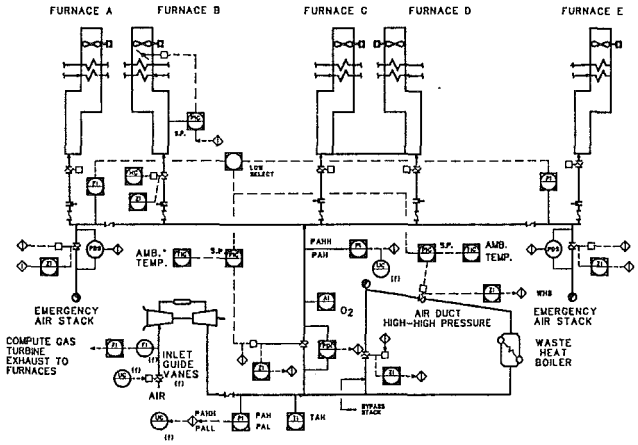


Fig. 7 Gas turbine integrated plant control schematic

will be closed and the damper in the main gas turbine exhaust ductwork will be open. The dampers at each furnace inlet are under control of oxygen analyzers in the furnace stacks and open further when any analyzer indicates low residual stack oxygen. The opening of any furnace intake damper allows the induced draft fan to draw more gas into the furnace burners. The cumulative effect of all furnaces determines the average pressure in the furnace intake manifold duct. Pressure indicators in the furnace intake manifold duct will indicate any change in average manifold pressure, signalling decreased or increased gas flow (oxygen) demand from the gas turbine. The pressure signals will activate the damper in the stack of the flywheel boiler, thereby causing more or less exhaust to be diverted to the boiler.

Any number of emergency trip signals from the gas turbine will initiate emergency decoupling of the gas turbine from the furnace exhaust/air supply system. Approximately two seconds after a turbine trip, the control system will initiate opening of the dampers in the ambient air inlets. These dampers will then fully open approximately 5 seconds later. Pressure in the intake manifold duct to the furnaces begins to decay from approximately 6 in. w.c. gage at the instant the gas turbine trips and subsequently reduces to a level of moderate vacuum as the furnace-induced draft fans commence to pull more draft at the arch of the furnaces. Since turbine exhaust flow takes a relatively long time to decay fully, the resulting fall in furnace duct manifold pressure will largely determine the ingress of ambient air to the ductwork system rather than the opening of the dampers in the air inlets. Ambient air from the air inlets will be aspirated into the system and mix freely with the decaying exhaust flow so that at no time during the transient operating condition will burners be starved for oxygen. During this transient condition, which is expected to last for a period of about 10 to 20 seconds, it is expected that oxygen supply to the system may dip to approximately 5 percent excess oxygen at furnace burners, thus never reaching substoichiometric conditions. A brief, moderate reduction in furnace firing (to 80 to 90 percent), however, may be necessary during the transient to stay above 5 percent excess oxygen, but this should not be sufficient to upset process operating conditions.

Following the transient dip in excess oxygen to the system, the main gas turbine exhaust duct damper will close to prevent drawing ambient air through the tripped turbine.

Figure 6 shows typical characteristic curves for the above described ambient air switchover, based on data from Bacsic (1982) and as indicated in the figure. Also shown in the figure is a steeper exhaust decay curve typical of a multishaft gas turbine, which would be optimal for a process compressor variable speed drive. This steeper decay would be more likely to produce substoichiometric (fuel rich) conditions in the furnace than the single-shaft characteristic. Single-shaft machines are therefore preferred in GTI applications where gas turbine trip protection is required.

The bypass stack, which is shown in the main exhaust ductwork near the point of turbine exhaust, is primarily for purposes of duct overpressure protection. The damper in the bypass stack will remain closed during normal gas turbine exhaust operation, except in those instances when the duct pressure is sensed to exceed a safe level for the integrity of the system.

It should also be mentioned that most plants require furnace startup using ambient air as the source of oxygen until such time that the gas turbine is brought on-line. The system therefore must be designed to permit gradual changeover to gas turbine exhaust as the oxygen source. A typical schematic diagram of a control system that facilitates the transient modes of operation discussed above is shown in Fig. 7.

## Gas Turbine Selection for Matched Oxygen Demand

During the earliest stages of an ethylene plant's conceptual design, the plant designer will determine the number and ther-

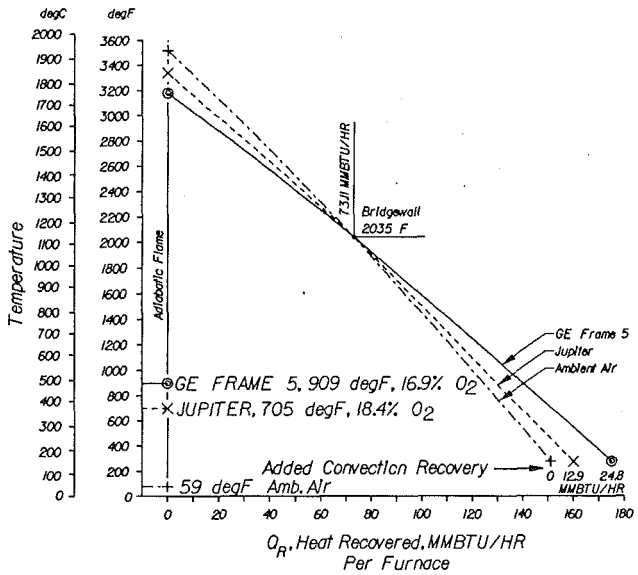


**Fig. 8 Heat recovery thermal profile**

mal size of the furnaces to be installed based on economic data made available by the plant owner. The data will be specific for feedstock and required production design capacity conditions. The number of furnaces is usually between three and nine, and may or may not include an inactive spare furnace, depending on the method of required periodic decoking and owner preference. The thermal size of each furnace is usually between 70 and 90 MMBtu/h radiant duty, depending on feedstock characteristics. The radiant duty of a furnace is the amount of heat absorbed in the cracking section.

At an early point in conceptual design, the economic feasibility of gas turbine integration with the furnaces must also be addressed and decided upon, since subsequent steps in the design of the convection sections of the furnaces, in particular, are dependent upon the decision to incorporate GTI, or not. In the evaluation process, it is important to know the maximum gas turbine power that may be utilized or exported by the owner. Knowledge of the maximum power limitations permits narrowing the turbine models for final selection.

**Oxygen Demand.** The oxygen demand for a single furnace is established by two conditions. The first is that the furnaces are "fully fired" at design operating conditions, in that nearly all available oxygen in the air or gas entering the furnace burners is consumed. Optimally, this means that oxygen available for combustion in conventional burners is about 110 percent of that required for stoichiometric firing conditions. Operating much below this level may result in unstable flame patterns and unburned fuel. The residual oxygen in the stack gas under these conditions may be 1.5 to 2 percent by weight, depending upon the initial weight percent of oxygen in the combustion gas. This is in a measurable range for stack gas $O_2$ analyzers used in furnace combustion control.

The second condition determining the oxygen requirement is that it must support the combustion of sufficient fuel to support the radiant duty, which, as defined above, is the amount of heat transferred from the hot gas to the cracking process fluid inside the pyrolysis coils in the radiant section of the furnace.

When gas turbine exhaust is used as the source of oxygen for furnace combustion, some of the oxygen originally in the intake air to the gas turbine compressor will have been used up in the primary GT combustor. While the oxygen in ambient air is about 23 percent by weight, gas turbines on the market range in exhaust oxygen content from 14.5 to 18.5 weight percent at design full-load operation. Another important variable among market gas turbines is exhaust temperature, which may be anywhere between 700 and 1100°F (371–593°C). These two parameters, $O_2$ content and temperature, are the most significant factors in determining the fuel and oxygen demand for each furnace under the above-discussed two conditions.

Figure 8 is a $T$–$Q$ plot allowing visualization of the foregoing thermal effects on a single furnace, keeping in mind that each of the gas turbines represented in the plot has sufficient exhaust flow to support several identical furnaces. Utilizing the concept of a single cooling curve starting at the AFT, as introduced in Fig. 3, two gas turbines having different exhaust $O_2$ content and temperature are compared with ambient air at 59°F (15°C). The cooling curves pivot about the bridgewall point, which represents the transition from the radiant to the convection section of the furnace as shown in Fig. 1. The bridgewall point occurs at the radiant duty and the "firebox" temperature, both of which remain relatively constant. It will be noted that the AFT is highest for ambient air and decreases with decreasing $O_2$ content. It is logical that ambient air with the largest temperature gain in the adiabatic flame would require the most fuel and oxygen. The two gas turbines shown do in fact save considerable fuel compared with ambient air operation. There is, however, a significant "side effect" with lower oxygen content. Since exhaust gas from the turbine contains more "inert" material to be heated, more fuel must be fired to attain the same temperature. The heat from the increased fuel shows up as additional available heat in the convection section. Because the heat required in the radiant section does not change, this added heat, in effect, gets "passed" from the radiant to convection zones. Theoretically, as the turbine exhaust $O_2$ content gets less and less, it is possible that *more* fuel will be required for the hot gas turbine exhaust than for much cooler ambient air. It will be seen presently that this phenomenon actually occurs for some gas turbine exhaust conditions.

**Oxygen and Power Range of Current Gas Turbine Market.** Table 1 is a list of gas turbines currently available on the world market in the range of applicability for direct exhaust GTI. The data are given for base rating, ISO ambient conditions (59°F, 15°C, sea level). Much of the data were obtained from, or calculated based on, data from manufacturers, but Gas Turbine World Performance Specs (1989) was the source of some data not otherwise available. One of the engines listed, the Mitsubishi MF-221B, is not yet on the market, but is included based on data provided by the manufacturer, who indicated near-future availability.

The machines are listed in descending order of total available oxygen, which is the product of exhaust mass flow and weight fraction of oxygen in the exhaust. These parameters are found in columns G, H, and I. The list is also in descending order of number of furnaces supported in an average ethylene plant, column J. It will be recalled that ethylene plants have from three to nine operating furnaces, but it should be recognized that the list is for 59°F ambient while most plants must operate in summer temperatures up to 100°F. Also, a margin for combustion control and decoking must be allowed, so the effective applicable range of number of furnaces in the list can vary between four and eleven.

The list is intended to represent single gas turbine units, which can support a given number of furnaces within the continuous applicable range of typical ethylene plants. As there appears to be a gap in the market of available single-unit gas turbines to support between 6.5 and 10.8 furnaces, two unit sets were listed in this range.

It will be noted that the order of power output, column D, does not correspond to the order of oxygen. The main reason for this is that the primary combustor firing temperature, column K, varies widely; the hotter machines producing more power with less oxygen available at exhaust. When the maximum power that may be economically utilized by the owner

**Table 1 Typical multiple furnace ethylene production facility: potential gas turbine base load performance for direct exhaust integration**

Ambient Temperature 59 degF (15 degC) - Relative Humidity 60% - NOx Control: Steam Inj. to 42 ppmvd unless "dry" indicated
GT and Furnace Fuel: Product Gas, Wt% $H_2/CH_4/C_2H_4$=1.95/97.92/.13 - Inlet Loss 3 to 4 "$H_2O$ - Exhaust Loss 3 to 14 "$H_2O$
Feedstock: Naphtha - Radiant Duty per Furnace: 80.38 MMBTU/Hr - Firebox at 2103 degF - Furnaces Fired at 10% Excess O2

| A No. Units | B Engine | C Supplier(s) | D Gen.MW | E Ht.Rate BTU/kwh | F GT Fuel MMBTU/hr | G Exh.Flow lb/hr | H Wt.%O2 at Exh. | I Avail. Exh.O2 lb/hr | J O2 Cap. No. of Furnaces | K Approx. Tlt degF | L Texh degF | M No. Shfts |
|---|---|---|---|---|---|---|---|---|---|---|---|---|
| 1. 1 | ABB GT-11 | Asea Brown Boveri | 71.900 Dry | 10970 | 788.74 | 2296491 | 16.32 | 374787 | 11.25 | 1874 | 968 | 1 |
| 2. 1 | Frame 7(EA) | G.E. or Licensees | 83.500 Dry | 10480 | 875.08 | 2351000 | 15.77 | 370753 | 10.91 | 2020 | 986 | 1 |
| 3. 2 | CW-191-PG | Westinghouse or Lic. | 37.930 | 13290 | 504.09 | 2077200 | 18.06 | 375225 | 10.81 | 1450 | 770 | 1 |
| 4. 2 | Frame 5(PA) | G.E. or Licensees | 51.428 Dry | 12071 | 620.79 | 1977494 | 16.90 | 334196 | 9.95 | 1755 | 909 | 1 |
| 5. 2 | Frame 6(B) | G.E. or Licensees | 77.862 | 10680 | 831.57 | 2185790 | 15.08 | 329595 | 9.30 | 2020 | 999 | 1 |
| 6. 2 | MF-221B | Mitsubishi | 59.000 | 10920 | 644.28 | 1742832 | 15.82 | 275699 | 8.14 | 2100 | 988 | 1 |
| 7. 2 | GT-35 Jupiter | Asea Brown Boveri | 32.720 Dry | 10535 | 344.71 | 1452000 | 18.39 | 267023 | 7.58 | 1508 | 705 | 3 |
| 8. 2 | H-25(A) | Hitachi | 46.248 Dry | 10728 | 496.14 | 1419538 | 16.21 | 230121 | 6.98 | 2300 | 994 | 1 |
| 9. 2 | SB-120 | Mitsui | 50.800 | 11388 | 578.52 | 1644930 | 15.61 | 256708 | 6.82 | 1832 | 892 | 1 |
| 10. 2 | MW-151 | Mitsubishi | 44.640 | 12006 | 535.95 | 1497522 | 15.70 | 235036 | 6.73 | 2000 | 971 | 1 |
| 11. 2 | Coberra 6462 | Cooper-Rolls | 48.200 Dry | 9114 | 439.28 | 1412770 | 16.50 | 233051 | 6.65 | 2128 | 882 | 3 |
| 12. 1 | ABB GT-8 | Asea Brown Boveri | 49.160 | 10657 | 523.90 | 1453000 | 15.41 | 223922 | 6.28 | 2100 | 977 | 1 |
| 13. 1 | V64 | Siemens, KWU | 54.200 | 10123 | 548.65 | 1382024 | 14.92 | 206143 | 5.75 | 2250 | 1004 | 1 |
| 14. 1 | CW251(B12) | Westinghouse or Lic. | 49.151 | 10436 | 512.96 | 1365780 | 15.16 | 207025 | 5.62 | 2150 | 957 | 1 |
| 15. 1 | CW-191-PG | Westinghouse or Lic. | 18.965 | 13290 | 252.04 | 1038600 | 18.06 | 187613 | 5.40 | 1450 | 770 | 1 |
| 16. 1 | Frame 5(PA) | G.E. or Licensees | 25.714 Dry | 12071 | 310.39 | 988747 | 16.90 | 167118 | 4.97 | 1755 | 909 | 1 |
| 17. 1 | Frame 6(B) | G.E. or Licensees | 38.931 | 10680 | 415.78 | 1092895 | 15.08 | 164798 | 4.65 | 2020 | 999 | 1 |
| 18. 1 | MF-221B | Mitsubishi | 29.500 | 10920 | 322.14 | 871416 | 15.82 | 137849 | 4.07 | 2200 | 988 | 1 |
| 19. 1 | LM5000(PC) | G.E. or Licensees | 36.160 | 9115 | 329.60 | 1017835 | 15.63 | 159067 | 3.90 | 2300 | 820 | 3 |
| 20. 1 | GT-35 Jupiter | Asea Brown Boveri | 16.360 Dry | 10535 | 172.35 | 726000 | 18.39 | 133511 | 3.79 | 1508 | 705 | 3 |
| 21. 1 | H-25(A) | Hitachi | 23.124 Dry | 10728 | 248.07 | 709769 | 16.21 | 115061 | 3.49 | 2300 | 994 | 1 |
| 22. 1 | SB-120 | Mitsui | 25.400 | 11388 | 289.26 | 822465 | 15.61 | 128354 | 3.41 | 1832 | 892 | 1 |
| 23. 1 | MW-151 | Mitsubishi | 22.320 | 12006 | 267.97 | 748761 | 15.70 | 117518 | 3.37 | 2000 | 971 | 1 |
| 24. 1 | Coberra 6462 | Cooper-Rolls | 24.100 Dry | 9814 | 236.51 | 706385 | 16.50 | 116525 | 3.33 | 2128 | 882 | 3 |
| 25. 1 | LM2500(PE) | G.E. or Licensees | 22.633 | 9345 | 211.51 | 551285 | 14.97 | 82511 | 2.21 | 2150 | 960 | 2 |

is rather small, the choice is frequently a cooler firing, and usually an older machine such as the Westinghouse CW-191-PG, which has a firing temperature of 1450°F (788°C).

Column M shows that some of the machines have multiple shafts, which is a typical characteristic of aeroderivatives. Because of the lower rotor spindown inertia and risk of fuel rich furnace conditions during transient switchover to ambient air, as was previously discussed, multishaft units are usually avoided in favor of the single-shaft industrial designs. Some of the very hot aeroderivatives are also low in percent fuel saved because of low exhaust oxygen content and temperature, as will be seen in the next section.

**Fuel Savings.** To be cogeneratively effective, the integration of gas turbine exhaust into an ethylene furnace must result in a saving of fuel compared to operation on ambient air. Otherwise, the gas turbine would be better installed as a standalone component, thus avoiding the expense of integration controls and ducting. Figure 9 shows an approximate two-dimensional, generalized, linear fit of the relations governing fuel saving relative to operation on ambient air. The percent saving is a function of temperature and oxygen content of the gas turbine exhaust at the point of entry into the furnace burners. The values given in columns H and L of Table 1 are roughly plotted on the continuum in Fig. 9, thus showing the percent fuel saving at design baseload for the various units. It should be kept in mind that the saving in fuel can often be improved by load and/or inlet guide vane position adjustments in consultation with the manufacturer. Also the savings shown are for an average furnace, and may be different for specific feedstocks and furnace design conditions.

The curved line at the left in Fig. 9 is the upper limit of furnace burner combustion stability, as defined by burner manufacturers according to Waibel (1989). To the left of this line, there is some risk of flameout due to insufficient oxygen and temperatures too low to maintain ignition. The curve shows that most gas turbines have sufficient oxygen content at temperatures high enough to avoid this danger. In some early GTI designs, including the one at Mossmorran, features were unnecessarily included to reduce exhaust temperature to 750°F (399°C) or below, apparently because burner problems were anticipated at elevated gas turbine exhaust temperatures.

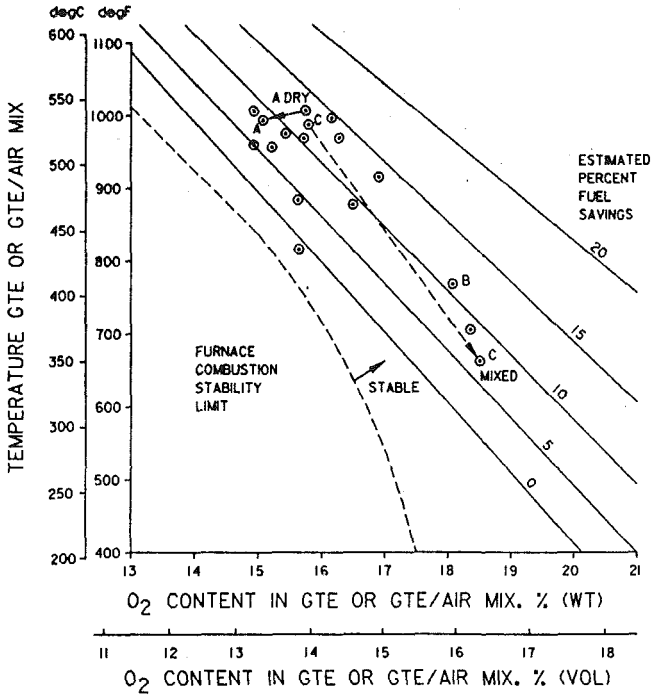


**Fig. 9 Estimated fuel savings versus gas turbine exhaust temperature and $O_2$ content**

The trend to zero fuel savings as oxygen content gets lower and lower, due to the increased mass flow of inert material and the increased fuel needed to heat it, as previously explained, can be easily seen in Fig. 9. In fact, one very hot aeroderivative machine having a low exhaust temperature plots slightly below zero fuel saving.

**$NO_x$ Control.** It is generally believed that any form of combustion gas preheating increases the formation of $NO_x$ because of the increase in adiabatic flame temperature. While true with ambient air preheat, this is not true with gas turbine exhaust integration, because the reduced oxygen content *lowers* the adiabatic flame temperature despite the elevated temperature of the gas. This effect can be seen in Fig. 8.

Most gas turbines can be brought below 50 ppmvd $NO_x$ at exhaust by steam or water injection. Typical low $NO_x$ furnace burner designs add about 35 ppmvd to bring the state-of-the-art $NO_x$ emissions at the furnace stack to approximately 85 ppmvd without further measures. At these levels, environmental restrictions in some Far-Eastern locations are requiring separate de-$NO_x$ facilities involving catalytic reduction.

The use of steam or water injection to control $NO_x$ has a very noticeable effect on fuel saving. Point A, at the upper part of the figure, is listed in Table 1 with steam injection to control $NO_x$ to 42 ppmvd. The arrow from point "A Dry" (without $NO_x$ control), shows that there is a loss of some 3.5 points in fuel saving due to the reduction in $O_2$ content caused by the increased moisture.

All engines listed in Table 1 require some steam or water injection to get below 50 ppmvd $NO_x$ at exhaust. Hotter engines usually require heavier injection quantities. Point A is for an engine with a firing temperature of 2020°F (1104°C). Engines cooler than this will therefore show a loss in fuel savings less than 3.5 points, while the reverse will be true for hotter engines.

To summarize regarding engine selection for GTI, the cooler running, single-shaft industrial designs are generally favored. In extremely power or premium fuel limited applications, extremely cool, older designs such as point B (firing temperature 1450°F, 788°C), are being utilized. Such a design still permits high furnace fuel savings, despite a low exhaust temperature, because of the high exhaust oxygen content.

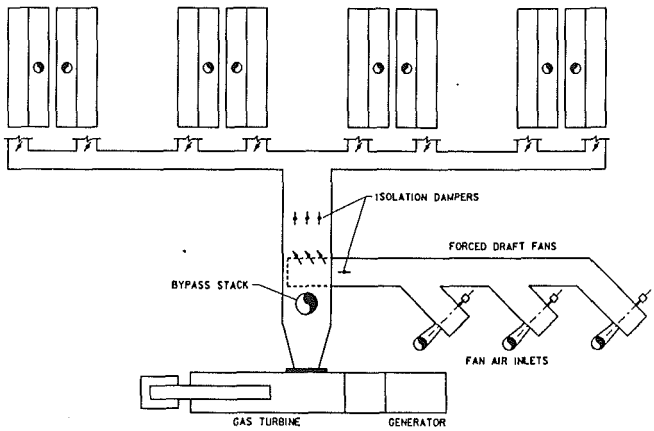


**Fig. 10 Gas turbine exhaust and forced draft fan flow arrangement**

## Partial Integration

When a plant owner determines that there is reduced demand for supplemental power that can be provided by a gas turbine, to such an extent that a matched exhaust furnace integration system will not be possible, the overall economic benefits of gas turbine integration diminish. This is because the exhaust quantities available from the turbine will not be sufficient to provide the total oxygen requirements for furnace combustion. An evaluation then must be made in consideration of some form of partial integration. Such systems may take the form of either integrating some of the furnaces totally with the turbine, with the remaining furnaces utilizing ambient air for combustion, or by supplementing the turbine exhaust products with forced draft ambient air and feed exhaust/air mix to all furnaces for combustion purposes. For either partial integration system, the economic benefits from fuel saving will not compare with those attainable with a matched system.

The simplest partial integration system, in consideration of operating controls, is one that has a fixed number of furnaces matched with the turbine for oxygen, with the others using only ambient air. Such a system, however, still requires a "Flywheel" boiler to handle exhaust surplus.

The partial integration system that utilizes supplementary forced draft ambient air is more complex in consideration of controls and system design requirements. Such a system, typical of several now being engineered for, or installed in, the Far East, is shown schematically in Fig. 10. The inherent reduction of temperature and increase of exhaust oxygen content by mixing ambient air is indicated by the dashed line from point C in Fig. 9. The concurrent reduction in fuel saving per furnace will also be noted in the figure.

This system must be able to maintain furnace operation when utilizing forced draft ambient air in the event of a turbine trip. A minimum practicable base air load, therefore, must be established for the forced draft fans to permit a safe changeover to forced draft air operation after a turbine trip. This means that for any ambient temperature condition other than winter, the forced draft fans will be expected to provide a greater quantity of air to the system, thus reducing the temperature of the exhaust gas/air mix, while increasing the percentage oxygen in the mixture. The cumulative effects of this manner of partial integration, however, are to reduce the amount of furnace fuel savings that are possible in comparison with systems employing some form of oxygen matching. One point in its favor, however, is that all furnaces would have the same convection section design, thus reducing furnace engineering costs.

A partial integration system employing forced draft fans is more difficult to justify economically because of the system's complexity. The system requires that costly mixing sections be

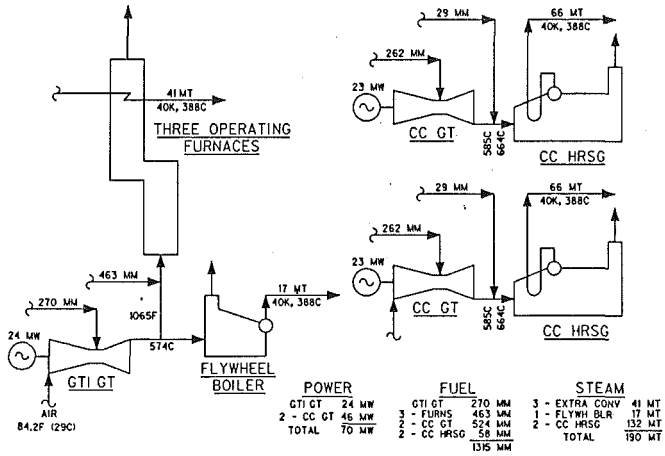


Fig. 11 Alternate A, with GTI

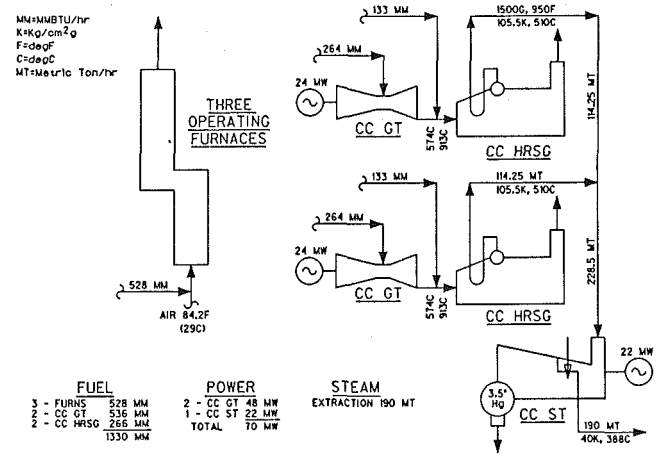


Fig. 12 Alternate B, no GTI, combined cycle central station

provided for the exhaust products and forced draft air to circumvent potential stratification of the colder ambient air, which could result in nonuniform oxygen distribution to burners. Unless the mixing sections are provided, however, furnace firing could be nonuniform due to varying oxygen composition in the mix to the burners and unstable flame propagation may result.

## Comparison With Other Means of Gas Turbine Cogeneration

The economics of direct exhaust GTI are very site specific, but can usually be justified in high fuel cost applications involving the ethylene plant alone. The ethylene facility is frequently in a refinery or petrochemical complex, however, where there is need for large amounts of heat in the form of high-pressure steam. In any such plant, if auxiliary boilers are being used to generate steam, thus burning fuel noncogeneratively for the separate production of heat, a significant economic advantage may be overlooked by not considering replacement of some of the heat with cogeneration, utilizing a combined cycle. Because of the high efficiency of the combined cycle, it is sometimes better to produce all power cogeneratively with high-pressure steam rather than use GTI at the ethylene furnaces.

A true combined cycle consists of a gas turbine, a heat recovery boiler and a *steam* turbine, either back-pressure or condensing, from which the needed steam is obtained by direct exhaust or extraction. In an earlier paper by one of the authors (Cooke, 1987), direct exhaust GTI in an ethylene plant was

**Table 2 Economic comparison for Figs. 11 and 12**

Configuration:

Alternate A: 1 gas turbine integrated into the ethylene furnaces (24 MW); 2 gas turbines with supplementary fired boilers in central utilities (46 MW).

Alternate B: 2 gas turbines (48 MW) and 1 steam turbine (22 MW) as a true combined cycle in central utilities.

Summary of results:

| | Alternate A | | Alternate B | |
|---|---|---|---|---|
| Total fuel fired | MMBtu/hr | (MMKcal/hr) | MMBtu/hr | (MMKcal/hr) |
| - Furnaces | 463 | (117) | 528 | (133) |
| - Gas turbines | 794 | (200) | 536 | (135) |
| - Boilers | 58 | (15) | 266 | (67) |
| - Total | 1315 | (332) | 1330 | (335) |
| Relative Cost (MM$U.S.) | | | | |
| - Furnaces | + 1.75 | | Base | |
| - Gas turbines | + 7.50 | | Base | |
| - Boilers | - 0.25 | | Base | |
| - Steam turbines | - 4.00* | | Base | |
| - Net Difference | + 5.00 | | Base | |

*Steam turbine power generation is not feasible in Alternate A.

shown to be considerably less effective, cogeneratively, than a combined cycle. In the latter, the steam and gas turbine cycles are combined in a special way that provides improved Carnot efficiency (i.e., thermal power conversion efficiency). This improves the cogenerative effect, which is saving of fuel by simultaneous, sequential production of heat and power together, rather than separately.

The foregoing can be demonstrated by an example in which application of direct exhaust GTI in an ethylene facility, where an off-site central utilities plant was also planned, was evaluated for an overseas owner. The utility need was for 70 MW of power and 190 metric tons (MT) per hour (418,950 lb/hr) of 40 kg/cm$^2$g, 388°C steam (569 psig, 730°F). Figure 11 shows Alternate A, with GTI, where the use of the gas turbine results in extra heat that cannot be utilized in the ethylene plant, from the flywheel boiler and the furnace convection section. This extra heat is equivalent to 58 MT/hr of steam, leaving 132 MT/hr for cogeneration in the utility plant with 46 MW of power. It is impractical to incorporate a steam turbine in the utility plant with this arrangement, because the power from GTI usurps the spot. The arrangement shown in Alternate B, without GTI (Fig. 12), allows an optimum combined cycle with a steam turbine operating at 1500 psig, 950°F (106 kg/cm$^2$g, 510°C), with extraction of the required steam. The increased fuel economy in the central utilities plant results in almost the same fuel for the two alternatives, but the capital cost with GTI and three gas turbines is considerably greater. Table 2 summarizes fuel and capital cost. As indicated, locating all gas turbines in central utilities (Alternate B) is the lower capital cost option and achieves essentially the same energy efficiency as Alternate A. Furthermore, by segregating the gas turbines and furnaces, greater operating flexibility and reliability is achieved. It is therefore concluded for this example that the best gas turbine application is to locate all turbines in central utilities.

## Conclusion

Gas turbine exhaust integration into the cracking furnace gas side provides additional shaft power and heat, which may improve the economics of operation, provided that purchased power and fuel costs are high enough to offset the capital costs of the gas turbine system with reasonably short payout. However, cracking furnace process systems themselves are usually more or less self-sufficient with regard to mechanical power, because the required shaft power for process gas compression is adequately covered by steam energy from cracked-gas quenching and furnace convection section heat recovery. Although a small part of the power from a thermally matched gas turbine system can probably be used electrically within the ethylene unit, there usually must be a need for power outside the immediate cracking plant, which would otherwise be furnished by less economical means such as purchase from the utility.

In a few plants, gas turbines driving process compressors have been utilized for exhaust integration. However, the majority of GTI applications involve steam turbines for compressor drive and single-shaft, power-generating gas turbines for exhaust integration. This results in simpler controls and a more economical arrangement.

Most of the current applications for direct exhaust GTI are in the Far East, where several are either already in operation, under construction, or being engineered by several U.S. firms. Some of these applications are characterized by low power demand and/or a shortage of premium fuel for firing the gas turbines. Owners are proceeding with GTI in these cases with favorable economics, in spite of the fact that some gas turbines utilized do not provide sufficient oxygen to support all ethylene furnaces. The gas turbines selected in most applications so far have favored cooler operating, single-shaft, industrial designs.

For ethylene plants in a complex where fuel is being burned noncogeneratively for the separate production of heat in auxiliary boilers, owners should alternatively consider replacement of some of the heat production by cogeneration utilizing a true combined cycle. This could provide a more cost-effective plant with simpler controls.

## References


Bacsic, G. J., 1982, "Process and Apparatus for Furnace Operation With Gas Seal," United States Patent No. 4,332,546, June 1.

Chambers, L. E., and Potter, W. S., 1974, "Design of Ethylene Furnaces," *Hydrocarbon Processing*, Jan.–Aug.

Cooke, D. H., 1987, "Combined Cycle Thermodynamic Inquiries and Options for Cogeneration Facilities in the Process Industry," ASME Paper No. 87-JPGC-Pwr-61; SWEC Paper No. TP 87-104.

Foerster, K. W., 1984, "The Fife Ethylene Project at Mossmorran/Scotland," *Machinery News*, Apr. (reprint available from MAN-GHH Corporation).

*Gas Turbine World*, 1989, "Performance Specs, 1989," Vol. 10, June, a Pequot Publication.

Waibel, R. T., 1989, Technical Director, Burner Division, John Zink Company, Private Communication, July.

# Performance Curves for Single-Stage Vapor Compression Cycles With Solution Circuit

**K. Amrane**

**M. V. Rane**

**R. Radermacher**

The University of Maryland,
Department of Mechanical Engineering,
College Park, MD 20742

*The performance curves for a single-stage vapor compression heat pump with solution circuit (VCHSC) and for its modified version, the cycle using a subcooler and a preheater, are obtained and are compared for the same total UA value including all heat exchangers. The two cycles are simulated at low and high temperature lifts. The weak solution concentration and flow rate are varied. The parameters studied are the cooling COP, the solution heat exchanger (SHX) effectiveness, the pressure ratio, the solution temperature glides in the absorber and the desorber, the desorber load, and the distribution of the UA value. Changing the weak solution concentration from 20 to 90 wt% ammonia increased the desorber load ten times. The cooling COP improved by as much as 20 percent by incorporating the preheater and the subcooler, for both the low and the high temperature lifts. Compared to the conventional ammonia vapor compression cycle, the modified VCHSC showed a maximum improvement in cooling COP of 88 and 35 percent for the low and high temperature lifts, respectively. The results indicate that VCHSC is a very versatile heat pump and/or refrigeration system suitable for a wide range of applications and changing operating conditions.*

## Introduction

Combinations of conventional compression and absorption heat pumps, if judiciously executed, can lead to advanced energy cycles with surprisingly interesting features (Alefeld, 1982, 1985). The particularity of one subset of such heat pumps, which may be seen as hybrids between conventional and absorption heat pumps, is that the input of energy to the cycles is in the form of work and is accomplished by mechanically compressing the refrigerant vapor. On the other hand, cooling and heating is achieved by desorbing and absorbing the vapor out of and into an absorbent. The weak solution at the outlet of the desorber is pumped to the absorber. This is achieved using a solution circuit as described below. The first concept of such heat pumps, which will be referred to in this text as vapor compression heat pumps with solution circuits (VCHSC), was proposed by Osenbrueck in 1895 (Morawetz, 1989). Since then, and mainly in the recent past, these cycles have been discussed repeatedly in the literature (Altenkirch, 1913; Mucic, 1984; Radermacher, 1986; Ahlby, 1987; Stokar, 1987). A historical survey on this matter can be found from Ahlby and Hodgett (1990) and Morawetz (1989). In this study, a design tool in the form of a computer simulation program is presented that allows the development and optimization of two versions of a VCHSC.

The objective of this study is to analyze the performance of a vapor compression heat pump with one solution circuit. A computer model based on steady-state operation of the system has been developed to assess the effect of temperature lift, mixture composition, heat exchanger size, and pump volumetric flow rate on the system's performance. A modified version of the heat pump is also investigated and its performance evaluated and compared to the basic cycle.

## Description of the Cycles

Figure 1 represents the vapor compression heat pump with one solution circuit in a pressure–temperature diagram. This representation has the advantage of indicating the pressure and temperature levels experienced by those heat exchangers (namely the absorber and the desorber) that accommodate a phase change. In addition, the horizontal length of each heat exchanger (except the solution heat exchanger) is indicative of the temperature change that the working fluid mixture undergoes during the phase change process. The cycle is composed of six main components: a desorber, an absorber, a solution heat exchanger, a compressor, a solution pump, and an expansion device. Figure 2 is a representation of the laboratory prototype heat pump in the single-stage configuration currently being tested at The University of Maryland. Details about the experimental setup have been presented by Rane et al. (1989). Heat from the heat source is transferred to the desorber, from which vapor containing the predominantly low boiling component of the working fluid mixture is generated and fed to the compressor, where it is compressed to a higher pressure level. The remaining solution, weak in refrigerant, is pumped to the high pressure level and circulated into the absorber,

Contributed by the Advanced Energy Systems Division for publication in the JOURNAL OF ENGINEERING FOR GAS TURBINES AND POWER. Manuscript received by the Advanced Energy Systems Division April 19, 1990; revision received September 17, 1990.

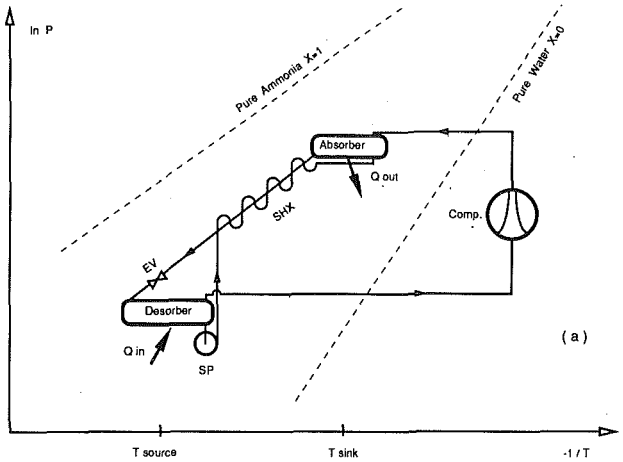


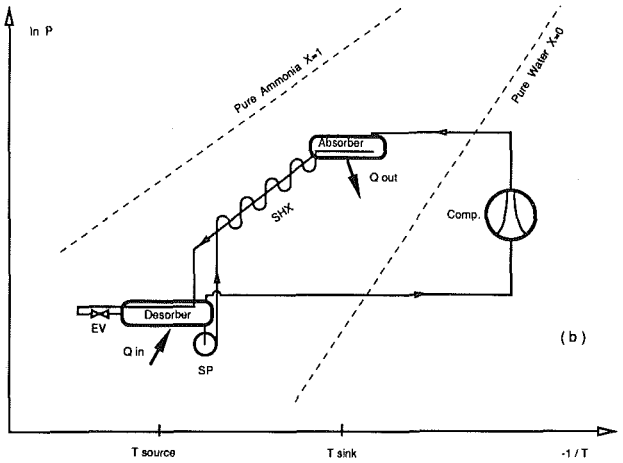


**Fig. 1 Ammonia–water single-stage vapor compression heat pump with solution circuit: (*a*) original, and (*b*) modified cycles**

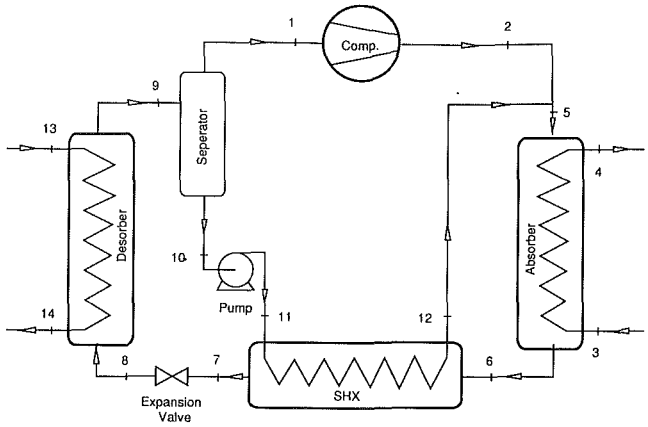


**Fig. 2 Single-stage VCHSC**

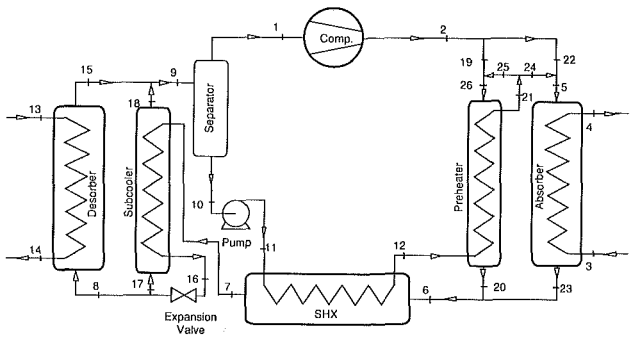


**Fig. 3 Modified version of single-stage VCHSC**

where it absorbs the vapor delivered by the compressor. The heat of absorption is transferred to the heat sink while the resulting strong solution leaving the absorber is brought into heat exchange with the weak solution in a solution heat exchanger and is finally expanded down to the low pressure. The desorption and absorption processes, although isobaric, are associated with a change in temperature of the working fluid, since the mixture composition varies. This variation of solution temperature will be referred to in this text as solution temperature glide. The solution temperature glide can be changed by changing the pump flow rate.

The basic cycle is modified by introducing two additional components, as shown in Fig. 3. Firstly, a preheater is used to heat the weak solution leaving the solution heat exchanger to a higher temperature. In the preheater, the weak solution picks up heat from the solution, which absorbs superheated vapor coming out of the compressor. Preheating increases the temperature of the solution at the inlet of the absorber, which influences the highest temperature in the absorber. Thus, by introducing a preheater, heat can either be delivered at a slightly higher temperature without increasing the absorber pressure or the absorber pressure can be reduced slightly if heat is to be delivered at the original temperature level.

Similarily, a subcooler is used to subcool the strong solution coming out of the solution heat exchanger, to a lower temperature. In the subcooler, the strong solution exchanges heat with the desorbing solution. Subcooling of the strong solution at the inlet of the expansion valve results in a reduction of the solution temperature at the inlet of the desorber, which is the minimum temperature in the desorber. This means, by introducing a subcooler, heat can either be picked up at a slightly lower temperature without decreasing the desorber pressure or the desorber pressure can be increased if heat is to be picked up at the same temperature level.

Thus, by introducing a preheater and a subcooler the pressure ratio encountered by the compressor can be reduced. This leads to reduced compressor work and increased COP. The preheater and the subcooler need not be independent units as it is assumed here; they can be integrated into the absorber and the desorber by using triple pass heat exchangers, as shown in Fig. 1(*b*).

## Computer Simulation Model

The computer simulation model is based on fundamental physical laws such as energy and mass balances and heat transfer relations. In order to study the thermodynamic performance of the heat pumps and simplify the model, the following assumptions were made:

1 Pressure drops due to friction in the system are negligible (except for the expansion valve).
2 Heat losses to the surroundings are negligible.
3 The state of the strong solution leaving the absorber is saturated.
4 Isentropic efficiency for the compressor is 70 percent, and the efficiency for the pump (not including the motor efficiency) is 70 percent.
5 Volumetric efficiency of the compressor is 100 percent.
6 The outlet conditions of the absorbing solutions at the outlet of the preheater and the absorber are identical.
7 The outlet conditions of the desorbing solutions at the outlet of the subcooler and the desorber are identical.

The last two assumptions are due to the fact that the modified cycle represents a system in which the absorber and desorber are triple pass heat exchangers.

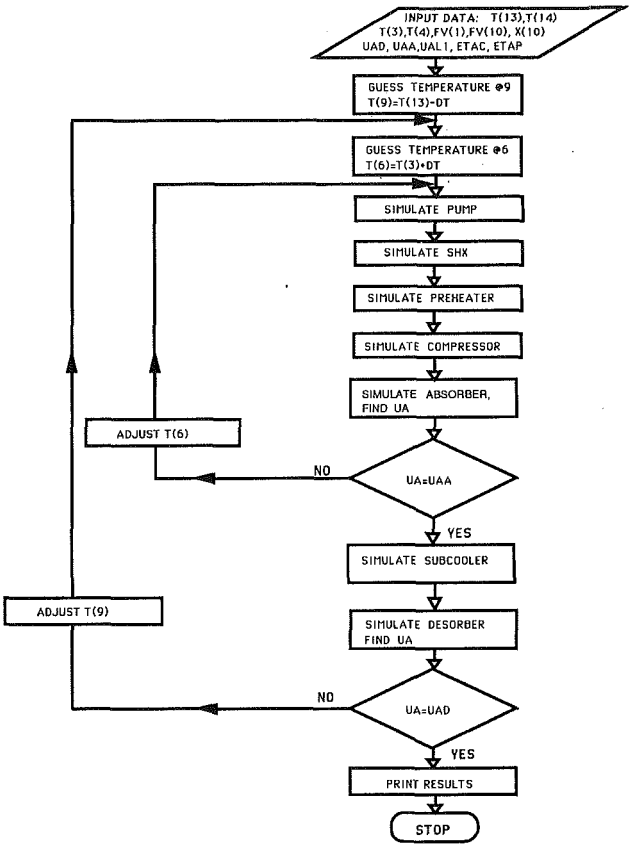


**Fig. 4 Model flowchart for the single-stage vapor compression heat pump with solution circuit**

The following equations can be written for each of the subunits constituting the system (it is here assumed that the heat sink and source of the heat pump are water streams):

*Energy balance*

heat exchangers $\Sigma(F*h)_{in}-\Sigma(F*h)_{out}=0$

compressor and pump $\Sigma(F*h)_{in}+W-\Sigma(F*h)_{out}=0$

*Refrigerant mass balance*

$$\Sigma(F*X)_{in}-\Sigma(F*X)_{out}=0.$$

*Overall mass balance*

$$\Sigma(F)_{in}-\Sigma(F)_{out}=0.$$

*Heat Transfer*

$$Q-(UA)\text{LMTD}=0.$$

where $F$ = mass flow rate; $h$ = enthalpy; $X$ = overall composition; $UA$ = product of the overall heat transfer coefficient and heat exchanger area; $W$ = compressor or pump work; $Q$ = heat transferred; LMTD: logarithmic mean temperature difference.

Input data to the program include the water inlet and outlet temperatures into the absorber and desorber, the weak solution concentration, and the volume flow rates of both the compressor and the pump. Also given are the products of the overall heat transfer coefficient and heat transfer area for all heat exchangers. With the given parameters, the program calculates the thermodynamic properties of the mixture at all points in the cycles. The cooling COP is also calculated, which is defined as the ratio of the desorber load to the sum of the compressor and the pump work inputs. The property data of the working fluid mixture, in our study ammonia-water, are taken from Ziegler and Trepp (1984) in the form of computer subroutines. The flowchart in Fig. 4 represents the model's logic, which is based on the successive substitution method and is completely described by Amrane et al. (1989).

**Table 1 Distribution of *UA* values for different heat exchangers after optimization of the cycles**

| *UA* values | Case 1 kW/°C | Case 2 kW/°C | Case 3 kW/°C | Case 4 kW/°C |
|---|---|---|---|---|
| Desorber | 4.50 | 4.25 | 4.50 | 3.90 |
| Subcooler | — | 0.20 | — | 0.40 |
| SHX | 0.60 | 0.30 | 1.30 | 0.70 |
| Preheater | — | 0.75 | — | 1.90 |
| Absorber | 5.90 | 5.50 | 5.20 | 4.10 |
| Total *UA* | 11.00 | 11.00 | 11.00 | 11.00 |

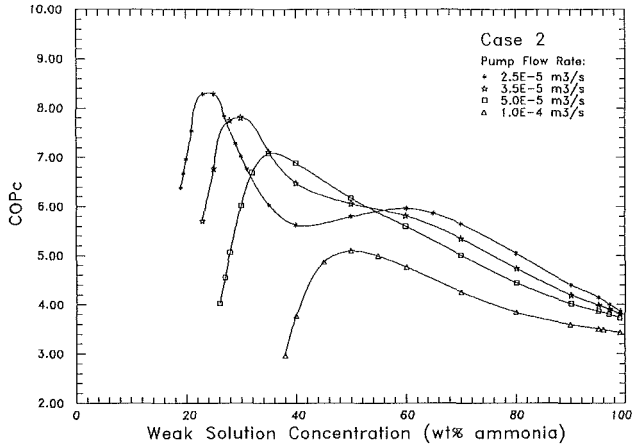


**Fig. 5 Variation of cooling COP with weak solution concentration for different solution flow rates**

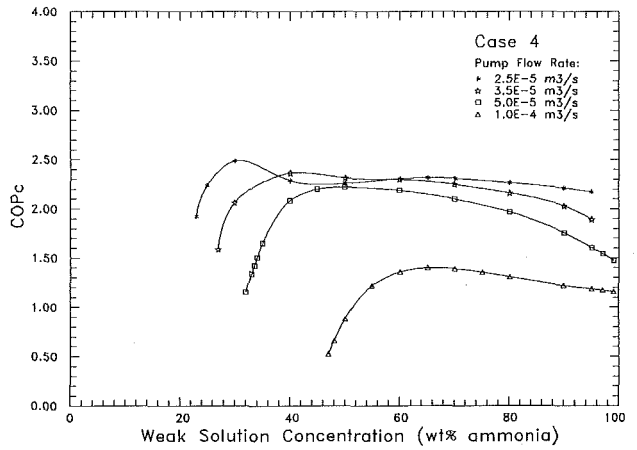


**Fig. 6 Variation of cooling COP with weak solution concentration for different solution flow rates**

## Results

**Simulation Conditions.** The performance curves for a single-stage VCHSC and its modified version (cycle with subcooler and preheater) are obtained by simulating the two cycles at two temperature lifts. The four cases are as follows:

Case 1: Single-stage VCHSC—low temperature lift
Case 2: Modified version—low temperature lift
Case 3: Single-stage VCHSC—high temperature lift
Case 4: Modified version—high temperature lift

The four cases were simulated at the following conditions:

1 Low temperature lift
(*a*) Heat source temperature
inlet $T(13)$ = 25°C and outlet $T(14)$ = 10°C

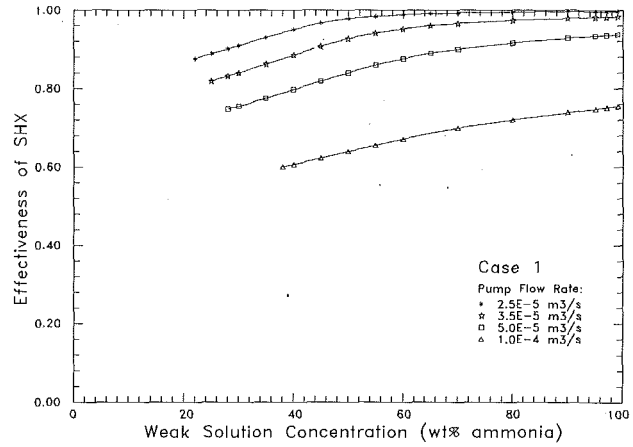


**Fig. 7 Variation of solution heat exchanger effectiveness with weak solution concentration and solution flow rate**

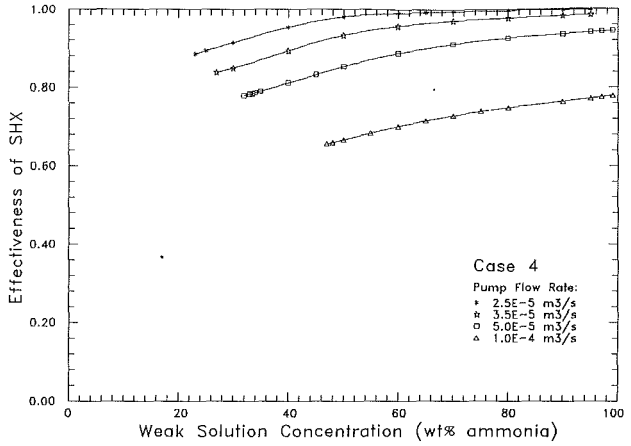


**Fig. 9 Variation of solution heat exchanger effectiveness with weak solution concentration and solution flow rates**

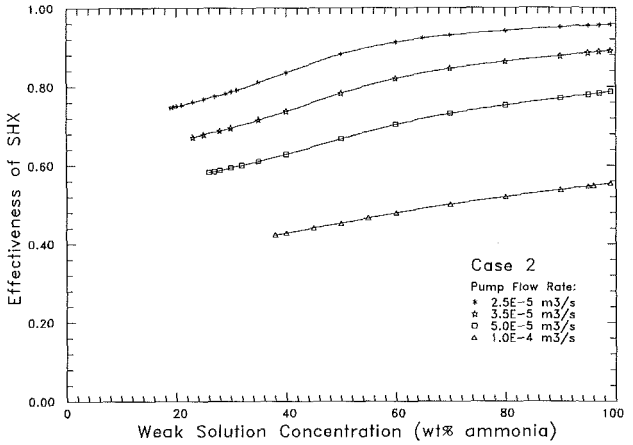


**Fig. 8 Variation of solution heat exchanger effectiveness with weak solution concentration and solution flow rate**

(*b*) Heat sink temperature
inlet $T(3) = 25°C$ and outlet $T(4) = 45°C$

2 High temperature lift

(*a*) Heat source temperature
inlet $T(13) = 15°C$ and outlet $T(14) = 0°C$

(*b*) Heat sink temperature
inlet $T(3) = 55°C$ and outlet $T(4) = 80°C$

The water temperatures at the inlet and outlet of the heat source and heat sink were specified as above. The mass flow rate of water was determined by the desorber and absorber loads.

3 The compressor volume flow rate was fixed at 0.01 $m^3/s$ for all cases.

4 Pump flow rates of $2.5*10^{-5}$, $3.5*10^{-5}$, $5.0*10^{-5}$, and $1.0*10^{-4}$ $m^3/s$ were studied. The pump flow rate is chosen as an independent variable because it influences the solution temperature glides and hence the performance of the VCHSC.

5 The sum of all *UA* values (products of overall heat transfer coefficients and the heat transfer areas) of all heat exchangers was assumed to be 11 kW/°C. This value was chosen because the absorber and the desorber LMTD's are about 5°C for a weak solution concentration of 50 wt% ammonia, and the pump flow rate is $5.0*10^{-5}$ $m^3/s$ for case 1. These values for the weak solution concentration and the pump flow rate were selected in the middle of the range of concentrations and flow rates investigated.

6 The optimal distribution of *UA* values among the different heat exchangers was obtained for each of the four cases. The *UA* values were optimized for maximum COP, at a weak solution concentration of 50 wt% ammonia, and pump flow rate of $5.0*10^{-5}$ $m^3/s$. Starting with a *UA* distribution of 5, 5, and 1 kW/°C for the desorber, the absorber, and the solution heat exchanger (SHX), respectively, the *UA*s were redistributed in successive steps so as to increase the cooling COP. This process was continued until no further improvement in COP was obtained. This required about 25 runs. The optimum allocations of *UA* values in the four cases are listed in Table 1. This distribution was then maintained for all other conditions.

7 The weak ammonia–water solution concentration was varied between 20 and 99 wt% ammonia.

The minimum weak solution concentrations investigated in this study are different for different simulation conditions because the absorber and/or the desorber appear oversized at very low concentrations, which lead to very low capacities.

**Results and Discussion.** Figure 5, which represents the variation of COP versus weak solution concentration for case 2, shows that the cooling COP peaks at two solution concentrations, 25 and 60 wt% ammonia, for the low solution flow rate of $2.5*10^{-5}$ $m^3/s$. On the other hand, the COP curves have only one peak, at 35 and 50 wt% ammonia, for the high solution flow rates of $5.0*10^{-5}$ and $1.0*10^{-4}$ $m^3/s$, respectively. On closer observation, it can be seen that as the solution flow rate increases, the two peaks merge. As the solution mass flow rate increases further, the peak in the COP curve shifts toward higher weak solution concentrations. Similar observations can be made from Fig. 6, which represents variation of COP versus weak solution concentration for case 4. The curves in Fig. 6 are relatively flat because of higher SHX effectivenesses, which is discussed later.

Variation of cooling COP with weak solution flow rate also shows that in most of the cases (for weak solution concentrations below 25 and above 55 wt% ammonia), the COP decreased with increase in solution flow rate. This is mainly due to two reasons: the decrease in the solution heat exchanger (SHX) effectiveness at higher mass flow rates, which is discussed next, and changes in the pressure ratio, as discussed later.

The variations of SHX effectiveness with weak solution concentration and flow rate for cases 1, 2, and 4 are plotted in Figs. 7, 8, and 9. For a particular temperature lift, as the solution flow rate increases, the SHX has to exchange more heat. This increases the LMTD (logarithmic mean temperature difference) in the SHX, thereby reducing the effectiveness. On the other hand, for a particular weak solution flow rate, as the weak solution concentration increases, the SHX effectiveness increases. The effectiveness increases because the SHX has to exchange less heat at higher solution concentrations, which is due to the reduced specific heat capacity at higher weak solution concentration (the product of density and spe-

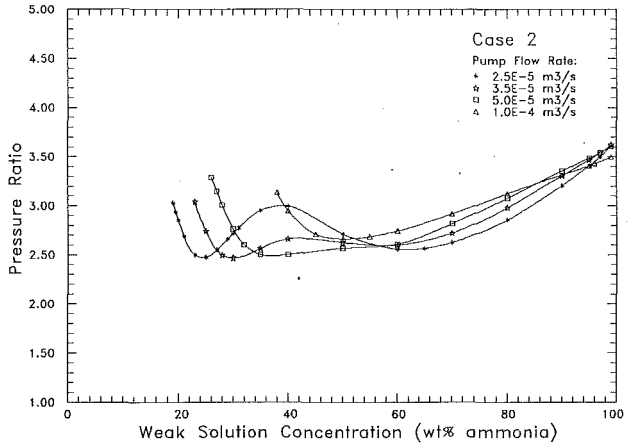


**Fig. 10 Variation of pressure ratio with weak solution concentration for different solution flow rates**

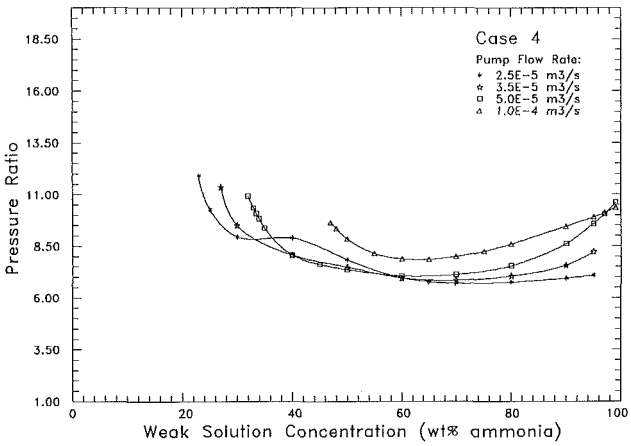


**Fig. 11 Variation of pressure ratio with weak solution concentration for different solution flow rates**

cific heat of the ammonia solution decreases with increase in the solution concentration).

The SHX effectiveness for case 1 (Fig. 7) is higher than that for case 2 (Fig. 8), because the optimized *UA* value for case 1 is significantly higher than that for case 2. Similar observations are made for cases 3 and 4.

Figures 10 and 11 show the variation of pressure ratio (the ratio of absorber to desorber pressure) with weak solution concentration for cases 2 and 4. As one would expect, the curves for the pressure ratio show the inverse behavior of the COP curves. Thus, the gain in COP is primarily a consequence of the reduction in pressure ratio. As the pressure ratio increases, the work increases, and consequently the COP decreases. The variation in the pressure ratio is dependent on the match in the temperature glides on the working fluid side and heat transfer fluid side of the desorber and absorber. At low solution flow rates, there is a good match in temperature glides at two different concentrations (Figs. 12, 13, 14, and 15). This is the reason that there are two maxima in the COP curves and two minima in the corresponding pressure ratio curves. At higher solution concentrations, the mismatch in the temperature glides leads to an increase in pressure ratio. This explains the decrease in COP at high concentrations, despite a small improvement in the SHX effectiveness (Figs. 5 and 6).

Variations in the solution temperature glide in the desorber for cases 3 and 4 are shown in Figs. 12 and 13, respectively. In these figures, the horizontal line at 15°C represents the temperature change of the source heat transfer fluid, which is fixed. Similarly, the solution temperature glides in the absorber for cases 3 and 4 are shown in Figs. 14 and 15, respectively,

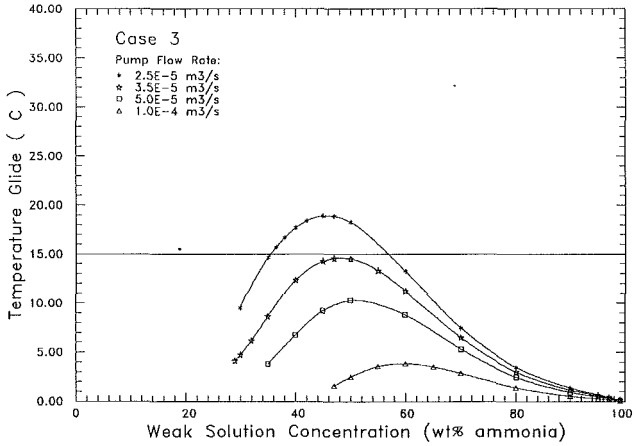


**Fig. 12 Variation of solution temperature glide in the desorber with weak solution concentration**

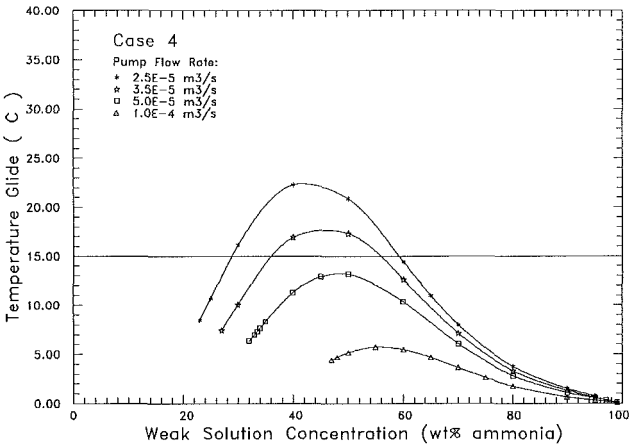


**Fig. 13 Variation of solution temperature glide in the desorber with weak solution concentration**

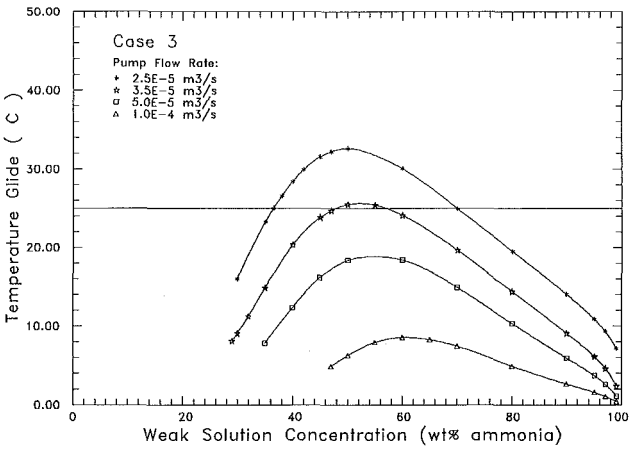


**Fig. 14 Variation of solution temperature glide in the absorber with weak solution concentration**

and the horizontal line at 25°C represents the change in temperature of the sink heat transfer fluid.

By comparing plots for cases 3 and 4 (Figs. 12 and 13), it can be seen that the solution temperature glide in the desorber and the absorber can be increased by introducing a subcooler and a preheater, respectively. The increase in the desorber solution temperature glide is due to the lowering of the temperature at the inlet of the desorber, while the increase in the absorber solution temperature glide is due to a higher inlet temperature in the absorber. These changes lead to lower pres-

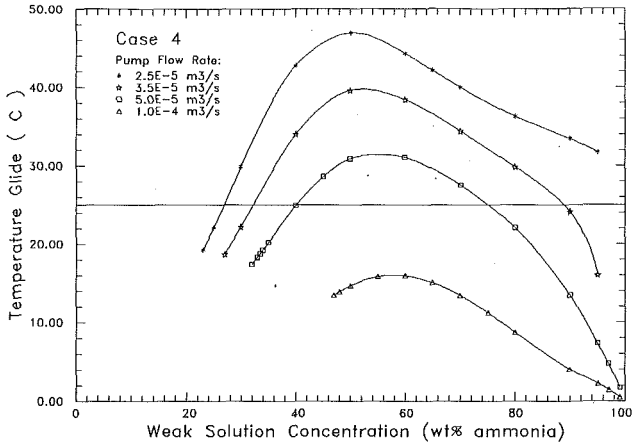


**Fig. 15 Variation of solution temperature glide in the absorber with weak solution concentration**

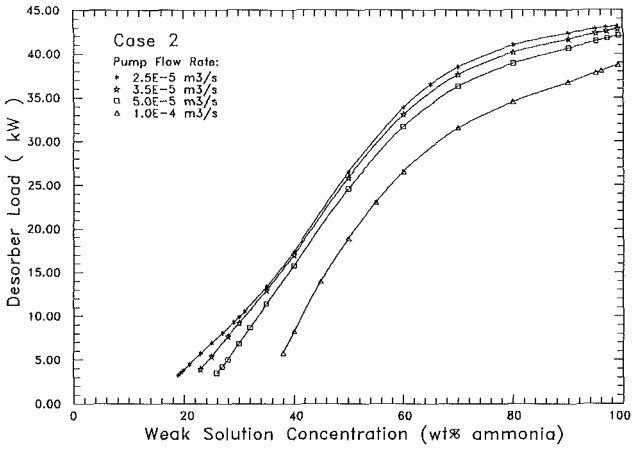


**Fig. 16 Variation of desorber load with weak solution concentration for different solution flow rates**

sure ratios and higher COPs. These effects are significant at low solution flow rates and at moderate concentrations. The cooling COP for case 2 is 20 percent higher than that for case 1 at a low solution flow rate of $2.5*10^{-5}$ $m^3/s$ and a weak solution concentration of about 25 wt% ammonia. However the improvement in COP decreases with increase in the solution flow rate and the weak solution concentration. This is because under these conditions the solution temperature glide is small, and so is the increase in glide. The improvement in COP for cases with high concentrations at low solution flow rates depends on how large the solution temperature glide is. Similar observations can be made by comparing cases 3 and 4.

Figure 16, which represents the variation of desorber load with weak solution concentration for case 2, shows that the desorber load changes significantly with changes in solution concentration. The desorber pressure increases with solution concentration. This increases the mass flow rate of vapor through the compressor, which leads to higher desorber loads. The desorber load can be increased by a factor of 10, by changing the weak solution concentration from 20 to 90 wt% ammonia.

The desorber load decreases with increase in the solution mass flow rate. As discussed earlier, increase in the solution flow rate decreases the SHX effectiveness. This increases the temperature and enthalpy of the weak solution at the inlet of the desorber, and thus leads to the decrease in desorber capacity. The curves for the desorber load are flatter at higher concentrations because the vapor pressure of the solution does not change significantly. The plots for cases 1, 3, and 4 are

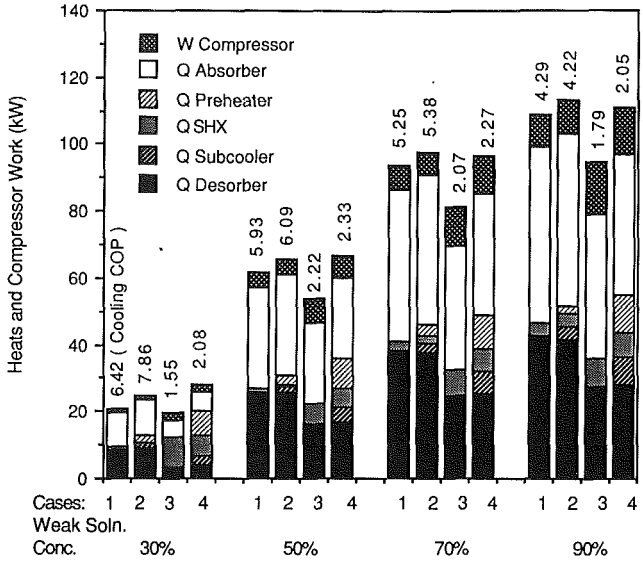


**Fig. 17 Performance comparison at different operating conditions**

similar to the one for case 2. In order to save space they are not included here.

It can be seen from the plots that the minimum weak solution concentrations investigated in this study are different for different simulation conditions. This is because at very low concentrations the desorber and/or the absorber effectiveness reaches 100 percent at a lower *UA* value than those specified in Table 1. In other words, the desorber and/or the absorber is oversized. It should be noted that the heat pump components are oversized when the heat pump is operated at low capacities, and are undersized for large loads.

Another important issue is that of friction in the reciprocating compressor (friction between the piston rings and the cylinder). The frictional loss for a reciprocating compressor, driven by a single-speed motor, will be almost constant, irrespective of the heat pump capacity. This means the assumption of constant isentropic efficiency is no longer valid. As the desorber load decreases, the isentropic work required to compress the vapor also decreases. Since the compressor friction is almost constant, the isentropic efficiency decreases with decrease is desorber capacity. This will lead to lower COPs than those predicted in this analysis. However, the assumption of constant isentropic efficiency will be reasonably good for a centrifugal compressor driven by a constant speed motor, because in this case the frictional loss will be proportional to the density of the vapor being compressed and so will be the isentropic work required and the capacity of the heat pump. This is also discussed by Buschmeier et al. (1990).

Figure 17 shows the heat exchanged in the different heat exchange units and the compressor work for the four cases at four different weak solution concentrations, for a pump flow rate of $3.5*10^{-5}$ $m^3/s$. The ratio of heat exchanged in the preheater to that exchanged in the absorber varies from 0.25 to 0.035 when the weak solution concentration changes from 30 to 90 percent. This is for the low temperature lift. For high temperature lift, this ratio varies from 1.13 to 0.27 for the same change in concentration. The considerable change in this ratio is indicative of the relative importance of the preheater for overall cycle performance. Similarly, the ratio of heat exchanged in the subcooler to that exchanged in the desorber varies from 0.13 to 0.1 for low temperature lift, and from 0.68 to 0.29 for high temperature lift. The ratio of total internal heat exchanged (that is, the sum of the heats exchanged in the subcooler, the SHX, and the preheater) to that of the desorber load varies from 0.51 to 0.23 for low temperature lift, and from 3.86 to 0.96 for high temperature lift. As discussed earlier,

the introduction of the subcooler and the preheater decreases the compressor work, but the desorber load remains unchanged. This results in improved COP. The above discussion reflects on the significance of including the subcooler and the preheater while operating the heat pump at high temperature lift and/or high solution temperature glide.

It is important to be able to estimate the optimum pump flow rate and weak solution concentration that would give maximum COP at any desired desorber load and temperature lift. The desorber load and compressor volumetric capacity essentially determine the weak solution concentration (Fig. 16 shows that the desorber load is not significantly altered at low solution flow rates or at high values of SHX effectiveness). Therefore, the only variable that needs to be optimized is the pump flow rate. The optimum pump flow rate is the one at which there is the best match in the temperature glides in the desorber and the absorber, provided the effectiveness of the SHX is 100 percent. However, in practice, the SHX effectiveness is less than 100 percent and so it shifts the optimum pump flow rate to a lower value than that determined by best match in temperature glides.

Simulation of the conventional ammonia vapor compression heat pump predicts a cooling COP of 4.39 and 1.85 at the low and high temperature lifts, respectively. The maximum cooling COP for the modified VCHSC is 8.3 for the low temperature lift. This is an improvement of 88 percent over the conventional ammonia cycle. The maximum improvement in cooling COP for the high temperature lift is 35 percent. Larger COP improvement is obtained for the low lift case because the ratios of the sink and the source heat transfer fluid temperature glides to the lift are higher (as can be seen on a $T$–$s$ diagram).

## Conclusions

An assessment of the potential of a vapor compression heat pump with solution circuit and its modified version (cycle with subcooler and preheater) has been made by developing and using a computer model.

Steady-state simulations show that the cooling COP curves peak at two weak solution concentrations for low solution flow rates, and at one weak solution concentration for high solution flow rates. Except at low solution flow rates and weak solution concentrations below 60 wt% ammonia, the COP decreases with increase in solution flow rate and concentration.

By introducing a subcooler and a preheater, the cooling COP increases by as much as 20 percent at the low concentrations, but the percentage improvement decreases as the weak solution flow rate and the concentration increases.

The SHX effectiveness decreases with increase in solution flow rate and increases with increase in weak solution concentration.

The pressure ratio is dependent on the match in the glides on the solution sides of the desorber and the absorber and the glides on the source and the sink, respectively.

The solution temperature glides in the absorber and the desorber peak at a particular concentration between 40 and 60 wt% ammonia. The glides decrease with increase in the solution flow rate. Introducing a subcooler and a preheater increases the solution temperature glides in the desorber and the absorber.

The desorber load increases by a factor of 10, by changing the weak solution concentration from 20 to 90 wt% ammonia.

The ratio of total internal heat exchanged to that of the desorber load increases significantly with increase in temperature lift.

The optimum solution pump flow rate is the one at which there is the best match in the temperature glides in the desorber and the absorber, provided the effectiveness of the SHX is 100 percent. At lower SHX effectiveness the optimum pump flow rate shifts to a lower value than that determined by best match in temperature glides.

The maximum improvements in cooling COP for the low and the high temperature lifts are 88 and 35 percent, respectively, as compared to the conventional ammonia vapor compression cycle.

## Acknowledgments

Support for this study by the National Science Foundation, the US Department of Energy, the American Society of Heating, Refrigerating and Air-Conditioning Engineers, Inc., and the University of Maryland, Engineering Research Center is gratefully acknowledged.

## References

Ahlby, L., 1987, "Compression/Absorption Cycles for Large Heat Pumps—System Simulation," Licentiate Thesis, Department of Heat and Power Technology, Chalmers University of Technology, Gothenburg, Sweden.

Ahlby, L., and Hodgett, D. L., 1990, "Compression Absorption Heat Pumps," presented at the 3rd International Energy Agency Heat Pump Conference, Tokyo, Japan, Mar. 12–15.

Alefeld, G., 1982, "Rules for the Design of Multistage Absorption and Compression Heat Pump" [in German], *Brenestoff-Warme-Kraft*, Vol. 34, pp. 142–162.

Alefeld, G., 1985, "Multi-stage Apparatus Having Working Fluid and Absorption Cycles, and Methods of Operation Thereof," U.S. Patent No. 4531374.

Altenkirch, E., 1913, "Reversible Absorption Machines," *Zietschrift für die gesamte Kalteindustrie*, Vol. 20, pp. 114–150.

Amrane, K., Radermacher, R., and Herold, K. E., 1989, "Simulation of an Ammonia–Water Vapor Compression Cycle With Solution Circuit," presented at the Int. District Heating and Cooling System Assoc. Annual Meeting, Virginia Beach, VA, June 18–27.

Buschmeier, M., Mulroy, W., and Didion, D., 1990, "An Initial Laboratory Evaluation of a Single Solution Circuit Cycle for Use With Nonazeotropic Refrigerants," Report for ORNL, Contract No. DE-AC05-840R21400, Mar.

Morawetz, E., 1989, "Sorption-Compression Heat Pumps," *International Journal of Energy Research*, Vol. 13, pp. 83–102.

Mucic, V., 1984, "A New Method of COP Increasing of Two Media Resorption-Compression Heat Pumps With Solution Circuit," Targung Zurich, VDI Berichte 539, Dusseldorf, VDI-Verlag, 10–12 Sept.

Radermacher, R., 1986, "Advanced Heat Pumps Cycles Using Zeotropic Refrigerant Mixtures and Solution Circuits," *ASHRAE Transactions*, Vol. 92, Part 2, Paper No. 2977.

Rane, M. V., Radermacher, R., and Herold, K. E., 1989, "Experimental Investigation of a Single Stage Vapor Compression Heat Pump With Solution Circuit," presented at the ASME Winter Annual Meeting, San Francisco, CA.

Stokar, M., 1987, "Compression Heat Pumps With Solution Circuit. Part 2: Sensitivity Analysis of Construction and Control Parameters," *International Journal of Refrigeration*, Vol. 10.

Ziegler, B., and Trepp, C., 1984, "Equation of State for Ammonia-Water Mixtures," *International Journal of Refrigeration*, Vol. 7, pp. 101–107.

**J. W. Murdock**
Associate Professor Emeritus,
Drexel University,
Philadelphia, PA 19104
Life Fellow ASME

**D. R. Keyser**
Senior Project Engineer,
Naval Air Development Center,
Warminster, PA 18974
Mem. ASME

# Theoretical Basis for Extrapolation of Calibration Data of PTC 6 Throat Tap Nozzles[1]

*Equations for the extrapolation of calibration data for ASME/PTC 6 throat tap nozzles are derived from boundary layer theory. The results match published coefficients with a maximum difference of +0.03 percent. It is also shown that the effects of transition in the boundary layer extend to throat Reynolds numbers in excess of 10,000,000, far beyond the capacity of any known calibration laboratory. The present PTC 6 requirement that calibration data must be in the fully turbulent range cannot be met with current facilities.*

## Introduction

This paper was developed because page and space limitations prevented us from including derivations in our original paper [1]. We have included all pertinent information from Hall's paper [2] so that each step may be followed without recourse to any other document.

We have also tried to include all pertinent information on flat plate boundary layer theory, which is the basis for our method of predicting the coefficient of discharge at higher Reynolds number using calibration data at lower Reynolds numbers. Theoretical numerical values needed for calculations were taken from Schlichting [3].

## Flat Plate Boundary Layer Theory

Figure 1 shows fluid approaching a flat plate with a uniform velocity profile of $U$. As the fluid passes over the plate, the velocity at the plate surface is zero and increases to $U$ at some distance from the surface. The region in which the velocity varies from 0 to $U$ is called the boundary layer. The thickness of this layer is $\delta$. For some distance along the plate, the flow within the boundary layer is laminar, with viscous forces predominating. As the inertia forces begin to exceed the viscous, in the transition zone a turbulent layer begins to form and increases as the laminar sublayer decreases.

Figure 2 shows the relation of a throat tap nozzle to Hall's [2] simplified nozzle. This model is a straight piece of pipe whose diameter equals the nozzle diameter, and whose length, $x_d$, is equal to the diameter. It is primarily the difference between the Hall's model and the real nozzle, with throat taps installed, which gave rise to the individual calibration number, $N$, a characteristic for each nozzle [1]. From the continuity equation for an incompressible fluid, the ideal flow rate, $Q_i$, with no boundary layer is given by equation (A12), but the actual flow is less than this. The theoretical coefficient of discharge is essentially an area ratio formed by removing the annulus of the boundary layer from the area available to the flow. There was considerable discussion concerning the use of Hall's simplified model for the throat tap nozzle as compared with the more sophisticated models in the literature. We continue to support the use of this model because it produces the same results without requiring extensive computer modeling. Further, the flow phenomena are physically correct, and it is easier to understand.

1 It provides a rational basis for extrapolation.

2 It agrees with published PTC 6 coefficients in all regions of interest.

3 The present PTC 6 method is impractical and does not take advantage of most of the calibration data.

From Hall's analysis [2] the four flow regions shown in Fig. 3 were presented in our paper [1]. The equations for each region are derived herein.

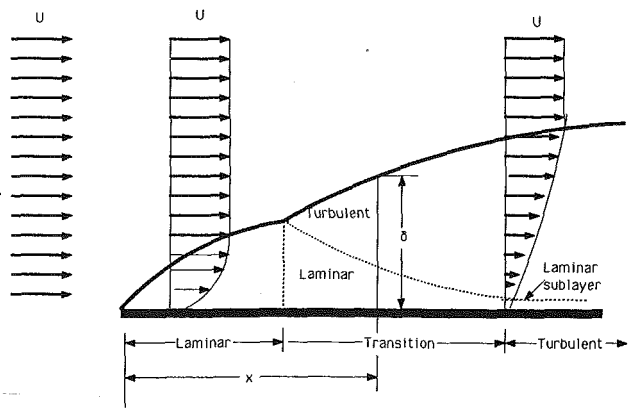


**Fig. 1 Boundary layer along a smooth flat plate**

[1]The opinions expressed in this paper are those of the authors, and do not necessarily reflect those of the Navy Department or the Naval Establishment at large.

Contributed by the Board on Performance Test Codes and presented at the Joint Power Generation Conference, Boston, Massachusetts, October 21-25, 1990. Manuscript received by the Board on Performance Test Codes July 1990. Paper No. 90-JPGC/PTC-1.

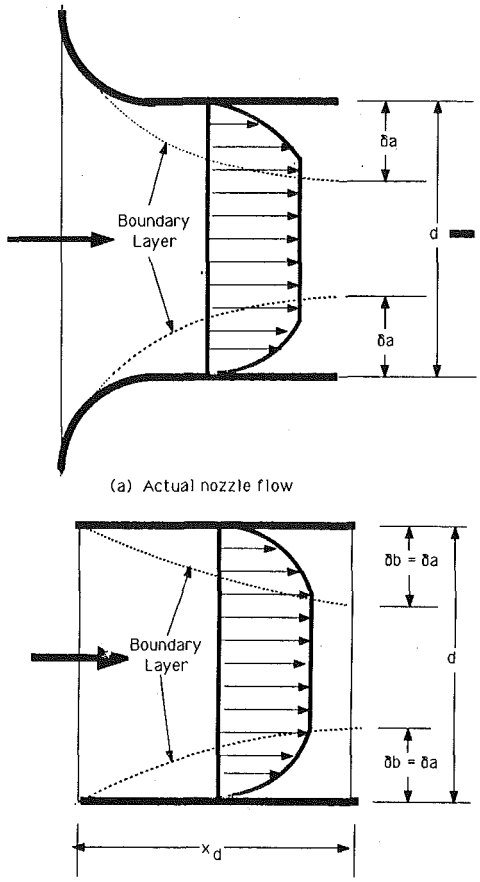


**Fig. 2 Transformation to Hall's simplified flow model**

Region I: Boundary layer wholly laminar ($Re_d < 5 \times 10^5$) (equation (A16))

$$\delta^*_{max} = \delta^*_L$$

Region II: Boundary layer partly laminar and partly turbulent, with laminar displacement thickness greater than turbulent, ($5 \times 10^5 < Re_d < 7 \times 10^5$) (equation (A22))

$$\delta^*_{max} = \delta^*_{Lt}$$

Region III: Boundary layer partly laminar and partly turbulent, with turbulent displacement thickness greater than laminar ($7 \times 10^5 < Re_d < 10^7$) (equation (A32))

$$\delta^*_{max} = \delta^*_{Tt}$$

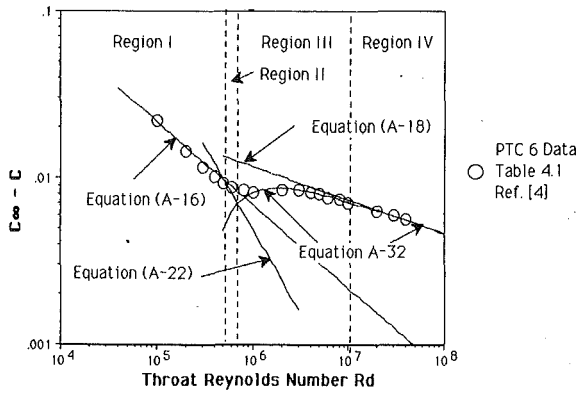


**Fig. 3 Flow regions**

Region IV: Boundary layer wholly turbulent ($Re_d > 10^7$)

$$\delta^*_{max} = \delta^*_T$$

Figure 3 is a Hall-type plot of the flow regions. Superimposed on this plot are the PTC 6 coefficients from Table 4.1 of [4]. Note that equation (A32) converges to equation (A18) at approximately $Re_d = 10^7$. This means that equation (A32) may be used for Region IV as well.

For extrapolation of PTC 6 calibration data, only Regions III and IV are of interest. From Appendix A, equation (A32), the boundary layer coefficient equation is:

$$C_b = C_{Tt} = 1 - \frac{T}{Re_d^{1/5}} \left(1 - \frac{Re_t}{Re_d}\left(1 - \frac{(H_T/H_L)^{5/4}(L/T)^{5/4}}{Re_t^{3/8}}\right)\right)^{4/5} \quad (1)$$

By using all the theoretical equations for $C_b$ for Regions I–IV, the boundary layer in Hall's model nozzle can be computed at the location of the throat tap pressure measurement. When this curve of boundary layer versus Reynolds number is inverted to calculate the theoretical coefficient of discharge, the traditional, familiar, and historical shape of the calibration curve is obtained, shown in Fig. 4. This is a most satisfying result, and it should remove all lingering doubts as to the correctness of our theoretical method. It only remains to customize, or fit, this equation to the individual calibration data for each peculiar nozzle, which is described in our parallel paper [8].

The pressure measured by a static pressure tap differs from the true static pressure, by an amount that depends upon the hole size and shape. Since static pressure measurement is not included in Hall's simplified nozzle, the complete equation requires a correction for this effect. Based on Rayle's analysis for a finite tap diameter [6], Benedict shows this value to be

## Nomenclature

$C$ = coefficient of discharge
$H$ = shape parameter = $\delta^*/\Theta$
$K$ = momentum coefficient
$L$ = laminar slope
Re = Reynolds number
$T$ = turbulent slope
$u$ = local velocity within boundary layer
$U$ = velocity outside the boundary layer
$x$ = distance from leading edge, flat plate
$\beta$ = $d/D$ = ratio of nozzle throat diameter to pipe internal diameter
$\delta^*$ = boundary layer displacement thickness
$\Theta$ = boundary layer momentum thickness
$\nu$ = fluid kinematic viscosity
$\rho$ = fluid density

**Subscripts**

$a$ = actual
avg = average
$b$ = based on boundary layer theory
$d$ = based on throat diameter
$i$ = ideal
$L$ = laminar
$m$ = measured
max = maximum
$o$ = beginning of turbulent boundary layer
$t$ = transition
$T$ = turbulent
$x$ = flat plate
$\infty$ = at $Re_d = \infty$
6 = for a PTC 6 throat tap nozzle

**Table 1 Values from Schlichting [3]**

| | | |
|---|---|---|
| $L$ | Laminar slope | 6.88 |
| $T$ | Turbulent slope | 0.185 |
| $H_L$ | Laminar shape parameter | 2.59 |
| $H_T$ | Turbulent shape parameter | 1.28 |
| $\mathrm{Re}_t$ | Transition Reynolds number | $5\times10^5$ |

**Table 2 Difference between published and calculated coefficients of discharge**

| Throat Reynolds Number $\mathrm{Re}_d$ | Discharge coefficients: PTC 6 1976 $C_6$ | Equation (2) $C_{(2)}$ | Difference $\Delta C$ |
|---|---|---|---|
| 1,000,000 | 0.9972 | 0.9972 | 0.0000 |
| 2,000,000 | 0.9970 | 0.9967 | 0.0003 |
| 3,000,000 | 0.9970 | 0.9969 | 0.0001 |
| 4,000,000 | 0.9972 | 0.9972 | 0.0000 |
| 5,000,000 | 0.9974 | 0.9974 | 0.0000 |
| 6,000,000 | 0.9978 | 0.9976 | 0.0002 |
| 8,000,000 | 0.9980 | 0.9980 | 0.0000 |
| 10,000,000 | 0.9983 | 0.9982 | 0.0001 |
| 20,000,000 | 0.9991 | 0.9991 | 0.0000 |
| 30,000,000 | 0.9994 | 0.9995 | −0.0001 |
| 40,000,000 | 0.9998 | 0.9999 | −0.0001 |

+0.0054 for a plenum inlet to the nozzle and +0.0056 for a beta ratio of 0.43 [7]. It is noted that Benedict, during an extended debate of this topic within the PTC 19.5 flow measurement committee, contended that this value was not a constant over the full range of flow. However, it was the collective judgment that the "tap correction" most likely is a constant coefficient of the dynamic pressure, similar to the drag coefficient data of a small hole in the skin of an aircraft. The answer to the question of whether or not this value is constant over regions III and IV cannot be known until data are obtained well beyond our present-day laboratory capacities.

In any case, the question of the absolute value of the "tap correction" becomes moot, since the individual nozzle calibration includes these effects as well as any small effects of beta ratio. Consequently we decided to use the plenum inlet correction in keeping with the philosophy of our simplified nozzle—making the theory no more complicated than necessary to match the data. As a result, we chose the plenum inlet value of 1.0054 for the theoretical coefficient of discharge (as the Reynolds number approaches infinity).

$$C = C_\infty - \frac{T}{\mathrm{Re}_d^{1/5}}\left(1-\frac{\mathrm{Re}_t}{\mathrm{Re}_d}\left(1-\frac{(H_T/H)_L^{5/4}(L/T)^{5/4}}{\mathrm{Re}_t^{3/8}}\right)\right)^{4/5} = 1.0054$$

$$-\frac{0.185}{\mathrm{Re}_d^{1/5}}\left(1-\frac{5\times10^5}{\mathrm{Re}_d}\left(1-\frac{(1.28/2.59)^{5/4}(6.88/0.185)^{5/4}}{(5\times10^5)^{3/8}}\right)\right)^{4/5} =$$

$$C = 1.0054 - \frac{0.185}{\mathrm{Re}_d^{1/5}}\left[1-\frac{361{,}239}{\mathrm{Re}_d}\right]^{4/5} \qquad (2)$$

Table 2 shows that the maximum difference between the present PTC 6 coefficient and that calculated using equation (2) is 0.03 percent at a throat Reynolds number of 2,000,000.

## Summary

Equation (2), finally developed in this paper, was derived from textbook boundary layer theory and well-developed static tap analysis. The combination of the two is an equation that predicts the published PTC 6 data within +0.0003 and −0.0001—a maximum of 3 parts in 10,000. This theory is valid throughout the range of usual nozzle calibrations and beyond without limit. It is therefore justified to use this equation for the extrapolation of nozzle calibration data from the laboratory to the test measurement installation. The following paper [8] describes the application, method, and extrapolation of calibration data to higher Reynolds numbers for individual nozzles.

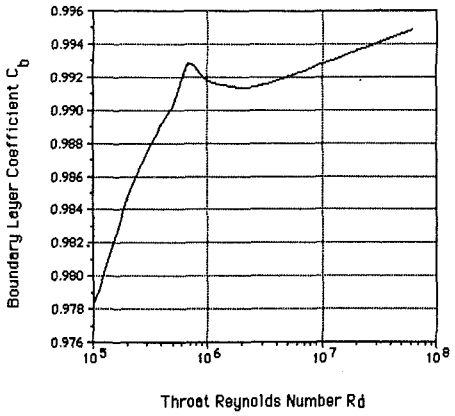


**Fig. 4 Theoretical form for the coefficient of discharge of an ASME/PTC 6 throat tap nozzle**

## References


1 Murdock, J. W., and Keyser, D. R., "A Method of Extrapolating Calibration Data for Flow Nozzles," presented at the Joint ASME/IEEE Power Generation Conference, Milwaukee, WI, Oct. 20–24, 1985; ASME Paper No. 85-JPGC-PTC-2.

2 Hall, G. W., "Application of Boundary Layer Theory to Explain Some Nozzle and Venturi Peculiarities," *Trans. IME, London*, Vol. 173, No. 36, 1959, pp. 837–870.

3 Schlichting, H., *Boundary Layer Theory* (English translation by J. Kestin), McGraw-Hill, 7th ed., 1979.

4 ASME/ANSI Performance Test Code for Stream Turbines—PTC 6 1976 (reaffirmed 1982).

5 Cotton, K. C., and Westcott, J. C., "Throat Tap Nozzles Used for Accurate Flow Measurements," ASME JOURNAL OF ENGINEERING FOR POWER, Vol. 82, Oct. 1960, pp. 247–263.

6 Rayle, R. E., "Influence of Orifice Geometry on Static Pressure Measurements," presented at the ASME Annual Meeting, Atlantic City, NJ, Nov. 22–Dec. 4, 1959; ASME Paper No. 59-A-234.

7 Benedict, R. P., "The Plenum Inlet Discharge Coefficient of an ASME Nozzle," ISA Flow Symposium, Saint Louis, MO, 1981, Paper No. C1.81-533.

8 Murdock, J. W., and Keyser, D. R., "A Method for the Extrapolation of Calibration Data of PTC 6 Throat Tap Nozzles," presented at the Joint ASME/IEEE Power Generation Conference, Boston, MA, Oct. 22–24, 1990; ASME Paper No. 90-JPGC/PTC-2, ASME JOURNAL OF ENGINEERING FOR GAS TURBINES AND POWER, Vol. 113, 1991, this issue.


## APPENDIX A

### Derivation of Equations

**Boundary Layer Thickness.** The boundary layer thickness is defined as that point where the local velocity $u$ is equal to the undisturbed velocity $U$. Figure 1 shows the boundary layer thickness $\delta$ at distance $x$ from the leading edge of the plate. Because of the difficulty in determining the exact point where $u = U$, this thickness is defined as that distance where $u = 0.99\,U$. With this definition, the following equations are obtained from Schlichting [3] and referenced.

For laminar layer flow:

$$\delta_L \approx 5\sqrt{\frac{x\nu}{U}} \approx \frac{5x}{\sqrt{\frac{xU}{\nu}}} \approx \frac{5x}{\mathrm{Re}_x^{1/2}} \qquad \text{(A1)}$$

[3, 7.35]

For turbulent layer flow:

$$\delta_T = 0.37x\left(\frac{xU}{n}\right)^{-1/5} = \frac{0.37x}{\mathrm{Re}_x^{1/5}} \qquad \text{(A2)}$$

[3, 21.8]

**Displacement Boundary Layer Thickness.** The boundary layer displacement thickness $\delta^*$ is defined as that thickness the layer would have if the flow in the layer were at the external velocity $U$. The displacement thickness is defined by equation (A-3) and illustrated by Fig. A1.

$$U\delta^* = \int_0^\delta (U-u)\,dy \text{ or } \delta^* = \int_0^\delta \left(1-\frac{u}{U}\right) dy \qquad \text{(A3)}$$

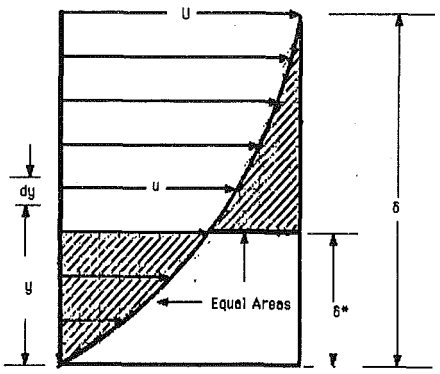


Fig. A1 Boundary layer displacement thickness

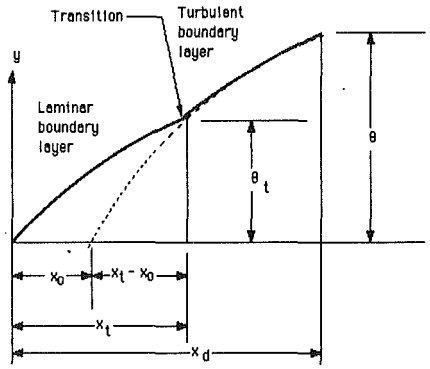


Fig. A2 Momentum boundary layer in transition

With this definition of displacement thickness, the following equations are obtained:

For laminar layer flow:

$$\delta_L^* = 1.7208\sqrt{\frac{\nu x}{U}} = \frac{1.7208x}{\sqrt{\frac{xU}{\nu}}} = \frac{1.7208x}{\mathrm{Re}_x^{1/2}} \qquad \text{(A4)}$$

[3, 7.37]

For turbulent layer flow:

$\delta_T^* = \frac{\delta_T}{8}$ from equation (A2)

$$\delta_T^* = \frac{\delta_T}{8} = \frac{0.37x}{8\mathrm{Re}_x^{1/5}} = \frac{0.04625x}{\mathrm{Re}_x^{1/5}} \qquad \text{(A5)}$$

[3, 21.6]

**Momentum Boundary Layer Thickness.** The loss of momentum in the boundary layer compared to the undisturbed flow gives rise to the momentum thickness, Θ, defined by equation (A6):

$$\theta = \int_0^\delta \frac{u}{U}\left(1 - \frac{u}{U}\right) dy \qquad \text{(A6)}$$

[3, 7.38]

For laminar layer flow:

$$\theta_L = 0.664\sqrt{\frac{\nu x}{U}} = \frac{0.664x}{\sqrt{\frac{Ux}{\nu}}} = \frac{0.664x}{\mathrm{Re}_x^{1/2}} \qquad \text{(A7)}$$

[3, 7.39]

For turbulent layer flow:

$$\theta_T = 0.036x\left(\frac{xU}{\nu}\right)^{-1/5} = \frac{0.036x}{\mathrm{Re}_x^{1/5}} \qquad \text{(A8)}$$

[3, 21.9]

**Shape Parameters.** The shape parameter, $H$, is a ratio of the displacement thickness $\delta^*$ to the momentum thickness, Θ:

$$H = \frac{\delta^*}{\theta} \qquad \text{(A9)}$$

For laminar layer flow:

$$H_L = \frac{\delta_L^*}{\theta_L} = \frac{1.7208x/\mathrm{Re}_x^{1/2}}{0.664x/\mathrm{Re}_x^{1/2}} \approx 2.59 \qquad \text{(A10)}$$

For turbulent layer flow:

$$H_T = \frac{\delta_T^*}{\theta_T} = \frac{0.04625x/\mathrm{Re}_x^{1/5}}{0.036x/\mathrm{Re}_x^{1/5}} \approx 1.28 \qquad \text{(A11)}$$

## Hall's Simplified Nozzle

Figure 2 shows the relation of a nozzle without throat taps to Hall's [2] simplified nozzle. This model is a straight piece of pipe whose diameter is the nozzle diameter and whose length is equal to the diameter. From the continuity equation for an incompressible fluid, the ideal flow with no boundary layer would be

$$Q_i = UA_i = U\frac{\pi d^2}{4} \qquad \text{(A12)}$$

but the actual flow, $Q_a$, is

$$Q_a = UA_a = U\frac{\pi(d - 2\delta_{\max}^*)^2}{4} = U\frac{\pi(d^2 - 4d\delta_{\max}^* + 4\delta_{\max}^{*2})}{4}$$

$$\approx U\frac{\pi(d^2 - 4d\delta_{\max}^*)}{4} \quad (\delta_{\max}^* \text{ small compared with } d) \qquad \text{(A13)}$$

$\delta_{\max}^*$ is the boundary layer affecting the downstream pressure measurement.

The theoretical coefficient of discharge is essentially an area ratio formed by removing the annulus of the boundary layer from the area available to the flow

$$C_b = \frac{Q_a}{Q_i} = \frac{U\pi(d^2 - 4d\delta_{\max}^*)/4}{U\pi d^2/4} = 1 - \frac{4\delta_{\max}^*}{d} \qquad \text{(A14)}$$

*Region I—Boundary Layer Wholly Laminar* ($\delta_{\max}^* = \delta^* L$). In this region the maximum displacement thickness is obtained from equation (A4) with the distance $x$ equal to the diameter, or:

$$\delta_{L\max}^* = \frac{1.7208x}{\mathrm{Re}_x^{1/2}} = \frac{1.7208d}{\mathrm{Re}_d^{1/2}} \qquad \text{(A15)}$$

Substituting equation (A15) into equation (A14) yields

$$C_b = C_L = 1 - \frac{4\delta_{\max}^*}{d} = 1 - \left(\frac{4}{d}\right)\left(\frac{1.7208d}{\mathrm{Re}_d^{1/2}}\right)$$

$$= 1 - \frac{6.88}{\mathrm{Re}_d^{1/2}} = 1 - \frac{L}{\mathrm{Re}_d^{1/2}} \qquad \text{(A16)}$$

where $L$ = the laminar slope.

Before we can derive the equations for Regions II and III, we must derive the equation for the fully turbulent boundary layer.

*Region IV—Boundary Layer Wholly Turbulent* ($\delta_{\max}^* = \delta_T^*$). In this region the maximum displacement thickness is obtained from equation (A5) with the distance $x$ equal to the diameter, or

$$\delta_{T\max}^* = \frac{0.04625x}{\mathrm{Re}_x^{1/5}} = \frac{0.04625d}{\mathrm{Re}_d^{1/5}} \qquad \text{(A17)}$$

Substituting equation (A17) into equation (A14)

$$C_b = C_L = 1 - \frac{4\delta^*_{\max}}{d} = 1 - \left(\frac{4}{d}\right)\left(\frac{0.04625d}{\mathrm{Re}_d^{1/5}}\right)$$
$$= 1 - \frac{0.185}{\mathrm{Re}_d^{1/5}} = 1 - \frac{T}{\mathrm{Re}_d^{1/5}} \quad \text{(A18)}$$

where $T$ = the turbulent slope.

*Region II—Boundary Layer Partly Laminar and Partly Turbulent, With the Laminar Displacement Thickness Greater Than the Turbulent.* This is a very narrow region, which could be ignored, except that it provides the physics of the beginning of the "transition hump" often discussed in the literature in connection with PTC-6 nozzle calibrations. Previously it had been assumed that once the data were "over the hump" the flow was in the fully developed turbulent region from which the $C_d$ could be extrapolated to Reynolds numbers beyond those obtained from the flow calibration laboratory. The maximum laminar displacement thickness will occur at the end of Region I, the transition point $x_t$. From equation (A4)

$$\delta^*_{L\max} = \frac{1.7208x_t}{\mathrm{Re}_t^{1/2}} \quad \text{(A19)}$$

Substituting equation (A19) into equation (A14)

$$C_b = C_{Lt} = 1 - \frac{4\delta^*_{\max}}{d} = 1 - \left(\frac{4}{d}\right)\left(\frac{1.7208x_t}{\mathrm{Re}_t^{1/2}}\right) = 1 - \frac{6.88x_t}{\mathrm{Re}_t^{1/2}} \quad \text{(A20)}$$

Noting that

$$\frac{x_t}{d} = \frac{\mathrm{Re}_t}{\mathrm{Re}_d} \text{ or } x_t = \frac{d\mathrm{Re}_t}{\mathrm{Re}_d} \quad \text{(A21)}$$

Substituting equation (A21) into equation (A20)

$$C_b = C_{Lt} = 1 - \frac{6.88x_t}{d\mathrm{Re}_t^{1/2}} = 1 - \frac{6.88(d\mathrm{Re}_t/\mathrm{Re}_d)}{d\mathrm{Re}_t^{1/2}} =$$
$$1 - \frac{6.88\mathrm{Re}_t^{1/2}}{\mathrm{Re}_d} = 1 - \frac{L\mathrm{Re}_t^{1/2}}{\mathrm{Re}_d} \quad \text{(A22)}$$

*Region III—Boundary Layer Partly Laminar and Partly Turbulent, With the Turbulent Displacement Thickness Greater Than the Laminar.* At the beginning point of Region III, the momentum boundary layer thickness, $\theta_t$, must be the same for both laminar and turbulent layers. The distance $x_0$ in Fig. A2 is the distance from the leading edge that a hypothetical fully turbulent boundary layer would begin in order to equal the momentum boundary layer thickness of $\theta_t$ at the transition point distance, $x_t$.

For laminar flow, from equation (A7)

$$\theta_L = \theta_t = \frac{0.664x_t}{\mathrm{Re}_t^{1/2}} = \frac{K_L x_t}{\mathrm{Re}_t^{1/2}} \quad \text{(A23)}$$

where $K_L$ is the laminar momentum coefficient

For turbulent flow, from equation (A8)

$$\theta_T = \theta_t = \frac{0.036(x_t - x_0)}{\left(\frac{(x_t - x_0)U}{\nu}\right)^{1/5}} = \frac{K_T x_t^{1/5}(x_t - x_0)^{4/5}}{\left(\frac{x_t U}{\nu}\right)^{1/5}} = \frac{K_T x_t^{1/5}(x_t - x_0)^{4/5}}{\mathrm{Re}_t^{1/5}} \quad \text{(A24)}$$

where $K_T$ is the turbulent momentum coefficient.

Equating (A23) and (A24)

$$\theta_t = \frac{K_T x_t^{1/5}(x_t - x_0)^{4/5}}{\mathrm{Re}_t^{1/5}} = \frac{K_L x_t}{\mathrm{Re}_t^{1/2}}$$
$$(x_t - x_0)^{4/5} = \left(\frac{K_L}{K_T}\right)\left(\frac{x_t}{x_t^{1/5}}\right)\left(\frac{\mathrm{Re}_t^{1/5}}{\mathrm{Re}_t^{1/2}}\right) = \frac{x_t^{4/5}}{\mathrm{Re}_t^{3/10}}\left(\frac{K_L}{K_T}\right)$$
$$x_t - x_0 = \frac{x_t}{\mathrm{Re}_t^{3/8}}\left(\frac{K_L}{K_T}\right)^{5/4} \quad \text{(A25)}$$

Solving equation (A25) for $x_0$

$$x_0 = x_t - \frac{x_t}{\mathrm{Re}_t^{3/8}}\left(\frac{K_L}{K_T}\right)^{5/4} = x_t\left(1 - \frac{(K_L/K_T)^{5/4}}{\mathrm{Re}_t^{3/8}}\right)$$

Note that $\frac{x_t}{x_d} = \frac{\mathrm{Re}_t}{\mathrm{Re}_d}$ so that

$$x_0 = \frac{x_d\mathrm{Re}_t}{\mathrm{Re}_d}\left(1 - \frac{(K_L/K_T)^{5/4}}{\mathrm{Re}_t^{3/8}}\right) \quad \text{(A26)}$$

Solving equation (A26) for $x_d - x_0$ (the distance from the origin of the hypothetical turbulent boundary layer)

$$x_d - x_0 = x_d - x_d\left(\frac{\mathrm{Re}_t}{\mathrm{Re}_d}\right)\left(1 - \frac{(K_L/K_T)^{5/4}}{\mathrm{Re}_t^{3/8}}\right)$$
$$= x_d\left(1 - \frac{\mathrm{Re}_t}{\mathrm{Re}_d}\left(1 - \frac{(K_L/K_T)^{5/4}}{\mathrm{Re}_t^{3/8}}\right)\right) \quad \text{(A27)}$$

The maximum turbulent displacement from equation (A5)

$$\delta^*_{\max} = \delta^*_{Tt} = \frac{0.04625(x_d - x_0)}{\left(\frac{(x_d - x_0)U}{\nu}\right)^{1/5}} = \frac{0.04625x_d^{1/5}(x_d - x_0)^{4/5}}{\mathrm{Re}_d^{1/5}} \quad \text{(A28)}$$

Substituting equation (A28) into equation (A14) and noting that for Hall's model nozzle, $x_d = d$:

$$C_b = C_{Tt} = 1 - \frac{4\delta^*_{\max}}{x_d} = \left(\frac{4}{x_d}\right)\left(\frac{0.04625x_d^{1/5}(x_d - x_0)^{4/5}}{\mathrm{Re}_d^{1/5}}\right)$$
$$= 1 - \frac{0.185}{\mathrm{Re}_d^{1/5}}\left(\frac{x_d - x_0}{x_d}\right)^{4/5} = 1 - \frac{T}{\mathrm{Re}_d^{1/5}}\left(\frac{x_d - x_0}{x_d}\right)^{4/5} \quad \text{(A29)}$$

Substituting equation (A27) into equation (A29)

$$C_b = C_{Tt} = 1 - \frac{T}{\mathrm{Re}_d^{1/5}}\left(\frac{x_d\left(1 - \frac{\mathrm{Re}_t}{\mathrm{Re}_d}\left(1 - \frac{(K_L/K_T)^{5/4}}{\mathrm{Re}_t^{3/8}}\right)\right)}{x_d}\right)^{4/5}$$
$$= 1 - \frac{T}{\mathrm{Re}_d^{1/5}}\left(1 - \frac{\mathrm{Re}_t}{\mathrm{Re}_d}\left(1 - \frac{(K_L/K_T)^{5/4}}{\mathrm{Re}_t^{3/8}}\right)\right)^{4/5} \quad \text{(A30)}$$

By definition

$$\frac{K_L}{K_T} = \frac{\theta_L}{\theta_T} = \frac{\delta^*_L/H_L}{\delta^*_T/H_T} = \frac{H_T}{H_L}\frac{L}{T} \quad \text{(A31)}$$

Substituting equation (A31) into equation (A30) gives (finally) the correct theoretical equation for the coefficient of discharge for a throat tap nozzle throughout both Regions III and IV.

$$C_b = C_{Tt} = 1 - \frac{T}{\mathrm{Re}_d^{1/5}}\left(1 - \frac{\mathrm{Re}_t}{\mathrm{Re}_d}\left(1 - \frac{(H_T/H_L)^{5/4}(L/T)^{5/4}}{\mathrm{Re}_t^{3/8}}\right)\right)^{4/5} \quad \text{(A32)}$$

This equation can be fitted easily to individual calibration data to account for minor differences in installation or manufacture.

## Coefficient of Discharge at $\mathrm{Re}_d = \infty$

The coefficient of discharge at Reynolds number of infinity is defined by equation (A33) as follows:

$$C_\infty = 1 + \text{ "Tap Correction"} \quad \text{(A33)}$$

and consequently the equation of the actual coefficient of discharge of an ASME/PTC 6 throat tap nozzle is simply equation (A32) plus the throat tap correction. This equation is valid throughout regions III and IV. The average value for this correction is +0.0054; however [4] permits a variation of ±0.0025 about this value.

**J. W. Murdock**
Associate Professor Emeritus,
Drexel University,
Philadelphia, PA 19104
Life Fellow ASME

**D. R. Keyser**
Senior Project Engineer,
Naval Air Development Center,
Warminster, PA 18974
Mem. ASME

# A Method for the Extrapolation of Calibration Data of PTC 6 Throat Tap Nozzles[1]

*This paper describes a precise method for extrapolating the coefficient of discharge of PTC 6 throat tap nozzles using all or most of the calibration data. The theoretical basis for this method is described in a parallel paper [3]. Numerical examples are given using actual calibration data to describe this method. Because this method permits the use of all calibration data at or above Reynolds numbers of 1,000,000, it is a clear improvement over the PTC 6-1976 method, which permits only the highest single point.*

## Introduction

Our general paper on this subject [1] was never published, so we were unable to respond in writing to the issues raised in the discussion that followed our presentation. The use of Hall's adaptation of flat plate boundary layer theory to a flow nozzle [2] generated most of the discussion that followed our presentation. We continue to support this analysis because:

1 It provides a rational basis for extrapolation.

2 It agrees with published PTC 6 coefficients in all regions of interest (see Fig. 1).

3 The present PTC 6 method is impractical and does not take advantage of most of the calibration data, and if strictly followed could not be used because of limitations of calibration facility capacities.

4 Any engineer can use this method. All the work can be performed on a simple hand-held calculator.

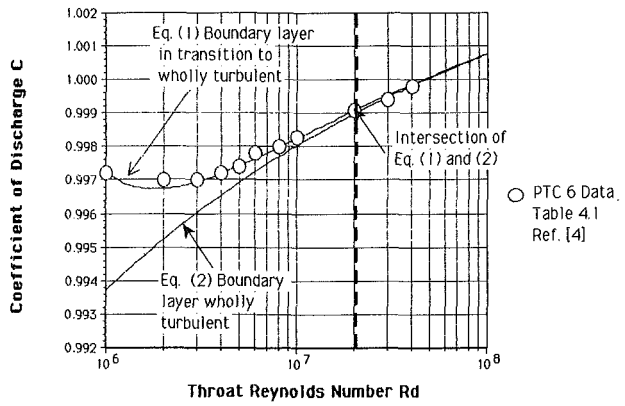


**Fig. 1 Discharge coefficients versus Reynolds number**

## PTC-6 Extrapolation Method

The present PTC 6 method for extrapolation is described in Par. 4.33 of PTC 6 [4]. This method permits extrapolation provided the calibration facility is capable of producing data in the *wholly turbulent boundary layer region*. Our study indicates that this is not possible since the boundary layer remains in transition to Reynolds numbers up to 20 million, well beyond the capability of any known calibration laboratory (see Fig. 1).

## Extrapolation Equation

In a parallel paper [3] we derived an equation based on boundary layer theory and a tap correction that matched the published PTC 6 data [4] within $+0.0003$ and $-0.0001$—a maximum of 3 parts in 10,000. This equation presented herein as equation (1) represents PTC 6 coefficients for a Reynolds number range of 1,000,000 to 40,000,000.

$$C_6 = 1.0054 - \frac{0.185}{\mathrm{Re}_d^{1/5}}\left[1 - \frac{361{,}239}{\mathrm{Re}_d}\right]^{4/5} \quad (1)$$

For a fully developed turbulent boundary layer our analysis indicated the following equation:

$$C_6 = 1.0054 - \frac{0.185}{\mathrm{Re}_d^{1/5}} \quad (\mathrm{Re}_d > 20 \times 10^6) \quad (2)$$

Figure 1 is a plot of equation (1) and equation (2) with the published PTC 6 points [4]. Examination of this curve indicates the following.

1 A fully developed turbulent boundary layer requires a minimum throat Reynolds number of 20,000,000.

2 Equation (1) is valid over the entire range of Reynolds numbers equal to or greater than 1,000,000.

3 Extrapolation of calibration data by an equation in the form of equation (2) will produce inaccurate results for all data below Reynolds number of 20,000,000.

4 The statement in Par. 4.33 of PTC 6 [4] quoted verbatim

[1]The opinions expressed in this paper are those of the Authors, and do not necessarily reflect those of the Navy Department nor the Naval Establishment at large.

Contributed by the Board on Performance Test Codes and presented at the Joint Power Generation Conference, Boston, Massachusetts, October 21-25, 1990. Manuscript received by the Board on Performance Test Codes July 1990. Paper No. 90-JPGC/PTC-2.

below is not correct. The italicized portions of the quoted text are those we found to be in error.

**"4.33—Transition Region.** At throat Reynolds numbers below *800,000* the nozzle boundary layer is laminar, at high throat Reynold numbers it is turbulent. In between these regions is a zone called the transition region. This transition region *should be established during calibration and avoided during the test.* Flow coefficients for the nozzles described in this Code have been found to be influenced by the transition at throat Reynolds numbers from 2.0 million to 3.5 million. It is *permissible to extrapolate the calibration curve when the nozzle is used beyond the range of the calibrating facility provided the level of the coefficient is established at Reynolds numbers higher than the transition region. This extrapolation should be parallel to the curve in Fig. 4.4* and subject to the restrictions of Par. 4.22(d)."

## Modified Murdock/Keyser Extrapolation Method

For extrapolating calibration data we recommend that a modified calibration number $\Delta N$ be used, where $\Delta N$ is defined by

$$\Delta N = (C_m - C_6) \times 10^4 \tag{3}$$

where $C_m$ is the coefficient obtained from a calibration (measured) and $C_6$ is calculated from equation (1). The extrapolating equation then becomes

$$C_m = 1.0054 - \frac{0.185}{\mathrm{Re}_d^{1/5}}\left[1 - \frac{361{,}239}{\mathrm{Re}_d}\right]^{4/5} + \frac{\Delta N_{\mathrm{avg}}}{10^4} \tag{4}$$

The $\Delta N$ must be within $+25$ and $-25$ in order to conform with the PTC 6 limit of $\pm 0.25$ percent.

To implement this procedure we recommend the following three-step method:

*Step A*—Compute values of $\Delta N$ using equation (3) for all calibration points of each tap set equal to or greater than a throat Reynolds number of one million.

*Step B*—Plot $\Delta N$ versus $\mathrm{Re}_d$ and examine plot to see whether this tap set meets the criterion of being within $\pm 25$.

*Step C*—Extrapolate $C_m$ values as needed using equation (4).

These steps are illustrated by three numerical examples in Appendix A.

## Summary

In this paper we have developed and described a precise method for extrapolating the coefficient of discharge of PTC 6 throat tap nozzles. The theoretical basis for this method is described in [3], where all equations are derived. Numerical examples using actual calibration data are used to illustrate this method. Example 3 shows that the "tap correction" is a constant up to throat Reynolds numbers of 8,500,000 and reinforces our contention that it is a constant over the entire range. It is shown that our proposed method of extrapolation is superior to the present PTC 6, which cannot be implemented. Nozzles cannot now be calibrated to throat Reynolds numbers of at least 20,000,000 to be in the fully developed turbulent range.

## References


1 Murdock, J. W., and Keyser, D. R., "A Method of Extrapolating Calibration Data for Flow Nozzles," presented at the Joint ASME/IEEE Power Generation Conference, Milwaukee, WI, Oct. 20–24, 1985; ASME Paper No. 85-JPGC-PTC-2.

2 Hall, G. W., "Application of Boundary Layer Theory to Explain Some Nozzle and Venturi Peculiarities," *Trans. IME, London*, Vol. 173, No. 36, 1959, pp. 837–870.

3 Murdock, J. W., and Keyser, D. R., "Theoretical Basis for Extrapolation of Calibration Data of PTC 6 Throat Tap Nozzles," presented at the Joint ASME/IEEE Power Generation Conference, Boston, MA, Oct. 22–24, 1990; ASME Paper No. 90-JPGC/PTC-1; ASME JOURNAL OF ENGINEERING FOR GAS TURBINES AND POWER, Vol. 113, 1991, this issue.

4 ASME/ANSI Performance Test Code for Steam Turbines—PTC 6 1976 (reaffirmed 1982).

5 Committee Correspondence—C. B. Scharp to J. W. Murdock May 4, 1984. Calibration Data for 8" Baltimore Gas & Electric Nozzle and for two 14 in. Westinghouse nozzles #35212 and 35214, all calibrated at Alden Research Laboratories.

6 American Electric Power—J. Friedman to D. Keyser, April 25, 1984, Calibration data on two throat tap nozzles #16-02558 and #16-02559. Throat diameter 7.500 in., $\beta = 0.500$. All calibrations performed at the same unspecified laboratory.

7 Power Technologies Inc.—J. C. Westcott to J. W. Murdock, February 26, 1990. Calibration data on one throat tap nozzle. Throat diameter 11.3171 in., pipe diameter 22.62, $\beta = 0.5003$, Calibrated at Alden Research Laboratories Sept. 7 and 8, 1989.


# APPENDIX A

## Numerical Examples

### Example One—Selection of Tap Sets From Calibration Data

The data used in this example are taken from [5] at throat Reynolds numbers equal to or greater than one million. The nozzle is 8 in. in diameter and was calibrated at Alden Research Laboratories 1 Aug. 1977. Four tap sets were calibrated, Tap Sets A and C being calibrated together, as were Tap Sets B and D. According to Par. 4.31 [4]

"Compliance with the above requirements is determined by the shape of the coefficient of discharge versus Reynolds number curve (see Fig. 4.4 and Table 4.1) which should be established by each set of taps. It is recommended that all four sets be calibrated and that the two sets, located 180 degrees apart, that comply most closely with Par. 4.22(d) be used for test."

#### Tap Set A

*Step A.* Calculated and calibrated values for this tap set are shown below. Average $\Delta N = -16$, $\sigma = 5$.

| Run | $\mathrm{Re}_d$ | $C_m$ | $C_6$ | $\Delta N$ |
|---|---|---|---|---|
| 5A | 1,118,000 | 0.9960 | 0.9970 | −10 |
| 8A | 1,347,000 | 0.9951 | 0.9968 | −17 |
| 4A | 1,523,000 | 0.9952 | 0.9968 | −16 |
| 9A | 1,714,000 | 0.9948 | 0.9967 | −19 |
| 3A | 1,892,000 | 0.9947 | 0.9967 | −20 |
| 10A | 2,134,000 | 0.9955 | 0.9968 | −13 |
| 2A | 2,312,000 | 0.9950 | 0.9968 | −18 |
| 11A | 2,601,000 | 0.9946 | 0.9968 | −22 |
| 1A | 2,825,000 | 0.9962 | 0.9969 | −7 |

*Step B.* Figure A1 is a plot of $\Delta N$ versus $\mathrm{Re}_d$ for Tap Set A. Examination of this graph indicates that all points are within both two standard deviations and the PTC 6 limit.

## Nomenclature

$C$ = coefficient of discharge
$n$ = number of data points
$\Delta N$ = modified calibration number $= 10^4(C_m - C_6)_{\mathrm{avg}}$
Re = Reynolds number
$\beta$ = ratio of nozzle throat diameter to pipe internal diameter

**Subscripts**

avg = average
$b$ = based on boundary layer theory
$d$ = based on throat diameter
$e$ = extrapolated
$m$ = measured
max = maximum
6 = PTC 6

*Step C.* Figure A2 shows the extrapolation of Tap Set A data. For a $\Delta N$ of $-16$, the equation for extrapolation becomes

$$C_m = 1.0054 - \frac{0.185}{\mathrm{Re}_d^{1/5}}\left[1 - \frac{361{,}239}{\mathrm{Re}_d}\right]^{4/5} + \frac{-16}{10^4}$$

$$= 1.0038 - \frac{0.185}{\mathrm{Re}_d^{1/5}}\left[1 - \frac{361{,}239}{\mathrm{Re}_d}\right]^{4/5} \quad \text{(A1)}$$

**Tap Set B**

*Step A.* Calculated and calibrated values for this tap set are shown below. Average $\Delta N = -15$, $\sigma = 5$.

| Run | $\mathrm{Re}_d$ | $C_m$ | $C_6$ | $\Delta N$ |
|---|---|---|---|---|
| 5B | 1,107,000 | 0.9963 | 0.9971 | −8 |
| 6B | 1,251,000 | 0.9958 | 0.9969 | −11 |
| 4B | 1,488,000 | 0.9955 | 0.9968 | −13 |
| 7B | 1,713,000 | 0.9951 | 0.9967 | −16 |
| 3B | 1,897,000 | 0.9949 | 0.9967 | −18 |
| 8B | 2,132,000 | 0.9945 | 0.9968 | −23 |
| 1B | 2,136,000 | 0.9958 | 0.9968 | −10 |
| 2B | 2,351,000 | 0.9948 | 0.9968 | −20 |
| 9B | 2,632,000 | 0.9948 | 0.9969 | −21 |

*Step B.* Figure A3 is a plot of $\Delta N$ versus $\mathrm{Re}_d$ for Tap Set B. Examination of this graph indicates that all points are within both two standard deviations and the PTC 6 limit. However, there seems to be a trend for decreasing $\Delta N$ with increasing $\mathrm{Re}_d$.

*Step C.* Figure A4 shows the extrapolation of Tap Set B data. For a $\Delta N$ of $-15$, the equation for extrapolation becomes

$$C_m = 1.0054 - \frac{0.185}{\mathrm{Re}_d^{1/5}}\left[1 - \frac{361{,}239}{\mathrm{Re}_d}\right]^{4/5} + \frac{-15}{10^4}$$

$$= 1.0039 - \frac{0.185}{\mathrm{Re}_d^{1/5}}\left[1 - \frac{361{,}239}{\mathrm{Re}_d}\right]^{4/5} \quad \text{(A2)}$$

**Tap Set C**

*Step A.* Calculated and calibrated values for this tap set are shown below. Average $\Delta N = -11$, $\sigma = 6$.

| Run | $\mathrm{Re}_d$ | $C_m$ | $C_6$ | $\Delta N$ |
|---|---|---|---|---|
| 5C | 1,118,000 | 0.9967 | 0.9970 | −3 |
| 8C | 1,347,000 | 0.9964 | 0.9968 | −4 |
| 4C | 1,523,000 | 0.9954 | 0.9968 | −14 |
| 9C | 1,714,000 | 0.9957 | 0.9967 | −10 |
| 3C | 1,892,000 | 0.9947 | 0.9967 | −20 |
| 10C | 2,134,000 | 0.9960 | 0.9968 | −8 |
| 2C | 2,312,000 | 0.9954 | 0.9968 | −14 |
| 11C | 2,601,000 | 0.9948 | 0.9968 | −20 |
| 1C | 2,825,000 | 0.9960 | 0.9969 | −9 |

*Step B.* Figure A5 is a plot of $\Delta N$ versus $\mathrm{Re}_d$ for Tap Set C. Examination of this graph indicates that all points are within both two standard deviations and the PTC 6 limit.

*Step C.* Figure A6 shows the extrapolation of Tap Set C data. For a $\Delta N$ of $-11$, the equation for extrapolation becomes

$$C_m = 1.0054 - \frac{0.185}{\mathrm{Re}_d^{1/5}}\left[1 - \frac{361{,}239}{\mathrm{Re}_d}\right]^{4/5} + \frac{-11}{10^4}$$

$$= 1.0043 - \frac{0.185}{\mathrm{Re}_d^{1/5}}\left[1 - \frac{361{,}239}{\mathrm{Re}_d}\right]^{4/5} \quad \text{(A3)}$$

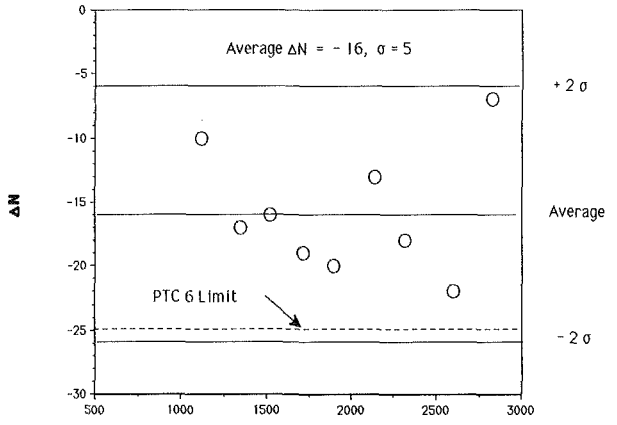


Fig. A1 Example 1, Tap Set A

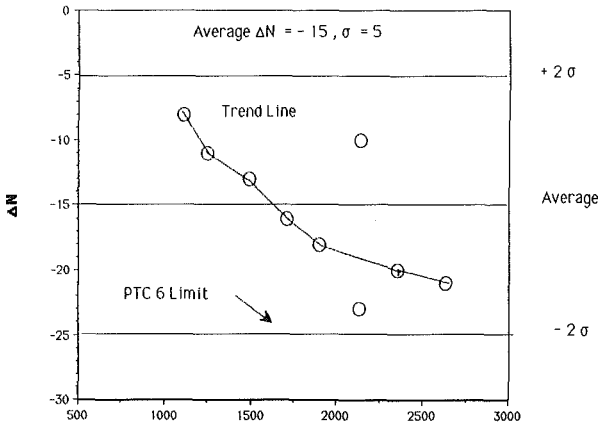


Fig. A3 Example 1, Tap Set B

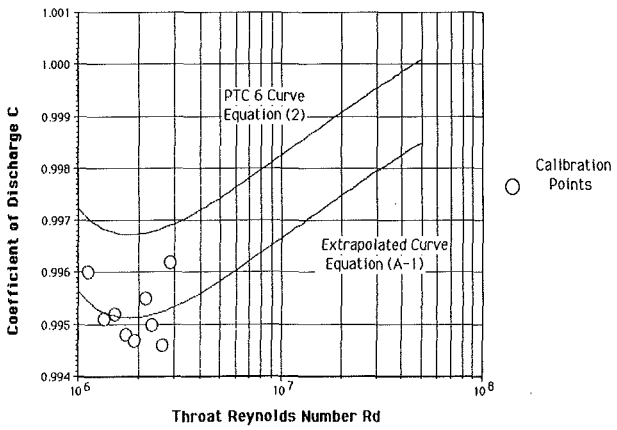


Fig. A2 Example 1: extrapolation of Tap Set A data

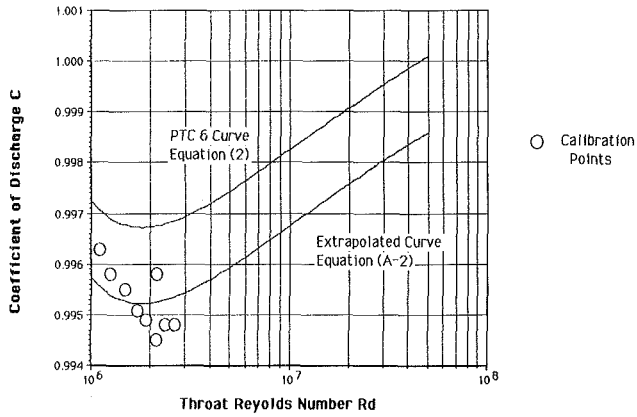


Fig. A4 Example 1: extrapolation of Tap Set B data

**Tap Set D**

*Step A.* Calculated and calibrated values for this tap set are shown below. Average $\Delta N = -12$, $\sigma = 4$.

| Run | $Re_d$ | $C_m$ | $C_6$ | $\Delta N$ |
|---|---|---|---|---|
| 5D | 1,107,000 | 0.9962 | 0.9971 | −9 |
| 6D | 1,251,000 | 0.9960 | 0.9969 | −9 |
| 4D | 1,488,000 | 0.9960 | 0.9968 | −8 |
| 7D | 1,713,000 | 0.9957 | 0.9967 | −10 |
| 3D | 1,897,000 | 0.9958 | 0.9967 | −9 |
| 8D | 2,132,000 | 0.9953 | 0.9968 | −15 |
| 2D | 2,351,000 | 0.9954 | 0.9968 | −14 |
| 9D | 2,632,000 | 0.9948 | 0.9969 | −21 |
| 1D | 2,877,000 | 0.9959 | 0.9969 | −10 |

*Step B.* Figure A7 is plot of $\Delta N$ versus $Re_d$ for Tap Set D. Examination of this graph indicates that all but one point is within two standard deviations and that all points are within the PTC 6 limit.

*Step C.* Figure A8 shows the extrapolation of Tap Set D data. For a $\Delta N$ of $-12$, the equation for extrapolation becomes

$$C_m = 1.0054 - \frac{0.185}{Re_d^{1/5}}\left[1 - \frac{361{,}239}{Re_d}\right]^{4/5} + \frac{-12}{10^4}$$

$$= 1.0042 - \frac{0.185}{Re_d^{1/5}}\left[1 - \frac{361{,}239}{Re_d}\right]^{4/5} \quad \text{(A4)}$$

**Tap Set Selection.** It is evident that Tap Sets A and C best meet the criteria of Par. 4.31 of [4] quoted above. The average $\Delta N$ of Tap Set A is $-16$ and that of Tap C is $-11$. For the combined set $\Delta N = -14$, the extrapolation equation becomes:

$$C_m = 1.0054 - \frac{0.185}{Re_d^{1/5}}\left[1 - \frac{361{,}239}{Re_d}\right]^{4/5} + \frac{-14}{10^4}$$

$$= 1.0040 - \frac{0.185}{Re_d^{1/5}}\left[1 - \frac{361{,}239}{Re_d}\right]^{4/5} \quad \text{(A5)}$$

*Step C.* Figure A9 shows the extrapolation of Tap Sets A and C data.

Note that this method tends to magnify small differences. If Tap Sets B and D had been chosen the combined set $\Delta N$ would have been $-13$ or only 0.01 percent different.

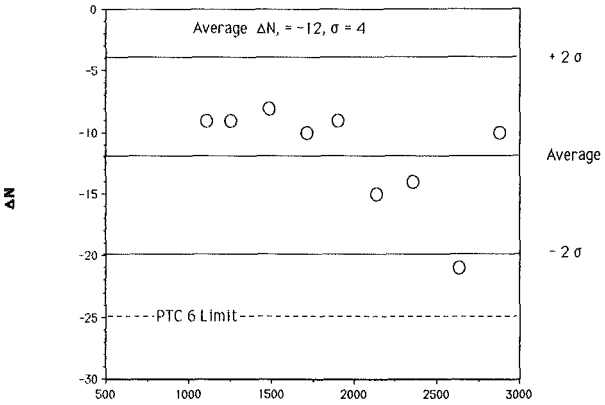


Fig. A7 Example 1, Tap Set D

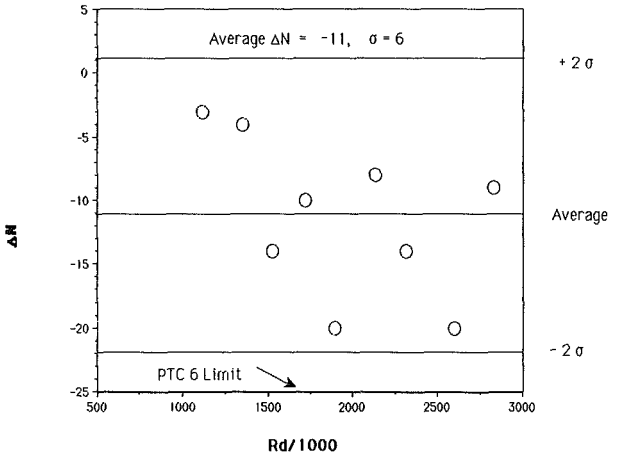


Fig. A5 Example 1, Tap Set C

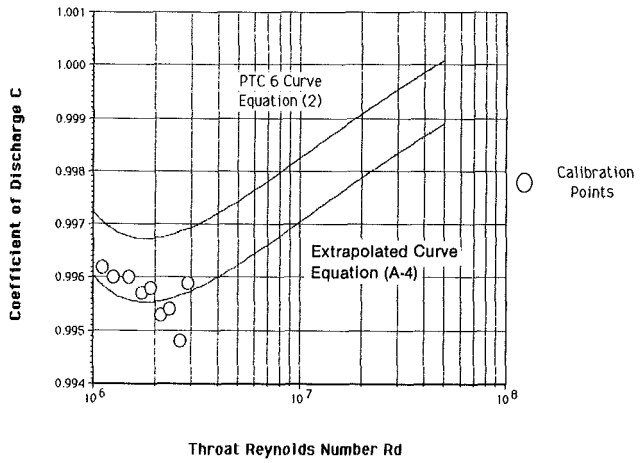


Fig. A8 Example 1: extrapolation of Tap Set D data

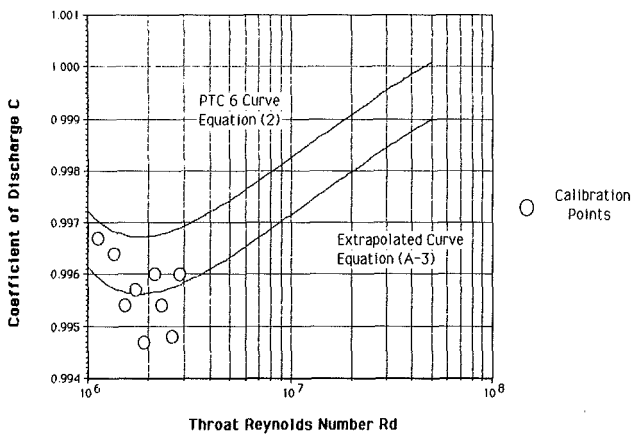


Fig. A6 Example 1: extrapolation of Tap Set C data

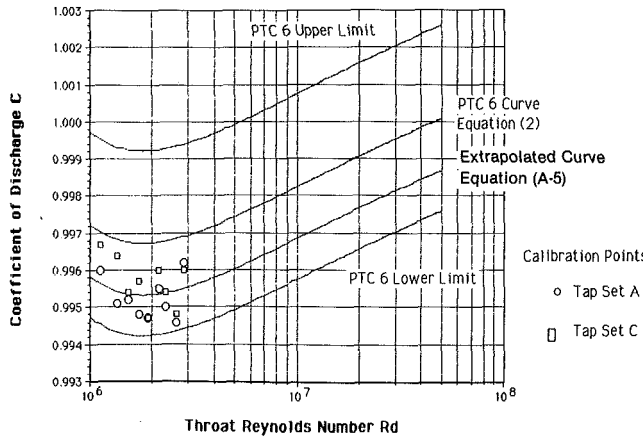


Fig. A9 Example 1: extrapolation of Tap Sets A and C

## Example Two—Preliminary, Pre and Post-Test Calibrations

The data used in this example are taken from [6] for all points of throat Reynolds number equal to or greater than one million. The nozzle used for this example had a throat diameter of 7.500 in. and a beta ratio of 0.500. The serial number of the example nozzle is #16-0558, Tap Set A. All calibrations were performed at the same (unspecified) laboratory. After the preliminary 1976 calibration, inspection revealed that there were some gouges in the entrance radii, which were removed by hand-polishing. The pre-test calibration was performed in 1978 and the post-test in 1979.

*Step A.* Calculated and calibrated values for all trials are shown below. The average $\Delta N$ for the pre-test calibration (after removal of gouges) was 16, $\sigma = 5$. For the post-trial $N = 16$ and $\sigma = 4$.

| Run | $Re_d$ | $C_m$ | $C_6$ | $\Delta N$ |
|---|---|---|---|---|
| *Calibration before gouge removal on inlet radii—1976* | | | | |
| 76A01 | 1,189,843 | 0.99495 | 0.99696 | −20 |
| 76A02 | 1,327,373 | 0.99582 | 0.99685 | −10 |
| 76A03 | 1,686,416 | 0.99687 | 0.99673 | 1 |
| 76A04 | 2,055,811 | 0.99714 | 0.99674 | 4 |
| 76A05 | 2,258,711 | 0.99752 | 0.99677 | 7 |
| 76A06 | 2,473,821 | 0.99849 | 0.99682 | 17 |
| 76A07 | 2,640,601 | 0.99815 | 0.99685 | 13 |
| 76A08 | 2,859,785 | 0.99854 | 0.99691 | 16 |
| 76A09 | 3,084,155 | 0.99840 | 0.99697 | 14 |
| 76A10 | 3,297,451 | 0.99818 | 0.99702 | 12 |
| 76A11 | 3,485,702 | 0.99720 | 0.99707 | 1 |
| 76A12 | 3,694,207 | 0.99693 | 0.99712 | −2 |
| 76A13 | 3,907,953 | 0.99704 | 0.99718 | −1 |
| 76A14 | 4,118,806 | 0.99738 | 0.99723 | 2 |
| *Pre-test calibration—1978* | | | | |
| 78A01 | 1,106,883 | 0.99997 | 0.99706 | 29 |
| 78A02 | 1,324,150 | 0.99865 | 0.99685 | 18 |
| 78A03 | 1,703,684 | 0.99855 | 0.99673 | 18 |
| 78A04 | 2,321,512 | 0.99842 | 0.99679 | 16 |
| 78A05 | 2,331,761 | 0.99813 | 0.99679 | 13 |
| 78A06 | 2,645,138 | 0.99806 | 0.99686 | 12 |
| 78A07 | 3,028,751 | 0.99824 | 0.99695 | 13 |
| 78A08 | 3,358,150 | 0.99875 | 0.99704 | 17 |
| 78A09 | 3,691,022 | 0.99875 | 0.99712 | 16 |
| 78A10 | 4,142,208 | 0.99929 | 0.99723 | 21 |
| *Post-test calibration—1979* | | | | |
| 79A01 | 1,203,785 | 0.99888 | 0.99695 | 19 |
| 79A02 | 1,407,805 | 0.99880 | 0.99680 | 20 |
| 79A03 | 1,825,274 | 0.99815 | 0.99672 | 14 |
| 79A04 | 2,515,829 | 0.99778 | 0.99683 | 10 |
| 79A05 | 2,549,283 | 0.99778 | 0.99683 | 9 |
| 79A06 | 2,936,981 | 0.99801 | 0.99693 | 11 |
| 79A07 | 2,944,684 | 0.99829 | 0.99693 | 14 |
| 79A08 | 3,285,975 | 0.99875 | 0.99702 | 17 |
| 79A09 | 3,638,720 | 0.99876 | 0.99711 | 17 |
| 79A10 | 4,009,605 | 0.99871 | 0.99720 | 15 |
| 79A11 | 4,376,199 | 0.99900 | 0.99729 | 17 |

*Step B.* Figure A10 is a plot of $\Delta N$ versus $Re_d$ for all calibrations. The effects of gouges on the inlet radii are clearly shown in the 1976 curve. All the data points for the 1978 calibration except one lie within both the PTC 6 limits and two standard deviations. All of the 1979 data lie within these limits. There are no trends and both calibrations have the same $\Delta N$ of 16.

*Step C.* Figure A11 shows the extrapolation of pre-test and post-test data. For a $\Delta N$ of 16

$$C_m = 1.0054 - \frac{0.185}{Re_d^{1/5}}\left[1 - \frac{361{,}239}{Re_d}\right]^{4/5} + \frac{16}{10^4}$$

$$= 1.0070 - \frac{0.185}{Re_d^{1/5}}\left[1 - \frac{361{,}239}{Re_d}\right]^{4/5} \quad \text{(A6)}$$

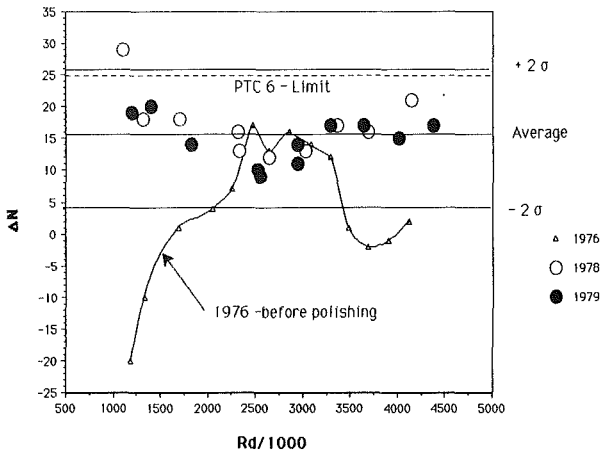


Fig. A10 Example 2: average pre and post-test 16, $\sigma = 5$

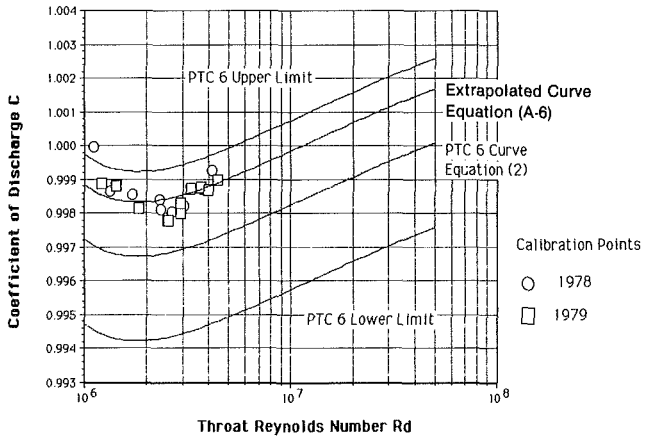


Fig. A11 Example 2: extrapolation of pre and post-test calibrations

## Example Three—Calibration at High Reynolds Numbers

The data used in this example were taken from [7]. The nozzle has a throat diameter of 11.3171 in. and is installed in a 24 in. pipe whose internal diameter is 22.62 in., with a beta ratio of 0.5003. The nozzle was calibrated at Alden Research Laboratories Sept. 7 and 8, 1989. Four sets of taps were installed, Tap Sets 1 and 2 being calibrated together, as were Tap Sets 3 and 4.

### Tap Set 1

*Step A.* Calculated and calibrated values for this tap set are shown below. Average $\Delta N = 16$, $\sigma = 3$.

| Run | $Re_d$ | $C_m$ | $C_6$ | $\Delta N$ |
|---|---|---|---|---|
| 24 | 3,660,000 | 0.9989 | 0.9971 | 18 |
| 1 | 4,025,000 | 0.9990 | 0.9972 | 18 |
| 2 | 4,262,000 | 0.9989 | 0.9973 | 16 |
| 3 | 4,530,000 | 0.9987 | 0.9973 | 14 |
| 4 | 4,781,000 | 0.9989 | 0.9974 | 15 |
| 23 | 4,794,000 | 0.9991 | 0.9974 | 17 |
| 5 | 5,026,000 | 0.9991 | 0.9974 | 17 |
| 6 | 5,258,000 | 0.9989 | 0.9975 | 14 |
| 7 | 5,507,000 | 0.9988 | 0.9975 | 13 |
| 10 | 5,763,000 | 0.9999 | 0.9976 | 23 |
| 9 | 5,990,000 | 0.9984 | 0.9976 | 8 |
| 8 | 6,000,000 | 0.9992 | 0.9976 | 16 |
| 11 | 6,249,000 | 0.9984 | 0.9977 | 7 |
| 22 | 6,287,000 | 0.9996 | 0.9977 | 19 |
| 12 | 6,525,000 | 0.9996 | 0.9977 | 19 |
| 13 | 6,739,000 | 0.9992 | 0.9978 | 14 |
| 14 | 6,957,000 | 0.9994 | 0.9978 | 16 |
| 15 | 7,280,000 | 0.9996 | 0.9979 | 17 |
| 16 | 7,535,000 | 0.9993 | 0.9979 | 14 |
| 17 | 7,766,000 | 0.9999 | 0.9979 | 20 |
| 18 | 8,000,000 | 0.9996 | 0.9980 | 16 |
| 19 | 8,255,000 | 0.9996 | 0.9980 | 16 |
| 21 | 8,533,000 | 0.9999 | 0.9981 | 18 |
| 20 | 8,538,000 | 0.9995 | 0.9981 | 14 |

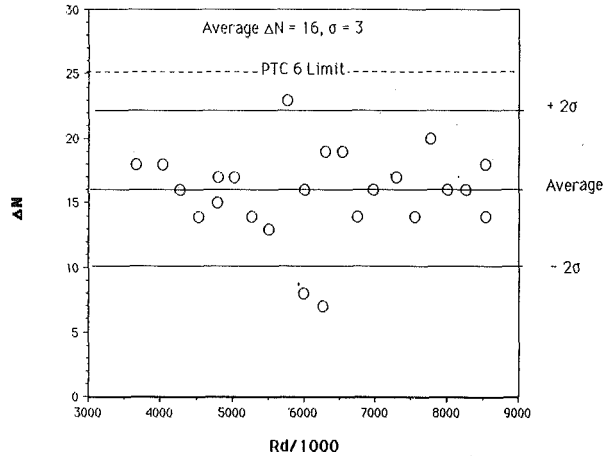


**Fig. A12 Example 3, Tap Set 1**

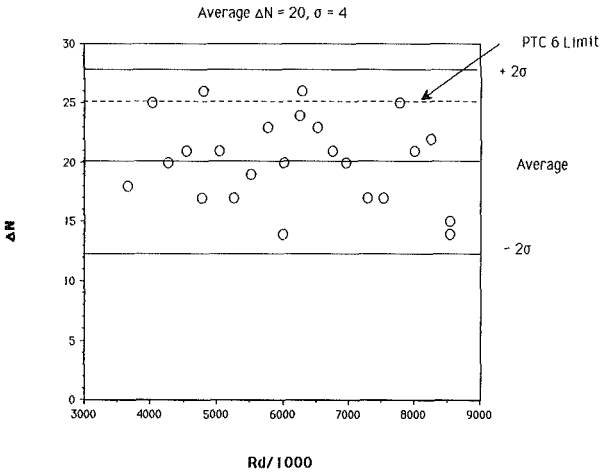


**Fig. A13 Example 3, Tap Set 2**

*Step B.* Figure A12 is a plot of $\Delta N$ versus $Re_d$ for Tap Set 1. Examination of this graph indicates that three points are outside the two standard deviation zone and all points are within the PTC 6 limit. Elimination of these points will not alter the average $\Delta N$ but would reduce the standard deviation to 2 and the remaining points would still be within $\pm 2\ \sigma$.

**Tap Set 2**

*Step A.* Calculated and calibrated values for this tap set are shown below. Average $\Delta N = 20$, $\sigma = 4$.

| Run | $Re_d$ | $C_m$ | $C_6$ | $\Delta N$ |
|---|---|---|---|---|
| 24 | 3,660,000 | 0.9989 | 0.9971 | 18 |
| 1 | 4,025,000 | 0.9997 | 0.9972 | 25 |
| 2 | 4,262,000 | 0.9993 | 0.9973 | 20 |
| 3 | 4,530,000 | 0.9994 | 0.9973 | 21 |
| 4 | 4,781,000 | 0.9991 | 0.9974 | 17 |
| 23 | 4,794,000 | 1.0000 | 0.9974 | 26 |
| 5 | 5,026,000 | 0.9995 | 0.9974 | 21 |
| 6 | 5,258,000 | 0.9992 | 0.9975 | 17 |
| 7 | 5,507,000 | 0.9994 | 0.9975 | 19 |
| 10 | 5,763,000 | 0.9999 | 0.9976 | 23 |
| 9 | 5,990,000 | 0.9990 | 0.9976 | 14 |
| 8 | 6,000,000 | 0.9996 | 0.9976 | 20 |
| 11 | 6,249,000 | 1.0001 | 0.9977 | 24 |
| 22 | 6,287,000 | 1.0003 | 0.9977 | 26 |
| 12 | 6,525,000 | 1.0000 | 0.9977 | 23 |
| 13 | 6,739,000 | 0.9999 | 0.9978 | 21 |
| 14 | 6,957,000 | 0.9998 | 0.9978 | 20 |
| 15 | 7,280,000 | 0.9996 | 0.9979 | 17 |
| 16 | 7,535,000 | 0.9996 | 0.9979 | 17 |
| 17 | 7,766,000 | 1.0004 | 0.9979 | 25 |
| 18 | 8,000,000 | 1.0001 | 0.9980 | 21 |
| 19 | 8,255,000 | 1.0002 | 0.9980 | 22 |
| 20 | 8,528,000 | 0.9995 | 0.9981 | 14 |
| 21 | 8,533,000 | 0.9996 | 0.9981 | 15 |

*Step B.* Figure A13 is a plot of $\Delta N$ versus $Re_d$ for Tap Set 2. Examination of this graph indicates that all points are within two standard deviations but two points are slightly (0.01 percent) above the PTC 6 limit.

**Tap Set 3**

*Step A.* Calculated and calibrated values for this tap set are shown below. Average $\Delta N = 16$, $\sigma = 3$.

| Run | $Re_d$ | $C_m$ | $C_6$ | $\Delta N$ |
|---|---|---|---|---|
| 24 | 3,654,000 | 0.9991 | 0.9971 | 20 |
| 1 | 4,023,000 | 0.9981 | 0.9972 | 9 |
| 2 | 4,261,000 | 0.9986 | 0.9973 | 13 |
| 3 | 4,528,000 | 0.9985 | 0.9973 | 12 |
| 4 | 4,779,000 | 0.9985 | 0.9974 | 11 |
| 23 | 4,793,000 | 0.9986 | 0.9974 | 12 |
| 5 | 5,026,000 | 0.9988 | 0.9974 | 14 |
| 6 | 5,259,000 | 0.9988 | 0.9975 | 13 |
| 7 | 5,508,000 | 0.9990 | 0.9975 | 15 |
| 10 | 5,759,000 | 0.9995 | 0.9976 | 19 |
| 9 | 5,994,000 | 0.9991 | 0.9976 | 15 |
| 8 | 5,997,000 | 0.9994 | 0.9976 | 18 |
| 11 | 6,248,000 | 0.9994 | 0.9977 | 17 |
| 22 | 6,284,000 | 0.9992 | 0.9977 | 15 |
| 12 | 6,524,000 | 0.9993 | 0.9977 | 16 |
| 13 | 6,743,000 | 0.9996 | 0.9978 | 18 |
| 14 | 6,956,000 | 0.9993 | 0.9978 | 15 |
| 15 | 7,280,000 | 0.9997 | 0.9979 | 18 |
| 16 | 7,530,000 | 0.9996 | 0.9979 | 17 |
| 17 | 7,764,000 | 1.0000 | 0.9979 | 21 |
| 18 | 8,000,000 | 0.9998 | 0.9980 | 18 |
| 19 | 8,257,000 | 0.9999 | 0.9980 | 19 |
| 21 | 8,529,000 | 0.9994 | 0.9981 | 13 |
| 20 | 8,533,000 | 0.9996 | 0.9981 | 15 |

*Step B.* Figure A14 is a plot of $\Delta N$ versus $Re_d$ for Tap Set 3. Examination of this graph indicates that all but one of the points are within two standard deviations, and that point is slightly (0.01) percent below this limit. All points are within the PTC 6 limit.

**Tap Set 4**

*Step A.* Calculated and calibrated values for this tap set are shown below. Average $\Delta N = 19$, $\sigma = 3$.

| Run | $Re_d$ | $C_m$ | $C_6$ | $\Delta N$ |
|---|---|---|---|---|
| 24 | 3,654,000 | 0.9987 | 0.9971 | 16 |
| 1 | 4,023,000 | 0.9998 | 0.9972 | 26 |
| 2 | 4,261,000 | 0.9992 | 0.9973 | 19 |
| 3 | 4,528,000 | 0.9984 | 0.9973 | 11 |
| 4 | 4,779,000 | 0.9988 | 0.9974 | 14 |
| 23 | 4,793,000 | 0.9998 | 0.9974 | 24 |
| 5 | 5,026,000 | 0.9989 | 0.9974 | 15 |
| 6 | 5,259,000 | 0.9990 | 0.9975 | 15 |
| 7 | 5,508,000 | 0.9992 | 0.9975 | 17 |
| 10 | 5,759,000 | 0.9996 | 0.9976 | 20 |
| 9 | 5,994,000 | 0.9998 | 0.9976 | 22 |
| 8 | 5,997,000 | 0.9994 | 0.9976 | 18 |
| 11 | 6,248,000 | 0.9998 | 0.9977 | 21 |
| 22 | 6,284,000 | 0.9999 | 0.9977 | 22 |
| 12 | 6,524,000 | 0.9996 | 0.9977 | 19 |
| 13 | 6,743,000 | 0.9997 | 0.9978 | 19 |
| 14 | 6,956,000 | 0.9997 | 0.9978 | 19 |
| 15 | 7,280,000 | 0.9996 | 0.9979 | 17 |
| 16 | 7,536,000 | 0.9998 | 0.9979 | 19 |
| 17 | 7,764,000 | 1.0002 | 0.9979 | 23 |
| 18 | 8,000,000 | 1.0000 | 0.9980 | 20 |
| 19 | 8,257,000 | 1.0000 | 0.9980 | 20 |
| 21 | 8,529,000 | 0.9997 | 0.9981 | 16 |
| 20 | 8,533,000 | 0.9998 | 0.9981 | 17 |

*Step B.* Figure A15 is a plot of $\Delta N$ versus $Re_d$ for Tap Set 4. Examination of this graph indicates that all but two points are within two standard deviations, one being 0.01 percent high and the other 0.02 percent low, below this limit. The high point is also 0.01 percent above the PTC 6 limit. Elimination of these points will change neither the average value of $\Delta N$ nor the standard deviation for this tap pair.

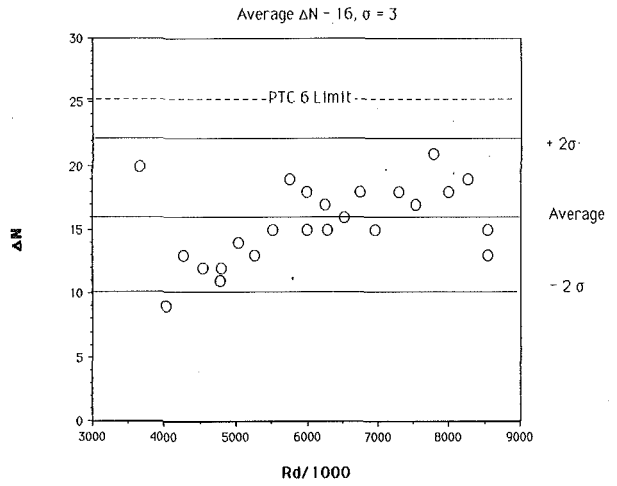


Fig. A14 Example 3, Tap Set 3

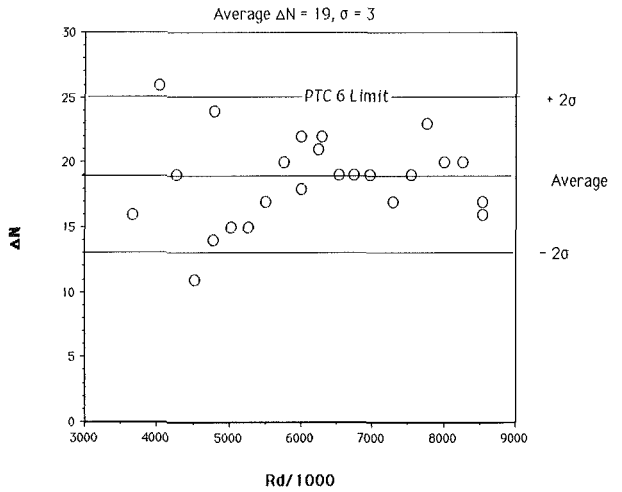


Fig. A15 Example 3, Tap Set 4

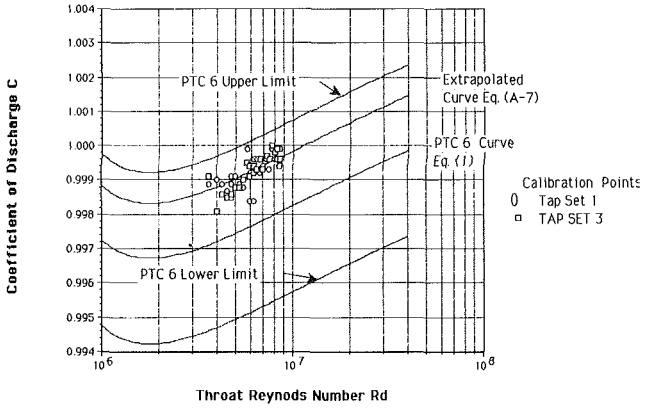


Fig. A16 Example 3: extrapolation of Tap Sets 1 and 3

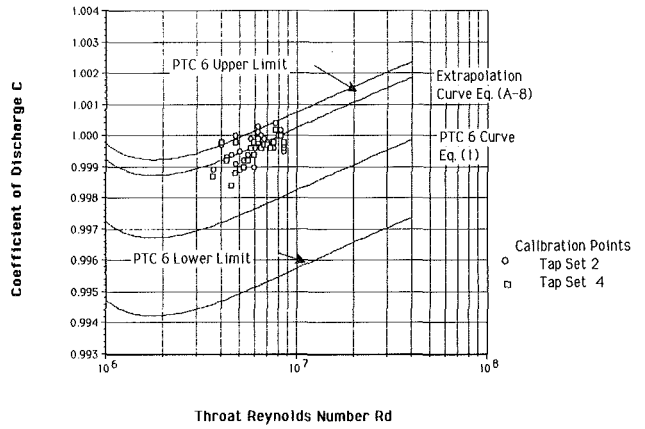


Fig. A17 Example 3: extrapolation of Tap Sets 2 and 4 calibration data

### Tap Sets 1 and 3

*Step C.* The average $\Delta N$ of both tap sets is 16 and their standard deviations are 3. For a $\Delta N$ of 16 the extrapolation equation becomes

$$C_m = 1.0054 - \frac{0.185}{\mathrm{Re}_d^{1/5}}\left[1 - \frac{361{,}239}{\mathrm{Re}_d}\right]^{4/5} + \frac{16}{10^4}$$

$$= 1.0070 - \frac{0.185}{\mathrm{Re}_d^{1/5}}\left[1 - \frac{361{,}239}{\mathrm{Re}_d}\right]^{4/5} \quad \text{(A7)}$$

Figure A16 shows the results of this extrapolation.

*Step C.* The average $\Delta N$ of Tap Set 2 is 20 with a sigma of 4, and for Tap Set 4, $\Delta N = 19$ with a sigma of 3. For a $\Delta N$ of $(20+19)/2 = 19.5 \approx 20$ the extrapolation equation becomes

$$C_m = 1.0054 - \frac{0.185}{\mathrm{Re}_d^{1/5}}\left[1 - \frac{361{,}239}{\mathrm{Re}_d}\right]^{4/5} + \frac{20}{10^4}$$

$$= 1.0074 - \frac{0.185}{\mathrm{Re}_d^{1/5}}\left[1 - \frac{361{,}239}{\mathrm{Re}_d}\right]^{4/5} \quad \text{(A8)}$$

Figure A17 shows the results of this extrapolation.

Comparison of Figs. A16 and A17 indicates clearly that Tap Sets 1 and 3 should be selected because all of the calibration data points are within the PTC 6 limits. Again, if the other combination were selected the difference would only be 0.04 percent.

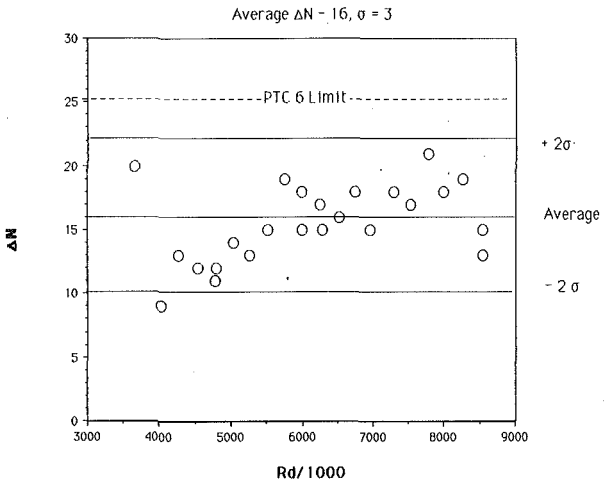


Fig. A14 Example 3, Tap Set 3

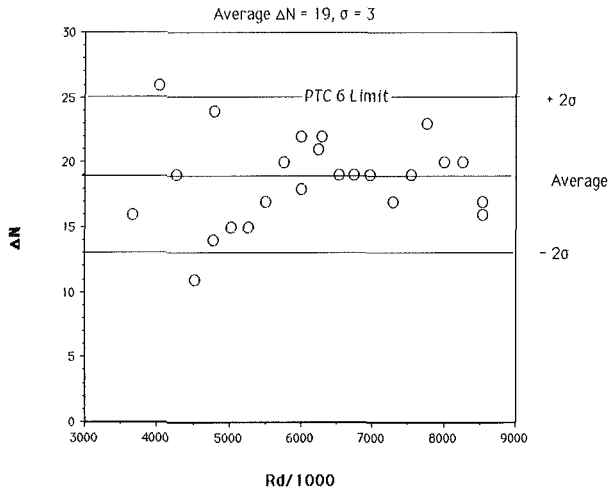


Fig. A15 Example 3, Tap Set 4

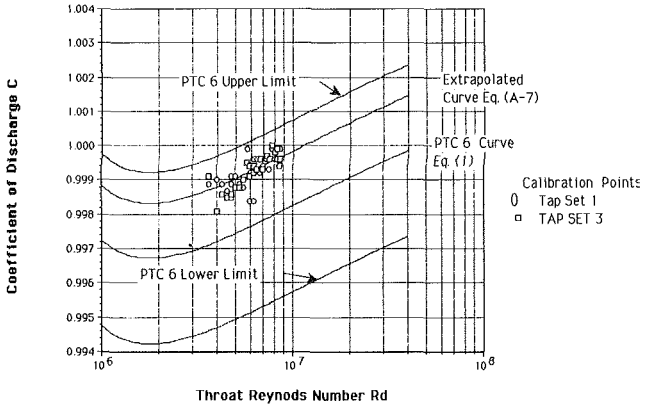


Fig. A16 Example 3: extrapolation of Tap Sets 1 and 3

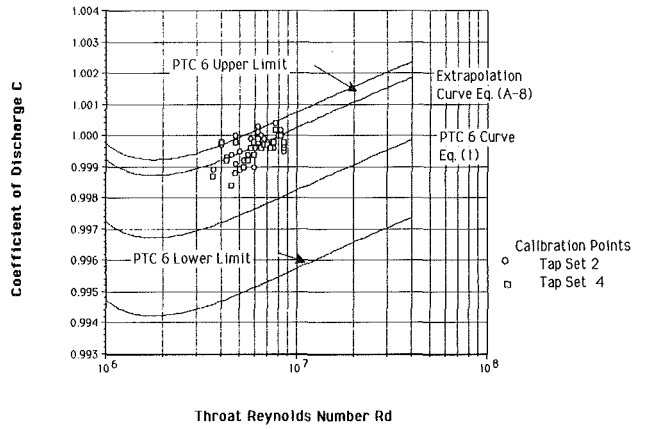


Fig. A17 Example 3: extrapolation of Tap Sets 2 and 4 calibration data

### Tap Sets 1 and 3

*Step C.* The average $\Delta N$ of both tap sets is 16 and their standard deviations are 3. For a $\Delta N$ of 16 the extrapolation equation becomes

$$C_m = 1.0054 - \frac{0.185}{\mathrm{Re}_d^{1/5}}\left[1 - \frac{361{,}239}{\mathrm{Re}_d}\right]^{4/5} + \frac{16}{10^4}$$

$$= 1.0070 - \frac{0.185}{\mathrm{Re}_d^{1/5}}\left[1 - \frac{361{,}239}{\mathrm{Re}_d}\right]^{4/5} \quad \text{(A7)}$$

Figure A16 shows the results of this extrapolation.

*Step C.* The average $\Delta N$ of Tap Set 2 is 20 with a sigma of 4, and for Tap Set 4, $\Delta N = 19$ with a sigma of 3. For a $\Delta N$ of $(20+19)/2 = 19.5 \approx 20$ the extrapolation equation becomes

$$C_m = 1.0054 - \frac{0.185}{\mathrm{Re}_d^{1/5}}\left[1 - \frac{361{,}239}{\mathrm{Re}_d}\right]^{4/5} + \frac{20}{10^4}$$

$$= 1.0074 - \frac{0.185}{\mathrm{Re}_d^{1/5}}\left[1 - \frac{361{,}239}{\mathrm{Re}_d}\right]^{4/5} \quad \text{(A8)}$$

Figure A17 shows the results of this extrapolation.

Comparison of Figs. A16 and A17 indicates clearly that Tap Sets 1 and 3 should be selected because all of the calibration data points are within the PTC 6 limits. Again, if the other combination were selected the difference would only be 0.04 percent.

## DISCUSSION

### F. H. Kindl[2]

The proper calibration of flow nozzles and improvement in the ability to extrapolate these data to power plant conditions is a subject that has fundamental interest for the PTC 6 committee. For this reason we wish to express our appreciation to the authors for their efforts on this subject. It should be noted that the committee has recognized that certain difficulties with use of the flow nozzle calibration and extrapolation techniques, as described in the 1976 version of the PTC 6 code, have been identified. A code revision aimed at overcoming these difficulties, along with incorporating other desirable changes, is currently under way. It is appropriate to mention that the authors had not seen all these proposed changes at the time they wrote their paper.

Following a study of the two papers we have the following observations, reservations, and comments:

- We have a fundamental concern about the ability of a "flat plate" analysis, such as Hall's, to describe the phenomena in the boundary layer transition region properly.
- The preceding notwithstanding, we are impressed with the fact that the extrapolation curve described by the authors follows the ASME PTC 6 data quite well, and for two of the three examples cited in the second of the two papers, the extrapolation procedure appeared to permit the use of data below the present Reynolds number limit set by PTC 6 of 3.5 million.

[2]Encotech, Inc., Schenectady, NY 12301.

• Considering the uncertainty of the ability to model an ASME nozzle with Hall's "flat plate" analysis, we consider their conclusions that:

— "The present PTC 6 requirement that calibration data must be in the fully turbulent range cannot be met with current facilities," and

— "The present PTC 6 method is impractical and does not take advantage of most of the calibration data, and if strictly followed could not be used because of limitations of calibration facility capacities."

to be overstated. The conclusion that the boundary layer transition to fully turbulent flow does not occur until a Reynolds number of 10 to 20 million seems likely to be a result of the simplifying assumptions used for the analysis.

The orderly transition from laminar to turbulent flow envisioned by the "Hall Flat Plate Nozzle" seems considerably oversimplified for the following reasons:

• Considerable emphasis is placed by Dr. Schlichting [8] on the importance of the pressure gradient in the flow in determining where and how transition to turbulent flow will take place. Hall's analysis assumes a gradient of zero, whereas potential flow analysis of an ASME nozzle by Mr. Sumner [9] shows both positive and negative gradients prior to the flow reaching the nozzle throat.

• Dr. Schlichting [8, Chap. XVII] describes at some length a "point of instability," which is then followed by a "point of transition," the difference in Reynolds number at which these occur, and the importance of the local pressure gradient in determining when these phenomena will take place. The simplified "Hall analysis" does not in any way recognize these phenomena.

In summary the committee would like to recognize that much progress in the understanding of boundary layer theory and related phenomena has come from the development of simplified models that were shown after extensive laboratory work to match experimental data. Preliminary work by the authors seems encouraging in this regard. However, the extent of the simplifications adopted to obtain the analytical results argues for caution in jumping to new conclusions. We wish to thank the authors for their efforts in helping to improve the understanding of this important area.

## References


8 Schlichting, H., *Boundary Layer Theory* (English translation by J. Kestin), 7th ed., McGraw-Hill, New York, 1979.

9 Albert, P. G., Sumner, W. J., and Halmi, D., "A Primary Flow Section for Use With the Alternative ASME Acceptance Test," ASME Paper No. 82-JPGC-PTC-4, 1982.


### J. Westcott[3]

The authors have presented an interesting approach for the evaluation of calibration data for flow sections with throat-tap nozzles. ANSI/ASME PTC 6 describes the expected attributes of this type of flow section. There are two requirements, which are that the calibration data must be within ± ¼ percent of the expected coefficient and that the resulting curve shall have the same shape as the expected curve. The procedure proposed by this paper does not provide for testing the second requirement. The assumption is made that the flow section is a *good* flow section and therefore the extrapolation can be accomplished using the calibration data and the expected coefficient curve shape. This assumption is also stipulated in the companion paper 90-JPGC/PTC-1. The conclusion of this paper states that since the developed equation reproduces the data contained in PTC 6, the equation is valid for the extrapolation of the coefficient to higher Reynolds numbers. This is correct. However, there is no demonstrated justification "*to use this equation for the extrapolation of nozzle calibration data from the laboratory to the test measurement installation.*"

In Appendix A of the second paper, three numerical examples are given. The first two examples are calibrations over a throat Reynolds number range of 1.1 to 2.9 million and 1.1 to 4.4 million. The third is for a range of 3.6 to 8.5 million. Only the third example has sufficient data for evaluation of the shape of the coefficient curve resulting from regression analysis of the data. The other two must assume that the nozzle characteristics provide the correct shape. Unfortunately PTC 6 does not specify a procedure for the evaluation of the coefficient curve shape resulting from the calibration data and there are many throat-tap nozzle flow sections, which are being used with the assumption that the actual coefficient has the same shape as the expected coefficient. Obviously this can introduce significant error when the extrapolation is large.

Example three shows a flow section, which has been calibrated to a Reynolds number of 8.5 million. Within the precision of the calibration, tap sets 1, 2, and 4 have a shape equivalent to the expected shape. Tap Set 3 has a shape that results in an increasing coefficient at a rate approximately 0.05 percent greater than the expected. The operating Reynolds number of this flow section is about 34 million and the precision of the calibration results in an additional uncertainty due to the calibration of less than ±0.1 percent. This evaluation is based on a regression analysis of the calibration data using an equation of the form

$$C_m = A + B(\log \mathrm{Re}_d)$$

Using this equation or the equation presented by the paper results in essentially the same results when extrapolated to higher Reynolds numbers. This is not unexpected since both forms adequately represent both the calibration data and the expected coefficient data.

This paper has provided a procedure for utilizing calibration data at lower Reynolds numbers than stated in PTC 6. The extrapolation is only valid when the coefficient shape is correct. The method described in the paper assumes that the shape is correct.

## Authors' Closure

We thank Mr. Westcott for his comments. We agree that all calibration data not in the turbulent boundary layer range can be extrapolated only by assuming a shape. This supports our contention that complete turbulence develops at a much higher Reynolds number than that stated in PTC 6.

Mr. Kindl's comments on behalf of the ASME PTC 6 committee are unfortunate because, if valid, they cast serious doubt on all existing extrapolations of throat tap nozzle calibration data. The source and derivation of the "typical curve" (Fig. 4.4 of PTC 6) is undocumented but is thought to originate from the Cotton and Westcott paper [10], which extends the work of Rivas and Shapiro [11] into the turbulent region. Neither of these papers take into account any axial or radial pressure gradients; they merely justify neglecting them. If our analysis is seriously flawed by neglecting pressure gradients and using a simplified nozzle, then the same is even more true for the PTC 6 basis for extrapolation. If the transition from laminar to turbulent boundary layer is not orderly, as Mr. Kindl suggests, then it will show up in the calibration data. We have not observed that phenomenon in calibrations at Reynolds numbers above 1,000,000.

If two methods are available that produce identical results, one simple and the other complex, either both are wrong or both correct. The PTC 6 committee can't have it both ways. In reply to the statement that our theory requires experimental

[3]Power Technologies, Inc., Schenectady, NY 12305.

• Considering the uncertainty of the ability to model an ASME nozzle with Hall's "flat plate" analysis, we consider their conclusions that:

— "The present PTC 6 requirement that calibration data must be in the fully turbulent range cannot be met with current facilities," and

— "The present PTC 6 method is impractical and does not take advantage of most of the calibration data, and if strictly followed could not be used because of limitations of calibration facility capacities."

to be overstated. The conclusion that the boundary layer transition to fully turbulent flow does not occur until a Reynolds number of 10 to 20 million seems likely to be a result of the simplifying assumptions used for the analysis.

The orderly transition from laminar to turbulent flow envisioned by the "Hall Flat Plate Nozzle" seems considerably oversimplified for the following reasons:

• Considerable emphasis is placed by Dr. Schlichting [8] on the importance of the pressure gradient in the flow in determining where and how transition to turbulent flow will take place. Hall's analysis assumes a gradient of zero, whereas potential flow analysis of an ASME nozzle by Mr. Sumner [9] shows both positive and negative gradients prior to the flow reaching the nozzle throat.

• Dr. Schlichting [8, Chap. XVII] describes at some length a "point of instability," which is then followed by a "point of transition," the difference in Reynolds number at which these occur, and the importance of the local pressure gradient in determining when these phenomena will take place. The simplified "Hall analysis" does not in any way recognize these phenomena.

In summary the committee would like to recognize that much progress in the understanding of boundary layer theory and related phenomena has come from the development of simplified models that were shown after extensive laboratory work to match experimental data. Preliminary work by the authors seems encouraging in this regard. However, the extent of the simplifications adopted to obtain the analytical results argues for caution in jumping to new conclusions. We wish to thank the authors for their efforts in helping to improve the understanding of this important area.

## References


8 Schlichting, H., *Boundary Layer Theory* (English translation by J. Kestin), 7th ed., McGraw-Hill, New York, 1979.

9 Albert, P. G., Sumner, W. J., and Halmi, D., "A Primary Flow Section for Use With the Alternative ASME Acceptance Test," ASME Paper No. 82-JPGC-PTC-4, 1982.


### J. Westcott[3]

The authors have presented an interesting approach for the evaluation of calibration data for flow sections with throat-tap nozzles. ANSI/ASME PTC 6 describes the expected attributes of this type of flow section. There are two requirements, which are that the calibration data must be within ± ¼ percent of the expected coefficient and that the resulting curve shall have the same shape as the expected curve. The procedure proposed by this paper does not provide for testing the second requirement. The assumption is made that the flow section is a *good* flow section and therefore the extrapolation can be accomplished using the calibration data and the expected coefficient curve shape. This assumption is also stipulated in the companion paper 90-JPGC/PTC-1. The conclusion of this paper states that since the developed equation reproduces the data contained in PTC 6, the equation is valid for the extrapolation of the coefficient to higher Reynolds numbers. This is correct. However, there is no demonstrated justification "*to use this equation for the extrapolation of nozzle calibration data from the laboratory to the test measurement installation.*"

In Appendix A of the second paper, three numerical examples are given. The first two examples are calibrations over a throat Reynolds number range of 1.1 to 2.9 million and 1.1 to 4.4 million. The third is for a range of 3.6 to 8.5 million. Only the third example has sufficient data for evaluation of the shape of the coefficient curve resulting from regression analysis of the data. The other two must assume that the nozzle characteristics provide the correct shape. Unfortunately PTC 6 does not specify a procedure for the evaluation of the coefficient curve shape resulting from the calibration data and there are many throat-tap nozzle flow sections, which are being used with the assumption that the actual coefficient has the same shape as the expected coefficient. Obviously this can introduce significant error when the extrapolation is large.

Example three shows a flow section, which has been calibrated to a Reynolds number of 8.5 million. Within the precision of the calibration, tap sets 1, 2, and 4 have a shape equivalent to the expected shape. Tap Set 3 has a shape that results in an increasing coefficient at a rate approximately 0.05 percent greater than the expected. The operating Reynolds number of this flow section is about 34 million and the precision of the calibration results in an additional uncertainty due to the calibration of less than ±0.1 percent. This evaluation is based on a regression analysis of the calibration data using an equation of the form

$$C_m = A + B(\log \mathrm{Re}_d)$$

Using this equation or the equation presented by the paper results in essentially the same results when extrapolated to higher Reynolds numbers. This is not unexpected since both forms adequately represent both the calibration data and the expected coefficient data.

This paper has provided a procedure for utilizing calibration data at lower Reynolds numbers than stated in PTC 6. The extrapolation is only valid when the coefficient shape is correct. The method described in the paper assumes that the shape is correct.

## Authors' Closure

We thank Mr. Westcott for his comments. We agree that all calibration data not in the turbulent boundary layer range can be extrapolated only by assuming a shape. This supports our contention that complete turbulence develops at a much higher Reynolds number than that stated in PTC 6.

Mr. Kindl's comments on behalf of the ASME PTC 6 committee are unfortunate because, if valid, they cast serious doubt on all existing extrapolations of throat tap nozzle calibration data. The source and derivation of the "typical curve" (Fig. 4.4 of PTC 6) is undocumented but is thought to originate from the Cotton and Westcott paper [10], which extends the work of Rivas and Shapiro [11] into the turbulent region. Neither of these papers take into account any axial or radial pressure gradients; they merely justify neglecting them. If our analysis is seriously flawed by neglecting pressure gradients and using a simplified nozzle, then the same is even more true for the PTC 6 basis for extrapolation. If the transition from laminar to turbulent boundary layer is not orderly, as Mr. Kindl suggests, then it will show up in the calibration data. We have not observed that phenomenon in calibrations at Reynolds numbers above 1,000,000.

If two methods are available that produce identical results, one simple and the other complex, either both are wrong or both correct. The PTC 6 committee can't have it both ways. In reply to the statement that our theory requires experimental

[3]Power Technologies, Inc., Schenectady, NY 12305.

B. W. Noel

H. M. Borella
Los Alamos National Laboratory,
Los Alamos, NM 87545

W. Lewis

W. D. Turley
EG&G Energy Measurements, Inc.,
Goleta, CA 93117

D. L. Beshears

G. J. Capps

M. R. Cates

J. D. Muhs

K. W. Tobin
Oak Ridge National Laboratory,
Oak Ridge, TN 37831

# Evaluating Thermographic Phosphors in an Operating Turbine Engine

*The results of a field test in a commercial turbine engine showed that we can remotely measure the temperature of engine components in operating engines using thermographic phosphors. The remote-measurement method exploits the temperature dependence of the characteristic decay time of the laser-induced fluorescence of thermographic phosphors. This paper summarizes recent work leading up to and including a successful test of the thermographic-phosphor method in an operating turbine engine.*

## Introduction

Over the past several years, we have developed a method of remote temperature measurement that uses thermographic phosphors (TPs). We apply the TP to a surface, excite the TP with UV light (whereupon it emits fluorescence in a spectrum of narrow lines whose characteristics are temperature dependent) and determine the surface temperature by measuring either the characteristic decay time of the laser-induced fluorescence (LIF) or the relative amplitudes of the emission lines.

We have used the method on rotating machinery, such as gas centrifuges (Cates et al., 1984) and developmental motors (Allison et al., 1988), in which the operating temperatures were near ambient. The method has been used to measure the temperature of the stationary surface of a variable-area ejector bathed in the high blackbody background from the augmenter flame of an operating turbine engine (Allison et al., 1987). We have recently been adapting the method to measure the surface temperature of components, such as stator vanes and turbine blades, in operating turbine engines (Noel et al., 1986). During this development, we studied the TP characteristics and their calibration, bonding methods, instrumentation development, and methods of data analysis (Noel et al., 1987). We also did a number of tests (Noel et al., 1989) that evaluated various aspects of the TPs' performance in high-temperature environments that simulate various aspects of an engine.

In this paper, we discuss the results of a test of the TP method in an operating turbine engine.

The purpose of the test was to demonstrate the feasibility of the method in an operating turbine engine. The main technical questions to be answered included the following:

1 Will the TP coatings survive in an engine environment?

2 Can an engine pyrometry probe be modified so that the TP coatings can be illuminated by UV and the LIF viewed by the probe optics?

3 Is it possible to detect the LIF from first-stage stator vanes in the presence of the large blackbody background from the burner?

4 Can the LIF signals be seen with a high enough signal-to-noise ratio (SNR) to extract the temperature data?

## Experimental Plan

We tested the method in a Pratt & Whitney (P&W) PW2037 commercial engine at a P&W test stand in East Hartford, CT.

Contributed by the International Gas Turbine Institute and presented at the 35th International Gas Turbine and Aeroengine Congress and Exposition, Brussels, Belgium, June 11-14, 1990. Manuscript received by the International Gas Turbine Institute February 15, 1990. Paper No. 90-GT-266.

We were able to use a pyrometer port located such that the pyrometer probe fits in a groove machined into one of the first-stage vanes on its downstream side. The vane is made of superalloy coated with a passivation layer.

Previous experience showed that, for stationary or periodically rotating structures, the LIF decay-time approach gave superior results compared with the approach using the ratio of emission-line amplitudes. We chose that method for this test.

Our initial choice of TP was europium-doped yttrium oxide, $Y_2O_3$:Eu; the 611-nm emission line from this TP is bright, its LIF decay times in the operating-temperature range of the engine fall well within the capabilities of the instrumentation, and it is the TP that we have most thoroughly studied and characterized. The 611-nm line of $Y_2O_3$:Eu is usable in the range from 650°C to >1200°C.

Earlier tests suggested that the TP should be electron-beam-deposited on the vanes, so that was done. In-laboratory evaluation of the virgin brightness of the TP-coated vane showed poor results; the brightness was less than 0.7 percent as bright as a reference sample of $Y_2O_3$:Eu powder. This situation was complicated by the fact that, during the electric-discharge machining of the pyrometer hole in the vanes, the passivation layer was removed in a region in and around the hole, where we planned to view with our probe. Our previous experience had shown that TPs bonded to nonpassivated areas either did not bond well or tended to come off after exposure to an oxidizing atmosphere. This occurs because the thin coating of TP is porous to oxygen, the metal oxidizes, and the oxide spalls when the metal cools, taking the TP with it. Figure 1 is a photograph of the vanes taken before the test. The figure shows the machined probe hole and the $Y_2O_3$:Eu coating, which emits yellow-orange LIF because it is illuminated by a UV lamp. The passivation layer is missing under the TP in the region adjacent to the hole. This fact made it necessary for us to view the region farther from the hole, at a distance of about 2 cm from the face of the probe.

Because of concerns about phosphor spalling and dimness of the electron-beamed $Y_2O_3$:Eu, we added three strips of TP mixed with a Sperex SP-115 inorganic high-temperature binder on top of the electron-beamed coating. The strips contained three different phosphors: $Y_2O_3$:Eu; europium-doped yttrium vanadate, $YVO_4$:Eu (a TP with a bright emission line at 618 nm that shows promise for high-temperature applications, but has not been as thoroughly characterized as $Y_2O_3$:Eu); and europium-doped scandium phosphate, $ScPO_4$:Eu (which, in theory, should be usable at higher temperatures than either $Y_2O_3$:Eu or $YVO_4$:Eu, but which is still in the developmental stage). The $ScPO_4$:Eu intensity turned out to be so low that, when the deposits were inadvertently removed in a degreasing operation, the $ScPO_4$:Eu was not replaced.

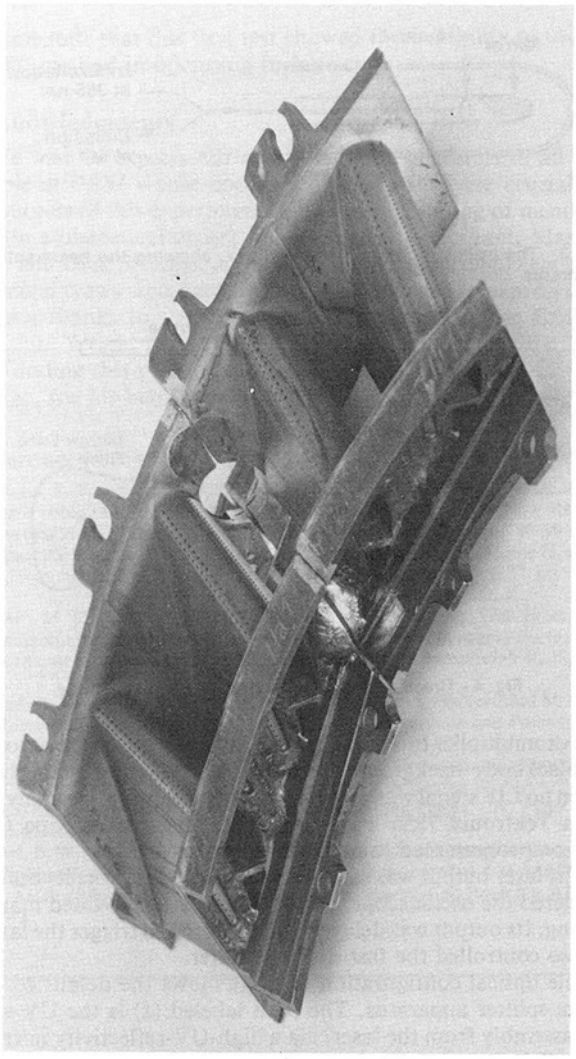

Fig. 1 Photograph of first-stage stator vanes for Pratt & Whitney PW2037 engine. One vane is coated with thermographic phosphor (TP) applied by electron-beam deposition. The vane assembly contains an electro-machined hole for insertion of either a pyrometer probe or the TP probe, which used a pyrometer-probe housing.

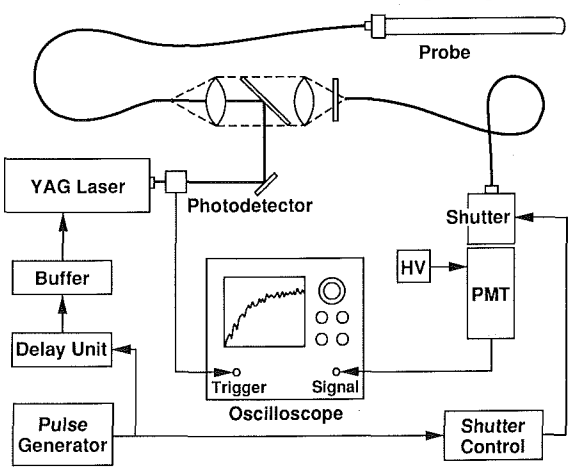


Fig. 2 Experiment setup. The YAG laser excites the TP on the vanes by way of the fiber optics to the probe. The return signal is detected by a photomultiplier tube (PMT) and analyzed in the waveform-processing oscilloscope.

## Instrumentation

The LIF-decay-time method requires a pulsed UV source having a pulse duration short relative to the decay time. In those experiments where ample SNR is available, it is possible to use a small nitrogen laser. In the present experiment, with long lengths of fiber optics, small-diameter probe optics, a relatively poor optical geometry, high blackbody background, and rather dim TPs, we chose to use a high-power Nd:YAG laser tripled to emit at 355 nm. The laser was set up in the control room adjacent to the test cell. The experiment setup is shown in Fig. 2. The UV laser light was coupled into a 600-$\mu$m-dia UV-grade glass-on-glass fiber-optic cable and launched into the probe through a beam-splitting apparatus. The probe also contained a 600-$\mu$m-dia UV-grade fiber. The probe optics focused the UV light on the TP-coated vane. The LIF return light was gathered by the same optics and fiber, returned to the beam-splitting apparatus, coupled into a 1000-$\mu$m-dia plastic-clad-silica fiber and sent to the data-gathering station, which was situated in another part of the control room. The LIF passed through a fast optical shutter before being detected by

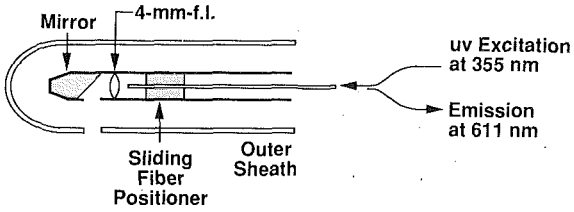


**Fig. 3 The optical configuration in detail, showing the beam-splitter apparatus**

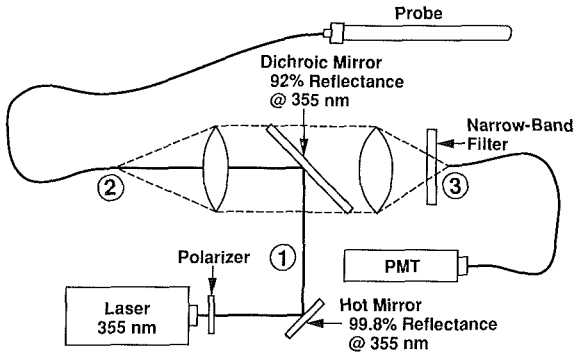


**Fig. 4 Cross-sectional view of the probe assembly**

a photomultiplier tube (PMT). The shutter reduced the amount of blackbody background seen by the PMT during the time when no LIF signal was present. The PMT output was analyzed by a Tektronix 7854 waveform-processing oscilloscope that was preprogrammed to accommodate the data.

The laser output was sampled by a photodetector; its output triggered the oscilloscope. A pulse generator provided master timing. Its output was delayed and buffered to trigger the laser; it also controlled the fast optical shutter.

The optical configuration (Fig. 3) shows the details of the beam-splitter apparatus. The path labeled (1) is the UV into the assembly from the laser, via a high-UV-reflectivity mirror. The dichroic mirror reflects most of the UV into the path labeled (2). The return signal from the probe contains both LIF and substantial reflected UV. On the return path, the dichroic mirror accepts the LIF, but rejects most of the UV. The narrowband filters were selected to pass only the 610-nm line of $Y_2O_3$:Eu and the 618-nm life of $YVO_4$:Eu. These filters rejected most of the remaining UV light.

The probe went through several revisions en route to its final form, which is shown in Fig. 4. This is a simpler configuration than the one described in Noel et al. (1989) and, despite the reduced overall optical-system efficiency, it was more convenient for this experiment.

## Results and Discussion

The various components were set up before the experiment in our laboratories for evaluation, calibration, and other pretesting. All the various pieces were then disassembled, moved to P&W, and reassembled.

The electron-beam-deposited $Y_2O_3$:Eu gave signals too small to be usable during the testing. Because the signals were even smaller than expected, we used a borescope to examine the vanes during periods when the engine was not running. The observations allowed us to get a qualitative feel for the rate of abrasion of the various TP coatings. The TP strips attached with the Sperex binder survived long enough (through about 15 h of engine running) to give useful data. Another factor that contributed to the low signals was the laser excitation. At 355 nm, the excitation efficiency was much lower than at the more desirable resonance excitations at 467 or 538 nm (for the $Y_2O_3$:Eu). These latter excitation wavelengths, which can be produced with a dye laser, are also better propagated by

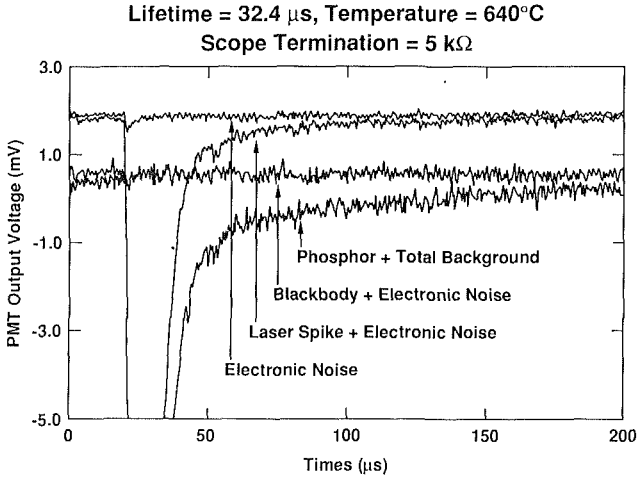


**Fig. 5 Reproduction of multiple oscilloscope traces, showing the various components of the signal**

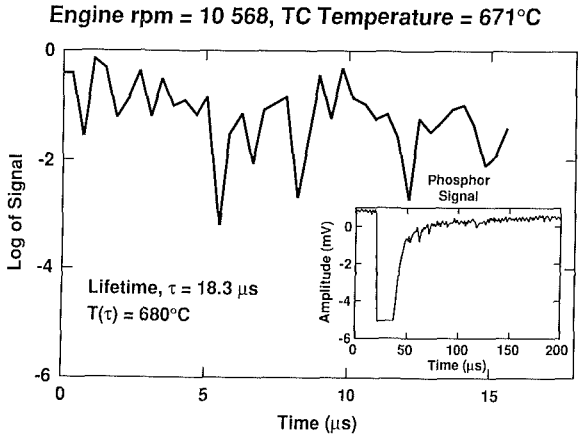


**Fig. 6 Reproductions of oscilloscope traces of raw data (inset) and logarithm of corrected data for the highest temperature (672°C) and highest engine rpm (10,568) during the experiment**

fiber optics. In terms of SNR, the $YVO_4$:Eu gave the best signals throughout the test. We therefore concentrated our efforts on observing signals from $YVO_4$:Eu.

The blackbody effects, which cause charge starvation when the PMT views the scene continuously, were mitigated well by the mechanical shutter up to the maximum temperatures observed, about 700°C.

Figure 5 is an overlay of several oscilloscope traces that illustrate the various components of the signal. The uppermost trace was obtained by blocking path (1) in Fig. 3; it shows only the electronic noise, which includes a few-hundred-microvolt excursion at the time the laser fires. The next lower trace was obtained by blocking path (2) of Fig. 3. It shows that, despite the precautions taken to exclude any laser light from the PMT, a large amount remains. The next trace was obtained by viewing a time region when there is no LIF, but there is blackbody background. The background causes a shift in the d-c level, as expected, but the signal is well within the dynamic range of the PMT; therefore, the signal neither saturates nor decreases the gain because of charge starvation. The lowermost trace is of the total composite signal. We extract the TP's decay time from such signals by painstakingly removing the background and finding the slope of a straight-line fit to the logarithm of the decay curve. The consistently repeatable results over a wide range of temperatures, geometries, and other parameters verify the utility of this simple approach.

The inset of Fig. 6 shows the worst-case data during this

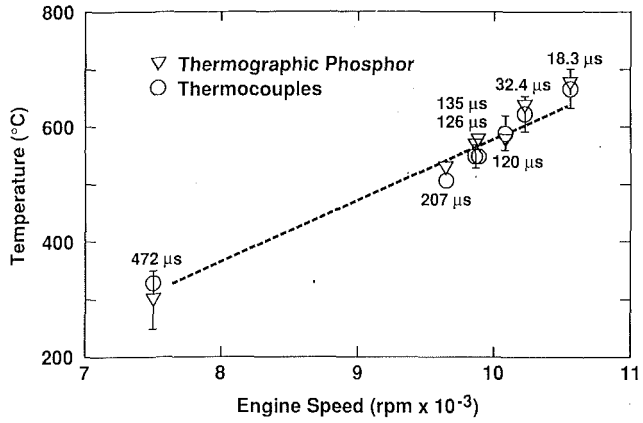


**Fig. 7 Temperature versus engine-speed data obtained using TPs and plotted on same scale as thermocouple data**

experiment: Taken at the highest temperature, the blackbody background is largest and the signal is the smallest. The logarithm can be fit to a reasonable straight line and, as discussed below, the results are acceptable. We did not treat these data to any statistical analysis to find the error bars because we considered such analysis to be outside the scope of the experiment.

Although we did this experiment to evaluate the TP method in an operating engine and not with the intention of acquiring data, we did acquire some data. The results are shown in Fig. 7. Our data are plotted here as a function of engine rpm from idle at about 7500 rpm, to 9643, 9864, 9885, 10,093, 10,225, and 10,568 rpm. Also plotted are the thermocouple data acquired by P&W personnel. The agreement is remarkably good. We conclude that this first test showed the feasibility of using the TP method in operating turbine engines.

## Acknowledgments

We wish to express our most profound gratitude to all the people at P&W whose cooperation and help were crucial to the success of this experiment. Especially deserving of mention are (in alphabetical order) Bill Atkinson, Al Brillant, Marcia Cyr, and Dick Strange, as well as all the engine engineers and the stand crews who participated. We also wish to express our deepest thanks to the Components Branch, Turbine Engine Division, Wright Research and Development Center (WRDC) for funding this project and to our colleague at WRDC, Bill Stange, for his helpful comments and suggestions.

## References

Allison, S. W., et al., 1987, "Remote Thermometry in a Combustion Environment Using the Phosphor Technique," *Proc. SPIE Conf. on Flow Visualization and Aero-Optics in Simulated Environments*, Vol. 788, pp. 90–99.

Allison, S.W., et al., 1988, "Monitoring Permanent-Magnet Motor Heating With Phosphor Thermometry," *IEEE Trans. Instrum. Meas.*, Vol. 37, pp. 637–641.

Cates, M. R., et al., 1984, "Applications of Pulsed-Laser Techniques and Thermographic Phosphors to Dynamic Thermometry of Rotating Surfaces," *ICALEO '84 Proceedings: Inspection, Measurement, and Control*, Vol. 45, pp. 4–10.

Noel, B. W., et al., 1986, "Proposed Laser-Induced Fluorescence Method for Remote Thermometry in Turbine Engines," *J. Propulsion and Power*, Vol. 2, pp. 565–568.

Noel, B. W., et al., 1987, "Evaluating and Testing Thermographic Phosphors for Turbine-Engine Temperature Measurements," presented at AIAA/SAE/ASME/ASEE 23rd Joint Propulsion Conference, San Diego, CA, Paper No. AIAA-87-1861.

Noel, B. W., et al., 1989, "Environmental Tests of Thermographic Phosphors for Turbine-Engine Temperature Measurements," presented at AIAA/ASME/SAE/ASEE 25th Joint Propulsion Conference, Monterey, CA; Paper No. AIAA-89-2913.

**J. M. Hager**
Vatell Corp.,
Blacksburg, VA 24060

**S. Simmons**
Mechanical Engineering Department.

**D. Smith**
Mechanical Engineering Department.

**S. Onishi**
Electrical Engineering Department.

Virginia Polytechnic Institute and State University,
Blacksburg, VA 24061

**L. W. Langley**
Vatell Corp.,
Blacksburg, VA 24060

**T. E. Diller**
Mechanical Engineering Department,
Virginia Polytechnic Institute and State University.
Blacksburg, VA 24061

# Experimental Performance of a Heat Flux Microsensor

*The performance characteristics of a heat flux microsensor have been measured and analyzed. This is a new heat flux gage system that is made using microfabrication techniques. The gages are small, have high frequency response, can measure very high heat flux, and output a voltage directly proportional to the heat flux. Each gage consists of a thin thermal resistance layer sandwiched between many thermocouple pairs forming a differential thermopile. Because the gage is made directly on the measurement surface and the total thickness is less than 2 μm, the presence of the gage contributes negligible flow and thermal disruption. The active surface area of the gage is 3 mm by 4 mm, with the leads attached outside this area to relay the surface heat flux and temperature signals. Gages were made and tested on glass and silicon substrates. The steady and unsteady response was measured experimentally and compared with analytical predictions. The analysis was performed using a one-dimensional, transient, finite-difference model of the six layers comprising the gage plus the substrate. Steady-state calibrations were done on a convection heat transfer apparatus and the transient response was measured to step changes of the imposed radiative flux. As an example of the potential capabilities, the time-resolved heat flux was measured at a stagnation point with imposed free-stream turbulence. A hot-film probe placed outside the boundary layer was used to provide a simultaneous signal showing the corresponding turbulent velocity fluctuations.*

## Introduction

There are many different methods for measuring heat flux to or from a surface, as reviewed by Jones (1977) and Diller and Telionis (1989). Techniques that are applicable in unsteady flows, however, are very few. Most heat flux gages have such long time constants that they cannot make time-resolved measurements in such flows. Several types have been developed recently that make use of thin films that have sufficient time response to be useful in making detailed measurements in unsteady flows.

Because the resistance of thin metal layers can be related to their temperature, they can be used for temperature measurement. When placed on a substrate, a thin metal film can be used to measure the transient surface temperature. If the thermal properties of the substrate are known, a change in the surface heat flux will create a predictable temperature response in the substrate. Conversely, measurements of the time–temperature history of the thin metal film coupled with the appropriate analytical model allow calculation of the surface heat flux history (Jones, 1977; Doorly and Oldfield, 1987; Keltner et al., 1988). The actual signal manipulation can be done with either analogue circuits or by digital signal processing. Because there is no steady-state response, however, such measurements are limited to transient, short-duration flows. Moreover, it is not a simple matter to obtain a reliable unsteady heat flux signal for such transient measurements (Dunn, 1986; George et al., 1987).

A second method using the thin-film resistance element is to measure the power dissipated when a current is passed through the element. Because the substrate always has a slow time response to temperature changes, the thin film must be maintained at a constant temperature. This is done by driving the thin-film resistance with a high-quality feedback control system, such as a constant-temperature anemometer controller

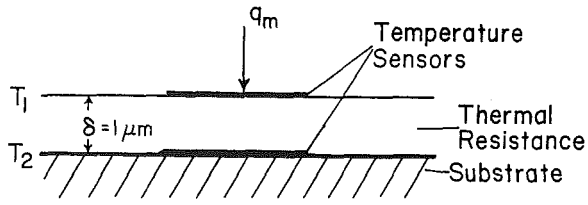


**Fig. 1 Layered heat flux gage**

Contributed by the International Gas Turbine Institute and presented at the 35th International Gas Turbine and Aeroengine Congress and Exposition, Brussels, Belgium, June 11–14, 1990. Manuscript received by the International Gas Turbine Institute, January 15, 1990. Paper No. 90-GT-256.

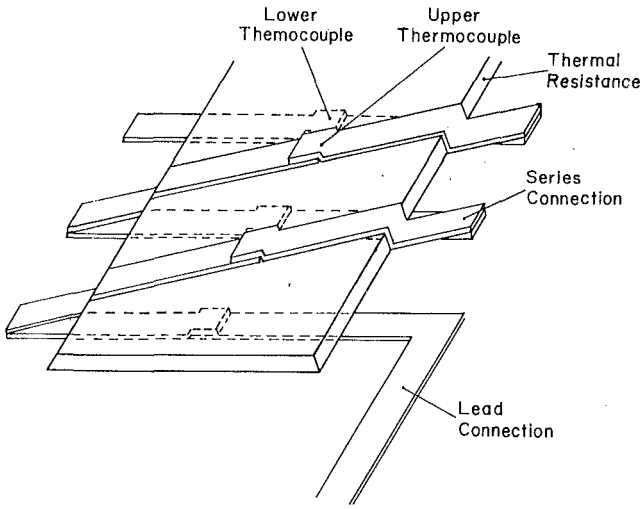


Fig. 2 Isometric view of gage configuration

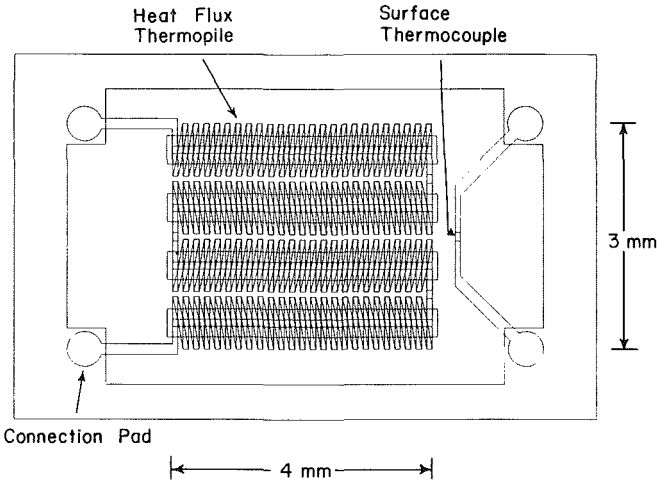


Fig. 3 Microsensor gage pattern overlay

(Campbell et al., 1989; Suarez et al., 1983; Boulos and Pei, 1974; Fitzgerald et al., 1981). Even with a good bridge controller, however, the frequency response is usually limited to about 100 Hz (Campbell et al., 1989). In addition, if the active resistance portion of the gage does not cover the entire gage surface, the resulting nonuniform temperature distribution degrades the transient response of the gage (Beasley and Figliola, 1988).

The third type is a layered heat flux gage as illustrated in Fig. 1. Such gages have been produced and used for many years. The measured temperature difference between $T_1$ and $T_2$ is ideally directly proportional to the heat flux. Because the thickness of the thermal resistance layer in designs previous to the microsensor has been greater than 25 $\mu$m, the time response is greater than 20 ms (Diller and Telionis, 1989). Epstein et al. (1985, 1986) incorporate metal resistance layers in such a gage to measure the temperatures $T_1$ and $T_2$. To overcome the limitation in time response, they effectively operate their layered gage in several different modes. At frequencies above 1500 Hz the rate of change of the temperature $T_1$ is used to determine the flux as with the transient gages described earlier. At low frequencies the steady response is used, and at intermediate frequencies the heat flux is reconstructed through numerical signal processing.

A layered gage using thermocouples for the temperature measurements is described in a paper by Hager et al. (1989). Because the gage was made with microfabrication techniques, the thermal resistance layer could be made two orders of magnitude thinner ($<1$ $\mu$m) than what had been used in previous designs. This provides a number of advantages for this microsensor. First, the time response is greatly reduced. Second, there is little concern for physical or thermal disruption of the surface, even for very high heat fluxes. The major drawback is that the temperature differences to be measured are typically very small. This is overcome by using microfabrication techniques to place many thermocouple pairs in series across the thermal resistance layer, which brings the signal back to a measurable level.

The initial heat flux microsensor was made by photolithography methods as reported by Hager et al. (1989). They reported preliminary results on the steady-state calibration and characterization of the transient response. The present paper reports on fabrication using sputtering with stencil masks. A detailed steady-state calibration and transient response characterization is reported along with samples of measurements of the effect of free-stream turbulence at a stagnation point. This is the first known report of simultaneous measurements of the time-resolved velocity and heat flux for this type of unsteadiness.

## Gage Design and Construction

As illustrated in Fig. 1, a heat flux microsensor is produced by fabricating a thermal resistance layer with temperature sensors on either side. Thermocouples are used to sense the temperature because the voltages produced by each thermocouple pair are additive when placed in series to form a differential thermopile. This is accomplished by depositing six different layers on an electrically insulated substrate. Strips of copper and nickel form the bottom thermocouples, silicon monoxide forms the thermal resistance layer, copper and nickel strips again form the top layer of thermocouples, and a silicon monoxide overcoat provides isolation. The four metal layers must be precisely registered so that the outside edges of all of the individual strips overlap the corresponding strips of the other layer to complete the series circuit. The positions and connections of these layers are illustrated in Fig. 2. The strips must wrap around the sides of the thermal resistance layer to complete the circuit.

Figure 3 shows the enlarged pattern for all six layers overlaid as a complete gage. Ninety-six thermocouples top and bottom are arranged in four rows with two copper signal leads leaving on the left side. In addition, a single thermocouple is positioned on the right side for surface temperature measurement with corresponding leads and pads for instrument connection. The pattern was changed from the earlier work of Hager et al. (1989) to implement a new masking production technique. Copper and nickel were chosen for the thermocouple materials because of their good thermoelectric potential, availability, and good adhesion.

Each of the layers is deposited using a high-vacuum sputtering apparatus. The layer pattern is created by a precisely etched stainless-steel mask clamped to the substrate. Each succeeding layer requires precise placement of a different mask.

## Nomenclature

$E_m$ = microsensor output, $\mu$V
$h_c$ = measured heat transfer coefficient, W/(m$^2$-K)
$q_m$ = convection heat flux of microsensor, W/cm$^2$
$S$ = sensitivity of microsensor, $\mu$V/(W/cm$^2$)
$T_1$ = temperature of upper gage surface, °C
$T_2$ = temperature of lower gage surface, °C
$T_a$ = temperature of air jet, °C
$T_m$ = temperature of microsensor surface, °C

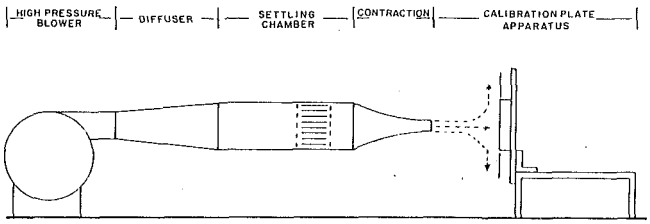


**Fig. 4 Heat flux calibration facility**

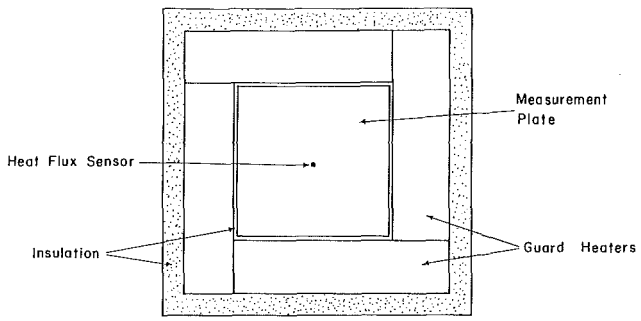


**Fig. 5 Heat flux calibration plate**

The mask and substrate are placed in a holder, which is placed in a stainless-steel chamber. The chamber is pumped to a high vacuum and purged with argon gas. A plasma is created by the rf discharge from a magnetron sputtering S-Gun at a chamber pressure of 2 mtorr. The plasma created between the primary and secondary targets of the material to be sputtered causes the target material molecules to be released toward the substrate. Under proper operation this provides a very pure, uniform, and controlled coating to be deposited on the substrate. The process is repeated for each of the layers, except the silicon-monoxide layer, which forms the thermal resistance. This was made by vapor deposition because the appropriate sputtering targets were not available. The only resulting difficulty is that the layer thickness is not well controlled, which makes prediction of the gage sensitivity more difficult.

## Gage Transient Analysis

A numerical finite-difference model was used to simulate the transient response of the gage. The heat transfer equations were formulated as an implicit finite-difference set of equations for the transient response of each layer and the substrate. Because of the large surface area to thickness ratio of the gage, the program assumes one-dimensional heat flow. Nodes were placed in the center of each layer.

Because of the different material composition of each layer, the thermal resistance between nodes was weighted for the thermal conductivity and thickness of the layers. The implicit formulation led to an $n \times n$ set of simultaneous algebraic equations, which had to be solved for each time step. A tridiagonal matrix solver was used in the program to solve the resulting matrices. The time step was increased geometrically with each step to minimize the number of steps required. The size of the time step was varied to insure negligible influence on the results. Sufficient spatial nodes were placed in the substrate to insure a semi-infinite boundary for the time period investigated.

The material properties used were those of the bulk properties except for those of the silicon monoxide layer. It was found from previous work (Hager et al., 1989) that the apparent thermal conductivity is an order of magnitude lower than the usual bulk values. Therefore, the estimated value of 0.1 W/m°C was used. The thermal diffusivity was assumed

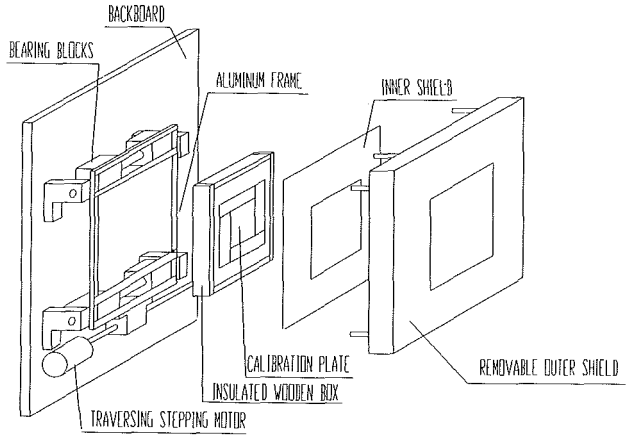


**Fig. 6 Calibration plate assembly**

to be the same as the bulk value. It was estimated that the metal layers covered only one-half of the surface area (equal spacing and strip width). The thermal resistance and capacitance of these layers were, therefore, taken as one-half of that of a full layer.

## Steady-State Calibration

A steady-state calibration was done using a modification of the technique described by Borell and Diller (1987). Because most of the applications of this gage are in convective environments, a convection calibration was considered most appropriate. The apparatus used by Borell and Diller consisted of a large air jet (10 cm × 10 cm), which was directed normal to a flat surface, as illustrated in Fig. 4. At the center of the surface is the calibration plate, which is heated from the backside by an electric resistance heater. Four heated guard plates surround the center plate to insure minimal heat loss from the edges of the center plate (see Fig. 5). This entire assembly is mounted in an insulated box, which is mounted on a track and is translated by a computer-controlled stepping motor. A flow shield surrounds the heated plates in such a way that as the plates are translated the air flow sees the same size surface. This assembly is shown schematically in Fig. 6. The apparatus allows the distribution of heat flux to be determined by a local heat flux gage without altering the flow field. Borell and Diller (1987) determined that for this impinging jet flow, the heat flux over the entire center calibration plate (15 cm × 15 cm) was nearly uniform (±5 percent).

According to the method of Borell and Diller (1987), the gage to be calibrated is placed in the middle of the center plate and the output is compared with the electric power supplied to the plate. The limiting error in the calibration is usually the uncertainty in voltage measurement from the gage itself. In the present case, because the microsensor could not be easily mounted into the calibration plate, the procedure was altered to allow a gage test assembly to be placed on the surface.

Microsensors were made on both silicon and glass substrates. These 2.5 cm × 1.9 cm substrates (1 mm thick) were placed in a special metal test holder with four spring clip connections to the gage terminals, allowing the measurement of the heat flux and surface temperature signals. The test assembly was affixed to the calibration plate using a thermally conductive paste. Eurotherm controllers and SCRs were used to power the heaters and maintain a constant temperature on both the center plate and the surrounding guard plates. The heat flux from the gage was determined from the heat transfer coefficient, $h_c$, previously measured using a Gardon (circular foil) gage in the middle of the calibration plate. For the conditions of the stagnation calibration tests the value of $h_c$ was found to be 104 W/m$^2$•K. The effect of the presence of the test holder, substrate, and spring clips was evaluated from a separate series

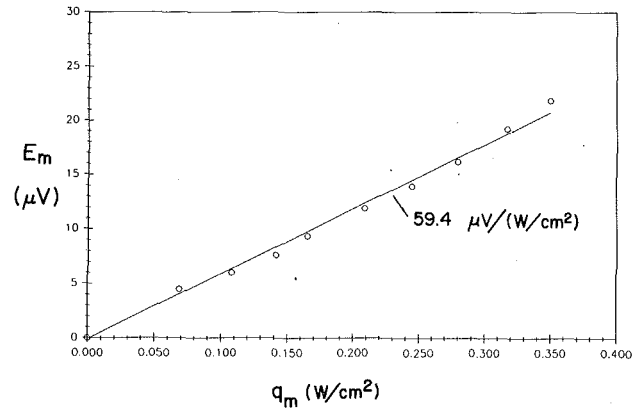


Fig. 7 Steady calibration results

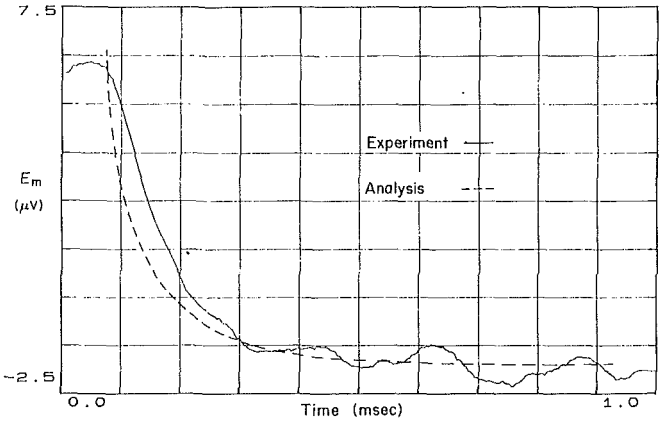


Fig. 8 Transient response to laser step function

of tests to be less than 2 percent. Because of the low operating temperatures used and the low surface emissivity (unoxidized metals), radiation effects were estimated to be less than one percent and were neglected.

$$q_m = h_c\ (T_m - T_a) \tag{1}$$

The microsensor surface temperature, $T_m$, was measured relative to an ice bath using the temperature calibration curve for copper–nickel thermocouples generated by Hager et al. (1989). Because the sputtered materials are very pure, the calibration curves for different thermocouples are very repeatable. The resulting heat flux calibration for a microsensor fabricated on Corning 7059 glass (using equation (1)) is shown in Fig. 7. The line shown is a least-square fit of the experimental data points with a slope of 59.4 $\mu$V/(W/cm$^2$), which is the sensitivity of the gage.

$$S = E_m/q_m \tag{2}$$

The sensitivity of this gage is about 1/3 that of the previous microsensor (Hager et al., 1989) because of a thinner thermal resistance layer and different fabrication processes. The corresponding 95 percent confidence interval determined from the data was ±4.5 percent. Based on the measurement uncertainty of only the voltage output (±0.5 $\mu$V), the average measurement uncertainty for these tests is almost 6 percent. Because the uncertainty is inversely proportional to the voltage output, however, it decreases rapidly as the measured heat flux increases.

## Prediction and Measurement of the Transient Gage Response

Because of the fast time response of the microsensor, an optical method of switching the heat flux incident on the gage was considered necessary to measure the response time. Using a mechanical chopper wheel with a laser, Hager et al. (1989) found that the gage responded faster than the rise time of the input signal, which was about 1 millisecond. To overcome this limitation for the present work, an rf modulating system was used with a Bragg cell. This provided a beam deflection in less than 10 nanoseconds. With proper alignment of the optics, the beam turns on or off in this time period over a wide range of frequencies ($10^{-1}$ Hz to $10^6$ Hz). Because the switching time is much faster than the gage response, the radiant flux appears as a nearly perfect square wave.

The radiation source used was a 5 W argon-gas continuous laser. Because the gage ceramic layers are transparent, a black coating was applied to the gage to absorb the energy at the gage surface. A Lumicolor black marker was successfully used in a similar application by Epstein et al. (1985). This coating was applied over the surface of the gage only for the laser tests. The output signal of the microsensor was run through a Dynamics differential amplifier to reduce the noise and amplify the signal before it was recorded by an HP Digital Signal Analyzer. The results are shown in Fig. 8 for one transient impulse. The gage response is less than 300 microseconds.

To model the transient response numerically, the marker layer over the gage had to be included. Unfortunately, the thickness was not very uniform, varying from 1 $\mu$m to 6 $\mu$m. An average value of 3 $\mu$m was chosen for the model. Appropriate thermal properties were assumed (thermal conductivity of 1.0 W/m °C and thermal diffusivity the same as bulk silicon monoxide). The numerical results for a silicon monoxide thermal resistance layer of 0.8 $\mu$m are shown on Fig. 8 with the experimental results. The match between experiments and analysis is encouraging. When the marker coating is removed, however, the predicted gage response time drops to less than 20 microseconds. This corresponds to a frequency response greater than 50 kHz. The large drop in response time is because it is approximately proportional to the square of the overall thickness and the marker layer was thicker than the entire gage. Better coating processes are being tested to allow a more direct measurement of this response time. Even the minimum response of 3 kHz, however, is sufficient for many new applications, as reported in the next section.

The effect of the substrate on gage response was also included in the transient model. The relatively low thermal conductivity of glass provided a good example of how a nonisothermal boundary condition affected the gage response. Two conclusions could be made from the results. First, the substrate had little effect on the response time of the microsensor. Second, the nodal temperatures of the microsensor layers followed the trend of the substrate surface temperature under all conditions tried. The response time of the gage was also not affected by the level of heat flux applied to the surface.

## Measurement of the Effect of Free-Stream Turbulence

To display one of the potential uses of the transient measurement capability of the gage, a turbulence grid was placed over the exit of the jet nozzle of the convection calibration apparatus (Fig. 4). The 1.25 cm square spacing of the grid created a high level of free-stream turbulence throughout the impinging flow field. To measure the local velocity fluctuations, a hot-film probe was placed near the stagnation point (where the heat flux gage was located) and out from the plate about 5 mm. It, therefore, measured the velocity fluctuations outside the boundary layer near the gage position. The probe was driven by an IFA-100 Constant-Temperature Anemometer. The signal was then linearized and run through a 3 kHz low-pass filter. The signal from the microsensor was also filtered at 3 kHz.

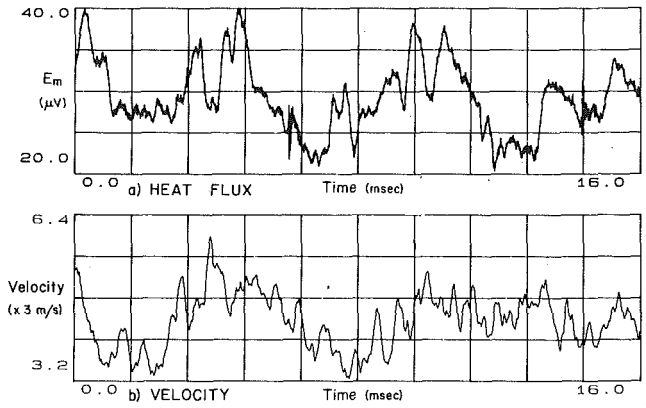


**Fig. 9 Simultaneous time records of turbulence at stagnation point**

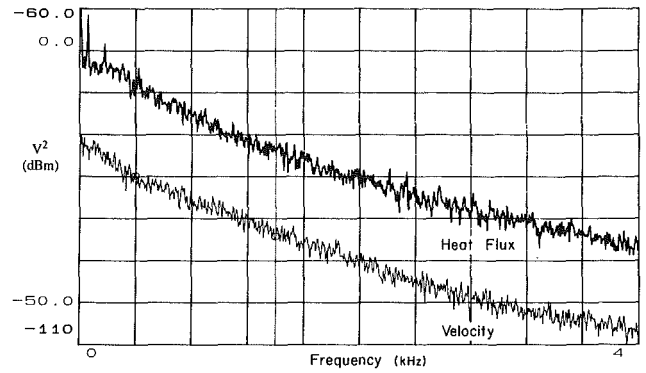


**Fig. 10 Frequency spectra of velocity and heat flux**

A sample of the simultaneous time traces is shown in Fig. 9. The measured free-stream turbulence level at the probe location was 17.2 percent rms. The correlation of the signals is striking even though the velocity probe only measures amplitude and not direction. The velocity signal appears to lead the heat flux, as might be expected based on previous analysis of unsteady flows at a stagnation point (Lighthill, 1954). To the authors' knowledge this is the first reported simultaneous measurement of the time-resolved velocity and surface heat flux due to free-stream turbulence.

Figure 10 shows the frequency spectrum of the velocity and heat flux signals. The velocity turbulence characteristics are similar to those measured earlier with this grid (Gundappa and Diller, 1985). The power spectrum of the heat flux follows almost exactly that of the velocity. This indicates that the size of the fluctuations in heat transfer responding to the velocity fluctuations are not a function of frequency.

As a final note, there has been considerable debate concerning how free-stream turbulence affects the heat transfer at a stagnation point. These time-resolved results taken with the new microsensor give some indication of the answers. The free-stream turbulence clearly penetrates the boundary layer to the surface and causes large local disturbances of the surface transport. This is in agreement with the earlier steady results of Van Fossen and Simoneau (1987) and the unsteady results of Doorly and Oldfield (1985). Moreover, the frequency content of the free stream appears to dominate the frequency content of the surface phenomenon. The boundary layer does not appear to have significant generation or alteration of the turbulence.

## Conclusions

Some of the characteristics and potential of the heat flux microsensor have been presented. Because the gages are thin and are made directly on the material surface, they do not alter the surface fluid flow or heat flux. Consequently, they can safely and accurately measure both heat flux levels and fast transients. The time response has been directly measured to 300 microseconds with predictions to less than 20 microseconds. Because of their high temperature capability and linear output they have a wide variety of applications. Future work includes fabrication on other substrates, particularly metals, which require an added dielectric coating. The example of the time-resolved effect of free-stream turbulence was briefly illustrated. The fundamental insight into this phenomenon provided by these measurements was demonstrated.

## Acknowledgments

This work was supported by the National Science Foundation under Grant No. CBT-8814364. The Government has certain rights on this material. The authors also acknowledge the cooperation of the Hybrid Microelectronics Laboratory of Virginia Polytechnic Institute and State University.

## References

Beasley, D. E., and Figliola, R. A., 1988, "A Generalized Analysis of a Local Heat Flux Probe," *J. Phys. E.: Sci. Instrum.*, Vol. 21, pp. 316–322.

Borell, G. J., and Diller, T. E., 1987, "A Convection Calibration Method for Local Heat Flux Gages," ASME *Journal of Heat Transfer*, Vol. 109, pp. 83–89.

Boulos, M. I., and Pei, D. C. T., 1974, "Dynamics of Heat Transfer From Cylinders in a Turbulent Air Stream," *Int. J. Heat Mass Transfer*, Vol. 107, pp. 767–783.

Campbell, D. S., Gundappa, M., and Diller, T. E., 1989, "Design and Calibration of a Local Heat-Flux Measurement System for Unsteady Flows," ASME *Journal of Heat Transfer*, Vol. 111, pp. 552–557.

Diller, T. E., and Telionis, D. P., 1989, "Time-Resolved Heat Transfer and Skin Friction Measurements in Unsteady Flow," *Advances in Fluid Mechanics Measurements, Lecture Notes in Engineering*, M. Gad-el-Hak, ed., Springer-Verlag, Berlin.

Doorly, D. J., and Oldfield, M. L. G., 1985, "Simulation of the Effects of Shock Ware Passing on a Turbine Rotor Blade," ASME JOURNAL OF ENGINEERING FOR GAS TURBINES AND POWER, Vol. 107, pp. 998–1006.

Doorly, J. E., and Oldfield, M. L. G., 1987, "The Theory of Advanced Multilayer Thin Film Heat Transfer Gauges," *Int. J. Heat Mass Transfer*, Vol. 30, pp. 1159–1168.

Dunn, M. G., 1986, "Time-Resolved Heat-Flux Measurements for the Rotor Blade of a TFE-731-2 HP Turbine," in: *Convective Heat Transfer and Film Cooling in Turbomachinery*, von Karman Inst. for Fluid Dynamics, Rhode Saint Genese, Belgium.

Epstein, A. H., Guenette, G. R., and Yuzhang, C., 1985, "High Frequency Response Heat Flux Gauge for Metal Blading," AGARD CP 390.

Epstein, A. H., Guenette, G. R., and Yuzhang, C., 1986, "High Frequency Response Heat Flux Gauge," *Review of Scientific Instruments*, Vol. 57, pp. 639–649.

Fitzgerald, T. J., Catipovis, N. M., and Javanovic, G. N., 1981, "Instrumented Cylinder for Studying Heat Transfer to Immersed Tubes in Fluidized Beds," *Ind. Eng. Chem. Fundam.*, Vol. 20, pp. 82–88.

George, W. K., Rae, W. J., Seymour, P. J., and Sonnenmeier, J. R., 1987, "An Evaluation of Analog and Numerical Techniques for Unsteady Heat Transfer Measurement With Thin Film Gauges in Transient Facilities," in: *Proc. of the 1987 ASME/JSME Thermal Engineering Joint Conf.*, P. J. Marto and I. Tanasawa, eds., ASME, New York.

Gundappa, M., and Diller, T. E., 1985, "The Effects of Freestream Turbulence and Flow Pulsation on Heat Transfer From a Cylinder in Crossflow," in: *Augmentation of Heat Transfer in Energy Systems*, P. J. Bishop, ed., ASME HTD-Vol. 52, pp. 29–36.

Hager, J. M., Onishi, S., Langley, L. W., and Diller, T. E., 1989, "Heat Flux Microsensors," in: *Heat Transfer Measurements, Analysis and Flow Visualization*, R. K. Shah, ed., ASME, pp. 1–8.

Jones, T. V., 1977, "Heat Transfer, Skin Friction, Total Temperature, and Concentration Measurements," in: *Measurement of Unsteady Fluid Dynamic Phenomena*, Hemisphere Pub. Corp., Washington, DC, pp. 63–102.

Keltner, N. R., Bainbridge, B. L., and Beck, J. V., 1988, "Rectangular Heat Source on a Semi-infinite Solid—An Analysis for a Thin Film Heat Flux Gage Calibration," ASME *Journal of Heat Transfer*, Vol. 110, pp. 42–48.

Lighthill, M. J., 1954, "The Response of Laminar Skin Friction and Heat Transfer to Fluctuations in the Stream Velocity," *Proc. Roy. Soc.*, Vol. A221, pp. 1–23.

Miller, C. G., 1985, "Refinement of an 'Alternate' Method for Measuring Heating Rates in Hypersonic Wind Tunnels," *AIAA J.*, Vol. 23, pp. 810–812.

Suarez, E., Figliola, R. S., and Pitts, D. R., 1983, "Instantaneous Azimuthal Heat Transfer Coefficients From a Horizontal Cylinder to a Mixed Particle Size Air-Fluidized Bed," ASME Paper No. 83-HT-93.

VanFossen, G. J., and Simoneau, R. J., 1987, "A Study of the Relationship Between Free-Stream Turbulence and Stagnation Region Heat Transfer," ASME *Journal of Heat Transfer*, Vol. 109, pp. 10–15.

# Service Temperature Estimation of Turbine Blades Based on Microstructural Observations

J. M. Aurrecoechea

W. D. Brentnall

J. R. Gast

Solar Turbines Incorporated,
San Diego, CA 92138

*Optical and electron metallographic (SEM) examination was performed on MAR-M-421 samples subjected to controlled furnace exposures, to quantify the microstructural changes associated with the prolonged high-temperature exposures. Gamma prime size measurements were used to generate a mathematical model, based on diffusion-controlled kinetics, designed to estimate temperatures. This computational technique was utilized to estimate exposure temperatures of turbine blades that had seen service in land-based gas turbine engines. The engines had accumulated from 1200 to more than 98,000 hours, operating under a variety of conditions. The procedure is generally applicable to commonly used gamma prime strengthened nickel-base superalloys.*

## Introduction

Nickel-base superalloys are used extensively in applications demanding high strength at elevated temperatures, for example in aircraft and land-based gas turbine engines. Many of these alloys derive their strength principally from the presence of an ordered FCC (L12) intermetallic phase, with an approximate composition of $Ni_3$(Al, Ti, Nb, Ta). This phase, commonly referred to as gamma prime, precipitates coherently in a nickel-rich fcc gamma matrix and acts as a barrier to movement of dislocations. Solid solution strengtheners and carbides also contribute to the strength of these alloys.

The strength of a given alloy is a function of volume fraction, particle size, shape, and composition of the gamma prime precipitate. Heat treatment can control these factors to varying degrees. However, substantial microstructural changes occur in these materials when subjected to prolonged elevated temperature exposures (Collins and Quigg, 1968; Collins, 1969). These microstructural variations have a significant effect, and usually an adverse one, on the mechanical properties of the alloy. The changes in mechanical properties can be caused by several time-dependent microstructural modifications, with coarsening or ripening of the gamma prime phase (Collins, 1974) having a major effect. Therefore, understanding of the gamma prime coarsening kinetics is important with respect to component life prediction and assessment, and heat treatments (including repair procedures).

Ardell and Nicholson (1966) demonstrated that gamma prime coarsening in simple binary Ni-Al alloys with low gamma prime volume fraction was in agreement with the volume diffusion-controlled coarsening theories formulated by Lifshitz and Slyozov (1961) and Wagner (1961). These models propose that the average particle radius increases linearly with time raised to the one-third power as described by the following equation:

$$(\bar{r}^3 - \bar{r}_o^3)^{1/3} = kt^{1/3} \tag{1}$$

where $\bar{r}$ = average radius of gamma prime spheres at time $t$ (for cuboidal gamma prime use $a/2$) where $a$ is the mean cube edge; $\bar{r}_o$ = average radius of gamma prime particles at time 0; $k$ = temperature-dependent rate constant; $t$ = time.

Additional work (Chellman and Ardell, 1974) showed that the coarsening behavior of gamma prime in binary Ni-Al and ternary Ni-Cr-Al alloys, with up to 0.60 volume fraction of gamma prime, also obeyed the $t^{1/3}$ law, thus indicating that the coarsening is independent of the gamma prime volume fraction. Furthermore, $t^{1/3}$ diffusion-controlled coarsening kinetics was found to be applicable to complex commercial superalloys (Van der Molen et al., 1971; Stevens and Flewitt, 1979).

The rate constant $k$ in equation (1) can be expressed as

$$k = \frac{8}{9}\frac{\gamma D C V^2}{RT} \tag{2}$$

where $\gamma$ = interfacial free energy of precipitate/matrix interface; $D$ = composite coefficient of diffusion for the various diffusing atom species; $C$ = molar concentration of gamma prime forming elements in equilibrium with a particle of infinite radius; $v$ = molar volume of precipitate; $R$ = gas constant; $T$ = absolute temperature. $\gamma$, $V$, and $R$ are independent of $T$. An Arrhenius model depicts the relationship between $D$ and $T$ as follows:

$$D = Ae^{(-Q/RT)} \tag{3}$$

where $A$ = const; $Q$ = activation energy for diffusion.

If the temperature dependency of $C$ can be disregarded, an Arrhenius relationship exists between $k$ and $T$ (Kolkman, 1981).

Contributed by the International Gas Turbine Institute and presented at the 35th International Gas Turbine and Aeroengine Congress and Exposition, Brussels, Belgium, June 11–14, 1990. Manuscript received by the International Gas Turbine Institute January 14, 1990. Paper No. 90-GT-23.

This relationship can be derived from equations (2) and (3) and expressed as

$$k^3 = (B/T)e^{(-Q/RT)} \quad (4)$$

where $B$ = const. Equation (4) can also take the following form:

$$\ln k^3 T = B - (Q/RT) \quad (5)$$

Therefore a plot of $k^3T$ versus $1/T$ results in a straight line with $Q/R$ as the slope from which $Q$ can be calculated. Once $Q$ is known, $T$ can be estimated. $k^3$ is first calculated from measured values of $\bar{r}$, $\bar{r}_o$, and $t$ using equation (1). Then $T$ is estimated by iteration on the $k^3T$ versus $1/T$ plot.

By means of the above technique, the size of the gamma prime precipitates can be used to estimate the average service temperature of a failed component. The technique can be applied to most gamma prime strengthened nickel-base superalloys.

Most studies regarding the microstructural stability of superalloys, including those mentioned above, have been based on elevated temperature furnace exposures for up to 5000 hours. Time and cost constraints make longer term studies unattractive. Therefore, a program involving the evaluation of blades removed from a number of engines that had accumulated 1200 to 98,000 hours was undertaken. The service temperatures of these blades were estimated by means of an Arrhenius relationship, which was derived using data obtained from samples subjected to controlled furnace exposures. In addition, microstructural features of the high time blade were compared with those of the furnace exposed samples.

## Sample Selection

A number of approximately 0.5 by 0.5 in. square airfoil segments were cut from several unused MAR-M-421 blades. Table 1 shows the nominal chemical composition of MAR-M-421. The blades had been fully heat treated using standard heat treatment parameters for MAR-M-421, according to the schedule outlined in Table 2. The airfoil segments were destined for a variety of furnace exposures.

For the test program, one first-stage turbine blade was removed from each of the twelve Centaur engines undergoing overhaul or repair. The blade alloy in all cases was MAR-M-421. Table 3 provides background information on the subject engines and blades.

## Experimental Procedure

**Furnace Exposure.** The airfoil segments sectioned from unused blades received static air furnace exposures at temperatures ranging from 1500°F (816°C) to 2100°F (1149°C). Exposure times varied from 1 to 5000 hours as shown in Table 4. The samples were air cooled upon removal from the furnace.

**Visual Examination of Blades.** The first-stage blades removed from service engines were examined visually to establish the extent (if any) of blade distress.

**Metallographic Sample Preparation.** The furnace exposure samples, the unexposed sample, and the twelve blades (according to the plan shown in Fig. 1) were sectioned. The specimens were mounted in bakelite and the mounted sections were wet ground on successively finer paper to 600 grit. They were then rough polished using 3-$\mu$m diamond. Final polishing was performed with a colloidal silica suspension. The specimens were etched for both light and electron microscopy using a molybdic acid etch consisting of 3 g $MoO_3$, 100 ml HCl, 100 ml $HNO_3$, and 100 ml $H_2O$.

**Gamma Prime Coarsening.** Gamma prime particle size measurements were made on the furnace exposed samples and on the baseline sample. Photographs of representative areas from each sample were taken with an ISI-SR-50 scanning electron microscope. Gamma prime particle size measurements were made and the average size of 20 particles per sample was calculated. The results were used to generate an $(\bar{r}^3 - \bar{r}_o^3)^{1/3}$ versus $t^{1/3}$ plot.

The $k$ values were determined from this plot and used to create a $k^3T$ versus $1/T$ plot. The $k$ values were introduced into a computer program designed to run iterative calculations on the $k^3T$ versus $1/T$ plot (see Appendix).

**Temperature Estimation.** Gamma prime particle size measurements were taken from 24 airfoil locations on each of the twelve blades (Fig. 2). In addition, gamma prime measurements were also obtained from a firtree section through each blade. Average gamma prime radii were calculated. Temperature estimates were obtained for the blade airfoil locations using the computer code incorporating the MAR-M-421 gamma prime coarsening data. The approximations and assumptions that were made when generating these temperature estimates were:

**Table 1 Nominal composition of MAR-M-421**

| Element | Wt. % | Element | Wt. % |
|---|---|---|---|
| Carbon | 0.15 | Niobium | 2.0 |
| Manganese | 0.20 Max. | Titanium | 1.75 |
| Silicon | 0.20 Max. | Aluminum | 4.25 |
| Chromium | 15.4 | Boron | 0.015 |
| Cobalt | 9.5 | Zirconium | 0.05 |
| Molybdenum | 2.0 | Iron | 1.0 Max. |
| Tungsten | 3.8 | Nickel | Bal. |

**Table 2 Heat treatment schedule for MAR-M-421**

1. 2100°F ± 25°F (1149°C ± 14°C) for 2 Hours ($7.2 \times 10^3$ s), (Vacuum - Rapid Cool).
2. 1950°F ± 25°F (1066°C ± 14°C) for 4 Hours ($1.44 \times 10^4$ s), (Vacuum - Rapid Cool).
3. 1400°F ± 25°F (760°C ± 14°C) for 16 Hours ($5.76 \times 10^4$ s), (Air - Air Cool).

**Table 3 Background information on blades evaluated**

| Engine/Blade Number | Application | Service Time Hours (s) |
|---|---|---|
| 1 | Power Generation | 46,000 ($1.66 \times 10^8$) |
| 2 | Gas Compression | 35,000 ($1.26 \times 10^8$) |
| 3 | Power Generation | 80,000 ($2.88 \times 10^8$) |
| 4 | Gas Compression | 25,000 ($9 \times 10^7$) |
| 5 | Gas Compression | 20,000 ($7.2 \times 10^7$) |
| 6 | Gas Compression | 1,200 ($4.32 \times 10^6$) |
| 7 | Power Generation | 36,700 ($1.32 \times 10^8$) |
| 8 | Gas Compression | 98,000 ($3.53 \times 10^8$) |
| 9 | Gas Compression | 40,000 ($1.44 \times 10^8$) |
| 10 | Gas Compression | 33,000 ($1.19 \times 10^8$) |
| 11 | Gas Compression | 4,000 ($1.44 \times 10^7$) |
| 12 | Gas Compression | 29,650 ($1.07 \times 10^8$) |

Table 4 Furnace exposure matrix

| EXPOSURE TEMPERATURE °F (°C) | EXPOSURE TIME (HOURS) 1 | 10 | 100 | 500 | 1000 | 2000 | 5000 |
|---|---|---|---|---|---|---|---|
| 1500 (816) | | | X | X | X | X | X |
| 1600 (871) | | | X | X | X | X | X |
| 1700 (927) | | | X | X | X | X | X |
| 1800 (982) | | | X | X | X | X | X |
| 1900 (1038) | | | X | X | X | X | |
| 2000 (1093) | | X | X | X | | | |
| 2100 (1149) | X | | | | | | |

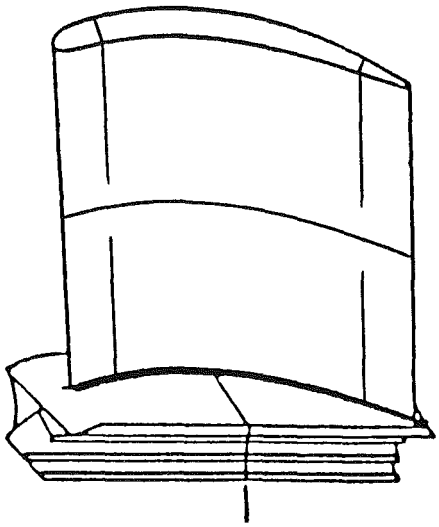

Fig. 1 Sectioning plan for metallographic examination of blades

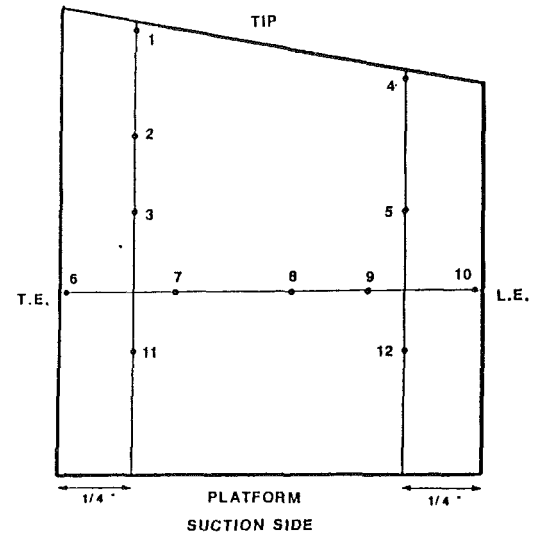


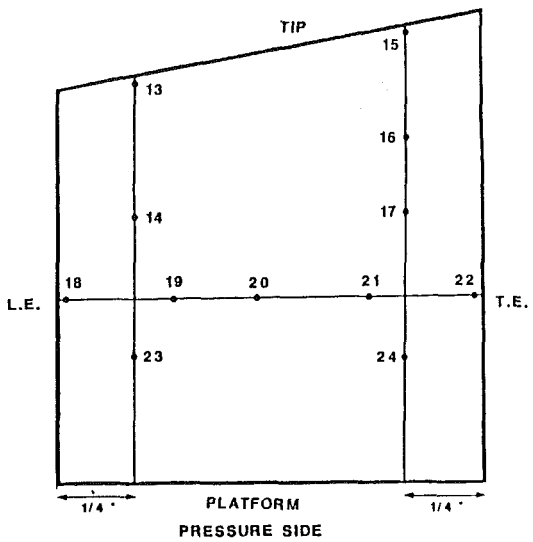


Fig. 2 Blade airfoil locations where maximum oxide penetration was measured; gamma prime temperature estimates were generated at approximately the same location

1 An average (constant) blade metal temperature profile was assumed throughout the operating life of the engines.

2 The service temperatures in the firtree area of the blades were not high enough to produce measurable gamma prime coarsening.

Assumption No. 1 is reasonable for turbine blades that have experienced relatively stable operating conditions such as is generally the case with many industrial gas turbine applications. Assumption No. 2 is valid for the engines under consideration where disk rim temperatures of less than 1250°F (677°C) are normally encountered.

**Metallographic Examination.** Light and electron metallography was performed on the sections prepared from the furnace exposure samples. The microstructural features observed on the high time blade were then compared with those of the furnace exposure samples.

## Results and Discussion

***Visual Examination of Blades.*** Several blades, identified as Nos. 1, 2, 3, and 10, showed no visible deterioration other than the normal discoloration. The distress on the remaining blades could be categorized as being minor (Nos. 4, 9, 11 and 12), intermediate (Nos. 5, 6, and 7), and severe (No. 8). Except for blade No. 8, deterioration was limited to an area between blade midspan and tip. Figure 3 shows the extent of the damage sustained by blade No. 8.

***Gamma Prime Coarsening.*** The gamma prime particle size measurements from the furnace exposure samples are shown in an $(r^3 - r_o^3)^{1/3}$ versus $t^{1/3}$ plot in Fig. 4. The data indicate that in the 1500° to 2000°F (816° to 1149°C) temperature range, the increase in particle radius can be described by equation (1). Therefore, between 1500° and 2000°F, gamma prime coarsening in MAR-M-421 follows the standard $t^{1/3}$ diffusion-controlled kinetics.

The rate constant $k$ increases with temperature as shown by the increasing slope of the lines in Fig. 4. The $k$ values determined from Fig. 3 are presented in a $k^3T$ versus $1/T$ plot (Fig. 5). The slope of the curve in Fig. 5 changes to a higher value for temperatures above 1900°F (1038°C). Nimonic 105 and Nimonic 115 display a similar behavior (Kolkman, 1981). The change in slope is probably due to the increase in solubility of Al and Ti with increasing temperature. The gamma prime solvus temperature for MAR-M-421 is between 2000° and 2100°F (1093° and 1149°C) and can be estimated to be about

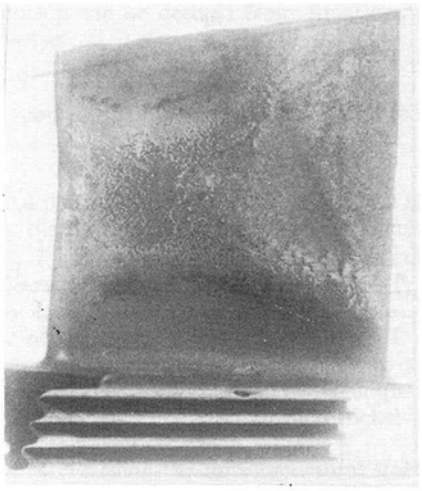

Fig. 3(*a*) Pressure side

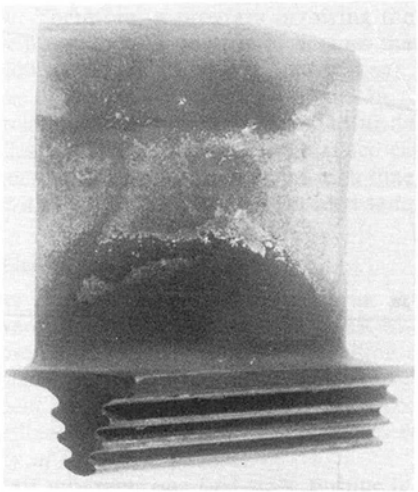

Fig. 3(*b*) Suction side

Fig. 3 Overall views of blade No. 8 (magnification: 1.7×)

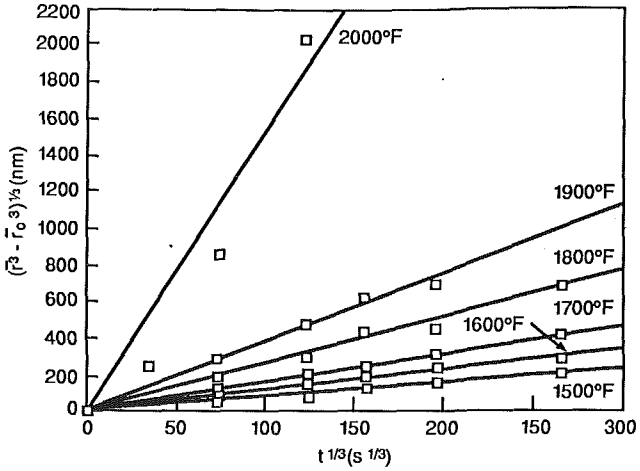


Fig. 4 Coarsening of cuboidal gamma prime in MAR-M-421

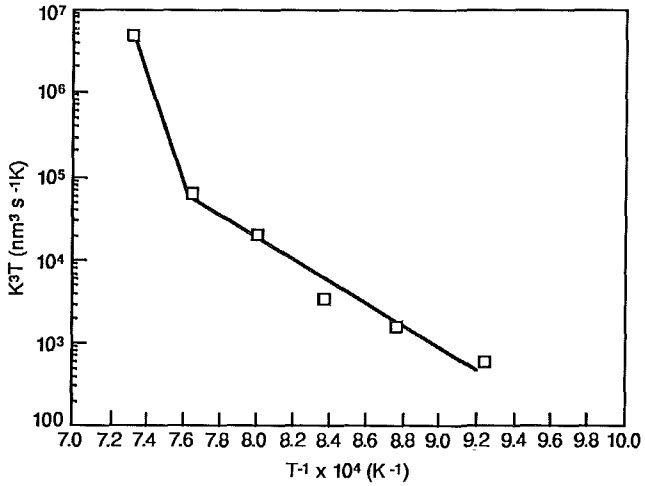


Fig. 5 Temperature dependence of rate constant *K*; the activation energy for coarsening is the slope of the line

2050°F (1121°C) based only on the amount of (Al + Ti + Nb + Ta) (Kolkman, 1981). Therefore, the temperature dependency of $C$ is significant and equations (4) and (5) would have to be rewritten as

$$k^3 = (B'C/T)e^{-(Q/RT)} \tag{6}$$

or

$$\ln(k^3T/C) = B' - (Q/RT) \tag{7}$$

Van der Molen et al. (1971) determined $C$ for the whole range of temperatures studied and used equations (6) and (7) to obtain a straight line relationship of $k^3t$ versus $1/T$ for U700.

The activation energy $Q$ for the coarsening of gamma prime in the furnace exposed samples was calculated from Fig. 5. The activation energy for the 1500° to 1900°F (816° to 1038°C) temperature range was 61.13 kcal mol$^{-1}$ ($2.56 \times 10^5$ J$^{-1}$ mol), which does not differ much from that for diffusion of aluminum or titanium in nickel and from that for coarsening of gamma prime in binary Ni–Al or Ni–Ti alloys (Table 5). However, the activation energy for the 1900° to 2000°F (1038° to 1093°C) range was 271.40 kcal mol$^{-1}$ ($11.38 \times 10^5$ J$^{-1}$ mol). The large discrepancy in the 1900° to 2000°F range is most likely due to the aforementioned temperature dependency of $C$. Van der Molen et al. (1971) measured a large increase in $C$ (70 percent) from 1600° to 2000°F (871° to 1093°C) for U700. A more detailed discussion concerning the accuracy of the activation energy values obtained using equations (4) and (5) is provided by Kolkman (1981).

An existing computer program was modified to incorporate the $k^3T$ versus $1/T$ curve. When applied to the gamma prime particle sizes of the furnace exposed MAR-M-421 samples, the temperature estimates were within −41 and +51°F (−23° and +28°C) of the actual exposure temperatures in the 1500° to 2000°F (816° to 1093°C) range. Taking into account furnace temperature fluctuations of +25°F (14°C), these deviations were considered to be reasonable.

**Temperature Estimation.** Based on the temperature estimates generated at the 24 locations shown in Fig. 2, the temperature ranges at the blade tip, 75, 50, and 25 percent airfoil span were determined. The results are shown in Table 6. In general, the highest temperature ranges are situated at 50 and 75 percent span. Peak temperatures are in locations at, or adjacent to, the airfoil leading edge (either 50 or 75 percent span) and in an area near the blade tip-trailing edge corner. There was no significant difference in average estimated temperatures between the airfoil pressure and suction sides.

Complete operational data on the engines from which the blades were removed was generally unavailable. Therefore, for the most part, it was not possible to establish any correlation between operating conditions and estimated blade temperatures. However, the gas temperatures immediately upstream of the third-stage turbine nozzles (T5) were approximately 1200–1300°F (649°–704°C) and 1670°F (910°C) for engines,

Table 5 Activation energy for element diffusion and gamma prime coarsening

| System or Alloy | Reference | Q Kcal mol-1 (J mol-1) |
|---|---|---|
| Al in Ni | Swalin & Martin (1965) | 64.4 ($2.7 \times 10^5$) |
| Ti in Ni | Swalin & Martin (1956) | 61.4 ($2.57 \times 10^5$) |
| in Ni-Al | Ardell & Nicholson (1966) | 64.4 ($2.7 \times 10^5$) |
| in Ni-Ti | Ardell (1970) | 67.5 ($2.83 \times 10^5$) |
| U700 | Van der Molen et al (1971) | 64.5 ($2.7 \times 10^5$) |
| IN-738 | Stevens & Flewitt (1979) | 64.3 ($2.69 \times 10^5$) |
| MAR-M-421(1) | Present Data | 61.13 ($2.56 \times 10^5$) |
| MAR-M-421(2) | Present Data | 271.40 ($1.14 \times 10^6$) |

(1)1500° - 1900°F (816° - 1038°C)
(2)1900° - 2000°F (1038° - 1093°C)

Table 6 Blade temperature estimates in °F (°C)

| Blade No. | Blade Tip | Location: Airfoil 75% Span | Airfoil 50% Span | Airfoil 25% Span |
|---|---|---|---|---|
| 1 | Up to 1350 (732) | Up to 1330 (721) | Up to 1300 (704) | Up to 1300 (704) |
| 2 | 1440-1445 (782-785) | 1390-1475 (754-802) | 1410-1475 (766-802) | 1370-1475 (743-802) |
| 3 | Up to 1325 (718) | Up to 1290 (699) | 1275-1365 (691-741) | Up to 1275 (691) |
| 4 | 1435-1480 (779-804) | 1435-1480 (779-804) | 1420-1470 (771-799) | 1430-1475 (777-802) |
| 5 | 1445-1530 (785-832) | 1520-1565 (827-852) | 1485-1555 (807-846) | 1485-1490 (807-810) |
| 6 | 1675-1730 (913-943) | 1670-1725 (910-941) | 1675-1735 (913-946) | 1605-1670 (874-910) |
| 7 | 1360-1490 (738-810) | 1440-1445 (782-785) | 1430-1495 (777-813) | 1380-1410 (749-766) |
| 8 | Up to 1400 (760) | 1400-1460 (760-793) | 1475-1575 (802-857) | 1380-1440 (749-782) |
| 9 | 1385-1445 (752-785) | 1380-1435 (749-779) | 1225-1370 (663-743) | 1225-1400 (663-760) |
| 10 | 1445-1490 (785-810) | 1455-1505 (791-818) | 1430-1485 (777-807) | 1445-1450 (785-788) |
| 11 | 1485-1555 (807-846) | 1525-1565 (829-852) | 1525-1560 (829-849) | 1525-1555 (829-846) |
| 12 | 1260-1440 (682-782) | 1395-1425 (757-774) | Up to 1320 (716) | 1260-1350 (682-732) |

Nos. 3 and 6, respectively. 1670°F (910°C) is considerably higher than the nominal peak T5 temperature and the peak estimated temperature [946°C (1735°F)] of the corresponding first-stage blade reflects the above discrepancy. The much lower T5 value for engine No. 3 resulted in a much lower peak temperature for blade No. 3 [741°C (1365°F)] when compared with blade No. 6.

**Metallographic Examination of Furnace Exposure Samples.** The microstructure of MAR-M-421 in the heat-treated condition consists of cuboidal gamma prime and a relatively smaller spheroidal gamma prime in a gamma matrix (Fig. 6). Intragrannular and grain boundary carbides can also be observed. The carbides display a mostly script-like morphology (probably an MC type carbide) although block carbides (probably an MC or an $M_6C$ type carbide) are also present.

The most obvious change resulting from exposures at intermediate temperatures (1500° to 1800°F, or 816° to 982°C) consists of the formation of grain boundary gamma prime films (Figs. 7*A*-7*D*). Blocky carbides, similar in appearance to carbides identified as $M_{23}C_6$ type in U-700, IN-100 (Collins, 1969), and René 80 (Collins, 1974), line the grain boundaries. Coarsening and spheroidization of the cuboidal gamma prime are also evident. With time at temperature, gamma prime coarsening and spheroidization progress, grain boundary gamma prime films widen, and the grain boundary carbides grow and become more continuous. These changes occur more rapidly with increasing temperature. Fine spheroidal gamma prime can only be observed at 1500°F for exposures under 1000 hours. After 5000, 1000, and 100 hours at 1600°, 1700°, and 1800°F, respectively, the script carbides begin to decompose. Decomposition of MC carbides has been formulated as MC plus gamma matrix dissociating into $M_6C$ and/or $M_{23}C_6$ plus gamma prime in several alloys by Danesi et al. (1966), Murphy et al. (1967), and Collins (1969, 1974).

At temperatures of 1900°F (1038°C) and above, gamma prime coarsening and spheroidization occur very rapidly. In addition, appreciable gamma prime solutioning can be observed at all exposure times. No attempt was made to identify and characterize the very fine spheroidal gamma prime particles, which usually form upon cooling after exposure at temperatures approaching the gamma prime solvus temperature. Complete gamma prime solutioning occurred after one hour at 2100°F (1149°C). Wide grain boundary gamma prime films and large grain boundary carbides are visible for exposures up to 500 hours at 1900°F. However, at longer times and higher temperatures, the grain boundary gamma prime films and carbides start to break down. Script carbides exist at 1900° and 2000°F up to 1000 and 10 hours exposure, respectively. After longer exposures, the script carbides appear to have decomposed.

**Metallographic Examination of Blades.** Examination of the blade sections revealed no indication of hot corrosion. However, evidence of high-temperature oxidation was found on most blades. Blades 1, 3, and 11 exhibited no measurable amount of oxidation. The depth of internal oxidation or maximum penetration was measured metallographically at 24 locations on the airfoil of the blades per Fig. 2. Total metal loss cannot be measured because the original blade thickness at the particular section examined is unknown. The results of the maximum penetration measurements are summarized in Table 7.

The maximum penetration varied considerably from blade to blade. The highest oxide depth ranges were generally located at 50 and 75 percent span. Furthermore, the greatest depths of internal oxidation were consistently found at an area at and adjacent to the airfoil leading edge between 50 and 75 percent span (locations 5, 9, 10, 14, 18 and 19) and at the blade tip-trailing edge corner (locations 1, 15, and 16). Therefore, the

Table 7 Depth of maximum oxide penetration in 0.001 in. (μm)

| Blade No. | Blade Tip | Location: Airfoil 75% Span | Airfoil 50% Span | Airfoil 25% Span |
|---|---|---|---|---|
| 2 | 0.4-3.2 (10-81) | 0.4-3.6 (10-91) | 0-3.6 (0-91) | 0-0.8 (0-20) |
| 4 | 2.8-4.8 (71-122) | 3.6-4.0 (91-102) | 3.6-5.6 (91-142) | 2.0-3.6 (51-91) |
| 5 | 1.6-5.2 (41-132) | 2.8-6.8 (71-173) | 2.8-8.0 (71-203) | 2.0-3.6 (51-91) |
| 6 | 0.8-4.0 (20-102) | 1.2-3.6 (30-91) | 1.6-4.0 (41-102) | 0.8-1.6 (20-41) |
| 7 | 2.0-7.6 (51-193) | 0.8-6.8 (20-173) | 0.8-9.2 (20-234) | 0.8-4.0 (20-102) |
| 8 | 2.4-8.8 (61-224) | 2.8-14.4 (71-366) | 4.4-17.2 (112-437) | 8.8-10.8 (224-274) |
| 9 | 1.6-3.2 (41-81) | 1.6-2.8 (41-71) | 0.8-2.0 (20-51) | 0.4-0.8 (10-20) |
| 10 | 2.0-4.8 (51-122) | 3.2-6.0 (81-152) | 1.6-5.2 (41-132) | 0.8-1.2 (20-30) |
| 12 | 2.8-6.0 (71-152) | 2.4-4.4 (61-112) | 0.8-2.0 (20-51) | 0.8-1.2 (20-30) |

Fig. 6(*a*) Optical (Mag: 1000×)

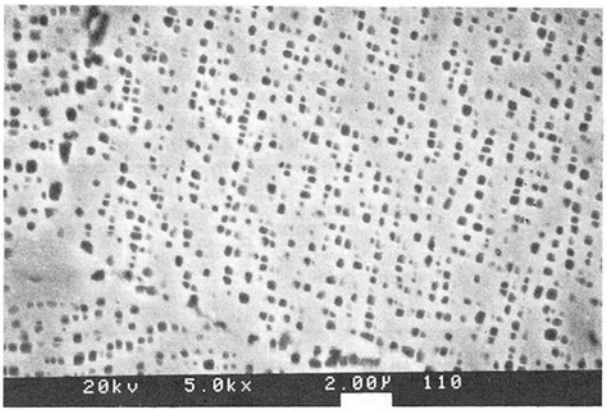


Fig. 6(*b*) SEM (Mag: 5000×)

Fig. 6 Microstructure of unexposed MAR-M-421 sample

areas of the blades exhibiting the greatest depths of oxidation corresponded to the areas where the highest temperatures were estimated. However, efforts to plot the individual values of maximum penetration versus the estimated temperature or a temperature-dependent parameter, such as the Larson–Miller parameter, did not yield meaningful correlations. Differing oxide scale spallation may have resulted in a variation in maximum penetration even between areas exposed to approximately the same temperatures.

Figure 8 illustrates the appearance of the external oxide scale and alloy depletion layer of blade No. 8. Dark and blocky internal oxides are uniformly distributed in the alloy depletion layer. Energy dispersive X-ray analysis showed that the oxide scale consisted of a mixture of chromium, nickel, cobalt, and titanium oxides and/or mixed oxides (spinels). Dark colored aluminum oxide ($Al_2O_3$) and gray colored chromium oxide ($Cr_2O_3$) particles are visible in areas of the alloy depleted zone adjacent to the external oxide scale. However, aluminum oxide was much more abundant than chromium oxide at areas of the alloy depleted zone away from the oxide scale.

These microstructures agree with the generally accepted theories of high temperature oxidation. MAR-M-421 has a relatively high chromium content (15.5 weight percent) and therefore is predominantly a $Cr_2O_3$ scale former. Selective oxidation of aluminum, which has the greatest affinity for oxygen, occurs underneath the external oxide scale. However, the amount of aluminum present in MAR-M-421 (4.25 weight percent) is insufficient to form a continuous $Al_2O_3$ layer. Once all the aluminum has been consumed, chromium also oxidizes internally. Eventually the aluminum and chromium depleted matrix oxidizes and a mixture of oxides results.

The metallographic sections obtained from blade No. 8, which had been in service for about 100,000 hours, were carefully examined to assess the microstructural changes associated with prolonged high-temperature exposure. The microstructures observed at the blade airfoil were compared with the microstructure at the blade firtree area.

Figure 9 shows that the blade firtree area microstructure does not differ greatly from that of the unexposed MAR-M-421 sample. Script and blocky carbides, similar to those of the unexposed sample, can be observed. The most patent difference is that the gamma prime in the blade firtree area is somewhat coarser than that in the unexposed sample. This difference is most likely attributable to variations, within the specified ranges, between the heat treatments received by the unexposed sample and blade No. 8.

The areas of the blade exposed to the highest temperatures (1500° to 1575°F or 816° to 857°C) display a number of microstructural alterations. The most obvious change is the spheroidization and coarsening of the cuboidal gamma prime (Fig. 10). The small spheroidal gamma prime is absent in these areas. Well-developed gamma prime films surround carbides and line grain boundaries. Blocky carbides, similar to but larger than those observed in the samples exposed between 1500° and 1800°F (816° and 982°C), are found along grain boundaries. The size of the gamma prime and of the intragranular carbides, and the width of the grain boundary gamma prime films, are not surprising, considering the extremely long service time accumulated by the blade. The service temperatures in these areas were not high enough to result in the noticeable decrease in gamma prime volume fraction from the levels observed in the blade firtree area.

An acicular phase is evident in some locations subjected to temperatures between 1500° and 1575°F (816° to 857°C) (Fig. 11). This phase resembles an acicular phase identified as an $M_6C$ type carbide in B-1900 (Danesi et al., 1966; Collins, 1969, 1974), in René 80 (Collins, 1974), and in MAR-M-200, MAR-M-246, and TRW-NASA VIA (Collins, 1969). Acicular $M_6C$ was observed after prolonged exposures at 1600° and 1800° F (871° and 982°C) in B-1900, between 1400° and 1600°F (760° and 871°C) in René 80, and between 1600° and 2000°F (871° and 1093°C) in MAR-M-200, MAR-M-246, and TRW-NASA VIA.

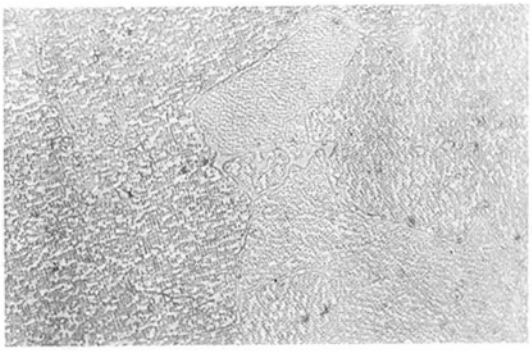

Fig. 7(*a*) 1500°F (816°C)/5000 hours (mag: 1000×)

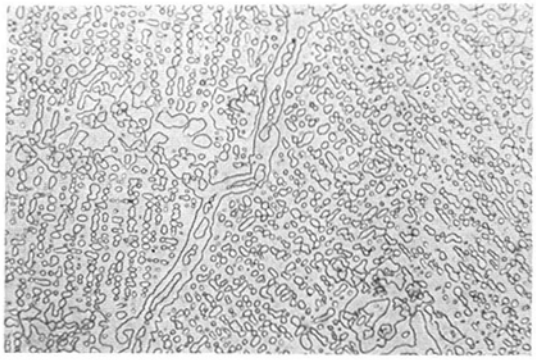

Fig. 7(*d*) 1800°F (982°C)/5000 hours (mag: 1000×)

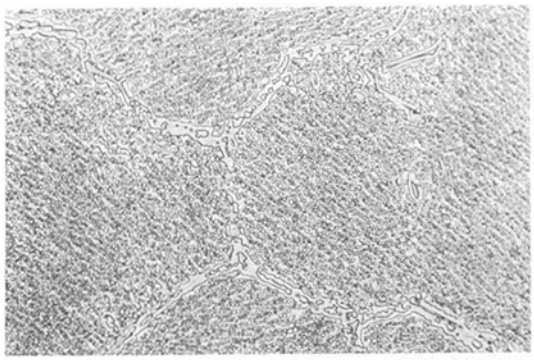

Fig. 7(*b*) 1600°F (871°C)/5000 hours (mag: 1000×)

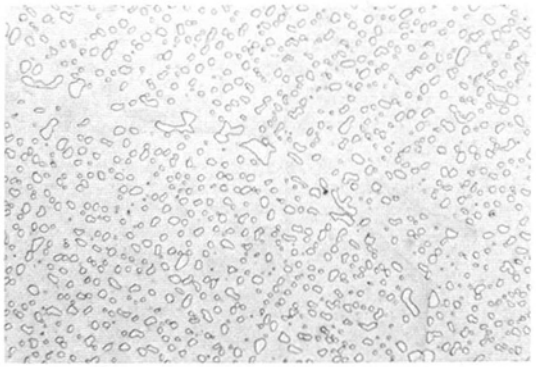

Fig. 7(*e*) 1900°F (1033°C)/5000 hours (mag: 1000×)

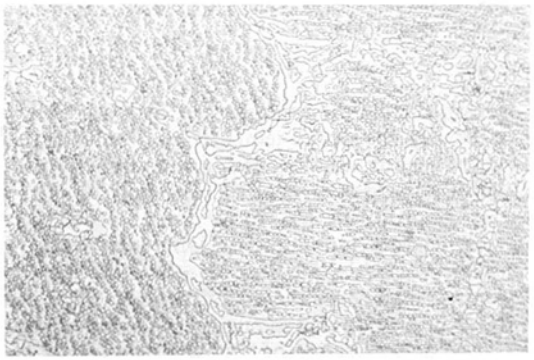

Fig. 7(*c*) 1700°F (927°C)/5000 hours (mag: 1000×)

Fig. 7(*f*) 2000°F (1093°C)/500 hours (mag: 1000×)

Fig. 7 Microstructure of furnace exposed MAR-M-421 samples

In areas exposed to temperatures between 1400° and 1500°F (760° and 816°C), degenerated script carbides are visible (Fig. 12). Similarly altered carbides were found in René 80 after prolonged exposure at 1700°F (927°C) (Collins, 1974). The resulting carbide was identified as an $M_{23}C_6$ type produced by the decomposition of the script-like MC carbide.

In certain locations exposed to temperatures between 1400° and 1500°F (760° and 816°C), directional gamma prime coarsening or rafting can be observed (Fig. 13). These locations correspond to areas where both the stress level and the temperature were relatively high. The phenomenon of rafting has been studied in single-crystal blade alloys and shown to be a function of time, temperature, and stress (Draper et al., 1989). No rafting was found near the blade tip where stresses were low and near the blade platform where the temperatures are relatively low. Rafting was observed at both the blade leading and trailing edges at approximately blade midspan and in both areas resulted in gamma prime elongated in a direction normal to the main stress axis. No rafting is visible in the unstressed exposure samples.

## Conclusions

Gamma prime coarsening in MAR-M-421 appears to follow a previously established model, which follows the standard $t^{1/3}$ diffusion-controlled kinetics. The activation energy $Q$ obtained for the 1500° to 1900° F (816° to 1038°C) range was fairly close to that reported for other alloys, despite disregarding the variation of $C$ with temperature. This temperature dependency is the most likely explanation for the extremely large value of $Q$ obtained for the 1900° to 2000°F (1038° to 1093°C) range. With these considerations in mind, the temperature estimates generated for the furnace exposure samples can be regarded as reasonably accurate.

Reasonably accurate estimates can also be achieved for turbine blades that have experienced relatively stable operating conditions. More uncertainties are involved when using the gamma prime coarsening method for estimating service temperatures of turbine blades subjected to complex and variable service conditions. However, when applied carefully the method can be a valuable tool for determining service conditions. The

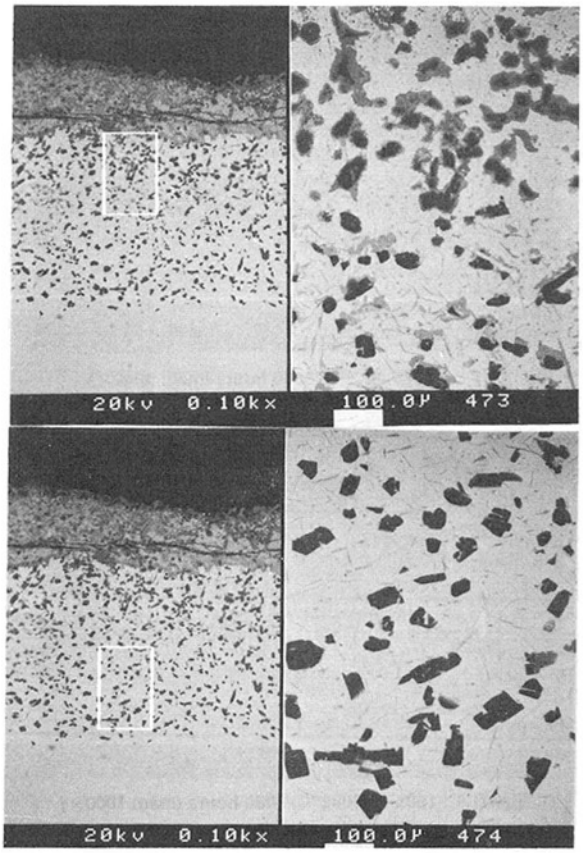


Fig. 8 Dual magnification (100×/500×) SEM micrographs showing evidence of high-temperature oxidation on blade No. 8; note change in microstructure of the internally oxidized alloy depletion zone as a function of the distance from the external oxide scale

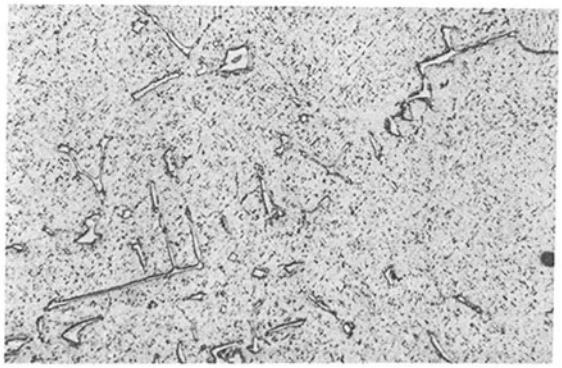

Fig. 9(*a*) MAG: 532×

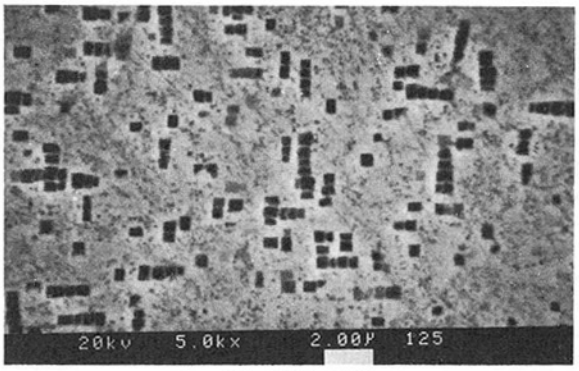


Fig. 9(*b*) MAG: 5000×

Fig. 9 Microstructure of firtree area of blade No 8

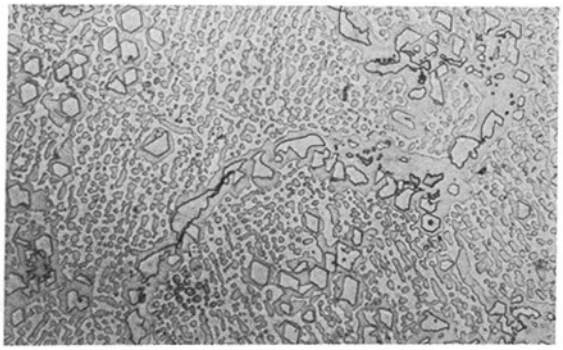

Fig. 10(*a*) MAG: 1000×

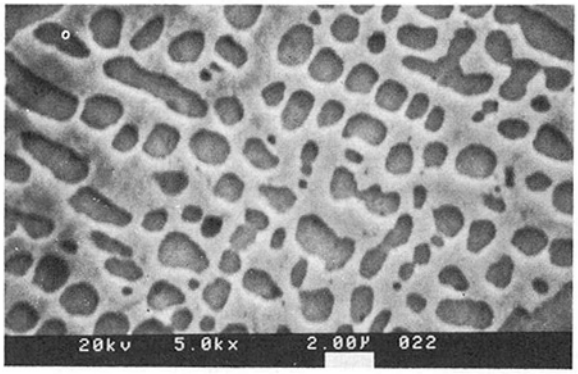


Fig. 10(*b*) MAG: 5000×

Fig. 10 Microstructure of areas in blade No. 8, which experienced temperatures above 1500°F (816°C)

model developed from the exposure test data was able to differentiate between the service temperature of a blade that was exposed at, or near to, nominal design temperature (blade No. 3) and that of a blade that experienced a short term overtemperature condition (blade No. 6) as well as providing fairly accurate temperature estimates for long-term service exposures. It also provides a method for obtaining temperature distributions or maps over the airfoil surface. Such data are of significant interest to design engineers for purposes of life prediction and determination of cooling effectiveness as in air cooled airfoils. The gamma prime coarsening method for temperature estimation of thermally exposed samples is generally applicable to all gamma prime strengthened nickel-base superalloys.

Metallographic examination of the furnace exposure samples revealed microstructural changes resembling those experienced by other gamma prime strengthened nickel-base superalloys. Gamma prime coarsening and spheroidization occurs more rapidly as exposure temperature increases. At 1900° and 2000°F (1038° and 1093°C) gamma prime solutioning is noticeable. Script and blocky carbides (probably MC type) are stable at 1500°F (816°C) and through 2000 hours at 1600°F (871°C). Decomposition of MC type carbides to $M_6C$ and/or $M_{23}C_6$ types, similar to that observed in other alloys is evident at 1600° to 1800°F (871° to 982°C). Script carbides are visible after short exposures at 1900°F (1038°C) but after 2000 hours, blocky carbides predominate. Blocky carbides are also present after 500 hours at 2000°F (1093°C).

The microstructure at the airfoil of blade No. 8 shows features similar to those seen in the furnace exposure samples. However, microstructural features such as grain boundary gamma prime films and decomposed carbides are present at areas of the blade exposed to temperatures (estimated) lower than those of the exposure samples. This would imply a different rate dependence with temperature for formation of

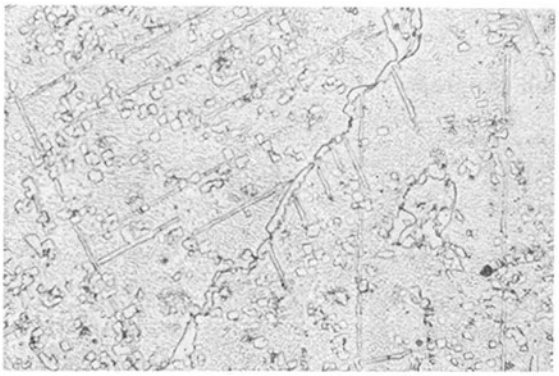

Fig. 11 Acicular phase found in some areas of blade No. 8, which experienced temperatures of 1500°F (816°C) (magnification: 532×)

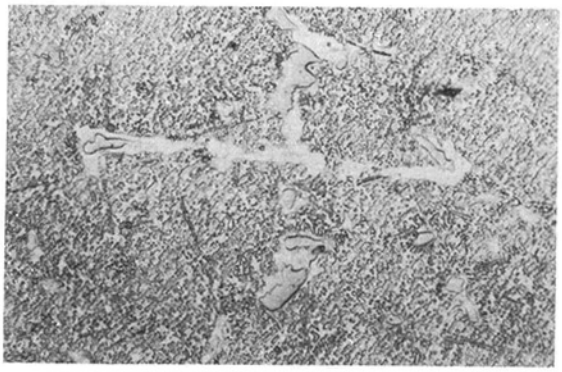

Fig. 12 Degenerated script carbide (magnification: 1000×)

gamma prime grain boundary films compared to gamma prime coarsening. The presence of the above features at lower temperatures reflects the extremely long service life of blade No. 8. Two features observed on blade No. 8 were not seen in the exposure samples. An acicular phase, possibly an $M_6C$ type carbide, and gamma prime rafting were unique to blade No. 8. Rafting resulted from a favorable combination of stress and temperature.

## References


Ardell, A. J., 1970, "The Growth of Gamma Prime Precipitates in Aged Ni-Ti Alloys," *Metallurgical Transactions*, Vol. 1, pp. 525–534.

Ardell, A. J., and Nicholson, R. B., 1966, "The Coarsening of Gamma Prime in Ni-Al Alloys," *Journal of Physics and Chemistry of Solids*, Vol. 27, pp. 1793–1804.


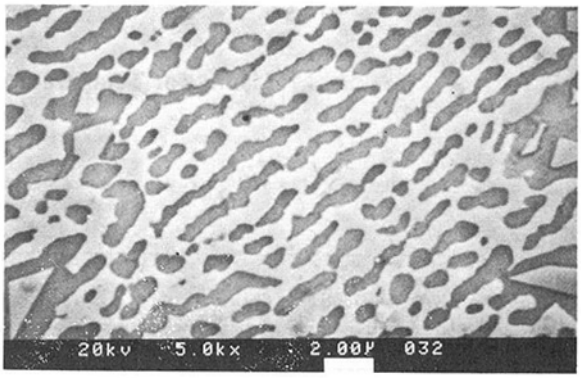


Fig. 13 Directional gamma prime coarsening or rafting observed at blade No. 8; midspan area near leading edge (magnification: 5000×)


Chellman, D. J., and Ardell, A. J., 1974, "The Coarsening of Gamma Prime Precipitates at Large Volume Fractions," *Acta Metallurgica*, Vol. 22, pp. 577–588.

Collins, H. E., 1969, "Relative Long-Time Stability of Carbide and Intermetallic Phases in Nickel-Base Superalloys," *Transactions of American Society for Metals*, Vol. 62, No. 1, pp. 82–104.

Collins, H. E., 1974, "The Effect of Thermal Exposure on the Microstructure and Mechanical Properties of Nickel-Base Superalloys," *Metallurgical Transactions*, Vol. 5, pp. 189–204.

Collins, H. E., and Quigg, R. J., 1968, "Carbide and Intermetallic Instability in Advanced Nickel-Base Superalloys," *Transactions of American Society for Metals*, Vol. 61, No. 1, pp. 139–148.

Danesi, W. P., Donachie, M. J., and Radavich, J. F., 1966, *Transactions of the American Society for Metals*, Vol. 59, pp. 505–516.

Draper, S., Hull, D., and Dreshfield, R., 1989, "Observations of Directional Gamma Prime Coarsening During Engine Operation," *Metallurgical Transactions A*, Vol. 20A, pp. 683–688.

Kolkman, H. J., 1981, "Coarsening and Solutioning of Precipitates in Superalloys," National Aerospace Laboratory, Amsterdam, The Netherlands, NLR TR 81114 U.

Lifshitz, I. M., and Slyozov, V. V., 1961, "The Kinetics of Precipitation From Supersaturated Solid Solutions," *Journal of Physics and Chemistry of Solids*, Vol. 19, pp. 35–50.

Murphy, H. J., Sims, C. T., and Heckman, G. R., 1967, "Long-Time Structures and Properties of Three High-Strength, Nickel-Base Alloys," *Transactions American Institute of Mining, Metallurgical, and Petroleum Engineers*, Vol. 239, pp. 1961–1978.

Stevens, R. A., and Flewitt, P. E. J., 1979, "The Effects of Gamma Prime Precipitate Coarsening During Isothermal Aging and Creep of the Nickel-Base Superalloy IN-738," *Materials Science and Engineering*, Vol. 37, pp. 237–247.

Swalin, R. A., and Martin, A., 1956, "Solute Diffusion in Nickel-Base Substitutional Solid Solutions," *Transactions American Institute of Mining, Metallurgical, and Petroleum Engineers*, Vol. 206, pp. 567–572.

Van der Molen, E. H., Oblak, J. M., and Kriege, O. H., 1971, "Control of Gamma Prime Particle Size and Volume Fraction in the High Temperature Superalloy Udiment 700," *Metallurgical Transactions*, Vol. 2, pp. 1627–1633.

Wagner, C., 1961, "Theorie der Alterung von Niederschlagen durch Umlösen (Ostwald-Reifung)," *Zeitschrift fuer Elektrochemie*, Vol. 65, pp. 581–591.

# APPENDIX

## Listing for Temperature Estimation Program

```
1000 '                                  ******************************
1020 '                                  *   GAMMA PRIME CALCULATION  *
1030 '                                  *    LAST REVISION 8-23-89   *
1050 '                                  ******************************
1060 '
2000 ' ------------------------------------------- FUNCTIONS ----------------------------------------------
2010 '
2020 DEF FNA (KT) = 13408.9 / (14.98314 - (LOG(KT)/LOG(10)))
2030 DEF FNB (KT) = 59528.23 / (50.25533 - (LOG(KT)/LOG(10)))
2050 '
3000 ' ------------------------------------------- DATA INPUT ---------------------------------------------
3010 '
3020 '
3030 KEY OFF: CLS
3050 INPUT "Total time (Hours) ................................";H
3060 INPUT "Initial gamma prime mean radius (nm).";R1
3070 LOCATE 4,1 :INPUT "Final gamma Prime mean radius (nm) . . .";R2
3080 '
3090 S=H*3600
3100 K=(R2^3-R1^3)/S
3110 Z=0    ' RESET TO ZERO FOR EACH RUN
3120 '
3130 PRINT "Total time at temp.  (Seconds) . . . . . .  " S
3140 PRINT "K^3= . . . . . .  "; K
3150 PRINT "Temp. range =  800  TO 2000 °K."
3160 LOCATE 10,25  :PRINT "
3170 LOCATE 25,1   :PRINT "CALCULATING";: LOCATE 10,1
3180 '
4000 '-------------------------------------------CALCULATIONS AND SEARCH LOOP ----------------------------
4010 '
4020 '
4030 T3=(T2-T1)/4
4040 FOR T= 800 TO 2000
4050    KT = K*T
4060    F = (T - 273) * 1.8 + 32
4080    IF F <= 1900 THEN X = FNA(KT)
4090    IF F >  1900 THEN X = FNB(KT)
4100    IF X >  T - .5 AND X < T +.5 THEN 5000
4110 NEXT T
4120 '
4130 PRINT "NO SOLUTION FOUND ": GOTO 6000
4140 '
5000 '------------------------------------------------------------------ OUTPUT ------------------------------
5010 '
5020 '
5030    PRINT "CALCULATED TEMPERATURE, "; T "°K              "; F "°F"
5040    PRINT "=================================          ============"
5050 '
6000 '------------------------------------------------------------------ END ---------------------------------
6010 '
6020 LOCATE 25,1 :PRINT "                  ";
6030 LOCATE 18,1
6040 PRINT "  1. RUN AGAIN "
6050 PRINT "  2. CHANGE FINAL RADIUS ONLY"
6060 PRINt "  3. END"
6070 PRINT "                              "
6080 LOCATE 21,1: INPUT "Enter selection #"; CH
6090 IF CH=1 THEN RUN
6100 IF CH=2 THEN GOTO 3070
6110 IF CH=3 THEN SYSTEM
```

# The Use of Semi-Conductor Sensors for Blade Surface Pressure Measurement in a Model Turbine Stage

R. W. Ainsworth

A. J. Dietz

Department of Engineering Science,
Oxford University,
Oxford OX1 3PJ United Kingdom

T. A. Nunn

Kulite Semi-Conductor Inc.,
Leonia, NJ

*The development of semi-conductor sensors particularly aimed at gas turbine technology applications is outlined. Methods of manufacture and means of utilizing some of the inherent advantages of this type of sensor are discussed. A novel technique, where miniature sensors are attached directly to the surface where the measurement is required, is described. This technique combines a high surface density of measurement points with a high frequency response capability. Detailed tests of the sensor's performance have been conducted and results obtained using this technology are presented. The performance tests include frequency response, base strain sensitivity, g sensitivity, and software temperature compensation schemes. Finally, possible future applications for these techniques in gas turbine technology are outlined.*

## Introduction

The Oxford Rotor Facility has been built in response to a need for accurate data obtained at conditions close to those found in the high-pressure stage of a modern aircraft gas turbine. The aims of the experiment are twofold. The first is to gain an understanding of the physics of this complex flow and the various phenomena present. The second is to provide detailed flowfield measurements for the validation of three-dimensional time-averaged and also unsteady flow prediction computer codes. Much experimentation has previously been carried out in two and three-dimensional cascades, and in rotating facilities with varying degrees of simulation. At Oxford, the turbine blade profile currently being tested in the Rotor Facility has already been extensively tested by Nicholson [1] and King [2] in a two-dimensional linear cascade and by Doorly et al. [3, 4, 5] with simulated wake and shock passing in his rotating bar experiment. As the understanding of the flow grows and the predictions become more complex, there is a corresponding need for increasingly accurate experimental simulations. The main problem faced by the experimenter is that the detailed and highly sensitive instrumentation required to record the flow information cannot survive in the hostile engine environment. This problem can be tackled from two directions: Either the important engine conditions (in terms of nondimensional parameters) may be simulated in a manner that allows complex instrumentation, but is nevertheless still a simulation, or, alternatively, the experimenter can try to make the instrumentation more durable so that it might survive an engine test, accepting a reduction in the accuracy and density of data obtained. Hence one must find a compromise between these two directions when choosing the best experiment to obtain a particular set of flow measurements. This paper outlines the experiment in the Rotor Facility at Oxford measuring the unsteady surface pressure field on rotating turbine blades and describes in detail the new pressure instrumentation techniques developed for this purpose.

## The Rotor Facility

The Oxford Rotor Facility [6] is a fully three-dimensional unsteady rotating experiment capable of simulating engine values of the important nondimensional groups including the Mach number, Reynolds number, and other flow and rotational parameters. A schematic is given in Fig. 1. The facility uses an Isentropic Light Piston Tunnel [7] as its source of air. This tunnel is a long pump tube containing a light piston driven by high-pressure air. The piston isentropically compresses the air ahead of it in the tube until a certain pressure and temperature are obtained. A fast-acting annular gate valve then opens explosively, allowing the air to pass through the working section containing the turbine mounted behind a nozzle guide vane ring. 200 ms of steady flow results. Prior to firing the tunnel, the working section is evacuated to less then 10 mb and the turbine is spun up to just below design speed with an airmotor. With the flow, the turbine accelerates through its design speed with the high-speed data acquisition occurring as it passes through this speed. A speed versus time plot for a typical run is given in Fig. 2.

Contributed by the International Gas Turbine Institute and presented at the 35th International Gas Turbine and Aeroengine Congress and Exposition, Brussels, Belgium, June 11–14, 1990. Manuscript received by the International Gas Turbine Institute January 24, 1990. Paper No. 90-GT-346.

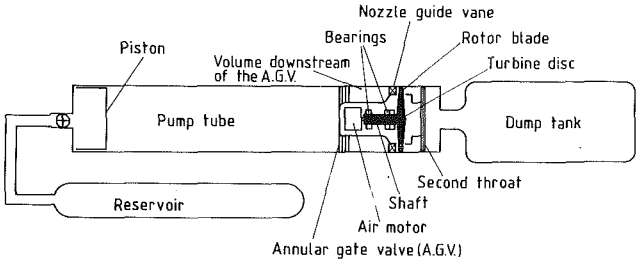


**Fig. 1 Layout of the OUEL transient turbine facility**

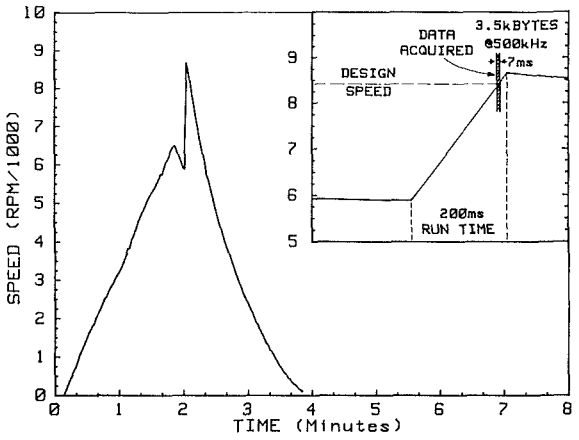


**Fig. 2 Operation of rotor facility**

During the data aquisition period the turbine completes one revolution. With 36 nozzle guide vanes, 36 nozzle guide vane passing events or wake interactions are available to study each run. The signals from the turbine are transmitted to the stationary frame via a 24-channel slip ring.

A transient facility such as this is a very good compromise when an accurate simulation with detailed instrumentation is required. The short run time allows the transducers to be calibrated immediately before and after each run, with the short time between runs unlikely to produce much variation in the calibration. The no-flow situation, while the turbine is spinning just before the tunnel is fired, gives a further measurement of the calibration with most of the possible errors present, including rotation-induced errors and noise. This is particularly valuable in checking the accuracy of the measurements made each run. The short run time is also low in cost and lends itself particularly well to heat transfer studies, as has been reported previously [8].

## Pressure Instrumentation Requirement

One of the main experiments to be performed on the Oxford Rotor Facility is to measure the surface pressure field on rotating turbine blades. To do this a pressure instrumentation system had to be developed utilizing a high surface density layout of high response transducers. The first step in this program was to look at the transducers currently available on the market. The most applicable of these were the low profile, absolute, semi-conducter sensors such as the Kulite LQ-047. This sensor uses a piezo-resistive chip of very small size, less than 1 mm in diameter, with good linearity and a high response. The total sensor size, however, is much larger due to the packaging necessary to make the wiring connections to the chip and also to protect the chip to ensure its survival. The smallest available sensors have a diameter of over 2 mm and a height of 1/2 mm. This size was too large for the detailed measurements required in the Oxford program with the blade sizes being used. The way forward was to reduce this packaging, making the chip and wiring more integral with the blade itself

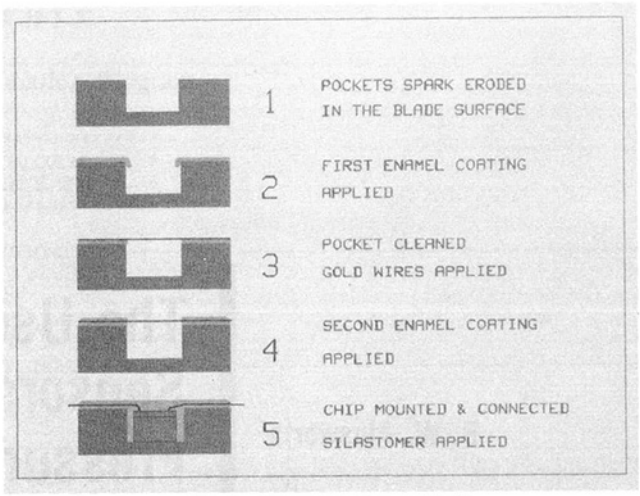


**Fig. 3 Chip mounting method**

and thus reducing each sensors's size. This is the technique developed at Oxford in association with Kulite.

## Production Method

The new mounting technique, shown in Fig. 3, is as follows:

(*a*) Pockets of a size just large enough to accommodate the chip were spark eroded into the turbine blade surface. An F306 Agemaspark spark erosion machine is used at Oxford and is capable of eroding holes of 75 $\mu$m $\pm$ 10 $\mu$m with a surface finish of 0.3 $\mu$m.

(*b*) A coating of vitreous enamel is then sprayed onto the blade. It is applied as a viscous liquid slip (frit materials plus mill additions) ground to a specific fineness and suspended in water. The resultant coating, after firing, is approximately 50 $\mu$m thick.

(*c*) 0.05-mm-thick gold wires are then laid down in tension on the enameled surface, with two wires across each pocket.

(*d*) A second coating of enamel is then applied such that the wiring is flush with the blade surface.

(*e*) After firing this coat, an ultrasonic drill is used to clear the pockets and flatten the pocket base. A thin coating of enamel is left on the side walls of the pocket for installation purposes. The drill also breaks the wires stretched across the pockets, leaving four exposed leads.

(*f*) The chip is mounted in the pocket with an epoxy glue and connected to the lead wires using a gold ball bonding technique.

(*g*) Finally, a silastomer is used to fill the holes till flush with the blade surface. The silastomer protects the transducer and ensures there is little aerodynamic disturbance due to the pocket.

The technique has been tested in the construction of a number of test specimens and actual blades. It has proved to be mechanically sound in manufacture, during thermal, strain, and rotation testing, and during experimentation in the facility. A packing density of up to three times that possible with current transducers can be achieved. Interruption of the blade surface curvature is therefore reduced and measurement points closer to the leading and trailing edges are possible. A blade specimen with 15 sensors mounted along the midheight section is shown in Fig. 4. The white squares visible are the pockets filled with silastomer. The buried wiring is also just visible running vertically down the blade.

## Transducer Accuracy

Having established the integrity of the technique, the next question concerns the accuracy of the measurements. To begin,

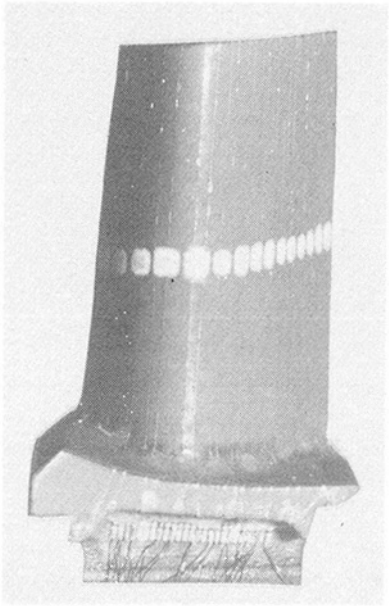

Fig. 4 Turbine blade instrumented with 15 sensors

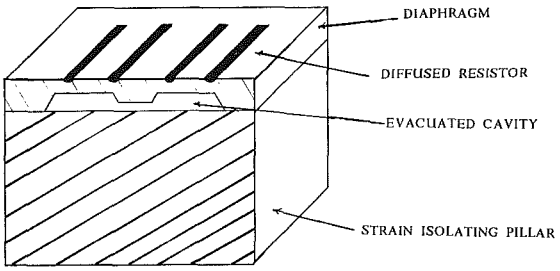


Fig. 5 Semi-conductor pressure transducer

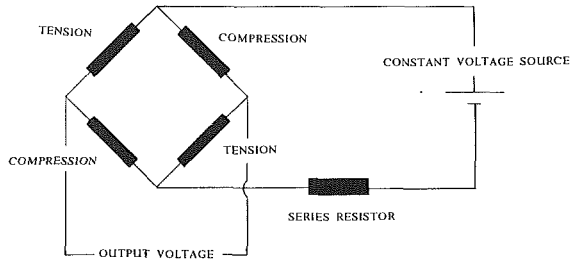


Fig. 6 Transducer circuit diagram

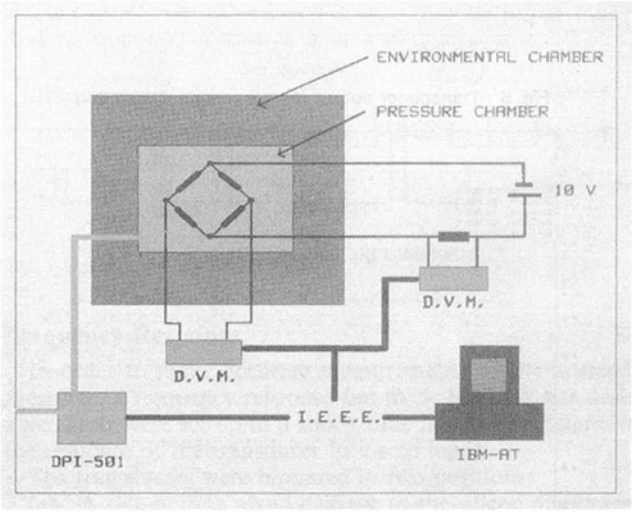


Fig. 7 Calibration facility

a brief description of the sensor is necessary. The semi-conductor pressure transducer consists of a silicon diaphragm bonded to a supporting pillar, with an evacuated cavity between (Fig. 5). A wheatstone resister bridge is diffused into the upper surface of this diaphragm. Strain intensifiers are etched into the other side, beneath the resistors. An anodic bond fixes the diaphragm to the pillar and seals the cavity between the two. The pillar acts to isolate the diaphragm from any base strain effects. The transducer is powered by a constant voltage source across the bridge, so that the bridge output depends on the balance of the resistors in the bridge. When pressure is applied to the transducer, the diaphragm deflects straining these resistors. They are positioned such that two are in tension and two in compression and experience a change in resistance, due to the piezo-resistive effect in the doped silicon, proportional to the strain in the diaphragm at that point. With careful positioning and matching of the resistors, an output voltage proportional to the applied pressure with good linearity and little hysteresis may be achieved.

Any change in the bridge resistances, not caused by pressure, can introduce errors into the measurements. The errors can be greatly reduced with careful calibration and/or compensation. Thermal sensitivity is the largest source of error but base strain sensitivity, acceleration sensitivity, and frequency response must also be investigated. The route chosen for the Rotor Facility pressure measurements was to calibrate the effect of a certain error source on the transducer output, then to measure the magnitude of that source in the actual experiment and with that knowledge to remove the error from the measured data during postprocessing of the results. This technique keeps the transducer-associated hardware as simple as possible while taking advantage of the extensive computer support already necessary for the data processing.

## Temperature Sensitivity

Temperature changes can affect the transducer's no-load output (null or offset sensitivity) and its pressure sensitivity (span sensitivity). If these two sensitivities are known, and the temperature of the bridge is measured in conjunction with its output, the transducer output may be corrected for temperature effects. The technique for measuring bridge temperature chosen at Oxford [9] was to place a resistor with a low Thermal Coefficient of Resistance (T.C.R.) in series with the transducer bridge in the power circuit as shown in Fig. 6. The total bridge resistance increases with temperature (due to a decrease in the mobility of the charge carriers in the doped impurity). With a constant voltage source the series resistor will act as a voltage divider, giving a bridge voltage that is proportional to the bridge resistance. If the T.C.R. of the bridge is known, its temperature may then be determined from measurements of the bridge voltage drop ($V_{br}$) or that across the series resistor ($V_s = V_{in} - V_{br}$, where $V_{in}$ is the constant voltage source). Hence three results are required for the temperature calibration of the chips: the span sensitivity, the offset sensitivity, and the T.C.R. of the bridge.

**Calibration Facility.** A computer-controlled calibration facility was constructed to permit precision testing of the transducers over a wide range of pressures and temperatures (Fig. 7). The facility consists of a Druck DPI 501 digital pressure controller linked to a pressure vessel inside an environmental chamber. The DPI 501, controlled by an IBM PC AT through an IEEE 488 bus interface, can control pressure to an accuracy of $\pm 0.007$ percent FS, the sensing element being a vibrating cylinder pressure transducer manufactured by Schlumberger.

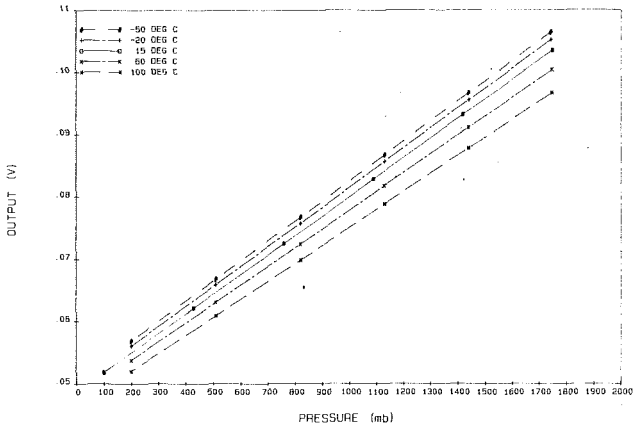


Fig. 8 Transdducer output from a sample calibration

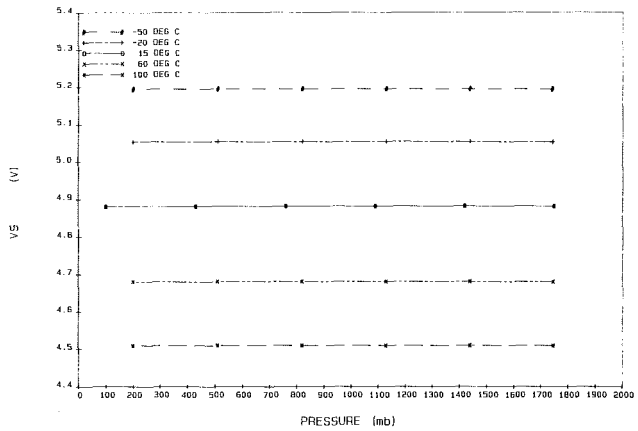


Fig. 9 Bridge voltage from a sample calibration

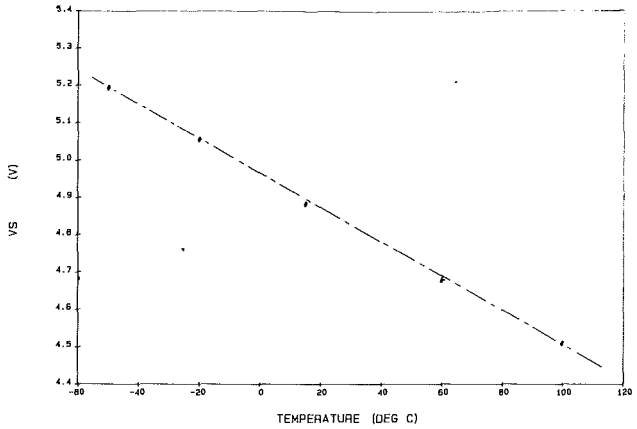


Fig. 10 Bridge voltage calibration

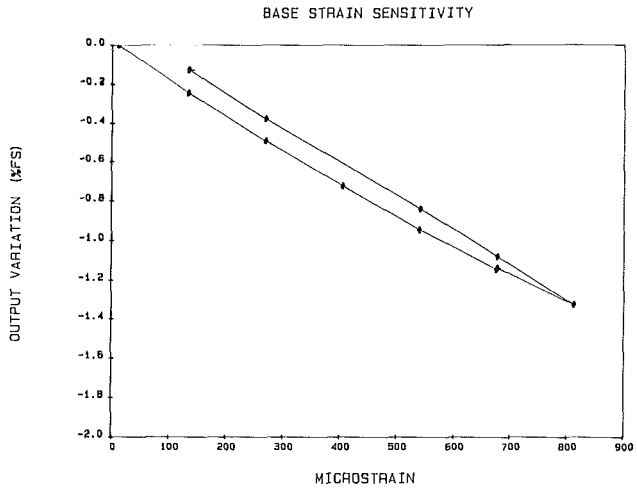


Fig. 11 Base strain sensitivity

The environmental chamber (Unilab Thermoduct), also controlled through an IEEE interface, can cycle between $-70°C$ and $+250°C$. Up to ten transducers at a time can be mounted in the test chamber with their outputs monitored on HP 3478A digital voltmeters and logged through the interface.

**Calibration Procedure.** The procedure used in obtaining the three required calibration results outlined above may be illustrated by following the calibration of a sample transducer. The voltage drop across the transducer bridge ($V_{br}$) and the transducer output voltage ($V_{out}$) were measured over the transducer's rated pressure range from $-50°C$ to $100°C$. The transducer was stabilized at each temperature and then calibrated over a minimum of two cycles, from 0 to FSD and back, with at least six pressures between. At each pressure, six measurements were taken at 30-second intervals to check that the voltages were stable. A plot of the calibration measurements of the sample transducer is given in Fig. 8. A similar plot of the calibration measurements of the transducer bridge voltage is given in Fig. 9.

**Temperature Coefficient of Resistance.** It can be seen from Fig. 9 that $V_{br}$ is insensitive to pressure. Hence an average value may be calculated at each temperature. A plot of this is given in Fig. 10 and by using a least-squares line fit the intercept $\alpha$ and slope $\beta$ may be determined. From these measurements the T.C.R. may be closely approximated using the equation

$$\text{T.C.R.} = \frac{R_s V_{in}\,\beta}{(V_{in}-\alpha)^2}\ \Omega/°\text{C} \quad \text{or} \quad \frac{100R_s V_{in}\,\beta}{(V_{in}-\alpha)^2 R_{br}}\ \%/100°\text{C}$$

where $V_{in}$ is the 10 V input voltage, $R_s$ the value of the series resistor, and $R_{br}$ the bridge resistance at a reference temperature, nominally 15°. For the transducer under consideration, the T.C.R. was calculated as 17.8 %/100°C and most of the transducers measured showed T.C.R.'s of this order. The linearity of the $V_{br}$ plot and its insensitivity to pressure changes show that the measurement of bridge voltage in a divided power circuit is a feasible way of recording bridge temperature. An accuracy of 2° was regularly achieved in the temperature calibrations.

**Span Sensitivity.** The type of semiconductor transducer used here has a negative span sensitivity. Hence when used with a series resistor in the circuit described above, the increase in bridge voltage with temperature due to the voltage divider compensates for the decreasing span. Choosing a series resistor that matched the bridge resistance was found to give good results. Any temperature sensitivity still remaining in the span may then be removed in the software compensation. For many of the transducers tested, however, the span sensitivity compensation provided by the sense resistor was such that no extra software compensation was necessary.

**Offset Sensitivity.** The sense resistor has no passive compensating effect on offset sensitivity. Rather than introducing further parallel resistors, it was decided to rely on the software corrections for the compensation of this variable. The data acquisition system being used allows the transducer output offsets to be zeroed with respect to a reference pressure just prior to the run. Bridge voltage is then recorded during the run to find the chip temperature change and corrections are applied to the initial zero using the calibrated offset sensitivity to correct for these temperature variations.

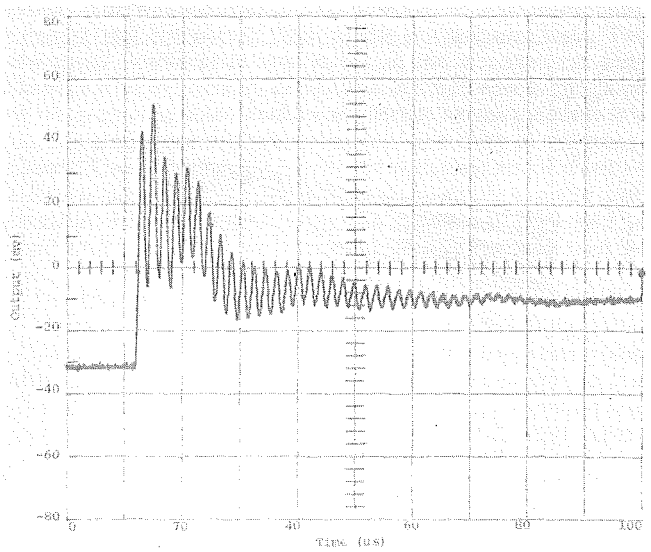


Fig. 12 Time response of a sensor with silastomer to a step input

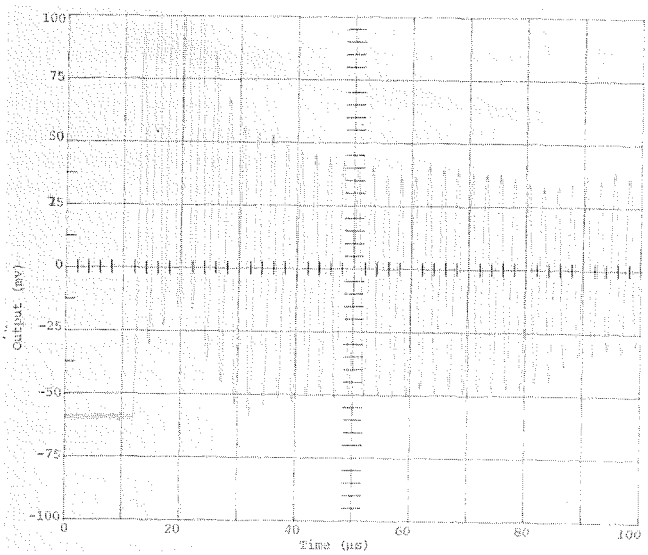


Fig. 13 Time response of a sensor without silastomer to a step input

With the very short run times of the facility, the small temperature gradients experienced, and the large thermal inertia of the silastomer-covered chips, only minor temperature effects are expected.

## Base Strain Sensitivity

A tensile specimen was constructed using the same technique that was to be applied to the blades in order to measure the base strain sensitivity of the sensors. The specimen was manufactured from Inco 718, machined with pockets to take the transducers, and coated with vitreous enamel in the usual way. It was mounted in an Instron tensile testing machine and tested to a base strain of 800 $\mu\epsilon$. Sheard [10] conducted a finite element analysis of the blade at design conditions and estimated the strain at the blade's midheight section to be of the order 200 $\mu\epsilon$. A plot of the tensile test results for one chip, aligned in the tensile specimen with its strain sensitive elements parallel to the load giving a worst case result, is shown in Fig. 11. The base strain sensitivity calculated from this plot is $-0.00164$ % FS/$\mu\epsilon$ giving a strain of $-0.33$ % FS at the midheight section at design speed.

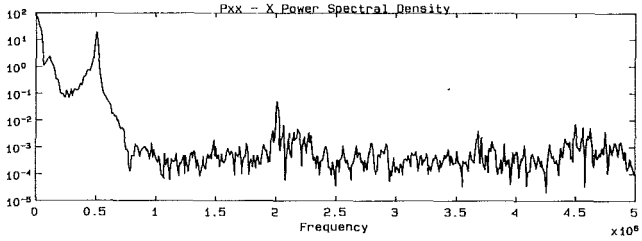


Fig. 14 Power spectral density

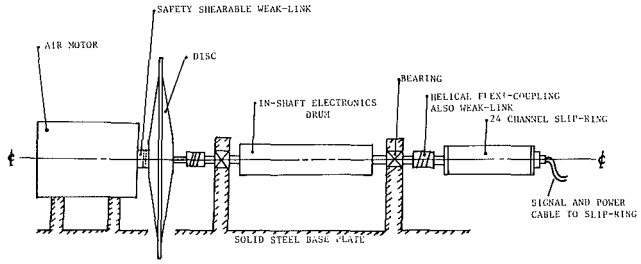


Fig. 15 Spinning rig schematic

## Frequency Response

In order to make accurate measurements of the unsteady pressures, a frequency response flat to > 100 kHz was desirable. Tests were set up in a shock tube in order to determine the response of the transducer to a step input.

The transducers were mounted in two positions:

(*a*) A side-port to avoid damage to the silicon diaphragm caused by the impact of particles from the nylon bursting diaphragm.

(*b*) An end-port where a greater likelihood of damage was possible.

The problem with position (*a*) was the finite time taken to traverse the silicon diaphragm, and the corresponding degradation of step input. In practice, however, little difference was observed between the two mounting positions, and transducers with and without silastomer covering their diaphragms were tested (Figs. 12 and 13, respectively). The effect of the silastomer was to dampen the transducer's response but this level of damping had little effect on the transducer's natural frequency. The natural frequency can be seen in the power spectral density plot, a sample of which is given in Fig. 14. Most transducers had a natural frequency of the order of 500 kHz, either with or without silastomer, easily satisfying the bandwidth requirements.

## Rotating Tests

A spinning rig (Fig. 15) was used to evaluate the performance of the transducers under rotating conditions before actual testing in the Rotor Facility. The aims of the test program in the spinning rig were to determine the level of acceleration sensitivity of the transducers, to measure the noise levels during rotation, and to test the proposed calibration/correction technique. If the technique worked, it would be possible to remove all the variations in the signal by using the calibration factors to reference the transducer outputs from runs at different conditions (pressure, temperature, speed, etc.) to a reference condition. The result should be a level curve when plotted against speed, time, etc. The acceleration sensitivity may be estimated from the data, which have been corrected for pressure, temperature, and base strain effects. The variation due to acceleration will be proportional to the square of the rotational speed, and a linear plot of transducer output versus speed squared will show the necessary calibration factor.

For these tests four sensors were mounted on a small circular

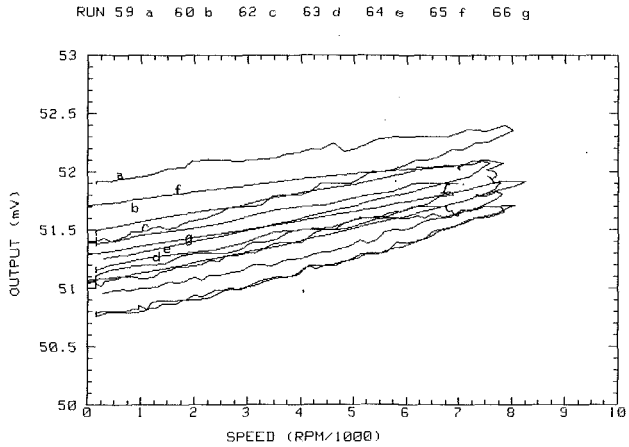


Fig. 16 Uncorrected transducer output data

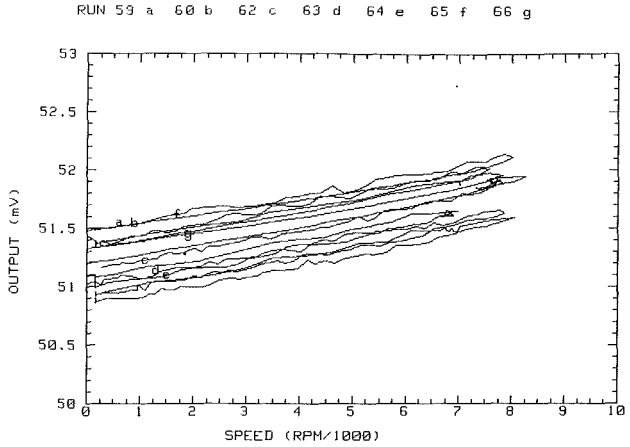


Fig. 18 Corrected for pressure variations

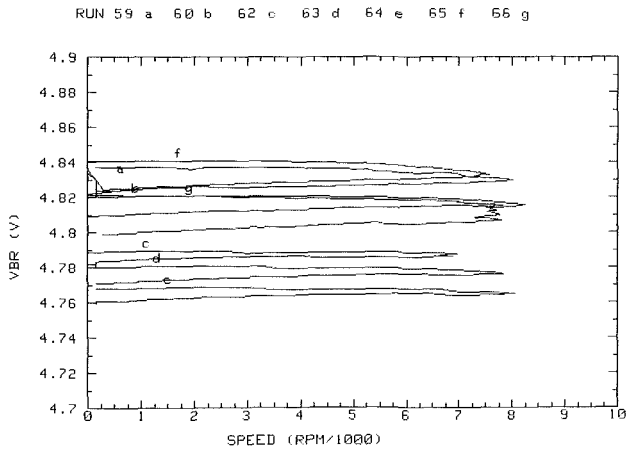


Fig. 17 Bridge voltage measurements

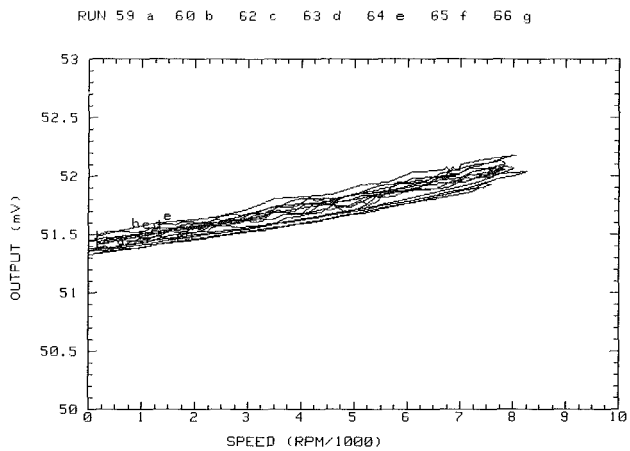


Fig. 19 Corrected for temperature variations

disk, which was then attached to the larger spinning disk at a radius equal to that of the blade midheight on the Rotor Facility. The whole assembly is housed within a pressure chamber allowing tests to be conducted at pressures ranging from 500 Pa to 350 kPa. Many of the systems used in the spinning rig are the same as those used on the Rotor Facility, including the airmotor, control program, and slipring, so that the results obtained here would be applicable to testing in the Facility. The tests presented here were conducted at low pressure with no signal conditioning. The transducer output was fed straight through the slipring and recorded by a CIL 6380 A/D convertor or a HP 3478a digital voltmeter (depending on the coupling and accuracy required). A plot showing the output from a sample transducer versus rotational speed for a number of different runs conducted over two days is shown in Fig. 16. The transducer outputs are affected by the pressure change during and between the runs, temperature variations, acceleration, and base strain. The precision of the measurements was increased for the last two runs, *f* and *g*, as no high-speed phenomena were detected at the previous higher sampling rate. The bridge voltage versus speed plots for these runs are given in Fig. 17.

The magnitude of each of the effects being considered may be seen if their particular calibrations are applied separately. Figure 18 shows the result after the correction of pressure variations in the test results. The transducer outputs have been referenced to a pressure of 30 mB. Using bridge voltage calibrations carried out in the Calibration Facility and the Bridge voltage measurements made during the tests (Fig. 17), temperature variations may also be corrected. With the runs referenced to 15°C the outputs collapse as shown in Fig. 19. The

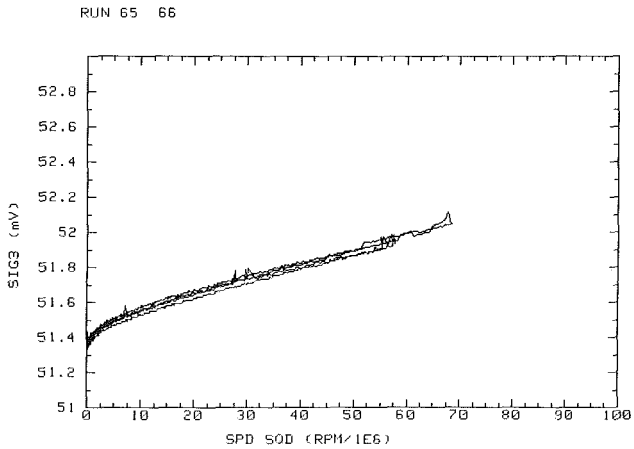


Fig. 20 Acceleration sensitivity

remaining variation in the output is due to the acceleration sensitivity of the transducer, its base strain sensitivity, and other factors such as aerodynamic effects resulting from the disk rotation.

The actual base strain experienced by the sensors during these tests is very low, of the order of 0.05 % FS, and so may be considered negligible. The acceleration sensitivity will be dependent on the square of the rotational speed and in Fig. 20 the corrected outputs from the last two runs are plotted against this. At speeds greater than 1000 rpm the plot is linear. The low-speed nonlinearity is probably due to aerodynamic

effects. This was ascertained by conducting tests at atmospheric pressure and comparing them to the low-pressure tests. The low-speed nonlinearity was larger in the atmospheric tests showing it to be pressure dependent. At high speeds the slope of the graph remained unchanged. Hence we may assume this slope is a measure of the acceleration sensitivity of the transducers. The transducers were aligned with their strain sensitive elements aligned in the radial direction, giving a worse case estimate. From the plot shown this estimate is 8E-9 % FS/rpm$^2$ or 0.5 % FS at design speed. This factor may then be used to correct for acceleration sensitivity.

The final plot of corrected transducer output versus speed is given in Fig. 21. An accuracy of ±0.2 % FS has been achieved for these runs. Hence the pressure instrumentation when combined with a calibration/correction technique can give results within the 1 % FS required for the pressure test program on the Rotor Facility. Noise levels measured during the rotating tests were less then 0.5 mV rms.

## Facility Data Acquisition System

The pressure instrumentation has been designed to be compatible with the existing data acquisition system used for heat transfer measurements in the Rotor Facility [8]. This allows easy instrumentation changes, a basic design aim of the Facility. Also the comparisons of pressure and heat transfer results recorded on the same turbine are made easier. Problems have been encountered in the past with the wiring in the rotating frame, but the technique in use at the present time seems satisfactory. The gold wires in the enamel are connected to thicker insulated copper wires at a solder pad bonded to the blade root. These copper wires are used to bridge the blade/disk gap to a permanent set of solder pads on the disk surface near the blade root fixing points. Thin steel shims insulated with a heat shrinking plastic are spot welded over the wires next to the pads to keep them in place. The copper wires are glued and supported with further shims down the disk to the 24-channel slipring, identical to that used on the spinning rig. The postslipring signal conditioning and Data Acquisition system is as reported in [8]. An amplifier based on the AMP-O5 fast response J-FET differential amplifier chip is used to boost the signals close to the slipring output before transmission to the data acquisition system. The signals are then sampled in two ways to obtain the time-averaged and unsteady traces. The d-c output is sampled at 434 Hz to determine the steady pressure measured by the transducer, the acquisition being performed by a PDP-11/34 computer after signal conditioning by CAS-8 amplifiers as described by Oldfield [11]. The signals are also recorded by two transient recorders. 3.5 kbytes of data are sampled at a rate of 500 kHz for 7 ms as the turbine passes through the design speed. This sampling rate is sufficient to be able to resolve the unsteady and periodic components of the flow. The bridge voltage excitation outputs are sampled on the PDP-11/34 computer and from them, the temperature corrections are applied to the d-c output signals. Any span sensitivity corrections needed can also be applied to the a-c sampled data.

Two speed encoder signals are also recorded, giving signals every 1 revolution and every 1/36 revolutions. The once per rev signal is used to determine the position of the instrumented blade with respect to the N.G.V. ring for phase-averaging purposes. The 36 per rev signal represents the nozzle guide

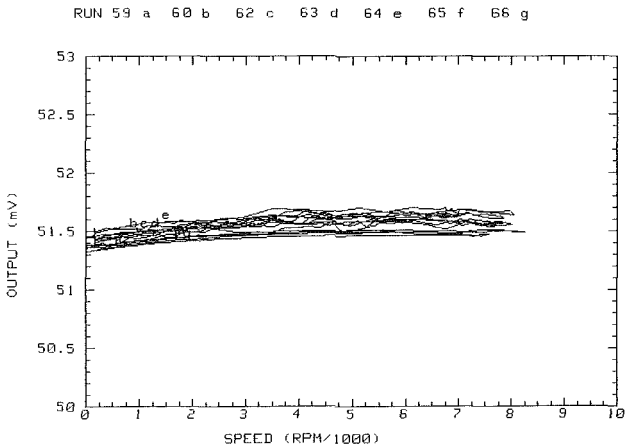


**Fig. 21 Final corrected plot**

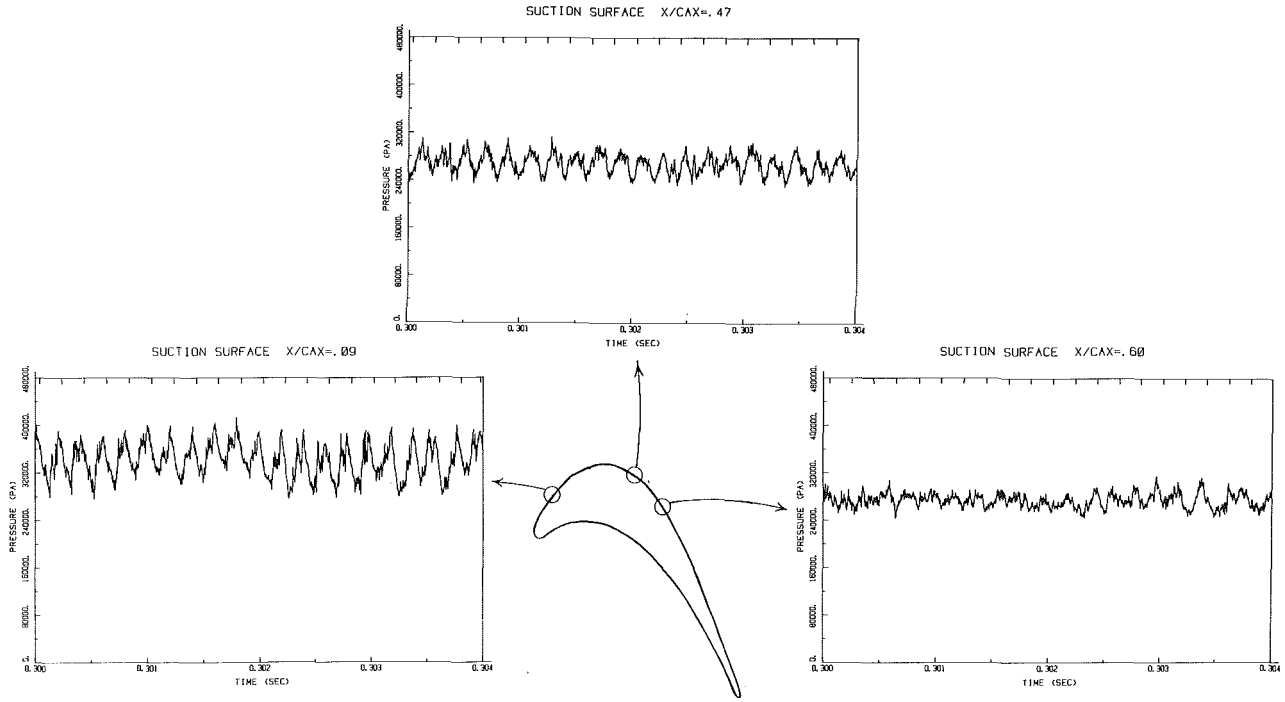


**Fig. 22 Unsteady surface pressure showing wake passing frequency**

vane passing frequency and is used to detect periodicity or wakes in the unsteady pressure trace.

## Provisional Results

The commissioning phase of the pressure instrumentation program has now been completed with steady and unsteady surface pressure data having been recorded on the instrumented blade shown in Fig. 4. Sample measurements, taken from 3 transducers positioned along the midheight suction surface streamline, are shown in Fig. 22. The output from the 36 line encoder disk is included at the top of each plot showing the nozzle guide vane passing frequency. The periodicity evident in the plots can be seen to be at the nozzle guide vane passing frequency, its effect decreasing toward the trailing edge. Further data and analysis will be reported at a later date.

## Conclusion

A technique for making measurements of the steady and unsteady surface pressure field on a rotating turbine blade has been outlined. A fully three-dimensional rotating turbine is used in the experiment, which closely simulates the flowfield through a high-pressure turbine stage. A new pressure measurement technique has been developed for this application, in which semi-conductor pressure sensors are attached directly to the blade surface in small pockets, with the connection wiring being buried between two enamel coatings on the blade surface.

This technique increases the density of measurement points possible while retaining the high-frequency response of the semi-conductor sensor. A calibration/correction technique for use with the sensors has been tested and the results proved satisfactory. The use of the transducers in the rotor facility itself is just beginning but the first set of results look very promising. Other applications for this technology are also being investigated, such as aerodynamic testing in the compressor stage, or on unsteady wedge and pyramid probes.

## Acknowledgments

The authors acknowledge gratefully the enthusiasm of R.P. Moores and A. Kurtz of Kulite Semi-Conductor International in supporting the work, and permitting its publication. The work of Billy Allan on the Spinning Rig, John Allen in technical support, and Kevin Grindrod in running the tunnel is also gratefully acknowledged.

## References

1 Nicholson, J. H., "Experimental and Theoretical Studies of the Aerodynamic and Thermal Performance of Modern Gas Turbine Blades," D. Phil. Thesis, University of Oxford, United Kingdom, 1981.

2 King, P., "Aerodynamics of High Performance Turbine Blading," D. Phil. Thesis, University of Oxford, United Kingdom, 1985.

3 Doorly, D. J., and Oldfield, M. L. G., "Simulation of Wake Passing in a Stationary Turbine Rotor Cascade," *J. Propulsion and Power*, Vol. 1, No. 4, July–Aug. 1985, p. 316.

4 Doorly, D. J., and Oldfield, M. L. G., "Simulation of the Effects of Shock Wave Passing on a Turbine Rotor Blade," ASME JOURNAL OF ENGINEERING FOR GAS TURBINES AND POWER, Vol. 107, No. 4, Oct. 1985, pp. 998–1006.

5 Doorly, D. J., Oldfield, M. L. G., and Scrivener, C. T. J., "Wake Passing in a Turbine Rotor Cascade," AGARD CP No. 390, *Heat Transfer and Cooling in Gas Turbines*, 1985.

6 Ainsworth, R. W., Schultz, D. L., Davies, M. R. D., Forth, C. P. J., Hilditch, M. A., Oldfield, M. L. G., and Sheard, A. G., "A Transient Flow Facility for the Study of the Thermofluid-dynamics of a Full Stage Turbine Under Engine Representative Conditions," ASME Paper No. 88-GT-144.

7 Schultz, D. L., Jones, T. V., Oldfield, M. L. G., and Daniels, L. C., "A New Transient Cascade Facility for the Measurement of Heat Transfer Rates," AGARD CP No. 229, *High-Temperature Problems in Gas Turbine Engines*, 1977.

8 Ainsworth, R. W., Allen, J. L., Davies, M. R. D., Doorly, J. E., Forth, C. J. P., Hilditch, M. A., Oldfield, M. L. G., and Sheard, A. G., "Developments in Instrumentation and Processing for Transient Heat Transfer Measurements in a Full Stage Model Turbine," ASME *Journal of Turbomachinery*, Vol. 111, Jan. 1989, pp. 20–27.

9 Epstein, A. H., "Measurement Techniques in Turbomachines," VKI Lecture Series 1985-03.

10 Sheard, A. G., D. Phil. Thesis, University of Oxford, United Kingdom, 1989.

11 Oldfield, M. L. G., Jones, T. V., and Schultz, D. L., "On-Line Computer for Transient Turbine Cascade Instrumentation," *IEEE Trans. on Aero. and Elec. Systems*, Vol. AES-14, No. 5, Sept. 1978, pp. 738–749.

**K. Mathioudakis**
Lecturer.

**A. Papathanasiou**
Research Associate.

**E. Loukis**
Research Assistant.

**K. Papailiou**
Professor.

Laboratory of Thermal Turbomachines,
National Technical University of Athens,
Athens, Greece

# Fast Response Wall Pressure Measurement as a Means of Gas Turbine Blade Fault Identification

*The distortions of the pressure field around rotating blades of turbomachinery components due to alterations of their shape can be utilized for the identification of faults related to the blading. Measurement of the unsteady pressure field near the wall provides information on such flow and pressure distortions and can thus be used for diagnostic purposes. An experimental investigation of the compressor rotating blade pressure field of an industrial gas turbine has been undertaken, in order to demonstrate the feasibility of the abovementioned principle. Various realistic gas turbine blade faults have been examined. Application of the appropriate processing techniques demonstrates that unsteady pressure measurements can be used to identify the occurrence of minor blade faults (not traceable by standard techniques) as well as the kind of fault. The proposed methodology has the potential for being incorporated in a computerized engine health monitoring system.*

## 1 Introduction

Methods for detecting the presence of faults in gas turbine components have received considerable attention recently. The diagnosis is achieved by measuring various physical quantities, appropriately processing the collected data and finally interpreting the reduced information. According to the kinds of measurements employed, different components and various categories of faults can be monitored. For example, aerothermodynamic measurements can be used to deduce the condition of the gas path components, while mechanical damages can be detected by vibration analysis (e.g., Mathioudakis et al., 1989a).

Most of the existing diagnostic techniques have the capability of identifying the component where a major fault is located. The reason for such fault identification is that the measured quantities, whether they are mean thermodynamic values or structural vibrations may not undergo a significant variation, unless the fault is of sufficient magnitude to produce visible changes in them, as for example discussed by Baines (1987). Such measurements will indicate the presence of severely damaged blades, while a minor shape modification of a few blades will not be felt. It is desirable, however, for a demanding engine monitoring system to be capable of identifying faults of small extent, in order to predict a later significant degradation or to locate failures that can grow very rapidly to catastrophic extent. A situation of one slightly bent or twisted blade, for example, which in itself might not significantly influence engine operation, can have catastrophic consequences if it results in a blade loss.

A method of diagnosing such minor faults on rotating turbomachinery blades is proposed in the present paper. The features of unsteady pressure signals related to rotating blades are utilized in order to extract diagnostic information about the blade condition. Such faults occupy the majority of steam turbine damages, as reported by Kaspar (1982) and Simmons and Smalley (1990). Methods applying the same principle have been discussed in the past by Barschdorf and Korthauer (1987), Barschdorf (1986), and Valero and Esquiza, (1988). Although several cases of turbomachines have been examined in the above references, they were mainly related to test models and no application to field gas turbines was reported. On the other hand, the main emphasis was concentrated on pattern recognition methods, but aspects related to operating conditions have not been mentioned.

The work presented here is based on experiments performed on a commercial gas turbine, functioning in conditions usually encountered in field operation. The feasibility of the employed procedure is demonstrated and the dependence on operating conditions is discussed. A feature of the proposed methodology is that it provides information that can be easily interpreted by expert systems used for condition monitoring.

## 2 Background

The time variation of pressure at a fixed location facing a blade row at the interior of a turbomachine casing is caused by the rotation of the blade-to-blade pressure field. The pressure field between blades of a turbomachinery cascade is determined by the geometry of the cascade and the operating conditions, namely, the flow conditions at cascade inlet and outlet.

Blade faults result in the distortion of the cascade geometry

Contributed by the International Gas Turbine Institute and presented at the 35th International Gas Turbine and Aeroengine Congress and Exposition, Brussels, Belgium, June 11–14, 1990. Manuscript received by the International Gas Turbine Institute January 17, 1990. Paper No. 90-GT-341.

and consequently will generate nonuniformities in the blade-to-blade pressure fields. For example, bending or twisting a blade results in destroying the periodicity of the pressure field between the blades. Blade erosion, corrosion, or fouling result in the alteration of the airfoil shape and consequently of the blade-to-blade pressure field. For all these blade fault categories, the resulting pressure field is directly related to geometric distortions. It is implied that knowledge of the initial intact, and the later distorted, pressure fields can lead to the identification of geometry alterations and finally to the blade faults. Also, the variation of the operating conditions of a compressor blade row corresponds to a change of the incidence angle of the blade airfoil, which affects the pressure distribution along the blade. These changes of the blade pressure field reflect upon the fluctuating pressure. The change of operating point might therefore influence the fluctuating pressure and, in such a case, this effect should be separated from the effect of blade faults.

In order to verify the abovementioned principles and demonstrates their practical implication, an experimental investigation of situations with different blade faults was undertaken. The tests that were performed and the corresponding experimental conditions are now described.

## 3 Experimental Investigation of Engine Faults

The Ruston Tornado Gas Turbine, described by Wood (1981) and Charchedi and Wood (1982), was the engine used as the test vehicle. Fast-response pressure transducers were flush mounted at the compressor inner casing wall. They were Kulite XST-190-25 SG type. The positioning and coding of the sensors on the compressor casing is schematically shown in Fig. 1. Data were acquired through a data acquisition system manufactured by LMS, with a total capacity of 32 channels and maximum total sampling frequency of 960 kHz. A key phasor signal and bearing proximity probe signals from the engine bearings were acquired simultaneously with unsteady pressure inside the compressor. All the data discussed in this paper have been acquired with a sampling frequency of 32 kHz and were low pass filtered at 16 kHz. Aerothermodynamic performance data were acquired by means of a data logging system described by Timperley and Smith (1983). Performance data provide information about operating conditions and cycle parameters for each operating point. In all the tests, data were collected at four operating points, hereafter designated as points A, B, C, and D, corresponding to nominal speed and full, 3/4, 1/2, and 1/4 load, respectively.

A number of blades of the compressor of the test engine were modified, in order to produce faults. Tests were conducted at four different configurations, which are now described:

*Test 1:* Datum test; this test provided the baseline data for all the subsequent tests with implanted faults. The compressor blading was in intact condition.

*Test 2:* Rotor fouling test; in order to examine the possibility of identifying fouling of an individual rotor, the stage 2 rotor of the compressor was coated with a textured paint. The paint layer roughens the blade surfaces and causes a slight alteration of their contour, thus simulating fouling of this rotor.

*Test 3:* Individual rotor blade fouling; the purpose of this test was to examine the possibility of identifying alteration in individual blades. Two blades of stage 1 rotor were painted with textured paint. The two painted blades are separated by five intact blades, as shown in Fig. 2(*a*). The painting of blades is expected to alter the aerodynamic pressure field around them due to two reasons: (*i*) alteration of the blade surface roughness: The surfaces of the painted blades are rougher than the intact ones; (*ii*) the layer of paint on the blade surface gives a slight modification of blade thickness. This results in a corresponding modification of blade shape, which in turn results in distorting the pressure field around the blade.

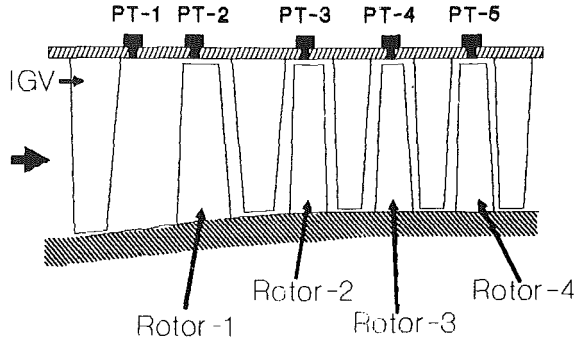


**Fig. 1 Compressor layout and positioning of fast-response pressure transducers**

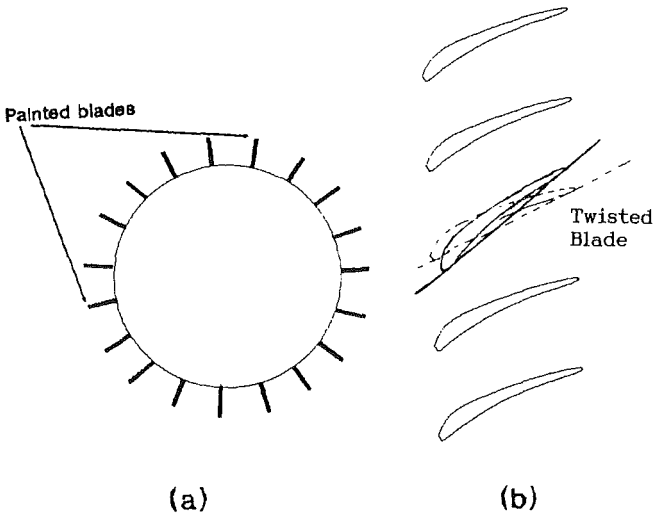


**Fig. 2 Position of painted blades and schematic of twisted blade of stage 1 rotor**

*Test 4:* Individual twisted blade; the purpose of this test was also to examine the possibility of locating alterations in individual rotor blades. This second kind of rotating blade alteration (the first being TEST-3) is also useful in determining whether the type of blade alteration can be identified, namely whether different rotating individual blade faults can be distinguished from each other. In our case it was desired to investigate whether painted blades (fouled) can be distinguished from twisted ones. A single blade of rotor 1 was twisted, as shown schematically in Fig. 2(*b*). The twisting of the blade tip was achieved by using a tool especially manufactured for this purpose. The magnitude of the twist angle was estimated to be approximately 8 degs. The change of blade stagger will result in a corresponding variation of incidence angle. Changes in incidence will result in changes of the blade pressure field, which are expected to be detectable by appropriate data capture.

The results obtained from the experimental study are now presented.

## 4 Measurement Results for Healthy and Faulty Operation

A series of tests were conducted with the engine operating at point A as described in section 3. Signals from pressure transducers installed in the inner surface of the compressor casing are shown in Fig. 3 and 4. The signals represent approximately one and a half periods of rotation and the sig-

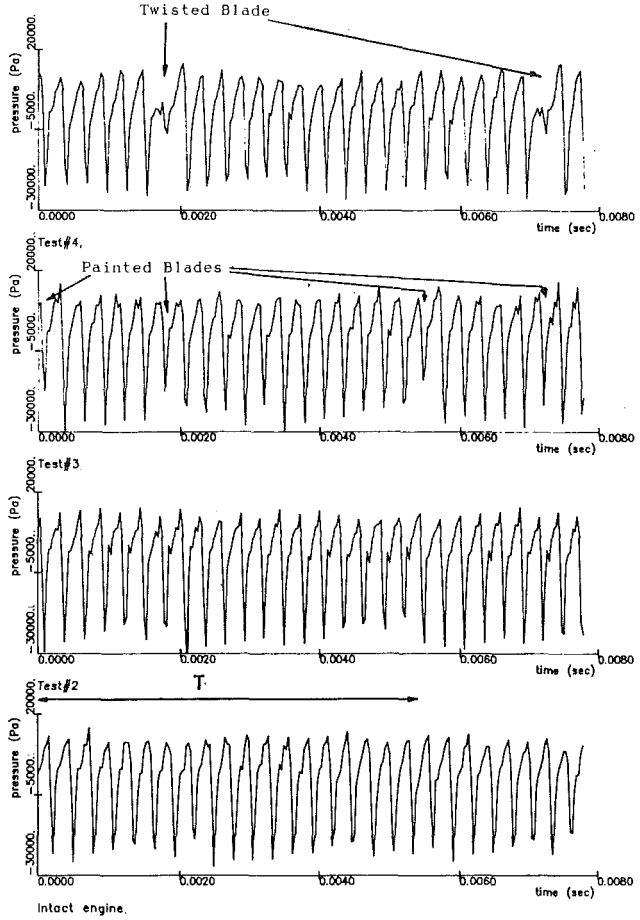


**Fig. 3 Pressure traces from pressure transducer 2 for the different tests**

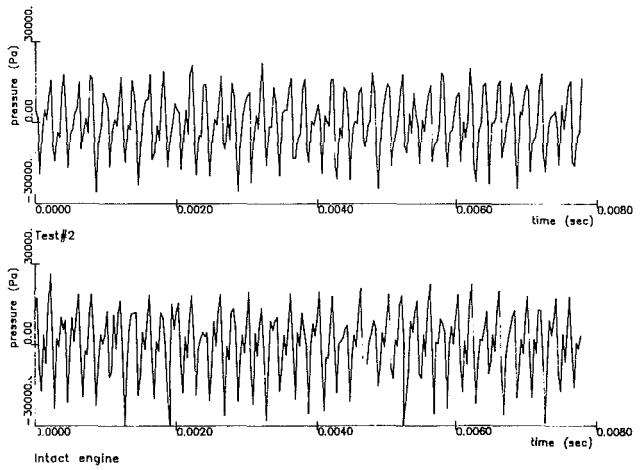


**Fig. 4 Pressure traces from pressure transducer 3 for tests 1 and 2**

natures of the individual blade passages are repeated. The existence of noise is evident and can be attributed to flow nonuniformities and rotational unsteadiness. In Fig. 3, the time traces from the pressure transducer PT-2 facing stage 1 rotor are displayed. For the fault of test 2, which is located on rotor stage 2, it can be seen that no obvious variation of the peaks can be deduced, with respect to the baseline. For the fault of test 3, where two blades on rotor stage 1 are fouled, a clear difference from baseline is observed, as shown by the arrows. Finally for the fault of test 4 the trace of the twisted blade is clearly distinguishable from the intact blades.

Time traces of the pressure transducer PT-3 facing stage 2 rotor for the cases of test 2 and the "healthy" engine are shown in Fig. 4. The introduction of fouling produces a reduction of the trace amplitude for the case of the fouled stage 2 rotor and distinct variation of the peak form per period. The time traces for test 3 and test 4 have also been examined and found by visual inspection almost identical to the intact engine ones. Information about the faults of stage 1 rotor is not obvious from such traces, because the flow recovers after passing through the stator cascade before entering the second rotor.

The raw signals contain the influence of the periodic components as well as of the random noise, which results in ambiguities in the interpretation, especially for the case of the painted blades. In order to remove this influence we apply phase averaging on the signals. The technique of phase averaging takes into account the variation of the period of rotation, and also gives the possibility to determine the location of the faulty blades, by using the key phasor signal as a reference. When the same key phasor is used for all cases, healthy and faulty, the circumferential position of a faulty blade is immediately determined. The phase-averaged signal from pressure transducer 2, facing rotor 1, for one twisted blade, is shown in Fig. 5(*a*). Comparison to the corresponding raw signal (Fig. 3) shows a more uniform distribution of peaks and valleys corresponding to blade passages, while the passage corresponding to the twisted blade is clearly identified. The same picture for the case of the two painted blades is shown in Fig. 5(*b*). For this case we see that the existence and location of the two painted blades is defined without ambiguity, which is not always true for the raw signal. On the raw signal (Fig. 3), the random influence might result in the ambiguity of the location of the painted blades, since some valleys corresponding to healthy blades look similar to the ones corresponding to the painted blades.

In order to reveal the harmonic content of the time signals, the power spectra have been calculated. Although the spectra extend to a frequency range of up to 16 kHz, the limitations in the frequency response of about 12 kHz of the transducers should be taken into account. A general feature of these spectra is that they consist of a broad-band component upon which pure tones are imposed at various multiples of the shaft rotational speed and predominant harmonics corresponding to the blade passing frequency of each stage.

The power spectra of the pressure transducer signals of the sensors facing stage 1 and stage 2 rotors are depicted in Figs. 6(*a*) and 6(*b*), respectively. When the pressure transducer PT-2 is examined, one notices a visible variation in the spectrum form, which makes evident the fault existence, for the cases of faults in tests 3 and 4. This variation appears mainly as an increase of the shaft rotational harmonics in the regions between the blade passing frequency of the first rotor. Almost no variation is observed for the fault at test 2. Also, an increase level of power can be observed in the entire broadband, which is caused by the implanted deficiencies. This variation makes the spectra from faulty engines clearly distinct from the datum baseline. The spectrum from PT-3 facing rotor stage 2 shows also a differentiation when the fouled staged 2 rotor is examined, but no visual differentiation can be revealed when the faults of tests 3 and 4 are present.

The power spectrum of pressure transducers PT1, PT3, PT4, and PT5 for test 4 are shown in Fig. 7, in order to indicate how the spectrum of measurements at different stages is influenced by the presence of a fault on rotor 1. The harmonic envelope in the spectrum of PT1 has developed when the fault was implanted. On the other hand, the spectra of PT3, PT4, and PT5 exhibit no visual change by the implantation of the fault on rotor 1. This indicates that the nonuniformity produced by the fault decays as it travels downstream through the compressor stages.

Further analysis has been applied upon the spectra by com-

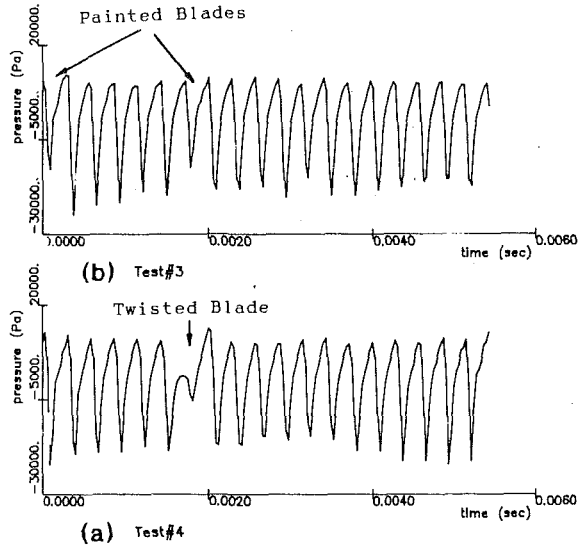


**Fig. 5 Phase-averaged pressure traces from pressure transducer 2, for tests 3 and 4**

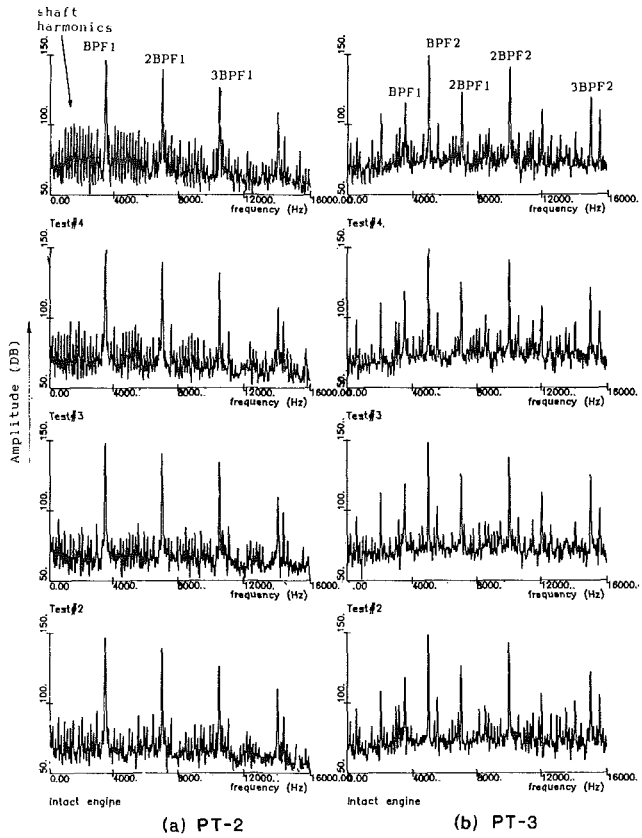


**Fig. 6 Power spectra of pressure measured by pressure transducer 2 and 3 for the different tests**

paring the amplitude at each frequency, and it is discussed in a later section.

## 5 Fault Indices

The power spectra from the pressure transducers were further processed in order to provide more information about differences arising from implanted faults. The algebraic manipulations to compare spectra from the "faulty" machines with the "healthy" one are now described.

The amplitudes of the power spectra at each frequency for

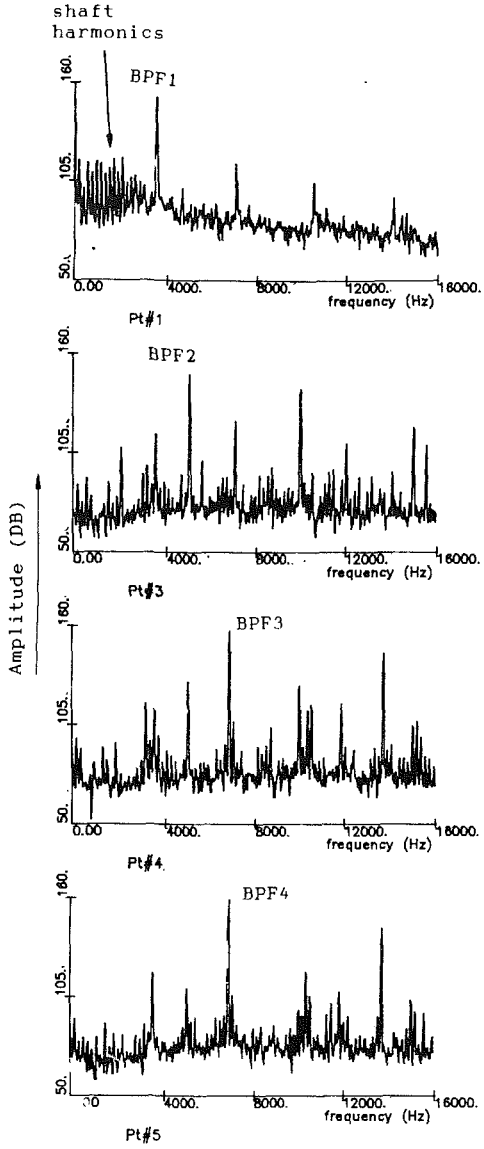


**Fig. 7 Power spectra of pressure measured by pressure transducers 1, 3, 4, and 5 for test 4**

the faulty engines were compared to the datum healthy machines by calculating various indices. After inspecting a number of indices, it was decided to adopt two of them:

*Index 1:* The difference of the amplitude logarithms of spectra from intact and faulty engines.

*Index 2:* The ratio of spectra amplitudes of faulty to the intact engines.

These two indices provided the clearest way, so far, for extracting fault signatures from power spectra.

Index 1 was applied to the output spectra from transducer PT-2 for engine tests 2, 3, and 4 at operating point A, and an example of results is shown in Fig. 8(*a*). Test 1 provided the results for the intact engine. When the fault of test 2 is examined, a variation on the entire broadband level can be seen, while an increase for tones without a specific pattern exists. Examining the fault of test 3, an increase in the overall power level can be noticed with an increase at the harmonic peaks at multiples of the shaft rotational harmonics. The signature of fault of test 4 becomes clear when the corresponding Index 1 is examined. A considerable increase in the shaft passing harmonics over the entire frequency range can be seen. Index 2 was also applied for all fault cases on signals from transducer PT-2 and the results are shown in Fig. 8(*b*). An increase in the

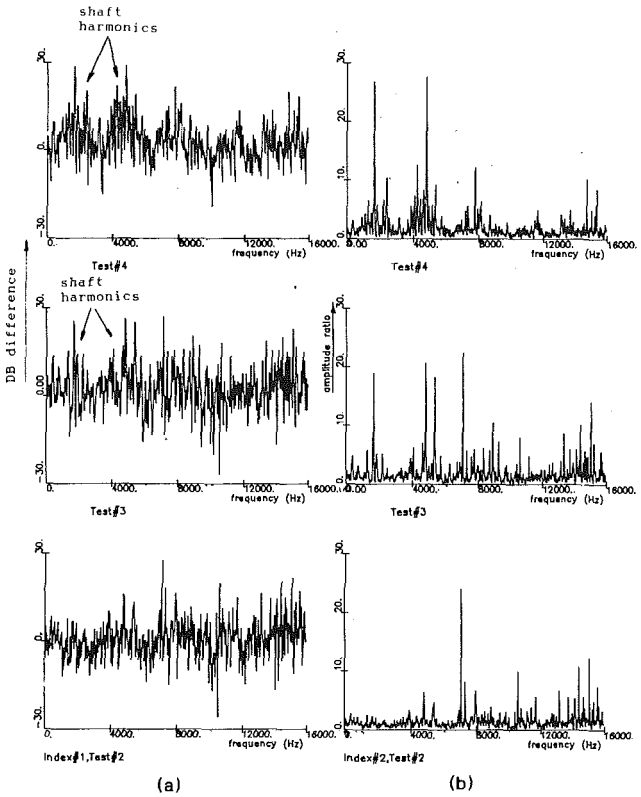


Fig. 8 Spectral comparison indices for pressure transducer 2 data: (*a*) index 1; (*b*) index 2

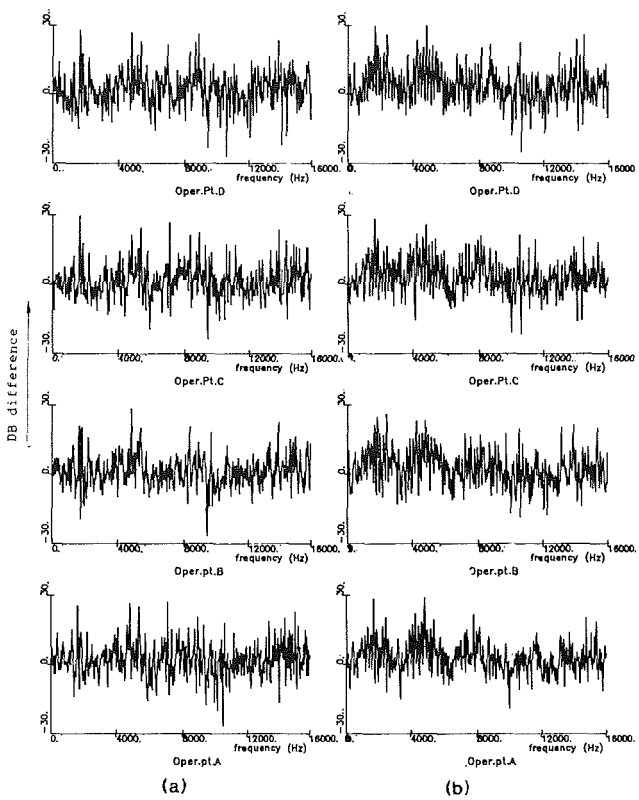


Fig. 9 Index 1 for different operating conditions: (*a*) tests 3; (*b*) test 4

broadband level for all the faults is seen. Inspection of either one of the indices shows that the signature of every fault is distinguished from the other two.

Similar analysis was performed upon the spectra from transducer PT-3 for all the cases of implanted faults, but the results are not presented here due to space limitations. When the indices were applied, there was a slight variation in the overall broadband level, and the defective stages corresponding blade passing frequency peaks. Most differentiation was observed for the fault of rotor stage 2, which faces PT-3. As a partial conclusion it can be stated that the comparison indices are very useful to identify a fault signature, but this signature becomes less traceable when the sensor is located downstream of the faulty stage.

In order to examine the dependence on operating conditions, for the faults of tests 3 and 4, Index 1 was applied to the power spectra of pressure transducer PT-2, when the machine is operating at points A, B, C, and D. This kind of variation of operating conditions is typical in power generation applications, where rotational speed remains unchanged and the output load varies. Figure 9 displays the application of Index 1 at the power spectra for faults of tests 3 and 4, respectively. It is seen that the influence of load upon the form of Index 1 is insignificant. The general qualitative form of the fault signatures is preserved regardless of load variations for both fault cases. The form is therefore preserved, even though the overall spectral energy varies with operating point, which was demonstrated by Mathioudakis et al. (1990). These observations indicate that the examined indices combined with selected spectra from sensors adjacent to faulty stages can provide a useful diagnostic tool.

Since phase averaging preserves the signal features, which are repeatable at the averaging period, it was thought that its application prior to power spectra calculation might enhance spectra and signatures, as long as periodic components are concerned. Employing such spectra for the calculation of Index 1 gives the result of Fig. 10, where a comparison to the corresponding index from raw data is presented. The indices from pressure transducer 2 for tests 3 and 4 are examined. It is noticed here that in the low-frequency range (up to two times the blade passing frequency of rotor stage 1) the index is significantly enhanced by predominance of information on harmonics, giving thus a picture of the envelope of the harmonics. On the other hand, at higher frequencies new information is added. This information should be examined very carefully, however, since the introduction of pseudo-periodic components is possible by the phase averaging, when the Nyquist frequency is approached.

## 6 Simulation of Blade Fault Signatures

The modification of the pressure field caused by the presence of a distorted blade in a rotating blade row can be calculated by means of flow analysis programs. Calculation of the pressure field for both the intact and the faulty blade row provides the possibility of reproducing pressure signals, which can then be processed in the same manner as the measured pressure signals discussed so far. The advantage of applying such a procedure is that signatures can be derived by analytical means and therefore the identification of faults can be done by comparison to these signatures, thus eliminating the need for performing tests and producing reference signatures for various blade faults. On the other hand, since the signatures are produced by calculation, such signatures can be derived for any other engine of known geometry, without the need for performing tests every time a different engine is considered.

The possibility of producing signatures by analytical means has been examined for one test case examined in this paper. The case of one twisted compressor rotor blade has been considered. The pressure field produced by the presence of one twisted blade in the stage 1 rotor was calculated by considering the following reasoning: Twisting of one blade, as shown in Fig. 2, causes a modification of the flow at the two blade

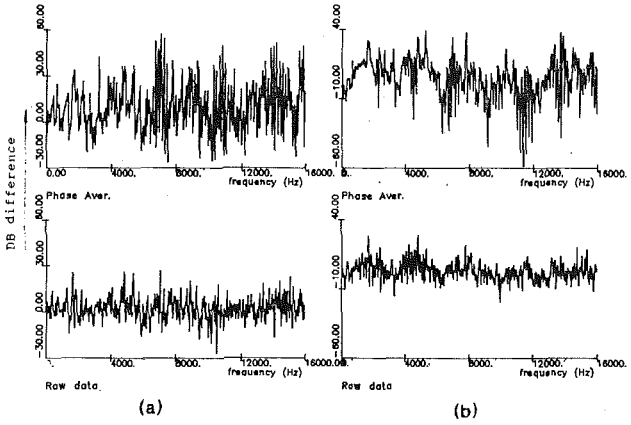


**Fig. 10 Index 1 calculated from phase-averaged pressure signals: (*a*) tests 3; (*b*) test 4**

passages adjacent to the blade. The distortion introduced by the blade causes a restriction of the flow in the passages and increases the incidence to the neighboring blades. The restriction is expected to be more severe for the blade on top of the twisted one in Fig. 2(*b*). The rest of the blades of the row are expected to operate at undistorted condition.

Following the above reasoning, the pressure fields around the twisted airfoil and the two airfoils from either side were calculated, while the rest of the blades of the rotor were considered to operate at the undistorted conditions for the same operating point. The pressure field calculation was done by very simple means, namely a singularity method (Wilkinson, 1967). By concatenating the calculated pressure fields, a pressure signal was produced, corresponding to the pressure signal of pressure transducer 2 in test 4. Similarly, a pressure signal was produced for the healthy rotor. The power spectrum calculation and application of Index 1 gave the signature of Fig. 11. The similarity to the corresponding measured signature, Fig. 8, is very good.

The accuracy of reproducing signature in this way depends on the sophistication of the flow analysis methods employed. It is remarkable that in the present case, a very simple flow analysis method was employed.

## 7 Signature Similarity Discriminants

It has been shown in the previous sections that the signatures of each fault are distinguishable and do not vary with engine load. This statement was based upon visual inspection of the corresponding figures. The similarity features observed on these figures can be mathematically formulated, in order to give objective criteria for comparison of the signatures. An example of application of such a procedure is described in this section.

A quantitative estimation of the similarity of two waveforms is known to be their cross-correlation coefficient (for definition, see for example Bendat and Piersol, 1971). If the indices are considered to constitute waveforms, their relative similarity can be expressed by such a coefficient. If certain signatures of a fault are considered as a reference, calculation of this coefficient for any signature derived from measurement data should give a value that would be indicative of their similarity to the particular fault signature.

This idea was applied to the fault indices calculated from the data of the present experiment. A reference signature was produced for the twisted blade fault. This signature was derived by averaging the values of Index 1 for each frequency over the four operating points of the engine. Index 1 was then calculated for every individual experiment and the correlation coefficient to that signature was calculated. The frequency range up to the second harmonic of the first rotor blade passing was con-

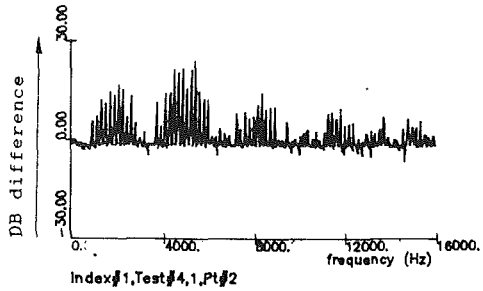


**Fig. 11 Index 1 for one twisted blade, produced by computation of the pressure signals**

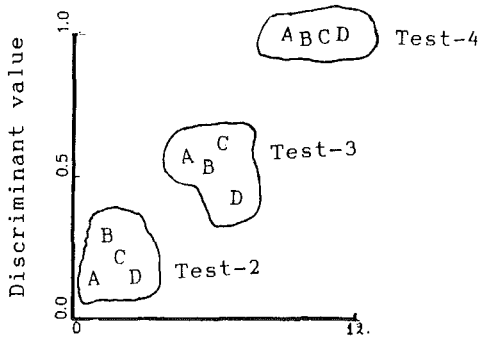


**Fig. 12 Discriminant for comparison of signatures of different tests to the reference signature of test 4**

sidered. The results of the calculation are shown in Fig. 12, where each letter represents the corresponding operating point. It is observed from this figure that data from test 4, namely one twisted blade, all give values very close to unity, indicating thus that the signatures are similar to the reference one. The values are much smaller for data from test 3, showing that these signatures are not similar to the reference and therefore, a different fault is present. Data from test 2 give even smaller values, indicating that the fault is not related to the reference one and yet different from fault 3. Similar conclusions have been reached by using as a reference the other two fault indices.

The above analysis shows that it is possible to decide whether a set of data can be classified as belonging to a particular class of faults, by simply observing the value of a single quantity, which can thus be used as a discriminant for fault classification. This choice of appropriate data organization and the derivation of several such discriminants is the subject of an investigation currently in progress by the authors.

## 8 Discussion

The analysis presented in the above sections has demonstrated the feasibility of detecting faults on rotating blades of gas turbine components. The particular feature of our investigation is that the experiments were performed on a commercial gas turbine operating under conditions that are the same as operating conditions in the field.

The faults that are detectable by the described procedure are of very small magnitude and cannot be detected by condition monitoring methods employing thermodynamic measurements. The deviations in performance caused by such faults are not of a magnitude sufficient to produce deviations in measured thermodynamic quantities. In this respect, the present method is complementary to performance condition monitoring, providing the capability of detecting the exact location and the kind of blade faults (in contrast to grossly detecting the component suffering from faults or deterioration). On the other hand, the variation in mechanical characteristics of the

engine shaft is also minor, and conventional monitoring systems (see for example Baines et al., 1987) cannot reveal the existence of those faults. This has also been experimentally verified during the present experiments. Shaft displacement signals acquired simultaneously with the pressure transducer signals gave no distinguishable signatures when the examined faults were implanted, as discussed by Mathioudakis et al. (1989b).

It was also demonstrated that discriminants can be derived from spectra and spectral indices. These discriminants are single numbers whose value can be used for identifying the kind of existing blade fault. The decision on the kind of fault is thus straightforward and can easily be performed by a computer program. This feature makes the procedure particularly suitable for incorporation into an expert system. From this point of view it meets current requirements of monitoring techniques, which aim to automate the procedure and eliminate the need of specialized personnel for interpreting the results of the measurements.

Finally, it should be mentioned that fast-response pressure transducer measurements, as the one reported here, can also be used for identification of another kind of operational malfunction, namely rotating stall in a compressor, which can lead to mechanical damage, as reported by Simmons and Smalley (1990). This possibility can be deduced from measurement results reported by Mathioudakis and Breugelmans (1988), as well as results from other investigations of this phenomenon. The occurrence of rotating stall is accompanied by the appearance of distinct waveforms in the measured pressure, corresponding to a rotational speed that is a fraction of the shaft rotational speed (namely the speed of rotation of stall cells).

## 9 Conclusions

A method for identification of rotating turbomachinery blade faults by measuring unsteady pressure at the inner casing surface has been presented. A commercial gas turbine was used as a test vehicle, and tests with different implanted blade faults were performed.

It was demonstrated that by calculating power spectra and subsequently producing spectral comparison indices, the kind of blade fault can be identified. The behavior of these indices was investigated and it was concluded that:

- The signatures are different for different blade faults.
- The signatures do not depend on the operating point, at least as long as the rotational speed remains the same.

Signatures for one of the experimentally tested faults were also produced by a simple computational procedure and they were found in very good agreement with the measured ones.

Finally, it was demonstrated that single-valued discriminants can be produced from the spectral indices, thus giving the possibility of introducing simple criteria for fault identification. This feature of the described procedure makes it suitable for inclusion in an expert system for fault diagnosis.

## Acknowledgments

The work reported in this paper has been carried out within the frame of research contract BRITE No. RI 1B-0159-F(CD). The authors express their thanks to the Hellenic General Secretariat for Research and Technology and the European Communities, for their financial support. Thanks are expressed to METRAVIB RDS and RUSTON GAS TURBINES, for providing the instrumentation and the test engine. The experiments were possible only by their cooperation. Special thanks are due to Mr. M. K. Smith for valuable discussions and suggestions and to Dr. P. Wetta for his excellent cooperation in preparing and executing the experiments.

## References

Baines, N., 1987, "Modern Vibration Analysis in Condition Monitoring," *Noise and Vibration Control Worldwide*, May, pp. 148–151.

Barschdorf, D., 1986, "Monitoring and Expert Systems for Automatic Failure Detection," presented at the Symposium Mantenimiento Predictive y Control de Maquinas Rotativas, Universidad de Oviedo, Gijon, Spain, July 15.

Barschdorf, D., and Korthauer, R., 1987, "Aspects of Failure Diagnosis on Rotating Parts of Turbomachines Using Computer Simulation and Pattern Recognition Methods," Paper No. H1, presented at the International Conference on Condition Monitoring, Brighton, United Kingdom, May, pp. 21–23.

Bendat, J. S., and Piersol, A. G., 1971, *Random Data: Analysis and Measurement Procedures*, Wiley-Interscience, New York.

Bloom, C., Isle, B., and Butler, A., 1989, "The Development and Delivery of Expert Systems for Special Environments," ASME Paper No. 89-GT-35.

Carchedi, F., and Wood, G. R., 1982, "Design and Development of a 12:1 Pressure Ratio Compressor for the Ruston 6-MW Gas Turbine," ASME JOURNAL OF ENGINEERING FOR POWER, Vol. 104.

Kaspar, K., 1982, "Altere Dampfturbinen im Kraftwerksbetrieb aus der Sicht des Maschinensversicherers," *VGB Kraftwerktechnik*, Vol. 62, No. 4, pp. 249–256.

Mathioudakis, K., and Breugelmans, F., 1988, "Three-Dimensional Flow Inside Deep Rotating Stalls of an Axial Flow Compressor," *Journal of Propulsion and Power*, May–June, pp. 263–269.

Mathioudakis, K., Stamatis, A., Loukis, E., and Papailiou, K., 1989a, "Computer Modeling and Data Processing Methods. An Essential Part of Jet Engine Condition Monitoring and Fault Diagnosis," presented at the 15th AIMS Symposium, Aachen, Federal Republic of Germany, Sept.

Mathioudakis, K., Papathanasiou, A., Loukis, E., Stamatis, A., and Papailiou, K., 1989b, "Noise/Vibration Imaging Techniques for Gas Turbine Investigations," Project Report No. 5, BRITE project No. 1368, June.

Mathioudakis, K., Loukis, E., and Papailiou, K. D., 1990, "Casing Vibration and Gas Turbine Operating Conditions," ASME JOURNAL OF ENGINEERING FOR GAS TURBINES AND POWER, Vol. 112, pp. 478–485.

Simmons, H. R., and Smalley, A. J., 1990, "Effective Tools for Diagnosing Elusive Turbomachinery Dynamics Problems in the Field," ASME JOURNAL OF ENGINEERING FOR GAS TURBINES AND POWER, Vol. 112, pp. 470–477.

Timperley, S., and Smith, M. K., 1983, "A Data-Logging and Performance Analysis System for Application to Industrial Gas Turbines," ASME Paper No. 83-GT-104.

Valero, M., and Esquiza, E., 1988, "Detection of Incipient Damage in Rotating Machinery by Noise Analysis," *Noise and Vibration Control Worldwide*, Oct., pp. 241–245.

Wilkinson, D. H., 1967, "A Numerical Solution of the Analysis and Design Problem for the Flow Past One or More Airfoils or Cascades," ARC Reports and Memoranda, No. 3545, Apr.

Wood, G. R., 1981, "The Ruston Tornado. A 6 MW Gas Turbine for Industrial Application," ASME Paper No. 81-GT-171.

**G. Merrington**
Aeronautical Research Laboratory,
Melbourne, Australia 3001

**Oh-Kyu Kwon**
Inha University,
Inchon, Korea

**G. Goodwin**
Newcastle University,
NSW, Australia 2308

**B. Carlsson**
Uppsala University,
Uppsala, Sweden

# Fault Detection and Diagnosis in Gas Turbines

*Modern military aircraft are fitted with Engine Monitoring Systems (EMS), which have the potential to provide maintenance personnel with valuable information for diagnosing engine faults and assessing engine condition. In this study, analytical redundancy methods have been applied to gas turbine engine transient data with the view to extracting the desired fault information. The basic idea is to use mathematical models to interrelate the measured variables and then monitor the effects of fault conditions on the new estimates of the model parameters. In most of the existing literature the models used are assumed to be perfect with the primary source of error arising from the measurement noise. In the technique to be described, a new method of quantifying the effects of changes in the operating conditions is presented when simplified models are employed. The technique accounts for undermodeling effects and errors arising from linearization of an inherently nonlinear system. Results obtained show a marked improvement over those obtained with traditional methods.*

## Introduction

Gas turbine performance degrades over time due to the influence of many effects, including tip clearance changes in the rotating components, seal wear, blade fouling, blade erosion, blade warping, foreign object damage, actuator wear, blocked fuel nozzles, and sensor problems. In some applications, such as in the commercial transport field, the availability of reliable cruise data facilitates the use of performance trending techniques for alerting maintenance personnel to emerging problems. However, the successful implementation of any trending techniques to gas turbine performance data still depends very largely on the skill and experience of the operator, especially when trying to diagnose some faults to module or line replaceable unit level. The situation is further exacerbated in the military arena because combat aircraft, in particular, seldom operate with their engines in a steady-state condition for extended periods. Thus, the selection of a suitable data capture window to provide maintenance personnel with reliable steady-state data is often difficult without resorting to dedicated tests, either on the ground or in-flight. In view of this, it would be convenient if operational transient engine data could be used for assessing engine condition and for diagnosing some of the more difficult engine faults.

Current generation military aircraft are often equipped with an Engine Monitoring System (EMS), which can be configured to capture selected engine data under certain conditions. These conditions include during flight when one or more of the measured parameters exceed predetermined limit values and during most take-offs. The take-off data, in particular, have the potential to provide a consistent data base for assessing engine condition, provided the analytical means are available for extracting the fault information. Because these data comprise engine accelerations from part-power positions, the current steady-state methods for assessing engine condition are not suitable. Methods have been developed for extracting fault information from gas turbine transient data [1, 4, 9, 13, 14, 17]. However, the methods differ in their ability to detect small changes, which usually accompany the presence of the degraded engine components.

In this paper, a new method of analyzing transient engine data is presented, which has the potential to detect the presence of degraded engine components from the actual EMS take-off measurements.

## Engine Fault Diagnosis and Condition Assessment

A fault may be defined as an abnormal change in the characteristics of a system, which gives rise to undesirable performance. The diagnostic tasks can be classified into three components [10], namely

- fault detection, i.e., making a binary decision between fault and no fault;
- fault diagnosis, i.e., isolating the source of the fault; and
- fault evaluation, i.e., characterizing the extent and significance of the failure.

Two related approaches can be used for fault detection, namely physical redundancy and analytical redundancy. The idea with physical redundancy is to use additional sensors to make independent measurements of the same parameter. In this way, sensor problems can be isolated by using a system of majority voting. The alternative is to use analytical redundancy where a model is used to interrelate two or more of the measured

Contributed by the International Gas Turbine Institute and presented at the 35th International Gas Turbine and Aeroengine Congress and Exposition, Brussels, Belgium, June 11–14, 1990. Manuscript received by the International Gas Turbine Institute January 24, 1990. Paper No. 90-GT-339.

variables and the model parameters are then monitored to determine the influence of any faults. For example, it could be convenient to measure speed and acceleration of a rotating component in an engine and in the fault-free case; these measurements are related by a known model (in this case the derivative of the speed should be the acceleration). If a fault condition exists then significant departures from the model can be expected. In a gas turbine, models can be used to relate various control input variables to various outputs. For example, changes in inputs, such as fuel flow and geometry, can be related to changes in the outputs, typically, spool speeds and pressures and temperatures throughout the gas path.

The idea with analytic fault detection is to examine critically the model used to interrelate the measured variables. Under fault-free conditions, estimates of the model parameters can be made along with the expected variation in the parameters due to inaccuracies in the modeling process. Typical inaccuracies include effects of undermodeling (where a simplified model is used for convenience to approximate the real system), linearization errors, and measurement noise. If, over a period of time, the new estimates of the model parameters fall outside the expected fault-free range, then a suspected fault condition exists. The particular way in which the estimated parameters vary from the nominal fault-free values will define a fault signature. This in turn can be used as an aid in diagnosing the cause of the suspected fault.

The key ingredient in an analytical redundancy approach is the mathematical model used to interrelate the measured variables. A typical model for an aircraft gas turbine engine [6, 19] can have up to six inputs and outputs with 20 or more state variables. In addition, a nonlinear model is usually required to describe the complex aerothermodynamic relationships over the full speed range of an engine. Thus, to gain insight into the fault detection problem, it is generally desirable to simplify the equations to something more manageable. Typically, linear models of order two or three are employed containing one or two inputs and outputs. The structure and the number of parameters to be used in these simplified models may depend on the operating conditions; for example, the most suitable model at part power may differ from that required at high power settings.

Some indication of the difficulty involved in diagnosing faults from transient data can be seen from the following example. The steady-state performance of a gas turbine can be defined within fairly close tolerances for a given operating condition as shown in Fig. 1, corresponding to sea-level-static test results from a turbofan engine over a range of inlet temperatures ($-5°C \le T_0 \le 45°C$). The uncertainty in the measured variables is minimized by allowing the engine to stabilize for long enough to reduce bulk temperature effects and averaging the measurements over a reasonable sampling period. However, results obtained from acceleration transients for the same engine do not produce a similar characteristic curve, but exhibit different profiles for each transient depending on the ambient conditions and the operating technique used Fig. 2. This is not surprising because of the increased effect of the changes in bulk temperature on the transient behavior compared to that of the steady state. Furthermore, the effect of measurement noise in the transient case cannot be so easily filtered as in the steady-state case. Thus, it is important that the fault detection procedures be capable of distinguishing between model changes resulting from nonfaulty conditions, such as changes in ambient conditions and/or operating procedures, from those introduced by faults.

## System Description and Parameter Estimation Procedure

There is a vast body of information on fault detection and diagnosis, for example, [2, 3, 10, 20]. In many cases the models used are assumed to describe the relationships between the various measurands accurately with the primary source of uncertainty being the measurement noise. This assumption leads to the conclusion that arbitrary small faults can be detected provided the system is observed for long enough [4]. In addition, the assumption of perfect modeling impacts upon the form of the individual parameter fault signatures used to distinguish between faulty and nonfaulty conditions.

All mathematical models are only approximate descriptions of real systems, As alluded to previously, the major sources of errors are measurement noise, undermodeling effects, and linearization errors. Thus a typical engine acceleration transient response can be represented by the following system description based on the Taylor series expansion of the input–output relationship:

$$y(k) = G(q^{-1})u(k) + G_\Delta(q^{-1})u(k) + G_{n\Delta}(q^{-1})u^2(k)\text{sign}(u(k)) + v(k)) + v(k) \quad (1)$$

where $q^{-1}$ denotes the delay operator, $G$ is the nominal model, $G_\Delta$ and $G_{n\Delta}$ denote the mismatched model due to undermodeling and linearization error, respectively, and $v$ is the

## Nomenclature

$B$ = numerator function in equation (1)
$C$ = uncertainty in the parameter space
$D$ = uncertainty in the frequency domain
$E$ = expectation in probability space
$F$ = denominator function in equation (2)
$G$ = nominal transfer function
$G_\Delta$ = mismatched model
$G_{n\Delta}$ = linearization error
$H$ = vector of impulse responses
$h$ = impulse response
$N$ = number of data points
$N_L$ = fan speed
$n$ = number of discrete frequencies in the range
$P$ = noise covariance matrix
$q^{-1}$ = delay operator
$Q$ = undermodeling covariance matrix
$R$ = covariance of unmodeled impulse response
$r$ = components of $R$
$S$ = vector of unmodeled response
$T_0$ = engine inlet temperature
$T_1$ = test variable in equation (16)
$T_2$ = test variable in equation (17)
$T_n$ = test based on measurement noise only
$T_{au}$ = standard cross validation test
$T_{f1}$ = test in the frequency domain
$T_{f2}$ = additional test in the frequency domain
$T_s$ = sampling period
$u$ = input signal value
$\underline{V}$ = measurement noise vector
$V$ = sensitivity of frequency response to parameter variations
$v$ = measurement noise
$W_F$ = fuel flow
$Y$ = output vector
$y$ = output signal value
$z^{-1}$ = $z$-transform variable
$\beta$ = decay parameter in covariance
$\delta_{kj}$ = delta function
$\theta$ = parameter vector
$\sigma^2$ = variance
$\tau$ = test variable
$\Phi$ = matrix of inputs
$\psi$ = matrix of inputs
$\psi_n$ = matrix of second-order inputs
$\omega$ = frequency in radians per second

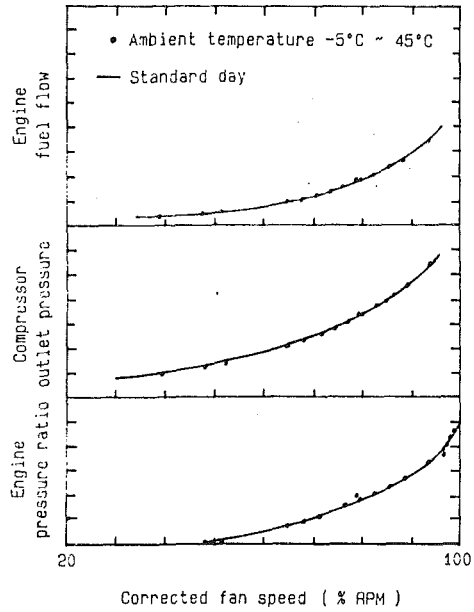


**Fig. 1 Steady-state turbofan data for various inlet temperatures**

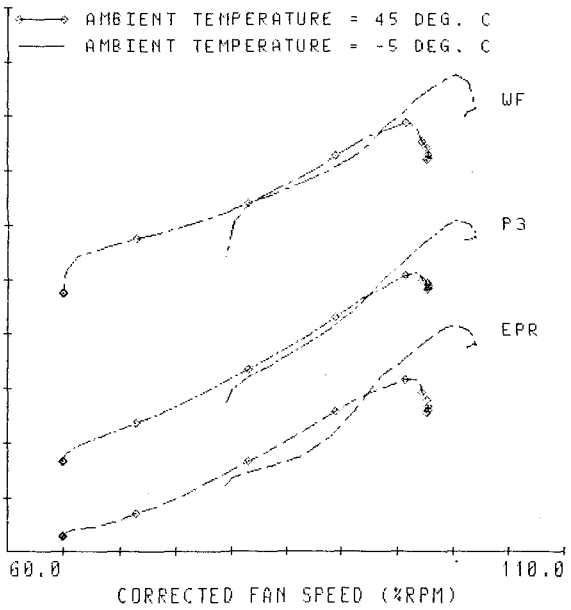


**Fig. 2 Turbofan acceleration response for different inlet temperatures**

measurement noise. This system description is depicted by Fig. 3.

The expansion given in equation (1) can be justified either in terms of linearization about an operating point or via a description of a nonlinear system in which the nonlinearity is represented as a static element on the input side [11].

We assume that $G$, $G_\Delta$, and $G_{n\Delta}$ are stable and causal and that $v$ is zero-mean white noise with variance $\sigma_v^2$. The nominal model is taken to be

$$G(z^{-1},\theta)=\frac{B(z^{-1},\theta,n_B)}{F(z^{-1},n_F)} \tag{2}$$

where $F(z^{-1}, n_F)$ is a predetermined denominator and

$$B(z^{-1},\theta,n_B)\triangleq b_1z^{-1}+b_2z^{-2}+\ldots\ldots+b_{n_B}z^{-n_B}$$

$$F(z^{-1},n_F)\triangleq 1+f_1z^{-1}+f_2z^{-2}+\ldots\ldots+f_{n_F}z^{-n_F}$$

$$\theta\triangleq[b_1,\ b_2,\ \ldots,\ b_{n_B}]^T$$

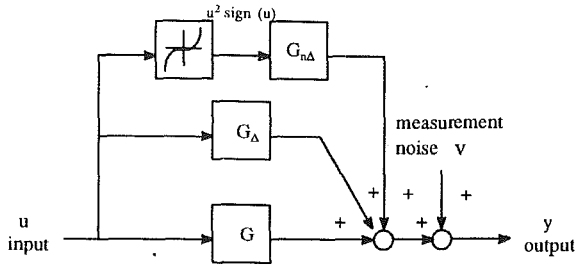


**Fig. 3 System description including undermodeling, linearization error, and measurement noise**

The denominator $F(z^{-1}, n_F)$ can be determined from *a priori* information about the system, e.g., approximate values of dominant poles or by some prior estimation experiments on the system. Note that any linear stable system can always be approximated by the nominal model equation (1) by adjusting the orders $n_B$ and $n_F$. Basically, errors in the denominator polynomial are corrected by adjustments to the numerator polynomial.

Using the system description equation (1) the system output has the following form:

$$y(k)=B(q^{-1},\theta,n_B)u_F(k)+\eta(k) \tag{3}$$

where

$$u_F(k)\triangleq\frac{1}{F(q^{-1},n_F)}u(k)$$

$$\eta(k)\triangleq G_\Delta(q^{-1})u(k)+G_{n\Delta}u^2(k)\text{sign}(u(k))+v(k)$$

Equation (3) can be represented in standard linear regression form as

$$y(k)=\phi^T(k)\theta+\eta(k) \tag{4}$$

where

$$\phi(k)\triangleq[u_F(k-1),\ u_F(k-2),\ \ldots,u_F(k-n_B)]^T \tag{5}$$

We define the estimated parameter using ordinary least squares as

$$\hat{\theta}\triangleq\text{argmin}\left\{\frac{1}{N}\sum_{k=1}^{N}[y(k)-B(q^{-1},\theta,n_B)u_F(k)]^2\right\} \tag{6}$$

Note that equation (6) corresponds to output error minimization. However, the ordinary least-squares method can be used to solve this problem due to the special form of the representation equation (2).

The least-squares method then gives the estimated parameters as

$$\hat{\phi}=[\Phi^T\Phi]^{-1}\Phi^TY \tag{7}$$

where

$$\Phi\triangleq[\phi(1),\ \phi(2),\ldots,\phi(N)]^T$$

$$Y\triangleq[y(1),\ y(2),\ldots,y(N)]^T \tag{8}$$

and $N$ is the number of data points.

From equation (5) and equation (6) we can also derive the following expression for the estimation error:

$$\theta\triangleq\hat{\theta}-\theta=[\Phi^T\Phi]^{-1}\Phi^TS \tag{9}$$

where

$$S\triangleq[\eta(1),\ \eta(2),\ldots,\eta(N)]^T \tag{10}$$

Using equation (4) and denoting the impulse response of $G_\Delta$ and $G_{n\Delta}$ as $\{h(\cdot)\}$ and $\{h_n(\cdot)\}$, respectively, $\eta(k)$ can be expressed as

$$\eta(k)=\sum_{i=0}^{k}h(i)u(k-i)$$

$$+\sum_{i=0}^{k}h_n(i)u^2(k-i)\text{sign}(u(k-i))+v(k)$$

assuming that $u(k)=0$ for $k\leq 0$ and $h(k)=h_n(k)=0$ for $k<0$. Then we obtain the following relationship from equation (10):

$$S=\Psi H+\Psi_n H_n+V \tag{11}$$

$$\Psi\triangleq\begin{bmatrix} u(1) & 0 & \\ u(2) & u(1) & 0 \\ \vdots & \vdots & \ddots \\ u(N) & u(N-1) & \cdots\ u(1) \end{bmatrix}$$

$$H\triangleq[h(0)\ h(1).\ .\ .\ .\ .\ .\ .\ .\ .\ h(N-1)]^T \tag{12}$$

$$V\triangleq[v(1)\ v(2).\ .\ .\ .\ .\ .\ .\ .\ .\ v(N)]^T$$

$$\Psi_n=\begin{bmatrix} u^2(1)\text{sign}(u(1)) & 0 & \\ u^2(2)\text{sign}(u(2)) & u^2(1)\text{sign}(u(1)) & 0 \\ \vdots & \vdots & \ddots \\ u^2(N)sign(u(N)) & u^2(N-1)\text{sign}(u(N-1)) & \cdots\ u^2(1)\text{sign}(u(1)) \end{bmatrix} \tag{13}$$

$$H_n=[h_n(0),\ h_n(1),\ \ldots,h_n(N-1)]^T$$

Before we can proceed we need to say something about the unmodeled impulse response $\{h(\cdot)\}$ and $\{h_n(\cdot)\}$. It would not make sense to assume these were known since they would then hardly qualify as being unmodeled dynamics. We overcome this dilemma by adopting a Bayesian point of view. We assume that *a priori* knowledge is available, which allows us to give a prior distribution to $\{h(\cdot)\}$ and $\{h_n(\cdot)\}$. This procedure is discussed in detail in [8], where the term "Stochastic Embedding" is used to describe the procedure of giving an *a priori* distribution to $\{h(\cdot)\}$. For our purposes here we will simply assume knowledge of the mean and covariance function for these distributions. We will later show how information about the second-order moments of $\{h(\cdot)\}$ and $\{h_n(\cdot)\}$ can be obtained from a series of experiments performed on nonfaulted systems. Given information about the second-order statistics of $h$, $h_n$, and $v$, we can then evaluate the expected value of the estimation error, $E\{\tilde{\theta}\tilde{\theta}^T\}$. This will be the basis of the fault detection method to be described below.

## Model-Based Fault Detection Method

We note that transient engine data are available from aircraft EMS. Thus in the sequel we assume that we have access to two sets of data, $I_n$ and $I_f$, where $I_n$ corresponds to nonfaulty data and $I_f$ corresponds to the suspected faulty data. The estimated parameter $\hat{\theta}$ and the corresponding nominal transfer function $G(z)$ may take different values in each experiment:

$$\hat{\theta}=\begin{cases}\hat{\theta}_n, & \text{for data set } I_n\\ \hat{\theta}_f, & \text{for data set } I_f\end{cases} \tag{14}$$

$$G(z^{-1},\hat{\theta})=\begin{cases}\hat{G}_n(z^{-1})=G(z^{-1},\hat{\theta}_n) & \text{for } I_n\\ \hat{G}_l(z^{-1})=G(z^{-1},\hat{\theta}_f) & \text{for } I_f\end{cases} \tag{15}$$

where $\hat{\theta}$ and $\hat{G}$ denote the estimated values of $\theta$ and $G$, respectively. We also assume that $H$, $H_n$, and $V$ are uncorrelated with one another.

The fault detection procedure now amounts to comparing $\hat{\theta}_n$ and $\hat{\theta}_f$ (or $\hat{G}_n$ and $\hat{G}_f$) and deciding whether the observed changes can be explained satisfactorily in terms of the effects of noise, undermodeling, and nonlinearity. If not, then we may conclude that a system fault has occurred. The covariance functions of $(\hat{\theta}_n-\hat{\theta}_f)$ and $(\hat{G}_n-\hat{G}_f)$ under nonfaulty condition will be used in this paper as measures of the uncertainty due to noise, undermodeling, and nonlinearity. An expression for the covariance of $\hat{\theta}_n-\hat{\theta}_f$ is as follows (see Appendix for proof):

$$C\triangleq\text{Cov}(\hat{\theta}_n-\hat{\theta}_f)=\text{E}\{[\hat{\theta}_n-\hat{\theta}_f]\ [\hat{\theta}_n-\hat{\theta}_f]^T\}$$

$$=[Q_n-Q_f]R[Q_n-Q_f]^T+[Q_{nn}-Q_{nf}]R_n[Q_{nn}-Q_{nf}]^T+[P_n] \tag{16}$$

where

$$Q_i\triangleq P_i\Phi_i^T\Psi_i,\quad Q_{ni}=P_i\Phi_i^T\Psi_{ni},\quad i=n,f$$

$$P_i\triangleq[\Phi_i^T\Phi_1]^{-1},$$

$$R\triangleq E[HH^T],\quad R_n\triangleq E\{H_nH_n^T\}$$

where $E$ denotes the expectation with respect to the underlying probability space, and $\Phi$, $\Psi$, and $\Psi_n$ are as in equations (8), (12), and (13), respectively.

The first and second terms on the right-hand side of equations (16) account for the effects of undermodeling, nonlinearities, and the difference in input signals for the two experiments. Note that if there is no undermodeling and no nonlinearity or if the inputs are identical, these terms vanish. The third term on the right-hand side of equation (16) corresponds to measurement noise. The higher the SNR (signal-to-noise-ratio) is, the smaller the norm of this term.

The matrix $C$ of equation (16) can now be used to formulate appropriate test variables for fault detection. For example, we may use

$$T_1=[\hat{\theta}_n-\hat{\theta}_f]^TC^{-1}[\hat{\theta}_n-\hat{\theta}_f] \tag{17}$$

$$T_2=[\hat{\theta}_n-\hat{\theta}_f]^T[\text{diag}(C)]^{-1}[\hat{\theta}_n-\hat{\theta}_f] \tag{18}$$

The test variables in equations (17), and (18) are based on a comparison between the observed value and the expected value of $[\hat{\theta}_n-\hat{\theta}_f]\ [\hat{\theta}_n-\hat{\theta}_f]^T$. If the test variable is larger than a fixed threshold we take this as evidence that the system parameters have changed (i.e., a fault has occurred).

It is straightforward to extend the result of Theorem 1 (see Appendix) to obtain uncertainty bounds in the frequency domain. The expected value of the difference between the estimated transfer functions in two nonfaulty experiments is evaluated in the following result; see Theorem 2 in Appendix.

$$D(\omega,n)\triangleq E\{\Delta\hat{G}(\omega,n)\Delta\hat{G}(\omega,n)\Delta\hat{G}(\omega,n)^*\}$$
$$=\overline{V}(\omega,n)C\,\overline{V}(\omega,n)^* \tag{19}$$

where

$$\overline{V}(\omega,n)\triangleq\left[\frac{\partial}{\partial\theta}G(e^{j\omega_1},\theta),\frac{\partial}{\partial\theta}G(e^{j\omega_2},\theta),\ldots,\frac{\partial}{\partial\theta}G(e^{j\omega_n},\theta)\right]$$

$$\Delta\hat{G}(\omega,n)\triangleq[\hat{G}_n(e^{j\omega_1})-\hat{G}_f(e^{j\omega_1}),\ldots,\hat{G}_n(e^{j\omega_n})-\hat{G}_f(e^{j\omega_n})]$$

$$\omega\triangleq[\omega_1,\omega_2,\ldots,\omega_n]^T$$

$G$ is the nominal transfer function, $C$ is as in equation (16),

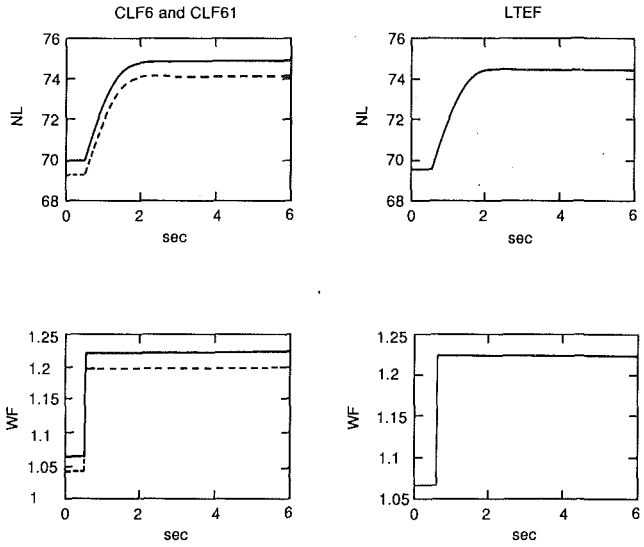


Fig. 4 Nonfaulty data sets (___ CLF6; ----CLF61) and faulty data set (LTEF) in aircraft engines

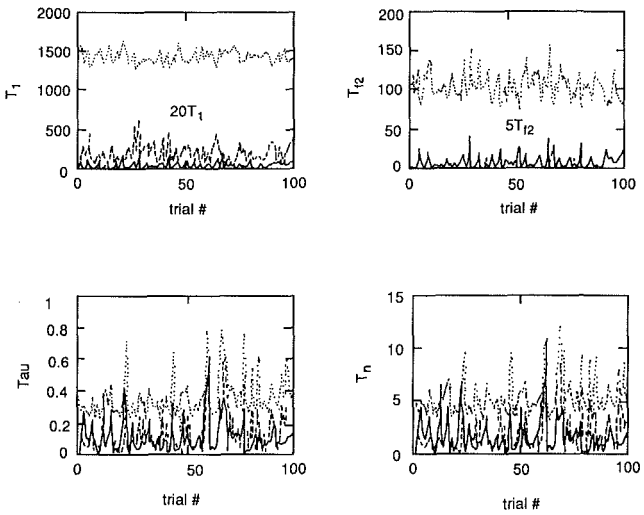


Fig. 5 Simulation results (___ NF1, nonfaulty case; --- NF2, nonfaulty case; . . . F3 faulty case)

the superscript * denotes the conjugate transpose, and $n$ is the number of frequencies of interest.

Based on the result in Theorem 2, we can develop test variables for fault detection in the frequency domain. For example, the frequency domain equivalents of equation (17) and (18) are

$$T_{f1} \triangleq \Delta\hat{G}^*(\omega, n)D(\omega, n)^{-1}\Delta\hat{G}(\omega, n), \quad n \le n_B \tag{20}$$

$$T_{f2} \triangleq \frac{1}{n}\sum_{i=1}^{n} |\hat{G}_n(e^{j\omega i}) - \hat{G}_f(e^{j\omega i})|^2/D_{ii}(\omega, n) \tag{21}$$

Of course, evaluation of the test variables $T_1$, $T_2$, $T_{f1}$, and $T_{f2}$ depends upon prior knowledge of $R$ and $R_n$. These data can be obtained from prior experimentation with nonfaulty systems based on some simplifying assumptions. For example, in recent literature on robust adaptive control [7, 15, 16], it has been assumed that the unmodeled dynamics are bounded by an exponential function. The corresponding stochastic assumption would be to assume

$$E\{h(k)h(j)\} = r(k)\delta_{k_j}$$

$$E\{h_n(k)h_n(j)\} = r_n(k)\delta_{k_j}$$

Table 1 Cases in aircraft engine fault detection simulation

| Case No. | Experiment n | Experiment f |
|---|---|---|
| NF 1 | CLF 6 | CLF 6 |
| NF 2 | CLF 6 | CLF 61 |
| F 3 | CLF 6 | LTEF |

Table 2 Summary of simulation results

| Case No. | $T_1$ | $T_{f2}$ | $\tau$ | $T_n$ |
|---|---|---|---|---|
| NF1 | 2.45 ± 2.42 | 1.30 ± 1.68 | 0.12 ± 0.12 | 1.81 ± 1.84 |
| NF2 | 9.67 ± 6.18 | 1.53 ± 1.68 | 0.14 ± 0.14 | 2.06 ± 1.96 |
| F3 | 1459.88 ± 85.07 | 105.76 ± 18.29 | 0.37 ± 0.13 | 5.48 ± 1.93 |

where

$$r(k) = \sigma_0^2 e^{-\beta k};\ k = 0, 1, \ldots . \tag{22}$$

$$r_n(k) = \sigma_n^2 e^{-\beta_n k};\ k = 0, 1, \ldots . \tag{23}$$

In equations (22) and (23), $2/\beta$ can be considered as the "average" time constant for the class of unmodeled dynamics. Given the simple description equations (22) and (23), we can estimate $\sigma_0^2$, $\sigma_n^2$, $\beta$, and $\beta_n$ from a sequence of prior experiments on nonfaulted systems.

## Application to an Aircraft Gas Turbine Engine

In order to illustrate the feature of the proposed method, we present some simulations for a military turbofan gas turbine engine. Exact models of aircraft engines are highly nonlinear [19] and thus simplified linearized models are usually employed [5, 12]. For example, taking the engine fuel flow $W_F$ as the input and the fan-spool speed $N_L$ as the output, an appropriate linearized nominal model is given as follows:

$$\Delta N_L(t) = \frac{b_{1c}p + b_{0c}}{p^2 + f_{1c}p + f_{0c}}\Delta W_F(t) \tag{24}$$

where $p$ denotes the differential operator.

Noise-free nonfaulty data sets (CLF6 and CLF61) and a faulty data set (LTEF) with $-2$ percent change in the low pressure turbine efficiency were chosen for the study (Fig. 4). Note that LTEF has the same operating point as that of CLF6 but that CLF61 has a different operating point with a very similar output to LTEF.

Taking noise and linearization errors into consideration, we can describe the underlying system by the following discretized model similar to equation (1) but with $G_\Delta = 0$:

$$\Delta N_L(k) = G(q^{-1})\Delta W_F(k) + G_{n\Delta}(q^{-1})[\Delta W_F(k)]^2 + v(k) \tag{25}$$

where

$$G(q^{-1}) = \frac{B(q^{-1}, \theta, n_B)}{F(q^{-1}, n_F)} = \frac{b_1 q^{-1} + b_2 q^{-2}}{1 + f_1 q^{-1} + f_2 q^{-2}}$$

We have applied the fault detection method to this problem, as shown in Table 1. The following constants were chosen: $T_s = 0.2$, $N = 350$, $n = 32$ between [0, 10] Hz, $\sigma_v^2 = 0.15^2$ (with a reference value of 100 percent) and the input $\Delta W_F$ was assumed to be corrupted by white noise with variance $\sigma_u^2 = 0.003^2$ (with a fuel range of 0 to 1). The fixed denominator was taken by prior experiments as $f_1 = -1.8238$ and $f_2 = 0.8294$ and the values of $\beta_n$ and $\sigma_n^2$ as $\beta_n = 0.0837$ and $\sigma_n^2 = 0.0818$.

Test variables $T_1$ and $T_{f2}$ of equations (17) and (20), respectively, have been adopted for fault detection and another test variable $\tau$ given by a standard cross validation test (18) has been also applied for the sake of comparison:

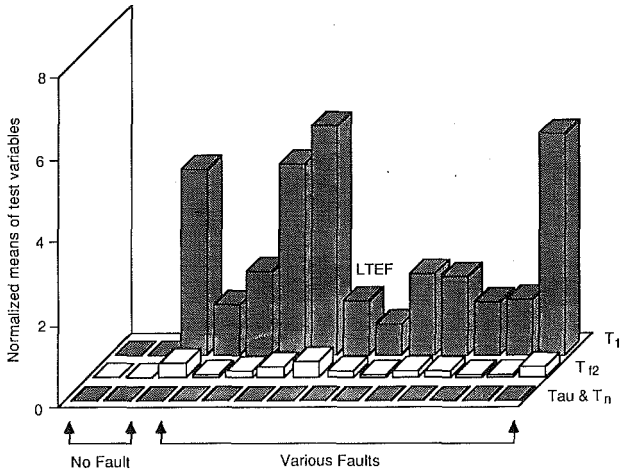


**Fig. 6 Simulation results for various kinds of fault in aircraft engines**

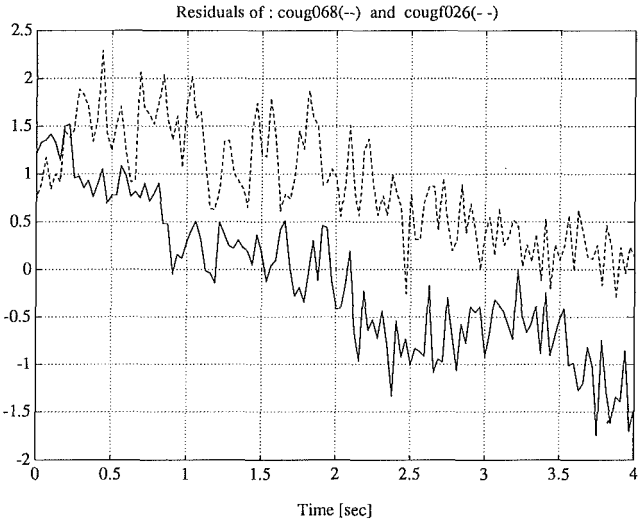


**Fig. 7 Residuals of "fault (---) and no-fault (___)" test runs**

$$\tau = \| Y_n - \Phi_n \hat{\theta}_f \|_2^2 - \| Y_n - \Phi_n \hat{\theta}_n \|_2^2$$

Also, a test was performed using the final term in equation (16) only to indicate the improvement resulting from the inclusion of undermodeling and linearization errors in the uncertainty bound. We denote this test variable as $T_n$.

The simulation results are shown in Fig. 5 and summarized in Table 2. Note that 100 trials were conducted with different noise realizations. These results show that the proposed fault detection method works very well even under the effect of linearization errors. Note that the cross validation test (18) and noise only test variable $T_n$ do not work well for this problem.

We simulated many other kinds of faults (11 causes in all) and in cases test variables $T_1$ and $T_{f2}$ gave consistent discrimination of the fault condition, as shown in Fig. 6.

A set of test runs of the cougar engine was performed by Aeronautical Research Laboratory in Melbourne. The data was divided into two sets, referred to as "no-fault" and "fault" tests. The no-fault runs consisted of snap and slower accelerations with a nozzle area of 115 percent. With the nozzle area increased to 120 percent snap accelerations runs were performed over the same speed ranges to yield the faulty data set.

The model described by equation (24) was fitted to the available data. Figure 7 shows residuals of "no-fault" and "fault" test runs. It is clear from Fig. 7 that the residuals of the "fault" test run are considerably higher than the "no-fault" test run, indicating the effectiveness of the method proposed for fault detection.

## Conclusions

A fault detection method for uncertain systems having undermodeling, linearization errors, and noise has been proposed. The key feature of this method is that it accounts for the effects of noise, model mismatch, and linearization errors. The method has been shown to work well on simulated gas turbine data and to outperform existing methods. This improvement is a consequence of the fact that the proposed method explicitly accounts for the effects of undermodeling and linearization errors in nonlinear systems.

## References


1 Baskiotis, C., Raymond, J., and Rault, A., "Parameter Identification and Discriminant Analysis for Jet Engine Mechanical State Diagnosis," *Proc. IEEE Conf. on Decision and Control and Sciences*, Fort Lauderdale, FL, 1979.

2 Basseville, M., and Benveniste, A., eds., *Detection of Abrupt Changes in Signals and Dynamical Systems*, Lecture notes in Control and Sciences, Vol. 77, Springer-Verlag, New York, 1986.

3 Basserville, M., "Detection of Changes in Signals and Systems—A Survey," *Automatica*, Vol. 24, pp. 309–326.

4 Carlsson, B., Salgado, M., and Goodwin, G. C., "A New Method for Fault Detection and Diagnosis," Technical Report EE8842, Dept. of Electrical Engr. and Computer Science, University of Newcastle, Australia, 1988; submitted to *Automatica*.

5 Dehoff, R. L., Hall, W. E., Jr., Adams, R. J., and Gupta, N. K., "F100 Multivariable Control Synthesis Program," AFAPL-TR-77-35, Vols. I and II, 1977.

6 Dehoff, R. L., and Hall, W. E., "Models for Jet Engine Systems, Part II, State Space Techniques and Modelling for Control," *Control and Dynamic Systems*, Vol. 14, 1978, pp. 259–299.

7 de Souza, C. E., Goodwin, G. C., and Mayne, D. Q., "An Adaptive Control Algorithm for Linear Systems Having Unknown Time Delay," *Automatica*, Vol. 24, 1988, pp. 327–341.

8 Goodwin, G. C., and Salgado, M. E., "Quantification of Uncertainty in Estimation Using an Embedding Principle," *International Journal of Adaptive Control and Signal Processing*, 1989, in press.

9 Henry, J. R., "CF-18 F404 Transient Performance Trending," AGARD CP NO. 448, Paper No. 37, Quebec City, 1988.

10 Isermann, R., "Process Fault Detection Based on Modelling and Estimation Methods—A Survey," *Automatica*, Vol. 20, 1984, pp. 387–404.

11 Ljung, L., *System Identification: Theory for the User*, Prentice Hall, Inc., Englewood Cliffs, NJ, 1987.

12 Merrill, W., "Identification of Multivariable High-Performance Turbofan Engine Dynamics From Closed Loop Data," *J. Guidance*, Vol. 7, 1984, pp. 677–683.

13 Merrington, G. L., "Identification of Dynamic Characteristics for Fault Isolation Purposes in a Gas Turbine Using Closed-Loop Measurements," AGARD CP No. 488, Paper No. 36, Quebec City, 1988.

14 Merrington, G. L., "Fault Diagnosis of Gas Turbine Engines From Transient Data," ASME JOURNAL OF ENGINEERING FOR GAS TURBINES AND POWER, Vol. 111, No. 2, 1989, pp. 237–243.

15 Middleton, R. H., Goodwin, G. C., Mayne, D. Q., and Hill, D. J., "Design Issues in Adaptive Control," *IEEE Trans. Automat. Contr.*, Vol. AC-33, 1988, pp. 50–58.

16 Praly, L., "Robustness of Indirect Adaptive Control Based on Pole Placement Design," *IFAC Workshop on Adaptive Control*, San Francisco, CA, 1983.

17 Smed, T. B., Carlsson, T. B., de Souza, C. E., and Goodwin, G. C., "Fault Detection and Diagnosis Applied to Gas Turbines," Technical Report EE8815, Dept. of Electr. Engr. and Computer Science, University of Newcastle, Australia, 1988.

18 Soderstrom, T., and Kumamaru, K., "On the Use of Kullback Discrimination Index for Model Validation and Fault Detection," Report UPTEC 8520R, Uppsala University, Sweden, 1985.

19 Szuch, J. R., "Models for Jet Engine Systems," *Control and Dynamic Systems*, Vol. 12, 1976, pp. 213–258.

20 Willsky, A. S., "A Survey of Design Methods for Failure Detection in Dynamic Methods—A Survey," *Automatica*, Vol. 12, 1976, pp. 601–611.

21 Zhang, C., Goodwin, G. C., and de Souza, C. E., "A Survey of Aircraft Engine Fault Detection and Diagnosis," Technical Report EE8735, Dept. of Electrical Eng. and Computer Science, University of Newcastle, Australia, 1987.


## APPENDIX

### Expression for the Uncertainty Bounds in the Parameter Space

**Theorem 1:** Given two sets of estimated parameters as in equation (14) for the underlying system of Fig. 3, the covar-

iance of $(\hat{\theta}_n - \hat{\theta}_f)$ is represented under nonfaulty condition as follows:

$$C \triangleq \text{Cov}\,(\hat{\theta}_n - \hat{\theta}_f) = E\{[\hat{\theta}_n - \hat{\theta}_f]\ \hat{\theta}_n - \hat{\theta}_f]^T\}$$

$$= [Q_n - Q_f]R[Q_n - Q_f]^T + [Q_{nn} - Q_{nf}]R_n[Q_{nn} - Q_{nf}]^T + [P_n] \quad \text{(A1)}$$

where

$$Q_i \triangleq P_i\Phi_i^T\Psi_i, \quad Q_{ni} = P_i\Phi_i^T\Psi_{ni}, \quad i = n, f,$$

$$P_i \triangleq [\Phi_i^T\Phi_i]^{-1},$$

$$R \triangleq E[HH^T], \quad R_n \triangleq E\{H_nH_n^T\}$$

where $E$ denotes the expectation with respect to the underlying probability space, and $\Phi$, $\Psi$, and $\Psi_n$ are in equations (18), (12), and (13) respectively.

**Proof:** By definition we have

$$C = E\{[\hat{\theta}_n - \hat{\theta}_f]\ [\hat{\theta}_n - \hat{\theta}_f]^T\}$$

$$= E\{[\hat{\theta}_n - \theta]\ [\hat{\theta}_n - \theta]^T\} + E\{[\hat{\theta}_f - \theta]\ [\hat{\theta}_f - \theta]^T\}$$

$$- E\{[\hat{\theta}_n - \theta]\ [\hat{\theta}_f - \theta]^T\} - E\{[\hat{\theta}_f - \theta]\ [\hat{\theta}_n - \theta]^T\} \quad \text{(A2)}$$

equation (19) and equation (12) give

$$\hat{\theta}_i - \theta = [\Phi_i^T\Phi_i]^{-1}\Phi_i^T S_i, \quad i = n, f$$

$$E[S_iS_j^T] = E\{[\Psi_i H + \Psi_{ni}H_n + V_i]\ [\Psi_j H + \Psi_{nj}H_n + V_j]^T\}$$

$$= \Psi_i R\Psi_j^T + \Psi_{ni}R_n\Psi_{nj}^T + \sigma_v^2 I\delta_{ij}, \quad j = n, f \quad \text{(A3)}$$

Substituting equation (A3) into equation (A2) gives equation (A1).

▽ ▽ ▽

## Expression of the Uncertainty Bounds in the Frequency Domain

**Theorem 2:** Given two sets of estimated transfer functions as in equation (15) under the same conditions as used in Theorem 1, we have:

$$D(\omega, n) \triangleq E\{\Delta\hat{G}(\omega, n)\Delta\hat{G}(\omega, n)^*\}$$

$$= \overline{V}(\omega, n)C\overline{V}(\omega, n)^* \quad \text{(A4)}$$

where

$$V(\omega, n) \triangleq \left[\frac{\partial}{\partial\theta}G(e^{j\omega_1}, \theta), \frac{\partial}{\partial\theta}G(e^{j\omega_2}, \theta \ldots, \frac{\partial}{\partial\theta}G(e^{j\omega_n}\theta)\right]^T$$

$$\Delta\hat{G}(\omega, n) \triangleq [\hat{G}_n(e^{j\omega_1}) - \hat{G}_f(e^{j\omega_1}), \ldots, \hat{G}_n(e^{j\omega_n}) - \hat{G}_f(e^{j\omega_n})]^T$$

$$\omega \triangleq [\omega_1, \omega_2, \ldots, \omega_n]^T,$$

$G$ is the nominal transfer function, $C$ is as in equation (A1), the superscript * denotes the conjugate transpose, and $n$ is the number of frequencies of interest.

**Proof:** The $i \times k$ element of the matrix $D(\omega, n)$ can be expanded as follows:

$$D_{ik}(\omega, n) = E\{[\hat{G}_n(e^{j\omega_i}) - \hat{G}_f(e^{j\omega_i})]\ [\hat{G}_n(e^{j\omega_k}) - \hat{G}_f(e^{j\omega_k})]^*$$

$$= E\{[\hat{G}_n(e^{j\omega_i}) - \hat{G}(e^{j\omega_i}, \theta)]\ [\hat{G}_n(e^{j\omega_k}) - \hat{G}(e^{j\omega_k}, \theta)]^*\}$$

$$+ E\{[\hat{G}_f(e^{j\omega_i}) - \hat{G}(e^{j\omega_i}, \theta)]\ [\hat{G}_f(e^{j\omega_k}) - \hat{G}(e^{j\omega_k}, \theta)]^*\}$$

$$- E\{[\hat{G}_n(e^{j\omega_i}) - \hat{G}(e^{j\omega_i}, \theta)]\ [\hat{G}_f(e^{j\omega_k}) - \hat{G}(e^{j\omega_k}, \theta)]^*\}$$

$$+ E\{[\hat{G}_f(e^{j\omega_i}) - \hat{G}(e^{j\omega_i}, \theta)]\ [\hat{G}_n(e^{j\omega_k}) - \hat{G}(e^{j\omega_k}, \theta)]^*\} \quad \text{(A5)}$$

We also have

$$\left[\frac{\partial}{\partial\theta}G(z^{-1}, \theta)\right]^T\theta_i = \frac{1}{F(z^{-1}, n_F)}\left[\frac{\partial}{\partial\theta}B(z^{-1}, \theta, n_B)\right]^T\hat{\theta}_i$$

$$= \frac{1}{F(z^{-1}, n_F)}[z^{-1}, z^{-2}, \ldots, z^{-n_B}][\hat{\theta}_i]$$

$$= \frac{B(z^{-1}, \hat{\theta}_i, n_B) - B(z^{-1}, \theta, n_B)}{F(z^{-1}, n_F)}$$

$$= \hat{G}_i(z^{-1}) - G(z^{-1}, \theta), \quad i = n, f \quad \text{(A6)}$$

Substituting equation (A6) into equation (A5) gives

$$D_{ik}(\omega, n)$$

$$= \left[\frac{\partial}{\partial\theta}G(e^{j\omega_i}, \theta)\right]^T E\{\hat{\theta}_n\hat{\theta}_n^T + \hat{\theta}_f\hat{\theta}_f^T - \hat{\theta}_n\hat{\theta}_n^T\}\left[\frac{\partial}{\partial\theta}G(e^{-j\omega_k}, \theta)\right]$$

$$= \left[\frac{\partial}{\partial\theta}G(e^{j\omega_i}, \theta)\right]^T C\left[\frac{\partial}{\partial\theta}G(e^{-j\omega_k}, \theta)\right]$$

which establishes equation (A4).

▽ ▽ ▽

D. E. Moellenhoff

S. Vittal Rao

Department of Electrical Engineering,
University of Missouri—Rolla,
Rolla, MO 65401

C. A. Skarvan

Allison Gas Turbine,
Division of General Motors Corp.,
Indianapolis, IN 46206-0420

# Design of Robust Controllers for Gas Turbine Engines

*This paper describes robust controller design methodologies for gas turbine engines. A linear state variable model for the engine is derived using partial derivatives. The Linear Quadratic Gaussian with Loop Transfer Recovery (LQG/LTR) and the Parameter Robust Linear Quadratic Gaussian (PRLQG) robust controller design methodologies have been used to design a controller for gas turbine engines. A new method is proposed by combining the features of LQG/LTR and PRLQG methods and yields good robustness properties with respect to both unstructured uncertainties in the frequency domain and structured parameter variations in the time domain. The new procedure is illustrated with the help of an aircraft gas turbine engine model.*

## 1 Introduction

In recent years, an increased amount of research effort has been directed toward the design of controllers for gas turbine engines. The control system is designed to meet specified steady-state performance requirements at different operating points and to have a safe and rapid transient response when moving from one operating point to another. A control strategy that can guarantee stability and provide satisfactory performance in the presence of model uncertainties is called a robust controller. The robustness problem has been studied in the single-input single-output (SISO) case for many years and much of the classical control theory deals with this in one way or another. These SISO methods are being extended to the multi-input multi-output (MIMO) cases. Among the various design methods for robust controllers, the linear quadratic Gaussian with loop transfer recovery (LQG/LTR) design procedure has many advantages [1]. This methodology will result in control systems with excellent stability robustness, command following, disturbance rejection, and sensor noise properties.

The linear quadratic Gaussian with loop transfer recovery (LQG/LTR) methodology [1, 2] is a design method for both SISO and MIMO linear systems, which produces controllers that are robust with respect to unstructured uncertainties. In many systems, however, information is available about the structure of the variations that can be expected in the model. In that case, the information should be used to improve the performance robustness of the system.

The Parameter Robust Linear Quadratic Gaussian (PRLQG) design method [3, 4] has been proposed to deal with parameter variations where information about the structure is available. In this method, the robustness properties are described in the time domain, while for the LQG/LTR, they are given in terms of the frequency domain. By itself, the PRLQG method has several limitations.

This paper presents a variation of the LQG/LTR method, incorporating aspects of the PRLQG method. The resulting procedure considers the robustness problem with respect to both the frequency domain with unstructured uncertainties, and the time domain with parameter variations of known structure.

Controller design for aircraft gas turbine engines is an area where structural information about the parameter variations is available. These variations arise due to changes in the engine operating environment corresponding to changes in ambient conditions, altitude, or airspeed. The effects of these environmental conditions on engine behavior should be used when designing a controller.

The modified PRLQG method is demonstrated by using an aircraft gas turbine engine system. The results are compared with a standard LQG/LTR design to show the types of improvement that can be obtained.

The paper is arranged in seven primary sections. Section II provides a brief description of gas turbine engines and then describes the derivation of the model for the Allison T56 engine. Section III reviews the basic LQG/LTR design methodology. The PRLQG method is described in Section IV. A new procedure by combining the PRLQG with the LQG/LTR method is developed and presented in Section V. Section VI contains robust controller design methods for gas turbine engines. A comparison of system response between proposed method and LQG/LTR method is also given in Section VI. Conclusions are given in Section VII.

## II Modeling of Gas Turbine Engines

The Allison T56 engine is a single-spool turbo-shaft engine and is used to power several types of propeller-driven aircraft. Due to the changes in engine behavior as the operating conditions vary, gas turbine engines are nonlinear systems. A linear

Contributed by the International Gas Turbine Institute and presented at the 35th International Gas Turbine and Aeroengine Congress and Exposition, Brussels, Belgium, June 11-14, 1990. Manuscript received by the International Gas Turbine Institute January 17, 1990. Paper No. 90-GT-113.

model framework can be developed at an operating point using partial derivatives [5]. The partial derivatives can be evaluated for each operating condition, through the use of a nonlinear simulation program on a digital computer.

The manipulative input variables are fuel flow ($\omega_f$) and propeller blade angle ($\beta$). The output variables are engine speed ($N_e$) and torque to the output shaft ($Q_1$). The linear model of the engine, incorporating partial derivatives, is shown in Fig. 1. An equivalent electrical circuit for the shaft, gearbox, and propeller system is shown in Fig. 2, where all quantities are referenced to engine speed.

The state of equations of the engine and propeller system are given by

$$\dot{\mathbf{x}}_p = \mathbf{A}_p\mathbf{x}_p + \mathbf{B}_p\mathbf{u} \qquad \mathbf{y} = \mathbf{C}_p\mathbf{x}_p + \mathbf{D}_p\mathbf{u} \tag{1}$$

where

$$\mathbf{x}_p = \begin{bmatrix} \Delta N_e \\ \Delta N_1 \\ \Delta Q_L \end{bmatrix} \quad \mathbf{u} = \begin{bmatrix} \Delta w_f \\ \Delta\beta \end{bmatrix} \quad \mathbf{y} = \begin{bmatrix} \Delta N_e \\ \Delta Q_1 \end{bmatrix} \tag{2}$$

and $\Delta$ represents change around the nominal operating point.

In matrix form the linear model can be summarized as follows:

$$\mathbf{A}_p = \begin{bmatrix} X_1 & 0 & C_1 \\ 0 & X_2 & C_2 \\ K & -K & 0 \end{bmatrix} \quad \mathbf{B}_p = \begin{bmatrix} X_3 & 0 \\ 0 & X_4 \\ 0 & 0 \end{bmatrix} \tag{3}$$

$$\mathbf{C}_p = \begin{bmatrix} 1 & 0 & 0 \\ 0 & X_5 & 0 \end{bmatrix} \quad \mathbf{D}_p = \begin{bmatrix} 0 & 0 \\ 0 & X_{10} \end{bmatrix} \tag{4}$$

where the $C$s and $K$ represent constants that are independent of the operating point. The $X$s represent elements that are functions of partial derivatives and therefore change as the operating conditions change. In order to obtain numerical values for the model, the partial derivatives were calculated at a given operating point using data from a nonlinear simulation program. Fourteen such operating points were selected and a linear model was evaluated for each. It is desirable to have one linear model as the nominal model to describe system operation over the entire flight envelope. Since linear models have been derived and validated at 13 other points encompassing most of the flight envelope, the types and magnitudes of the parameter variations expected in the nominal model can be assessed quite easily.

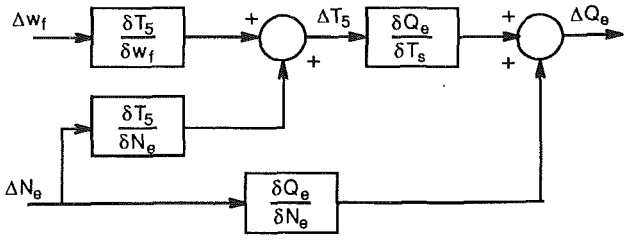


Fig. 1 Linear model of the engine

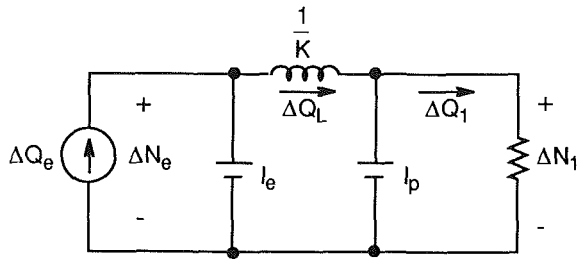


Fig. 2 Equivalent electrical circuit of the shaft gearbox and propeller

## III Robust Controller Design Methodology

A controller is said to be robust if the performance characteristics of the closed-loop system remain satisfactory even when the system is subjected to uncertainties. Among the various design methods for robust controllers, the linear quadratic Gaussian with loop transfer recovery (LQG/LTR) design procedure [1] has many advantages. This methodology will result in systems with excellent stability robustness, command following, disturbance rejection, and noise suppression properties. A brief review of this methodology is given in this section.

Consider a system represented by

$$\dot{x} = Ax + Bu + \Gamma\xi \tag{5}$$

$$y = Cx + Du + \eta \tag{6}$$

## Nomenclature

ARE = Algebraic Ricatti Equation
GM = Gain Margin
$G(s)$ = nominal transfer function of the plant
$\hat{G}(s)$ = transfer function of the perturbed model
$I$ = identity matrix
KF = Kalman filter
$K(s)$ = transfer function of the controller
LQG/LTR = Linear Quadratic Gaussian with Loop Transfer Recovery
LQR = Linear Quadratic Regulator
$L(s)$ = multiplicative frequency domain representation of model uncertainties
$m$ = number of inputs in the model
MIMO = Multi-Input Multi-Output
$n$ = number of states in the model
$N_e$ = engine speed
$N_p$ = propeller speed
$N_1$ = propeller speed referenced to engine speed
$p$ = number of outputs in the model
PM = Phase Margin
PR = Parameter Robust Controller
PRLQG = Parameter Robust Linear Quadratic Gaussian
$Q_L$ = load torque
$Q_1$ = torque delivered to the propeller
SISO = Single-Input Single-Output
$T_5$ = temperature at the turbine inlet
TFL = Target Feedback Loop
$u$ = input vector
$x$ = vector of state variables
$y$ = output vector
$\beta$ = propeller blade angle
$\Delta$ = perturbation parameter
$\zeta, \eta$ = Gaussian white noise processes
$\Phi$ = $(SI-A)^{-1}$
$\omega_f$ = fuel flow

where $\xi$ and $\eta$ are uncorrelated, Gaussian white noise processes.

The LQG/LTR procedure essentially consists of designing a target feedback loop (TFL) and synthesizing the compensator $K(s)$ so that the loop transfer function matrix is close to that of TFL. The output version of the procedure can be summarized as follows:

1 Define a nominal model of the gas turbine engine. Augment pure integrators to the plant for zero steady state tracking error. Define the stability and performance barriers in the frequency domain.

2 For the loop broken at output, design a Kalman filter by adjusting the weighting matrices to meet the robustness specifications at high and low frequencies.

3 Design a linear quadratic regulator for recovering the stability margins of the closed loop systems.

4 Verify the closed-loop performance of the system.

The LQG/LTR controller methodology was successfully employed to design robust controllers for gas turbine engines [6, 7]. We have also used this methodology to design controllers for the Allison T56 engine and the results are presented in Section VI.

## IV Parameter Robust Linear Quadratic Gaussian Methods

Tahk and Speyer [3, 4] have presented the parameter robust linear quadratic Gaussian (PRLQG) controller design method for systems that are robust with respect to structured parameter variations in the state space model representations. These variations are represented in the time domain using an internal feedback loop (IFL) modeling technique. Many of the design steps in this method are very similar to those in the LQG/LTR methods; however, the motivation is somewhat different. The salient features of this method are presented in this section.

**Internal Feedback Loop (IFL) Modeling of Uncertainties.** Consider a system represented in state space form

$$\dot{x} = Ax + Bu \tag{7}$$

$$y = Cx \tag{8}$$

where some of the elements of the $A$ matrix are uncertain. The perturbed system can be described as

$$\dot{x} = (A + \Delta A)x + Bu = (A - MLN)x + Bu \tag{9}$$

where $M$, $L$, and $N$ are matrices chosen to represent the information known about the uncertainties in $A$. Define an additional input $w$ and output $z$ such that

$$w = -Lz \tag{10}$$

$$z = Nx \tag{11}$$

then

$$\dot{x} = Ax + Bu + Mw \tag{12}$$

$$x = (SI - A)^{-1}[Bu + Mw] = \Phi Bu + \Phi Mw \tag{13}$$

$$\begin{bmatrix} y \\ z \end{bmatrix} = \begin{bmatrix} C\Phi B & C\Phi M \\ N\Phi B & N\Phi M \end{bmatrix} \begin{bmatrix} u \\ w \end{bmatrix} \tag{14}$$

Define an output feedback controller $u(s) = r(s) - K(s)y(s)$ where $r(s)$ is the reference input. The dependence on $s$ will be dropped to simplify notation. Let $G = C\Phi B$. The resulting system

$$\begin{bmatrix} y \\ z \end{bmatrix} = \begin{bmatrix} G(I+KG)^{-1} & (I+GK)^{-1} \\ N\Phi B(I+KG)^{-1} & N\Phi M - (I+KG)^{-1}KC\Phi M \end{bmatrix} \begin{bmatrix} r \\ w \end{bmatrix} \tag{15}$$

is drawn in Fig. 3 where the uncertainty is represented by the feedback loop [3, 4]. Let $G_{22}$ be the transfer function between $z$ and $w$, given by

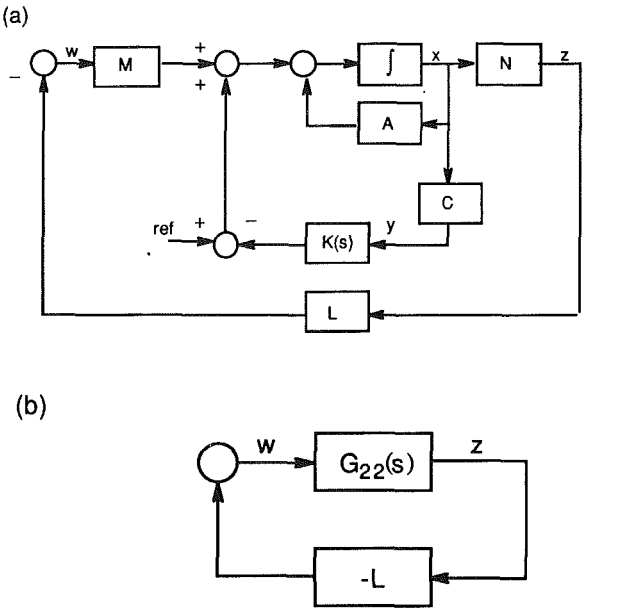


**Fig. 3 Two input-two output system with uncertainties represented by IFL: (*a*) detailed block diagram; (*b*) simplified block diagram**

$$G_{22} = N\Phi M - N\Phi B(I+KG)^{-1}KC\Phi M \tag{16}$$

Tahk and Speyer [3, 4] have shown that if $\Gamma$ is column similar to $M$, then the closed-loop system poles due to $K_f$ will be insensitive to parameter variations in $A$, which are described by $M$, as $\mu \to 0$. By a dual procedure, it can be shown that if $H$ is row similar to $N$, then the closed-loop poles due to $K_c$ will be insensitive to parameter variations described by $N$, as $\rho \to 0$. A simple procedure for the selection of the matrices $M$, $L$, and $N$ is given by Tahk and Speyer [4].

**Limitations.** A controller designed using the procedure outlined above will produce a system that is insensitive to parameter variations. However this PRLQG method has a severe limitation. This limitation is evident from Kalman filter loop properties equation. For a small value of a design parameter $v$ [3], the singular values of the target feedback loop (TFL) get very large, causing a large bandwidth. This causes large overshoots and rapid oscillations in the time response of the system. Many real system components such as pumps, actuators, and other hardware have limited rate of change or maximum output capabilities.

The LQG/LTR method avoids this problem because the asymptotic procedure does not change the loop shape. This procedure assures that as the weighting matrix gets large the frequency domain properties of the total open loop system approach those of the TFL. It is suggested by Tahk and Speyer [3, 4] that the PRLQG procedure be substituted for the recovery procedure of the LQG/LTR to decrease the sensitivity to parameter variations. This will make the regulator poles (for the case of output uncertainties) insensitive to parameter variations; however, the frequency domain properties of the TFL are no longer preserved.

## V Proposed Combined Method

A combined robust controller design method utilizing the ideas of the PRLQG and LQG/LTR is developed in this section. This combination of the methods guarantees stability robustness with respect to unstructured perturbations, and performance robustness with respect to known parameter variations. This procedure considers the closed-loop system performance in both time and frequency domains.

Often it is necessary to augment integrators to the input of the plant in order to guarantee steady-state matching between the reference inputs and the outputs of the system. These integrators are actually part of the controller, but for design purposes they are assumed to be part of the plant model.

$$\begin{bmatrix} \dot{x}_i \\ \dot{x}_p \end{bmatrix} = \begin{bmatrix} 0 & 0 \\ B_p & A_p \end{bmatrix} \begin{bmatrix} x_i \\ x_p \end{bmatrix} + \begin{bmatrix} I \\ 0 \end{bmatrix} u \tag{17}$$

$$y = [D_p \; C_p] \begin{bmatrix} x_i \\ x_p \end{bmatrix} \tag{18}$$

where $A_p$, $B_p$, $C_p$, and $D_p$ are the state space model matrices of the plant. The vector $x_i$ represents the state variables of the integrators.

The uncertainties are assumed to occur at the output. Now the system performance will be determined by

$$\sigma[C\Phi K_f] \cong \frac{1}{\sqrt{\mu}} \sigma[C\Phi\Gamma] \tag{19}$$

At low frequencies this becomes

$$C\Phi\Gamma \cong \frac{1}{s}[C_p(-A_p)^{-1}B_p + D_P]\,\Gamma_L = \frac{1}{s}[\text{LFP}] \tag{20}$$

For high frequencies

$$C\Phi\Gamma \cong \frac{1}{s}[D_p\Gamma_L + C_p\Gamma_H] = \frac{1}{s}[\text{HFP}] \tag{21}$$

In the standard matching procedure for the LQG/LTR, both LFP and HFP are set equal to the identity matrix. This eliminates much design flexibility. For performance robustness, assume HFP and LFP are diagonal matrices. For diagonal matrices, the singular values are equal to the magnitudes of the diagonal elements, which makes the frequency domain properties easy to see. This defines some relationships between elements in $\Gamma$, which depend on the values of the unaugmented plant model matrices $A_p$, $B_p$, $C_p$, and $D_p$. Selecting $\Gamma$ in this way assures that the TFL will have an approximately constant $-20$ dB per decade slope for each singular value. In order to bring the maximum and minimum singular values together, the diagonal elements of HFP should be approximately equal and the diagonal elements of LFP should also be approximately equal. Thus we would like HFP and LFP to be approximately equal to scalar multiples of the identity matrix; however, we do not restrict them to be exactly equal to the identity matrix. In general the high-frequency behavior is most important for determining the bandwidth of the system and for meeting the stability robustness requirements set by the unstructured uncertainties $L(s)$. Therefore it is usually more critical to have HFP approximate a scalar multiple of the identity matrix than it is for LFP to do so. The remaining elements of $\Gamma$ are then selected, either by trial and error, or by relationships derived by setting diagonal elements of HFP or LFP equal to each other. The key to this method comes from the PRLQG development. For insensitivity to parameter variations $\Gamma$ should be approximately column similar to $M$. In other words, the rows of $A$ that are subject to variations should correspond to the rows of $\Gamma$ which have the largest values. With $\Gamma$ selected in this manner, $K_f$ can be calculated using the algebraic Riccati equation where $\mu$ is chosen to raise or lower the TFL for bandwidth or stability robustness constraints. Then $K_f$ should also be column similar to $M$, or at least have its largest values in the rows corresponding to the perturbed rows of the $A$ matrix.

Using this approach, the TFL will have an approximately uniform slope of $-20$ dB per decade, the bandwidth can be fixed by selecting $\mu$, and the KF poles should be relatively insensitive to the parameter variations described by $M$. If the regulator gain $K_c$ is calculated using the loop transfer recovery (LTR) procedure, that is if $K_c = (1/\rho)B^TP$, where $P$ is the solution of algebraic Riccati equation

$$A^TP + \text{PA} + Q_{co} + q^2C^TC - \frac{1}{\rho}PBB^TP = 0 \tag{22}$$

and $q$ is large, then the open-loop system $G(s)K(s)$ will have the same frequency domain properties as the TFL, except at high frequencies where $\sigma[G(s)K(s)]$ will exhibit $-40$ dB per decade rolloff. An example of this method will be given in the next section.

A similar procedure could be used to make the regulator poles insensitive to parameter variations in $A$ by replacing $C$ with $N$ and letting $\rho$ get small. However, if this is done, the frequency domain properties of $G(s)K(s)$ will change and will no longer approximate those of the TFL. The control engineer should be aware of this since $C$ matrix can sometimes be changed by the selection of sensor locations in the physical system. If that were the case, from a robust controller point of view, the best configuration would make the $C$ matrix row similar to $N$, or at least have nonzero elements in rows that correspond to the rows of $A$ that are subject to variations. For uncertainties at the plant input, the recovery procedure is enhanced with respect to parameter variations if the $B$ matrix is column similar to $M$. The structure of the $B$ matrix is affected by locations of the actuators, that is the manipulative variables, of the system.

We note that $K_f$ is only approximately similar to $M$ in the sense that rows corresponding to perturbed rows of the $A$ matrix have the larger entries. Also $\mu$ does not approach zero, but is just small enough to satisfy bandwidth requirements. For complete insensitivity to parameter variations, all the rows of $K_f$ corresponding to rows of $A$, which are definitely known, would have to be identically equal to zero and $\mu$ would have to be very small. However, insensitivity to parameter variations is not the only consideration in control system design. Nominal performance and noise rejection, for example, are extremely important and thus tradeoffs must be made. What this new procedure provides is a way to include some consideration of parameter variations in the design of an LQG/LTR controller.

## VI Robust Controller Design for Gas Turbine Engines

The proposed method described in Section V is illustrated by designing a robust controller for an engine propeller system. The results of the controllers are compared with a robust controller designed by using the standard LQG/LTR procedure.

The mathematical model of the engine-propeller system is described in Section II. The control strategy is to vary the output torque corresponding to the power level requests from the pilot or flight computer, while maintaining constant engine speed. Speed regulation is important for efficient propeller operation, and also for generators or accessories that are driven from the gearbox. The actuators in the propeller are limited according to the maximum rate of change of the blade angle, so the bandwidth of the controller is limited. Also temperatures in the engine are directly related to fuel flow, which means that overshoots in the fuel flow are associated with temperature overshoots, and therefore should be avoided if possible.

The linear models are fairly accurate from a transient point of view, but steady-state errors will be present if the operating conditions change. For this reason, integrators will be augmented to the inputs to the plant to insure steady-state matching of the reference and the feedback signals from the torque and speed sensors. The singular value plots of the augmented plant are shown in Fig. 4. Note that the maximum and minimum singular values are considerably different, which is reflection of the differences between the dynamics associated with the input and output variables.

**(a) Uncertainties Due to Operating Point Variables.** Of the 14 linear models available, one nominal model was selected

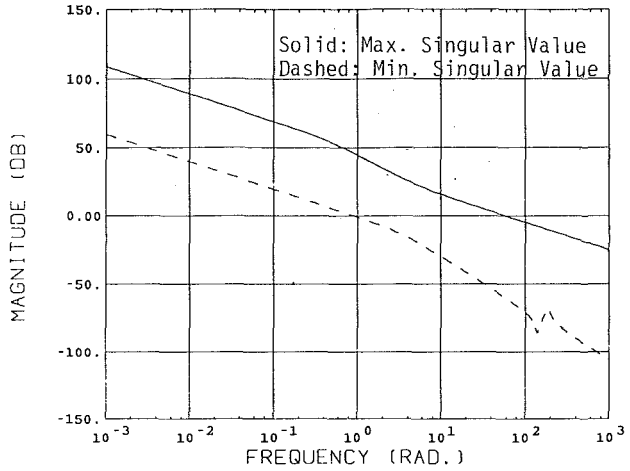


Fig. 4 Singular value plots of the plant with integrators

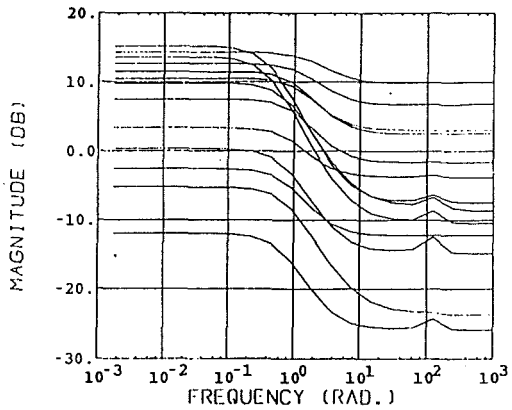


Fig. 5 Singular value plots of $L(s)$

to represent the plant characteristics. The other 13 models are used to define variations or uncertainties in the nominal model.

$$\bar{\sigma}[L(s)] = \bar{\sigma}[\hat{G}(s)G^{-1}(s) - I] \tag{23}$$

where $G(s)$ is the nominal model and $\hat{G}(s)$ the perturbed model corresponding to the other operating points. The maximum singular values of $L(s)$ calculated using linear models at 13 different operating points in the flight envelope is shown in Fig. 5. From the figure it is concluded that the system bandwidth should be limited to less than 10 rad/s.

**(b) Standard LQG/LTR Design.** The first step in designing a LQG/LTR controller for uncertainties at the output is to select $\Gamma$ and $\mu$ such that the TFL has good frequency domain properties. The singular values of the plant are not close together, so the matching procedure is used. Setting $\mu = 0.1$ results in the TFL shown in Fig. 6 and has an appropriate crossover frequency. The resulting matrices are

$$\Gamma = \begin{bmatrix} 0.0907 & 1.0404 \\ -0.0907 & 0.0171 \\ 1.0 & 0.0 \\ 1.0 & 0.0 \\ 0.0 & 0.0 \end{bmatrix}$$

$$K_f = \begin{bmatrix} 0.2877 & 3.2962 \\ -0.0068 & 0.0539 \\ 3.1653 & 0.0 \\ 3.1542 & -0.0023 \\ -0.0011 & 3.1618 \end{bmatrix} \tag{24}$$

The LQR gain $K_c$ is found using the standard recovery procedure. In this case $q = 25$ gave adequate recovery without requiring excessive gains in the LQR. The matrix $K_c$ is given by

$$K_c = \begin{bmatrix} 11.7 & -3.0 & 15.18 & 5.64 & -0.0465 \\ -3.0 & 1471.0 & -2.11 & -6.55 & -0.0325 \end{bmatrix} \tag{25}$$

The resulting open-loop singular values are shown in Fig. 7. The stability margins for the system are

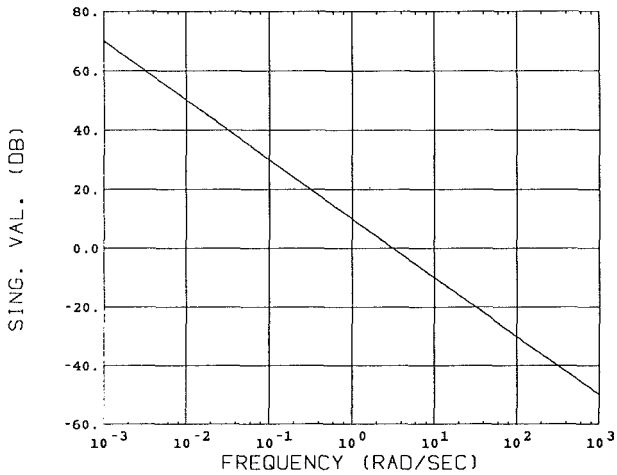


Fig. 6 Target feedback loop

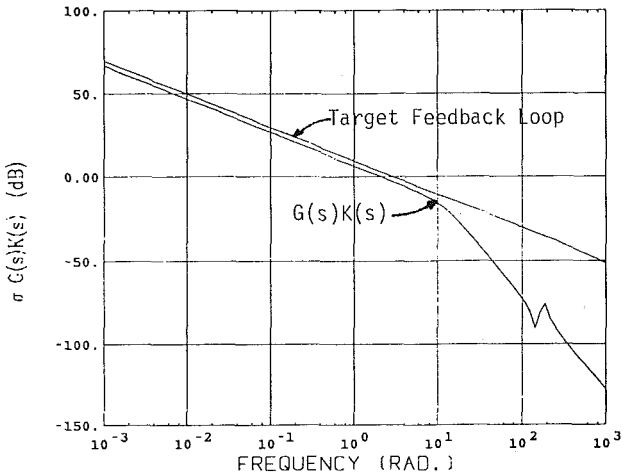


Fig. 7 Singular value plot of $G(s)K(s)$ for the LQG/LTR design

$$-5.06 \text{ dB} < \text{GM} < 13.58 \text{ dB}$$
$$-46.6 \text{ deg} < \text{PM} < 46.6 \text{ deg} \tag{26}$$

**(c) Design Using Proposed Method.** In this design method, the same system and models will be used; however, the information about parameter variations will be utilized.

Consider the augmented system matrix $A$ given by

$$A = \begin{bmatrix} 0 & 0 & 0 & 0 & 0 \\ 0 & 0 & 0 & 0 & 0 \\ X_3 & 0 & X_1 & 0 & C_1 \\ 0 & X_4 & 0 & X_2 & C_2 \\ 0 & 0 & K & -K & 0 \end{bmatrix} \quad (27)$$

where the $X$s are the elements that change as the operating conditions change. In this case, $M$ should have zeros in rows one, two, and five, and $N$ should have zeros in column five. For insensitivity to parameter variations, $K_f$ should be approximately column similar to $M$, that is, $K_f$ should have its largest entries in rows three and four. The $K_f$ from the LQG/LTR design does not meet this requirement. By using the proposed method, the matrix $\Gamma$ was determined such that the entries in rows three and four are large compared to the other rows while at the same time yielding a target feedback loop that has good frequency domain properties.

The matrix $\Gamma$ was chosen to be

$$\Gamma = \begin{bmatrix} 0.3626 & 1.0294 \\ -0.0086 & 0.0168 \\ 2.0 & 0.0 \\ 4.0 & 8.0 \\ 1.0 & 2.0 \end{bmatrix} \quad (28)$$

The bandwidth requirements are satisfied with $\mu = 0.1$. The Kalman gain matrix $K_f$ is given by

$$K_f = \begin{bmatrix} 2.4296 & 2.4513 \\ -0.0019 & 0.0598 \\ 16.0736 & -0.06595 \\ -4.3394 & 6.392 \\ -20.8338 & -1.7926 \end{bmatrix} \quad (29)$$

A plot of the target feedback loop for this design is shown in Fig. 8.

The LQR gain $K_c$ will be the same as in equation (25) since the recovery procedure guarantees that the frequency domain properties of $G(s)K(s)$ will be similar to those of the TFL. The stability margins are

$$-4.69 \text{ dB} < \text{GM} < 10.9 \text{ dB} \quad (30)$$
$$-42.0 \text{ deg} < \text{PM} < 42.0 \text{ deg}$$

which are slightly worse than the LQG/LTR controller, but not significantly different.

Figure 9 shows the step response of the system with this new controller, and with the LQG/LTR controller, at the nominal operating point.

To assess performance robustness, the time response to a step input in torque reference is computed when the controller remains fixed, but the plant model is changed to that of a different operating point. The results from the two operating points that exhibit the most deviation from the nominal point are shown in Figs. 10 and 11. Note that when the plant model and the model imbedded in the controller are not the same, the separation principle no longer applies, and the closed-loop poles are not equal to the filter poles and the regulator poles. In the frequency domain, the two controllers exhibit similar properties, as one would expect since the TFL is approximately that of an integrator in both cases. The time responses show that the parameter robust (PR) controller exhibits improved

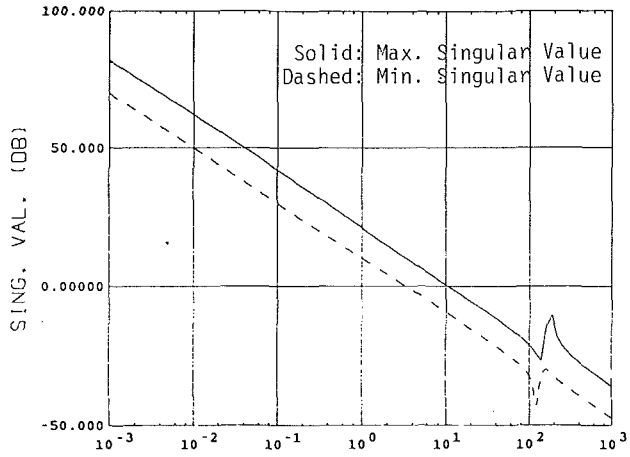


*Fig. 8 Singular value plot of target feedback loop for the PR design*

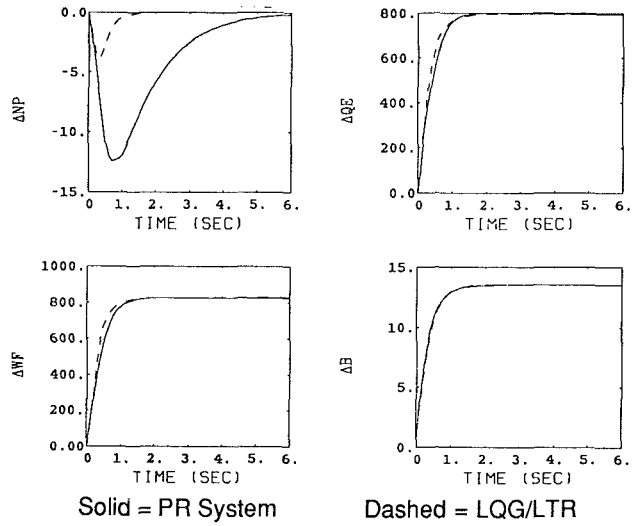


**Fig. 9 Transient response to a step in torque reference at the nominal operating point**

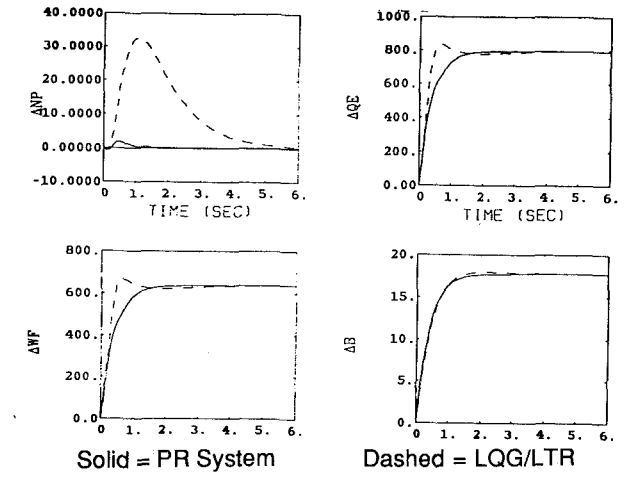


**Fig. 10 Transient response to a step in torque reference at operating point 232**

performance robustness properties in the presence of parameter variations. Although the speed change in the nominal case is slightly more for the PR controller, it is improved for both the off-nominal points. Also the PR controller eliminates the

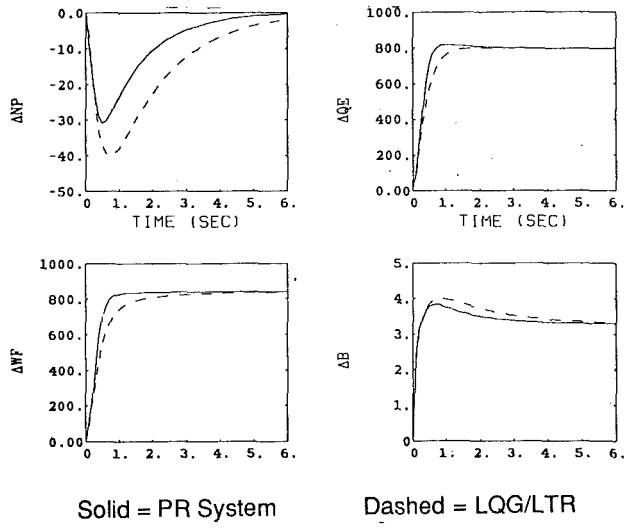


**Fig. 11 Transient response to a step in torque reference at operating point 214**

overshoot in fuel flow, and corresponding temperature, that appears with the LQG/LTR design at point 232.

It should be noted that the PR procedure was not used in either case in the design of $K_c$, yet the results are good. The main reason for this can be seen by observing the $C$ matrix of the augmented plant model.

$$C = \begin{bmatrix} 0.0 & 0.0 & 1.0 & 0.0 & 0.0 \\ 0.0 & X_{10} & 0.0 & X_5 & 0.0 \end{bmatrix} \tag{31}$$

$X_{10}$ is the largest entry, on the order of 50, in the nominal model while $X_5$ is roughly 0.1. The largest variations in the nominal $A$ matrix occur in $X_4$, which corresponds to the second column. The variations in $X_3$ and $X_1$, that is columns one and three, are relatively small. Consequently, the $C$ matrix of the model is close to the $N$ matrix, which would have been chosen for the PR procedure for $K_c$. One would expect that if the $C$ matrix had not been approximately similar to $N$, the performance robustness, especially for the LQG/LTR, would not have been as good. This illustrates the fact that selection of the $C$ matrix, or the $B$ matrix for input uncertainties, can have a significant effect on the robustness of the system.

## VII Conclusions

Robust controller design methodologies were applied to design controllers for gas turbine engines, which are subject to both structured parameter variations and unstructured uncertainties.

The stability robustness properties of the LQG/LTR methodology with respect to unstructured uncertainties were discussed. In order to deal with both stability and performance robustness in the time domain, for structured parameter variations, the PRLQG methodology was described.

These two methodologies were compared in order to illustrate their respective strengths and weaknesses. Then a new PR design procedure was suggested, which combines aspects of both LQG/LTR and the PRLQG. This new approach is particularly useful when the plant is subject to parameter variations of a known structure.

Gas turbine engines for aircraft are an example of a situation where structured parameter variations are well defined. A description of this type of system was given, as well as a specific example illustrating the modeling techniques.

Finally, the suggested PR controller design procedure was applied to an aircraft gas turbine engine example to illustrate the method and results. Comparisons were made between the PR Controller and a standard LQG/LTR controller for the same system. It was shown that the PR design method yielded improved performance robustness with identical controller structure and only a minimal increase in design computations.

## Acknowledgments

The authors would like to thank Mr. William R. Schnell and Mr. Tom Scott of Allison Gas Turbine Division for their constant encouragement and support.

## References

1 Doyle, J. C., and Stein, G., "Multivariable Feedback Design: Concepts for a Classical/Modern Synthesis," *IEEE Transactions on Automatic Control,* Vol. AC-26, No. 1, Feb. 1981, pp. 4–16.

2 Stein, G., and Athans, M., "The LQG/LTR Procedure for Multivariable Feedback Control Design," *IEEE Transactions on Automatic Control,* Vol. AC-32, No. 2, Feb. 1987, pp. 105–114.

3 Tahk, M., and Speyer, J. L., "Modeling of Parameter Variations and Asymptotic LQG Synthesis," *Proceedings of the 25th Conference on Decision and Control,* Athens, Greece, Dec. 1986, pp. 1459–1465.

4 Tahk, M., and Speyer, J. L., "A Parameter Robust LQG Design Synthesis With Applications to Control of Flexible Structures," *Proceedings of the 1987 American Control Conference,* Minneapolis, MN, Vol. 1, June 1987, pp. 386–392.

5 Rao, S. V., Moellenhoff, D., and Jaeger, J. A., "Linear State Variable Dynamic Model and Estimator Design for Allison T406 Gas Turbine Engine," ASME Paper No. 88-GT-239, 1988.

6 Pfiel, W. H., Athans, M., and Spang, H. A., "Multivariable Control of the GE T700 Engine Using the LQG/LTR Design Methodology," presented at the 1986 American Control Conference, Seattle, WA, June 1986.

7 Athans, M., Kapasouris, P., Kappos, E., and Spang, H. A., "Linear-Quadratic Gaussian With Loop Transfer Recovery Methodology for the F-100 Engine," *Journal of Guidance, Control, and Dynamics,* Vol. 9, No. 1, Jan.–Feb. 1986, pp. 45–52.

H. Kumakura

T. Matsumura

E. Tsuruta

A. Watanabe

Central Engineering Laboratories,
Nissan Motor Co., Ltd.,
Yokosuka, Kanagawa, Japan

# A Control System for a High-Quality Generating Set Equipped With a Two-Shaft Gas Turbine

*A control system has been developed for a high-quality generating set (150-kW) equipped with a two-shaft gas turbine featuring a variable power turbine nozzle. Because this generating set satisfies stringent frequency stability requirements, it can be employed as the direct electric power source for computer centers without using constant-voltage, constant-frequency power supply systems. Conventional generating sets of this kind have normally been powered by single-shaft gas turbines, which have a larger output shaft inertia than the two-shaft version. Good frequency characteristics have also been realized with the two-shaft gas turbine, which provides superior quick start ability and lower fuel consumption under partial loads.*

## Introduction

Demands for high-quality electric power sources for emergency use are continually growing, along with the increasing number of intelligent buildings or computer centers where there are many computers that require a constant supply of high-quality electric power [1]. In 1982, Nissan Motor Company utilized automotive gas turbine technology to develop a two-shaft gas turbine for an emergency generating set, which provided very quick starting performance [2–4]. Subsequently, we started a new engine project that has resulted in the present high-quality generating set.

Conventional generating sets of this kind have normally been powered by single-shaft gas turbines, which have a larger output shaft inertia than the two-shaft version. The new generating set employs a two-shaft regenerative gas turbine, which consumes less fuel under a partial load. The adoption of a new control scheme using a variable nozzle for active power control achieves superior frequency characteristics.

This paper compares the transient response of single and two-shaft gas turbines using simulation models incorporating experimental control gains. The results show that the two-shaft engine employing an accurate feed-forward control procedure displays better frequency control than a single-shaft version without this control scheme. The control scheme applies feed-forward control to both the variable nozzle angle and gas generator speed. Experimental results for the control scheme are also presented.

## System Design

Superior frequency characteristics and lower fuel consumption under partial loads were two requirements for the new generating set. A regenerative heat exchanger was adopted to reduce fuel consumption across the entire load range. It also lowers the exhaust gas temperature so that special heat-proof exhaust facilities are not needed.

The selection of a single or two-shaft version is an important question when configuring the gas turbine. A two-shaft version was selected for use in the emergency generating set developed earlier. The advantages of the two-shaft version include its quick starting performance and step load capacity. A two-shaft version can start more quickly because of the low inertia of the gas generator shaft. This is a valuable attribute for emergency use. A two-shaft version can also restore the output shaft speed within a safe turbine inlet temperature range following a substantial drop in shaft speed owing to the application of a large step load. By contrast, with a single-shaft version, there is a possibility the engine may stop so as to avoid an abnormally high turbine inlet temperature since the load capacity depends on the shaft speed. Even though conventional generating sets of this type have normally been powered by a single-shaft version, we re-evaluated the possibility of using a two-shaft version in order to take advantage of its strong points.

Figure 1 illustrates the newly developed engine and Table 1 lists the generating set specifications.

The power source requirements of computer manufacturers are given in Table 2 along with the development targets. On these targets, the voltage regulation capacity depends mainly on how closely the generator is controlled. It was concluded that the requirement could be satisfied using conventional technology. The main issue was to improve the frequency regulation capacity. Since the generator shaft would be connected tightly to the engine shaft, it was necessary to assure a stable and accurate engine output shaft speed.

## Evaluation of Shaft Speed Stability

The two-shaft engine for emergency generating use was not equipped with either a variable turbine nozzle or any other

Contributed by the International Gas Turbine Institute and presented at the 35th International Gas Turbine and Aeroengine Congress and Exposition, Brussels, Belgium, June 11–14, 1990. Manuscript received by the International Gas Turbine Institute January 24, 1990. Paper No. 90-GT-340.

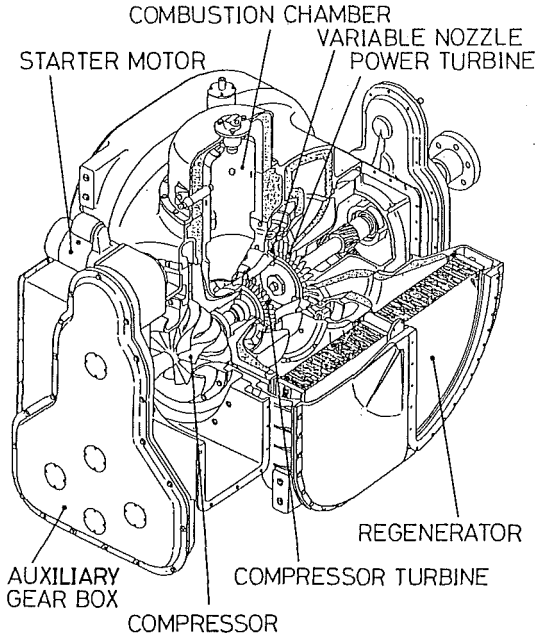


**Fig. 1 Cutaway model of TR230G engine**

**Table 1 Generating set specification**

| | |
|---|---|
| CONFIGURATION | 2-shaft regenarative engine |
| COMPRESSOR | Radial (single stage) 1:40 |
| COMPRESSOR TURBINE | Axial (single stage) |
| POWER TURBINE | Axial (single stage) |
| GAS GENERATOR (GG) SHAFT SPEED | 40,000 rpm (design) |
| POWER TURBINE SHAFT SPEED | 26,500 rpm |
| ENGINE OUTPUT SHAFT SPEED | 3,000 rpm |
| RATED SHAFT POWER | 220 kW |
| GENERATED POWER | 150 kW |

**Table 2 Requirements for computer power sources and development targets**

| MAKER | TOLERANCE FOR VOLTAGE CHANGE | | TOLERANCE FOR FREQUENCY CHANGE |
|---|---|---|---|
| | STEADY | TRANSIENT | |
| I B M | ±10% | +15%, -18% | ±1% |
| HITAC | ±10% | +15%, -18% | ±1% |

| DEVELOPMENT TARGETS | TOLERANCE FOR VOLTAGE CHANGE | | TOLERANCE FOR FREQUENCY CHANGE | |
|---|---|---|---|---|
| | STEADY | TRANSIENT | STEADY | TRANSIENT |
| | ±2% | ±15% | ±0.25% | ±1% |

variable mechanism. The new engine would have to accelerate the gas generator shaft speed under load conditions, which would mean there could be a time lag caused by gas generator inertia. Therefore, a two-shaft version with a variable nozzle, which allows more power control flexibility, was selected as a candidate for comparison with the single-shaft version.

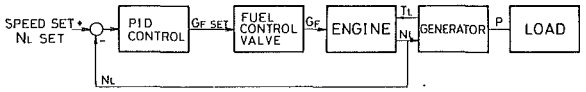


NL SET: reference shaft speed
GF SET: fuel flow rate signal
TL : drive torque for generator
NL : shaft speed
GF : fuel flow rate
P : electric power

**Fig. 2 Control block diagram (single-shaft)**

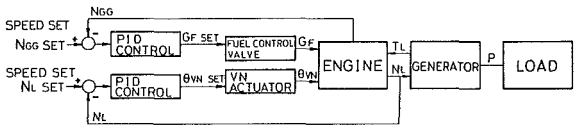


NGG SET : reference gas generator shaft speed
NGG : gas generator shaft speed
θVN SET : variable nozzle angle signal
θVN : variable nozzle angle

**Fig. 3 Control block diagram (two-shaft)**

Figures 2 and 3 show the control block diagrams for the single-shaft version and two-shaft version.

It was thought that a quick response was needed in the feedback control loop for the output shaft speed. For this reason, a quick-operating variable nozzle was included as an input in the control loop for the two-shaft version (Fig. 3). In the evaluation of shaft speed stability, the gas generator speed was controlled at 95 percent of the design value. Although not a good control scheme for lowering the fuel consumption of the two-shaft version, it was expected that this scheme would provide the quickest response. As the first step in the evaluation, this control scheme was selected for assessment.

The important points in the evaluation were to estimate both the output shaft inertia and control gains of each version.

In this 220–250 kW gas turbine engine class, the output shaft inertia of the two-shaft version was estimated at about 2.0 $kgm^2$ (for a shaft of 3000 rpm) from our former engine data. On the other hand, the inertia of the single-shaft version was estimated about 6.0 $kgm^2$ (for a shaft of 3000 rpm) based on typical engine dimension data.

In estimating the control gain, we had experimental data on the two-shaft version, but no experience in driving a single-shaft engine and could not obtain relevant data from other materials. This made it necessary to estimate the control gain from the values for the two-shaft version. The control gain for the two-shaft version was estimated from the gain margin and phase margin, and a controller for the single-shaft version was then designed for use in simulations.

Figure 4 shows the simulation model of the two-shaft version used in estimating the gain margin and phase margin. The two-shaft engine was expressed as a nine-dimensional model. The characteristics of two inputs, first-order lag and dead time, were modeled. For the single-shaft version, a six-dimensional model was used in which the power turbine was eliminated.

Figures 5 and 6 show the Nichols charts obtained with the two-shaft engine model and experimental control gain. According to these results, there is about an 8-dB gain margin and a 40 deg phase margin in the output shaft speed loop, and about a 7-dB gain margin and a 60 deg phase margin in the gas generator shaft speed loop. These are proper values for this kind of application.

A controller was designed for the single-shaft version using a method in which the PID gain was changed experimentally until the same margins as those in Fig. 6 were obtained. The result is given in Fig. 7. Using these simulation models, the

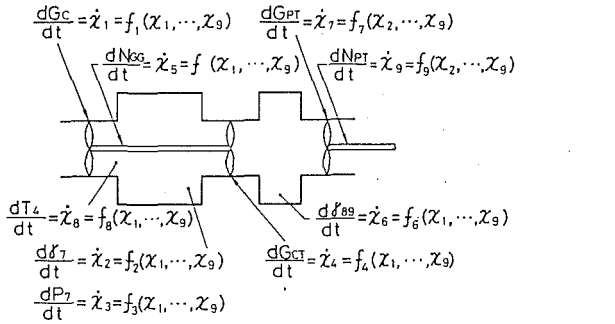


Gc : compressor flow rate
$\delta_7$ : specific gravity in C.C. (combustion chamber)
$P_7$ : pressure in C.C.
$G_{CT}$: compressor turbine flow rate
$N_{GG}$: gas generator shaft speed
$\delta_{89}$ : specific grarity in interstage duct
$G_{PT}$ : power turbine flow rate
$T_4$ : air temperature at heat exchanger outlet
$N_{PT}$ : power turbine shaft speed

**Fig. 4 Simulation model of two-shaft gas turbine**

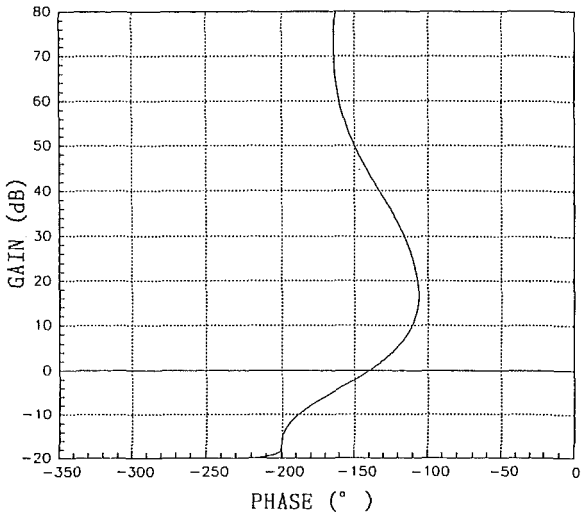


**Fig. 5 Nichols chart of variable nozzle—output shaft speed control (two-shaft)**

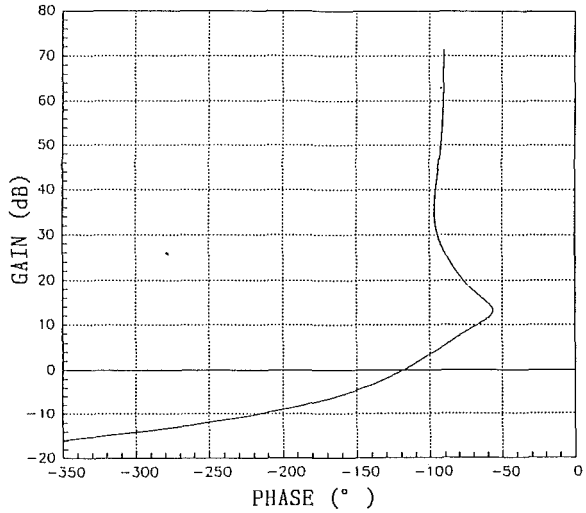


**Fig. 6 Nichols chart of fuel flow rate—gas generator shaft speed control (two-shaft)**

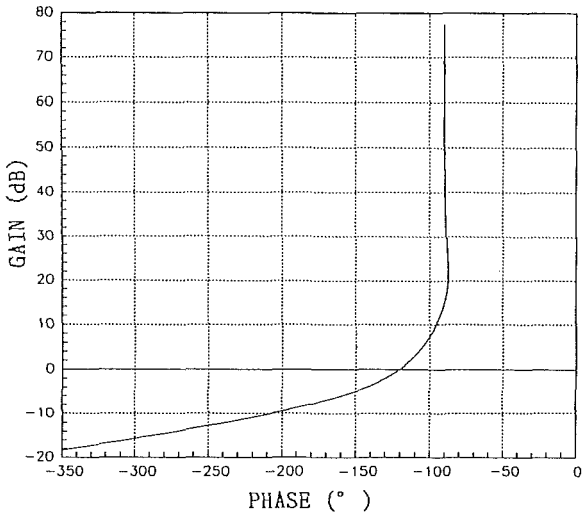


**Fig. 7 Nichols chart of fuel flow rate—output shaft speed control (single-shaft)**

characteristics of the single and two-shaft versions were compared for various step loads.

Figure 8 shows the calculated results, assuming a step load change of 0–70 percent. The results indicate that the speed changes of both versions were about 0.8 percent at the point where the output shaft inertia was 15 kgm$^2$. A single-shaft version has a larger engine shaft inertia than a two-shaft version (6 kgm$^2$ versus 2 kgm$^2$) and consequently it can stabilize speed changes using a smaller generator (9 kgm$^2$ versus 13 kgm$^2$ at a total inertia of 15 kgm$^2$).

Calculations were also made for maximum variable nozzle speeds of 200 deg/s and 500 deg/s, but the results showed no noticeable difference.

To maintain a steady speed change level (± 0.25 percent), both the single and two-shaft versions would have to suppress speed changes to a much lower level than 0.8 percent. If only feedback control was used, larger control gains would have to be selected to suppress speed changes. However, the gain margin and phase margin for both versions had already been checked, and clearly there was no surplus margin for either of them. A feed-forward control scheme was then investigated for the purpose of improving engine response.

If generator load changes can be detected at high speed, a controller is able to determine a suitable control input for the engine using a feed-forward map to suppress output shaft speed changes to the desired lower level. In the case of a single-shaft version, a map of load changes and fuel flow rate changes can be used. For a two-shaft version, two maps can be used, one of load changes and variable nozzle angle changes, and the other of load changes and reference gas generator speed changes.

Pulse width modulation type fuel injectors were adopted in TR230G to regulate the fuel flow rate. These injectors have a good transient response and are relatively inexpensive because they can be obtained by modifying automotive engine injectors. A similar fueling system had already been adopted in the emergency generating set developed earlier. The TR230G engine can operate on either kerosene or light fuel (JIS No. 2) without changing a fuel nozzle. However, the difference in fuel properties and temperature would cause the fuel flow rate to fluctuate when the same injector duty ratio is used.

According to our experiments, this fluctuation had a maximum change of about 30 percent in our simulated condition. If a real fuel flow rate is used as the feed-forward input, compensation must be provided for the fluctuation. On the other hand, the control procedure shown in Fig. 9 can be used with a two-shaft engine. The reference shaft speed and reference angle, which are very easy to detect accurately, can be

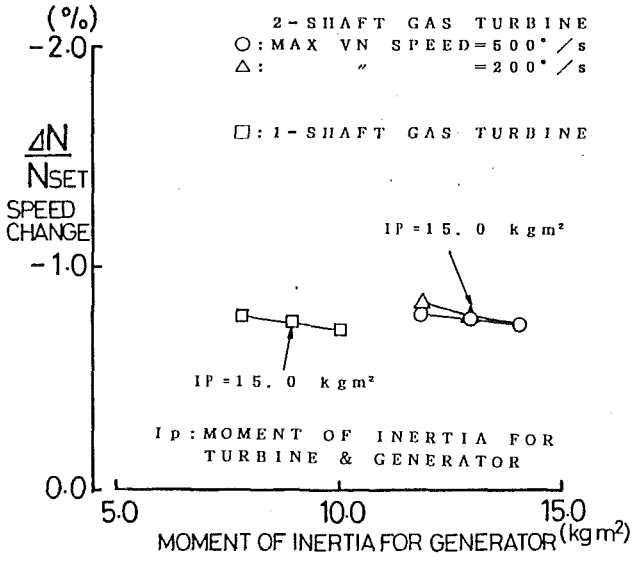


Fig. 8 Influence of output shaft inertia on speed change (calculated)

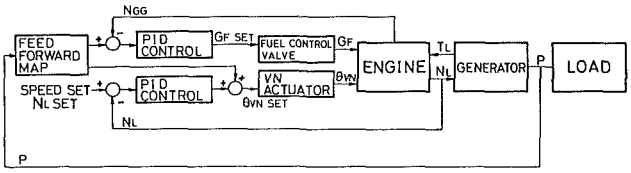


Fig. 9 Control block diagram with feed-forward control (two-shaft)

used for the feed-forward inputs. The gas generator shaft speed and variable nozzle angle can be treated as corrected values, taking into account the compressor inlet conditions.

Figure 10 shows that the feed-forward control procedure has a large effect on assuming speed stability.

When feed-forward control is applied, the variable nozzle maximum speed has a large effect on control performance. An increase from 200 deg/s to 300 deg/s is significant, and the effect on control performance decreases as the variable nozzle maximum speed becomes higher, e.g., from 400 deg/s to 500 deg/s.

The results of these investigations indicate there are two ways to satisfy the stringent speed stability requirement. The first is to use a system with a large output shaft inertia and large control gains. The second is to use a feed-forward control procedure with a quick response to load changes. Feed-forward control can easily be adopted to a two-shaft version with a variable nozzle to achieve accurate control. The simulation results show that a two-shaft engine employing feed-forward control provides speed change control performance that is equal to or higher than that of a single-shaft version without this control.

## Evaluation of Fuel Consumption

Figure 11 shows the fuel consumption characteristics of the single-shaft gas turbine, two-shaft gas turbine (fixed geometry), and two-shaft gas turbine with a variable nozzle.

The control method used in Fig. 10 is to keep the gas generator shaft speed at a high and constant level and to control the shaft speed only by means of the variable nozzle. To improve fuel consumption under partial loads, the two-shaft engine with a variable nozzle has to be driven at low gas generator speeds as much as possible. However, at lower gas generator speeds, the transient response of the two-shaft engine with a variable nozzle approaches that of the two-shaft engine with

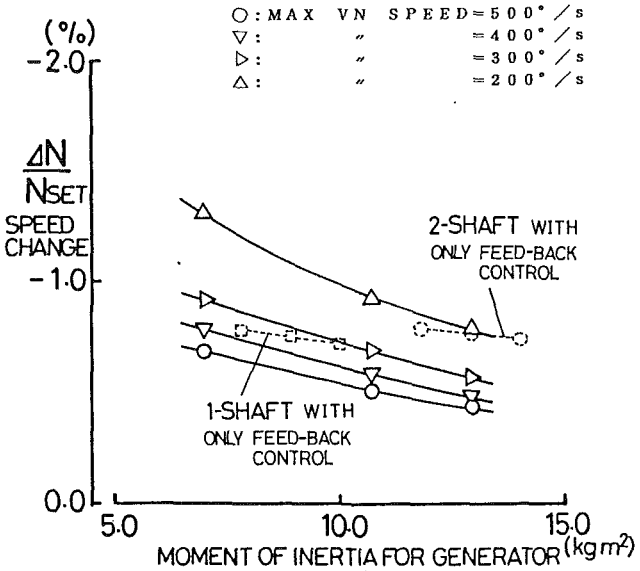


Fig. 10 Influence of feed-forward control (calculated)

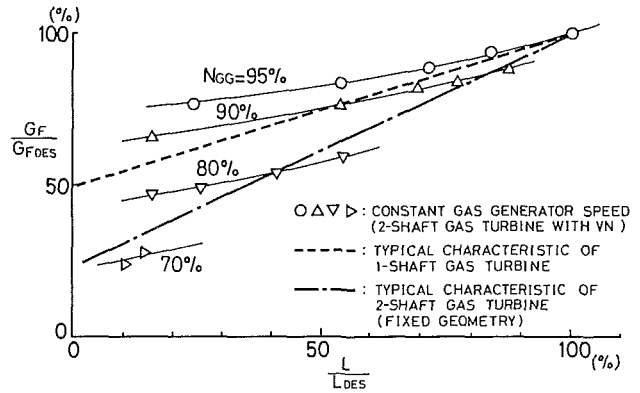


Fig. 11 Fuel consumption characteristics of single-shaft and two-shaft gas turbines

fixed geometry. This result suggests there is a tradeoff between fuel consumption and transient response with the two-shaft engine equipped with a variable nozzle.

Using a simulation model, we investigated the tradeoff between transient response and idle fuel flow rate over a load change of 0–70 percent. The control system used in the calculations employed the two feed-forward controls shown in Fig. 9, i.e., load relative to variable nozzle angle and load relative to reference gas generator speed. The transient response of the actuator for the newly developed variable nozzle was also used in the calculations. The results obtained are presented in Fig. 12. The transient response of the two-shaft engine with a variable nozzle did not decline until the gas generator shaft reached nearly 80 percent of its speed. This indicates the generating set has the potential to stabilize speed changes within 1 percent under a load change of 0–70 percent with a little less than 40 percent of the rated fuel flow rate, which is 20 percent less than the typical value for the single-shaft version. If the idle gas generator speed is reduced to less than 80 percent, the acceleration lag of the gas generator has a large effect on transient response and control performance becomes worse. In this region, the turbine inlet temperature limit during acceleration greatly affects control performance. The control performance of the two-shaft engine with fixed geometry is shown in Fig. 12 as reference data. With an idle gas generator speed of about 65 percent, the idle fuel flow rate

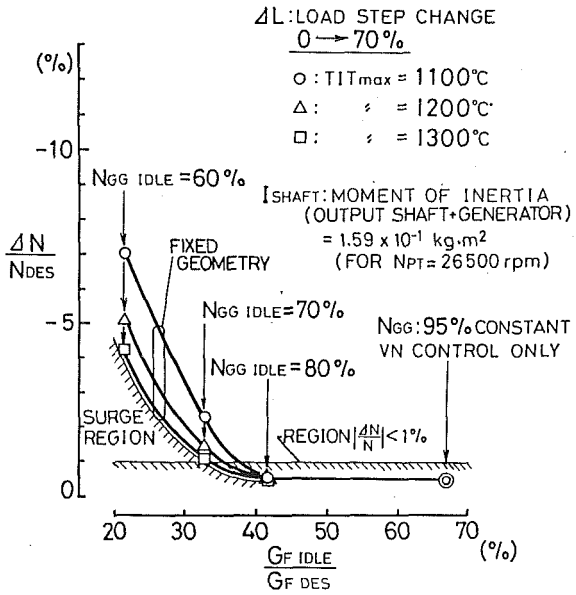


Fig. 12 Relation between idle fuel rate and speed change (calculated)

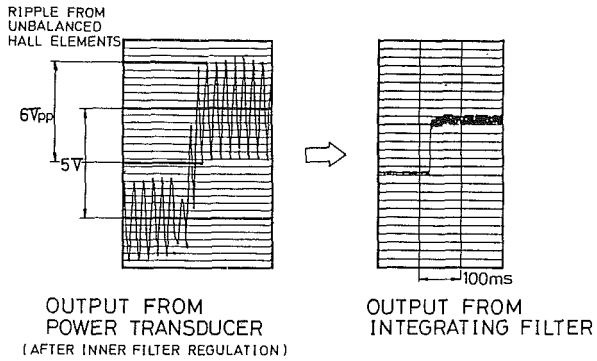


Fig. 13 Response of power transducer

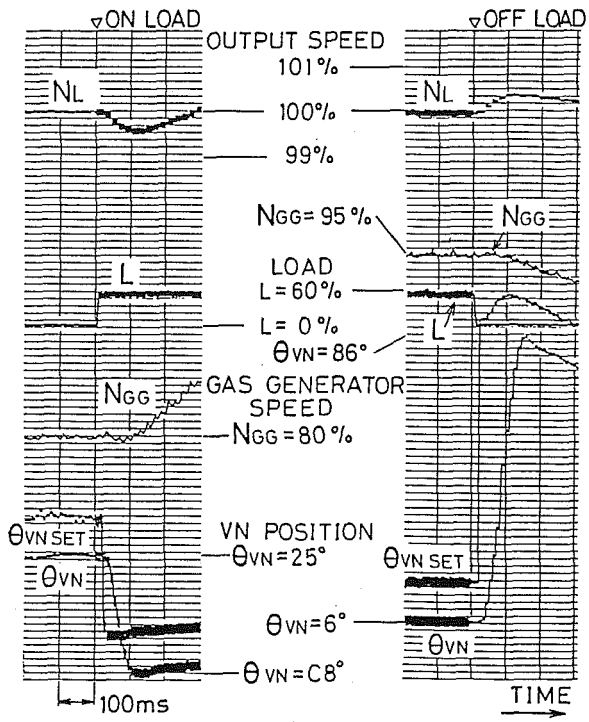


Fig. 14 Experimental results (0↔60 percent load)

is small, but the response is very slow due to the shaft acceleration lag.

The use of the two-shaft engine with a variable nozzle makes it possible to select performance combinations to satisfy different requirements. The same generating set can be configured to provide either superior frequency control plus acceptable fuel consumption or lower fuel consumption plus satisfactory frequency control. Based on the results of the investigations, we decided to use the two-shaft version with a variable nozzle in order to make the most of these advantages.

## Development of Sensor and Actuator

The foregoing investigations indicated that the system would require high-speed sensing of load changes and high engine response. Based on the simulation results, several requirements were set for the sensor and actuator. It was found that the conventional sensing method and actuator were not capable of meeting those requirements, indicating that new devices would have to be developed.

### Sensor

To sense load changes directly and cope with them by means of feed-forward control, a high response power transducer is needed. Many generating sets employ current transducers for this purpose because of the cost factor. Since the new generating set, however, has a very quick response to load changes, a power transducer of the Hall element type was provided in order to avoid any effects to the control performance resulting from lower power factor. Power transducers of the Hall element type on the market are built with filters to smooth signals from the Hall element and other noise. Their response time (interval until output of step input reaches ± 1 percent of the final value) is typically about 500 ms. That figure was regarded as being too slow to cope with load changes by means of feed-forward control. Based on simulation results, the target response time was set as under 20 ms.

When the frequency characteristic of the low-pass filters was raised to the point where the noise problem could be avoided, the response time met the requirement, but there were big ripples on the signal of the generating frequency. The ripples showed a relatively large value of 6 Vp-p when the total signal change was 5 V (Fig. 13). To maintain the desired response time and smooth the ripples simultaneously, we tried an integral treatment of the generating frequency period. The result is shown on the right side of Fig. 13.

### Actuator

The fuel supply system and variable nozzle actuator must have a high response in order to utilize the high response and accurate signals effectively. It was noted earlier that PWM injectors were adopted in the fuel supply system to assure quick response.

The target speed for the variable nozzle actuator was set at 500 deg/s at maximum speed based on simulation results. The hydraulic circuit was modified to provide higher oil pressure, lower pressure loss in the pipes, and larger capacity for the servovalve. The resulting response obtained with the new variable nozzle system reaches about 1000 deg/s at maximum speed.

## Experimental Results

Figure 14 shows the experimental results, indicating the main changes in parameter values during load changes. The idle gas generator speed was set at 80 percent in this experiment. In the case of step loading (left side of Fig. 14), C8° in the figure means 8 deg closer to the design angle. In this load region, a

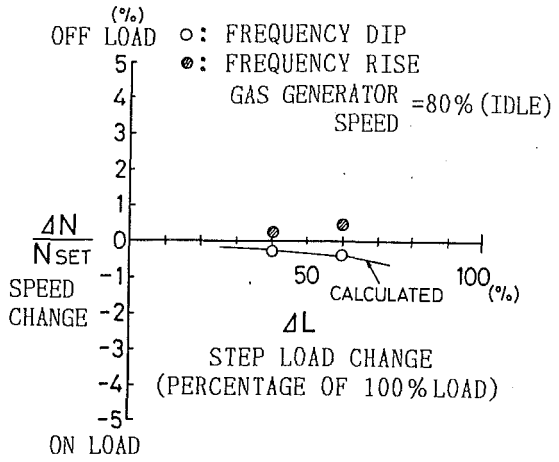


**Fig. 15 Transient response to step load change**

major portion of the engine response is related to the variable nozzle, so the output shaft speed starts to recover before the gas generator speed begins to accelerate. A similar situation is seen on the right side of Fig. 14.

Figure 15 shows the experimental results for load changes along with the simulation results. Good agreement is seen between the experimental and calculated results, indicating that each part fulfilled its function in the system.

The durability of the variable nozzle is a very important factor in ensuring the desired control performance in this system [5, 6]. To insure nozzle durability, optimal clearances were selected around the hot movable section, ceramic coatings were applied on sliding faces, metal materials were chosen, and the durability of the actuator was improved. A $10^6$ rubbing durability test was conducted on the new variable nozzle system under the rated turbine inlet temperature. Sliding faces showed no abnormal wear and the potentiometers had no trouble in detecting the variable nozzle angle.

## Summary

1 A two-shaft engine with a variable nozzle has a high capability for meeting stringent frequency stability requirements. This capability results from effective use of the variable nozzle angle and the gas generator speed, which are very easy to sense accurately for use in feed-forward control.

2 The load sensing speed and actuator response were improved through effective use of feed-forward control. The load sensing response time was reduced to less than 20 ms and the variable nozzle provides a maximum speed of over 500 deg/s as well as sufficient durability.

3 A two-shaft engine with a variable nozzle provides good control performance and fuel consumption under partial loads. There is no serious decline in control performance with an idle fuel flow rate, which is 40 percent of the rated fuel flow rate in our application.

## References

1 Itoi, T., "Gas Turbine for Emergency Use," *Journal of the Gas Turbine Society of Japan*, Vol. 14, No. 53, June, 1986.

2 Ito, T., et al., "Development of a Controller for Automotive Gas Turbine," *Preprints of the Gas Turbine Society of Japan*, 1974/6, pp. 167–172.

3 Kobayashi, O., et al., "Development of Generating Set for Emergency Use Equipped With Gas Turbine," Nissan Technical Report, 1982/12, pp. 142–154.

4 Fujikawa, Y., et al., "The Development of the Quick-Start Gas Turbine Standby Generator Set," ASME Paper No. 80-GT-115.

5 Cadwell, R. G., et al., "The Ford Turbine—An Engine Designed to Compete With the Diesel," SAE Paper No. 720168.

6 Carriere, D. L., et al., "Variable Power Turbine Nozzle System Mechanical Development," ASME Paper No. 77-GT-105.

T. H. Barmby

A. Cleveland
React Energy Ltd.,
Calgary, Alberta, Canada

# Control Systems for Turbo Expanders in Pressure Reduction Service

## Introduction

This paper considers some of the aspects of control of a turbo expander used in pressure reduction service to generate electricity. The parameters governing the performance of the expander and the connection of the expander generator system into a grid or electric supply system are discussed and the practical requirements of a suitable control system are outlined. The essential elements of a system to provide stability and control of certain selected parameters are described and extensions of control to include other functions and to provide additional data for evaluation are reviewed.

## Control of Pressure by Means of a Turbo Expander

A turbo expander may be used in place of a regulating valve to control a pressure reduction. In many such installations the power available from the expander is used to generate electricity, which ensures that the energy that would otherwise be wasted in a valve is put to use. A turbo expander used in pressure reduction service has to be controlled to:

(A) ensure that speed is compatible with the requirements of the generator and the electrical system fed by that generator;

(B) ensure that the discharge pressure from the turbo expander is maintained at the required level and with the same stability that would be provided by a valve;

(C) ensure that the power output can be controlled such that it meets the requirement of the electric system into which it feeds.

In addition to these output control functions, a turbo expander has to have alarms and trips to protect it against overspeed, low lube oil pressure and flow, high lube oil temperature, seal leakage and motoring, i.e., the generator driving the expander as a motor. These essential elements of protection need not in fact be monitored, although it is customary to provide indication of an alarm or trip condition. The customer may require a readout of certain of these operating parameters and annunciation of the trips. These facilities are in addition to the basic control functions listed above. The basic functions for operational control are shown in table 1 and those required for unit safety are shown in Table 2.

**Table 1 Operational control parameters**

| | |
|---|---|
| Discharge pressure | - measured at outlet of turbo expander |
| Speed | - measured on generator shaft |
| Power output | - measured on generator output |

**Table 2 Unit safety and protection**

| | |
|---|---|
| Overspeed | - measured on turbine shaft |
| High lube oil temperature | - measured on turbine drain |
| Low lube oil pressure | - measured on pump delivery |
| Seal leakage | - measured on return oil line (pressure) |
| Overcurrent<br>Reverse current<br>Phase imbalance<br>Generator overload | - measured in control panel |

## Control and Power

Before considering the best way of accomplishing the control function, it is necessary to look at the way in which the performance, that is, the power output, of the turbo expander can be controlled. Power output on pressure let down for a given gas depends upon the pressure ratio, the gas flow, and the inlet gas temperature. To illustrate this it is necessary to look at the expansion formula. The expansion process is calculated by the following formula:

$$\text{Power output} = ZRT_1 \left[\frac{K}{K-1}\right]\left[1-\left(\frac{P_2}{P_1}\right)\frac{K-1}{K}\right]\times M\times\mu$$

where $P_1$ = inlet pressure; $P_2$ = discharge pressure; $T_1$ = inlet temperature; $z$ = compressibility factor; $K$ = ratio of specific heats; $\mu$ = expander efficiency; $M$ = mass flow.

Mass flow is a function of fluid density and flow area in the expander nozzles. In a turbo expander with fixed nozzles the flow is a function of the nozzle area and pressure at the nozzle inlet. Since the nozzles normally operate choked, an increase in throughput can only be obtained by an increase in upstream pressure. Placing a variable orifice (valve) upstream of the nozzles provides a means of control. The graph in Fig. 1 shows how the flow varies with valve position and pressure ratio across the nozzles. The system pressure ratio is constant; the flow is increased as the pressure ratio across the nozzles increases. Figure 2 shows how the flow in MMSCFD varies with these changes in pressure ratio and valve position.

## Turbo Expander Flow Control

With this one valve control it is possible to regulate discharge pressure or power output. When the turbine is coupled to an induction generator we can also have speed control. Without going too deeply into induction motor and generator char-

Contributed by the International Gas Turbine Institute and presented at the 35th International Gas Turbine and Aeroengine Congress and Exposition, Brussels, Belgium, June 11–14, 1990. Manuscript received by the International Gas Turbine Institute January 1990. Paper No. 90-GT-349.

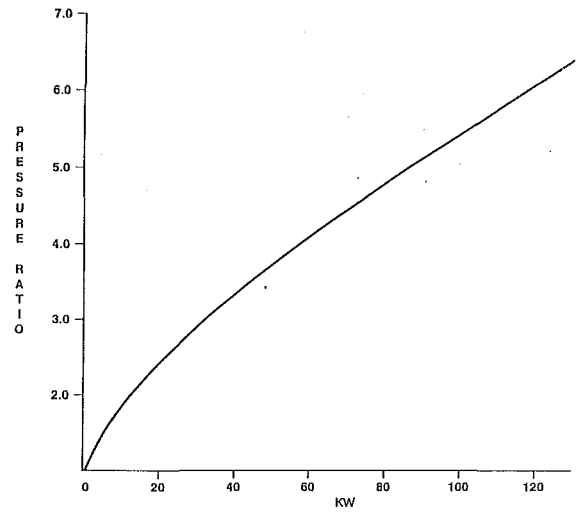


Fig. 1 Simons Valley single turbine calibration: Nozzle 7, 2/12/88

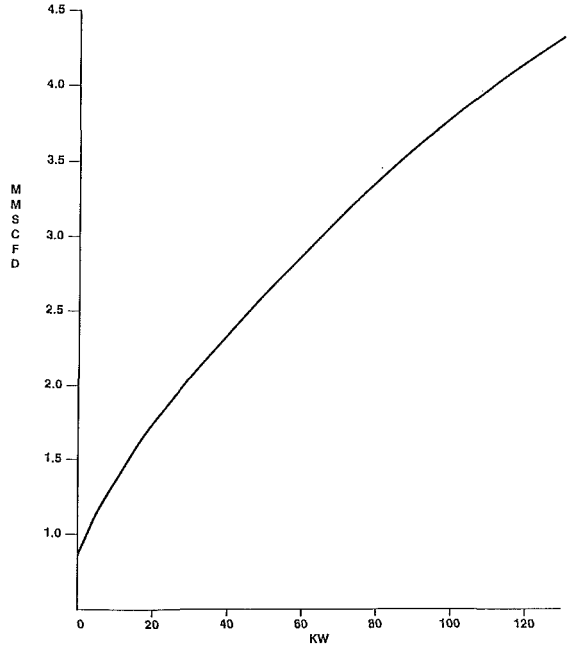


Fig. 2 Simons Valley single turbine: Nozzle 7, 2/12/88

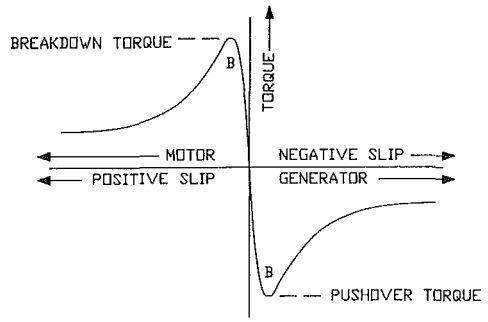


Fig. 3 Torque speed characteristic of an induction machine

acteristics, it will be seen from Fig. 3, that as the speed of induction motor is increased by driving it above synchronous speed, power is produced, and that power varies with speed. Speed will increase until the torque produced by the turbine matches the torque required by the generator. An increase of torque will increase the speed of the generator and hence increase the power until balance is once again achieved. With an induction generator therefore speed is self-regulating be-

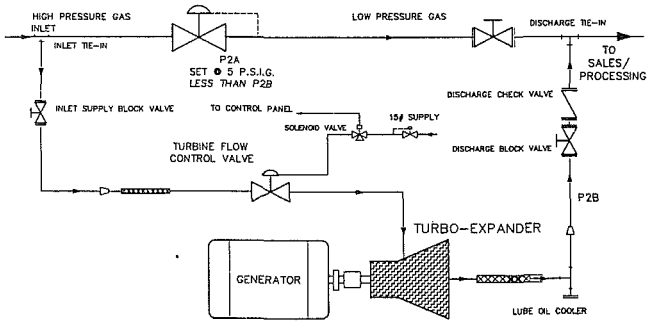


Fig. 4

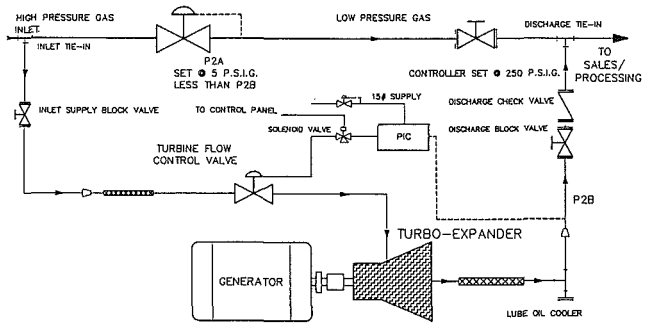


Fig. 5

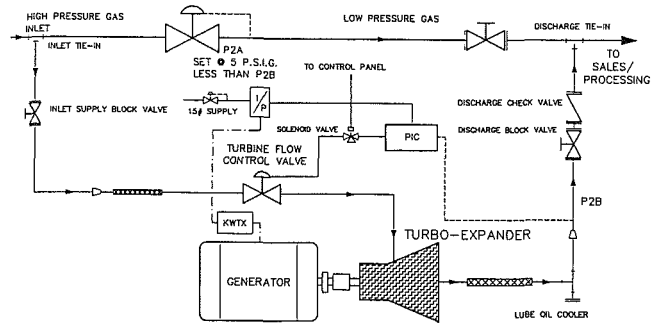


Fig. 6

cause the excitation of the machine is tied to the grid and need not be considered as a control parameter. We therefore have the option of controlling discharge pressure or power output. In most pressure reduction installations the turbo expander will be in parallel with the existing regulating valve and with this valve working the discharge pressure will be controlled by the regulating valve. The expander will then operate between the pressure limits determined by the upstream pressure and the fixed downstream pressure.

When the turbo expander is operating in parallel with an existing regulating valve and the flow through the system is greater than the expander can handle, the system will behave as a parallel regulator stream. That is, the downstream pressure will be controlled by the regulator valve and the turbo expander flow control valve will open fully in order to maximize the pressure upstream of the nozzles and thereby ensure the maximum flow through the turbo expander.

In the event that the regulating valve is out of circuit and the turbo expander alone is controlling the pressure, then a pressure signal from the discharge side fed to the control valve of the expander will modulate the flow through the expander such that a pressure drop across the control valve plus the pressure drop across the nozzles will equal the desired pressure drop for the system.

When power output control is desired, then a power output

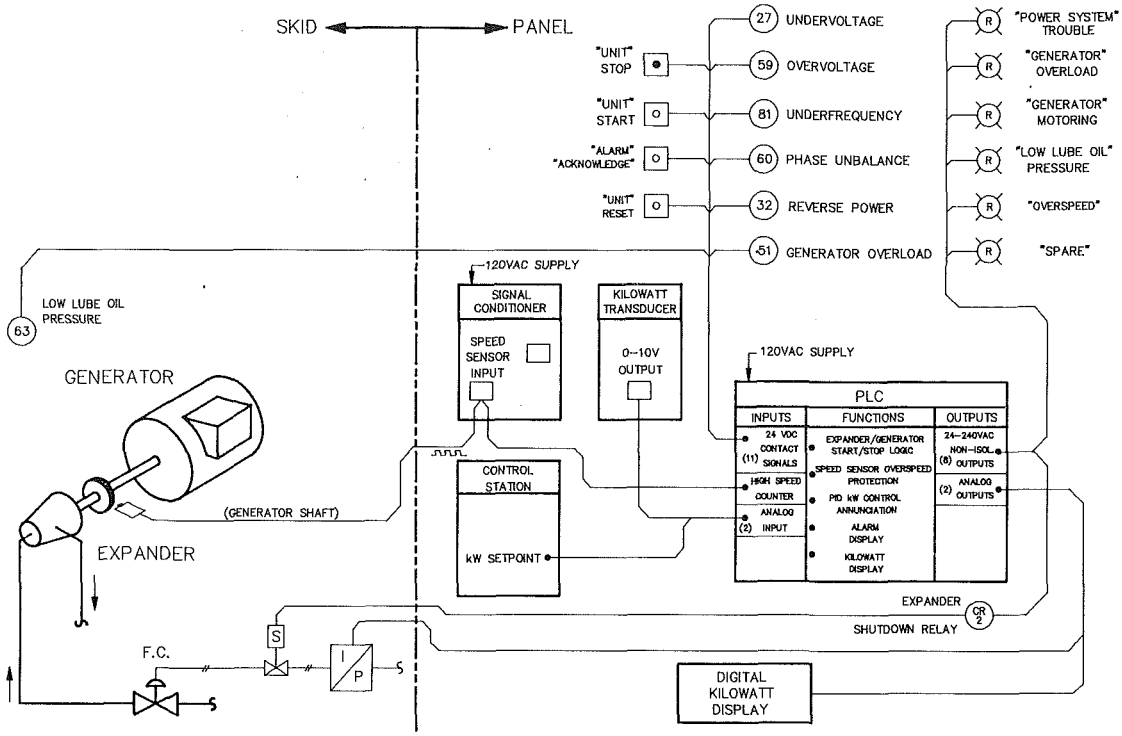


**Fig. 7 Typical logic ladder diagram**

signal can be fed to the control valve and flow modulated until the required output power is achieved. With this control, however, the discharge pressure may vary unless the expander is operated in parallel with a regulating valve.

## Development of the Control System

The requirement of the control system for the turbo expander can be summarized as:

(*a*) means of operating the flow control valve to respond to a pressure or a power output signal.

(*b*) protection for the turbine, gearbox, and generator, from overspeed, lube, or seal failure, loss of gas flow, and loss of electrical grid.

As already explained, with an induction generator the primary control element in the turbo generator package becomes the generator itself. It was found that by installing a generator approximately 10 percent larger in maximum power capability than the power that could be developed from the turbo expander, the generator limits the speed. The speed control system was therefore in place. In the induction generator, as discussed in the first part of the paper, the frequency and voltage are controlled by the grid itself; the speed of the generator only increases or decreases the amount of current produced. Therefore as long as the turbine cannot produce more power than the generator can absorb, the speed control loop becomes self-limiting. The remaining control function becomes that of controlling the flow or the pressure downstream of the turbo expander.

In addition to these functions it is necessary to have assurance that oil pressure, oil temperature, the lube system, and the seal system are functioning, and on the electrical side overload relays, phase imbalance relays, undercurrent and overcurrent relays, and reverse current relays are all correctly in circuit. The purpose of the reverse current relay is to shut the unit down when the gas flow has decreased to such an extent that the turbine is no longer providing sufficient power to drive the generator and therefore the generator becomes a motor and tries to drive the turbine.

This type of control package is the simplest control package required by the turbo expander (Fig. 4). This embodies the very basic functions only for turbo generator operation and safety. This type of package is used where the inlet pressure is reasonably constant, the discharge pressure is required to be held constant, and the flow does not vary significantly. This kind of system is suitable for fuel gas letdown to boiler packages, gas turbines, and large gas-driven reciprocating engines.

The next stage in sophistication in the control package is generally specified for gas pressure regulating systems for gas distribution companies. In this case the upstream pressure may fluctuate quite widely between 20 and 30 percent, although the downstream pressure will remain more or less constant. In this case, it is necessary to incorporate a flow or pressure-regulating device, which is usually a linear control valve.

The regulating valve is operated by a pressure pilot, which will work to try to maximize the amount of power available under any set of given conditions within the limitations of maintaining the constant downstream pressure (Fig. 5).

In this case, with the inlet pressure varying over a range, the turbo expander would normally be designed to maximize the power output of the system at the lower level of inlet pressure. With a fixed guide vane machine the number of inlet nozzles to the turbine will be chosen such that the flow at this pressure will be sufficient to generate the maximum rated power output. When the pressure is increased at inlet above this nominal level the pressure control valve will come into play to cut the pressure between the inlet manifold and the inlet to the nozzle and thus maintain this constant flow, constant-pressure condition, through the turbine. This method of control has been found to give the maximum output of kilowatts over the course of the year and ensures that the requirement of downstream pressure can be maintained.

A further variation on this is to use the kilowatt output of the generator as the control function (Fig. 6). In this case the control loop still retains the inlet governor valve and the pressure pilot but is cascaded with a kilowatt transducer working off the generator. The kilowatt transducer sends a 4–20 mA signal to *I/P*, which sends a 3–15 lb air signal to the control valve. This signal keeps the generator system at maximum output. If the kilowatt transducer calls for more output from

the generator than the gas system requires or is able to deliver at the downstream pressure then the pressure control will override the kilowatt transducer. This is the most sophisticated type of control loop required by this type of generator system and is used where flows are great enough and the downstream pressure constant enough so that the generator output can be maximized. This system is particularly valuable in multiple parallel expander installations such as would be used on a large plant or in a large regulating station.

The functions of the control system have been dealt with considering three levels of sophistication of control. In addition to these three levels of sophistication, a number of devices can be attached to any one of these control systems to allow data to be read out or fed into a higher level control such as that employed on a gas distribution system. These monitoring devices can cover the whole range of functions on the expander generator from system pressures and flows through speed to lube oil system pressure and temperatures. The utility and value of these data is a matter for the discretion of the individual user. With an induction generator, for example, speed is an interesting parameter to observe but it has very little importance because it is directly tied to generator power output and grid frequency. It would therefore be more useful to monitor power output rather than speed. Similarly, with a simple unit like the expander generator, provided the lubrication system is functioning, remote information on pressures and temperatures may not be particularly useful, the system should be able to look after itself.

However, each operator will wish to determine the necessity for the monitoring of specific functions and all of these functions relating to the operation of the machine can be readily added to the basic control system package.

## Summary and Conclusions

The simple turbo expander operating in pressure reduction service can be readily controlled using only an upstream valve modulated by power output, pressure, or speed. With an induction generator speed is regulated within narrow limits by the grid to which it is connected. The system can therefore be made to operate on either power output or pressure according to the customers' requirements. The functions needed to be monitored for control and safety are thus limited and the basic control system can be made very simple. Customers' needs, however, may dictate a more thorough knowledge of the machine's operation by reporting conditions at regular intervals or continuously and these functions can readily be added to the control system. The cost of these additional functions, however, may be considerable, and it should be carefully considered whether the benefits are not outweighed by the economics. We should not lose sight of the basic premise that the turbo expander is a means of recovering energy otherwise wasted in pressure reduction and that its function is that of a regulating valve. It should not therefore require any more attention or surveillance than a valve, provided it is capable of monitoring and responding to upset conditions that threaten its integrity.

## References

Cleveland, A., 1986, "Energy Recovery With Turbo Expanders," ASME Paper No. 86-GT-66.

Cleveland, A., 1988, "Turbo Expanders for Energy Recovery; Design and Installation of a 250 kW Unit," ASME Paper No. 88-GT-266.

Simms, J. S., 1989, "Design of a 500 kW Turbo Expander," ASME Paper No. 89-GT-225.

# Dynamic Simulation of Compressor Station Operation Including Centrifugal Compressor and Gas Turbine

**K. K. Botros**
NOVA HUSKY Research Corporation,
Calgary, Alberta, Canada

**P. J. Campbell**

**D. B. Mah**
NOVA Corporation of Alberta,
Edmonton, Alberta, Canada

*Dynamic simulation of the operation of a compressor station requires mathematical modeling of the dynamic behavior of the compressor unit and various piping elements. Such models consist of large systems of nonlinear partial differential equations describing the pipe flow together with nonlinear algebraic equations describing the quasi-steady flow through various valves, constrictions, and compressors. In addition, the models also include mathematical descriptions of the control system, which consists of mixed algebraic and ordinary differential (mad) equations with some inequalities representing controllers' limits. In this paper a numerical technique for the solution of the gas dynamics equations is described, based on the transfer matrix formulation relating the state vector time difference at one side of an element to that on the other side. This approach facilitates incorporation of all element transfer matrices into an overall transfer matrix according to the system geometric connectivity. The paper also presents simulation results and comparison with actual field measurements of three case histories: (1) simulation of a compressor surge protection control process; (2) unit startup; and (3) slow transient of a compressor station responding to changes in the discharge pressure set point. Good agreement between simulation results and field measurements is demonstrated.*

## Introduction

The technology relating to gas pipeline transient flow simulation is mature. Today, transient models of large gas pipeline networks for off-line purposes are generalized to the point that almost any practical network or straight line system can be readily simulated. The literature contains a vast amount of papers dealing with the subject of dynamic simulation of compressible gas flow in pipes. From an analysis point of view, these papers may be divided into two main categories: slow or rapid transients, for which formulations of the mathematical models are slightly different. Several different methods of solution for the pertinent one-dimensional conservation equations have been developed. The choice of a particular method is partly dependent upon the requirements of the system such as the degree of accuracy, size of the system, imposition of boundary conditions, variation of wave speed, and the type of transient. A good review paper on the various numerical methods applied is by Thorley and Tiley [1].

The dynamic behavior of the gas flow within a compressor station not only depends on the dynamic behavior of each piping element, including the compressor itself, but also interacts strongly with the unit and station control system. The literature related to compressor station dynamic simulation including control systems is scarce. Some simulation programs exist already [2, 3], but only for networks including compressor stations where the detailed dynamic behavior of the control system is greatly simplified so as to observe only crucial set points and machine limitations. A rather practical model based on solving only the continuity and momentum equations coupled with the ordinary differential equations describing the control system was described in [4], and applied in chemical plants. Simplified dynamic simulation for the evaluation of new compressor controllers were performed by Van Zee [5]. Boyce et al. [6] and Stanley and Bohannan [7] indicated the need for such coupling particularly at the design phase so as to assess the dynamic performance of the station and the effectiveness of its control system.

The work presented in this paper was motivated by this need. A computer program has been developed that deals with two levels of computations: (*a*) the gas dynamics of the piping system, and (*b*) the associated control loop response. The paper first describes briefly the mathematical models for the gas flow dynamics, which consists of large systems of nonlinear hyperbolic partial differential equations together with nonlinear algebraic equations describing the quasi-steady flow through various valves, constrictions, compressors, and their drivers. Secondly, a mathematical description of the control system,

Contributed by the International Gas Turbine Institute and presented at the 35th International Gas Turbine and Aeroengine Congress and Exposition, Brussels, Belgium, June 11–14, 1990. Manuscript received by the International Gas Turbine Institute January 23, 1990. Paper No. 90-GT-344.

which consists of mixed algebraic and ordinary differential (mad) equations with some inequalities representing controller's limits, is presented.

Solution of the above two systems of equations is performed in a stepwise and sequential manner so as to close the feedback loop of information transferred between the two systems. Results and comparison with actual field measurements of gas recycling during the process of unit surge protection at a compressor test loop, and unit startup, are presented. The third example represents a slow transient of a variable speed compressor responding to changes in the discharge pressure set point.

## Governing Equations for Yard Piping Elements

**Straight Pipe.** The general continuity, momentum, and energy equations for one-dimensional unsteady compressible fluid flow in a pipe can be written after some manipulation in the conservation form [8, 9]:

$$\frac{\partial U}{\partial t}+\frac{\partial F}{\partial x}+H=0 \tag{1}$$

where $U$ is the dependent state-space vector and $F=F(U)$, $H=H(U)$ are both functions of $U$, i.e.,

$$U=\begin{bmatrix}\rho\\ \dot{m}\\ P\end{bmatrix};\qquad F=\begin{bmatrix}G\\ G^2/\rho+P\\ \left(\frac{G}{\rho}\right)_n P+(c^2\rho)_n\left(\frac{G}{\rho}\right)\end{bmatrix};$$

$$H=\begin{bmatrix}0\\ \frac{f}{2D}\frac{G|G|}{\rho}\\ -\phi_1\frac{G^2|G|}{\rho^3}-\phi_2\frac{T_a-T}{\rho}\end{bmatrix};\quad \begin{matrix}G=\rho u=\dot{m}/A\\ \phi_1=\frac{f}{2DC_v}\left(\frac{\partial P}{\partial T}\right)_v\\ \phi_2=\frac{4h}{DC_v}\left(\frac{\partial P}{\partial T}\right)_v\end{matrix}$$

In reviewing the work of many authors on the solution of the above set of hyperbolic partial differential equations (P.D.E.), it is evident that the choice of a particular scheme or method of solution depends on the type of application. In the current application of compressor station dynamics, both slow and rapid transients can be anticipated. For example, transients caused by changes in compressor set points to meet certain demand requirements are considered slow. In this case, considerable savings in computational time and hence cost will be made by utilizing an implicit finite difference scheme, which does not require a small time step for stability. However, if rapid transients are being considered, such as those caused by a compressor surge protection system, blowdown and startup/shutdown of unit(s), a small time step is required and a scheme such as Euler explicit finite difference may be satisfactory. We have, therefore, adopted the generalized time differencing scheme of Beam and Warming [10], which allows for the selection of various known schemes upon setting two independent parameters $[\theta, \eta]$. For example, for $[\theta, \eta]$ equal to [0, 0], the Euler explicit scheme is invoked, while [1, 0] corresponds to Euler implicit, [1/2, 0] Crank–Nicolson; [1, 1/2] three-point backward; [0, −1/2] Leapfrog. The scheme, after linearization, can be put in a "delta" form relating the change in the state vector $\Delta U_1$ at one side (node) of a finite pipe element to the other side $\Delta U_2$ (see Fig. 1*a*) via a $[3\times 6]$ matrix $[T]$, i.e.,

$$[T]\begin{bmatrix}\Delta U_1\\ \Delta U_2\end{bmatrix}=[R] \tag{2}$$

where

$$\Delta U=U_{n+1}-U_n$$

and $[R]$ is the right-hand-side vector of length $[3\times 1]$. The subscripts $(n+1)$ and $(n)$ refer to the time step indices. Both $[T]$ and $[R]$ are functions of the pipe geometric dimensions, mean flow parameters, gas properties, and heat transfer parameters. This formulation of the transfer matrix concept was necessary in order to facilitate integration of the element transfer matrices into an overall transfer matrix according to the system geometric connectivity between the various elements.

**Constriction Elements.** For flow constriction elements such as elbows, reducers, orifices, and valves, a quasi-steady flow can be assumed at each time step of the numerical solution. The following equations can then be applied:

*Continuity*:

$$F_1=\dot{m}_1-\dot{m}_2=0 \tag{3}$$

## Nomenclature

$A$ = pipe cross-sectional area
$c$ = speed of sound
$C_p$ = specific heat at constant pressure
$C_v$ = specific heat at constant volume
$D$ = pipe inside diameter
$E$ = error
$f$ = Darcy friction factor (or function of)
$F$ = function of $U$
$G$ = mass flow per unit area
$H$ = function of $U$
$H_p$ = compressor polytropic head
$k$ = isentropic exponent
$K$ = proportional gain
LHV = Lower Heating Value of fuel
$\dot{m}$ = mass flow rate
$\dot{m}_f$ = fuel mass flow rate
$n$ = polytropic exponent
$N$ = compressor speed
$N_c$ = normalization constant
$N_G$ = gas generator speed
$P$ = static pressure
$Q_a$ = actual inlet flow to compressor
$[R]$ = right-hand-side vector
$s$ = Laplace variable
$t$ = time
$T$ = absolute temperature
$T_d$ = derivative time constant
$T_i$ = integral time constant
$[T]$ = transfer matrix
$u$ = mean flow velocity
$U$ = state space vector
$v$ = specific volume
$V$ = volume
$V_s$ = bias
$W_t$ = turbine output power
$x$ = axial dimension
$X$ = position
$y$ = control signal vector
$Z_a$ = average compressibility factor
$\alpha_1, \alpha_2, \alpha_3$ = constants
$\Delta$ = forward difference
$\zeta$ = damping coefficient
$\eta_m$ = mechanical efficiency
$\eta_p$ = compressor polytropic efficiency
$\eta_t$ = turbine thermal efficiency
$\theta, \eta$ = two parameters in Beam & Warming Scheme
$\lambda_i$ = Runge–Kutta weights
$\xi$ = pressure loss coefficient
$\rho$ = density
$\tau$ = time constant
$\phi_1, \phi_2$ = function defined in the text
$\omega_n$ = natural frequency

**Subscripts**

$a$ = surrounding
$n$ = time step $(n\cdot\Delta t)$
$oi$ = stagnation condition at section $i$
1 = section 1
2 = section 2
3 = section 3

*Pressure loss equation*:

$$F_2 = P_{01} - P_{02} - \xi\left(\frac{1}{2}\rho_1 u_1^2\right) = 0$$

$$F_2 \simeq P_1\left[1 + \frac{k_1 - 1}{2}\left(\frac{\dot{m}_1}{\rho_1 A_1 c_1}\right)^2\right]^{\frac{k_1}{k_1 - 1}}$$

$$- P_2\left[1 + \frac{k_2 - 1}{2}\left(\frac{\dot{m}_2}{\rho_2 A_2 c_2}\right)^2\right]^{\frac{k_2}{k_2 - 1}} - \xi\left(\frac{\dot{m}_1^2}{2\rho_1 A_1^2}\right) = 0 \quad (4)$$

*Energy equation*:

$$F_3 = h_{01} - h_{02} = 0 \quad (5)$$

where the subscripts 1 and 2 refer to upstream and downstream conditions of the element as shown in Fig. 1(*b*), $\xi$ is the pressure loss coefficient, $k_1$, $k_2$, $c_1$, $c_2$ are evaluated for the real gas from a state equation (BWRS or AGA-8 equations of state) at conditions 1 and 2.

Equations (3)–(5) can be linearized and put in a delta form similar to that developed for a pipe [i.e., equation (2)] so as to be readily adaptable to the overall system transfer matrix. The first-order Taylor expansion can be used, which results in the following transfer matrix formulation:

$$\left[\frac{\partial F}{\partial U_1}, \frac{\partial F}{\partial U_2}\right]\begin{bmatrix}\Delta U_1 \\ \Delta U_2\end{bmatrix} = [-F]_n \quad (6)$$

where $F$ is the transposition of $[F_1, F_2, F_3]$; and $\partial F/\partial U_1$, and $\partial F/\partial U_2$ are the Jacobian matrices evaluated at the time step $(n \cdot \Delta t)$. This formulation also leads to a $[3 \times 6]$ transfer matrix on the left-hand side of equation (6).

In a similar manner, finite difference formulations based on a quasi-steady flow through various elements (Fig. 1) such as a volume element, e.g., a station gas scrubber, combining and dividing Tee-elements, various types of valves, were developed (see [11]).

## Governing Equation for Turbomachinery

**Variable Speed Centrifugal Compressor.** The dual-shaft gas turbine/compressor arrangement is considered here, which is comprised of two basic functional sections: the gas generator and the power turbine, as shown in Fig. 1(*f*). Although the speed of the gas generator ($N_G$) is different from that of the power turbine and compressor speed ($N$), it is closely associated with the power level required by the load. Both speeds are protected against overspeed by speed controllers. Modeling of this system requires attention and special consideration to the fact that there are two mechanically independent but thermodynamically coupled shafts.

In the following formulation, the compressor system is assumed to respond to any perturbation in a quasi-steady manner. Linearization via first-order Taylor expansion with Jacobians evaluated at time $(n \cdot \Delta t)$ will be applied to the governing equations for both the centrifugal compressor and the gas turbine driver. This will furnish the relationship between the perturbed quantities of the gas flow on both sides of the compressor similar to that for other elements discussed above. The complication in the present formulation, however, arises from the introduction of the speeds ($N$) and ($N_G$) and the coupling between the compressor and the driver.

The governing equation of gas flow through the centrifugal compressor can be approximated by the polytropic process [12], i.e.,

*Continuity*:

$$F_1 = \dot{m}_1 - \dot{m}_2 = 0 \quad (7)$$

*Polytropic pressure ratio*:

$$F_2 = P_1/\rho_1^n - P_2/\rho_2^n = 0 \quad (8)$$

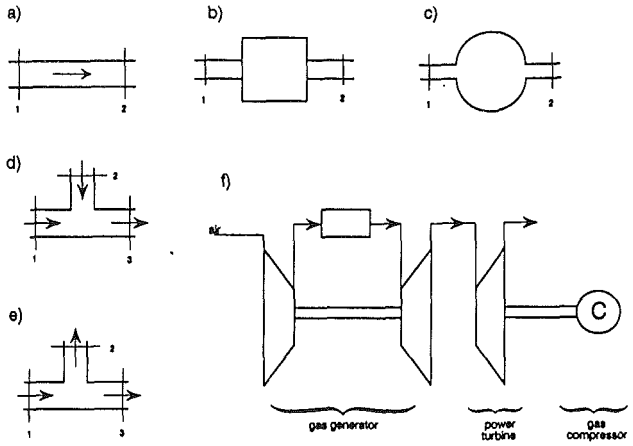


**Fig. 1 Schematics of various gas piping elements**

*Polytropic head (energy)*:

$$F_3 = \frac{Z_a R T_1}{(n-1)/n}\left[(P_2/P_1)^{\frac{n-1}{n}} - 1\right] - H(Q_a, N) = 0 \quad (9)$$

where the polytropic head ($H_p$) for the compressor is function of the actual inlet flow to the compressor ($Q_a$) and the compressor speed ($N$). A quadratic polynomial function was used alongside the affinity laws to determine $H_p$ ($Q_a$, $N$) and also for the compressor polytropic efficiency $\eta_p(Q_a, N)$, where $\eta_p$ is defined as

$$\eta_p = \left(\frac{n}{n-1}\right) / \left(\frac{k}{k-1}\right) \quad (10)$$

and ($n$) is the polytropic index and ($k$) is the isentropic exponent at average suction and discharge conditions.

Linearization of the above equations results in

$$\left[\begin{array}{c:c:c} & 0 & \\ \frac{\partial F}{\partial U_1}, \frac{\partial F}{\partial U_2} & 0 & \\ & \frac{\partial F_3}{\partial N} & \end{array}\right]_n \begin{bmatrix}\Delta U_1 \\ \Delta U_2 \\ \Delta N\end{bmatrix} = \begin{bmatrix}-F_1 \\ -F_2 \\ -F_3\end{bmatrix}_n \quad (11)$$

where $F$ is the transposition of $[F_1, F_2, F_3]$ and the Jacobians $\partial F/\partial U_1$, $\partial F/\partial U_2$ and the right-hand-side vector are evaluated at the current time step $(n \cdot \Delta t)$.

For the constant speed compressors, $\Delta N = 0$, and hence the above equation reduces to the typical $[3 \times 6]$ transfer matrix formulation in the form

$$\left[\frac{\partial F}{\partial U_1}, \frac{\partial F}{\partial U_2}\right]\begin{bmatrix}\Delta U_1 \\ \Delta U_2\end{bmatrix} = \begin{bmatrix}-F_1 \\ -F_2 \\ -F_3\end{bmatrix}_n \quad (12)$$

which is a sufficient equation regardless of the driver. For a variable speed compressor, however, information regarding $\Delta N$ must be determined from the gas turbine performance characteristics as is shown below.

**Gas Turbine.** The power turbine output power ($W_t$), gas turbine overall thermal efficiency ($\eta_t$) or specific fuel consumption, exhaust gas temperature, and inlet mass flow rate of air are all functions of the inlet air temperature and pressure, gas generator speed ($N_G$) and power turbine speed ($N$). For a given site condition, therefore, $W_t = W_t(N, N_G)$ and $\eta_t = \eta_t(N, N_G)$.

Gas turbine manufacturers usually furnish the above performance characteristics of the gas turbine either in a chart or empirical format. In the first case, it was found that cubic polynomial least-square approximation of the performance

characteristics of these two functions results in a good representation of the data when the following affinity laws were used:

$$(W_t/N_G^{\alpha_2}) = f(N/N_G^{\alpha_1}) \tag{13}$$

$$(\eta_t/N_G^{\alpha_3}) = f(N/N_G^{\alpha_1}) \tag{14}$$

where $\alpha$, $\alpha_2$, and $\alpha_3$ are constants determined from two corresponding points (maximum power line) at two different $N$ and $N_G$, for a given site condition.

Returning to the requirement of determining $\Delta N$ in terms of gas flow perturbations (i.e., equation (11)), variation in compressor speed is connected to the fuel rate delivered to the gas turbine, which is governed by the fuel control system. The power turbine output power ($W_t$) is related to the fuel rate ($\dot{m}_f$) and gas turbine overall thermal efficiency $\eta_t$, i.e.,

$$F_4 = W_t(N, N_G) - \dot{m}_f(t) \cdot LHV \cdot \eta_t(N, N_G) = 0 \tag{15}$$

where LHV is the Lower Heating Value of the fuel used. Linearization of the above equation at time $(n \cdot \Delta t)$ gives

$$\left(\frac{\partial F_4}{\partial N}\right)\Delta N + \left(\frac{\partial F_4}{\partial N_G}\right)\Delta N_G = -F_4 \tag{16}$$

where the Jacobian derivatives can be evaluated from equations (13) and (14).

Furthermore, the machine matching between the compressor and the power turbine requires that the output power from the power turbine ($W_t$) times a mechanical efficiency ($\eta_m$) must be equal to the gas compressor power, i.e.,

$$F_5 = \frac{H_p(Q_a, N) \cdot \dot{m}_1}{\eta_p(Q_a, N)} - \eta_m W_t(N, N_G) = 0 \tag{17}$$

and linearization at time $(n \cdot \Delta t)$ gives

$$\left(\frac{\partial F_5}{\partial \rho_1}\right)\Delta\rho_1 + \left(\frac{\partial F_5}{\partial \dot{m}_1}\right)\Delta\dot{m}_1 + \left(\frac{\partial F_5}{\partial N}\right)\Delta N + \left(\frac{\partial F_5}{\partial N_G}\right)\Delta N_G = -F_5 \tag{18}$$

Equations (16) and (18) above can be solved together to determine $\Delta N$ and $\Delta N_G$ in terms of $\Delta\rho_1$ and $\Delta\dot{m}_1$. The expression for $\Delta N$ can then be substituted into the compressor equation (11) to reveal the formal transfer matrix for the compressor in the normal form, i.e.,

$$[T]_c \begin{bmatrix} \delta U_1 \\ \delta U_2 \end{bmatrix} = [R] \tag{19}$$

where $[T]_c$ is the required $[3 \times 6]$ compressor transfer matrix and $[R]$ is the corresponding $[3 \times 1]$ right-hand-side vector. After the solution of the state-space vector $U$ is obtained for the entire system at time $(n+1)\Delta t$, equations (16) and (18) are then used to update the values of $(N)$ and $(N_G)$ at this time step.

It should be emphasized that the compressor and driver shaft inertias are neglected in the above formulation, and should be accounted for, particularly in relatively larger units. Other piping elements such as control valves, relief valves, conventional, and nonslam check valves were also included in the simulation, but are omitted in this paper due to space limitations.

## Dynamic Representation of the Control System

In any realistic simulation of compressor station dynamics, the response of the control system and its control elements must be included. In the last section, the mathematical descriptions of the dynamic behavior of gas through various gas-handling elements and devices were presented. Typically, these elements are connected with some sort of autonomous control system whose behavior is very important for any simulation of the flow transients.

The purpose of the station control system is to provide a collection of automatic functions so that the station operator may make major decisions, but not have continually to adjust the setting of a valve or the speed of each compressor unit, etc. Additionally, the control system permits remote operation from a central gas control location so as to provide overall operational integrity of the gas transmission network in an efficient and safe manner.

In the field, these functions are accomplished using a number of standard control elements, such as sensors, controllers, actuators, relays, ramp generators, filters, etc. All control circuits, whether pneumatic or electronic, can be described by a set of ordinary differential equations (O.D.E.) in the form

$$\frac{dy}{dt} = f(y) \tag{20}$$

together with a set of subsidiary nonlinear algebraic equations in the form

$$F(y) = 0 \tag{21}$$

where $(y)$ is a vector representing the state variable of measurements, control equipment, and controllers' outputs, and $F$ is the transposition of $[F_1, F_2, \ldots]$. The following is a brief description of the basic control elements and the respective governing control equations.

**PID Controller.** The output signal $y_3(t)$ from a PID controller is related to the control signal $y_1(t)$ and the set point signal $y_2(t)$ (see Fig. 2*a*) via the known equation

$$y_3 = K\left[E + T_d\frac{dE}{dt} + \frac{1}{T_i}\int_0^t E dt\right] + V_s \tag{22}$$

where $E$ = error = $(y_1 - y_2)/N_c$.

The derivative term in the above equation is approximated by a backward two-point difference form, while the integral term is approximated by the trapezoidal summation. This yields equation (22) above, a linear algebraic equation in $y_1$, $y_2$, and $y_3$.

Anti-reset windup is incorporated in the PID controller to help avoid problems related to saturation at the full limits of the controller output.

**Dynamic Actuator/Positioner.** The actuator is the part of a control loop that is attached directly to the station piping elements and adjusts the connected element setting in response to time-varying input signals from a controller, sensor, or relay. Second-order actuators are modeled by describing the varying relation between the actuator position $X$, input signal $(y_1)$, and the actual position $(y_2)$ (see Fig. 2*b*) via

$$\frac{d^2y_2}{dt^2} + 2\zeta\omega_n\frac{dy_2}{dt} + \omega_n^2[y_2 - X(y_1)] = 0 \tag{23}$$

where $\zeta$ and $\omega_n$ are the actuator constants (damping coefficient and natural frequency, respectively), that determine its response. The above second-order ordinary differential equation can be converted into two first-order ordinary differential equations in accordance with the system equation (20).

**Low-Pass Filter.** A low-pass filter provides a slowly varying output signal, which tends asymptotically to the input signal. Examples of such control devices in the field are ramp generators and first-order actuators. The rate of change of the output signal depends on the time constant $(\tau)$ of the filter. The equation governing the relation of the output signal $(y_2)$ to the input signal $(y_1)$ (see Fig. 2*c*) is given by

$$\tau\frac{dy_2}{dt} = (y_1 - y_2) \tag{24}$$

which is a first-order ordinary differential equation.

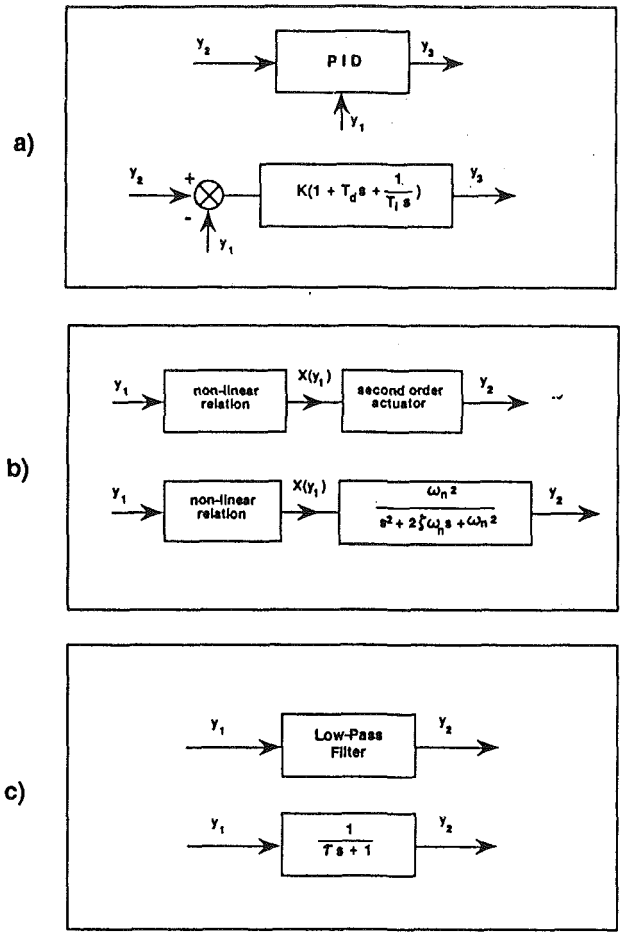


Fig. 2 Schematics of basic control elements, and the corresponding Laplace transform

The above three control elements constitute the basic building blocks for a variety of other control elements, filters, and compensators that can be found in the field. For example, a lead-lag filter or a lag-lead filter can be simulated by a PD controller and a ramp generator in series; a washout filter can be modeled as a differentiator (i.e., only the derivative component in a PID controller) and a ramp generator also in series. Once the Laplace transform of a control element is known, it is possible to construct from the building blocks of the above three basic elements the required model and proceed with the simulation. Other control elements such as comparators, multipliers, etc., can be mathematically described by equation (21).

## Closed-Loop Simulation

The mathematical description presented in the above three sections indicates that two levels of interconnected computations exist, which must be solved either simultaneously in a parallel mode, or sequentially. The first level is the gas dynamics part of the flow-handling piping system in the compressor station. This level of computation involves a solution of a set of mixed nonlinear P.D.E. and algebraic equations with appropriate boundary conditions and elements setting dictated by the control system. The other level of computation solves the dynamic behavior of the station control system, which involves a set of mixed nonlinear algebraic and O.D.E. together with boundary conditions represented by set points and measured quantities. Figure 3 illustrates schematically the closed-loop simulation of these two levels of computations. In the present work, computations were performed sequentially,

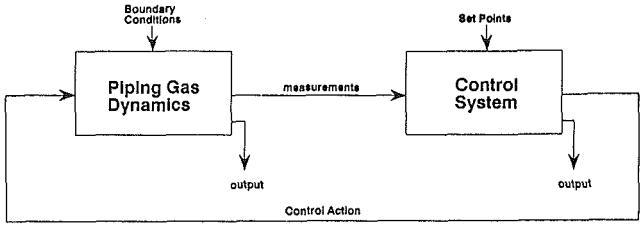


Fig. 3 Closed-loop dynamic simulation process

although a parallel computer technique can lend itself quite well in this application.

The basic framework for the simulation model adopted for the piping system is the nodal approach, in which the system is said to be comprised of nodes and elements connecting these nodes. The relationship between the state-space vector on each side of each element is formulated in a delta form using the concept of the transfer matrix (see equation (2)) and properly pooled in the system overall transfer matrix relating all space vectors at all system nodes. An effective solution technique, which takes advantage of the sparse characteristics of the system matrix, was implemented. The technique is based on a sparse variant of Gaussian elimination for the solution of a symmetric systems of equation (13). The system of equations is closed by proper description of the number and type of boundary conditions in accordance with the system characteristics equation for the hyperbolic type of P.D.E.

As for the control system, solution of the mixed algebraic and ordinary differential equations (equations (20) and (21)) is required. In the literature one finds very few algorithms for solving numerically such systems. One method [14] is to transform the algebraic equations into O.D.E., which, combined with the original O.D.E., can be solved relatively easily by standard numerical techniques. Another method stems from the multivalue method proposed by Gear [15], which replaces the system of the mixed equations by a system of purely algebraic equations obtained by substituting the finite difference approximations for all of the derivative terms. In the present work, simple $m$-stage Runge-Kutta method of the following form was considered for the part of equations represented by equation (20):

$$\begin{aligned} y_{n+1}^{(1)} &= y_n + \lambda_1 \cdot \Delta t f(y_n) \\ y_{n+1}^{(2)} &= y_n + \lambda_2 \cdot \Delta t f(y_{n+1}^{(1)}) \\ y_{n+1}^{(r)} &= y_n + \lambda_r \cdot \Delta t f(y_{n+1}^{(r-1)}) \\ y_{n+1} &= y_n + \Delta t f(y_{n+1}^{(m-1)}) \end{aligned} \tag{25}$$

where the subscripts $n$ and $n+1$ denote time levels, the superscript denotes stage number, and $\lambda_r$ are the Runge-Kutta weights. Notice that each stage has the form of the explicit Euler method advancing the dependent variable from $y_{n+1}^{(r-1)}$ to $y_{n+1}^{(r)}$ with time step size $\lambda_r \Delta t$. The weights $\lambda_r$ may be chosen in a variety of ways, to maximize either accuracy, the size of the stability region, or a combination of both. In the present application, it is better to maximize the size of the stability region while keeping the order of approximation to first order. Van der Houwen [16] calls this class "stabilized Euler formulas" and gives the expressions defining the weights. For example, the weights for a four-stage solution are

$$\lambda_1 = 1/64;\ \lambda_2 = 1/20;\ \lambda_3 = 5/32;\ \text{and}\ \lambda_4 = 1.$$

As for the other part of the control system equations represented by the nonlinear algebraic equations (21), a first-order Taylor expansion was assumed; i.e.,

$$F(y_n) + \left(\frac{\partial F}{\partial y}\right)_n (y_{n+1} - y_n) = 0 \tag{26}$$

The above set of equations (25) and (26) form a sparse system of linear equations, which were also solved by the sparse variant

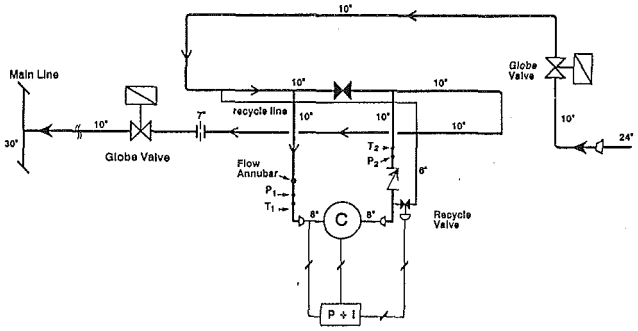


Fig. 4 Schematic of a single unit compressor station

of Gaussian elimination technique for the solution of asymmetric systems of equations resulting from the network type of the control systems.

A computer program (TRAN) has been developed that incorporates the above techniques and methods of solution. The program is PC-based and features user-friendly interfaces for preprocessing, execution monitoring, and postprocessing.

## Simulation Results and Comparison With Field Measurements

The following are three examples of dynamic simulation of a compressor station during transient operation. The examples are taken from compressor stations in the gas transmission system of NOVA Corporation of Alberta. The first two examples represent rapid transients and compressor surge protection and startup, while the third demonstrates a slow transient of a compressor station responding to changes in the discharge pressure set point.

**(i) Compressor Surge Protection Control.** This example involves field measurements of a single unit compressor station, the layout of which is shown schematically in Fig. 4. The objective was to assess the effectiveness of the surge protection control system as the field personnel indicated that the recycle valve tends to oscillate violently (from 0 to 50 percent open) when the compressor operators close to the surge control line. A field test was conducted and measurements were taken while the compressor was running at approximately constant speed of 18,000 rpm. The station suction and discharge valves were used to throttle the flow and thereby bring the compressor operating point toward the surge region. Measurements of the suction and discharge static pressures and temperatures, and differential pressures across the suction side annubar and the discharge side orifice meter, were recorded. Recycle valve position was also observed during the test. The measured data are plotted in indicative Fig. 5 for a period of 100 seconds taken during operation at the surge control line while the surge protection control system was activated. Obviously, this surge control system is shown to be unstable as manifested by the pressure and flow oscillations (Fig. 5*a* and 5*c*, respectively) and the resulting cyclic behavior on the compressor performance map (Fig. 5*d*). Dynamic simulation of the station with its control system was performed using TRAN. The surge controller was a PI controller whose settings at the time of the test were $K=5.0$ and $T_i=1/9.5$ seconds. With these settings and system boundary conditions, the simulation resulted in a remarkably good agreement with the field measurements as is demonstrated by corresponding Figs. 6. The recycle valve position (Fig. 6*e*) shows oscillations between $\approx 0$–50 percent open as has been observed during the test but was not measured and recorded due to lack of valve position indicator on the valve. Although pressure and flow oscillations both through the compressor and the recycle line agree very well with those measured in the field, the temperature oscillations predicted

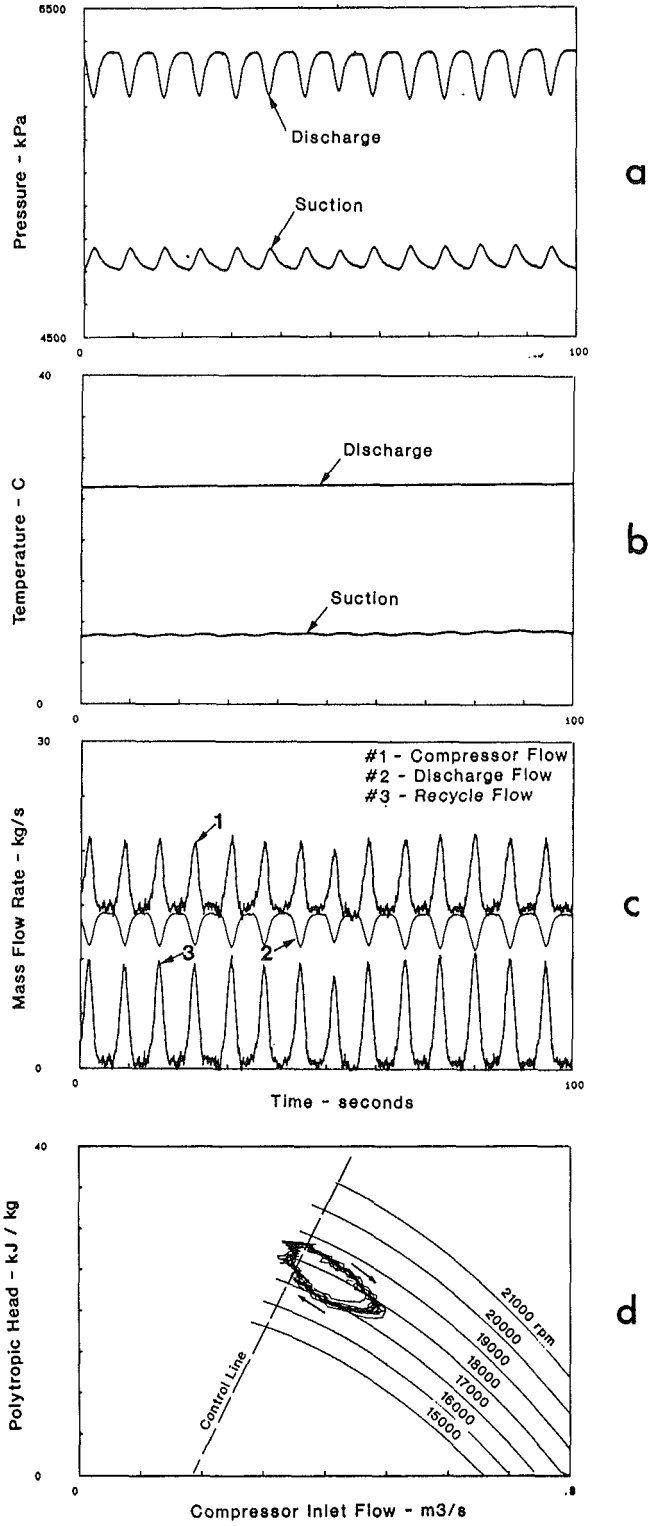


Fig. 5 Field measurements during the process of compressor surge protection of the system shown in Fig. 4

by the simulation do not agree with those measured (compare Fig. 5*b*, and Fig. 6*b*). This is due to the slow dynamic response of the temperature gages placed in relatively high thermal capacitance jackets. However, the mean temperatures agree very well in both cases.

The constants representing the damping coefficient ($\zeta$) and natural frequency of the actuator ($\omega_n$) of the recycle valve had to be estimated from the simplified control feedback loop shown in Fig. 7. In this feedback loop, the transfer function

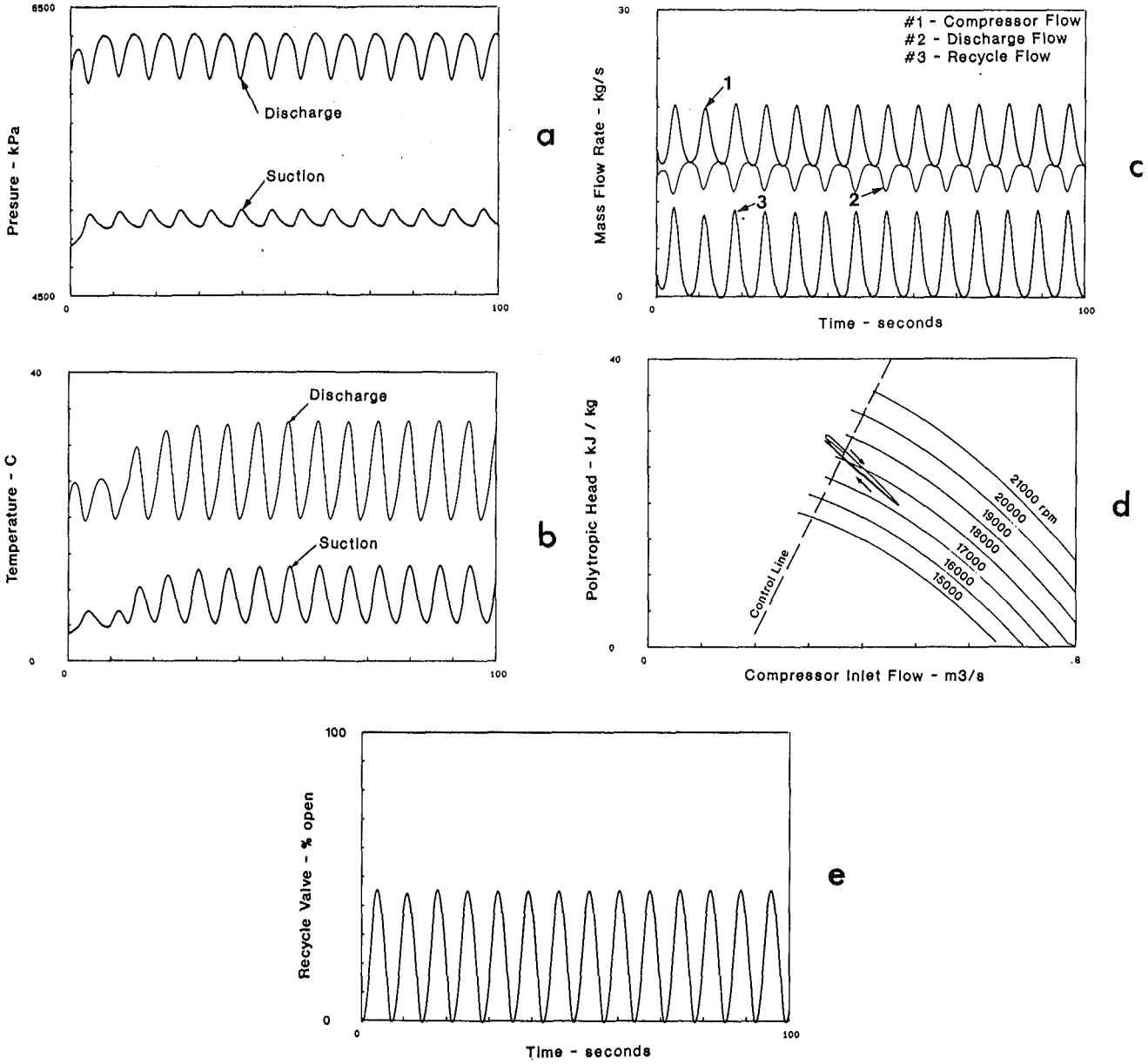


**Fig. 6 Simulation results during the process of compressor surge protection of the system shown in Fig. 4**

of the process representing the piping dynamics is assured unity with respect to flow and pressure only and not to temperature. The open loop transfer function of the feedback loop represented in Fig. 7 is

$$K\left(1+\frac{1}{T_i s}\right)\left(\frac{\omega_n^2}{s^2+2\zeta\omega_n s+\omega_n^2}\right)$$

while the root locus of the closed-loop system is determined from solving the characteristic equation

$$T_i s^3+2T_i\zeta\omega_n s^2+(K+1)T_i\omega_n^2 s+K\omega_n^2=0$$

Since measurements were showing steady oscillation at a period of 7.2 seconds (see Fig. 5*c*), i.e., at frequency $\omega=0.873$ rad/s, then two roots of the characteristic equation must be $\pm i\omega$. Equating both real and imaginary parts of the left-hand side of the equation to zero yields

$$\omega_n=0.356 \text{ and } \zeta=11.12$$

for $K=5.0$ and $T_i=1/9.5$ seconds. The root locus of the feedback control loop shown in Fig. 7 is plotted in Fig. 8, where the three poles of the open-loop transfer function are located at 0.0, $-0.0161$, and $-7.9005$. Only the first two poles are shown in Fig. 7 since the third one goes to the zero at $-1/T_i$, i.e., to $-9.5$ and hence has no influence on the control loop stability. The root locus plot of Fig. 8 indicates that stability will improve for a value of gain less than 5.0, and the lower this value, the higher damping that will be achieved. A value of $K=0.5$ was therefore chosen and introduced to TRAN for full dynamic simulation. The results obtained confirmed the above analysis and are shown in corresponding Figs. 9. Remarkable damping and suppression of oscillations were also achieved in the field with this lower value of $K$. The results of a subsequent field test (with $K=0.5$) are shown in Fig. 10.

This example demonstrates that small adjustment of the PI controller can lead to a remarkable improvement in the control process. Full dynamic simulation is useful in selecting the appropriate parameter(s) to adjust in order to achieve best results, before final implementation is executed in the field.

**(ii) Compressor Startup.** In normal operation of a gas compressor station, a unit can be started either manually or

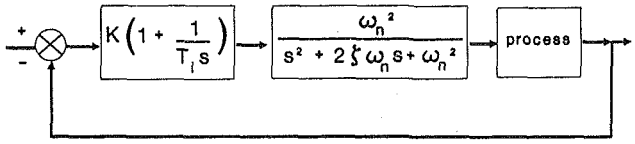


Fig. 7 Closed-loop representation of the surge control system of Fig. 4

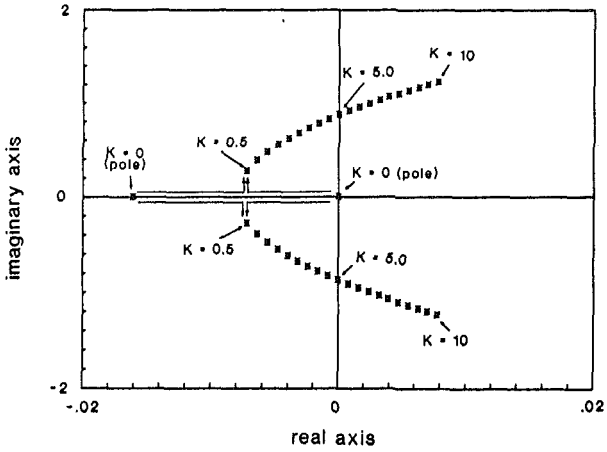


Fig. 8 Root locus of the closed-loop control system of Fig. 7

remotely with automatic valve sequencing. Typically after purging and pressurizing the compressor casing to the suction pressure, the unit suction, discharge, and recycle valves are opened and the starter is switched on, accelerating the compressor to an idle (warmup) speed. When the gas turbine combustion pressure reaches a certain pressure, the starter drops out. After a warmup period, the compressor speed is then ramped up to a higher speed. At a certain speed the recycle valve is closed, allowing the unit discharge pressure to increase to a pressure slightly higher than the line discharge pressure at which point the unit check valve will open.

Simulation of the startup period from idling to on-line conditions for the compressor set of Fig. 4 was performed and compared to actual field measurements. During testing, the discharge line pressure was only 55 kPa higher than the suction pressure, and therefore during idling at speed = 9400 rpm, the unit check valve was open allowing gas to flow to the discharge line as well. Figure 11 presents comparisons between simulation results and actual field measurements during 100 seconds covering the ramp-up period. Prior to time zero and up to 25 seconds in Fig. 11, the compressor was idling at 9400 rpm, after which a ramp signal at a rate of 50 rpm per second was issued to the ramp generator. At time 80 seconds, another signal was issued to close the recycle valve while ramping continued.

Applying the above two signals (ramping and recycle valve closure) to the unit fuel system resulted in the fuel rate profile shown in Fig. 11(*a*) from the simulation. Comparisons with field measurements of suction and discharge pressures and temperatures, compressor and recycle flows are shown in Fig. 11(*b*), Fig. 11(*c*), and Fig. 11(*d*), respectively. A plot of the process on the compressor performance map is shown in Fig. 11(*e*).

Good agreement between simulated results and measurements is demonstrated except for the temperature profiles. This is again due to the thermal capacitance of the thermal wells in which the temperature probes are placed.

**(iii) Compressor Station Set Point Change.** Compressor station dynamic operation during slow transients has been

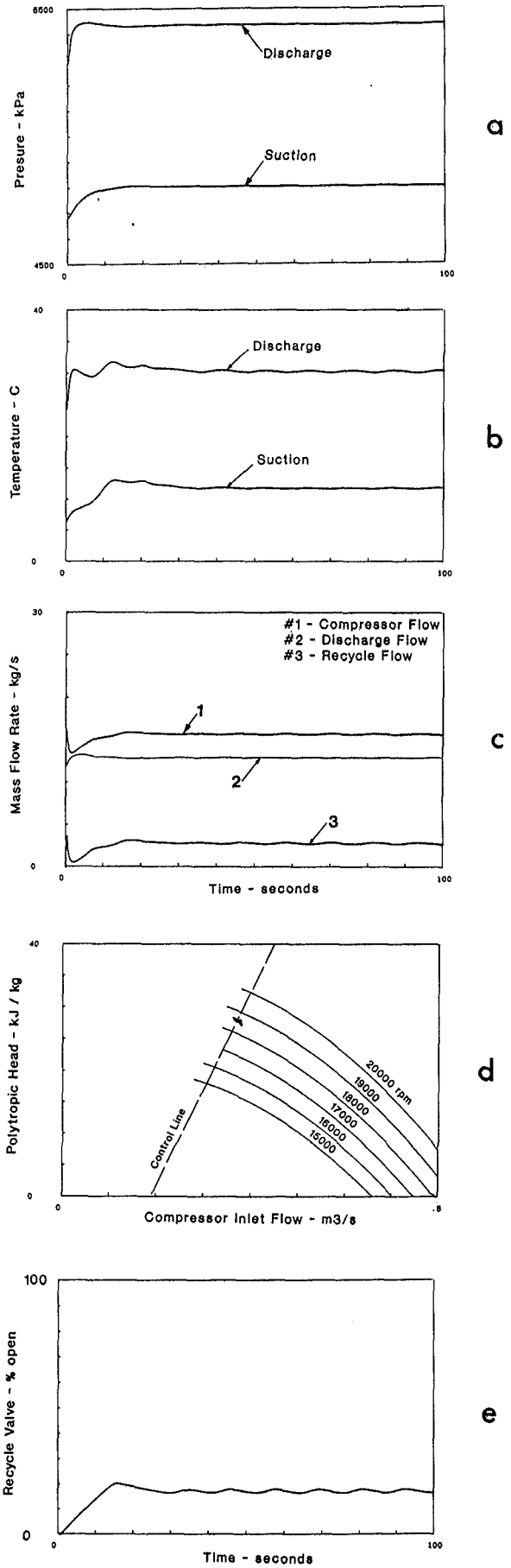


Fig. 9 Simulation results during the process of compressor surge protection ($k = 0.5$)

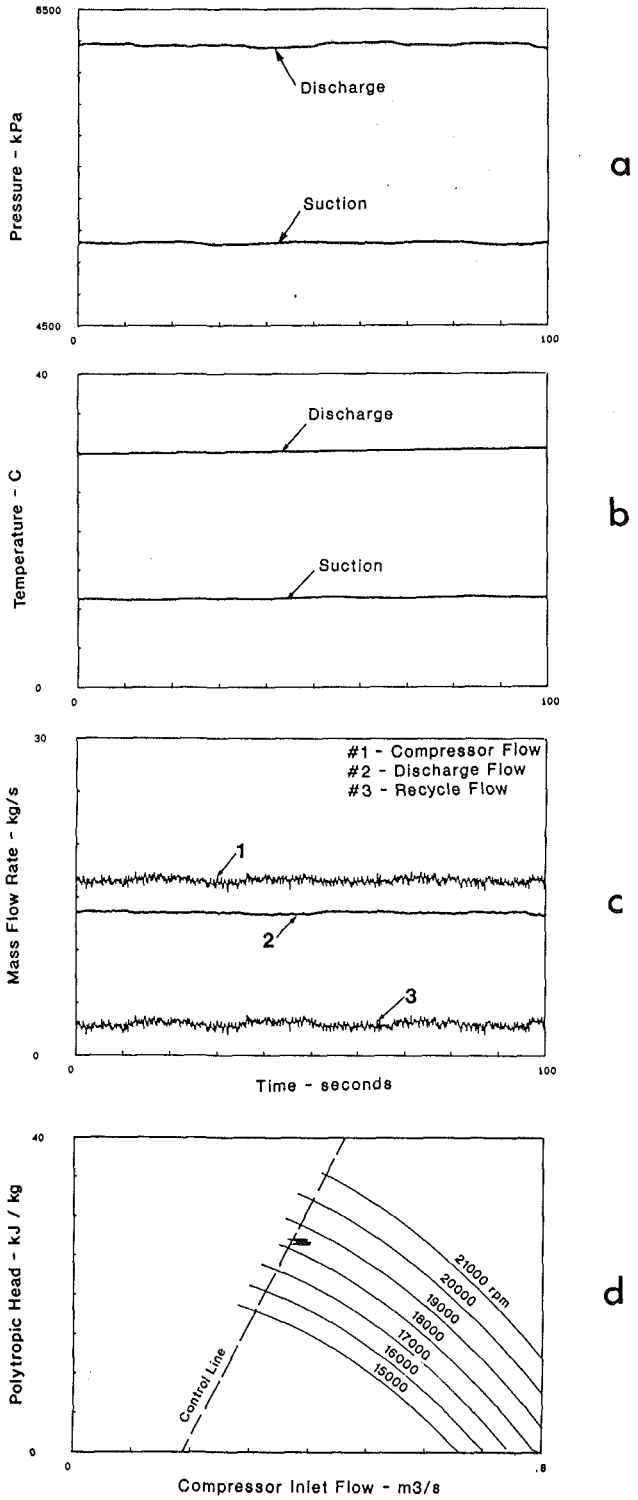


**Fig. 10 Field measurements during the process of compressor surge protection ($k = 0.5$)**

simulated by TRAN and the results were compared with actual field measurements from telemetered data at one of NOVA's compressor stations. The station contains two compressor units in series as shown in Fig. 12. For the comparison period, only unit #1 was running. Mainline flow conditions were relatively stable far upstream (approx. 82 km). A flow-controlled meter station is located approximately 66 km downstream of the compressor station where the flow demand during a six hour period is shown in Fig. 13(*b*). The flow demand prior to this period was 376 standard $m^3/s$. In order to meet this demand,

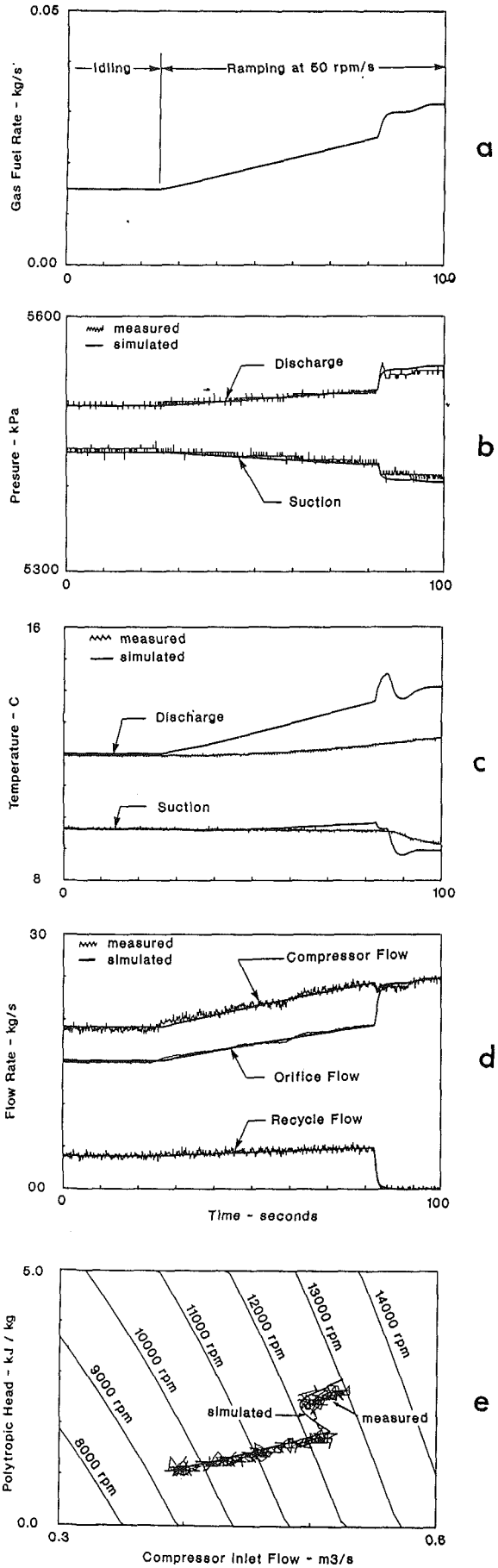


**Fig. 11 Comparison between simulation results and field measurements during startup of the compressor of Fig. 4**

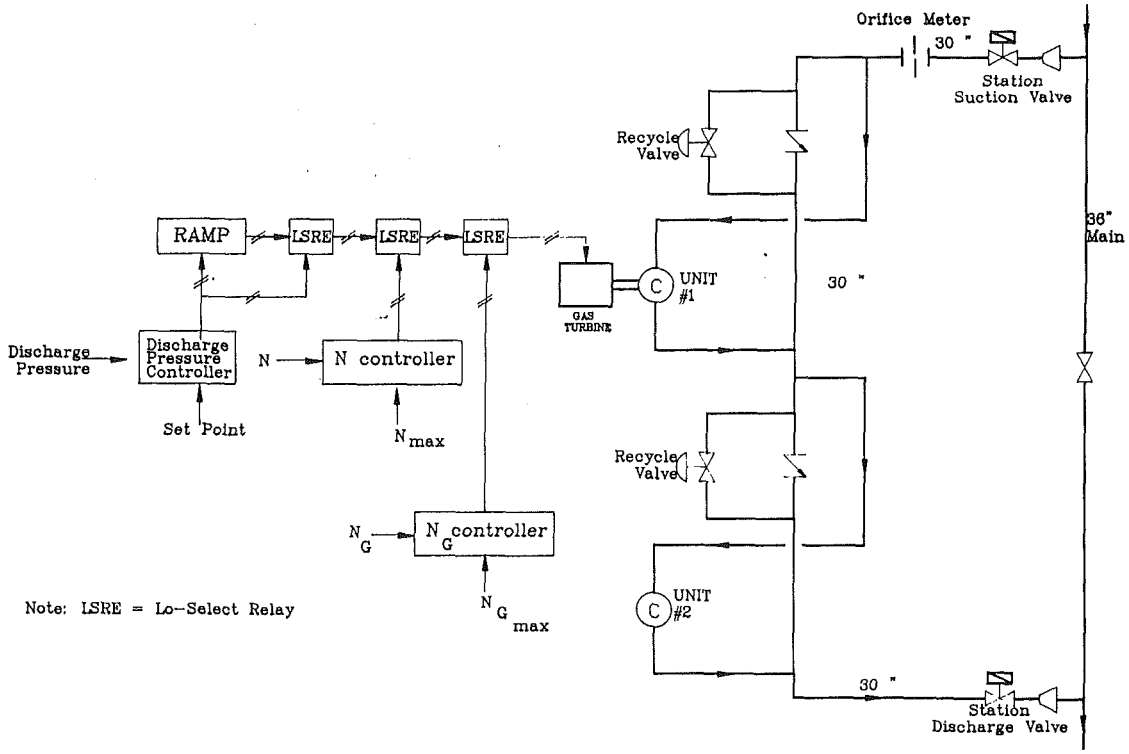


**Fig. 12 Schematic of a two-unit compressor station and its fuel control system**

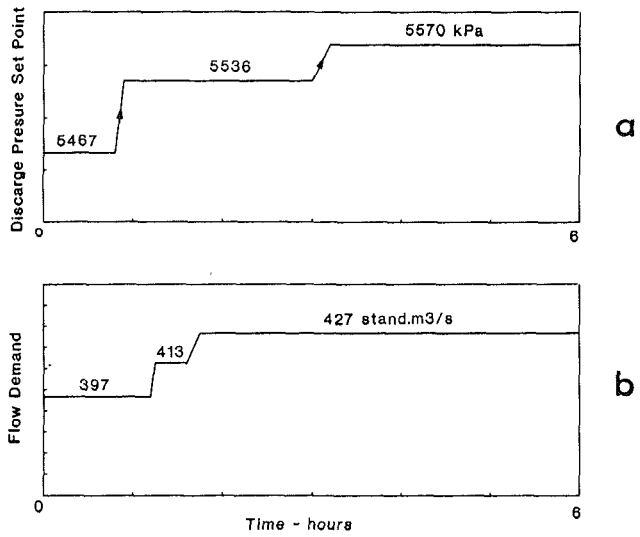


**Fig. 13 Discharge pressure control and flow demand for a six-hour period**

a remote set point change in the station discharge pressure control (DPC) was issued from the Gas Control Centre in a manner shown in Fig. 13(*a*). The sequence of compressor unit operations required to drive the unit toward the set point pressure was directed by the on-site station control system, which is simplified by the set of controllers shown on the left-hand side of Fig. 12.

Telemetry and calculated information is updated instantaneously in the Gas Control Centre on a four-minute scan basis. A twelve-minute average is calculated from three consecutive four-minute scans.

Figure 14 shows some of the telemetered data, namely, suction and discharge pressures, station flow measured by the station orifice meter, and the calculated ($H_p$-$Q_a$) plot during the same six hour period.

Dynamic simulation for the station configuration including the simplified control system shown in Fig. 12 was conducted. The mainlines upstream and downstream of the facility were simulated via capacitance (volume) and resistance elements. Boundary conditions upstream were taken at constant pressure of 5343 kPa and temperature of 15°C, while at the downstream end, the flow demand of Fig. 13(*b*) was imposed. The DPC set point pattern of Fig. 13(*a*) was then introduced in the simulation and the results obtained are shown in indicative Figs. 15. It can be shown that these results compare very favorably with the telemetered information (Fig. 14). The following observations can also be made:

- A very significant peak in station flow follows each major DPC set point increase. This is attributed to the dynamic behavior of the discharge pressure controller and its interaction with other controllers. In this example, due to the large capacitance of the discharge mainline, the discharge pressure cannot follow immediately the DPC and hence a controller error will persist for a while. This will result in increasing the fuel rate to the gas turbine and hence its gas generator speed (see Fig. 15*d*) to the maximum dictated by the $N_G$ controller. At this time, the $N_G$ controller will take over the control command until the discharge pressure increases (due to packing of the mainline) and the error in the discharge pressure controller decreases. Eventually, the latter controller restores its primary function of controlling the fuel rate to the gas turbine.
- Although the results of the station flow obtained by TRAN and that telemetered are similar, there is a shift in their relative magnitude of approximately 5–6 percent. This can be attributed to the accuracy of the flow rate measurement by the station orifice meter.
- The peaks in Fig. 14 are somewhat distorted and appear different to those in Fig. 15 due to the difference in resolution. The points in Fig. 14 were taken every twelve minutes while the calculated data in Fig. 15 are every ten seconds.

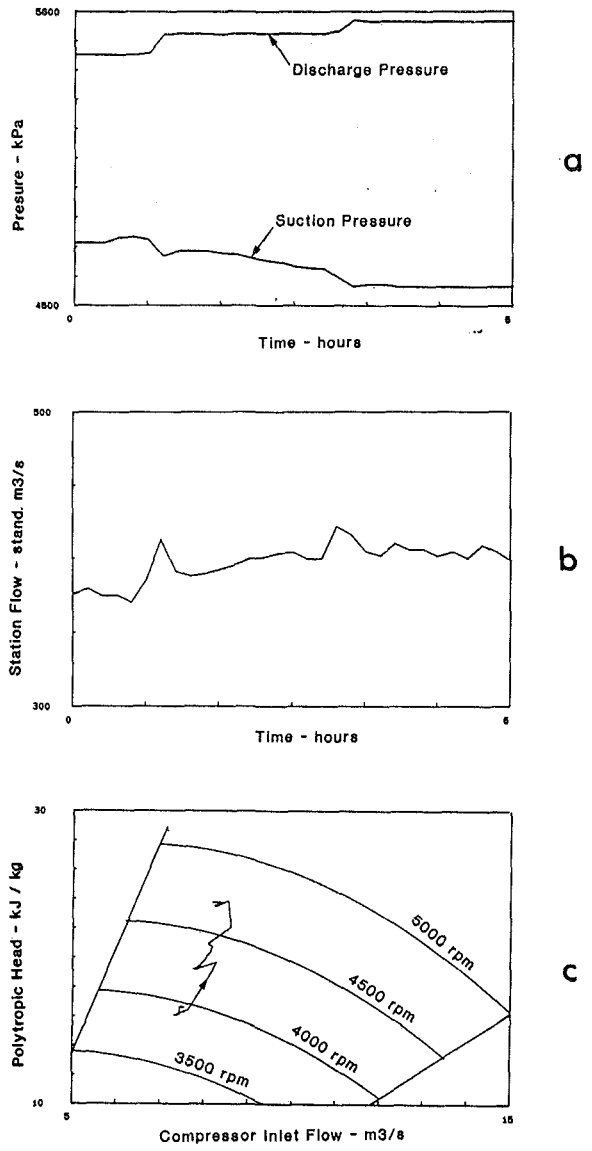


Fig. 14 Twelve-minute average telemetry and calculated information during the six-hour period of Fig. 13

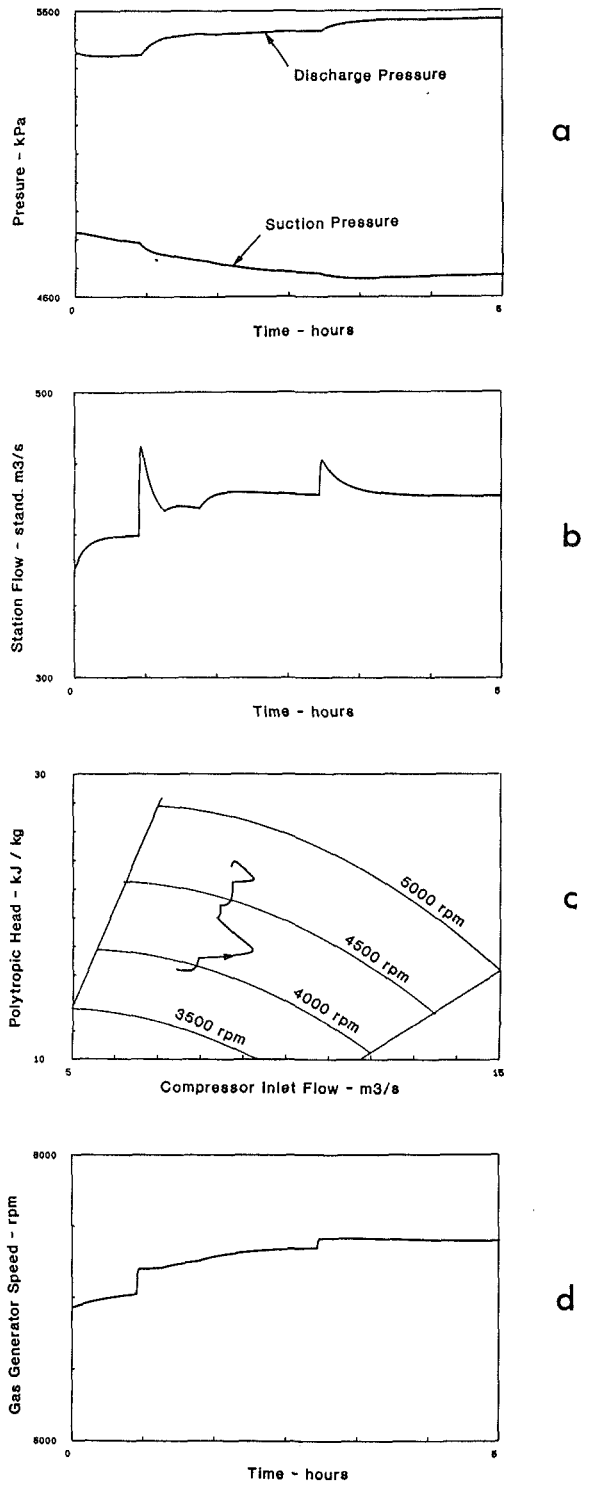


Fig. 15 Simulation results during the six-hour period

## Concluding Remarks

Simulation of the dynamic gas flow within a compressor station requires mathematical modeling of the gas dynamics of the flow through the compressor and the associated yard piping, together with mathematical descriptions of the control system and turbine driver. The type of equations and method of solution are different for the gas dynamics part than those for the control system, and therefore, dynamic modeling of the station requires two levels of computations that are performed sequentially in a closed-loop fashion.

The transfer matrix approach is a useful tool in modeling gas transients in geometrically complicated networks such as those found in compressor station yard piping. Once a transfer matrix is formulated for each element in the system, an overall transfer matrix for the entire network can be easily constructed and subsequently solved with a sparse solver routine.

Good agreement between the simulation results and actual field measurements was obtained.

## Acknowledgment

The work presented here is part of a research project sponsored by NOVA Corporation of Alberta and the permission to publish it is hereby acknowledged.

## References

1 Thorley, A. R. D., and Tiley, C. H., "Unsteady and Transient Flow of Compressible Fluids in Pipelines—A Review of Theoretical and Some Experimental Studies," *Heat and Fluid Flow*, Vol. 8, No. 1, Mar. 1987.

2 Turner, W. J., and Simonson, M. J., "Compressor Station Transient Flow Modeled," *Oil and Gas J.*, May 20, 1985, pp. 79–83.

3 Turner, W. J., Simonson, M. J., "A Compressor Station Model for Transient Gas Pipeline Simulation," Pipeline Simulation Interest Group Annual Meeting, Chattanooga, TN, Oct. 18–19, 1984.

4 Bender, E., "Simulation of Dynamic Gas Flows in Networks Including

Control Loops," *Computers and Chemical Engineering*, Vol. 3, 1979, pp. 611–613.

5 Van Zee, G. A., "Control System Design for a Centrifugal Compressor Using Dynamic Simulation," *Automatic Control, World Congress*, Vol. 2, 1987, pp. 363–368.

6 Boyce, M. P., et al., "Tutorial Session on Practical Approach to Surge and Surge Control Systems," *Proceedings of the 12th Turbomachinery Symposium*, Texas A&M University, 1983, pp. 145–173.

7 Stanley, R. A., and Bohannan, W. R., "Dynamic Simulation of Centrifugal Compressor Systems," *Proceedings of the 6th Turbomachinery Symposium*, Texas A&M University, 1977.

8 Picard, D. J., and Bishnoi, P. R., "The Importance of Real-Fluid Behavior and Nonisentropic Effects in Modelling Decompression Characteristics of Pipeline Fluids for Application in Ductile Fracture Propagation Analysis," *Can. J. Chem. Eng.*., Vol. 66, Feb. 1988, pp. 3–12.

9 Issa, R. I., and Spalding, D. B., "Unsteady One-Dimensional Compressible Frictional Flow With Heat Transfer," *J. Mech. Eng. Sciences*, Vol. 14, No. 6, 1972, pp. 365–369.

10 Beam, R. M., and Warming, R. F., "An Implicit Finite-Difference Algorithm for Hyperbolic Systems in Conservation Law Form," *J. Comp. Phys.*, Vol. 22, 1976, pp. 87–110.

11 Botros, K. K., Mah, D. B., and Campbell, P. J., "Dynamic Simulation of Compressor Station Installations Including Control Systems," *Pipeline Simulation Interest Group Annual Meeting*, El Paso, TX, Oct. 19–20, 1989.

12 Schultz, J. M., "The Polytropic Analysis of Centrifugal Compressors," ASME JOURNAL OF ENGINEERING FOR POWER, Vol. 84, Jan. 1962, pp. 69–82.

13 Duff, I. S., "MA28—A set of FORTRAN subroutines for Sparse Unsymmetrical Linear Equations," Computer Sciences and Systems Division AERE HARWELL, R. 8730, Oxfordshire, United Kingdom, Nov. 1980.

14 Audry-Sanchez, J., "On the Numerical Solution of Differential Algebraic Equations," *Can. J. Chem. Eng.*, Vol. 66, Dec. 1988, pp. 1031–1035.

15 Gear, C. W., *Numerical Initial Value Problems in Ordinary Differential Equations*, Prentice-Hall, Englewood Cliffs, NJ, 1971.

16 Van der Houwen, P. J., *Construction of Integration Formulas for Initial Value Problems*, North Holland Publishing Company, Amsterdam–New York–Oxford, 1977.

T. M. Tan

C. M. Pastore

F. K. Ko

Fibrous Materials Research Center,
Drexel University,
Philadelphia, PA 19104

# Engineering Design of Tough Ceramic Matrix Composites for Turbine Components

*This paper provides a review of the material design concepts for the toughening of ceramic matrix composites by three-dimensional fiber architecture. To establish a communication link between the structural and the materials engineers, an integrated design methodology is presented with an example. Through a Fabric Geometry Model (FGM), the contribution of three-dimensional fiber architecture is translated into a stiffness matrix for finite element structural analysis. With the feedback from the structural analysis, this design methodology provides an effective means to screen reinforcement materials systems for three-dimensional fabric-reinforced composite components.*

## 1 Introduction

In order to reach the U.S. goal of doubling the thrust-to-weight ratio of propulsion systems by the year 2000, there is an urgent need for new engineering materials. Among these materials systems, fiber-reinforced ceramic matrix composites are receiving increased attention owing to their high-temperature capabilities and the toughening properties provided by the fibrous reinforcement.

Until recently, most ceramic matrix composites were reinforced by short fibers, laminates, or filament wound systems. The delamination potential of these material systems results in relatively low stress catastrophic failure, typically occurring at matrix microcracking levels. To improve the interlaminar strength and reduce the potential for brittle failure, the concept of structural toughening of ceramic matrix composites by three-dimensional fiber architecture was demonstrated using Nicalon SiC in LAS glass matrix (Ko et al., 1987a). It was found that the through thickness strength of the three-dimensional braided composite was greater than that of the laminated and stitched composites by an order of magnitude (from 3 to 30 MPa) while achieving a fracture toughness of greater than 10 MPa$\sqrt{\text{m}}$.

As shown in a review article (Ko, 1989), there is a large family of candidate fiber architectures available for the reinforcement of ceramic matrix composites. These textile structures not only provide a mechanism for structural toughening via crack bridging and crack deflection, but also facilitate high-temperature composite processing into net or near-net shape structural parts. In order to facilitate the adaptation of the new material design concepts to the development of composite turbine components, there is a need to establish a communication link between materials engineers and structural designers. Specifically, the engineering design of three-dimensional composite turbine components requires the integration of microstructural analysis on the unit cell fiber architecture level, including the material properties and preform manufacture parameters, as well as macrostructural analysis by finite ele-

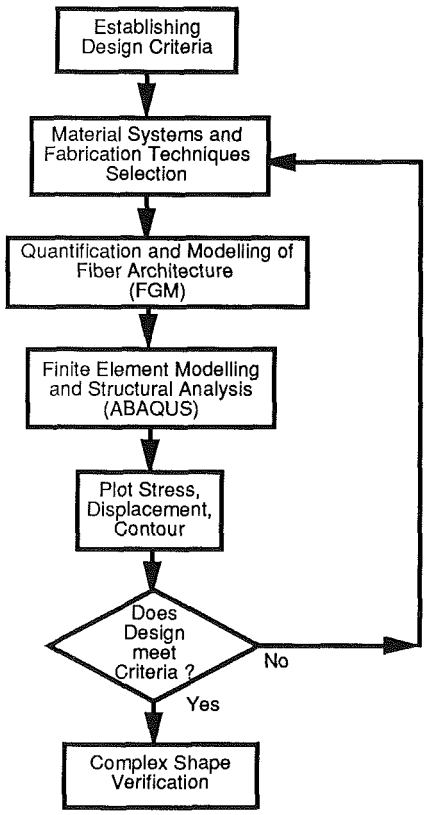


**Fig. 1 An integrated design methodology for three-dimensional fabric composite structures**

Contributed by the International Gas Turbine Institute and presented at the 34th International Gas Turbine and Aeroengine Congress and Exhibition, Toronto, Ontario, Canada, June 4–8, 1989. Manuscript received at ASME Headquarters February 14, 1989. Paper No. 89-GT-294.

ment modeling, as illustrated in Fig. 1. For this paper, the three-dimensional braided structure (Ko and Pastore, 1985) is employed as an example to illustrate the integrated design methodology established at Drexel University for silicon carbide fiber-reinforced glass ceramic matrix composite turbine blade structures.

## 2 Unit Cell Modeling

The engineering design and analysis of a three-dimensional fabric composite structural component requires the knowledge of not only the properties of fiber, matrix, and fiber-matrix interface, but also the geometric arrangement of the fabric reinforcement. The geometry of fiber architecture resulting from a particular fabrication technique dictates the fiber orientation and fiber volume fraction, and will strongly influence the integrity and performance of the composite structure, as well as the processability of the composite system. Likewise, from a structural analyst's point of view, it is important that the mechanical behavior of these three-dimensional fabric composite systems can be determined based on their fiber architectures and the properties of constituents. For this purpose, a Fabric Geometry Model, which combines textile engineering methodology and modified lamination theory, has been developed to characterize the fabric composites (Whyte, 1986; Ko et al., 1987b).

**2.1 Quantification of Fabric Geometry.** The first step in the geometric modeling of fabric-reinforced composites is the identification of the orientation of the yarns in the three-dimensional network. Figure 2 shows a typical three-dimensional braided rectangular composite panel with an enlarged view of a topological unit cell, which repeats itself throughout the structure. Representing thickness, width, and height, $U$, $V$, and $W$, respectively, of the unit cell are related by the following equation:

$$W=\frac{\sqrt{U^2+V^2}}{\tan\theta} \tag{1}$$

where $\theta$ is the interior angle defining the orientation of the yarn with respect to the longitudinal axis of the panel. With this relation it is possible to identify the angle $\theta$ associated with a particular fabric system, or to determine the value of $W$ necessary to manufacture a fabric with fiber orientation $\theta$.

Once the interior angle $\theta$ is identified for a given system, the relation between the desirable fiber volume fraction and the total number of yarns needed in the fabric composite can be established as follows (Whyte, 1986; Ko et al., 1987b):

$$N_y=\frac{C_d A_c \rho \cos\theta}{D_y} V_f \tag{2}$$

where $N_y$ = total number of yarns in the fabric; $C_d = 9\times10^5$, a constant; $A_c$ = cross-sectional area of finished composite ($cm^2$); $\rho$ = density of fiber ($g/cm^3$); $\theta$ = interior angle, defined in equation (1); $D_y$ = linear density of fiber (denier); $V_f$ = fiber volume fraction.

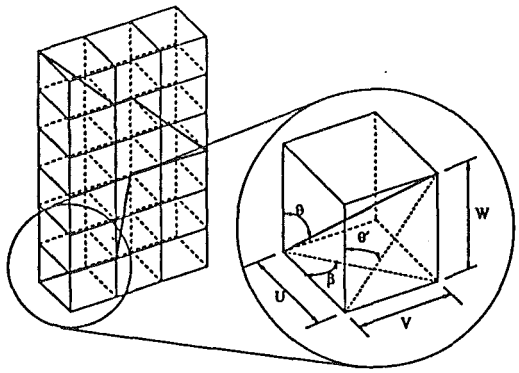


**Fig. 2 Unit cell and typical path of a yarn in a three-dimensional braided rectangular panel**

Depending on the fiber architecture of a given fabric system, there is an upper limit on the fiber volume fraction attainable. For three-dimensional braided composite, it can be shown that the highest fiber volume fraction attainable is approximately 68 percent (Whyte, 1986).

**2.2 Fabric Geometry Model.** Once the fabric geometry is quantified, the results can be used together with the fiber and matrix properties to predict the mechanical properties of a fabric composite system through a modified lamination theory. From the geometry of a unit cell associated with a particular fiber architecture, different systems of yarn can be identified whose fiber orientations are defined by their respective interior angle $\theta$ and azimuthal angle $\beta$ (Whyte, 1986). The angles of the braiding yarn system in a three-dimensional braided structure, for instance, are shown in Fig. 2. Assuming each system of yarn can be represented by a comparable unidirectional lamina with an elastic stiffness matrix defined as (Whitney, 1987)

$$[C]=\begin{bmatrix} C_{11} & C_{12} & C_{13} & 0 & 0 & 0 \\ C_{12} & C_{22} & C_{23} & 0 & 0 & 0 \\ C_{13} & C_{23} & C_{33} & 0 & 0 & 0 \\ 0 & 0 & 0 & C_{44} & 0 & 0 \\ 0 & 0 & 0 & 0 & C_{55} & 0 \\ 0 & 0 & 0 & 0 & 0 & C_{66} \end{bmatrix} \tag{3}$$

where

$$C_{11}=\frac{(1-\nu_{23}^2)E_{11}}{K}$$

$$C_{22}=C_{33}=\frac{(1-\nu_{12}\nu_{21})E_{22}}{K}$$

$$C_{12}=C_{13}=\frac{(1+\nu_{23})\nu_{21}E_{11}}{K}$$

## Nomenclature

$A_c$ = cross-sectional area of the finished composite, $cm^2$
$a_i$ = CTE of composite
$[C]$ = elastic stiffness matrix
$C_d$ = $9\times10^5$, a constant
$D_y$ = linear density of fiber, denier
$E_{i,j}$ = elastic modulus of composite
$E_m$ = elastic modulus of matrix
$G_{i,j}$ = shear modulus of composite
$k_i$ = proportional volume
$l_i, m_i, n_i$ = direction cosines
$N_y$ = total number of yarns in the three-dimensional braid
$T$ = transportation tensor
$U$ = thickness of the unit cell
$V$ = width of the unit cell
$V_f$ = fiber volume fraction
$W$ = height of the unit cell
$\beta$ = azimuthal angle
$\theta$ = fiber orientation or interior angle
$\nu_{i,j}$ = Poisson ratio
$\rho$ = fiber density, $g/cm^3$

$$C_{23} = \frac{(\nu_{23} + \nu_{12}\nu_{21})E_{22}}{K}$$

$$C_{44} = G_{23}; \quad C_{55} = G_{13}; \quad C_{66} = G_{12}$$

and

$$K = 1 - 2\nu_{12}\nu_{21}(1 + \nu_{23}) - \nu_{23}^2$$

then the elastic stiffness matrix, $[C']$, of this yarn system in the longitudinal direction of the panel can be expressed as

$$[C'] = [T][C][T]^{-1} \tag{4}$$

in which the transformation matrix (Whyte, 1986)

$$[T] = \begin{bmatrix} l_1^2 & m_1^2 & n_1^2 & 2m_1n_1 & 2l_1n_1 & 2l_1m_1 \\ l_2^2 & m_2^2 & n_2^2 & 2m_2n_2 & 2l_2n_2 & 2l_2m_2 \\ l_3^2 & m_3^2 & n_3^2 & 2m_3n_3 & 2l_3n_3 & 2l_3m_3 \\ l_2l_3 & m_2m_3 & n_2n_3 & m_2n_3 + m_3n_2 & l_2n_3 + l_3n_2 & l_2m_3 + l_3m_2 \\ l_1l_3 & m_1m_3 & n_1n_3 & m_1n_3 + m_3n_1 & l_1n_3 + l_3n_1 & l_1m_3 + l_3m_1 \\ l_2l_1 & m_2m_1 & n_2n_1 & m_1n_2 + m_2n_1 & l_1n_2 + l_2n_1 & l_1m_2 + l_2m_1 \end{bmatrix}$$

and

$$l_1 = \cos\theta \qquad m_1 = 0 \qquad n_1 = -\sin\theta$$
$$l_2 = \sin\theta\cos\beta \qquad m_2 = \sin\beta \qquad n_2 = \cos\theta\cos\beta$$
$$l_3 = \sin\theta\sin\beta \qquad m_3 = -\cos\beta \qquad n_3 = \cos\theta\cos\beta$$

where the angles $\theta$ and $\beta$ have been defined previously. It is noted that the material properties of a unidirectional lamina, $E_{11}$, $E_{22}$, $G_{12}$, ..., can be easily obtained using the well-established micromechanics relationships (Jones, 1975).

With the elastic stiffness matrix of each yarn system determined, the total elastic stiffness matrix, $[C^c]$, of the composite panel can be obtained by the equation

$$[C^c] = \sum_i k_i [C']_i \tag{5}$$

where $k_i$ is the fractional volume of the $i$th yarn system (Ko et al., 1987b).

The Fabric Geometry Model (FGM) described in this section has also been extended to characterize the strength and nonlinear stress–strain behavior of various fabric composite systems ranging from polymer to metal and ceramic matrix composites. A detailed formulation of this model can be found from Ko et al. (1985) and Whyte (1986).

## 3 Design Criteria and Fabrication Techniques

In establishing the design criteria for near-net shape manufacturing of fabric composite structures, the requirements that need to be satisfied include strength, stiffness, and geometry. For instance, when designing a composite turbine blade, the structure must be able to survive a certain level of centrifugal force due to a given level of rotational speed and the thermal loading due to heated gas flow from the combustion chamber. In order to assess the fatigue life of the turbine blade, the natural frequencies of the blade must also be known. On the other hand, the aerodynamic analysis of a turbine rotor may impose certain restrictions on the thickness of blades, and the fiber architecture used may have to provide the structure with enough fiber volume fraction in some critical areas and directions.

The selection of material systems and fabrication techniques will greatly influence the mechanical properties of the composite system and the responses of structural components, and is therefore the most important step in this design framework. For each material system and fabrication technique that was selected as possible candidate, the corresponding fiber architecture and material properties can be identified using the Fabric Geometry Model. Structural analysis of the blade may then be conducted using the finite element method to verify whether the selected material system and fabrication technique meet the design criteria, and fabrication technique may be modified accordingly. This process may be iterated until a final design with an optimal fiber architecture and proven structural behavior is identified.

## 4 Structural Analysis of a Composite Turbine Blade

In this section, the finite element model and procedure used for the structural analysis of a three-dimensional fabric composite blade are described along with typical results. The structural analysis of the composite blade is performed using a general purpose finite element code (ABAQUS Manuals, 1982). Based on hypothetical blade specifications, a three-dimensional model is first generated on a CAD system; the coordinates of the geometry for constructing a finite element mesh are then obtained from this model. Thirty-six 20-mode three-dimensional isoparametric elements are used to model the blade, resulting in a total of 720 nodes. Figure 3 shows the finite element mesh established for the turbine blade.

After consideration of several fabrication techniques with different fiber volume fractions, a final design was chosen. The mechanical properties for each fiber architecture are computed from the Fabric Geometry Model. Illustrated herein is a three-dimensional braided Nicalon SiC structure in a lithium alumina silicate (LAS III) ceramic matrix. The input material

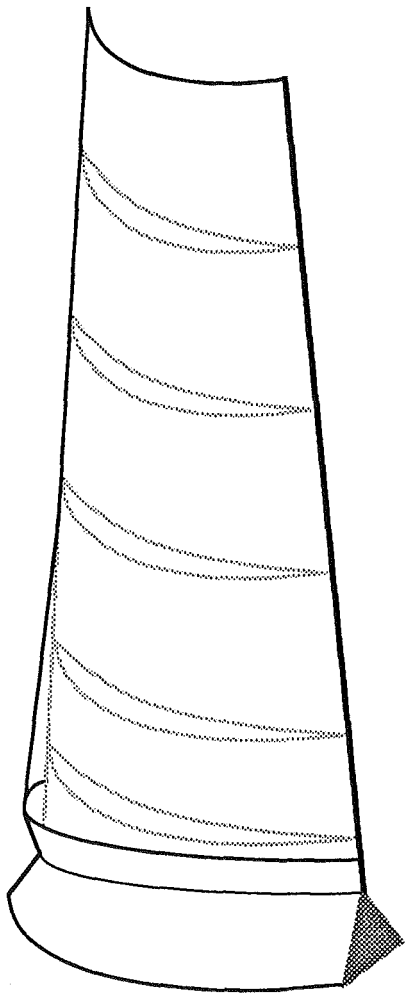

Fig. 3(*a*) Low-pressure turbine blade

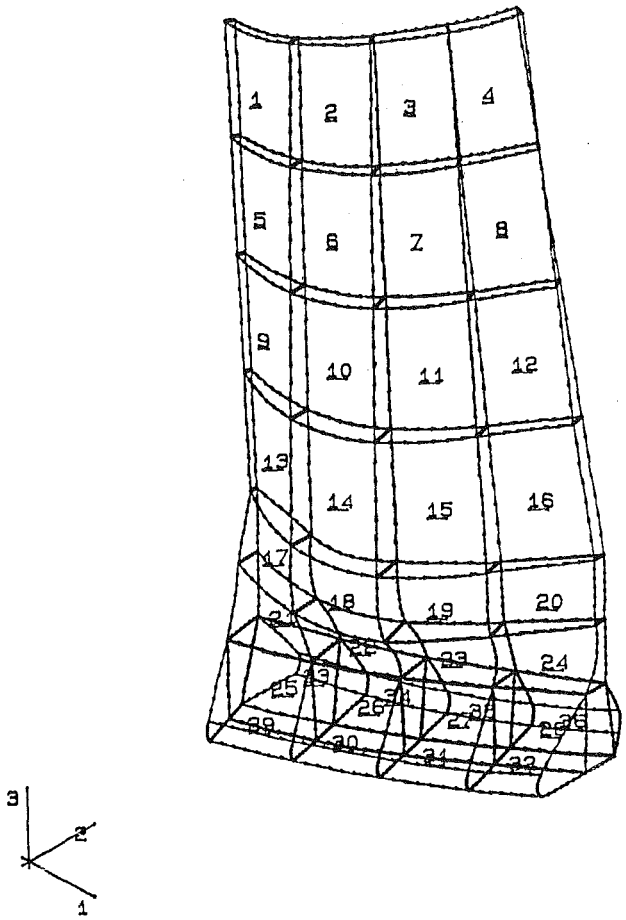


Fig. 3(*b*) Hypothetical turbine blade showing finite element mesh for Fig. 3(*a*)

**Table 1 Materials properties**

| Nicalon SiC | LASIII | |
|---|---|---|
| $E_{11}$(GPa) | 139 | 181 |
| $E_{22}$(GPa) | 32 | 181 |
| $E_{33}$(GPa) | 32 | 181 |
| $G_{12}$(GPa) | 43 | 60 |
| $\rho_{12}$(g/cm$^3$) | 0.20 | 0.26 |
| $\alpha(10^{-6}/°C)$ | 3.1 | 1.6 |

**Table 2 Geometric parameters**

| | |
|---|---|
| Braid construction | 1×1 |
| Braiding angle $\theta$ | ±20 |
| $V_f$ | 0.4 |

properties and structural parameters for the computation of the system stiffness matrix are presented in Tables 1 and 2.

The resulting elastic stiffness matrix and the coefficients of thermal expansion for the shank region are given by

$$\begin{pmatrix} 157.6 & 49.4 & 50.2 & 0.4 & 1.2 & 1.2 \\ 49.4 & 156.1 & 52.3 & -0.2 & -0.4 & -0.9 \\ 50.1 & 52.3 & 156.5 & -0.2 & -0.9 & -0.4 \\ 0.4 & -0.2 & -0.2 & 46.7 & -0.6 & -0.6 \\ 1.2 & -0.4 & -0.9 & -0.6 & 43.9 & 0.4 \\ 1.2 & -0.9 & -0.4 & -0.6 & 0.4 & 41.9 \end{pmatrix} \text{(GPa)}$$

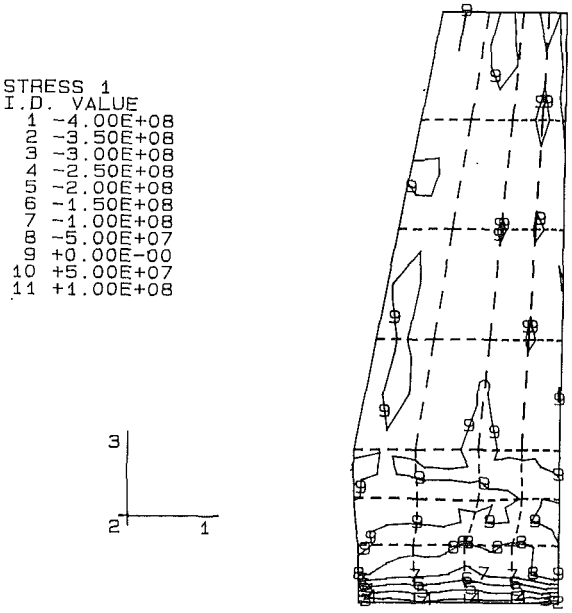


Fig. 4 Typical stress distribution for axial stresses

with

$\alpha_1 = 1.53 \times 10^{-6}$

$\alpha_2 = 1.61 \times 10^{-6}$

$\alpha_3 = 1.65 \times 10^{-6}$

and those of the dovetail region are given by

$$\begin{pmatrix} 154.3 & 51.0 & 51.0 & 1.9 & 2.3 & 2.3 \\ 51.0 & 153.9 & 54.0 & -1.0 & -0.6 & -2.0 \\ 51.0 & 54.0 & 153.9 & -1.0 & -2.0 & -0.6 \\ 1.9 & -1.0 & -1.0 & 49.5 & -1.1 & -1.1 \\ 2.3 & -0.6 & -2.0 & -1.1 & 43.5 & 1.7 \\ 2.3 & -2.0 & -0.6 & -1.0 & 1.7 & 43.5 \end{pmatrix} \text{(MPa)}$$

with

$\alpha_1 = 1.53 \times 10^{-6}$

$\alpha_2 = 1.61 \times 10^{-6}$

$\alpha_3 = 1.65 \times 10^{-6}$

respectively.

With the stiffness matrix generated according to the input material and geometric properties, one can examine the response of the three-dimensional composite system to a given thermomechanical condition. For a fixed boundary condition on the bottom surface of the blade, assuming a 1000°C operating temperature and a rotational speed of 4500 rpm, we can evaluate the centrifugal force field as well as the displacement contour on the turbine blade.

Figures 4 and 5 illustrate typical stress distributions on the tension surface of the blade for axial (1) and radial (3) stresses, respectively. Using this preliminary analysis of this component, the axial stresses in the blade are relatively constant at a value of 50 MPa. In the radial direction, stresses on the shaft of the blade are in the range of 50–80 MPa, with an expected stress concentration at the dovetail region, reaching a predicted level of 170 MPa. Figure 6 shows a typical shear stress distribution (1, 3). Shearing is relatively constant, in the range of 0–40 MPa. The radial displacement of the tension surface of the blade is shown in Fig. 7. Maximum tip displacement is predicted at 12 mm.

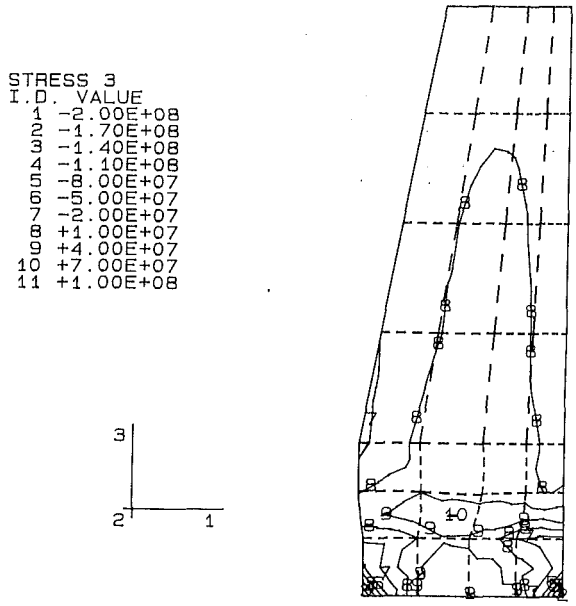


Fig. 5 Typical stress distribution for radial stresses

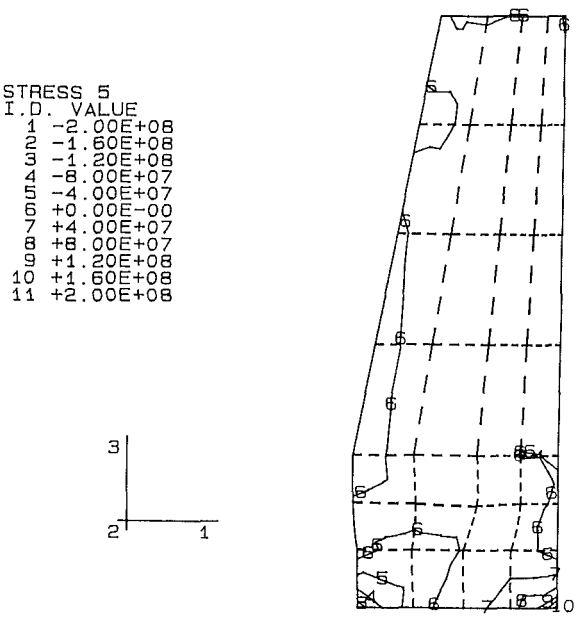


Fig. 6 Typical shear stress distribution

To determine the critical natural frequency of the blade, an eigenvalue analysis was carried out. Figures 8 and 9 show the first two natural modes of the blades. The original mesh is shown with dashed lines, the displaced mesh with solid lines. The frequencies associated with these modes are $2.126 \times 10^6$ rad/s for mode 1, and $2.742 \times 10^6$ rad/s for mode 2.

## 5 Conclusion

In this paper, the recent development of an integrated design methodology for three-dimensional fabric composite structural components was summarized. The procedure for design and analysis of a composite engine rotor was presented as an illustrating example. Emphases were put on the Fabric Geometry Model (FGM) for quantifying and modeling fiber architectures, and finite element structural analysis procedure. This work has laid the foundation for the further development of

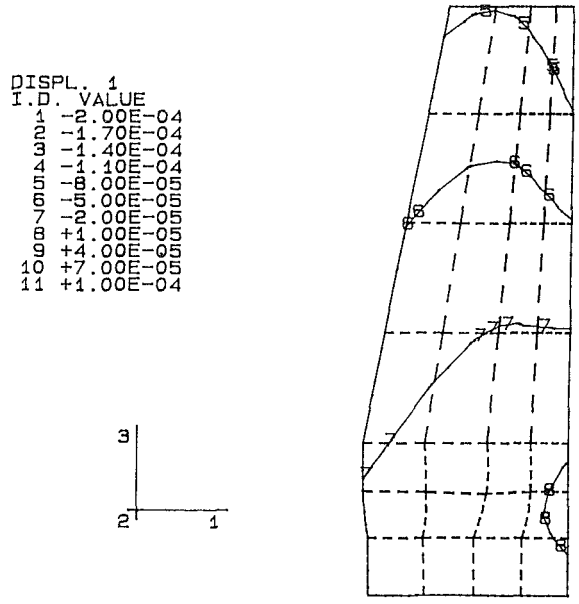


Fig. 7 Radial displacement of blade tension surface

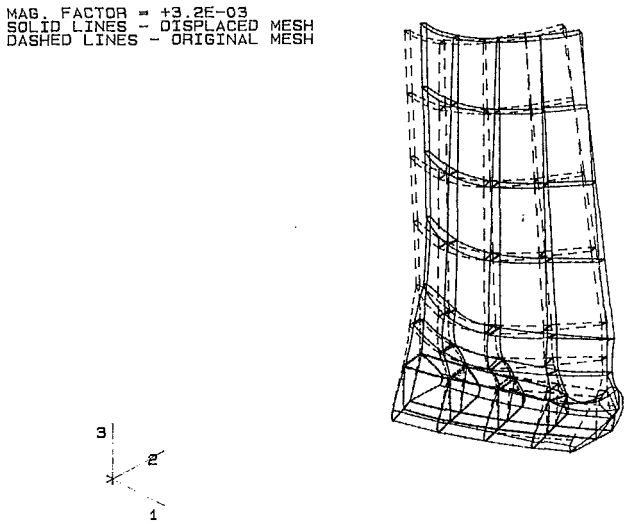


Fig. 8 Natural mode of the blade: $2.126 \times 10^6$ rad/s (mode 1)

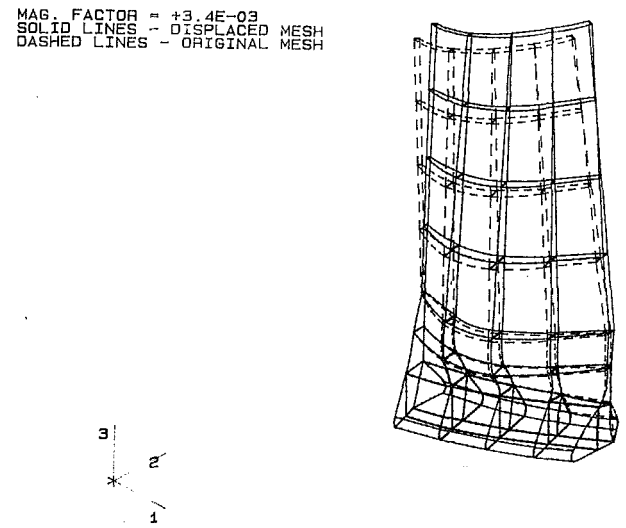


Fig. 9 Natural mode of the blade: $2.742 \times 10^6$ rad/s (mode 2)

integrated design methodology where the concept of FGM will be directly incorporated into finite element analysis procedure.

## References


"ABAQUS Theory and User's Manuals," 1982, Version 4, Hibbit, Karlsson and Sorensen, Inc., Providence, RI.

Jones, R., 1975, *Mechanics of Composite Materials*, McGraw-Hill, New York, p. 90.

Ko, F. K., and Pastore, C., 1985, "Structure and Properties of an Integrated 3-D Fabric for Structural Composites," *Recent Advances in Composites in the United States and Japan*, J. R. Vinson and M. Taya, eds., American Society for Testing and Materials, Philadelphia, PA, pp. 428-439.

Ko, F. K., Koczak, M., and Layden, G., 1987a, "Structural Toughening of Glass Matrix Composites by 3-D Fiber Architecture," *Ceramic Engineering and Science Proceedings*, Vol. 8, No. 7-8, The American Ceramic Society, July-Aug., pp. 822-831.

Ko, F., Pastore, C., Lei, C., and Whyte, D., 1987b, "A Fabric Geometry Model for 3-D Braid Reinforced FP/Al-Li Composites," 1987 International SAMPE Metals Conference: *Competitive Advances in Metals/Metals Processing*, Aug. 18-20, Cherry Hill, NJ.

Ko, F. K., 1989, "Preform Fiber Architecture for Ceramic Matrix Composites," *Bulletin American Ceramic Society*, Feb.

Whitney, J., 1987, *Structural Analysis of Laminated Anisotropic Plates*, Technomic Pub., p. 11.

Whyte, D., 1986, "On the Structure and Properties of 3-D Braided Composites," Ph.D. Thesis, Drexel University, Philadelphia, PA.